# Università di Torino

## Scuola di Dottorato in Scienza ed Alta Tecnologia

### Dottorato di Ricerca in Fisica ed Astrofisica

XXVIII ciclo

Tesi di Dottorato

---

# New Developments in Cosmology

---

Stefano Gariazzo

Relatore:  Prof. Nicolao Fornengo
Co-relatore:  Dott. Carlo Giunti

Coordinatore del Dottorato: Prof. Mauro Gallio

Anni Accademici: 2012/2013 – 2013/2014 – 2014/2015 – 2015/2016

Settore Scientifico–disciplinare di afferenza: FIS/02

# Università di Torino

## Scuola di Dottorato in Scienza ed Alta Tecnologia

### Indirizzo di Fisica ed Astrofisica

XXVIII ciclo

Tesi di Dottorato

# New Developments in Cosmology

Stefano Gariazzo

Relatore: Prof. Nicolao Fornengo
Co-relatore: Dott. Carlo Giunti

Torino, 22 March 2016

# Abstract (English)

The evolution of the Universe is well described by the Standard Model of Cosmology, parameterized through the so-called $\Lambda$CDM ($\Lambda$ + Cold Dark Matter) model, based on the theory of General Relativity. The $\Lambda$CDM model has been widely studied in the past, and the fundamental parameters that describe it have been constrained using several different experimental measurements. In the last years, the accurate observations of the Cosmic Microwave Background (CMB) anisotropies allowed to improve considerably the constraining power of the cosmological analyses, opening the way to precision cosmology. Cosmology can help in studying constraints on the content of the Universe at all times, and precision measurements of the cosmological observables can improve even our knowledge on particle physics. For example, constraints on the absolute neutrino mass scale or on the presence of additional neutrinos beyond the three standard ones can be derived using cosmological data.

The last results released by the Planck collaboration are in strong agreement with the $\Lambda$CDM model and there is no strong evidence that the $\Lambda$CDM model may be incomplete. Despite the overall robustness, however, some small inconsistencies appear. For example, the local determinations of the Hubble parameter $H_0$ and of the matter fluctuations at small scales $\sigma_8$ are in tension with the estimates obtained from the analyses of CMB data in the context of the $\Lambda$CDM model. We show that the presence of a light sterile neutrino or a thermal axion may reduce these tensions, suppressing the matter fluctuations at small scales and increasing the Hubble parameter. These two light particles are motivated by the phenomenology of short-baseline neutrino oscillations and by the strong CP problem in Quantum ChromoDynamics, respectively. We present also the most recent constraints on the sterile neutrino and on the thermal axion properties.

Another indication that not all the predictions of the standard cosmological model are complete is related to the possible presence of features in the Primordial Power Spectrum (PPS) of curvature perturbations. The initial fluctuations were generated during the early inflationary phase of the Universe evolution and they are the initial conditions for the subsequent evolution. As a consequence, features in the PPS can be reconstructed observing the WMAP and Planck spectra of CMB temperature anisotropies at large scales. The assumptions on the PPS shape, however, are crucial for all the cosmological analyses. If inflation is realized in a non-standard scenario, the PPS may have a non-standard shape and if it does not have the standard power-law shape, the cosmological constraints can be (strongly) biased. We study how the constraints on the properties of massless and massive neutrinos and of thermal axions change when a free PPS shape is considered instead of the usual power-law one. In addition, we study also how the constraints on primordial non-Gaussianities change in the context of a scenario involving "inflationary freedom".

We also show that a possible solution to the small $H_0$ and $\sigma_8$ tensions may come from an additional non-gravitational interaction between dark matter and dark energy, if dark energy decays into dark matter. This is not forbidden by any current observation, and this possibility opens a new window to study the dark sector of our Universe.

# Abstract (Italiano)

L'evoluzione dell'Universo è ben descritta dal modello cosmologico standard, parametrizzato attraverso il cosiddetto modello $\Lambda$CDM ($\Lambda$ + Cold Dark Matter - materia oscura fredda) e basato sulla teoria della Relatività Generale. Il modello $\Lambda$CDM è stato ampiamente studiato in passato, e i parametri che lo descrivono sono strettamente vincolati dalle numerose osservazioni sperimentali. Negli ultimi anni le accurate misure della radiazione cosmica di fondo (CMB, da Cosmic Microwave Background) hanno incrementato notevolmente la precisione delle determinazioni nelle analisi, aprendo la strada alla cosmologia di precisione. Oggi i dati cosmologici ci permettono di studiare il contenuto dell'Universo a tutte le epoche e le misure di precisione delle osservabili cosmologiche permettono di migliorare anche la nostra conoscenza della fisica delle particelle. Per esempio, dai dati cosmologici si possono ottenere vincoli sulla scala di massa dei neutrini e sulla eventuale presenza di neutrini aggiuntivi in aggiunta ai tre neutrini standard.

Gli ultimi risultati pubblicati da parte della collaborazione Planck sono in notevole accordo con le predizioni del modello $\Lambda$CDM e non compare nessuna evidenza significativa che il modello $\Lambda$CDM possa essere incompleto. Al di là della robustezza generale, comunque, ci sono alcune piccole discrepanze. Per esempio, le misure locali del parametro di Hubble $H_0$ e delle fluttuazioni di materia a piccola scala $\sigma_8$ sono in tensione con le stime ottenute dalle analisi dei dati della CMB nel contesto del modello $\Lambda$CDM. Mostreremo che la presenza di un neutrino sterile leggero o di un assione termico può ridurre tali tensioni, sopprimendo le fluttuazioni di materia a piccola scala e incrementando il parametro di Hubble. Queste due particelle leggere emergono rispettivamente come soluzione alle anomalie nei dati delle oscillazioni dei neutrini a corto raggio o al problema della CP forte nella cromodinamica quantistica. Presenteremo quindi i vincoli più recenti sulle proprietà di tali particelle.

Un'altra indicazione che non tutte le predizioni del modello cosmologico standard sono complete è collegata alla forma dello spettro di potenza iniziale (PPS, da Primordial Power Spectrum) delle fluttuazioni di curvatura. Queste condizioni iniziali sono state generate durante il periodo di inflazione all'inizio dell'Universo e ne determinano l'evoluzione successiva. Le assunzioni sulla forma del PPS sono cruciali per tutte le analisi cosmologiche. Le osservazioni delle anisotropie di temperatura della CMB osservate dagli esperimenti WMAP e Planck suggeriscono la presenza di una forma anomala del PPS. Se l'inflazione non può essere descritta nella maniera più semplice e il corrispondente PPS può deviare dalla legge di potenza standard, i risultati delle analisi cosmologiche possono esserne influenzati. Studieremo come i vincoli sulle proprietà dei neutrini (massivi o privi di massa) e sugli assioni termici sono influenzate dalla libertà nella forma del PPS, se questo può differire dalla normale legge di potenza. In aggiunta valuteremo anche come i vincoli sulle non-Gaussianità primordiali possono cambiare nel contesto di questa "libertà inflazionaria".

Una diversa possibilità per risolvere le tensioni riguardanti $H_0$ e $\sigma_8$ è collegata alla possibile esistenza di una nuova interazione, di tipo non-gravitazionale, fra materia oscura ed energia oscura, in particolare se coinvolge energia oscura che decade in materia oscura. Questa interazione non è proibita da nessuna osservazione corrente e rappresenta una possibiltà di aprire una nuova finestra sullo studio delle componenti oscure del nostro Universo.

# Contents

# Contents

# Introduction

Recently the Nobel Prize in Physics was awarded to Takaaki Kajita and Arthur B. McDonald "for the discovery of neutrino oscillations, which shows that neutrinos have mass", a result that confirms the hypothesis proposed almost sixty years ago by B. Pontecorvo [1]. Pontecorvo was the first to suggest that neutrinos may exist in different flavors and that they can oscillate. Since the proposal of Pontecorvo, many years were needed to measure neutrino oscillations, but finally this achievement opened a new window on physics, imposing the existence of the mass of at least two neutrinos. Neutrino oscillations, indeed, require that the three neutrino mass eigenstates have different masses $m_i$ (with $i = 1, 2, 3$). These masses can be measured in neutrino oscillation experiments, as we will discuss in details in Chapter 4. The quantities that allow to describe the oscillations between the three different flavor neutrinos are the squared-mass differences[1] $\Delta m_{21}^2$, $\Delta m_{31}^2$, $\Delta m_{32}^2$ and the elements of the so-called PMNS mixing matrix, originally proposed by Z. Maki, M. Nakagawa, S. Sakata [2] to describe the neutrino oscillation proposed by B. Pontecorvo [1]. One standard possibility to write the unitary mixing matrix for the three neutrino mixing paradigm is written in Eq. (4.10). Nowadays, most of the elements of the PMNS matrix are well determined (see e.g. Ref. [3]) by the numerous experiments that probe neutrino oscillations at different energies and distances.

Not all the quantities required to describe the neutrino physics, however, are well known at present times. The mixing matrix in the standard parameterization of Eq. (4.10) is described using 6 parameters: three mixing angles $\vartheta_{12}$, $\vartheta_{23}$ and $\vartheta_{13}$, one Dirac phase $\eta_{13}$ and two Majorana phases $\lambda_{21}$ and $\lambda_{31}$, that are physical only if neutrinos are Majorana particles. The mixing angles are known with good precision, apart for $\vartheta_{23}$, that is nearly maximal and we do not know if it is larger or smaller than $45°$. The present knowledge about the phases, instead, is rather poor. We have small indications that the favored value for the Dirac phase, that may provide CP violation in the lepton sector, is close to $3\pi/2$ [4], but the statistical significance is small.

One of the interesting open questions concerns the nature of neutrinos. All the known particles in the Standard Model (SM) of Particle Physics are Dirac particles, but neutrino is actually the only candidate for being a Majorana particle. If they are Majorana particles, neutrinos coincide with their own antiparticles and processes that violate the conservation of the lepton number are possible. The most studied process of this kind is the neutrinoless double $\beta$-decay, that however has never been observed [5]. Double-$\beta$ decay processes are possible for particular unstable atoms, that may decay simultaneously through the emission of two electrons, normally accompanied by the emission of two electron antineutrinos. For these atoms, the observation of the double $\beta$-decay is possible only because the single $\beta$-decay is forbidden by the kinematics. If the neutrino is Majorana, however, in a small fraction of the cases the neutrino is emitted and immediately absorbed inside the decaying nucleus, that undergoes a double-$\beta$ decay emitting only two electrons, with a violation of the lepton number. Neutrinoless double $\beta$-decay is nowadays the only process that could allow to measure the Majorana phases that appear in the mixing matrix, since they are relevant only for processes that distinguish the Majorana nature of the neutrinos [5].

Another crucial unknown point is the absolute scale of the neutrino masses. Measurements of the neutrino mixing give information on the mass differences, but we cannot learn from

---

[1] We use the convention $\Delta m_{ij}^2 = m_i^2 - m_j^2$.

neutrino oscillation experiments what is the mass of the lightest neutrino, that is $m_1$ in the normal ordering and $m_3$ in the inverted ordering. The absolute neutrino mass scale can be directly determined measuring the endpoint of the spectrum of the released electron in $\beta$-decay processes (see e.g. Ref. [6]) or through the kinematics of neutrinoless double $\beta$-decay processes [5], if neutrinos are Majorana particles. Currently, the direct measurements of the neutrino masses through $\beta$-decay experiments provide an upper limit on the neutrino mass scale of about 2.2 eV [7]. The future experiment KATRIN should reach a sensitivity of about 0.2 eV using the decay of tritium atoms [8].

Another unknown point pertains the squared mass differences. The squared-mass difference $\Delta m_{21}^2$ is fully known thanks to the matter effect in the oscillations inside the sun, also called the MSW effect after S.P. Mikheev, A.Yu. Smirnov and L. Wolfenstein [9–11]. On the other hand, we know only the absolute values of the squared-mass differences $\Delta m_{31}^2$ and $\Delta m_{32}^2$. As a consequence, we know that the mass $m_2$ of the eigenstate $\nu_2$ is larger than the mass $m_1$ of the eigenstate $\nu_1$, but we do not have information on the ordering of the third mass eigenstate. The neutrino mass ordering may be $m_1 < m_2 < m_3$ (normal ordering) or $m_3 < m_1 < m_2$ (inverted ordering), depending on the sign of $\Delta m_{31}^2$ (or of $\Delta m_{32}^2$). Future experiments will investigate the neutrino mass ordering, trying to measure the matter effects on neutrino oscillations in the Earth [12, 13] or using the phase difference in the oscillations of reactor electron antineutrinos, given by the different sign of the squared-mass differences $\Delta m_{31}^2$ and $\Delta m_{32}^2$ in the oscillation probability formula [14].

Short Baseline (SBL) neutrino oscillation experiments suggest that the standard description of the three neutrino mixing may be incomplete, since several anomalies appear (see Section 4.2 or Ref. [15]). The global fit of SBL neutrino oscillation data improves if one assumes an additional neutrino mass eigenstate $\nu_4$ with $\Delta m_{41}^2 \simeq 1 \, \text{eV}^2$ (see Section 4.3). To the new neutrino mass eigenstate, a new flavor eigenstate should correspond. This is called a "sterile" flavor state, since it is not coupled to the SM Lagrangian, but its interactions with the SM particles and with the other neutrinos are possible only through neutrino oscillations. The existence of the fourth neutrino state and the SBL anomalies will be tested in future SBL neutrino oscillation experiments.

Direct mass detection and oscillation experiments, however, are not the only way that we have to test the unknown neutrino properties, although they represent the strongest tests that can be performed, since their results are model independent. Another exciting field of research, indeed, is cosmology. From various cosmological measurements it is possible to derive constraints on the absolute scale of neutrino masses and on the existence of additional particles. In this case, however, the results are obtained in the context of a specific cosmological model.

The standard description of our Universe is based on the theory of General Relativity of A. Einstein [16], proposed one hundred years ago. The Standard Model of Cosmology, also called the *Hot Big Bang model* and described in Chapter 1, predicts that the Universe started its evolution in a very dense and hot configuration, that expanded for about 13 billions years to become what we observe nowadays. A crucial evidence in favor of the Big Bang model was the detection of the Cosmic Microwave Background (CMB) radiation [17], that is the thermal radiation left over from the time of recombination. It is the oldest light in the Universe, originated when the photon energy decreased enough to become smaller than the electron binding energy inside the hydrogen atoms. Recombination indicates in fact the time at which the electrons and the protons started to be bounded together in the hydrogen atoms. Before recombination the Compton scattering of electrons and the presence of high energy photons prevented those stable bounds and the photons were continuously scattered. After recombination, instead, the density of free electrons diminished drastically, the photons started to propagate freely and the CMB radiation was generated. Further details are presented in the description of the CMB radiation and of its anisotropies developed in Chapter 2.

The CMB radiation has become one of the pillars of the modern cosmology. After the first

detection by A.A. Penzias and R.W. Wilson [17], who were awarded the Nobel prize in 1978, the discovery of the CMB anisotropies beyond the monopole and the dipole by the COBE experiment in 1992 [18] opened the window to a new way to test the evolution of the Universe. With the precision measurements of the CMB spectrum obtained by the WMAP [19] and Planck [20, 21] experiments, we have the possibility of testing the cosmological models with great accuracy and to derive constraints on the cosmological parameters.

CMB observations, extensively discussed in Sec. 3.1, are not the only robust measurements that can be used to constrain the cosmological models. Baryon Acoustic Oscillations (see Section 3.2), for example, represent a robust tool that can give strong constraints on the evolution using geometrical methods. Other tests of the Universe evolution at late times are the measurements of the Hubble parameter, that gives the expansion rate today (see Sec. 3.3), of the redshift-distance relation through the observations of SuperNovae (see Sec. 3.4), and of the late time matter distribution through the full power-spectrum of matter fluctuations (see Sec. 3.5), the cluster counts (see Sec. 3.6) and the weak lensing detection through the observations of the cosmic shear (see Sec. 3.7).

In this dissertation we will use CMB data, together with the other observations of the Universe, to derive constraints on neutrino physics. These constraints are model-dependent, in the sense that they depend on the assumptions in the context of the Hot Big Bang model. Additional mechanisms or phenomena that are not considered in the standard description of the Universe evolution can dramatically change these results. In our case, however, we will focus mainly on the most simple parameterization of the hot Big Bang model, that is the so-called $\Lambda$CDM model (see Section 2.5), after the names of the cosmological constant $\Lambda$ and of the cold dark matter (CDM), that are the most abundant constituents of the Universe today. We will detail extensively the properties of the cosmological constant and of cold dark matter in the first two Chapters.

Cosmology cannot probe all the neutrino properties that we listed above: the cosmological evolution is basically insensitive to the mixing of three neutrinos. On the contrary, cosmological measurements provide strong constraints on the neutrino masses and on the existence of additional particles that were relativistic in the early Universe, as the 1 eV mass sterile neutrino that we mentioned above. These quantities can be constrained since the presence of massive neutrinos has an impact on the CMB anisotropies and on the other cosmological quantities, as we will describe in details in Section 4.4. Part of the analyses presented in this Thesis have the aim of studying the compatibility of the light sterile neutrino motivated by the SBL oscillations with the most recent cosmological measurements, constraining the effects that this additional neutrino has on the various observables. These analyses will be presented in Chapters 5 and 6, based on Refs. [22–24] and [25, 26], respectively.

The presence of neutrinos in cosmology may be particularly significant to solve the small tensions that are present in the $\Lambda$CDM model. These regards the CMB estimates and the determinations at small redshift of the Hubble parameter $H_0$ and of the clustering parameter $\sigma_8$, that measures the matter fluctuations inside a sphere of $8h^{-1}$ Mpc radius. An additional light particle that is relativistic at the time of matter-radiation equality and that becomes non-relativistic at late times can reduce the amount of matter fluctuations at small scales thanks to its free-streaming properties (see Section 4.4.3 for the neutrino case): this goes in the required direction to reconcile local and cosmological estimates of $\sigma_8$. At the same time, the presence of additional "dark radiation" (i.e. relativistic particles, apart for photons) in the early Universe requires an increase of the cold dark matter energy density and of the cosmological constant energy density at all times, in order to avoid a shift of the matter-radiation equality epoch that would alter significantly the CMB spectrum. This has the direct consequence of increasing the predictions of $H_0$, reducing the difference between the local measurements and the cosmological estimates for that parameter.

A crucial problem that appears when one tries to constrain the neutrino properties from cosmology is that from neutrino oscillations we expect that the sterile neutrino is in full equilibrium with the active neutrinos in the early Universe: the contribution to the radiation

energy density of a sterile neutrino should be equal to the contribution of each active neutrino. The expectation does not correspond to the results, however, since the analyses of the most recent CMB data indicate with high precision that there are approximately three neutrino-equivalent particles, and the existence of a fourth one is strongly disfavored (see Chapter 5). This is known as the thermalization problem of the sterile neutrino. In the context of the standard cosmological model, if there are four neutrinos, one of them cannot be in equilibrium with the others, possibly as a consequence of some new physical mechanism in particle physics: we will list some possibilities proposed in the literature in Section 5.4.

The thermalization problem can be solved in a different way that does not involve new particle physics mechanisms. If a new cosmological mechanism induces some effects in the evolution that compensate the changes arising from the presence of an additional particle (the sterile neutrino), the tension may disappear. One possibility is the scenario of "inflationary freedom". Inflation is the initial phase of the Universe expansion, during which the distances were stretched exponentially for a very short time. Inflation is required to explain the "horizon" and the "flatness" problems, that we will treat in Chapter 1, as well as the extreme large scale homogeneity and isotropy of the Universe. The simplest inflationary models predict an initial power spectrum of curvature fluctuations that is a simple power-law. Observations of the CMB spectrum suggests that there may be deviations from such a featureless spectrum, especially at large scales. If deviations from the power-law form exist also at small scales, as a consequence of some freedom in the inflationary scenarios, the effects of the additional dark radiation may be erased in the final results by the shape of the initial power spectrum of the Gaussian density fluctuations and the final power spectrum of CMB anisotropies would be almost unchanged. We study this possibility in Chapter 6, where we test the degeneracies between the primordial power spectrum (PPS) of scalar perturbations and the neutrino properties. These degeneracies may give a partial solution to the thermalization problem, that is still present when the recent CMB polarization data by Planck are considered in the analyses.

The light sterile neutrino, however, is not the only candidate that could help solving the $H_0$ and the $\sigma_8$ tensions. Among the other possibilities, we studied the thermal axion as a candidate of dark radiation. Axions were proposed by R.D. Peccei and H.R. Quinn [27,28] to solve the strong CP problem in Quantum Chromodynamics, as we will explain in Section 7.1. If one considers a thermal production mechanism [29–31], it turns out that the axion can have a mass of the order of 1 eV, it contributes to the radiation energy density in the early Universe and it has free-streaming properties. In brief, it behaves approximately as a massive neutrino and therefore it can provide a solution to the $H_0$ and the $\sigma_8$ tensions. In Chapter 7, based on Refs. [26,32], we will show the most recent constraints on the thermal axion mass that arise from the cosmological analyses. Also in this case we will study the degeneracies within the context of inflationary freedom, as we did for the neutrino properties.

Another analysis that we will present concerns the possible existence of non-Gaussianities, i.e. deviations from the Gaussian distribution, in the initial fluctuations that evolved to generate the CMB anisotropies and the structures that we observe in our Universe. Non-Gaussianities are expected to be generated during inflation, and the presence of non-Gaussianities produces a distortion of the CMB (or matter) power spectrum. Since non-Gaussianities and the initial power spectrum of scalar fluctuations are both expected to be generated during inflation by the same mechanism, there is the concrete possibility that they produce similar distortions in the observed power spectrum of CMB (or matter) fluctuations. In Chapter 8 we show that the distortions of the matter power spectrum generated by non-Gaussianities may be mimicked by deviations of the power spectrum of initial fluctuations from the simple power-law. The immediate consequence is that the results obtained for the non-Gaussianities may be significantly biased if some scenario involving "inflationary freedom" is assumed. We devote Chapter 8 to test and discuss these degeneracies, following the analyses published in Ref. [33].

Up to now, we considered extensions of the $\Lambda$CDM model including some new mechanism

in the very beginning of the Universe life, possibly connected with some particle physics model of inflation, or some new particles that arise from some model in particle physics (sterile neutrinos, thermal axions). These additional particles, however, are expected to give only a minor fraction of the total energy density of the nowadays Universe. The largest fraction of the Universe content today [21] is provided by two fluids for which we do not have a well assessed explanation in terms of particle physics: the cold dark matter and the cosmological constant, accounting for 26% and 69% of the total energy density today, respectively. Cold dark matter indicates some massive component that does not interact electromagnetically. The cosmological constant, or in general the "dark energy", is a diffuse fluid that is responsible of the accelerated expansion of the Universe at late times. These fluids are known only for their gravitational interaction and nothing else is known about them. In a minimal scenario, dark matter and dark energy do not have interactions apart for gravity, but some non-gravitational coupling between them cannot be excluded. In Chapter 9, based on Ref. [34], we will study exactly this case: a phenomenological non-gravitational coupling between dark matter and dark energy, and we will show how this coupling influences the Universe evolution. We will explore two possibilities: dark matter decaying in dark energy or dark energy decaying in dark matter. Using cosmological data that probe different times, we will study the compatibility of the coupled scenario with the current cosmological measurements, with a particular focus on the small tensions concerning the Hubble parameter $H_0$ and the clustering parameter $\sigma_8$.

Chapter 10, the last of this Thesis, contains a resume and a brief discussion of our results.

# Part I

# Overview of Standard Cosmology

# Chapter 1

# The Standard Model of Cosmology

The evolution of our Universe is currently well described by the so-called *Standard Model of Cosmology*, or *Hot Big Bang Model*. This model is based on the renowned theory of General Relativity, presented by A. Einstein in 1915 and published in 1916 [16]. The fundamental elements of the cosmological model are the *Cosmological Principle*, which states that the Universe is homogeneous and isotropic on large scales, and the *Einstein Equations*, which describe the evolution of a physical system under the action of gravity. In this first Chapter we will describe the Standard Model of Cosmology, particularly focusing on the equations that govern the thermal history of the Universe and the evolution of perturbations. Since we will not develop the full calculations, we suggest further readings for more details, e.g. Ref. [35]. We will work in natural units through all the text.

## 1.1 Short Evolution History

In the Big Bang model, the Universe started from a very hot and dense plasma, that cooled down during the expansion. The initial phases of the Universe are not well known, since we do not have any confirmed theory to explain physics at extremely large energies: a complete theory of quantum gravity is required to fully describe the initial phase of the Universe.

Possibly in the very early Universe an inflationary phase occurred. Inflation is a theory that predicts an exponential expansion during which the scale factor $a$ grows as $a(t) = \exp(Ht)$, where $H$ is the Hubble factor (see Eq. (1.1)). Inflation requires a constant energy density, with the consequence that the first Friedmann equation (see Sec. 1.5) becomes $H^2 \simeq const$. Using the cosmological constant notation, this becomes $H \simeq \sqrt{\Lambda_I/3}$, where $\Lambda_I$ is the cosmological constant during inflation.

Inflation was proposed firstly in the eighties [36–43] to solve the *horizon* and the *flatness* problems. The *horizon* problem is connected to the fact that we observe an extreme homogeneity between sky regions that are separated by distances between them larger than the horizon radius. These regions were not in causal contact in the past if the standard evolution, without inflation, is assumed. It appears unlikely that widely separated regions that could not be in causal contact in the past can be so similar today. This is not true if the Universe expanded exponentially in the early phases of its history, since regions that were in causal contact before the end of inflation were stretched and widely separated. Initial perturbations that were similar before the end of inflation evolved independently after inflation, possibly until today.

The *flatness* problem indicates the fact that the curvature of the Universe is very close to 1 today: the strongest constraints come from the Planck collaboration [21], which estimated that the curvature energy density is $\Omega_k^0 = 0.000 \pm 0.005$ [44], using the Planck full mission data on the CMB spectrum (see Section 1.5). Going back in time, the bounds become very stringent, since in a not flat and decelerating Universe the curvature increases during the expansion (see Section 1.5): for example, at the time of Big Bang Nucleosynthesis (BBN) the

total energy density $\Omega_{\text{tot}} = 1 - \Omega_k$ must fulfill the requirement $|\Omega_{\text{tot}} - 1| \lesssim 10^{-18}$, in order to be compatible with the Planck bound today. Since at earlier epochs the value would be even smaller, this was considered as a fine-tuning problem. In the context of inflation, this problem is solved by the exponential expansion which dilutes the curvature: since the relation is $|\Omega_{\text{tot}} - 1| \propto \exp(-\sqrt{4\Lambda_I/3}\, t)$ during inflation, the longer was inflation, the closest $\Omega_{\text{tot}}$ was to 1 at its end. To solve both the flatness and the horizon problems, inflation should have lasted for at least 50 to 60 *e-foldings*, a unit that measures the exponential variation of the scale factor: $N$ e-foldings correspond to an increase in the scale factor $a(t_{\text{end}}) = e^N a(t_{\text{start}})$, or equivalently $N = \ln(a(t_{\text{end}})/a(t_{\text{start}}))$.

As we will see in Section 1.9, inflation is usually modeled with the introduction of a scalar field $\phi$, called *inflaton*, that mimics the cosmological constant behavior when rolling down a slowly varying potential $V(\phi)$. Inflation ends when the scalar field decays into other particles, with a consequent energy transfer to the plasma. This phase takes the name of *reheating*, since the temperature of the plasma of coupled particles is raised with the increase of its energy.

The Universe temperature continuously decreases. As the temperature decreases, the kinematics of the processes occurring in the plasma changes and some particles that were abundant in the early Universe cannot be produced at later times: for unstable particles, this means that they start to disappear, being the production and decay processes out of equilibrium. At the same time, some of the symmetries that were perfect in the hot Universe start to spontaneously break: after the electroweak symmetry breaking the bosons of the weak interaction and most of the fermions start to have a mass. Since they are still very energetic, each of them behave as relativistic particles until the temperature falls below its mass; in other cases, such as for the $t$ quark, the mass is so high that they never behave as relativistic particles. The quarks still cannot be confined in hadrons since their kinetic energy is too high. As the temperature decreases, however, the kinetic energies decrease and at a certain point the quarks can be confined: this is the transition to the hadron epoch.

Before this time, depending on its mass and its interaction rates, DM can decouple. When the DM particles can annihilate but they cannot be produced because of the kinematics, they stop interacting and they are *freezed-out*, i.e. they stop interacting and their energy density is simply diluted with the evolution. The annihilation rate depends on the squared number density, and consequently it decreases while the Universe expands. At a temperature of around $1\,\text{MeV}$, the equilibrium of neutrino-electron interactions is broken and also the existing neutrinos decoupled from the rest of the plasma: the relic neutrinos give origin to the *Cosmic Neutrino Background* (CNB), the neutrino analogous of the Cosmic Microwave Background (CMB) radiation, composed by the cosmological photons. The CNB today is very hard to detect directly, since these neutrinos have an extremely low energy. We have a number of indirect signals that the number of relativistic species at CMB decoupling is compatible with the presence of three relic neutrinos, but we are still not sure that these additional particles are truly the standard neutrinos.

Shortly after neutrino decoupling, the mean photon temperature becomes too small to allow the production of electron-positrons pairs and also the electrons start to decouple. The energy density of electrons is transferred to photons through the annihilation process $e^+e^- \to 2\gamma$. In this phase the photons are reheated by this energy transfer, and from now on the photon temperature is higher than the neutrino temperature.

During the hadron epoch, neutrinos play a role in the interactions that bring protons and neutrons to equilibrium: the number of neutrinos have an impact on the relic neutron-to-proton ratio, that in turn influences the relic abundances of light elements after the BBN. As the photon energy diminishes below 0.1 MeV, photons are no more able to break the nuclear bounds and the light nuclei can be produced in hadron scatterings. Starting from protons and neutrons, the first element that is created is deuterium, $^2H$. Inelastic scattering of deuterium and other nucleons originates $^3He$, $^4He$, $^7Li$ and some unstable elements such as $^3H$, $^7Be$, that decay in $^3He$ and $^7Li$.

After the production of the light nuclei, photons have enough energy to break electron-nucleus bounds and matter is still ionized. After matter-radiation equality, that is the time at which the Universe evolution started to be dominated by the matter energy density, photons and relic neutrinos become less and less important for the evolution of the Universe and the matter perturbations can start growing under the effect of gravity. While the photons continue to cool down, their temperature diminishes below $T \simeq 0.1\,\mathrm{eV}$. At this point their energy becomes small enough to allow the creation of atoms: photons are no more energetic enough to break the electron-nucleus bounds and finally the Universe becomes transparent to photons, that start to move freely. This is the time of recombination, when the CMB was originated. Since CMB photons interacted rarely in the following epochs, the study of the CMB anisotropies gives us information on the Universe at the time of recombination, that occurred about 380.000 years after Big Bang. In the same way, the CNB anisotropies would give us information on the Universe at the time of neutrino decoupling, that occurred about 1 second after Big Bang. The detection and the study of the CNB anisotropies are far away from our current technological capabilities, however.

After CMB decoupling, the evolution of the matter perturbations under the gravitational attraction leads to the creation of the structures we observe today, linearly at the beginning and passing to a non-linear evolution after some time. The last part of the Universe evolution, finally, is no more dominated by matter at large scales: an accelerated expansion of the largest scales was discovered in the observation of far SuperNovae. This cannot be the result of a matter dominated phase of the evolution, but it can be explained assuming that the Universe entered a Dark Energy (DE) dominated phase that is responsible of the accelerated expansion.

After this qualitative introduction, we are going to face in details some of the calculations that must be deployed in order to obtain the theoretical predictions from the Standard Model of Cosmology. In particular, we are interested in obtaining the predictions for the power spectra of CMB anisotropies. In the second part of this Thesis these predictions will be compared with the various experimental results (presented in Chapter 3) and we will derive constraints on the quantities that describe the Universe. The goal of this Chapter is to present all the necessary mathematical tools and to obtain the evolution equation for the perturbations that describe the Universe. In Chapter 2 we will use these results to study in details the spectrum of the CMB anisotropies and to show how they are influenced by the various cosmological parameters. Chapter 4, finally, is devoted to introduce the neutrinos and their properties, with a particular focus on their impact in cosmology.

## 1.2 The Expanding Universe

The expansion of the Universe is a very well assessed fact: at earlier times the distances between us and distant galaxies were smaller than today. The expanding behavior can be described using a scale factor $a = a(t)$, where today we have $a_0 = a(t_0) = 1$ [1] and $a(t < t_0) < 1$. Using the scale factor we can define the *comoving distance* as the physical distance in units of the scale factor. If two points are at rest in the expanding Universe, the comoving distance between them is constant during the Universe evolution. On the contrary, the physical distance evolves with time, since it is proportional to the scale factor. The comoving distance is used to measure the distances between two points in the *comoving frame*, that is the reference frame where the coordinates of an observer at rest do not change during the Universe evolution. An observer at rest has constant comoving coordinates and evolving physical coordinates, that scale with $a$.

We must also introduce the geometry of the space-time. There are three possibilities: the Universe can be *flat*, *open* or *closed*. The flat Universe is an Euclidean Universe, where if two particles start to move parallely, their motions will be parallel until they travel freely. In an open (closed) Universe, instead, the particles will diverge (converge) during their motion even if they move parallely at the beginning. A flat, open or closed Universe has null, negative

---

[1] We will use the subscript 0 to refer to the today values of the related quantities.

or positive curvature, respectively. We will see that in General Relativity the geometrical properties of the space-time are related to energy: when the energy density is equal to the critical density, the Universe is flat and its curvature is null. Observations suggest that we live in a Universe that is flat (or very close to flat).

In the context of General Relativity, the expansion history of the Universe can be described by the time evolution of the scale factor $a(t)$. The *Hubble factor* $H(t)$ is defined to encode this time dependency:

$$H(t) \equiv \frac{\dot{a}}{a} \,, \tag{1.1}$$

where the dot indicates the derivative with respect to time, $\dot{a} = da/dt$. It is interesting to measure the value of the Hubble factor today, $H_0 = H(t_0)$: this quantity is related to the critical energy density today, as we will discuss in Section 1.5.

The Hubble factor today $H_0$, also called Hubble constant, is interesting also for another reason. Consider two observers that are at rest in the comoving frame: they are moving away from each other with a velocity that depends on the evolution of the scale factor. At low redshifts, the relative recessional velocity of two observers $v$ and their distance $d$ are related by the *Hubble law*:

$$v = H_0 \, d \,, \tag{1.2}$$

where $H_0$ is measured to be about 70 Km s$^{-1}$ Mpc$^{-1}$ (see Section 3.3), or equivalently the dimensionless Hubble constant is $h \simeq 0.7$, where $h$ is defined as $h \equiv H_0/(100 \text{ Km s}^{-1} \text{ Mpc}^{-1})$. We will discuss in more detail the Hubble law in Section 1.6.

## 1.3 Friedmann-Lemaître-Robertson-Walker Metric

Under the assumption of the *Cosmological Principle*, the most important properties of the Universe are homogeneity and isotropy. The observations of the galaxy distribution in the Universe and of the Cosmic Microwave Background (CMB) radiation are in strong agreement with the hypothesis of the Cosmological Principle at scales larger than 100 Mpc: the Universe looks statistically the same from all the possible points of view, in all the possible directions in which it is observed. These properties corresponds to homogeneity, that is invariance under translations, and isotropy, that is invariance under rotations. If we can state that at large scales there are no privileged positions and directions, this is not true at small scales, at which the Universe is highly inhomogeneous: we will need to introduce some perturbations to the homogeneous background and study them separately. The background evolution is important since it gives the general behavior of the Universe, while all the structures of the visible Universe can be generated only by the small perturbations that we will introduce in Section 1.8.

Homogeneity and isotropy of the Universe can be encoded into a coordinate system where the metric of the space-time does not depend on the position (in cartesian coordinates). In the space-time reference frame described by the coordinates $x^\mu = (x^0, x^i)$ [2], where $x^0 = t$ is the time component and $x^i$ are the three space components, one can write the distance between two points:

$$ds^2 \equiv g_{\mu\nu} dx^\mu dx^\nu \,, \tag{1.3}$$

where $ds^2$ is the squared distance between the points separated by $dx^\mu$ and $g_{\mu\nu}$ is the metric that describes the geometrical properties of the space-time. We use the convention that repeated indices are summed over.

The metric $g_{\mu\nu}$ must be a symmetric $4 \times 4$ tensor, with 4 diagonal and 6 off-diagonal independent components. The metric for a homogeneous and isotropic Universe is called Friedmann-Lemaître-Robertson-Walker (FLRW) metric. If one considers a local observer, general relativity can be approximated with the theory of special relativity, described in

---

[2] We use the convention that greek letter indices span the space-time coordinates $(0, \ldots, 3)$ and latin letter indices span the space coordinates $(1, \ldots, 3)$.

the Minkowsky space-time with metric $\eta_{\mu\nu} = \mathrm{diag}(-1, +1, +1, +1)$. The FLRW metric $g_{\mu\nu}$ can be approximated by $g_{\mu\nu} \simeq \eta_{\mu\nu}$ only locally. From the isotropy of the Universe we can infer that the off-diagonal terms, $g_{\mu\nu}$ with $\mu \neq \nu$, must vanish, since there are no privileged directions. From the property of homogeneity we infer that $g_{\mu\nu}$ (in cartesian coordinates) must be independent on the spatial coordinates, since there are no privileged observers. For a flat Universe, the metric can then be written in the form

$$g_{\mu\nu} = \begin{pmatrix} -1 & 0 & 0 & 0 \\ 0 & a^2(t) & 0 & 0 \\ 0 & 0 & a^2(t) & 0 \\ 0 & 0 & 0 & a^2(t) \end{pmatrix} \tag{1.4}$$

and Eq. (1.3) becomes:

$$ds^2 = -dt^2 + a^2(t)\delta_{ij}dx^i dx^j \ , \tag{1.5}$$

where we $\delta_{ij} = \mathrm{diag}(+1, +1, +1)$ is the Kronecker delta in an Euclidean space.

To describe a closed or an open Universe, it is convenient to use spherical coordinates in the space and introduce a new parameter: the curvature of the space-time, $k$. The distance $ds^2$ can be written as

$$ds^2 = -dt^2 + a^2(t) \left\{ \frac{dr^2}{1 - kr^2} + r^2(d\theta^2 + \sin^2\theta d\phi^2) \right\} \ , \tag{1.6}$$

where $(r, \theta, \phi)$ are the usual spherical coordinates. The curvature is $k = 0$ for a flat Universe, $k = +1$ for a closed Universe or $k = -1$ for an open Universe. We will consider now the case of a flat Universe.

Given the metric $g_{\mu\nu}$, it is possible to study the free motion of a particle in the space-time. It is necessary to obtain the *Christoffel symbols* $\Gamma^\rho_{\mu\nu}$, by definition symmetric in the $\mu$ and $\nu$ indices:

$$\Gamma^\rho_{\mu\nu} \equiv \frac{g^{\rho\tau}}{2} \left( \partial_\mu g_{\nu\tau} + \partial_\nu g_{\mu\tau} - \partial_\tau g_{\mu\nu} \right) \ , \tag{1.7}$$

where we introduced the notation $\partial_\mu g_{\nu\tau} = \partial g_{\nu\tau} / \partial x^\mu$. It is worth noting that the Christoffel symbols are not tensors, since they do not transform in the correct way under changes in the coordinate system.

The *geodesic* is the trajectory of a particle in the space-time, in absence of any forces: it is the generalized concept of straight line in presence of a non-trivial metric. The Christoffel symbols appear in the *geodesic equation*:

$$\frac{d^2 x^\mu}{d\lambda^2} = -\Gamma^\mu_{\alpha\beta} \frac{dx^\alpha}{d\lambda} \frac{dx^\beta}{d\lambda} \ , \tag{1.8}$$

where $\lambda$ can be any scalar monotonic parameter that describes the position on the geodesic, for example the conformal time $\eta$ that we will introduce in Sec. 1.6. To compute the geodesics, one should calculate the components of the Christoffel symbols from the metric $g_{\mu\nu}$, using the definition in Eq. (1.7), and insert them in Eq. (1.8). For a flat Universe with the FLRW metric written in cartesian coordinates in Eq. (1.4), most of the derivatives of $g_{\mu\nu}$ vanish and most of the components $\Gamma^\rho_{\mu\nu}$ vanish. We have:

$$\Gamma^0_{0\mu} = \Gamma^0_{\mu 0} = 0 \, , \tag{1.9}$$

$$\Gamma^0_{ij} = \delta_{ij} \dot{a} \, a \, , \tag{1.10}$$

$$\Gamma^i_{0j} = \Gamma^i_{j0} = \delta_{ij} \frac{\dot{a}}{a} \, , \tag{1.11}$$

$$\Gamma^i_{\alpha\beta} = 0 \quad \text{otherwise.} \tag{1.12}$$

The Christoffel symbols are necessary to define the *Ricci tensor*, symmetric in the indices $\mu$ and $\nu$, that we will use to write the Einstein equations:

$$R_{\mu\nu} \equiv \partial_\alpha \Gamma^\alpha_{\mu\nu} - \partial_\nu \Gamma^\alpha_{\mu\alpha} + \Gamma^\alpha_{\beta\alpha} \Gamma^\beta_{\mu\nu} - \Gamma^\alpha_{\beta\nu} \Gamma^\beta_{\mu\alpha} \, . \tag{1.13}$$

The trace of the Ricci tensor is named *Ricci scalar*:

$$\mathcal{R} \equiv R^{\mu}_{\ \mu} = g^{\mu\nu} R_{\mu\nu}, \tag{1.14}$$

where $g^{\mu\nu} = \mathrm{diag}(-1, a^{-1}, a^{-1}, a^{-1})$ is the inverse of $g_{\mu\nu}$.

In a FLRW Universe the Ricci tensor and the Ricci scalar can be easily calculated. The Ricci tensor is diagonal and its components are

$$R_{00} = -3\frac{\ddot{a}}{a}, \tag{1.15}$$

$$R_{ij} = \delta_{ij}\left(2\dot{a}^2 + a\ddot{a}\right), \tag{1.16}$$

while the Ricci scalar is simply the trace of the Ricci tensor:

$$\mathcal{R} = 6\left(\frac{\ddot{a}}{a} + \frac{\dot{a}^2}{a^2}\right). \tag{1.17}$$

These are the quantities to be used in the Einstein equations, that we will discuss in the following Section. After the introduction of the perturbations to the homogeneous and isotropic Universe, the metric will become more complicate. We will discuss the perturbed Universe in Section 1.8.

## 1.4 Einstein Equations

The evolution with time of the Universe can be derived from the *Einstein equations*:

$$G_{\mu\nu} = 8\pi G\, T_{\mu\nu}, \tag{1.18}$$

where $G_{\mu\nu} \equiv R_{\mu\nu} - 1/2\,\mathcal{R}\,g_{\mu\nu}$ is the Einstein tensor and $G = 6.67 \times 10^{-11}\mathrm{m}^3\,\mathrm{s}^{-2}\,\mathrm{Kg}^{-1}$ is the Newton constant.

The symmetric tensor $T_{\mu\nu}$ is the stress-energy tensor, that contains all the information about the energy content of the Universe. For a perfect, isotropic and homogeneous fluid, it can be written as

$$T_{\mu\nu} = \mathrm{diag}(\rho, p, p, p), \tag{1.19}$$

where $\rho$ and $p$ are the energy density and the pressure of the fluid, respectively. The definitions of $\rho$ and $p$ involve the momentum distribution function $f$. Using here the capital letter to denote the momentum $P$, density and pressure are defined as:

$$\rho = g \int \frac{d^3 P}{(2\pi)^3}\, f(P)\, E(P), \tag{1.20}$$

$$p = g \int \frac{d^3 P}{(2\pi)^3}\, f(P)\, \frac{P^2}{3E(P)}, \tag{1.21}$$

where $g$ is the degeneracy of the species.

Due to conservation laws, the covariant derivatives of the stress-energy tensor must vanish:

$$D_\mu T^\mu_\nu \equiv \partial_\mu T^\mu_\nu + \Gamma^\mu_{\alpha\mu} T^\alpha_\nu - \Gamma^\alpha_{\mu\nu} T^\mu_\alpha = 0. \tag{1.22}$$

This is the General Relativity equivalent of the continuity equation and of the Euler equations in the classical theory. For the perfect fluid with stress-energy tensor in Eq. (1.19), the $\nu = 0$ component of Eq. (1.22) is

$$\dot{\rho} + 3\frac{\dot{a}}{a}(\rho + p) = \dot{\rho} + 3\frac{\dot{a}}{a}(1 + w)\rho = 0, \tag{1.23}$$

where we used the equation of state $\rho = wp$ for the fluid we are considering. This equation can be rearranged to obtain the relation between $\rho$ and $a$ for different fluids:

$$\dot{\rho} + 3\frac{\dot{a}}{a}(\rho + P) = a^{-3}\frac{\partial(\rho\, a^{3(1+w)})}{\partial t} = 0, \tag{1.24}$$

which in turn gives that $\rho\, a^{3(1+w)}$ is constant over time. Since different fluids have a different equation of state, the scaling of the energy density is different during the expansion: for radiation, the name used to indicate any relativistic fluid, $w = 1/3$ and $\rho_r \propto a^{-4}$, while for non-relativistic matter $w = 0$ and $\rho_m \propto a^{-3}$.

Since our Universe is not made of a single perfect fluid, but rather it is a mixture of different components with different properties, the fact that the energy densities of different fluids evolve differently imply the possibility of having different phases in the Universe history. The Big Bang model predicts an initial radiation dominated phase, when all species were relativistic, followed by a matter dominated phase, when most of the species become non-relativistic and their total energy density diminishes more slowly than the radiation energy density. Moreover, observations show that in the recent history the Universe expansion is accelerated, thus suggesting a new phase in the evolution. The current phase cannot be a radiation dominated or a matter dominated phase, since these components do not give an accelerated expansion: it is necessary to introduce then something like a cosmological constant $\Lambda$, which has a negative pressure: the corresponding equation of state parameter is $w = -1$ and $\rho_\Lambda$ is constant over time (see Eq. (1.24)). It is possible to include the cosmological constant in the stress-energy tensor and consider it as a new fluid. If today the Universe is in a $\Lambda$-dominated phase, the expansion is accelerated: this can be seen from the solutions of the Einstein Equations, in particular from the solution of the time-time component, that we are going to treat.

## 1.5  Friedmann Equations

If we insert the Eq. (1.19) into Eq. (1.18), for a FLRW Universe where the Ricci tensor and the Ricci scalar are those written in Eqs. (1.15), (1.16) and (1.17), we obtain two different independent differential equations, corresponding to the 00 and the $ii$ component of the tensor equation. They are the so-called Friedmann Equations:

$$H^2 = \left(\frac{\dot{a}}{a}\right)^2 = \frac{8\pi G}{3}\,\rho, \tag{1.25}$$

$$\dot{H} + H^2 = \frac{\ddot{a}}{a} = -\frac{4\pi G}{3}\,(\rho + 3p), \tag{1.26}$$

where $\rho = \sum \rho_i$ and $p = \sum p_i$ are the total energy density and pressure of the Universe, respectively. The total density and pressure include the contributions from all the existing species: photons, baryons, dark matter (DM), cosmological constant, neutrinos. At different times, some of these species contribute as relativistic components, being referred to as radiation, (baryons and neutrinos before the non-relativistic transition, photons), or as non-relativistic components, falling into the category of matter (baryons and neutrinos after the non-relativistic transition, DM[3]). The cosmological constant component ($w = -1$) can be described by some unknown species that contributes with a negative pressure. It is also possible that there is some fluid that contributes with a negative pressure but does not have a constant equation of state $w = -1$. In this case the component that substitutes the cosmological constant is usually referred to as Dark Energy (DE) and it can have a generic $w < -1/3$, required to have an accelerated expansion, with a possible dependence $w(t)$. Moreover, if the Universe is not flat, the curvature $k$ can be described as an additional functional fluid in the Friedmann Equations: one can compute the Ricci tensor for a curved FLRW Universe, obtaining an additional term in Eq. (1.25). This can be considered as the contribution of the curvature fluid, described by an energy density $\rho_k = -3k/(8\pi G a^2)$ and an equation of state $w_k = -1/3$.

---

[3]In the very early Universe, also DM may have been relativistic, thus accounting as radiation, but this depends on the specific model.

From Eq. (1.25) one can define the *critical energy density*:

$$\rho_c(t) \equiv \frac{3H(t)^2}{8\pi G},\tag{1.27}$$

which is the total energy density of a flat Universe at a given time. Its value today, $\rho_c^0$, depends only on the current value of the Hubble parameter $H_0$. Using the critical density we can define the *density parameter* as the ratio between the absolute energy density $\rho$ and the critical density $\rho_c$, for each different species $i$:

$$\Omega_i \equiv \frac{\rho_i}{\rho_c},\tag{1.28}$$

where, for example, $i = \Lambda, k, m, r$ for cosmological constant, curvature, matter and radiation. In term of the density parameters of the different species, the first Friedmann Equation becomes:

$$H^2 = H_0^2(\Omega_\Lambda^0 + \Omega_k^0 a^{-2} + \Omega_m^0 a^{-3} + \Omega_r^0 a^{-4}),\tag{1.29}$$

where we used the results of Eq. (1.24) for the different fluids.

As an example, the matter contribution at the time of matter-radiation equality takes into account baryons and charged leptons plus the DM component that was non-relativistic at decoupling, named Cold Dark Matter (CDM), and eventually other non-relativistic species, such as massive neutrinos after their non-relativistic transition. At least two neutrinos, in fact, must have small but non-zero masses, whose values are currently unknown. The neutrino mass is requested to explain the flavor oscillations, that we will discuss in Chapter 4. The consequence is that at different times each neutrino can contribute to $\Omega_r$ or to $\Omega_m$, depending on its mass: a relativistic neutrino is considered radiation, while a non-relativistic neutrino accounts as matter. Each massive neutrino, hence, can account as radiation in the early Universe and as matter when it becomes non-relativistic in the late Universe. Eventually, if there are very light massive neutrinos ($m_\nu \lesssim T_\nu^0$), some of them can be still relativistic today. The correct behavior at all times must be evaluated numerically and the non-relativistic transition of each neutrino can leave an imprint on the cosmological observables. We will discuss the neutrino effects in cosmology in Section 4.4.

From Eq. (1.29), the most important lesson we can learn is that the evolution of the Universe depends on the relative amounts of energy density corresponding to each fluid. At different times, one of the contributions is usually dominant and the evolution rate $H = \dot{a}/a$ has a different behavior. Recently the Planck collaboration determined the density parameters for the different fluids, using the CMB measurements of the Planck satellite [21, 44]: these determinations tell us that we have approximately $\Omega_\Lambda^0 \simeq 0.69$ for the cosmological constant, $\Omega_c^0 \simeq 0.26$ for the CDM, $\Omega_b^0 \simeq 0.05$ for the baryons and $\Omega_r^0 \simeq 10^{-5}$ for the relativistic components. Thus the cosmological constant gives the main contribution to the total energy density and the Universe is in a $\Lambda$-dominated ($\Lambda$D) phase. If we go back in time, however, while $a$ decreases other contributions in Eq. (1.29) start to dominate, due to their different evolution with $a$: before the $\Lambda$D phase there was a matter-dominated (MD) phase, while at the beginning of the evolution the larger energy density was $\Omega_r$ and the Universe was in a radiation-dominated (RD) phase. Even if from Eq. (1.29) we can expect also a curvature-dominated phase, the current analyses show that the Universe is almost flat, and we will neglect the possibility that the space-time is open or closed. The constraint of the Planck collaboration on the curvature is $\Omega_k^0 = 0.000 \pm 0.005$ [44].

If we consider $a = 1$ in Eq. (1.29), finally, we obtain the following relation between all the density parameters:

$$\Omega_\Lambda^0 + \Omega_k^0 + \Omega_m^0 + \Omega_r^0 = 1.\tag{1.30}$$

We conclude defining the dimensionless quantity $\omega_i = \Omega_i h^2$, where $h$ is the reduced Hubble parameter and $i$ indicates all the possible fluids. The dimensionless density parameter $\omega_i$ is proportional to the physical density of the component $i$ at present time and we will use it in the following Chapters.

Coming back to the second Friedmann equation, we can rewrite Eq. (1.26) evaluated today in terms of the *deceleration parameter*, named $q_0$:

$$q_0 \equiv -\left(\frac{\ddot{a}}{a}\right)_{t=t_0} \frac{1}{H_0^2} \,, \tag{1.31}$$

that is positive for a decelerated expansion and negative for an accelerated expansion of the Universe. Using the equation of state of the different fluids and the definition of $H_0$, it is possible to write:

$$q_0 = \frac{1}{2} \sum_i \Omega_i^0 \left(1 + 3w_i\right) . \tag{1.32}$$

If the cosmological constant $\Lambda$ or any other fluid with $w < -1/3$ dominates, $q_0$ can be negative, corresponding to an accelerated expansion.

## 1.6 The Hubble Law and Distance Measurements

One of the most difficult measurements in the Universe are distance estimations. A fundamental distance is the comoving distance, that is the distance of two points in the comoving frame and does not depend on the scale factor. The physical distance, instead, depends on the comoving distance and on the evolution history.

One important quantity is the distance that light can have traveled since $t = 0$. Since in a time $dt$ light can travel a distance $dx = dt/a$, the total comoving distance is

$$\eta = \int_0^t \frac{dt}{a(t)} \,, \tag{1.33}$$

that is the maximum distance at which information can be propagated in a time $t$, in the comoving frame: regions separated by distances greater than $\eta$ are not causally connected. We can think to $\eta$ as the size of the *comoving horizon*. As it is a monotonically increasing variable, $\eta$ can be considered as a *conformal time*, that describes the photon path and can be used conveniently in place of the time $t$ in a number of calculations we will discuss in the following. The corresponding physical distance, that is the farthest distance we can observe today, is called the *horizon distance*:

$$d_H(t_0) = a(t_0) \int_0^t \frac{dt}{a(t)} \,. \tag{1.34}$$

where $a(t_0) = 1$ in the usual convention. Points separated by a distance greater than the horizon distance are not in causal contact.

Using the FLRW metric in polar coordinates in Eq. (1.6), the *physical distance* among two objects at a time $t$ can be written as

$$d_p(t) = a(t) \int_0^r \frac{dr}{\sqrt{1 - kr^2}} \,, \tag{1.35}$$

that for a flat Universe ($k = 0$) becomes

$$d_p(t) = a(t)\, r \,. \tag{1.36}$$

In absence of peculiar motions in the comoving frame, i.e. if $\dot{r} = 0$, the relative velocity between the considered objects depends on their distance:

$$v \equiv \dot{d}_p = \dot{a}(t)\, r = H(t)\, d_p \,. \tag{1.37}$$

When $t = t_0$ we obtain the *Hubble Law*:

$$v = H_0\, d_p \,, \tag{1.38}$$

which tells us that the relative velocity is higher for distant objects and it is a strong probe of the expansion of the Universe.

To measure the Hubble parameter $H_0$, one should obtain the distance and the velocity. The latter one is straightforward since it can be related to the redshift, $z$. Due to cosmic expansion, the light emitted by a distant observer is stretched while traveling towards us, since the emitter is receding with respect to us. It is convenient to define this stretching of the wavelength of the emitted light in term of the redshift $z$:

$$1 + z \equiv \frac{\lambda_o}{\lambda_e} = \frac{a(t_o)}{a(t_e)}, \tag{1.39}$$

that can be interpreted as a Doppler effect between two objects with a relative velocity. Subscripts $o$ and $e$ refer to the observer and the emitter, respectively. Usually the observer corresponds to an experiment performed today on Earth and consequently the redshift is related to the scale factor $a_e = a(t_e)$ at the emission time $t_e$, since $a(t_0) = 1$:

$$1 + z = a_e^{-1}. \tag{1.40}$$

In General Relativity, however, the stretching of the wavelengths does not arise only from something equivalent to the Doppler effect that occurs for the acoustic and electromagnetic waves, but also from the Universe expansion, that dilutes the photon energy in a larger portion of space. Moreover, the photons may be redshifted (or blueshifted) by changes in the space-time properties or in the gravitational potential along the photon path: a photon is redshifted when exiting a region with large gravitational potential and it is blueshifted when leaving a region with small gravitational potential.

The most difficult part of the process to determine $H_0$ is the determination of the distance $d_p$. The redshift can be used to connect the physical distance $d_p(t_0)$ and the *luminous distance* $d_L$ of an object. The luminous distance $d_L$ is defined as the distance at which an observer $P_0$ at $t = t_0$ measures a flux $f$ from a source $P$, emitting a power $L$ in light:

$$d_L = \left(\frac{L}{4\pi f}\right)^{1/2}. \tag{1.41}$$

The spherical surface centered in $P$ and passing through $P_0$ at a time $t_0$ has an area $4\pi a_0^2 r^2$. Since the expansion causes the photon to be redshifted by a factor $a_0/a_e$ during the travel, we can derive the relation between the luminous and the physical distance:

$$d_L = \frac{r}{a_e} = (1 + z)\, d_p, \tag{1.42}$$

where we used Eq. (1.36) at $t = t_0$.

Determinations of the luminous distance are complicated by the fact that we usually do not know the magnitude of the power $L$ for a given astrophysical object. This is not true for particular objects, that are supposed to behave as *standard candles*: they have always the same luminosity and we can obtain their luminous distance simply measuring at Earth the flux they produce. Commonly used standard candles are, for example, the Cepheids variable stars, since their intrinsic brightness is related to the period of variation. Other standard candles are type Ia SuperNovae (SN Ia), which have always the same emission power since they originate in a standard way: when one of the two elements in a binary system is a white dwarf, it can gradually accrete mass from the binary companion. If the mass of the white dwarf is sufficient, during the accretion the core can reach the ignition temperature for the carbon fusion. At this point, a large part of the matter in the white dwarf undergoes a runaway reaction, releasing enough energy to unbind the star in a supernova explosion.

Another method to determine distances is to consider the angular size $\delta\theta$ of a given object of length $l$, aligned perpendicularly to the line of sight. Its *angular diameter distance, $d_A$,* is

$$d_A = \frac{l}{\delta\theta} \tag{1.43}$$

and it can be related to the physical distance through:

$$d_A = \frac{d_L}{(1+z)^2} \, . \tag{1.44}$$

As for the luminous distance, determinations of the angular diameter distance suffer the fact that it is difficult to know the size $l$ of generic objects. In the context of cosmological observations, the angular diameter distance is especially used to study the separation distance of the galaxies. In fact, due to Baryon Acoustic Oscillations (BAO), generated by the balance of the gravitational potential and the radiation pressure between photons and baryons in the early Universe, there is a preferred separation distance between galaxies. Since this typical distance depends on the evolution properties, it can be used to constrain the cosmological parameters. We will discuss BAO results in detail in Section 3.2.

## 1.7 Boltzmann Equation

In the hot and dense primordial Universe, the interactions among particles were much more frequent than today and the species were maintained in equilibrium in most of the cases. During the cooldown of the Universe, due to a decrease of the particle number densities caused by the expansion, at certain times interactions were not able to maintain the chemical and thermal equilibrium between the involved species: most of the species decoupled from the rest of the primordial plasma at the corresponding decoupling time. This is a result arising from non-equilibrium phenomena, encoded in the *Boltzmann equation*, which formalizes the fact that the rate of variation for a given species is the difference between the production and annihilation rates.

We want to describe now the Boltzmann equation in a simple case. Suppose we are interested in the number density of a species 1, $n_1$. Let us assume that the species 1 is non-relativistic. Suppose also that the only process involving the species 1 is its annihilation with another species 2, during which elements of the species 3 and 4 are produced. The inverse process must be considered as well. The interaction is then summarized by $1 + 2 \leftrightarrows 3 + 4$. Under these assumptions, the integrated Boltzmann equation in the expanding Universe is:

$$
\begin{aligned}
a^{-3}\frac{d(n_1 a^3)}{dt} = &\int \frac{d^3 p_1}{2E_1(2\pi)^3} \int \frac{d^3 p_2}{2E_2(2\pi)^3} \int \frac{d^3 p_3}{2E_3(2\pi)^3} \int \frac{d^3 p_4}{2E_4(2\pi)^3} \\
&\times (2\pi)^4 \delta(E_1 + E_2 - E_3 - E_4)\delta^3(p_1 + p_2 - p_3 - p_4)|\mathcal{M}|^2 \\
&\times \{f_3 f_4(1 \pm f_1)(1 \pm f_2) - f_1 f_2(1 \pm f_3)(1 \pm f_4)\} \, .
\end{aligned} \tag{1.45}
$$

In the previous equation $n_i$, $f_i$, $p_i$ and $E_i$ are the number density, the distribution function, the momentum and the energy of the species $i$. In the last line, the plus sign is for bosons and the minus sign is for fermions: the terms $(1 \pm f_i)$ represent the phenomena of Bose enhancement and Pauli blocking, respectively. In the absence of interactions, Eq. (1.45) says that the density times the scale factor to the third is conserved: this is a consequence of the expanding Universe, and number densities of the particles scale with $a^{-3}$. The interaction is encoded in the matrix element $\mathcal{M}$ in the second line of the right-hand side and the last line tells us that the production rate of the particle 1 is proportional to the abundance of the particles 3 and 4, $f_3$ and $f_4$, while the disappearance rate is proportional to the abundances of the particles 1 and 2, $f_1$ and $f_2$. The Dirac delta functions in the second line give the four-momentum conservation. Finally, the integrals sum over all the possible momenta: either the matrix element and the distribution functions, even if not explicitly written, depend on the particle momenta.

Equation (1.45) refers to the particle 1, but corresponding equations hold for the other particles. In practice, the *kinetic equilibrium* is typically enforced by the interactions, since scattering processes are fast enough to make all the particles have a distribution that is close to a Bose-Einstein or a Fermi-Dirac. This simplifies a lot the calculation. All the uncertainty

in the correct form of the distribution of each species is encoded in a single function of time $\mu$, that is the chemical potential if annihilations process are also in equilibrium. In this case we can write

$$f_j = \frac{1}{e^{(E_j - \mu_j)/T_j} \pm 1} , \qquad (1.46)$$

where $-1$ is for bosons and $+1$ is for fermions. Since we are interested in temperatures smaller than $E - \mu$, the $\pm 1$ term in the denominator is much smaller than the exponential and the distribution functions can be approximated with:

$$f_j \simeq e^{\mu/T} e^{-E/T} . \qquad (1.47)$$

With this approximation, we show now that the last line in Eq. (1.45) can be simplified. The number density of a species is defined as

$$n_i = g_i e^{\mu_i/T} \int \frac{d^3 p}{(2\pi)^3} e^{-E_i/T} , \qquad (1.48)$$

where $g_i$ is the degeneracy of the species $i$. The equilibrium number density can be written under the approximation of $m_i \ll T$ (relativistic) or $m_i \gg T$ (non-relativistic):

$$n_i^{(0)} = \begin{cases} g_i \frac{T^3}{\pi^2} & \text{for } m_i \ll T \\ g_i \left(\frac{m_i T}{2\pi}\right) e^{-m_i/T} & \text{for } m_i \gg T \end{cases} . \qquad (1.49)$$

The out of equilibrium expression is then $n_i = n_i^{(0)} e^{\mu_i/T}$: using Eq. (1.47) and this last expression we can rewrite the last line of Eq. (1.45) as

$$e^{-(E_1 + E_2)/T} \left( \frac{n_3 n_4}{n_3^{(0)} n_4^{(0)}} - \frac{n_1 n_2}{n_1^{(0)} n_2^{(0)}} \right) , \qquad (1.50)$$

where we also used the energy conservation condition.

We can define $\langle \sigma v \rangle$, the thermally averaged cross section, as

$$\langle \sigma v \rangle = \frac{e^{-(E_1 + E_2)/T}}{n_1^{(0)} n_2^{(0)}} \int \frac{d^3 p_1}{2E_1 (2\pi)^3} \int \frac{d^3 p_2}{2E_2 (2\pi)^3} \int \frac{d^3 p_3}{2E_3 (2\pi)^3} \int \frac{d^3 p_4}{2E_4 (2\pi)^3}$$
$$\times (2\pi)^4 \delta(E_1 + E_2 - E_3 - E_4) \delta^3(p_1 + p_2 - p_3 - p_4) |\mathcal{M}|^2 . \qquad (1.51)$$

This definition allows us to rewrite in a more compact way the Boltzmann equation:

$$a^{-3} \frac{d(n_1 a^3)}{dt} = n_1^{(0)} n_2^{(0)} \langle \sigma v \rangle \left( \frac{n_3 n_4}{n_3^{(0)} n_4^{(0)}} - \frac{n_1 n_2}{n_1^{(0)} n_2^{(0)}} \right) . \qquad (1.52)$$

This last expression is an ordinary differential equation for $n_1$ that can be applied to study the freeze-out of DM. Similar calculations can be exploited to derive the Boltzmann equations needed to solve different scenarios, such as the BBN and the recombination, that corresponds to the electron-photon decoupling and gives rise to the last scattering surface. The calculations in these two cases would be slightly different, since the approximations we adopted here for non-relativistic species are not valid for all the species involved in the different processes.

Through the Boltzmann equation it is possible to write the equilibrium distributions and track the evolution into the out-of-equilibrium phases for each species. For stable particles, the distribution function after decoupling evolves simply following the expansion history. Tracking the full evolution it is then possible to obtain the relic DM density today or, using the corresponding Boltzmann equations, the abundances of the light nuclei produced in the early Universe and the isotropic photon distribution at the last scattering, that evolved into the isotropic part of the CMB that we can observe today. We will not treat the applications of this unperturbed Boltzmann equation in detail: we suggest Refs. [35, 45] to the interested reader. In the next Section, however, we will present the perturbed treatment that is used to obtain the Boltzmann equation for the photon perturbations, necessary to calculate the expected spectrum of the CMB anisotropies. Before this, however, we must update our treatment to include the perturbations of the space-time metric and of the distribution functions for each species.

## 1.8 The Perturbed Universe

### 1.8.1 Metric

If we look at the Universe near us today we have the immediate impression that the hypothesis of the *Cosmological Principle* we introduced at the beginning of this Chapter cannot be valid at small scales. At short distances the Universe is not homogeneous and isotropic, with the direct consequence that the results we presented up to now are just approximations of the full solutions for the evolution. To describe the perturbed Universe, it is possible to define a perturbed metric, that is no more characterized by one single function of time ($a$), but it depends on two additional functions $\Psi$ and $\Phi$, both of which are functions of space and time. The perturbations are described by $\Psi$, that corresponds to the Newtonian potential, and by $\Phi$, that describes the perturbations to the spatial curvature. We will treat them as small quantities, using series expansions truncated at the first order and neglecting second order terms. To write the perturbed metric, we must choose a *gauge*, because there is some freedom in selecting the variables used to describe the fluctuations. The physical results are insensitive to the gauge choice, but the complexity of the calculation can vary from gauge to gauge. In the *conformal Newtonian* gauge, the perturbed metric is

$$g_{00}(\vec{x}, t) = -1 - 2\Psi(\vec{x}, t) \tag{1.53}$$

$$g_{0i}(\vec{x}, t) = 0 \tag{1.54}$$

$$g_{ij}(\vec{x}, t) = a^2(t)\left(1 + 2\Phi(\vec{x}, t)\right)\delta_{ij}. \tag{1.55}$$

We adopt the sign convention that positive $\Psi$ and negative $\Phi$ correspond to underdense regions, while negative $\Psi$ and positive $\Phi$ correspond to overdense regions.

We limit ourselves to the treatment of the scalar perturbations in the metric and we neglect the other possibilities: vector and tensor perturbations. The former ones arise from the generalization of a rotational fluid, producing vortex motions that rapidly decays. They are not predicted by the standard cosmological model. The latter ones, instead, describe the contribution of tensor components, such as gravitational waves. These additional components would require additional functions to be parameterized: we will not discuss all the details and we will only mention some of the main results.

We want now to derive the Einstein Equations in the perturbed Universe. To do this, we must first calculate the Christoffel symbols, to get the Ricci tensor and the Ricci scalar. Let us look at the first order terms in the Christoffel symbols, starting from $\Gamma^0_{\mu\nu}$:

$$\Gamma^0_{\mu\nu} = \frac{1}{2}g^{0\alpha}(\partial_\nu g_{\alpha\mu} + \partial_\mu g_{\alpha\nu} - \partial_\alpha g_{\mu\nu}), \tag{1.56}$$

where the only nonzero component of $g^{0\alpha}$ is $g^{00} = -1 + 2\Psi$ and we can write

$$\Gamma^0_{\mu\nu} = \frac{-1 + 2\Psi}{2}(\partial_\nu g_{0\mu} + \partial_\mu g_{0\nu} - \partial_0 g_{\mu\nu}). \tag{1.57}$$

Neglecting the second order terms, we get

$$\Gamma^0_{00} = \partial_0\Psi \tag{1.58}$$

$$\Gamma^0_{0i} = \Gamma^0_{i0} = \partial_i\Psi = ik_i\Psi \tag{1.59}$$

$$\Gamma^0_{ij} = \delta_{ij}a^2[H + 2H(\Phi - \Psi) + \partial_0\Phi], \tag{1.60}$$

Using the metric in Eqs. (1.53) to (1.55) we can calculate also the other Christoffel symbols:

$$\Gamma^i_{00} = \frac{\partial_i\Psi}{a^2} \tag{1.61}$$

$$\Gamma^i_{0j} = \Gamma^i_{j0} = \delta_{ij}(H + \partial_0\Phi) \tag{1.62}$$

$$\Gamma^i_{jk} = [\delta_{ij}\partial_k + \delta_{ik}\partial_j + \delta_{jk}\partial_i]\Phi, \tag{1.63}$$

We can also express all these equations in the Fourier space, simply replacing $\partial_i$ with $ik_i$ and each quantity with its Fourier transformed, such as $\Psi$ with $\widetilde{\Psi}$. The Fourier convention we adopt is:

$$A(\vec{x}) = \int \frac{d^3k}{(2\pi)^3} e^{i\vec{k}\cdot\vec{x}} \, \widetilde{A}(\vec{k}) \,. \tag{1.64}$$

We will mostly work in Fourier space from now on, and we will neglect the $\sim$ notation for all the quantities when it will be clear that the quantities will be in the Fourier space.

The calculation of the Ricci tensor is a mechanical process that requires the Christoffel symbols and some algebra. The results are:

$$R_{00} = -3\frac{\ddot{a}}{a} - \frac{k^2}{a^2}\Psi - 3\partial_0^2\Phi + 3H\partial_0(\Psi - 2\Phi) \tag{1.65}$$

$$R_{ij} = \delta_{ij}\left[\left(2a^2H^2 + a\ddot{a}\right)\left(1 + 2\Phi - 2\Psi\right)\right.$$
$$\left. + a^2H\partial_0(6\Phi - \Psi) + a^2\partial_0^2\Phi + k^2\Phi\right] + k_ik_j(\Psi + \Phi) \,, \tag{1.66}$$

where we adopted $k^2 = \delta_{ij}k^ik^j$.

The contraction of the Ricci tensor with the metric gives the perturbed Ricci scalar:

$$\mathcal{R} = (-1 + 2\Psi)\left(-3\frac{\ddot{a}}{a} - \frac{k^2}{a^2}\Psi - 3\partial_0^2\Phi + 3H\partial_0(\Psi - 2\Phi)\right)$$
$$+ \left(\frac{1 - 2\Phi}{a^2}\right)\left\{3\left[\left(2a^2H^2 + a\ddot{a}\right)\left(1 + 2\Phi - 2\Psi\right)\right.\right.$$
$$\left.\left. + a^2H\partial_0(6\Phi - \Psi) + a^2\partial_0^2\Phi + k^2\Phi\right] + k^2(\Phi + \Psi)\right\} \,, \tag{1.67}$$

that becomes Eq. (1.17) at zero-order when $\Psi$ and $\Phi$ vanish. The first-order part is:

$$\delta\mathcal{R} = -12\Psi\left(H^2 + \frac{\ddot{a}}{a}\right) + 2\frac{k^2}{a^2}\Psi + 6\partial_0^2\Phi$$
$$- 6H\partial_0(\Psi - 4\Phi) + 4\frac{k^2}{a^2}\Phi \,. \tag{1.68}$$

To write the Einstein Equations in terms of the perturbed quantities we will start from Eq. (1.18), but we have to deal with the perturbed stress-energy tensor, before. To obtain the first-order part of the stress-energy tensor, however, it is necessary to study the first-order terms in the distribution function $f_i$ for the different species, generalizing the treatment of the Boltzmann equation in Section 1.7 to the case of a non-homogeneous Universe.

## 1.8.2   Boltzmann Equations

We discussed in Section 1.7 the integrated version of the Boltzmann Equation in the context of the homogeneous and isotropic Universe, but we are now interested in the anisotropies of the distribution of cosmic photons for the CMB observations and in the inhomogeneities of the matter distribution, that originated the structures in the current Universe through the gravitational evolution. These perturbed distributions are difficult to calculate, since in the hot plasma before CMB decoupling photons interact mainly with electrons through the Compton scattering and electrons are coupled to protons. Moreover, all the mentioned species, plus neutrinos and DM, are coupled to gravity. Therefore, it is necessary to solve simultaneously the Boltzmann equation for each component, to obtain the distribution functions $f_i$ for all the species. The Boltzmann equation in its differential form can be schematically written as

$$\frac{df}{dt} = \mathcal{C}[f] \,, \tag{1.69}$$

where $\mathcal{C}$ contains all the possible collision terms. For a non-interacting species this equation reduces to $df/dt = 0$, that is nontrivial to solve since the phase space elements change with time, as a consequence of the nontrivial metric.

We want now to write the Boltzmann equation for photons. It is convenient to express the total derivative in Eq. (1.69) as a sum of partial derivatives. The momentum vector is defined as

$$P^\mu = \frac{dx^\mu}{d\lambda}\,, \tag{1.70}$$

where $\lambda$ is a monotonic parameter that describes the particle path. Since the photon is massless,

$$P^2 = g_{\mu\nu}P^\mu P^\nu = 0 \tag{1.71}$$

and there are only three independent components of $P^\mu$. Defining the generalized magnitude of the momentum $p^2 = g_{ij}P^i P^{j\,4}$ , we can eliminate the time component of $P^\mu$, using the metric in Eqs. (1.53)-(1.55):

$$P^0 = \frac{p}{\sqrt{q+2\Psi}} \simeq (1-\Psi)\,p\,, \tag{1.72}$$

that is the perturbed version of $E = pc$ and it can be used to eliminate $P_0$ in favor of $p$. From this equation we learn also that photons lose energy when exiting an overdense region. Now we can re-express the total derivative in Eq. (1.69):

$$\frac{df}{dt} = \frac{\partial f}{\partial t} + \frac{\partial f}{\partial x^i}\cdot\frac{dx^i}{dt} + \frac{\partial f}{\partial p}\cdot\frac{dp}{dt} + \frac{\partial f}{\partial \hat{p}^i}\cdot\frac{d\hat{p}^i}{dt}\,, \tag{1.73}$$

where $\hat{p}^i$ is the direction of $P^i$. The last term of this expression is at second order in the perturbations, since $f$ does not depend on $\hat{p}^i$ at zero order and in absence of the potentials $\Psi$ and $\Phi$ the photon goes straight, hence $d\hat{p}^i/dt$ is also a first order term.

We can rewrite the second term:

$$\frac{dx^i}{dt} = \frac{dx^i}{d\lambda}\frac{d\lambda}{dt} = \frac{P^i}{P_0}\,, \tag{1.74}$$

where we used the definition of $P^\mu$. Since $P^i = C\hat{p}^i$ and $p^2 = a^2(1+2\Phi)C^2$ (from the definition of $p^2$), we can always write

$$P^i = p\,\hat{p}^i\frac{1-\Phi}{a}\,, \tag{1.75}$$

and from Eq. (1.74) we obtain

$$\frac{dx^i}{dt} = \frac{\hat{p}^i}{a}(1+\Psi-\Phi)\,. \tag{1.76}$$

For an overdense region the term in parentheses is less than one, meaning that photons slow down. Anyhow, in Eq. (1.73) $dx^i/dt$ multiplies a first order term, since the momentum distribution at zero order does not depend on the position, and we can neglect the potentials in Eq. (1.76).

The last term we have to deal with is $dp/dt$. For sake of brevity we do not present the complete calculations, that involves the Christoffel symbols of the perturbed metric. It is fully deployed, for example, in Ref. [35]. Neglecting the second order terms in $\Psi$ and $\Phi$, the result is

$$\frac{1}{p}\frac{dp}{dt} = -H - \frac{\partial\Phi}{\partial t} - \frac{\hat{p}^i}{a}\frac{\partial\Psi}{\partial x^i}\,. \tag{1.77}$$

The change in the photon momentum is described by a term accounting for the momentum loss due to Hubble expansion ($H$) plus two terms that depend on the perturbations: if a photon is traveling in a deepening gravitational well from one side it loses energy since the curvature is increasing ($\partial\Phi/\partial t$), but from the other side it gains energy because it is pulled towards the center ($\hat{p}^i \cdot \partial\Psi/\partial x^i$).

---

[4]Since in this section we will not need to denote the pressure, we use $p$ to indicate the generalized magnitude of the momentum.

We can finally write the left-hand term of Eq. (1.69):

$$\frac{df}{dt} = \frac{\partial f}{\partial t} + p\frac{\hat{p}^i}{a} \cdot \frac{\partial f}{\partial x^i}\frac{\partial f}{\partial p}\left(H + \frac{\partial \Phi}{\partial t} + \frac{\hat{p}^i}{a}\frac{\partial \Psi}{\partial x^i}\right). \tag{1.78}$$

The next step requires to expand the perturbed photon distribution function. Following Ref. [35], we define

$$f(\vec{x}, p, \hat{p}, t) = \left[\exp\left(\frac{p}{T(t)(1 + \Theta(\vec{x}, \hat{p}, t))}\right) - 1\right]^{-1}, \tag{1.79}$$

where we expanded the temperature at zero-order as a function of time only, for the properties of homogeneity and isotropy of the Universe, while the perturbations are included in a small function of space and momentum ($\Theta$). We can then expand $f$ in terms of the perturbation:

$$f = f^{(0)} - p\frac{\partial f^{(0)}}{\partial p}\Theta, \tag{1.80}$$

where $f^{(0)}$ is the Bose-Einstein distribution with $\mu = 0$ (Eq. (1.46)).

If we set the collision term to zero, the zero-order term of Eq. (1.78) becomes:

$$\left.\frac{df}{dt}\right|_{\text{zero order}} = \frac{\partial f^{(0)}}{\partial t} - Hp\frac{\partial f^{(0)}}{\partial p} = 0. \tag{1.81}$$

For the first order, we have to extract all the terms proportional to $\Psi$, $\Phi$ or $\Theta$ in Eq. (1.78), using the perturbed version of $f$. The result gives

$$\left.\frac{df}{dt}\right|_{\text{first order}} = -p\frac{\partial f^{(0)}}{\partial p}\left(\frac{\partial \Theta}{\partial t} + \frac{\hat{p}^i}{a}\frac{\partial \Theta}{\partial x^i} + \frac{\partial \Phi}{\partial t} + \frac{\hat{p}^i}{a}\frac{\partial \Psi}{\partial x^i}\right). \tag{1.82}$$

We may note that only physical distances ($ax^i$) appear in the equation. The first two terms in the parentheses account for free-streaming, while the last two terms arise from gravity.

Now we should calculate the collision term for the processes involving photons. For the epoch we are interested in, photons interact only with electrons through Compton scattering. We skip all the calculations and we go directly to the final result. To write the collision term, we need to define the *monopole* part of the perturbation to the distribution function, that is independent of the direction vector:

$$\Theta_0(\vec{x}, t) = \frac{1}{4\pi}\int d\Omega\, \Theta(\hat{p}, \vec{x}, t), \tag{1.83}$$

where $\Omega$ is the solid angle element spanned by $p$. The collision term is then [35]

$$\mathcal{C}[f(\vec{p})] = -p\frac{\partial f^{(0)}}{\partial p}n_e\sigma_T(\Theta_0 - \Theta(\hat{p}) + \hat{p}\cdot\vec{v}_b), \tag{1.84}$$

where $n_e$ is the electron number density, $\sigma_T$ is the Thomson cross section and $\vec{v}_b = \vec{v}_e$ is the baryon velocity, carried by electrons, that is small. In particular, if $\vec{v}_b$ is negligible the collision term drives $\Theta$ to $\Theta_0$, hence all the higher moments are damped and only the monopole term survives; if $\vec{v}_b$ is not negligible, instead, the last term produces a dipole moment in addition to the monopole.

With these results we can finally write a linear equation for the perturbations to the photon distribution:

$$\frac{\partial \Theta}{\partial t} + \frac{\hat{p}^i}{a}\frac{\partial \Theta}{\partial x^i} + \frac{\partial \Phi}{\partial t} + \frac{\hat{p}^i}{a}\frac{\partial \Psi}{\partial x^i} = n_e\sigma_T\left[\Theta_0 - \Theta(\hat{p}) + \hat{p}\cdot\vec{v}_b\right]. \tag{1.85}$$

It is convenient to move to the Fourier space and to switch to the conformal time $\eta$. We can change each time derivative into a conformal time derivative introducing a $a^{-1}$ factor:

from now on, the overdots will indicate conformal time derivatives. The advantage of the Fourier transform is that all the $\partial/\partial x^i$ becomes $k_i$ and the Fourier amplitudes obey ordinary differential equations. Moreover, if the background is smooth and the perturbations are small, the space dependence is only encoded in the perturbation variables: the Fourier transform of Eq. (1.85) originates a set of uncoupled differential equations for each mode and the Fourier modes can be evolved independently. In the case of the CMB perturbations, their smallness persists also today and the Fourier transforms are extremely useful. On the contrary, for the matter perturbations the nonlinearities occur at small scales after some time and the Fourier transforms lose part of their appeal.

Before writing the Fourier transformed version of Eq. (1.85), we define some useful quantities. The cosine of the angle between the photon direction $\hat{p}$ and the wavenumber $\vec{k}$ is

$$\mu \equiv \frac{\vec{k} \cdot \hat{p}}{k} \,. \tag{1.86}$$

A photon traveling along the gradient (parallel to $\vec{k}$) corresponds to $\mu = 1$, while a photon moving in a direction where the temperature does not change has $\mu = 0$.

The optical depth $\tau$, defined as the integral of the scattering rate along the line of sight and measuring the total amount of interactions that a photon experienced between $\eta$ and $\eta_0$, is

$$\tau(\eta) \equiv \int_\eta^{\eta_0} d\eta' \, n_e \sigma_T a \,. \tag{1.87}$$

With these definitions, we have finally the equation for the evolution of the perturbation to the photon distribution function:

$$\dot{\widetilde{\Theta}} + ik\mu\widetilde{\Theta} + \dot{\widetilde{\Phi}} + ik\mu\widetilde{\Psi} = -\dot{\tau} \left( \widetilde{\Theta}_0 - \widetilde{\Theta} + \mu\widetilde{v}_b \right), \tag{1.88}$$

where $\widetilde{\Theta}$ is defined through Eq. (1.64).

With similar calculations, it is possible to derive the corresponding equations for dark matter and baryon perturbations: in these cases we will find also an equation for the evolution of the velocity. Naming $f_{dm}$ the momentum distribution of DM, we can define

$$\delta_{dm}(\vec{x}, t) \equiv \frac{n_{dm} - n_{dm}^{(0)}}{n_{dm}^{(0)}} = \frac{\rho_{dm} - \rho_{dm}^{(0)}}{\rho_{dm}^{(0)}} \,, \tag{1.89}$$

$$v_{dm}^i \equiv \frac{1}{n_{dm}} \int \frac{d^3 p}{(2\pi)^3} f_{dm} \frac{p\hat{p}^i}{E} \,, \tag{1.90}$$

where we used the definition

$$n_{dm} \equiv \int \frac{d^3 p}{(2\pi)^3} f_{dm} \,. \tag{1.91}$$

Due to the tight Coulomb scattering, overdensities of electrons and protons are forced to a common value. The same happens for the electron and proton velocity anisotropies, that are maintained in equilibrium by the interactions. For the baryons, considering together protons and electrons[5], the same definitions adopted for the quantities $\delta_{dm}$ and $v_{dm}$ can be used to define $\delta_b$ and $v_b$, just substituting $f_{dm}$ with $f_b$.

With these definitions, the perturbation equations become:

$$\dot{\widetilde{\delta}}_{dm} + ik\widetilde{v}_{dm} + 3\dot{\widetilde{\Phi}} = 0 \,, \tag{1.92}$$

$$\dot{\widetilde{v}}_{dm} + \frac{\dot{a}}{a}\widetilde{v}_{dm} + ik\widetilde{\Psi} = 0 \,, \tag{1.93}$$

$$\dot{\widetilde{\delta}}_b + ik\widetilde{v}_b + 3\dot{\widetilde{\Phi}} = 0 \,, \tag{1.94}$$

---

[5]Electrons, having a smaller mass than protons, contribute less to the energy density when they are non-relativistic.

$$\dot{\widetilde{v}}_b + \frac{\dot{a}}{a}\widetilde{v}_b + ik\widetilde{\Psi} = \dot{\tau}\frac{1}{R}\left(3i\widetilde{\Theta}_1 + \widetilde{v}_b\right),\tag{1.95}$$

where we defined the ratio

$$R = \frac{3\rho_b}{4\rho_\gamma}\,.\tag{1.96}$$

The difference between Eq. (1.93) and Eq. (1.95) is a consequence of the electromagnetic interaction between baryons and photons. Here we used the definition of the first moment of $\Theta$:

$$\widetilde{\Theta}_1 = i\int_{-1}^{1}\frac{d\mu}{2}\mu\widetilde{\Theta}(\mu)\,.\tag{1.97}$$

Forgetting all the $\sim$, the relevant quantities to describe the perturbations for non-relativistic particles are $\delta_{dm}$, $\delta_b$ and $v$, $v_b$: all of them are functions of $k$, $\eta$. For relativistic particles, more information is needed: they have a monopole and a dipole perturbation (corresponding to $\delta_{dm}$ and $v_{dm}$ for non-relativistic dark matter), but all the higher moments as well. In other words, the photon perturbation $\Theta(k, \mu, \eta)$ (the Fourier transform of $\delta T/T$) and its equivalent for neutrinos $\mathcal{N}(k, \mu, \eta)$ (defined in Chapter 4) depend also on the propagation direction. The general definition of the higher moments for the temperature perturbations is:

$$\Theta_l(k, \eta) \equiv \frac{1}{(-i)^l}\int_{-1}^{1}\frac{d\mu}{2}\,\mathcal{P}_l(\mu)\,\Theta(k, \mu, \eta)\,,\tag{1.98}$$

where we used the Legendre polynomial of order $l$, $\mathcal{P}_l$. The higher moments describe the perturbations of the temperature field at increasingly smaller scales. A similar definition applies to the massless neutrino distribution, while massive neutrinos require an additional treatment (see Subsection 4.4.2).

The inverse relation of Eq. (1.98) reads:

$$\Theta(k, \mu, \eta) = \sum_l (-i)^l\,(2l+1)\,\Theta_l(k, \eta)\,\mathcal{P}_l(\mu)\,,\tag{1.99}$$

which can be inserted into Eq. (1.88) to obtain an infinite hierarchy of coupled equations for the multipole moments $\Theta_l$:

$$\dot{\Theta}_0 = -k\Theta_1 - \dot{\Phi}\tag{1.100}$$

$$\dot{\Theta}_1 = \frac{k}{3}(\Theta_0 - 2\Theta_2 + \Psi) + an_e\sigma_T\left(\frac{iv_b}{3} - \Theta_1\right)\tag{1.101}$$

$$\dot{\Theta}_l = \frac{k}{2l+1}\left[l\,\Theta_{l-1} - (l+1)\,\Theta_{l+1}\right] - an_e\sigma_T\Theta_l \qquad \forall l \geq 2\,.\tag{1.102}$$

### 1.8.3 Einstein Equations

With the definitions of the perturbations presented above, we can finally derive the Einstein Equations in the perturbed Universe.

The first order component of $G_{\mu\nu}$ can be calculated using the Ricci tensor and the Ricci scalar written in Eqs. (1.65) to (1.67), together with the perturbed metric in Eqs. (1.53) to (1.55). We obtain for the time-time component:

$$\delta G^0{}_0 = -6H\partial_0\Phi + 6H^2\Psi - 2\frac{k^2}{a^2}\Phi\,.\tag{1.103}$$

This has to be used with the time-time component of the stress-energy tensor, that is the energy density of all the particles in the Universe (see Eq. (1.19)) and that can be obtained as the sum of the integrals over the distribution functions of each species:

$$T^0{}_0(\vec{x}, t) = -\sum_i g_i\int\frac{d^3p}{(2\pi)^3}E_i(p)f_i(\vec{p}, \vec{x}, t)\,,\tag{1.104}$$

where $g_i$ is the degeneracy of the states (spin), $E_i = \sqrt{p^2 + m_i^2}$ and $i$ represents all the species. The result gives

$$
\begin{aligned}
T^0_{\ 0} = - &\rho_\gamma(1 + 4\Theta_0) && \text{(photons)} \\
- &\rho_{dm}(1 + \delta_{dm}) && \text{(DM)} \\
- &\rho_b(1 + \delta_b) && \text{(baryons)} \\
- &\rho_\nu(1 + 4\mathcal{N}_0) && \text{(massless neutrinos)}\,,
\end{aligned} \tag{1.105}
$$

where we used the perturbation variables for each species. The perturbation variables for the neutrinos, $\mathcal{N}_l$, will be discussed in the Chapter 4. We can now write the time-time component of the Einstein equations in the perturbed space, that is the first of the two equations we are going to obtain. Changing again to the conformal time, it is:

$$
k^2\Phi + 3\frac{\dot{a}}{a}\left(\dot{\Phi} - \Psi\frac{\dot{a}}{a}\right) = 4\pi G a^2(4\rho_\gamma\Theta_0 + 4\rho_\nu\mathcal{N}_0 + \rho_{dm}\delta_{dm} + \rho_b\delta_b)\,, \tag{1.106}
$$

that is the first evolution equation for $\Psi$ and $\Phi$.

To obtain the second evolution equation, we have to focus on the spatial part of the Einstein tensor. It is convenient to introduce the projection operator $(\hat{k}_i\hat{k}^j - \delta^j_i/3)$ and to consider only the longitudinal and traceless part of $G^i_j$:

$$
(\hat{k}_i\hat{k}^j - \delta^j_i/3)G^i_j = \frac{2}{3a^2}k^2(\Phi + \Psi)\,, \tag{1.107}
$$

where the terms proportional to $\delta_{ij}$ are killed by the projection operator. In the same way we can obtain the projection of $T^i_j$:

$$
(\hat{k}_i\hat{k}^j - \delta^j_i/3)T^i_j = \sum_i g_i \int \frac{d^3p}{(2\pi)^3}\frac{p^2(\mu^2 - 1/3)}{E_i(p)}f_i(\vec{p})\,, \tag{1.108}
$$

where $(\mu^2 - 1/3)$ is proportional to the second Legendre polynomial $\mathcal{P}_2(\mu)$, hence it picks up the quadrupole part of the distribution. Baryons and DM do not have a quadrupole term, that exists only for photons and neutrinos and is related to their *anisotropic stress*. The second evolution equation becomes

$$
k^2(\Phi + \Psi) = -32\pi G a^2(\rho_\gamma\Theta_2 + \rho_\nu\mathcal{N}_2) \tag{1.109}
$$

and we learn that $\Phi$ and $\Psi$ have opposite sign if the quadrupole moments $\Theta_2$ and $\mathcal{N}_2$ are null. In the practice, the photon quadrupole is large only when the photon density becomes small and the main contribution to the sum comes from the collisionless neutrino quadrupole in the early Universe, when radiation is dominant.

## 1.9 Adiabatic Initial Conditions

### 1.9.1 Initial Conditions

The solution of the Boltzmann equations requires a set of initial conditions that must be fixed. We recall that, at first order, we have two equations for baryons and CDM, plus an infinite set of equations for photons. All the multipoles above the first two, however, are negligible in the tightly-coupled limit, since the Thomson scattering term in Eq. (1.88) forces $\Theta$ to be equal to $\Theta_0 + \mu v_b$: a monopole part plus a dipole term aligned with $v_b$, while all the higher multipoles are suppressed. To compute the power spectrum of the CMB anisotropies or of the matter perturbations, it is convenient to choose the initial conditions in the tightly-coupled regime and for scales larger than the Hubble horizon, in order to apply this simplification. In this case, given $N$ species, we have to deal only with $2N$ first-order equations, one for the monopole and one for the bulk velocity of each species. Half of the

$2N$ corresponding initial conditions seed decaying modes that we do not observe today. The combination of $N$ non-decaying solutions must be identified when studying the mechanisms of generating the initial conditions (inflation or other scenarios).

One particular combination has a simple physical interpretation: in a homogeneous Universe, the Friedmann equations, together with the equations of particle physics and thermodynamics, allow us to determine the evolution of the background densities $\rho_i^{(0)}$ and pressures $p_i^{(0)}$ for each species $i$. The simplest realization of an inhomogeneous Universe that we can think of is the following: assume that some physical mechanism introduces a local time-shift, which accounts for the fluctuations during inflation[6]. In this situation, we have the simplest realization of an inhomogeneous Universe, where we can write the inhomogeneous densities and pressures:

$$\rho_i(i, \vec{x}) = \rho_i^{(0)}(t + \delta t(\vec{x})) \simeq \rho_i^{(0)}(t) + \dot{\rho}_i^{(0)}(t)\delta t(\vec{x}) , \tag{1.110}$$

$$p_i(i, \vec{x}) = p_i^{(0)}(t + \delta t(\vec{x})) \simeq p_i^{(0)}(t) + \dot{p}_i^{(0)}(t)\delta t(\vec{x}) . \tag{1.111}$$

We assume that the time-shift function $\delta t(\vec{x})$ is the same for all the species and it is at first order in the perturbation. Using the two last equations and the conservation equation (1.23) we obtain

$$\frac{\delta \rho_i}{\rho_i^{(0)} + p_i^{(0)}} = \frac{\dot{\rho}_i^{(0)}}{\rho_i^{(0)} + p_i^{(0)}}\delta t(\vec{x}) = -3\frac{\dot{a}(t)}{a(t)}\delta t(\vec{x}) , \tag{1.112}$$

that is independent on the species $i$.

In this perturbed Universe, at least for wavelengths larger than the Hubble horizon, all the species have an adiabatic sound speed $c_{a,i}$, defined as the ratio $\delta p_i / \delta \rho_i$:

$$\frac{\delta p_i(t, \vec{x})}{\delta \rho_i(t, \vec{x})} = \frac{\dot{p}_i^{(0)}(t)}{\dot{\rho}_i^{(0)}(t)} \equiv c_{a,i}^2(t) . \tag{1.113}$$

The total perturbations are also described by an effective sound speed $c_s$:

$$c_s^2(t) \equiv \frac{\sum_i \dot{\rho}_i^{(0)}(t)c_{a,i}^2(t)}{\sum_i \dot{\rho}_i^{(0)}(t)} , \tag{1.114}$$

that we can use to write the total pressure perturbation as

$$\delta p(t, \vec{x}) = c_s^2(t)\delta \rho(t, \vec{x}) . \tag{1.115}$$

If we do not assume the conditions in Eqs. (1.110) and (1.111), instead, we can only write the total pressure perturbation as a sum over $N$ independent functions of $\vec{x}$:

$$\delta p(t, \vec{x}) = \sum_i c_{s,i}^2(t)\delta \rho_i(t, \vec{x}) , \tag{1.116}$$

that can be eventually rearranged using the entropy perturbations. For any set of perturbations satisfying Eqs. (1.110) and (1.111), hence, the fluctuations of the total effective fluid have adiabatic properties and the solutions of the perturbation equations are *adiabatic* or *isentropic*, while in the more general case the solutions involve entropy perturbations. In the simplest case, one can use the set of Equations (1.110) and (1.111) plus the other $2N$ Boltzmann equations to obtain a basis of two independent sets of initial conditions. If the basis is chosen appropriately, one of the solutions becomes rapidly negligible: this is called the *decaying* mode, while the other one is the *growing* mode.

The full calculation of the adiabatic initial conditions is performed, for example, in Chapter 6 of Ref. [35]. The initial conditions for each variable can be calculated as a function

---

[6]For example, in the single-field inflation scenario, the only clock in the quasi-De Sitter Universe is represented by the inflaton, whose fluctuations can be seen as local shifts with respect to the average time.

of the gravitational potential at early times, from the Boltzmann equations: the problem reduces then to calculate the initial conditions for the gravitational potential $\Phi$ only. For the photon and neutrino monopoles it is possible to find

$$\Theta_0(k, \eta_i) = \mathcal{N}_0(k, \eta_i) = \Phi(k, \eta_i)/2 \,, \tag{1.117}$$

at the early time $\eta_i$. For the baryon and DM perturbations, the adiabatic solution is

$$\delta_{dm} = \delta_b = 3\Theta_0 \,. \tag{1.118}$$

Finally, the appropriate initial conditions for bulk velocities and dipole moments are:

$$\Theta_1 = \mathcal{N}_1 = \frac{iv_b}{3} = \frac{iv_{dm}}{3} = -\frac{k\Phi}{6aH} \,. \tag{1.119}$$

### 1.9.2 Initial Curvature Perturbations

To calculate the initial conditions for the curvature perturbations, we must make some assumptions for the physical process that excites the growing mode in the very early Universe. Inflation can be the mechanism that does the job, being responsible for the initial perturbations in the early Universe.

Inflation was firstly proposed in 1981 [36–43] to explain two theoretical problems affecting the Big Bang model: the horizon and the flatness problems, that we discussed in Section 1.1. One possible implementation of the inflationary mechanism requires the existence of a generic scalar field $\phi(\vec{x}, t)$, which we call the inflaton. The inflaton is required to contribute with a negative $\rho_\phi + 3p_\phi$, that can be calculated from the stress energy tensor of $\phi$:

$$T^\alpha{}_\beta = g^{\alpha\nu} \, \partial_\nu\phi \, \partial_\beta\phi - g^\alpha{}_\beta \left( \frac{1}{2} g^{\mu\nu} \, \partial_\mu\phi \, \partial_\nu\phi + V(\phi) \right) \,, \tag{1.120}$$

where $V(\phi)$ is the potential of $\phi$. The homogeneous zero-order part of the field, $\phi^{(0)}$, gives the homogeneous density and pressure:

$$\rho_\phi = \frac{1}{2} \left( \frac{d\phi^{(0)}}{dt} \right)^2 + V(\phi^{(0)}) \,, \tag{1.121}$$

$$p_\phi = \frac{1}{2} \left( \frac{d\phi^{(0)}}{dt} \right)^2 - V(\phi^{(0)}) \,, \tag{1.122}$$

having considered the diagonal components of $T^\alpha{}_\beta$ and Eq. (1.19). If the potential is larger than the kinetic energy, the field gives a negative pressure. This can happen, for example, if the scalar field is trapped in a false vacuum, where it has small or vanishing kinetic energy since it is at a minimum, but not in the true minimum: the consequence is that the pressure is negative, the density is almost constant and the Universe is in a phase of exponential expansion. The scenario with a scalar field trapped in a false vacuum is not viable, since the inflaton cannot exit the false vacuum unless it tunnels quantum mechanically. Detailed calculations showed that the exponential expansion of the regions in the false vacuum prevents the transition of the full Universe to the true vacuum state. [46, 47].

To avoid the problem of the Universe never reaching the true vacuum, mechanisms involving a scalar field slowly rolling down a potential energy hill were proposed [37, 41]. If the potential is not too steep, the inflaton energy density remains almost constant and after some time it comes to dominate, providing the desired exponential expansion. From the Friedmann equation (1.25) it is possible to derive the second-order differential equation for $\phi$:

$$\ddot{\phi}^{(0)} + 2aH\dot{\phi}^{(0)} + a^2 V' = 0 \,, \tag{1.123}$$

using the dots to indicate derivatives with respect to the conformal time $\eta$ and the primes to indicate the derivatives with respect to the inflaton $\phi$.

Slow roll is usually quantified through two small parameters, $\epsilon_{\text{SR}}$ and $\eta_{\text{SR}}$[7] that vanish when $\phi$ is constant, since $H^2 \propto (\rho_\phi)$. We define

$$\epsilon_{\text{SR}} \equiv \frac{d(H)^{-1}}{dt} = \frac{-\dot{H}}{aH^2} \,, \tag{1.124}$$

that is always positive since $H$ is decreasing. In the inflationary era, $\epsilon_{\text{SR}}$ is typically small, while it can be large during the radiation or matter era, during which its definition is valid, but it loses its original meaning. The complementary parameter $\eta_{\text{SR}}$ is instead:

$$\eta_{\text{SR}} \equiv \frac{1}{H} \left( \frac{d^2\phi^{(0)}}{dt^2} \right) \left( \frac{d\phi^{(0)}}{dt} \right)^{-1} = \frac{-1}{aH\dot{\phi}^{(0)}} \left( 3aH\dot{\phi}^{(0)} + a^2 V' \right) \,, \tag{1.125}$$

where we used Eq. (1.123) to eliminate the second derivative of $\phi^{(0)}$.

Our goal at this point is to predict the statistical properties of the perturbations at a time $\eta$, given the initial conditions inferred from inflation. One of the assumptions is that the perturbations have a gaussian distribution at the beginning. This is preserved until the evolution remains in the linear regime. Under this assumption, the statistical properties of the fluctuations can be entirely encoded in the two-point correlation function. For a stochastic gaussian field, different wavevectors are uncorrelated and the two point correlation function in the Fourier space is

$$\langle A^\dagger(\vec{k}, t) A(\vec{k}', t) \rangle \equiv (2\pi)^3 \delta^3(\vec{k} - \vec{k}') \, P_A(k) \,, \tag{1.126}$$

where the coefficient $P_A(k)$ is called the power spectrum of the quantity $A$. In a statistically isotropic Universe, the power spectrum is a function of the wavenumber $k$ only, not of its direction $\hat{k}$.

We want now to derive the Primordial Power Spectrum (PPS) of the initial curvature fluctuations, from which it is possible to derive the power spectra for the other quantities using the relations presented in the previous Subsection. Inflation is expected to excite also tensor fluctuations, or gravitational waves. These are not coupled to the energy density and do not affect the growth of large scale structures of the Universe, but they induce fluctuations in the CMB. A detection of gravitational waves from the primordial Universe would be a strong evidence of inflation, but so far they were not observed. We will not treat tensor perturbations here, but the interested reader can find details of the calculations in Ref. [35]. We report here only the PPS that can be obtained for the initial tensor perturbations:

$$P_T(k) = \frac{8\pi G H^2}{k^3} \,, \tag{1.127}$$

under the assumption that $H$ is constant. More generally, $H$ has to be evaluated at the time when each mode leaves the horizon. Since the expression of the PPS of tensor perturbations is remarkably simple, a detection of gravitational waves would give us a measure of the Hubble rate during inflation. Since the inflaton energy density is usually dominated by its potential energy, $H^2 \propto \rho/m_{\text{Pl}}^2$ is proportional to the inflaton potential $V$. The PPS $P_T$ is consequently proportional to $V(\phi)$.

The calculation of the initial scalar fluctuations is more complicated. All the density and metric perturbations are generated by quantum fluctuations in the values of the inflaton field. While tensor perturbations are not coupled to any of the other perturbation variables, however, scalar perturbations couple to energy density fluctuations. Firstly we decompose the inflaton field in a background and a perturbed component:

$$\phi(\vec{x}, t) = \phi^{(0)}(t) + \delta\phi(\vec{x}, t) \,. \tag{1.128}$$

---

[7]We use the subscript "SR" to distinguish the slow roll parameter $\eta_{\text{SR}}$ from the conformal time $\eta$.

If we completely neglect the metric perturbations, we can derive a spectrum for $\delta\phi$ that is similar to $P_T$, since in this approximation both the quantities are decoupled from the metric perturbations:

$$P_{\delta\phi} = \frac{H^2}{2k^3}\,. \tag{1.129}$$

It is possible to show that the approximation under which $\Psi$ and $\Phi$ are negligible works well in a particular gauge, called *spatially flat slicing*. In this gauge the metric is simple in its spatial part:

$$ds^2 = -(1+2A)\,dt^2 - 2a\,\partial_i B\,dx^i\,dt + \delta_{ij}\,a^2\,dx^i\,dx^j\,, \tag{1.130}$$

where the functions $A$ and $B$ characterize the perturbations. Under this assumption, Eq. (1.129) is exact, since the inflaton perturbations are decoupled from the metric ones. It is then necessary to find a way to convert back the quantities to the conformal Newtonian gauge. This is possible since there is a gauge-invariant variable that is proportional to $\delta\phi$:

$$\zeta = -\Phi_H - \frac{iaH}{k}v\,, \tag{1.131}$$

where $\Phi_H$ is the Bardeen's potential and $v$ is the Bardeen's velocity, that in the spatially flat slicing is

$$v = ikB - \frac{ik\,\dot\phi^{(0)}\,\delta\phi}{(\rho+p)\,a^2}\,. \tag{1.132}$$

In the spatially flat slicing the Bardeen's potential is $\Phi_H = aHB$ and the gauge-invariant quantity $\zeta$ becomes:

$$\zeta = -\frac{aH}{\dot\phi^{(0)}}\delta\phi\,. \tag{1.133}$$

With this relation we can immediately obtain the PPS for $\zeta$, from Eq. (1.129):

$$P_\zeta = \left(\frac{aH}{\dot\phi^{(0)}}\right)^2 P_{\delta\phi} = \left.\frac{2\pi G H^2}{\epsilon_{\mathrm{SR}}k^3}\right|_{aH=k}\,. \tag{1.134}$$

This is the power spectrum of a gauge-invariant quantity: if we compute $\zeta$ in the conformal Newtonian gauge we can relate $P_\zeta$ to $P_\Phi$, and then we can use the relations in Eqs. (1.117)–(1.119) to obtain the power spectra for all the other quantities.

In the conformal Newtonian gauge the Bardeen's potential is $\Phi_H = -\Phi$, so we have

$$\zeta = -\Psi - \frac{ik_i\,\delta T^0{}_i\,H}{k^2(\rho+p)}\,. \tag{1.135}$$

It is possible to demonstrate that $\zeta$ is conserved on super-horizon scales: we can then evaluate the last expression after inflation and we obtain a general result. If we calculated the stress-energy tensor for the inflaton perturbations, we would find out that in the conformal Newtonian gauge, after inflation, $\zeta = 3\Phi/2$. Assuming that $\Phi = -\Psi$ in absence of anisotropic stress (see Eq. (1.109)), we can finally use the spectrum $P_\zeta$ to obtain:

$$P_\Psi = P_\Phi(k) = \left.\frac{8\pi G}{9k^3}\frac{H^2}{\epsilon_{\mathrm{SR}}}\right|_{aH=k}\,, \tag{1.136}$$

which tells us that the ratio of the scalar to the tensor modes is of order $\epsilon_{\mathrm{SR}}^{-1}$, so that the scalar modes dominate over the tensor ones. With this solution and the results we presented in Eqs. (1.117)–(1.119) it is then possible to calculate the spectra of the initial perturbations for the other quantities, relating them to the initial power-spectrum $P_\Phi(k)$ through the definition in Eq. (1.126).

A spectrum with constant $k^3 P(k)$ is called a *scale-invariant* or *scale-free* spectrum. Both the tensor and the scalar perturbations have an almost scale-free power spectrum, where

the deviation from scale-invariance is proportional to the slow roll parameters and it is typically small. The scale-invariant spectrum is also referred to as "Harrison-Zel'dovich-Peebles spectrum", from the names of the people that proposed it well before that inflation was developed [48–50]. The observations nowadays point towards a scalar perturbation spectrum that is slightly away from scale-invariance, while the tensor spectrum has never been measured. The deviation from scale invariance can be parameterized through the spectral indices $n_s$ and $n_T$, for scalar and tensor perturbations respectively. The spectra indices and the amplitudes of the PPS are defined using:

$$P_T(k) = \left.\frac{8\pi G H^2}{k^3}\right|_{aH=k} = C_T \, k^{n_T-3} \,, \tag{1.137}$$

$$P_\Phi(k) = \left.\frac{8\pi G H^2}{9\epsilon_{\mathrm{SR}} k^3}\right|_{aH=k} = \delta_H^2 \left(\frac{k}{H_0}\right)^{n_s-1} \frac{50\pi^2}{9k^3} \left(\frac{\Omega_m}{D_1(a=1)}\right)^2 \,, \tag{1.138}$$

where in this convention $\delta_H$ and $C_T$ are the amplitudes of the power spectra of scalar and tensor modes, $\Omega_m$ is the fraction of critical density provided by matter and $D_1$ is the *growth function* of matter perturbations.

It is possible to relate the spectral indices to the slow roll parameters using the logarithmic derivatives with respect to $k$:

$$\frac{d\ln(P_T)}{d\ln k} = n_T - 3 \,, \tag{1.139}$$

from which we can obtain the relationship between the tensor spectral index and $\epsilon_{\mathrm{SR}}$, that is

$$n_T = -2\epsilon_{\mathrm{SR}} \,. \tag{1.140}$$

A similar relation can be derived for the scalar spectral index, depending on both $\epsilon_{\mathrm{SR}}$ and $\eta_{\mathrm{SR}}$:

$$n_s = 1 - 4\epsilon_{\mathrm{SR}} - 2\eta_{\mathrm{SR}} \,. \tag{1.141}$$

Please note that in this convention the scale-invariant spectrum correspond to $n_T = 0$ and $n_s = 1$.

We conclude mentioning that many authors use the notation $\mathcal{P}_A$ for the rescaled power spectrum:

$$\mathcal{P}_A(k) \equiv \frac{k^3}{2\pi^2} P_A(k) \,. \tag{1.142}$$

With this definition $\mathcal{P}_A$ represents the contribution of each logarithmic interval in the Fourier space to the two-point correlation function in the real space. For practical reasons, if one does not deal with a specific inflationary model, but rather is interested in studying the cosmological evolution, the simplest way to write the power spectra of scalar and tensor perturbations is:

$$\mathcal{P}_t(k) = A_T \left(\frac{k}{k_*}\right)^{n_T} \tag{1.143}$$

$$\mathcal{P}_s(k) = A_s \left(\frac{k}{k_*}\right)^{n_s-1} \,, \tag{1.144}$$

where $k_*$ is the pivot scale and the spectral indices are the same for each $P_x$ and $\mathcal{P}_x$.

It is convenient to parameterize the power spectrum of tensor fluctuations in terms of the amplitude of the spectrum scalar modes $A_s$ and of the tensor-to-scalar ratio $r_{k_\star}$, defined at the scale $k_\star$:

$$r_{k_\star} \equiv \frac{\mathcal{P}_t(k_\star)}{\mathcal{P}_s(k_\star)} \,. \tag{1.145}$$

With this definition of $r_{k_\star}$ and assuming $r = r_{k_*}$, we have

$$\mathcal{P}_t(k) = r \cdot A_s \left(\frac{k}{k_*}\right)^{n_T} \,. \tag{1.146}$$

From Eqs. (1.137) and (1.138) we can see that the tensor-to-scalar ratio is proportional to the slow roll parameter $\epsilon_{\mathrm{SR}}$ and is is typically small. In particular, under the hypothesis of single-field slow-roll inflation, the tensor-to-scalar ratio is $r = \epsilon_{\mathrm{SR}} = -n_T/2$.

Finally, we can relate the slow-roll parameters to the inflaton potential and to its derivatives:

$$\epsilon_{\mathrm{SR}} = \frac{1}{16\pi G} \left( \frac{V'}{V} \right)^2 , \tag{1.147}$$

$$\eta_{\mathrm{SR}} = \epsilon_{\mathrm{SR}} - \frac{1}{8\pi G} \frac{V''}{V} , \tag{1.148}$$

$$\tag{1.149}$$

where the primes denote derivatives with respect to the zero-order field $\phi^{(0)}$. These relations allow to write the spectral indices and the tensor-to-scalar ratio as functions of $V$ and its derivatives:

$$n_s - 1 = 2\frac{V''}{V} - 3 \left( \frac{V'}{V} \right)^2 , \tag{1.150}$$

$$n_T = -4 \left( \frac{V'}{V} \right)^2 , \tag{1.151}$$

$$r = 8 \left( \frac{V'}{V} \right)^2 . \tag{1.152}$$

Measurements of a scale dependence of the spectral indices and of the tensor-to-scalar ratio, then, can give information on the shape of the inflaton potential and consequently on the inflationary mechanism.

# Chapter 2

# Cosmic Microwave Background Radiation

With the quantities and the definitions presented in the previous Chapter, we now study the solutions of the Einstein and Boltzmann Equations for the perturbations to the photon distribution function. We will show the main features of the power spectrum of the CMB anisotropies and we will describe how the theoretical predictions are influenced by variations of the different cosmological parameters.

## 2.1 Power Spectrum

The goal of a stochastic theory is to predict the statistical properties of some physical quantity at a time $t$, given the initial conditions at a time $t_{\text{in}}$. In the case of the theory of cosmological perturbations, we want to obtain the statistical properties of the perturbations for some cosmological quantity, such as the cosmological photon distribution function, to be tested against the experimental measurements. Assuming that the initial fluctuations are Gaussian, as the current observations suggest, it is possible to convert all the information encoded in the CMB maps in the power spectrum of a two-point correlation function, at least until the perturbations remain in the linear regime.

The temperature anisotropy in the direction $\hat{n}$ can be expanded in spherical harmonics using

$$\frac{\delta T}{T}(\hat{n}) \equiv \sum_{lm} a_{lm} Y_{lm}(\hat{n}) \,. \tag{2.1}$$

This is related to the photon perturbation $\Theta$ at the time $\eta_0$, in the direction $-\hat{n}$ and at the position of the observer. The $a_{lm}$ coefficients can be extracted from the sky map with

$$a_{lm} \equiv (-1)^l \int \frac{d^3k}{2\pi^2} Y_{lm}(\hat{k}) \Theta_l(\eta_0, k) \,, \tag{2.2}$$

where $\hat{k}$ is the direction of $\vec{k}$ and $\Theta_l$ is the photon perturbation in the Fourier space, defined in Eq. (1.98). This equations tells us that there is a linear relation between the Fourier modes $\Theta_l$ and the multipoles $a_{lm}$: to any set of Gaussian-distributed cosmological perturbations it corresponds a set of Gaussian-distributed $a_{lm}$. This situation is particularly interesting since the statistics of a set of Gaussian-distributed $a_{lm}$ is fully described by the two point correlation function, $\langle a_{lm} a_{l'm'}^* \rangle$. Eq. (2.2) also implies that different (theoretical) multipoles are uncorrelated, as they are different modes of a gaussian random field. If the power spectrum in the Fourier space is isotropic, depending on the modulus of $\vec{k}$ but not on its direction, the harmonic power spectrum is also isotropic and does not depend on $m$:

$$C_l \equiv \langle a_{lm} a_{lm}^* \rangle \,, \qquad \forall m. \tag{2.3}$$

Under the assumption of ergodicity, it is possible to build an estimator for the true power spectrum, since at a given $l$ all the multipoles $a_{lm}$ should have the same variance $C_l$. In the ideal case the best estimator would be:

$$C_l^{\text{obs}} \equiv \frac{1}{2l+1} \sum_{m=-l}^{l} \left| a_{lm}^{\text{obs}} \right|^2 . \tag{2.4}$$

This is not a realistic way to calculate the spectrum, since in the real case the sky coverage is not complete and the observation is affected by the instrumental noise and the contamination of the anisotropic emission (galaxy, point sources): in this situation, building the optimal estimator is a complicated task that we will not discuss.

Since we can observe only one realization of the theory that describes the evolution of the primordial perturbations, we can expect that the statistical fluctuations of the observed spectrum have an impact on our best estimator. It is easy to compute the average deviation at a given $l$ using an ideal full-sky experiment. Each $C_l^{\text{obs}}$ as computed in Eq. (2.4) is obtained as the mean of $(2l+1)$ independent numbers, each of them with mean zero and variance $C_l$, so that the $C_l^{\text{obs}}$ obey a $\chi^2$ distribution with $(2l+1)$ degrees of freedom. The mean and variance of this distribution are $C_l$ and $\sqrt{2/(2l+1)}\, C_l$, respectively. The distribution is asymmetric around its peak, especially at low $l$, where the variance is larger. This is a consequence of the fact that we have less independent realizations of the same cosmic evolution at low $l$ (large angles). This variance plays the role of a theoretical error on the best estimator and it is called *cosmic variance*. Independently of the experimental errors, the cosmic variance is the minimum error for the CMB power spectrum at the multipole $l$, as a consequence of the fact that we can observe one single realization of the evolution history. As we will discuss in Sec. 3.1, the most recent measurements of the CMB spectrum are limited by the cosmic variance in a very wide range of multipoles.

## 2.2  Power Spectrum and Transfer Functions

We mentioned that the power spectrum of a given quantity $A$, in the statistically isotropic Universe we are studying, does not depend on the wavevector direction $\hat{k}$. In the same way, we can note that the differential equations for the perturbations we presented in the previous Chapter are also independent of $\hat{k}$. As a consequence, the system of linear equations must be solved only once for each wavenumber $k$, given an arbitrary set of initial conditions. For example, we could assume that the solution is normalized to $\Theta_0(\eta_{\text{in}}, \vec{k}) = 1$. In this case, the power spectrum of $\Theta_l$ at a given time will be the product of the power spectrum of $\Theta_0$ at $\eta_{\text{in}}$ multiplied by the square of the solution $\Theta_l(\eta, \vec{k})$ (see the definition in Eq. (1.126)).

The initial normalization, in an Universe with only adiabatic conditions, often refers to a dimensionless quantity $\mathcal{R}$, called the comoving curvature perturbation. In the comoving gauge, $\mathcal{R}$ represents the local fluctuation of the spatial curvature, in comoving units. In the Newtonian gauge this is defined as

$$\mathcal{R} \equiv \Psi - \frac{1}{3} \frac{\delta\rho_{\text{tot}}}{\rho_{\text{tot}}^{(0)} + p_{\text{tot}}^{(0)}} . \tag{2.5}$$

With this assumption, all the evolution equations of the perturbations can be solved using the arbitrary condition $\mathcal{R}(\eta_{\text{in}}, \vec{k}) = 1$ and the power spectrum of a given quantity $f$ will be then the square of the solution multiplied by the initial power spectrum of $\mathcal{R}$. In other words, one should solve the evolution equations for some renormalized variables

$$f(\eta, k) \equiv f(\eta, \vec{k}) / \mathcal{R}(\eta_{\text{in}}, \vec{k}) , \tag{2.6}$$

where we adopted the notation used in Ref. [51] to distinguish the *transfer functions* $f(\eta, k)$, depending on $k$, from the corresponding not normalized quantity $f(\eta, \vec{k})$, depending on $\vec{k}$. Here $f$ indicates one of the perturbation functions we defined in the previous Chapter: $\Theta_l$,

$\delta$, $\delta_b$, and so on. Once one has the solution for the transfer function $f(\eta, k)$ at any time $\eta$, the power spectrum of $f(\eta, \vec{k})$ can be obtained from the initial spectrum of $\mathcal{R}$ multiplying by the square of the transfer function corresponding to $f$, that is $f(\eta, k)$ (see the definition in Eq. (1.126)):

$$\mathcal{P}_f(\eta, k) = \mathcal{P}_\mathcal{R}(k) \left[ f(\eta, k) \right]^2 . \tag{2.7}$$

## 2.3 Acoustic Oscillations

While a precise solution of the system of differential equations that describe the cosmological perturbations can be obtained numerically, several analytical approximations were developed in the past, see e.g. Ref. [52]. These approximations helped in understanding all the complex physical phenomena that occurred during the evolution. The full analytical treatment is beyond the scope of this thesis and we will only give a qualitative description of the CMB spectrum.

When photons and baryons can be considered as a single tightly-coupled fluid, the sound speed of the perturbations in the fluid is

$$c_s^2 \equiv \frac{1}{3(1 + R)} , \tag{2.8}$$

where $R$ is the baryon to photon ratio defined in Eq. (1.96). The ratio $R$ increases with the scale factor, as the photon and baryon densities scale differently. The sound speed is then $c_s = 1/\sqrt{3}$ during radiation domination, when $R$ is small, and decreases slowly to zero.

When the sound speed is different from zero, acoustic waves propagate in the fluid. Since the primordial perturbations drive the system locally out of equilibrium, gravitational attraction and radiation pressure are not exactly compensated at each point and the acoustic waves propagate causally. The maximal distance at which they propagate is the *sound horizon*. The comoving sound horizon, that is the comoving distance traveled by the wavefront in a time $\eta - \eta_\mathrm{in}$, is given by

$$r_s(\eta) \equiv \int_{\eta_\mathrm{in}}^{\eta} c_s(\eta') \, d\eta' . \tag{2.9}$$

If $\eta_\mathrm{in} \ll \eta$, this quantity does not depend on the initial time.

Acoustic waves are density waves in the coupled fluid, whose perturbations can be encoded in the variations of the temperature $\Theta_0(\eta, k)$. However, the system does not behave like a simple harmonic oscillator. This is the consequence of several phenomena: first of all, the ratio $R$ increases with time, changing the sound speed and other properties of the fluid, like its inertia. Secondly, the gravitational forces are seeded by the overdensities of the baryon-photon fluid, but also by those of the other species, as CDM or neutrinos. All these effects are taken into account in the second-order differential equation for $\Theta_0$:

$$\ddot{\Theta}_0 + \frac{\dot{R}}{1 + R}\dot{\Theta}_0 + k^2 c_s^2 \, \Theta_0 = -\frac{k^2}{3}\Psi - \frac{\dot{R}}{1 + R}\dot{\Phi} - \ddot{\Phi} . \tag{2.10}$$

We analyze now the different terms that appear in this equation.

### 2.3.1 Diffusion Damping

When all the electrons were ionized, before recombination, the photons had a mean free path that was much smaller than the size of the Universe. As a consequence of Compton scattering, the electron-proton fluid was tightly coupled with the photons. In the tight-coupling approximation, the scattering rate of the photons is much larger than the expansion rate and their trajectory can be described as a random walk, with photons taking a random direction after each interaction with an electron. Since the interaction rate of the photons $\Gamma_\gamma$ can be obtained from the Thomson scattering ($\Gamma_\gamma = a n_e \sigma_T$) and the comoving mean free

path of the photons is $r_\gamma = \delta\eta = (an_e\sigma_T)^{-1}$, an approximated expression for the comoving distance traveled by a photon between an early time $\eta_{\text{in}}$ and a time $\eta$ will be

$$r_d^2(\eta) \simeq \int_{\eta_{\text{in}}}^{\eta} d\eta\, \Gamma_\gamma\, r_\gamma^2 \simeq \int_{\eta_{\text{in}}}^{\eta} \frac{d\eta}{an_e\sigma_T}\,. \tag{2.11}$$

If $\eta_{\text{in}} \ll \eta$, $r_d$ does not depend on $\eta_{\text{in}}$. Photon diffusion erases all the perturbations with a wavenumber greater than $k_d = 2\pi/r_d$, corresponding to small distances.

The damping effect, together with the driving contribute given by the gravitational terms in the right hand side of Eq. (2.10), leads to an interesting phenomenology for the acoustic oscillations, that we will study in three different stages: radiation domination, matter domination before photon decoupling and evolution after the photon decoupling. This discussion is essential for understanding how the different cosmological parameters can affect the CMB spectrum.

### 2.3.2  Constant Acoustic Oscillations during Radiation Domination

During radiation domination it is easy to obtain approximated analytic solutions, since one can work in the limit $R = 0$ or $c_s = 1/\sqrt{3}$, valid when baryon and CDM perturbations are negligible with respect to photon perturbations. From the Einstein equations it is possible to find a second order differential equation only for the perturbations of the fluid we consider. The growing solution corresponds to constant transfer functions outside the sound horizon: in this regime, the propagation of acoustic waves is negligible since the comoving wavelength is much larger than the comoving sound horizon and the modes are frozen at their initial values. Inside the sound horizon, instead, the photon density modes oscillate with a constant amplitude and metric fluctuations decay with time. The effects driven by the metric terms in Eq. (2.10) are negligible with respect to photon pressure forces and if we use $k\eta \gg 1$ the driving term on the r.h.s. can be neglected. We obtain hence the equation of a simple harmonic oscillator.

### 2.3.3  Damped Acoustic Oscillations after Equality

After matter-radiation equality and before photon decoupling, several phenomena modify the evolution. As the baryon fraction $R$ starts to increase, the sound speed decreases, affecting the amplitude of the acoustic oscillations. At the same time, the increase of the baryon fraction forces an increase of the coupling between the fluid and gravity, and the zero-point of the oscillations is shifted. If we neglect the time variation of $\Phi$ in Eq. (2.10), the zero point of temperature oscillations corresponds to $k^2 c_s^2 \Theta_0 = -k^2\Psi/3$, that is $\Theta_0 = -(1 + R)\Psi$. For a gravitational potential well with $\Psi < 0$ the value of $\Theta_0$ that corresponds to the equilibrium of the oscillations increases with $R$.

After matter-radiation equality, non-relativistic matter components start to influence the metric perturbations so that $\Phi$ and $\Psi$ do not decay as quickly as during the radiation domination, inside the Hubble radius. The gravitational driving terms of Eq. (2.10) become then more important and alter the behavior of the acoustic oscillations.

Finally, when the fluid exits the tight-coupling approximation regime, oscillations are damped at wavelengths smaller than the diffusion length of the photons, as we mentioned earlier.

At the equality, temperature oscillations are roughly symmetric around the zero-point $\Theta_0 = \Phi$ inside the sound horizon and constant at larger scales, where metric fluctuations are negligible. At decoupling, the amplitude of photon oscillations is reduced on all the sub-horizon scales: with respect to the zero-point at equality, the zero-point of the oscillations is shifted down, with a consequent enhancement of the amplitude of the odd peaks with respect to the even ones. These effects, plus the damping at small scales, are essentially controlled by the duration of the transition between equality and decoupling, by the baryon fraction $R$ at decoupling and by the value of the diffusion length $r_d$.

### 2.3.4   Gravitational Clustering after Decoupling

After decoupling, photons stop interacting with the rest of the plasma and the calculation of the perturbations concerns the self-gravitation of non-relativistic matter components. The evolution of matter perturbations leads to structure formation. In the real Universe we cannot use the approximation that $\Phi = -\Psi$ is constant over time at all scales, valid in the ideal matter dominated Universe, since at the beginning of the matter dominated era a residual decay of $\Phi$ and $\Psi$ perturbations occurs. Moreover, during the DE dominated stage a similar decay occurs. The presence of massive neutrinos, finally, breaks the approximation that $\Phi = -\Psi$ is always valid at small scales.

## 2.4   Temperature Anisotropies

### 2.4.1   Numerical Calculation

As we stated in Section 2.1, the main goal of the cosmological evolution theory is to predict the CMB spectrum, or the final spectrum of the perturbations as a function of the cosmological parameters.

One possible way to do this is to adopt a brute-force method and to integrate all the equations (1.100) to (1.102) with at least $l_{\max}$ multipoles for the photon perturbations, between an initial time $\eta_{\mathrm{in}}$ and today. The temperature anisotropy spectrum up to $l_{\max}$ is then given by:

$$C_l = \frac{1}{2\pi^2} \int \frac{dk}{k} [\Theta_l(\eta_0, k)]^2 \mathcal{P}_{\mathcal{R}}(k) \,. \tag{2.12}$$

The hierarchy of coupled photon equations is infinite, but any numerical algorithm can integrate only a finite number of multipoles. A truncation of the multipole series is needed, but this can cause a reflection of power-down at lower multipoles. Even if it is possible to avoid such a power-down with an appropriate choice of $k_{\max} \simeq l_{\max}/\eta_0$, that ensures that only the photon transfer functions $\Theta_l(\eta, k)$ with $l \gtrsim l_{\max}$ vanish, the brute-force approach is extremely time-consuming from the computational point of view.

A much more convenient approach is the so called *line-of-sight* approach. For convenience, in this Subsection we will return to the description in the real space. The same calculations can be transposed in the Fourier space using the spherical Bessel functions (see Ref. [53]). Consider a photon traveling along a geodesic between the last scattering and us: we know that the geodesic is not a straight line, since the gravitational lensing effects modify the photon path. These, however, are second-order effects and we are considering only the first-order perturbations: the geodesic is then approximated as a straight line, since we are neglecting the spatial curvature. A photon reaching us from the direction $-\hat{n}$ traveled in the direction $\hat{n} \equiv \hat{p}$ from the last scattering surface. Its comoving coordinates at the time $\eta$ were $\vec{x} = -(\eta_0 - \eta)\,\hat{n}$, so that the variation in the radial coordinate is $dr = -d\eta$. A function $\mathcal{F}(\vec{x}, \hat{n}, \eta)$ evolves along the trajectory according to the total derivative

$$\frac{d\mathcal{F}}{d\eta} = \dot{\mathcal{F}} + \hat{p} \cdot \vec{\nabla} \mathcal{F} \,, \tag{2.13}$$

using the straight line approximation $d\hat{n}/d\eta = 0$. It is convenient to consider the function $\mathcal{F} = \Theta(\vec{x}, \hat{n}, \eta) + \Psi(\vec{x}, \eta)$ and to integrate the Boltzmann equation over the photon trajectory. We can use the optical depth $\tau(\eta)$ written in Eq. (1.87) to define the visibility function $g(\eta) = -\dot{\tau}e^{-\tau}$, that represents the probability for a photon reaching us today to have experienced its last scattering at the time $\eta$. The last scattering time $\eta_{\mathrm{LS}}$ can be defined as the time that gives the maximum of $g$. With these definitions, using the Boltzmann equation (1.88) and multiplying by $e^{-\tau(\eta)}$, we obtain:

$$\frac{d}{d\eta}[e^{-\tau(\eta)}(\Theta + \Psi)] = g(\eta)(\Theta_0 + \Psi + \hat{n} \cdot \vec{v}_b) + e^{-\tau(\eta)}(\dot{\Psi} - \dot{\Phi}) \,. \tag{2.14}$$

Integrating along the line of sight between an early time $\eta_{\rm in} \ll \eta_{\rm LS}$, when $e^{-\tau(\eta_{\rm in})} \simeq 0$, and today, when $e^{-\tau(\eta_0)} = 1$, we obtain the temperature anisotropy as seen by the observer in the direction $\hat{n}$:

$$\Theta(\vec{o}, \hat{n}, \eta_0) = -\Psi(\eta_0, \vec{o}) + \int_{\eta_{\rm in}}^{\eta_0} d\eta \left[ g(\eta)(\Theta_0 + \Psi + \hat{n} \cdot \vec{v}_b) + e^{-\tau(\eta)}(\dot{\Psi} - \dot{\Phi}) \right], \qquad (2.15)$$

where $\vec{o}$ refers to the observer position, fixed at the origin for simplicity. The first term on the r.h.s. gives a local isotropic redshift or blueshift of incoming photons due to the local metric fluctuation today at the observer position, that is usually small and we will neglect it. The integral shows us that the observed temperature anisotropy in a given direction depends on two terms: the sum $(\Theta_0 + \Psi + \hat{n} \cdot \vec{v}_b)$ around the time of decoupling (when $g$ is not negligible) and the sum $(\dot{\Psi} - \dot{\Phi})$ between decoupling and today (when $e^{-\tau}$ is not negligible).

Interestingly, from Eq. (2.15) we learn that the photon perturbations $\Theta_l$ for $l > 1$ are not needed to compute CMB anisotropies, meaning that this method is then much more economic than the brute-force method.

Equation (2.15) shows that four quantities are required to obtained the temperature fluctuations: $\Phi$, $\Psi$, $\Theta_0$ and $v_b$. Since these must be obtained from the Einstein equations, however, also the density perturbations and the bulk velocities for the other species must be calculated. To obtain a good precision on the first multipoles of the temperature anisotropy, though, also the modes with $l > 2$ must be calculated. An economic truncation scheme requires the calculation up to $l_{\rm max}^{\gamma} \simeq \mathcal{O}(10)$ to obtained a sufficient precision on the $C_l$ up to $l_{\rm max} \simeq \mathcal{O}(10^3)$ [54]. As for the brute-force approach, $l_{\rm max}$ determines the maximum wavenumber $k_{\rm max} \simeq l_{\rm max}/\eta_0$ at which the source function has to be evaluated, corresponding to the information about perturbations on the last scattering surface as seen today under an angle $\theta \simeq \pi/l_{\rm max}$. The advantage of the line-of-sight approach over the brute-force method is then given only by the factor $l_{\rm max}^{\gamma}/l_{\rm max}$, that allows to gain few orders of magnitude in computation time. The line-of-sight approach, used by all the modern Boltzmann codes, was firstly implemented in CMBFAST [55].

### 2.4.2   Physics of the CMB Anisotropies

We want now to look at Eq. (2.15) to study how the different terms contribute to the CMB spectrum.

The most obvious contribution to the observed temperature fluctuations in one direction is given by the temperature fluctuations at the last scattering in the same direction, corrected by a gravitational shift [56]: this contribution comes from the $g(\eta)(\Theta_0 + \Psi)$ term in Eq. (2.15). Ideally, in the instantaneous decoupling limit the last scattering surface can be seen as a flat surface rather than a thick shell, corresponding to a rapid increase of the mean free path of the photons from 0 to infinity at $\eta = \eta_{\rm LS}$. In this limit, the visibility function can be replaced by a Dirac delta $\delta(\eta - \eta_{\rm LS})$ and the integral of $g(\eta)(\Theta_0 + \Psi)$ gives the *Sachs-Wolfe (SW) contribution*:

$$\Theta^{\rm SW}(\vec{o}, \hat{n}, \eta_0) \simeq \Theta_0(\vec{x}_{\rm LS}, \hat{n}, \eta_{\rm LS}) + \Psi(\eta_{\rm LS}, \vec{x}_{\rm LS}), \qquad (2.16)$$

where $\vec{x}_{\rm LS} = (\eta_{\rm LS} - \eta_0)\hat{n}$.

For super-horizon scales and during matter-domination it is possible to derive the relation $\Theta_0 = -2/3\Psi$. In a CMB map smeared over small scale fluctuations, the SW contribution becomes then

$$\Theta^{\rm SW,smoothed}(\vec{o}, \hat{n}, \eta_0) \simeq -\frac{1}{2}\Theta_0(\vec{x}_{\rm LS}, \hat{n}, \eta_{\rm LS}) \simeq \frac{1}{3}\Psi(\eta_{\rm LS}, \vec{x}_{\rm LS}). \qquad (2.17)$$

This Equation tells us that hot regions in the observed CMB map correspond to cold regions at the last scattering: the reason is that photons leaving an overdense region lose part of their energy to exit the gravitational potential well.

The second contribution from the integral in Eq. (2.15) comes from the term proportional to $\vec{v}_b$. Photons are emitted from the coupled baryon-electron fluid with a peculiar velocity
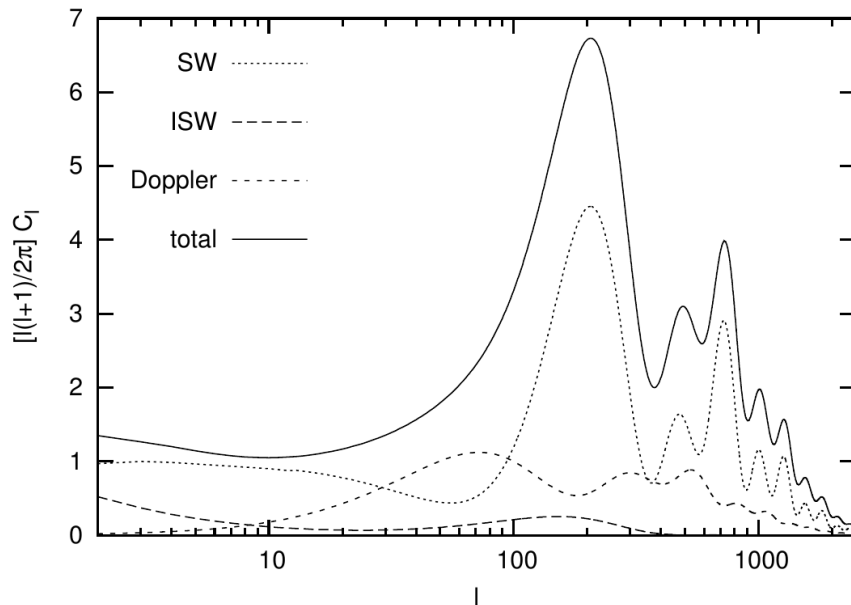
Figure 2.1: Full spectrum of CMB temperature anisotropies and individual contributions from the SW term, the Doppler term and the ISW term. The full spectrum is given by the sum of the above terms, plus the contributions coming from their correlations. The spectrum is obtained numerically in a flat Universe without considering neutrino perturbations. From [51].

that is different from point to point. When they are projected along the line-of-sight, this velocity induces a Doppler shift in the photon wavelength. In the instantaneous decoupling limit, the *Doppler contribution* is:

$$\Theta^{\text{Doppler}} \simeq \hat{n} \cdot \vec{v}_b(\eta_{\text{LS}}, \vec{x}_{\text{LS}}) \,. \tag{2.18}$$

Photons traveling from the last scattering surface to a today observer encounter several metric fluctuations: every time they enter or exit a gravitational potential well, they are blueshifted or redshifted. The term in Eq. (2.15) that encodes this phenomenon is the one containing to $e^{-\tau}(\dot{\Psi} - \dot{\Phi})$. In a static Universe, variations in $\Psi$ correspond to the presence of over- or under-dense regions, while variations in $\Phi$ encode a local correction to the average time-dilation, responsible for the gravitational redshift during the Universe expansion. Since the Universe is not static, the photon does not encounter the same gradient when entering or exiting a local metric fluctuation: while traveling along the line-of-sight, photons take a cumulative temperature shift, accounted by the integral of $\dot{\Psi}$ and $\dot{\Phi}$. The combination of these shifts is the *Integrated Sachs-Wolfe (ISW) contribution* to the temperature fluctuations. In the instantaneous decoupling limit, $e^{-\tau}$ can be replaced by the Heaviside function $\theta(\eta - \eta_{\text{LS}})$ and the ISW contribution becomes

$$\Theta^{\text{ISW}}(\vec{o}, \hat{n}, \eta_0) \simeq \int_{\eta_{\text{LS}}}^{\eta_0} d\eta \, (\dot{\Psi} - \dot{\Phi}) \,. \tag{2.19}$$

### 2.4.3 Features of the CMB spectrum

With the various contributions to the CMB spectrum we just mentioned and the $C_l$ formula in Eq. (2.12) it is possible to obtain the shape of the features of the CMB spectrum. An example of the full temperature power spectrum is plotted in Fig. 2.1.

In the Fourier space, the photon transfer function $\Theta(\eta, k)$ can be written using the spherical Bessel functions $j_l(x)$, that are peaked near $x \simeq l$. Since the visibility function $g$ is peaked around recombination and the PPS of curvature perturbations $\mathcal{P}_{\mathcal{R}}$ is nearly scale-independent, we can derive mathematically a simple result: in the Fourier space, the SW

contribution to the $C_l$ multiplied by $l^2$ is qualitatively similar to the square of the SW contribution to the transfer function, namely

$$l^2 C_l \propto [\Theta(\eta_{\mathrm{LS}}, k) + \Psi(\eta_{\mathrm{LS}}, k)]^2_{k=l/(\eta_0 - \eta_{\mathrm{LS}})} \,. \tag{2.20}$$

This comes from the fact that the anisotropy multipoles at a given $l$ come mainly from the Fourier modes at $\lambda \simeq 2\pi a(\eta_{\mathrm{LS}})/k$ on the last scattering surface, that are seen today under an angle $\theta = \lambda/d_A(\eta_{\mathrm{LS}}) \simeq 2\pi/l$. In a flat space, $d_A(\eta_{\mathrm{LS}}) = a(\eta_{\mathrm{LS}})/(\eta_0 - \eta_{\mathrm{LS}})$, that gives $2\pi/l \simeq 2\pi/[k(\eta_0 - \eta_{\mathrm{LS}})]$. The full calculation is more complex, since a given wavenumber contributes to an ensemble of multipoles and the relation we presented above gives only the value of $l$ corresponding to the maximum contribution for a given $k$. To develop a qualitative description of the CMB spectrum, however, the approximation we adopted is sufficient.

We can look at the dotted line in Fig. 2.1, that represents the SW contribution to the CMB spectrum. At large scales (small $l$), the nearly flat behavior gives the so-called SW plateau, that corresponds to the modes that are outside the sound horizon at decoupling, which are still frozen. From $l \simeq 100$ we can distinguish the acoustic peaks we discussed in the previous Section, which are modulated by the various effects already described. We can see that the odd peaks are enhanced with respect to the even ones, as a consequence of the high baryon fraction (see Subsection 2.3.3). The first peak is given by the correlation length on the last scattering surface that corresponds to the sound horizon at decoupling, while all the other peaks represent the higher harmonics of the same feature. These peaks are damped according to the diffusion damping effect described in Subsection 2.3.1, that gives a factor $e^{-(l/l_d)^2}$, with $l_d \simeq k_d(\eta_0 - \eta_{\mathrm{LS}}) \simeq 2\pi(\eta_0 - \eta_{\mathrm{LS}})/r_d$. The damping effect is usually referred to as *Silk damping* [57].

The second contribution comes from the Doppler term (short-dashed line in Fig. 2.1). On super-Hubble scales (at small $l$) the contribution of the Doppler term is negligible, since perturbations are frozen and the velocities in the baryon-photon fluid are very small. At smaller scales, instead, the contribution is sourced by $\vec{v}_b$, that exhibits the same oscillatory pattern as $\Theta_0$, but with a shift of $\pi/2$, as for any oscillator.

The last contribution comes from the ISW terms. These would vanish if the evolution between decoupling and today occurred in a perfectly matter-dominated Universe, since in this case the metric perturbations would be static everywhere and at any time. Instead, the ISW term contributes in two different phases of the Universe history. The first one is at the time of decoupling, since the Universe is at the beginning of the matter-dominated phase and the metric perturbations are still decaying together with the photon perturbations: the residual time variation of $\Psi$ and $\Phi$ gives the Early ISW (EISW) effect. Secondly, at late times the Universe enters a $\Lambda$-dominated phase and the metric fluctuations start decaying again. This Late ISW (LISW) effect can be considered as a secondary anisotropy, since it comes from gravitational interactions involving free-streaming photons that travel through neighboring galaxy clusters. We can identify the EISW and the LISW terms as two separate contributions to the long-dashed line in Fig. 2.1. The EISW term cannot affect modes that were outside the sound horizon at decoupling, so it is negligible at very large scales: it gives the maximum contribution at $l \simeq 200$ and it tends to decrease at larger $l$, as a consequence of the $k^{-2}$ coefficient in the Doppler term. The EISW then contributes with an enhancement of the first acoustic peak. The LISW contribution, instead, is present at any times, since it is related to a decay of metric fluctuations at all scales caused by the Universe entering a DE-dominated phase. Since this effect decreases for the same reason of the EISW effect, it is peaked at $l = 2$ and it becomes sub-dominant for $l \gtrsim 30$.

## 2.5   Parameter Dependence

Up to now we presented how the CMB temperature spectrum looks like, but we did not focus on how the different features are affected by variations in the fundamental cosmological parameters that we want to infer from the observations. Before we describe how we can

parameterize the standard cosmological model and we study how the parameters change the CMB spectrum, however, we should discuss one last effect that is caused by astrophysical phenomena after photon decoupling.

During the formation of the first stars, at redshift of order ten, the Universe was partly reionized by the light produced by the new stars. A small fraction of CMB photons is then scattered by the free electrons that are created in this context. This effect is negligible for modes that entered the horizon well after the reionization epoch ($l < l_{\text{step}}$, with $l_{\text{step}} \simeq 40$), but it leads to a scale-independent suppression of the CMB spectrum at smaller scales. The effect is accounted by a factor $e^{-\tau_{\text{re}}}$, where $\tau_{\text{re}}$ measures the optical depth to reionization: this quantity is constrained to be $\tau_{\text{re}} \simeq 0.1$ by current observations. The damping of the spectrum at $l \gg l_{\text{step}}$ is completely parameterized by $\tau_{\text{re}}$, while around $l \simeq l_{\text{step}}$ the suppression depends on the details of the reionization history, which are not well constrained by the current data.

Now we have all the ingredients to describe how the cosmological quantities influence the CMB spectrum, restricting ourselves to a flat Universe with three massless neutrinos: we will describe the parameterization and the neutrino effects in Section 4.4. We emphasize that considering a Universe without neutrino perturbations is not a realistic scenario, but we want focus on the neutrino contribution separately. We refer to the standard cosmological model as to the $\Lambda$CDM model, from the names of the cosmological constant $\Lambda$ and of CDM, that are two of the components of the Universe. In the $\Lambda$CDM model, we need six parameters to describe all the phenomena we encountered:

- to parameterize the PPS of scalar perturbations, we use its amplitude $A_s$ and its tilt $n_s$, see Eq. (1.144);

- the baryon density fraction today is given by $\omega_b = \Omega_b h^2$;

- we can use either the CDM density fraction $\omega_c = \Omega_c h^2$ or the total matter density fraction $\omega_m = \omega_b + \omega_c$. The former is more convenient if we consider additional massive components, for example massive neutrinos;

- the optical depth to reionization, $\tau_{\text{re}}$;

- if we assume a spatially flat Universe, we can consider either the cosmological constant density fraction $\Omega_\Lambda$ or the Hubble parameter today, $H_0$ or $h$, since for a fixed $\omega_m$ they are related by $h = \sqrt{\omega_m/(1 - \Omega_\Lambda)} = H_0/(100 \text{ Km s}^{-1} \text{ Mpc}^{-1})$. Since in the analyses reported in the second part of this Thesis we will use the public Boltzmann solver CAMB [58], instead, we adopt a different parameterization for the $\Lambda$CDM model, that considers the characteristic angular size of the fluctuations in the CMB, also called the acoustic scale $\theta$, in place of the Hubble parameter. Since the acoustic scale is determined from the positions of the acoustic peaks, its measurement is quite robust and stable to changes in data combinations and in the assumed cosmological model. The situation is similar to that of the BAO feature in the context of the large scale structure surveys, with the advantage that the CMB acoustic peaks develop in a completely linear regime.

Since the CMB measurements give a very precise determination of the photon temperature today, we consider $\omega_\gamma = \Omega_\gamma h^2$ as a fixed parameter. Since we fixed the amount of the other species (three massless neutrinos) contributing to the radiation energy density $\omega_R$ at the time of matter-radiation equality, the redshift of equality depends only on $\omega_m$. In the same way the redshift of coincidence, that occurs when the energy densities of matter and cosmological constant are equal, is fixed by $\Omega_\Lambda$.

Given this set of parameters, we can list how they control the features of the CMB temperature spectrum: we follow the treatment of Ref. [51]. The shape of the CMB spectrum is controlled by:

**(C1)** the peaks location, depending on the angle $\theta = d_s(\eta_{\text{LS}})/d_A(\eta_{\text{LS}})$. The sound horizon at decoupling $d_s$ is controlled by the expansion history, controlled by $\omega_m$ through the

redshift of matter-radiation equality, and by the sound speed at decoupling, affected by changes in $\omega_b$. The angular diameter distance, instead, depends on the expansion history after decoupling and is controlled by $\Omega_\Lambda$ or $h$, governing the coincidence redshift.

**(C2)** the relative amplitude of odd to even peaks, that depends on the balance between gravity and pressure in the photon-baryon fluid through the ratio $\omega_b/\omega_\gamma$;

**(C3)** the amplitude of all the peaks, depending on the expansion rate between equality and decoupling. Since decoupling is fixed by the interactions and by the evolution rate, the amplitude of the peaks is affected mainly by the redshift of equality ($\propto \omega_m/\omega_R$): for an earlier equality (higher $\omega_m$) the peaks are smaller, because the damping of acoustic oscillations lasts longer. Moreover, if there is more time between equality and decoupling, the EISW effect is reduced and the first peak gets an even smaller contribution.

**(C4)** the envelope of the secondary peaks, depending on the angle $\theta = \lambda_d(\eta_{\text{LS}})/d_A(\eta_{\text{LS}})$. The diffusion length $\lambda_d = a\, r_d$, controlled by the expansion history and recombination history before decoupling, depends essentially on the electron number $n_e$, that is the quantity in Eq. (2.11) that changes more before recombination, and on the conformal time at decoupling, $\eta_{\text{LS}}$. In the $\Lambda$CDM model, $n_e$ is fixed and the integral in Eq. (2.11) essentially does not depend on the expansion and on the electron fraction before equality. The angle $\theta$, then, depends essentially on $\omega_m$ (entering $\lambda_d$) and on $\Omega_\Lambda$ (entering $d_A$).

**(C5)** the normalization of the power spectrum of initial fluctuations $A_s$, being the CMB spectrum proportional to $\mathcal{P}_\mathcal{R}$.

**(C6)** the tilt $n_s$, for the same reason.

**(C7)** the duration of the $\Lambda$-dominated phase. The part of the spectrum where the $n_s$ contribution is more evident is indeed the SW plateau. Here, however, a contribution from the LISW effect enhances the first multipoles. It depends on $\Omega_\Lambda/\Omega_m = \Omega_\Lambda/(1-\Omega_\Lambda)$ for a flat Universe: for a larger $\Omega_\Lambda$, the $\Lambda$-domination is longer and the LISW contribution is enhanced.

**(C8)** the optical depth to reionization $\tau_{\text{re}}$. Due to reionization, the behavior of the CMB spectrum at $l \gtrsim 40$ is different from that at $l \lesssim 40$: the suppression at high $l$ depends on $\tau_{\text{re}}$. This effect is not degenerate with the damping of acoustic oscillations, that affects only the multipoles starting from an higher $l$ and not in a constant way. If one considers the entire CMB spectrum, the step at $l \simeq 40$ breaks also the degeneracy with $A_s$.

The effects we listed do not take into account a number of other tiny dependences that play a very small role in modeling the CMB spectrum. Some of these dependencies would concern the electron density $n_e$ and the redshift of recombination $\eta_{\text{LS}}$, that depends marginally on the baryon density and on the primordial Helium fraction, usually denoted with $Y_p$. These parameters affect the sound horizon at decoupling (Eq. (2.9)), the duration of the transition from equality to recombination and the photon diffusion length (Eq. (2.11)), with also a small impact on the effects **(C1)**, **(C3)** and **(C4)**. The magnitude of these effects, however, is much smaller than the magnitude of the primary effects **(C1)**–**(C8)**: the baryon density impact through $z_{\text{LS}}$ is much smaller than its effect on the relative magnitude of the peaks, and in the range currently allowed by the experimental data the effect of $Y_p$ is negligible. The approximation of considering a fixed recombination history, therefore, is very strong for most of the purposes.

We listed eight different characteristics of the CMB spectrum that can be controlled by only six parameters, but until few years ago the CMB measurements were not precise enough to strongly constrain all the $\Lambda$CDM parameters, since most of the effects listed above can

be distinguished only with very precise measurements. Cosmic variance at low-$l$ and instrumental noise at high-$l$ lead to partial parameter degeneracies inside the experimental error. The situation changed with the data release of the Planck experiment, that measured the CMB spectrum in a wide range of multipoles, obtaining an with unprecedented precision for the high-$l$ part of the spectrum, up to $l \simeq 2500$. After having analyzed the full experimental data, the Planck collaboration recently released the temperature and the polarization spectra, these latter ones measured for the first time at high multipoles. The joint analysis of temperature and polarization data allows to reduce or break the degeneracies among the different parameters and to improve the strength of the constraints on the cosmological parameters. We will discuss in more detail the CMB experimental results in the dedicated Section 3.1.

## 2.6  Polarization spectra

The CMB spectrum is not only characterized by temperature fluctuations: since Thomson scattering depends on the polarization of the photons, when isotropy disappears at the time of recombination the quadrupole momentum $\Theta_2(\eta, \vec{x})$ of the growing anisotropies is responsible for a net polarization of the scattered photons. As a consequence, a polarization pattern appears on the last scattering surface. This is strongly correlated with the temperature pattern.

Photon polarization at last scattering can be detected as a vector field on a sphere and can be decomposed in two modes: an $E$-polarization (gradient field) and a $B$-polarization (curl field) component. As for temperature, it is possible to define an harmonic power spectrum for the $E$ and $B$ modes auto-correlation and for the various cross-correlation terms: the different possibilities are given by

$$C_l^{XY} = \langle a_{lm}^X a_{lm}^{*Y} \rangle, \qquad \forall m, \tag{2.21}$$

where $X, Y \in \{T, E, B\}$.

Polarization of the type $B$ is related to the gravitational waves arising from inflation. Gravitational waves are coupled only to species having non-negligible tensor degrees of freedom, that are contained in the non-diagonal part of the spatial stress-energy tensor $\delta T_{ij}$. These degrees of freedom vanish for CDM, due to the smallness of the velocity dispersion, and also for baryons and tightly-coupled photons, due to the isotropic pressure enforced by interactions: the only species coupled to gravitational waves are photons, after decoupling, and other collisionless species, before their non-relativistic transition (neutrinos, for example). The influence of neutrinos on tensor anisotropies was studied in Ref. [59] and implemented in `CAMB` [58]. The neutrino contribution to CMB anisotropies, however, can be only significant for modes crossing the horizon during radiation domination or soon after matter-radiation equality, i.e. on small scales.

For parity invariance, the $TB$ and $EB$ cross-correlation spectra are zero after the last scattering, but they can be generated at the level of secondary anisotropies through the weak lensing of last scattering photons. Primary $B$ modes can be generated only if some tensor fluctuations exist in the early Universe, and they contribute to the CMB temperature spectrum only at small multipoles (typically $l < 150$). Scalar fluctuations do not contaminate the primordial tensor anisotropies, but the main contribution to the $B$-modes auto-correlation spectrum comes from a leak from $E$- to $B$-type polarization driven by gravitational lensing effects on small scales. Consequently, the $C_l^{BB}$ spectrum is dominated by tensor perturbations only at large scales. Since the $B$-type polarization is subdominant with respect to temperature and $E$-type polarization, the detection of the contribution to the CMB spectra of primordial tensor perturbations is a complicated experimental task. We will discuss the current status of the experimental results in Section 3.1.

The calculation of the spectra $C_l^{TE}$ and $C_l^{EE}$, instead, can be performed with the same procedure we presented for the temperature anisotropies, with the introduction of a new degree of freedom, whose evolution can be described by a new Boltzmann equation. The result of the calculation is a second hierarchy of differential equations for polarization anisotropies,

coupled to the infinite set of equations describing the temperature perturbations. The contribution of polarization to the evolution of temperature perturbations is small, so that our treatment of the temperature perturbations is a very good approximation of the full calculation. We will not describe in details the calculation of the polarization spectra, nor the different impact that some physical effects, such as reionization, have on the $TE$ and $EE$ spectra. We conclude just remembering the importance of measuring and analyzing the CMB polarization spectra to help removing parameter degeneracies in the $\Lambda$CDM model.

# Chapter 3

# Cosmological Measurements

This Chapter is devoted to describe all the cosmological measurements that we will consider in our following analyses. We firstly review the status of CMB experiments (Section 3.1), and then we present the other experimental data: Baryon Acoustic Oscillations (BAO, Section 3.2), local measurements of the Hubble parameter $H_0$ (Section 3.3), distance calibration with the SuperNovae of type Ia (Section 3.4), constraints on the matter power spectrum (Section 3.5), abundance of galaxy clusters (Section 3.6) and cosmic shear observations (Section 3.7).

## 3.1 Cosmic Microwave Background Radiation

The CMB was discovered accidentally by Penzias and Wilson in 1965 [17], who received the Nobel prize for their amazing discovery. Since then the CMB science had a terrific improvement. The first detection of the CMB anisotropies above the dipole was achieved by the COBE experiment in 1992 [18], which stimulated a new generation of CMB detectors that culminated with WMAP [19] and Planck. Most of the analyses we will present in the following chapters are based on the measurements of the CMB anisotropies, mainly as detected by the Planck satellite. These results are described in Subsection 3.1.1. We discuss also the results obtained by Earth-based high-precision experiments such as ACT and SPT (Subsection 3.1.2) and the constraints from the $B$-mode polarization experiments, such as the recent claims by BICEP2 and BICEP/Keck, and the joint analysis presented by the BICEP/Keck and Planck collaborations (Subsection 3.1.3).

### 3.1.1 Planck

Planck is a space-based mission designed to measure with extreme accuracy the spectra of CMB anisotropies, both in temperature and polarization. Launched in 2009, Planck probes the microwave emission at nine different frequencies, using two different instruments: the Low Frequency Instrument (LFI) and the High Frequency Instrument (HFI). The different frequencies are used to separate the foreground contributions, mainly coming from the Milky Way, from the signal of the CMB. HFI completed its survey in January 2012, while LFI collected data until October 2013. The data were analyzed and published in two branches. The first release, in 2013, contained the data of the first 15.5 months of operations [20]. With the second release in 2015 [21] all the maps were published, but the analyses still requires further studies of the polarization spectra and a third version of the likelihood codes is expected.

#### CMB temperature and polarization

The Planck collaboration released the first public data and codes in 2013 [20]. In this release, only the full temperature spectrum obtained by the Planck data was presented [60]. The CMB temperature auto-correlation spectrum is obtained from LFI and HFI data using

different methods for the low-$l$ and for the high-$l$ part of the spectrum, that would require otherwise an enormous computation time. The spectrum at low multipoles, $2 \leq l \leq 49$, is obtained from the maps between 30 and 353 GHz, using a fraction of sky equal to 91%. For the spectrum at high multipoles, $l \geq 50$, the maps at 100, 143 and 217 GHz were considered and a Gaussian approximation was adopted. As the polarization data from the Planck satellite were not satisfactory at the time of the first release, the Planck collaboration decided to include the WMAP polarization likelihood for the low multipoles [19, 61] at $l \leq 23$ (denoted WP).

In the second data release [21], the Planck collaboration presented the full mission data obtained by the Planck satellite. The analyses of the CMB maps to obtain the spectra and the likelihood were also improved. The second public likelihood code includes the $E$-mode polarization through the $TE$ cross-correlation and the $EE$ auto-correlation spectra. The low-$l$ likelihood includes temperature and polarization up to $l = 29$, for a total sky fraction of 94%, and it is obtained from the 70 GHz (LFI) map, cleaned with the measurements of the 30 GHz (LFI) and the 353 GHz (HFI) for the polarized synchrotron and dust templates, respectively [62]. The high-$l$ part of the spectrum, instead, is obtained with the same Gaussian approximation adopted in the first release, but for the multipoles $30 \leq l \leq 2500$. For the temperature spectrum, the HFI maps at 100, 143 and 217 GHz were used with the 66%, 57% and 47% of the sky retained, respectively. For the polarization spectra, instead, the same HFI maps were used with a fraction of sky of 70%, 50% and 41%, respectively, to exclude the sky regions where the dust signal is larger.

**CMB lensing**

The presence of large scale structures induces a dependency in the CMB observables that is connected with gravitational lensing. Late time geometry and clustering can then have an impact on CMB the fluctuations, which in turn can be used to probe the strength of the gravitational accretion after recombination. Being originated at the last scattering, the CMB fluctuations are more affected by the lensing due to structures at $z \simeq 2$, that is half-way to the last-scattering surface, while important effects at low multipoles ($l \leq 60$) are caused also by sources at smaller redshift.

Gravitational lensing in CMB maps is mainly observed as a smoothing of the acoustic peaks and troughs in the temperature and polarization maps, a conversion from $E$- to $B$-mode polarization and a production of late-time non-Gaussianities, that have the form of a non-zero connected 4-point function. The temperature and polarization likelihoods from Planck include the smoothing effect, that is then considered in all the analyses, but it is possible to study separately the measurements of the power spectrum $C_l^{\phi\phi}$, where $\phi$ is the lensing potential. This spectrum is extracted from the 4-point correlation functions involving both temperature and polarization, as discussed in Refs. [63] and [64] for the 2013 and 2015 releases, respectively. The power of these lensing measurements is that they allow to constrain the late-time expansion, the geometry and the clustering of matter using CMB data alone.

The CMB lensing likelihood is constructed as a simple Gaussian approximation of the estimated $C_l^{\phi\phi}$, covering the multipole range $40 \leq l \leq 400$. The lower limit of this interval is conservatively chosen in order to avoid problems in the difficult reconstruction of the lensing potential at large scales, that is the consequence of the large "mean-field" due to survey anisotropies. A less conservative choice could involve multipoles starting from $l = 8$. The upper limit, instead, is fixed to exclude the multipoles at which there is a marginal evidence of residual systematics in the reconstruction of the lensing deflections from the temperature maps only [64].

### 3.1.2 High-multipoles Experiments

The advantage of earth-based CMB missions is that they have an higher angular resolution, but they are limited in the sky coverage. Detections from earth-based experiments can

help to study the high-$l$ tail of the CMB spectrum after appropriate calibrations with the low-$l$ spectrum observed by space-based missions. The study of the high-$l$ tail of the CMB spectrum allows to constrain better the nuisance parameters used in the likelihood codes to model some unresolved foreground contributions, such as the kinetic SZ effect. In part of the following analyses we will consider the results presented by the two experiments ACT and SPT, that we introduce now.

The Atacama Cosmology Telescope (ACT) was settled in the Chilean Andes and it mapped the sky in two distinct regions: the equatorial stripe (ACTe) along the celestial equator and a stripe along $-55°$ of declination, that is called the southern stripe (ACTs). Observations lasted from 2007 to 2010 and covered approximately 600 deg$^2$ of sky. The ACT survey covered the multipole ranges $540 \leq l \leq 9440$ at the frequency of 148 GHz and $1540 \leq l \leq 9440$ at the frequency of 218 GHz [65].

The South Pole Telescope (SPT) observed a different portion of sky of 2540 deg$^2$ at $2000 \leq l \leq 11\,000$ [66]. In our analyses we used the incomplete results obtained for $650 \leq l \leq 3000$ at the frequency of 150 GHz [67, 68] and for $2000 \leq l \leq 10\,000$ at the frequencies of 95, 150 and 210 GHz, obtained observing a region of 800 deg$^2$ [69].

For the ACT/SPT data we use the prescriptions and the likelihood code described in Ref. [70].

### 3.1.3 Tensor Perturbations

We stated that the search of primordial tensor perturbations is of crucial importance for studying inflation. The tensor fluctuations, however, have an amplitude that is suppressed with respect to scalar fluctuations, and therefore it is much more difficult to detect them experimentally.

In 2014, the BICEP2 experiment reported the first claim [71] for the detection of a signal of $B$-mode polarization anisotropies, that they associated to primordial tensor modes. If the BICEP2 signal had been caused by the existence of primordial gravitational waves, a preference for a tensor-to-scalar ratio $r \simeq 0.2$ would have been reported, in apparent conflict with the Planck and WMAP constraints $r \lesssim 0.1$ [19, 44, 72], that however are highly model dependent. A subsequent study performed by the Planck collaboration showed that the BICEP2 experiment observed a region were a non-negligible contamination from dust emission was present [73]. After some months the BICEP collaboration presented updated results that consider in addition of the data taken by the Keck array [74, 75]. The signal of the existence of $B$-modes was reported by the BICEP/Keck (BK) collaboration, but not in association with their possible primordial origin. In fact, a joint analysis of the BICEP/Keck and Planck collaborations [76] finally demonstrated the dust origin of the measured $B$-modes. After removing the dust contribution, the signal of primordial tensor modes disappears and the constraints on the tensor-to-scalar ratio are compatible with $r = 0$. As a consequence, we do not have any evidence that inflationary tensor modes exist.

Several other experiments aim to measure the signals of primordial gravitational waves. The largest contribution to the $B$-mode polarization spectrum, however, comes from the leak of $E$-mode polarization, that are partially converted into $B$-modes through gravitational lensing. The first detection of the lensing $B$-mode spectrum comes from the SPTPol experiment [77, 78]. This detection is not important for constraining inflation, since it does not concern primordial tensor modes, but it confirms the predictions of General Relativity about gravitational lensing.

## 3.2 Baryon Acoustic Oscillations

BAO measurements and their implications in cosmology has been reviewed in Refs. [79, 80]. We present a less detailed treatment for length purposes.

Acoustic oscillations imprint a characteristic scale in the clustering of matter, providing a cosmological *standard ruler* that can be measured in the power spectrum of CMB fluctuations

and of large-scale structures, at small redshift [49,50,81–83]. The BAO distance is computed from first principles, differently than the distance measurements that involve SN Ia, which are calibrated against objects in the local Universe [84–86]. The sharpening of the BAO precision at higher redshifts, the difference between absolute and relative measurements and the completely independent systematic uncertainties make the BAO and SN Ia methods highly complementary tools to measure the cosmic expansion history and to test DE models. Combining the SN Ia results for relative distances and the BAO measurements, it is possible to derive constraints on $H_0$ using an *inverse distance ladder*. This essentially requires to use the SN Ia data to transfer the information on the absolute calibration of the BAO scale from the intermediate redshifts, where it is measured with high precision, to $z = 0$. The line-of-sight detection of BAO, indeed, allows to obtain a direct determination of the expansion rate $H(z)$ at the probed redshift, in addition to the transverse direction detection that allows to obtain the angular diameter distance $d_A(z)$.

### 3.2.1 BAO Physics

The imprint of the BAO is visible in the matter power spectrum at late times. We discussed in the previous Chapter the coupled baryon-photon oscillations, consequence of the competing forces of gravity and radiation pressure. We want now to qualitatively describe how they influence the matter distribution at late times. For this purpose, we can consider a single, spherical density perturbation that propagates outwards in the tightly coupled fluid as an acoustic wave with a speed $c_s$, written in Eq. (2.8). Fig. 3.1, from Ref. [87], contains useful plots to help visualizing the phenomena we are going to describe. At the beginning, the photon (red line) and baryon (blue line) perturbations move together, dragging the dark matter (black line) perturbations through gravity (top right panel). Matter perturbations moves also outwards, but delayed (top left panel) because the interaction is only gravitational, while photons and baryons interact mainly electromagnetically. At the time of photon decoupling, the radiation pressure on the baryons disappears and the baryon wave stalls (middle left panel). Neutrinos (green line), that are already decoupled, and photons free stream away, forming the Cosmic Neutrino Background (CNB) and the CMB radiation (middle right panel). The characteristic radius of the spherical shell formed by the stalled baryon wave is imprinted in the baryon density as a significant excess at this time. From now on, the gravitational interaction is the only force that drives the evolution, affecting dark matter and baryons. Since the dark matter and the baryon profiles are peaked at different radii, what happens is that the dark matter pulls baryons towards the peak in the origin, while baryons continue to drag the dark matter towards the overdensity at ~150 Mpc (bottom left panel). The final profiles have a significant overdensity near the center and a smaller peak (bottom right panel) at the scale $r_{drag}$, that is the sound horizon at the end of the baryon drag.

As it is impressed in the dark matter and baryon distributions, the slight excess at $r_{drag}$ appears also in the distribution of galaxies we can observe today. As firstly suggested in Ref. [88], this feature can be used to constrain the cosmological parameters. To do this, one has to reconstruct the typical distance that, at each different redshift, has the role of a statistical standard ruler. The easiest way to distinguish it is through the two-point correlation function or through its Fourier counterpart, the power spectrum. In the power spectrum, the excess at the galaxy separation distance $r_{drag}$ appears in the forms of oscillations, that are typically easy to recognize. The line-of-sight and the tangential Fourier oscillating modes can be measured separately, so that both the Hubble parameter $H(z)$ and the angular diameter distance $d_A(z)$ can be measured. The experimentally observed modes, however, contain components of both, and consequently $H(z)$ and $d_A(z)$ are partially anti-correlated.

For the BAO analyis, the situation is different from the analyses where the data points are fixed and the different models must be fitted. To compute the data points, indeed, a redshift-distance relation must be assumed to convert the points from the redshift space, after which the power spectrum is constructed, to the physical space, and vice versa. The dependence on the fiducial model is typically ignored in the analyses involving BAO data,
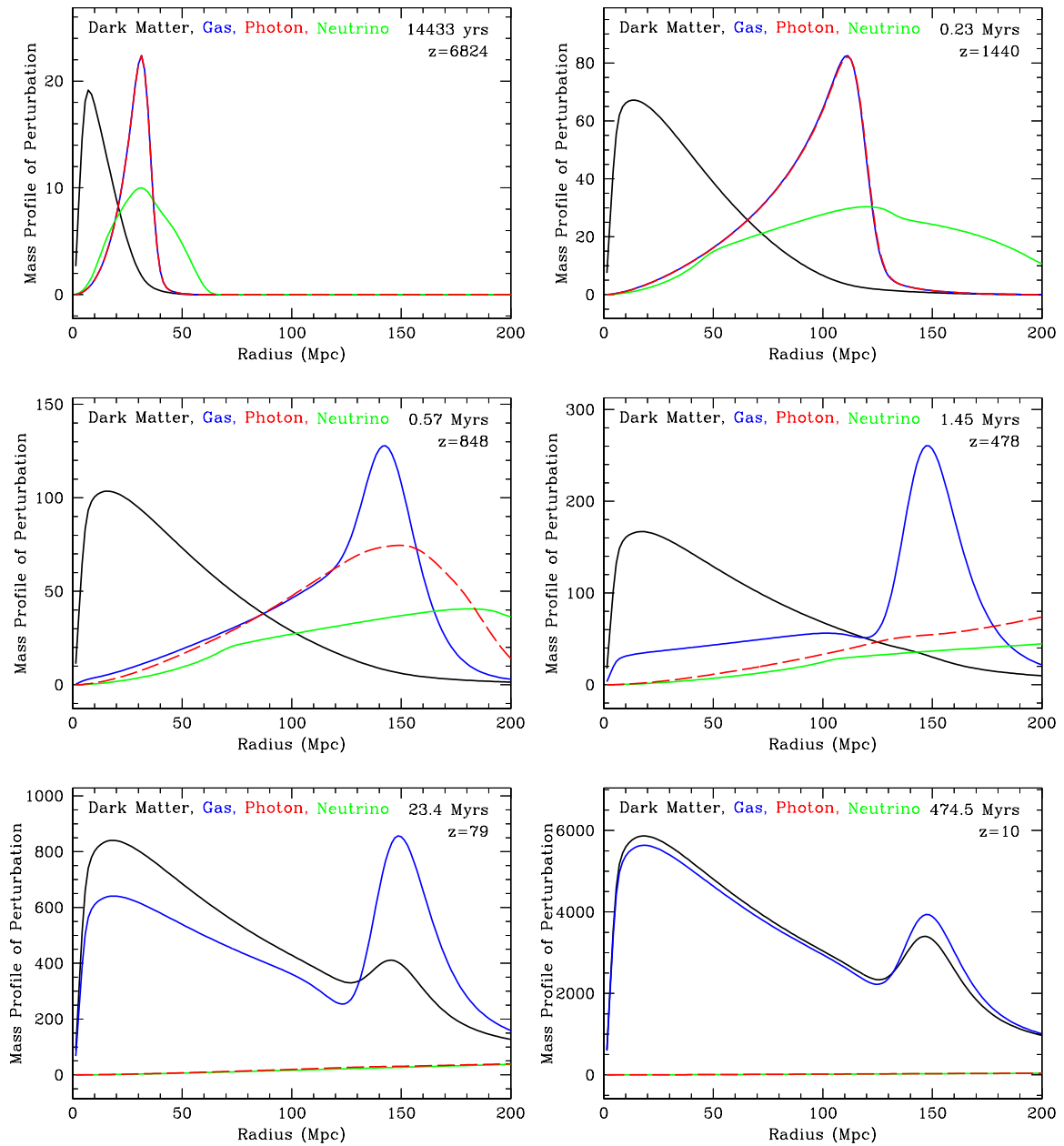
Figure 3.1: Evolution of the radial mass profile versus the comoving radius of an initially point-like overdensity located at the origin. The perturbations in dark matter (black), baryons (blue), photons (red) and neutrinos (green) are plotted. The perturbations are evolved from early times ($z = 6824$, top left) to $z = 10$ (bottom right), long after the recombination. At the initial time, photons and baryons travel outwards as a pulse. The drag of the coupled baryon-photon fluid on dark matter is only gravitational and it produces a delayed enhancement of the cold dark matter profile (top right). The photon and the baryon profiles decouple at recombination (middle left), when the photons leak away from the baryons. After recombination is complete (middle right), the photons continue to free-stream away. Gravitational instability now takes over, and the overdensities start to grow (bottom left). Dark matter pulls baryons towards the central overdensity, while baryons drag dark matter towards the overdensity at 150 Mpc, that is still visible in the mass profile at late times (bottom right). From Ref. [87].

since the results are almost insensitive to this choice, if one does not range far from the assumed fiducial model. We will explore this point more in details in the next subsection, where we will discuss the analyses of the BAO data.

### 3.2.2 BAO Analysis

In a flat Universe, the comoving angular diameter distance $d_M(z)$ is

$$d_M(z) = \frac{c}{H_0} \int_0^z dz' \frac{H_0}{H(z')} . \tag{3.1}$$

The comoving angular diameter distance $d_M$ must not be confused with the proper angular diameter distance $d_A$ we introduced in Section 1.6. They are related by $d_M = d_A(1 + z)$. From Eq. (1.44) we obtain that the luminosity distance $d_L$, relevant to supernovae, is $d_L = d_M(1 + z)$.

The Hubble factor in Eq. (3.1) can be calculated from the Friedmann equation (1.25) with the contributions of the energy densities of all the species existing in the Universe. The densities of CDM and baryons scale as $a^{-3}$, while that of DE depends on the equation of state, being proportional to $a^{-3(1+w)}$. We will discuss in more details the aspects of neutrino cosmology in the dedicated Chapter 4, but we anticipate here that the most complicate energy density dependence to be obtained is for the energy density of massive neutrinos, since they behave differently when relativistic or non-relativistic. The contribution of neutrinos, photons and other relativistic particles can be written as [80]

$$\Omega_{\nu+r}(a) = \frac{C}{H_0^2} \left[ T_\gamma^4 + T_\nu^4 \sum_i I(m_i/k_B T_\nu) \right] , \tag{3.2}$$

where $C$ is a normalization constant, obtained as a combination of fundamental constants, and $k_B$ is the Boltzmann constant. The photon temperature $T_\gamma$ scales with $a^{-1}$, as the neutrino temperature $T_\nu = T_\gamma(4/11)^{1/3}g_s$. The factor $g_s = (3.046/3)^{1/4}$ encodes the small reheating of the neutrinos at the electron decoupling. The integral $I$ is defined as [80]

$$I(r) = \frac{15}{\pi^4} \int_0^\infty dx\, x^2 \frac{\sqrt{x^2 + r^2}}{e^x + 1} \tag{3.3}$$

and must be evaluated separately for the different neutrino mass eigenstates. For massless neutrinos $I(0) = 7/8$, while for heavy neutrinos ($r \gg 1$) it tends to $I(r) \simeq 45\,\zeta(3)\,r/(2\pi^4)$, where $\zeta$ is the Riemann function. In the limit $r \gg 1$, the integral $I(r)$ scales with $a$ and the energy density scales correctly with $a^{-3}$, as for pressureless matter (CDM, baryons).

The BAO scale is set by the radius of the sound horizon at the time of photon decoupling (the end of the baryon drag), $r_{\rm drag}$, that can be written as

$$r_{\rm drag} = \int_{z_{\rm drag}}^\infty \frac{c_s(z)}{H(z)} dz , \tag{3.4}$$

where $z_{\rm drag}$ is the redshift of the drag epoch, when photon-baryon decoupling occurred, and the sound speed $c_s$ is defined in Eq. (2.8). The definition in Eq. (3.4) is sufficiently accurate for reasonable variations of the fiducial model, but it must be evaluated numerically with a full Boltzmann code computation to obtain very precise BAO measurements.

The robustness of BAO measurements comes from the fact that a sharp feature in the correlation function cannot be mimicked by any kind of systematics. The BAO scale is determined assuming a set of fiducial parameters in the cosmological model, to define the redshift-distance relation. In an isotropic fit, that does not distinguish the directions parallel and perpendicular to the line-of-sight, the measurement is encoded in the parameter $\alpha$, that is the ratio of the measured BAO scale divided by the one predicted by the fiducial model. In an anisotropic fit, instead, the ratios perpendicular and parallel to the line of sight, $\alpha_\perp$ and

| Name | Redshift | $D_V/r_{\mathrm{drag}}$ | $D_M/r_{\mathrm{drag}}$ | $D_H/r_{\mathrm{drag}}$ | $r_{off}$ |
|---|---|---|---|---|---|
| SDSS (DR7) | 0.35 | $8.88 \pm 0.17$ | | | |
| 6dFGS | 0.106 | $3.047 \pm 0.137$ | – | – | – |
| MGS | 0.15 | $4.480 \pm 0.168$ | – | – | – |
| BOSS DR9 | 0.57 | $13.67 \pm 0.22$ | | | |
| BOSS DR11 LOWZ | 0.32 | $8.467 \pm 0.167$ | – | – | – |
| BOSS DR11 CMASS | 0.57 | – | $14.945 \pm 0.210$ | $20.75 \pm 0.73$ | $-0.52$ |

Table 3.1: BAO constraints used in the following Chapters. These values are taken from [89] (SDSS DR7), [90] (6dFGS), [91] (MGS), [92] (BOSS DR9), [93] (BOSS DR11).

$\alpha_\parallel$, must be considered separately. The errors on $\alpha_\perp$ and $\alpha_\parallel$ are usually correlated within the same redshift slice in a real survey, but they are uncorrelated across different redshift slices. Even if the values of $\alpha$ are derived within a fiducial model, the BAO feature is independent of the choice of the fiducial model, within a reasonable range.

While the various $\alpha$ are determined for a specific fiducial model, the conversion to any other model is straightforward. In an anisotropic fit, a measurement at redshift $z$ of the parameter $\alpha_\perp$ constrains the ratio of the comoving angular diameter distance to the sound horizon at the same redshift:

$$\frac{D_M(z)}{r_{\mathrm{drag}}} = \alpha_\perp \frac{D_{M,\mathrm{fid}}(z)}{r_{\mathrm{drag,fid}}}\,, \tag{3.5}$$

while a measurement of the parameter $\alpha_\parallel$ constrains the Hubble parameter $H(z)$:

$$\frac{D_H(z)}{r_{\mathrm{drag}}} = \alpha_\parallel \frac{D_{H,\mathrm{fid}}(z)}{r_{\mathrm{drag,fid}}}\,, \tag{3.6}$$

having defined

$$D_H(z) = 1/H(z)\,. \tag{3.7}$$

In the isotropic case, instead, the analysis measures a combination of these distances. If the redshift-space distortions are weak, the constrained quantity is the volume averaged distance $D_V$, defined as

$$D_V(z) = [zD_M^2(z)D_H(z)]^{1/3}\,. \tag{3.8}$$

The constraint from the isotropic fit is then:

$$\frac{D_V(z)}{r_{\mathrm{drag}}} = \alpha \frac{D_{V,\mathrm{fid}}}{r_{\mathrm{drag,fid}}}\,. \tag{3.9}$$

The BAO measurement allows to constrain the cosmological parameters through their impact on the sound horizon radius $r_{\mathrm{drag}}$ and on the distances $D_H$ and $D_M$. For standard cosmological models, the error on $r_{\mathrm{drag}}$ as obtained from the CMB analyses is small with respect to the errors on the BAO measurements, so the constraints come mainly from the distances $D_M$ and $D_H$ (or $D_V$ for the isotropic analyses). We show in Table 3.1 the results in terms of $D_M/r_{\mathrm{drag}}$, $D_H/r_{\mathrm{drag}}$ or $D_V/r_{\mathrm{drag}}$ for the different experiments we will consider in the cosmological analyses presented in the following Chapters. The quoted redshift is usually an effective redshift, determined using the statistical contributions of each sample to the BAO measurement. Since the anisotropic analyses yields to anti-correlated errors on $D_M$ and $D_H$, the last column of Tab. 3.1 contains the correlation coefficient in the relevant case.

### 3.2.3 BAO measurements

The most precise BAO measurements today come from the analysis of the Baryon Oscillation Spectroscopic Survey (BOSS) DR12 galaxy sample [94, 95], that is the final BOSS release. BOSS uses the same telescope of the original Sloan Digital Sky Survey (SDSS), with

improved spectrographs. The total sample is composed of two distinct subsets of galaxies, selected by different color cuts and luminosity fluxes: the CMASS sample within $0.43 < z < 0.7$, corresponding to an approximately constant threshold for the galaxy stellar masses, and the LOWZ sample, in the range $0.15 < z < 0.43$. Both the samples are analyzed with reconstruction algorithms in order to partly revert the non-linear effects and to improve the measurement precision. In part of the analyses presented in the next Chapters we will use the former BAO data obtained from the BOSS samples as presented in the DR9 [92,96] and DR11 [93] releases (Tab. 3.1). In DR9, the CMASS statistics was not sufficient to perform an anisotropic analysis, as it has been done in DR11 and DR12 instead. Since the LOWZ sample is smaller, only in the DR12 the anisotropic analysis has been performed on it, while in DR11 the results were firstly reported only for the isotropic fit.

Part of the analyses presented in the next Chapters involves other BAO measurements from the SDSS, namely the SDSS DR7 isotropic results [89,97,98] and the recent re-analysis of the SDSS main galaxy sample (MGS) data [91], that uses reconstruction to improve the former BAO measurement. Further BAO measurements include the results from the Six Degree Field Galaxy Survey (6dFGS) [90,99], which carries small statistical weight due to the less precise constraints, and the results from the WiggleZ survey [100,101], which sample a fraction of sky that partly overlaps with the BOSS volume. Due to the overlap with the more precise BOSS data, we do not consider the WiggleZ BAO measurements in our calculations.

We will not discuss, finally, the constraints on the BAO feature at high redshifts, $z > 2$, which can be obtained from the auto-correlation of the Lyman-$\alpha$ forest fluctuations in the spectra of high-redshift quasars. The first detection of the BAO scale from the Lyman-$\alpha$ forest was firstly obtained by BOSS DR9 [102–104], following the pioneering work [105].

### 3.2.4 Redshift-Space Distortions

The growth rate of the cosmic structures is a strong test for discriminating between different cosmological models. The evolution of these structures takes place in a Universe where all the material moves within the comoving frame, so that also the galaxies follow this peculiar velocity field. The observed galaxy redshift depends both on the peculiar velocities of the objects and on the global recessional velocity induced by the Hubble flow. If only the Hubble flow is considered when converting from redshifts to distances, the local velocities cause a distortion of the redshift reconstruction. These distortions are referred to as Redshift-Space Distortions (RSD, see e.g. Ref. [106]). RSD are more important for near objects, since the velocity caused by the Hubble flow is small and the peculiar motions can be relevant.

In the context of the standard General Relativity predictions for the growth rate, it is possible to derive a relation at linear order between the redshift-space galaxy power spectrum $P_{gg}^s$ and the real-space matter power spectrum $P_{mm}^s$. This relation includes a dependence on the angle to the line of sight [107, 108]:

$$P_{gg}^s(k, \mu) = P_{mm}^s(k)(b_\delta + b_v f \mu^2), \qquad (3.10)$$

where $b_\delta$ accounts for a linear deterministic bias between galaxy and matter overdensity fields, $b_v$ allows for a linear bias between galaxy and matter velocity distributions, usually assumed to be one, $f$ is the logarithmic derivative of the growth factor with respect to the scale factor and $\mu$ is the cosine of the angle to the line of sight. We learn from Equation (3.10) that the component owing to RSD depends only on cosmological quantities: the growth rate, depending on the redshift, and the amplitude of matter fluctuations at a given time. It has been shown that the parameter combination $f(z)\sigma_8(z)$ is a good discriminant between models of modified gravity that can be tested with RSD [109] The parameter $\sigma_8$ is the root mean square of the amplitude of matter fluctuations inside a sphere of $8h^{-1}$ Mpc radius.

The dominant non-linear contribution to the RSD signal, at small scales, is due to the peculiar motions of the galaxies inside the DM halos. The peculiar velocities can be large enough that, when misinterpreted as Hubble velocities, lead to a stretching of the galaxy clusters reconstruction in the real space along the line-of-sight. The shape of the cluster in

the real space after the wrong reconstruction is referred to as "Fingers of God" (FoG). This effect can be approximated with an additional term in Eq. (3.10) that reduces the power at small scales. The approximations, however, are not very accurate and a precise description still requires the higher-order solutions in perturbation theory [110–113].

RSD are related to distance measurements and not to angles, but the distortions may affect also angles reconstruction. This happens for example when determining projected angular clustering of galaxies, if the samples are selected using redshift-dependent quantities. In general, clusters and voids within a sample tend to "push-in" and "push-out" the near galaxies, respectively, so that both positive and negative overdensities are increased, with a consequent distortion of the reconstructed power spectrum.

Currently, the most recent constraints on the RSD signal come from the BOSS experiment we mentioned in the discussion dedicated to BAO. In particular, the last results come from BOSS DR12 [114], but in our analyses we shall use the results given by the analysis of the BOSS DR11 data, presented in Ref. [115]. Other experiments that presented results on the RSD are 6dFGS [116], WiggleZ [117], BOSS-CMASS with other different analysis methods [118, 119] and the VIMOS Public Extragalactic Redshift Survey (VIPERS) [120].

## 3.3 Hubble parameter

We include in some of our analyses the constraints on the Hubble parameter $H_0$, the expansion rate of the Universe today, as determined in the local Universe.

The Hubble parameter can be constrained by CMB observations in the context of the $\Lambda$CDM model. The bounds on $H_0$ from CMB are typically lower than the local measurements [44, 72]. One must remember that $H_0$ constraints from CMB are derived results and they are considerably model dependent, but they have the advantage of not suffering the existence of systematics in the measurement. The most recent Planck result in the $\Lambda$CDM model is $H_0 = 67.3 \pm 1.0$ Km s$^{-1}$ Mpc$^{-1}$, obtained using CMB temperature autocorrelation and polarization on large scales only [44]. Let us emphasize, however, that the Planck value of $H_0$ reported above has been obtained assuming the standard $\Lambda$CDM cosmological model. If one extends the $\Lambda$CDM model, the results for $H_0$ can change significantly. For example, if one considers as an additional parameter the effective number of relativistic degrees of freedom $N_{\text{eff}}$ that we will introduce in Chapter 4, the analysis of CMB data lead to[1] $H_0 = 68.0^{+2.6}_{-3.0}$ km s$^{-1}$ Mpc$^{-1}$.

The cosmological constraint can be compared with the results obtained by local determinations, that in turn can suffer the existence of unaccounted systematics, but do not depend on a specific cosmological model. Using the SN Ia detected by HST, with Cepheid-calibrated distances, the authors of Ref. [121] found $H_0 = 73.8 \pm 2.4$ Km s$^{-1}$ Mpc$^{-1}$. Using the same SN Ia set with different calibrations for the distance it is possible to derive some slightly different value: for example, when a new calibration of the NGC 4258 distance is used to calibrate the HST Cepheid distances, it is possible to obtain $H_0 = 72.0 \pm 3.0$ Km s$^{-1}$ Mpc$^{-1}$ [122]. A different reanalysis of the HST SNe leads to $H_0 = 70.6 \pm 3.3$ Km s$^{-1}$ Mpc$^{-1}$ (using NGC 4258 as a distance anchor) and to $H_0 = 72.5 \pm 2.5$ Km s$^{-1}$ Mpc$^{-1}$ (averaging over three different distance-calibration methods) [123]. Other calculations show that $H_0 = 74.3 \pm 2.6$ km s$^{-1}$ Mpc$^{-1}$, obtained by the Carnegie Hubble Program [124] through a recalibration of the secondary distance methods used in the HST Key Project, or $H_0 = 78.7 \pm 4.5$ km s$^{-1}$ Mpc$^{-1}$, from the strong gravitational lensing time delay measurements of the system RXJ1131-1231, observed as part of the COSmological MOnitoring of GRAvitational Lenses (COSMOGRAIL) project [125].

The significance of the tension between local and CMB results on $H_0$ depends hence on the calibrations of the SN Ia distances. The result $H_0 = 70.6 \pm 3.3$ Km s$^{-1}$ Mpc$^{-1}$ obtained in Ref. [123] is consistent with the CMB result within $1\sigma$, but typically other determinations are in tension with the Planck result at the level of 2 to $3\sigma$. If a reliable determination of $H_0$

---

[1] See page 185 of the tables with 68% limits available at `http://wiki.cosmos.esa.int/planckpla/index.php/File:Grid_limit68.pdf`.

from local measurements will be confirmed in the future, we will have a strong evidence that the $\Lambda$CDM model is not complete.

## 3.4   Supernovae

As we mentioned earlier, Supernovae of the type Ia (SN Ia) are believed to be standard candles, that means that a SN Ia has always the same luminosity. Under this hypothesis, SN Ia are one of the best probes to verify the redshift-distance relation, since they provide a direct measurement of the luminosity distance, independently of the redshift determination. For this reason, SN Ia can be used to constrain the Universe expansion history. We shall include in the following analyses the constraints obtained using the Joint Lightcurve Analysis (JLA) compilation [126], which include the SN Ia observations obtained by the SDSS-II and SNLS collaborations, for a total of 740 SN Ia. The dataset includes several samples at low-redshift from different experiments ($z < 0.1$), the observations from all the seasons of the SDSS-II ($0.05 < z < 0.4$), and those collected by SNLS in three years ($0.2 < z < 1$), plus a number of SN Ia at high redshift ($0.8 < z < 1.2$) from HST.

## 3.5   Matter Power Spectrum

The gravitational collapse, that started to act in the initial phases of the Universe evolution, formed a number of structures that fill the Universe. These structures are observed through the light they emit when the gas is compressed and heated. The analysis of this light permits to test our theoretical models of structure formation, starting from the tiny density fluctuations that were generated during inflation. The increasing precision of the experiments requires a correspondingly good precision in the predictions from theory, from which we want to obtain the shape of the galaxy power spectrum (or the correlation function). At the linear level, we can make predictions using perturbation theory. The problems appear when we want to go beyond the linear theory, since the relationship between the observed galaxy power spectrum and the prediction for the matter power spectrum is complicated by the existence of non-linear structure formation, galaxy bias, and redshift space-distortions. The non-linear structure formation occurs when the density perturbations become large and the linear perturbation theory fails to describe them. While the linear theory is sufficient to describe CMB fluctuations, at low-redshift the matter power spectrum is the consequence of some non-linear evolution that can be estimated by numerical simulations [112, 127, 128] and then applied as a correction to the linear prediction using an algorithm as `Halofit` [129].

Beside the non-linear evolution, there is the problem that observations are affected by redshift-space distortions, as discussed in the previous Section, and by the problem of the galaxy bias. We observe the distribution of galaxies, but the theoretical predictions are obtained for the distribution of the total matter fluctuations, that include also DM. The complex phenomena that involve baryons in star and galaxy formation cause a slight decoupling between galaxies and matter. The simplest possibility is to assume the idea of the linear bias [130]: an overall, shape-independent amplitude that scales from the matter power spectrum to the galaxy power spectrum. The bias parameter is directly related to the history of galaxy formation of each population, and it is different for different populations of galaxies. For this reason, we expect that the bias parameter evolves with redshift and with the environment of each population, so that it is also scale-dependent. Today, numerical simulations of galaxies allow to predict the bias for each population of galaxies.

After considering all these effects that go beyond the linear regime, the theory is quite robust at low values of the comoving wavenumber $k$ (large scales), where the large-scale clustering can be treated as linear. The difference between the different models starts to increase at smaller scales, approximately for $k > 0.2h$ Mpc$^{-1}$.

The WiggleZ Dark Energy survey measured the matter power spectrum in four redshift bins and seven regions on the sky, giving 28 separate power spectra in total [101]. All of these

spectra are publicly available, including the window functions and covariance matrices. We use the measured matter power spectra in the four redshift bins $0.1 < z < 0.3$, $0.3 < z < 0.5$, $0.5 < z < 0.7$ and $0.7 < z < 0.9$. Since the analysis of the matter power spectrum is limited by the poor theoretical modeling of a number of effects, such as non-linearities, galaxy bias and redshift-space distortions, the WiggleZ collaboration presented several different methods for modeling the theoretical power spectrum and tested them against the N-body simulations named "Gigaparsec WiggleZ" (GiggleZ). The WiggleZ likelihood and published results take into account these analyses.

## 3.6 Cluster Counts

Another powerful probe to constrain the growth of cosmic structures is the abundance of galaxy clusters. The reliability of this probe is based on the calibration of the mass-observable relation, which is currently the largest uncertainty. It is the same problem we discussed for the RSD and the determination of the matter power spectrum. The cosmological information enclosed in the cluster abundance is encoded in a constraint on the so-called cluster normalization condition [131–133], that is the combination

$$\sigma_8 \left( \frac{\Omega_m}{\alpha} \right)^{\beta} , \qquad (3.11)$$

where $\alpha$ is a fiducial value adopted in each analysis and $\beta$ depends on the measured redshift. The full calculation of the cluster counts requires a hard and time consuming computation, that involves a geometrical determination of the cosmological volume element and that considers the number of halos for different redshift and mass bins.

We will use the measurements of the Chandra Project [134, 135], that observes galaxy clusters in the X-rays constraining $\sigma_8(\Omega_m/0.25)^{0.47} = 0.813 \pm 0.013$ and from the 2013 and 2015 release of Planck [136, 137], that counts the clusters through the Sunyaev-Zel'dovich effect. The Sunyaev-Zel'dovich (SZ) effect [49, 138] is the result of high energy electrons distorting the CMB spectrum through inverse Compton scattering, in which the low energy CMB photons receive an average energy boost during collision with the high energy cluster electrons. Observed distortions of the CMB spectrum are used to detect the density perturbations of the Universe. The Planck 2013 cluster count result can be written as $\sigma_8(\Omega_m/0.27)^{0.3} = 0.782 \pm 0.01$, obtained with a fixed mass bias, or as $\sigma_8(\Omega_m/0.27)^{0.3} = 0.764 \pm 0.025$, if the mass bias is free to vary. The Planck collaboration improved the analyses of the cluster counts in the 2015 release, taking into account with increased accuracy the possible dependence on the bias between the galaxy and the matter distribution. In this last case we do not write constraints in the form of Eq. (3.11), since additional dependencies on the nuisance parameters used to model the uncertainties have been introduced.

Some of the results from the cluster counts are in tension with the CMB constraints on $\sigma_8$, that is higher when obtained from the CMB than when obtained from local measurements. If more measurements of cluster counts are compared, however, it seems that there is not a clear indication that the cluster count measurements are in tension with the CMB predictions. A comparison between different methods is proposed for example in Ref. [139], where in Fig. 2 the constraints on $\sigma_8$ from the $\Lambda$CDM predictions obtained from CMB analyses are compared with the results of several experiment that probe the cluster counts detected through X-ray, optical and SZ surveys. The fact that some of the reported results are in good agreement with the CMB predictions may indicate that the anomalous measurements suffer the presence of unaccounted systematics, that possibly lead to a wrong estimate of the mass calibration (see also the discussion in Ref. [44]).

The tension between local and cosmological estimations of $\sigma_8$ may be the indication that our comprehension of the systematic effects that affect the experimental measurements is rather limited, but also that the $\Lambda$CDM model is incomplete and that some new physics is required. For example, the free-streaming of a massive neutrino or of a different light particle

would reduce the value of $\sigma_8$ on small scales and possibly reconcile local and cosmological measurements (see e.g. Refs. [22, 140] and the discussion in the following Chapters).

## 3.7 Cosmic Shear

The presence of large scale structures along the line of sight causes a distortion of the shape of distant galaxies, that can be used to constrain the growth of fluctuations.

Today, the largest weak lensing (WL) survey is the Canada-France-Hawaii Telescope Lensing Survey (CFHTLenS) [141, 142]. This experiment provides results from 2 types of analysis: from the analyses of 2D data to estimate the shear correlation functions $\xi^\pm$ from 0.9 to 296.5 arcmin [141], and from observations of the tomographic blue galaxy sample, that allows to estimate the shear correlation functions in six redshift bins, in the angular range $1.7 < \theta < 37.9$ arcmin. [142]. These two determinations are not independent and we will use only the results of the tomographic survey.

Since the non-linear scales contribute significantly to $\xi^\pm$, it is important to have a good modeling of the non-linear evolution to avoid the introduction of systematics in the analysis. The analyses at the angular scales probed by both the 2D and the tomographic data, however, may be affected by the poor knowledge of the non-linear evolution and by the consequent incomplete theoretical modeling. To avoid the uncertainties related to the numerical calculations in the non-linear regime, the CFHTLenS collaboration proposed a set of "conservative" cuts on the observed data. For the 2D analysis, the authors of Ref. [141] propose to exclude angular scales $\theta < 17'$ for $\xi^+$ and $\theta < 54'$ for $\xi^-$. For the tomographic analysis, instead, different cuts are proposed for each redshift bin. In the two lowest redshift bins, angular scales $\theta < 3'$ are excluded for $\xi^+$ and $\theta < 30'$ are excluded for $\xi^-$. In the two central redshift bins, the exclusions concern $\theta < 30'$ only for $\xi^-$, while no cuts are applied for $\xi^+$. Finally, in the highest redshift bins only a cut $\theta < 16'$ is applied to calculate $\xi^-$ [142]. The Planck collaboration argued that these "conservative" cuts may be insufficient if one wants to investigate extensions of the $\Lambda$CDM model [44, 143] and they proposed a set of "ultra-conservative" cuts, that consists in completely removing the $\xi^-$ analysis and restricting to angular scales $\theta > 17'$ for $\xi^+$, both in the 2D and the tomographic surveys. At the small scales relevant for the CFHTLenS experiment the effects of baryonic feedback and intrinsic alignment can also be important, but our knowledge and theoretical description of these effects is quite limited nowadays. More detailed discussions can be found in Refs. [44, 141, 142].

Even if one applies the ultra-conservative cuts, however, in the context of the $\Lambda$CDM model the Planck results are in substantial tension with the CFHTLenS results. According to the author of Ref. [144], this is a conclusion that cannot be obtained simply by studying the marginalized posterior probabilities for the cosmological parameters. The tension can be explained invoking the presence of some unaccounted systematics in the analysis of the experimental data or of an incomplete modeling of the theoretical predictions, but can also be the result of the existence of new physics beyond the standard model. The importance of precise local measurements is therefore high, since local measurements are not dependent on a specific cosmological model and they can help to explore cosmology in a model-independent way [145].

A recent analysis [146] of the CFHTLenS data that takes into account several astrophysical systematics, however, shows that the tension between Planck and the cosmic shear measurements disappears when the systematics are considered jointly. They find that the two data concordance tests are in agreement, and that the level of concordance between the two datasets depends on the exact details of the systematic uncertainties included in the analysis. The results of the concordance tests based on the Bayesian evidence and on information theory range from decisive discordance to substantial concordance while the treatment of the systematic uncertainties becomes more conservative. The least conservative scenario is the one most favored by the cosmic shear data, but it is also the one that shows the greatest degree of discordance with Planck. A future, robust result from local measurements that

will take into account all the possible systematics will either confirm the tension with CMB estimates of the cosmological quantities, probing that the $\Lambda$CDM model is incomplete and possibly suggesting us where to look for new physics, or confirm that the tension that we observe now is just due to an incomplete knowledge of some astrophysical phenomenon. These results are confirmed by an independent analyses by other authors [147].

# Chapter 4

# Neutrino Physics

*Part of this Chapter is based on Ref. [15].*

After the proposal of Pauli in 1930, who conjectured the neutrino to explain the problem of the $\beta$ decay spectrum, several years passed before the neutrino was firstly observed in 1956 by Cowan et al. [148]. B. Pontecorvo was the first to guess that more than a single flavor of neutrinos could exist, and also he proposed the possibility that the neutrinos oscillate between the different flavors. Only 30 years later neutrino oscillations were finally observed in the SuperKamiokande and in the Sudbury Neutrino Observatory experiments, which was recently awarded with the 2015 Nobel Prize in Physics. The discovery of neutrino oscillations was the definitive confirmation of the fact that neutrinos are massive particles, but their masses are much smaller than the masses of all the other particles in the Standard Model of electroweak interactions.

In this Chapter we will firstly introduce and discuss the most important aspects of the neutrino theory in particle physics, the short-baseline neutrino oscillation anomaly and its explanation with a light sterile neutrino, and finally we will show how cosmology can help to constrain the neutrino absolute mass scale and other properties.

## 4.1  Neutrino Masses and Oscillations

The electroweak interactions are described by the Standard Model (SM) of particle physics [149–151], a fantastic theory, based on the $SU(2)_L \times U(1)_Y$ gauge symmetry, which can explain the majority of terrestrial experimental observations. The SM does not account for neutrino masses, whose existence have been firmly verified by the measurement of neutrino oscillations in atmospheric, solar and long-baseline neutrino oscillation experiments (see e.g. Refs. [152–157]). The SM can be extended to include neutrino masses simply through the introduction of singlet fields for the $SU(2)_L \times U(1)_Y$ gauge symmetry, which are traditionally called *right-handed neutrino* fields or *sterile neutrino* fields. They are *right-handed* since they do not transform under the $SU(2)_L$ transformations. Assuming that they have zero hypercharge, they can be called *neutrino* fields since they are neutral. Finally, they are *sterile*, because they do not have SM electroweak interactions. These right-handed sterile neutrino fields are included in many models which extend the SM (see e.g. Refs. [158–163]). In the following we consider the general theory of neutrino mixing that includes the three standard active left-handed flavor neutrino fields $\nu_{eL}$, $\nu_{\mu L}$, $\nu_{\tau L}$ plus $N_s$ sterile right-handed flavor neutrino fields $\nu_{s_1 R}$, ..., $\nu_{N_s R}$. We can use these fields to write the most general Lagrangian mass term, that is[1]

$$\mathcal{L}_{\text{mass}} = \frac{1}{2} \nu_L^{(\text{F})T} \, \mathcal{C}^\dagger \, M \, \nu_L^{(\text{F})} + \text{h.c.} \,, \tag{4.1}$$

---

[1] In the following we will adopt the convention that the superscript "(F)" indicates the flavor basis, while the superscript "(M)" indicates the mass basis.

where $\mathcal{C}$ is the unitary charge-conjugation matrix[2], such that $\mathcal{C}\gamma_\mu^T\mathcal{C}^{-1} = -\gamma_\mu$ and $\mathcal{C}^T = -\mathcal{C}$, and

$$\nu_L^{(F)} = \begin{pmatrix} \nu_L^{(a)} \\ \nu_R^{(s)c} \end{pmatrix}, \qquad \nu_L^{(a)} = \begin{pmatrix} \nu_{eL} \\ \nu_{\mu L} \\ \nu_{\tau L} \end{pmatrix}, \qquad \nu_R^{(s)c} = \begin{pmatrix} \nu_{s_1 R}^c \\ \vdots \\ \nu_{s_{N_s} R}^c \end{pmatrix}. \tag{4.2}$$

Here we used the superscripts "(a)" and "(s)" to indicate the column matrices of active and sterile neutrino fields, respectively. For any field $\psi$ the charge-conjugated field $\psi^c$ is given by $\psi^c = \mathcal{C}\overline{\psi}^T$. Charge conjugation transforms the chirality of a field: for example, $\psi_R^c$ is left-handed. In general, the mass matrix $M$ is a complex symmetric matrix, which can be diagonalized with the unitary transformation

$$\nu_L^{(F)} = \mathcal{U}\,\nu_L^{(M)}, \qquad \text{with} \qquad \nu_L^{(M)} = \begin{pmatrix} \nu_{1L} \\ \vdots \\ \nu_{NL} \end{pmatrix}, \tag{4.3}$$

where $N = 3 + N_s$ is the total number of neutrino fields. The $N \times N$ unitary matrix $\mathcal{U}$ has the property that

$$\mathcal{U}^T M \mathcal{U} = \text{diag}(m_1, \dots, m_N)\,, \tag{4.4}$$

where $m_1, \dots, m_N$ are real and positive masses (see Refs. [152, 164]). Using the definitions we just presented, the Lagrangian mass term (4.1) becomes

$$\mathcal{L}_{\text{mass}} = -\frac{1}{2}\sum_{k=1}^{N} m_k \overline{\nu_k}\nu_k, \tag{4.5}$$

where $\nu_k = \nu_{kL} + \nu_{kL}^c$ are massive Majorana neutrino fields, since they satisfy the Majorana constraint $\nu_k = \nu_k^c$. This means that, in the general case of active-sterile neutrino mixing, the massive neutrinos are Majorana particles[3].

The unitary transformation (4.3) has physical effects connected with the non-invariance of the weak interaction Lagrangian under a rephasing of the lepton fields. We can write the leptonic charged-current weak interaction Lagrangian in a matrix form, using the flavor basis where the mass matrix of the charged leptons, $\ell_e \equiv e$, $\ell_\mu \equiv \mu$, $\ell_\tau \equiv \tau$, is diagonal:

$$\mathcal{L}_{\text{CC}} = -\frac{g}{\sqrt{2}}\overline{\ell_L}\gamma^\rho\nu_L^{(a)}W_\rho^\dagger + \text{h.c.} = -\frac{g}{\sqrt{2}}\overline{\ell_L}\gamma^\rho U\nu_L^{(M)}W_\rho^\dagger + \text{h.c.}\,, \tag{4.6}$$

where we used

$$\ell_L = \begin{pmatrix} e \\ \mu \\ \tau \end{pmatrix}, \qquad \nu_L^{(a)} = U\nu_L^{(M)} \qquad \text{and} \qquad U = \mathcal{U}|_{3\times N}\,. \tag{4.7}$$

The $3 \times N$ rectangular matrix $U$ is formed by the rows of $\mathcal{U}$ corresponding to the active neutrinos and it can be parameterized with a number of mixing parameters smaller than those necessary for the unitary matrix $\mathcal{U}$. This is a consequence of the fact that weak interactions are not affected by the arbitrariness of the mixing in the sterile sector. It is possible to show [152] that the mixing matrix $U$ can be written in terms of $3 + 3N_s$ mixing angles and $3 + 3N_s$ physical phases, divided into $1 + 2N_s$ Dirac phases and $N - 1$ Majorana phases. A convenient scheme for this parameterization is

$$U = \left[\left(\prod_{a=1}^{3}\prod_{b=4}^{N}W^{ab}\right)R^{23}W^{13}R^{12}\right]_{3\times N}\text{diag}\left(1, e^{i\lambda_{21}}, \dots, e^{i\lambda_{N1}}\right). \tag{4.8}$$

---

[2] We use the notations and conventions in Ref. [152].

[3] However, it is not excluded that the mixing is such that there are pairs of Majorana neutrino fields with exactly the same mass which form Dirac neutrino fields.

The unitary $N \times N$ matrix $W^{ab} = W^{ab}(\theta_{ab}, \eta_{ab})$ represents a complex rotation in the $a$-$b$ plane, described by a mixing angle $\theta_{ab}$ and a Dirac phase $\eta_{ab}$:

$$\left[ W^{ab}(\vartheta_{ab}, \eta_{ab}) \right]_{rs} = \delta_{rs} + (c_{ab} - 1)(\delta_{ra}\delta_{sa} + \delta_{rb}\delta_{sb}) + s_{ab} \left( e^{i\eta_{ab}} \delta_{ra}\delta_{sb} - e^{-i\eta_{ab}} \delta_{rb}\delta_{sa} \right), \quad (4.9)$$

where $c_{ab} \equiv \cos\vartheta_{ab}$ and $s_{ab} \equiv \sin\vartheta_{ab}$. The matrix $U$ in Eq. (4.8) is insensitive to the order of the product of the of $W^{ab}$ matrices. The orthogonal matrix $R^{ab} = W^{ab}(\theta_{ab}, 0)$ represents a real rotation in the $a$-$b$ plane. We indicate with the square brackets with subscript $3 \times N$ the fact that the enclosed $N \times N$ matrix is truncated to the first three rows. The diagonal matrix on the right of Eq. (4.8) collects the Majorana phases $\lambda_{21}, \dots \lambda_{N1}$, which are physical only if massive neutrinos are Majorana particles. The product of $W^{ab}$ matrices in Eq. (4.8), finally, contains a number of unphysical phases among the $\eta_{ab}$, which can be eliminated for each value of the index $b = 4, \dots, N$ (see Ref. [152]).

In the limit of vanishing active-sterile mixing, the mixing matrix in the scheme (4.8) reduces to the three-neutrino ($3\nu$) mixing matrix in the standard parameterization

$$U^{(3\nu)} = \left[ R^{23} W^{13} R^{12} \right]_{3\times3} \mathrm{diag}\left( 1, e^{i\lambda_{21}}, e^{i\lambda_{31}} \right)$$

$$= \begin{pmatrix} c_{12}c_{13} & s_{12}c_{13} & s_{13}e^{-i\eta_{13}} \\ -s_{12}c_{23} - c_{12}s_{23}s_{13}e^{i\eta_{13}} & c_{12}c_{23} - s_{12}s_{23}s_{13}e^{i\eta_{13}} & s_{23}c_{13} \\ s_{12}s_{23} - c_{12}c_{23}s_{13}e^{i\eta_{13}} & -c_{12}s_{23} - s_{12}c_{23}s_{13}e^{i\eta_{13}} & c_{23}c_{13} \end{pmatrix} \begin{pmatrix} 1 & 0 & 0 \\ 0 & e^{i\lambda_{21}} & 0 \\ 0 & 0 & e^{i\lambda_{31}} \end{pmatrix}. \tag{4.10}$$

We can now study the neutral-current Lagrangian:

$$\mathcal{L}_{\mathrm{NC}} = -\frac{g}{2\cos\vartheta_{\mathrm{W}}} \overline{\nu_L^{(\mathrm{a})}} \gamma^\rho \nu_L^{(\mathrm{a})} Z_\rho = -\frac{g}{2\cos\vartheta_{\mathrm{W}}} \overline{\nu_L^{(\mathrm{M})}} \gamma^\rho U^\dagger U \nu_L^{(\mathrm{M})} Z_\rho. \tag{4.11}$$

Given that the mixing matrix $U$ is a rectangular $3 \times N$ matrix formed by the first three rows of the unitary matrix $\mathcal{U}$, we have

$$UU^\dagger = \mathbf{1}_{3\times3}, \qquad \text{but} \qquad U^\dagger U \neq \mathbf{1}_{N\times N}. \tag{4.12}$$

Therefore, the GIM mechanism [165] is not operative in neutral-current weak interactions [166] and it is possible to have neutral-current transitions among different massive neutrinos.

The effective number of active neutrinos contributing to the decay of the $Z$-boson is not affected, or is marginally affected by the introduction of sterile neutrinos. This number has been determined with high precision by the LEP experiments [167]:

$$N_\nu^{(Z)} = 2.9840 \pm 0.0082. \tag{4.13}$$

In the following we will consider sterile neutrinos with masses around 1 eV, for which $N_\nu^{(Z)}$ is given by [168, 169]

$$N_\nu^{(Z)} = \sum_{j,k=1}^{N} \left| \sum_{\alpha=e,\mu,\tau} U_{\alpha j}^* U_{\alpha k} \right|^2 = 3. \tag{4.14}$$

For this reason the high-precision LEP measurement of $N_\nu^{(Z)}$ gives no constraint on the number and mixing of these light sterile neutrinos.

If we want to study neutrino oscillations in vacuum, we can conveniently use the following general expression of the probability of $\overset{(-)}{\nu_\alpha} \to \overset{(-)}{\nu_\beta}$ oscillations [170, 171]:

$$P_{\overset{(-)}{\nu_\alpha} \to \overset{(-)}{\nu_\beta}} = \delta_{\alpha\beta} - 4 \sum_{k\neq p} |U_{\alpha k}|^2 \left( \delta_{\alpha\beta} - |U_{\beta k}|^2 \right) \sin^2\Delta_{kp}$$

$$+ 8 \sum_{\substack{j>k \\ j,k\neq p}} |U_{\alpha j} U_{\beta j} U_{\alpha k} U_{\beta k}| \sin\Delta_{kp} \sin\Delta_{jp} \cos(\Delta_{jk} \overset{(+)}{-} \eta_{\alpha\beta jk}), \tag{4.15}$$

where

$$\Delta_{kp} = \frac{\Delta m_{kp}^2 L}{4E}, \qquad \Delta m_{jk}^2 = m_j^2 - m_k^2, \qquad \eta_{\alpha\beta jk} = \arg\left[U_{\alpha j}^* U_{\beta j} U_{\alpha k} U_{\beta k}^*\right]. \qquad (4.16)$$

Here $p$ is an arbitrary fixed index, which can be chosen in the most convenient way depending on the case under consideration. The choice of $p$ forces to have only one possibility for $j$ and $k$ such that $j > k$. As a consequence, in the case of three-neutrino mixing, there is only one interference term in Eq. (4.15).

The measurements of neutrino oscillations determined the existence of two squared-mass differences, which guarantee that at least two neutrino mass eigenstates are massive. The analyses of the oscillations of neutrinos coming from the Sun lead to the solar squared-mass difference

$$\Delta m_{\text{SOL}}^2 \simeq 7.5 \times 10^{-5} \,\text{eV}^2, \qquad (4.17)$$

while from oscillations of neutrinos produced during the cosmic rays interactions with the atmosphere it is possible to determine the atmospheric squared-mass difference

$$\Delta m_{\text{ATM}}^2 \simeq 2.4 \times 10^{-3} \,\text{eV}^2. \qquad (4.18)$$

We can conveniently label the masses of the three light neutrinos according to the convention

$$\Delta m_{\text{SOL}}^2 = \Delta m_{21}^2 \ll \Delta m_{\text{ATM}}^2 = \frac{1}{2}\left|\Delta m_{31}^2 + \Delta m_{32}^2\right|, \qquad (4.19)$$

although different definitions has been adopted in the literature (see e.g. Ref. [172]). The sign of $\Delta m_{\text{SOL}}^2$ is determined thanks to the matter effect in the neutrino oscillations in the Sun, that give rise to the Mikheev-Smirnov-Wolfenstein (MSW) effect [9–11] (see also Ref. [152,173]). On the contrary, we do not know the sign of $\Delta m_{\text{ATM}}^2$ and the absolute value in Eq. (4.19) is necessary. As a consequence, there are two possible orderings of the neutrino masses: the normal ordering (NO) with $m_1 < m_2 < m_3$ and $\Delta m_{31}^2, \Delta m_{32}^2 > 0$, and the inverted ordering (IO) with $m_3 < m_1 < m_2$ and $\Delta m_{31}^2, \Delta m_{32}^2 < 0$.

According to Eq. (4.10), the mixing in the $3\nu$ paradigm can be described with 3 mixing angles, one Dirac phase and 2 Majorana phases (given that the neutrinos are Majorana particles). We report in Table 4.1 the results of the determination of the mixing angles and the squared-mass differences as obtained in Ref. [174] from a global fit of neutrino oscillation data (see also Refs. [175,176]). The angle $\vartheta_{23}$ is the more uncertain, since its value is known to be close to maximal ($\pi/4$), but it can be smaller or larger than $\pi/4$. For the Dirac CP-violating phase $\eta_{13}$ we have indications in favor of $\eta_{13} \approx 3\pi/2$ [4], corresponding to maximal CP violation, but at $3\sigma$ all the values of $\eta_{13}$ are allowed, including the CP-conserving values $\eta_{13} = 0, \pi$.

We can extend the framework of $3\nu$ mixing with the introduction of non-standard massive neutrinos. The requirement, however, is that mixing between active and non-standard neutrinos is small, since we do not want to spoil the successful $3\nu$ mixing explanation of solar, atmospheric and long-baseline neutrino oscillation measurements. The non-standard massive neutrinos must be then mostly sterile and in the following we will always assume the constraint

$$|U_{\alpha k}|^2 \ll 1 \qquad (\alpha = e, \mu, \tau; \ k = 4, \ldots, N). \qquad (4.20)$$

Even if more than one sterile neutrino has been considered in the literature, we consider only the so-called 3+1 scheme, where the "+1" refers to a non-standard massive neutrino, mostly sterile, at the eV scale. It generates a new squared-mass difference

$$\Delta m_{\text{SBL}}^2 \sim 1 \,\text{eV}^2, \qquad (4.21)$$

that allows to explain the anomalies found in some short-baseline (SBL) neutrino oscillation experiments (see Section 4.2). We assume that the three standard massive neutrinos are much lighter than the eV scale. A different possibility would concern an inverted sterile ordering,

| parameter | mass order | best fit | $1\sigma$ range | $2\sigma$ range | $3\sigma$ range |
|---|---|---|---|---|---|
| $\Delta m^2_{\text{SOL}}/10^{-5}\,\text{eV}^2$ | | 7.54 | $7.32 - 7.80$ | $7.15 - 8.00$ | $6.99 - 8.18$ |
| $\sin^2\vartheta_{12}/10^{-1}$ | | 3.08 | $2.91 - 3.25$ | $2.75 - 3.42$ | $2.59 - 3.59$ |
| $\Delta m^2_{\text{ATM}}/10^{-3}\,\text{eV}^2$ | NO | 2.43 | $2.37 - 2.49$ | $2.30 - 2.55$ | $2.23 - 2.61$ |
| | IO | 2.38 | $2.32 - 2.44$ | $2.25 - 2.50$ | $2.19 - 2.56$ |
| $\sin^2\vartheta_{23}/10^{-1}$ | NO | 4.37 | $4.14 - 4.70$ | $3.93 - 5.52$ | $3.74 - 6.26$ |
| | IO | 4.55 | $4.24 - 5.94$ | $4.00 - 6.20$ | $3.80 - 6.41$ |
| $\sin^2\vartheta_{13}/10^{-2}$ | NO | 2.34 | $2.15 - 2.54$ | $1.95 - 2.74$ | $1.76 - 2.95$ |
| | IO | 2.40 | $2.18 - 2.59$ | $1.98 - 2.79$ | $1.78 - 2.98$ |

Table 4.1: Values of the neutrino mixing parameters obtained in Ref. [174] with a global analysis of neutrino oscillation data in the framework of three-neutrino mixing with the normal ordering (NO) and the inverted ordering (IO).

where the additional neutrino has a mass much smaller than the active neutrinos, which have then almost degenerate masses at the eV scale in order to generate the same $\Delta m^2_{\text{SBL}} \sim 1\,\text{eV}^2$. This possibility is strongly disfavored by cosmological measurements [44] and by the experimental bounds on neutrinoless double-$\beta$ decay, assuming that massive neutrinos are Majorana particles (see Ref. [5]). In any case, the 3+1 scheme must be considered an effective mixing scheme, since possible additional non-standard massive neutrinos beyond the first one are allowed, if their mixing with the three active neutrinos is sufficiently small to be negligible in the analysis of the data of current experiments.

We want now to consider Eq. (4.15) to obtain the effective oscillation probabilities in short-baseline experiments, for which $\Delta_{21} \ll \Delta_{31} \ll 1$. Consider the general $3+N_s$ case in which $\Delta m^2_{k1} \approx \Delta m^2_{\text{SBL}}$ and $\Delta_{k1} \approx 1$ for $k \geq 4$. Choosing $p = 1$ in Eq. (4.15), we obtain

$$
P^{(\text{SBL})}_{\overset{(-)}{\nu_\alpha} \to \overset{(-)}{\nu_\beta}} \simeq \delta_{\alpha\beta} - 4 \sum_{k=4}^{N} |U_{\alpha k}|^2 \left( \delta_{\alpha\beta} - |U_{\beta k}|^2 \right) \sin^2 \Delta_{k1}
$$
$$
+ 8 \sum_{k=4}^{N} \sum_{j=k+1}^{N} |U_{\alpha j} U_{\beta j} U_{\alpha k} U_{\beta k}| \sin \Delta_{k1} \sin \Delta_{j1} \cos(\Delta_{jk} \overset{(+)}{-} \eta_{\alpha\beta jk}). \tag{4.22}
$$

Let us consider the survival probabilities of active neutrinos: we can define the effective amplitudes

$$
\sin^2 2\vartheta^{(k)}_{\alpha\alpha} = 4|U_{\alpha k}|^2 \left( 1 - |U_{\alpha k}|^2 \right) \simeq 4|U_{\alpha k}|^2 \qquad (\alpha = e, \mu, \tau; \, k \geq 4), \tag{4.23}
$$

where we have taken into account the constraint in Eq. (4.20). The quadratically suppressed terms can be dropped in the survival probabilities, and we obtain

$$
P^{(\text{SBL})}_{\overset{(-)}{\nu_\alpha} \to \overset{(-)}{\nu_\alpha}} \simeq 1 - \sum_{k=4}^{N} \sin^2 2\vartheta^{(k)}_{\alpha\alpha} \sin^2 \Delta_{k1} \qquad (\alpha = e, \mu, \tau). \tag{4.24}
$$

Each effective mixing angle $\vartheta^{(k)}_{\alpha\alpha}$ parameterizes the disappearance of $\overset{(-)}{\nu_\alpha}$ due to its mixing with $\overset{(-)}{\nu_k}$.

We can now consider the probabilities of short-baseline $\overset{(-)}{\nu_\alpha} \to \overset{(-)}{\nu_\beta}$ transitions between two different active neutrinos or an active and a sterile neutrino. The transition amplitudes are defined as

$$
\sin^2 2\vartheta^{(k)}_{\alpha\beta} = 4|U_{\alpha k}|^2 |U_{\beta k}|^2 \qquad (\alpha \neq \beta; \, k \geq 4), \tag{4.25}
$$

which allow us to write the transition probabilities as

$$
P^{(\text{SBL})}_{\overset{(-)}{\nu_\alpha} \to \overset{(-)}{\nu_\beta}} \simeq \sum_{k=4}^{N} \sin^2 2\vartheta^{(k)}_{\alpha\beta} \sin^2 \Delta_{k1}
$$

$$+ 2 \sum_{k=4}^{N} \sum_{j=k+1}^{N} \sin 2\vartheta_{\alpha\beta}^{(k)} \sin 2\vartheta_{\alpha\beta}^{(j)} \sin \Delta_{k1} \sin \Delta_{j1} \cos(\Delta_{jk} \overset{(+)}{-} \eta_{\alpha\beta jk}) . \qquad (4.26)$$

We can see from the first line that each effective mixing angle $\vartheta_{\alpha\beta}^{(k)}$ parameterizes the amount of $\overset{(-)}{\nu_\alpha} \to \overset{(-)}{\nu_\beta}$ transitions due to the mixing of $\overset{(-)}{\nu_\alpha}$ and $\overset{(-)}{\nu_\beta}$ with $\overset{(-)}{\nu_k}$. The second line in Eq. (4.26), instead, is the interference between the contributions of $\overset{(-)}{\nu_k}$ and $\overset{(-)}{\nu_j}$, depending on the same effective mixing angles.

From Eqs. (4.23) and (4.25) we can see that for each value of $k \geq 4$ the transition amplitude $\sin 2\vartheta_{\alpha\beta}^{(k)}$ and the disappearance amplitudes $\sin 2\vartheta_{\alpha\alpha}^{(k)}$ and $\sin 2\vartheta_{\beta\beta}^{(k)}$ depend only on the elements in $k^{\text{th}}$ column of the mixing matrix $\mathcal{U}$ and are related by[4]

$$\sin^2 2\vartheta_{\alpha\beta}^{(k)} \simeq \frac{1}{4} \sin^2 2\vartheta_{\alpha\alpha}^{(k)} \sin^2 2\vartheta_{\beta\beta}^{(k)} \qquad (\alpha = e, \mu, \tau) . \qquad (4.27)$$

The importance of this relation is crucial for the acceptance or rejection of the $3+N_s$ mixing schemes with sterile neutrinos through their test against the experimental results, because it constrains the oscillation signals that can be observed in short-baseline experiments, both in the appearance and disappearance channels. In particular, the amplitudes of the short-baseline transition probabilities between active neutrinos are quadratically suppressed since both $\sin^2 2\vartheta_{\alpha\alpha}^{(k)}$ and $\sin^2 2\vartheta_{\beta\beta}^{(k)}$ are small for $\alpha, \beta = e, \mu, \tau$.

In the case of 3+1 neutrino mixing [177–180], we have $\Delta m_{41}^2 = \Delta m_{\text{SBL}}^2$ and $\Delta_{41} \sim 1$ in short-baseline experiments. The transition and survival probabilities become

$$P_{\overset{(-)}{\nu_\alpha} \to \overset{(-)}{\nu_\beta}}^{(\text{SBL})} \simeq \sin^2 2\vartheta_{\alpha\beta} \sin^2 \Delta_{41} \quad (\alpha \neq \beta), \qquad P_{\overset{(-)}{\nu_\alpha} \to \overset{(-)}{\nu_\alpha}}^{(\text{SBL})} \simeq 1 - \sin^2 2\vartheta_{\alpha\alpha} \sin^2 \Delta_{41} , \qquad (4.28)$$

where the transition and survival amplitudes are

$$\sin^2 2\vartheta_{\alpha\beta} = 4|U_{\alpha4}|^2 |U_{\beta4}|^2 \quad (\alpha \neq \beta), \qquad \sin^2 2\vartheta_{\alpha\alpha} = 4|U_{\alpha4}|^2 \left(1 - |U_{\alpha4}|^2\right) . \qquad (4.29)$$

The appearance-disappearance constraint is [177, 178]

$$\sin^2 2\vartheta_{\alpha\beta} \simeq \frac{1}{4} \sin^2 2\vartheta_{\alpha\alpha} \sin^2 2\vartheta_{\beta\beta} \qquad (\alpha = e, \mu, \tau) . \qquad (4.30)$$

In Eq. (4.28), the transition and survival probabilities depend only on the largest squared-mass difference, that in the 3+1 scheme is $\Delta m_{41}^2 = \Delta m_{\text{SBL}}^2$, and on the absolute values of the elements in the fourth column of the mixing matrix. There is no difference between the transition probabilities of neutrinos and antineutrinos, since the absolute values of the elements $U_{\alpha4}$ do not depend on the CP-violating phases. Even in the presence of CP-violating phases in the mixing matrix, signals of CP violation cannot be measured in short-baseline experiments, but it must be searched for in experiments sensitive to the oscillations generated by the smaller squared-mass differences $\Delta m_{\text{ATM}}^2$ [181–183] or $\Delta m_{\text{SOL}}^2$ [184].

## 4.2   Short-baseline Anomalies and Constraints

The measurements obtained in short-baseline neutrino oscillation experiments require the existence of at least one additional squared-mass difference, $\Delta m_{\text{SBL}}^2$, which is much larger than $\Delta m_{\text{SOL}}^2$ and $\Delta m_{\text{ATM}}^2$. Three types of experiments give indications in favor of $\Delta m_{\text{SBL}}^2$: the reactor antineutrino anomaly, the Gallium neutrino anomaly, and the LSND anomaly.

---

[4] This relation was derived in the case of 3+1 mixing (see Eq. (4.30)) in Refs. [177, 178].

### 4.2.1 The reactor Antineutrino Anomaly

In the literature, one can find a discrepancy between the rate of $\bar{\nu}_e$ observed in several short-baseline reactor neutrino experiments and the value expected from the calculation of the reactor neutrino fluxes [162, 185, 186], which predict more events than those observed. Many authors studied this discrepancy [162, 187–199], that is referred to as the *reactor antineutrino anomaly.*

The significance of the reactor anomaly depends on the uncertainties of the reactor antineutrino flux, that is calculated from the available database information on nuclear decays and from the electron spectra associated with the fission of $^{235}$U, $^{239}$Pu, and $^{241}$Pu measured at ILL in the 80's [200–203]. These determinations of the values and uncertainties of the reactor antineutrino fluxes have been presented in Refs. [162, 185, 186]. There have been, however, some debate [204–211], especially after the discovery of an excess at about 5 MeV in the reactor antineutrino spectrum measured by the RENO [212], Double Chooz [213] and Daya Bay [214] experiments.

The main process involved for neutrino detection in reactor experiments is the inverse neutron decay process

$$\bar{\nu}_e + p \to n + e^+ \tag{4.31}$$

that occurs in liquid-scintillator detectors. This detection process has a cross section $\sigma_{\bar{\nu}_e p}(E_e) \propto E_e p_e$ (see Refs. [152, 215, 216]), where $E_e$ and $p_e$ indicate the positron energy and momentum, respectively. The recoil energy of the neutron is small and it can be neglected. The neutrino energy $E$ can be calculated from the kinetic energy $T_e$ of the positron, that can be measured, through the relation

$$E \simeq T_e + m_e + m_n - m_p \simeq T_e + 1.8\,\text{MeV}\,, \tag{4.32}$$

where $m_p$ and $m_n$ are the proton and neutron masses, respectively. As a consequence, the threshold for the detection process is about $1.8\,\text{MeV}$ for the neutrino energy.

The anomaly is usually parameterized using the ratio $R \equiv N_{\text{exp}}/N_{\text{cal}}$ of the measured ($N_{\text{exp}}$) and calculated ($N_{\text{cal}}$) number of electron antineutrino events in reactor experiments at different distances $L$. The average ratio of the values $R$ obtained in several different experiments [217–228] is $\overline{R} = 0.933 \pm 0.021$, indicating a deficit with a statistical significance of about $3.1\sigma$ (see also Ref. [15]).

One possible explanation of the reactor antineutrino anomaly is the existence of neutrino oscillations with an oscillation length shorter than about 20 m. From the relation between the squared-mass difference $\Delta m^2$ and the corresponding oscillation length $L^{\text{osc}}$, that is

$$L^{\text{osc}} = \frac{4\pi E}{\Delta m^2} \simeq 2.5\,\frac{E\,[\text{MeV}]}{\Delta m^2\,[\text{eV}^2]}\,\text{m}\,, \tag{4.33}$$

given that the average energy of the antineutrinos detected in a reactor experiment is about 4 MeV, these oscillations require a squared-mass difference

$$\Delta m^2_{\text{SBL}} \gtrsim 0.5\,\text{eV}^2\,. \tag{4.34}$$

### 4.2.2 The Gallium Neutrino Anomaly

The second anomaly we present is the Gallium neutrino anomaly [194, 229–234], a disappearance of $\nu_e$ measured in the short-baseline Gallium radioactive source experiments GALLEX [235–237] and SAGE [229, 238–240]. The detectors of the GALLEX and SAGE solar neutrino experiments have been tested with intense artificial $^{51}$Cr and $^{37}$Ar radioactive sources, which produce electron neutrinos through the electron captures

$$e^- + {}^{51}\text{Cr} \to {}^{51}\text{V} + \nu_e, \qquad e^- + {}^{37}\text{Ar} \to {}^{37}\text{Cl} + \nu_e\,. \tag{4.35}$$

The radioactive source was placed near the center of the detector of each experiment, which detected electron neutrinos with the reaction

$$\nu_e + {}^{71}\text{Ga} \to {}^{71}\text{Ge} + e^-\,. \tag{4.36}$$

The total detection cross section of this reaction is given by

$$\sigma = \sigma_{\text{gs}} \left( 1 + \xi_{175} \frac{\text{BGT}_{175}}{\text{BGT}_{\text{gs}}} + \xi_{500} \frac{\text{BGT}_{500}}{\text{BGT}_{\text{gs}}} \right), \tag{4.37}$$

where $\sigma_{\text{gs}}$ indicates the cross sections of the transitions from the ground state of $^{71}$Ga to the ground state of $^{71}$Ge, $\text{BGT}_{\text{gs}}$ is the corresponding Gamow-Teller strength, and $\text{BGT}_{175}$ and $\text{BGT}_{500}$ are the Gamow-Teller strengths of the transitions from the ground state of $^{71}$Ga to the two excited states of $^{71}$Ge at about 175 keV and 500 keV (see e.g. Ref. [15]). The coefficients of $\text{BGT}_{175}/\text{BGT}_{\text{gs}}$ and $\text{BGT}_{500}/\text{BGT}_{\text{gs}}$ are determined by phase space: $\xi_{175}(^{51}\text{Cr}) = 0.669$, $\xi_{500}(^{51}\text{Cr}) = 0.220$, $\xi_{175}(^{37}\text{Ar}) = 0.695$, $\xi_{500}(^{37}\text{Ar}) = 0.263$ [241].

Bahcall [241] calculated accurately the cross sections of the transitions from the ground state of $^{71}$Ga to the ground state of $^{71}$Ge:

$$\sigma_{\text{gs}}(^{51}\text{Cr}) = 55.3 \times 10^{-46}\,\text{cm}^2, \qquad \sigma_{\text{gs}}(^{37}\text{Ar}) = 66.2 \times 10^{-46}\,\text{cm}^2, \tag{4.38}$$

and [194, 242]

$$\text{BGT}_{\text{gs}} = 0.0871 \pm 0.0004. \tag{4.39}$$

The Gamow-Teller strengths $\text{BGT}_{175}$ and $\text{BGT}_{500}$ have been measured in 1985 in the $(p, n)$ experiment of Krofcheck et al. [243, 244] and in 2011 in the $(^3\text{He}, {}^3\text{H})$ experiment of Frekers et al. [245] with higher precision.

In analogy with the reactor anomaly, the results for the Gallium anomaly are usually reported in terms of the ratio $R \equiv N_{\text{exp}}/N_{\text{cal}}$ of the measured number of electron neutrino events ($N_{\text{exp}}$) and the one calculated ($N_{\text{cal}}$) with the Frekers et al. Gamow-Teller strengths. The average ratio calculated with the results obtained in the GALLEX and SAGE radioactive source experiments is $\overline{R} = 0.84 \pm 0.05$, indicating a deficit with a statistical significance of about $2.9\sigma$.

The average neutrino travels distances in the GALLEX and SAGE radioactive source experiments equal to $\langle L \rangle_{\text{GALLEX}} = 1.9\,\text{m}$ and $\langle L \rangle_{\text{SAGE}} = 0.6\,\text{m}$. The produced neutrinos may have different energies, depending on the electron-capture channel. The largest branching ratios are for the $E = 747\,\text{keV}$ neutrino for $^{51}$Cr and for the $E = 811\,\text{keV}$ neutrino for $^{37}$Ar, while the complete list of neutrino energies and the corresponding branching ratios can be found for example in Tab. 2 of Ref. [15]. From Eq. (4.33) we can estimate that the Gallium neutrino anomaly can be explained by neutrino oscillations if they are generated by a squared-mass difference

$$\Delta m^2_{\text{SBL}} \gtrsim 1\,\text{eV}^2. \tag{4.40}$$

### 4.2.3 The LSND Anomaly

Finally, the LSND experiment [246, 247] observed an excess of electron antineutrino events in a beam of muon antineutrinos produced by $\mu^+$ decay at rest,

$$\mu^+ \to e^+ + \nu_e + \bar{\nu}_\mu. \tag{4.41}$$

The energy spectrum of the muon antineutrinos is $\phi_{\bar{\nu}_\mu}(E) \propto E^2 (3 - 4E/m_\mu)$ (see Ref. [216]) for neutrino energies $E$ smaller than $E_{\text{max}} = (m_\mu - m_e)/2 \simeq 52.6\,\text{MeV}$. The experiment used a detector filled with liquid scintillator to detect electron antineutrino events at a distance $L \simeq 30\,\text{m}$ through the inverse neutron decay process (4.31). The energy range is $20 \lesssim E_e \lesssim 60\,\text{MeV}$ for the energy $E_e$ of the detected positron.

From Eq. (4.33) and for the energy range of LSND, we can estimate that the $\bar{\nu}_e$ appearance signal can be explained by $\bar{\nu}_\mu \to \bar{\nu}_e$ oscillations generated by a squared-mass difference

$$\Delta m^2_{\text{SBL}} \gtrsim 0.1\,\text{eV}^2. \tag{4.42}$$

The statistical significance of the electron antineutrino appearance signal at LSND is of about $3.8\sigma$. We must note, however, that the similar KARMEN experiment [248, 249] did

|  | GLO | PrGLO | noMB | noLSND |
|---|---|---|---|---|
| $\chi^2_{\mathrm{min}}$ | 306.0 | 276.3 | 251.2 | 291.3 |
| NDF | 268 | 262 | 230 | 264 |
| GoF | 5% | 26% | 16% | 12% |
| $(\chi^2_{\mathrm{min}})_{\mathrm{APP}}$ | 98.9 | 77.0 | 50.9 | 91.8 |
| $(\chi^2_{\mathrm{min}})_{\mathrm{DIS}}$ | 194.4 | 194.4 | 194.4 | 194.4 |
| $\Delta\chi^2_{\mathrm{PG}}$ | 13.0 | 5.3 | 6.2 | 5.3 |
| $\mathrm{NDF}_{\mathrm{PG}}$ | 2 | 2 | 2 | 2 |
| $\mathrm{GoF}_{\mathrm{PG}}$ | 0.1% | 7% | 5% | 7% |
| $\Delta\chi^2_{\mathrm{NO}}$ | 49.2 | 47.7 | 48.1 | 11.4 |
| $\mathrm{NDF}_{\mathrm{NO}}$ | 3 | 3 | 3 | 3 |
| $n\sigma_{\mathrm{NO}}$ | $6.4\sigma$ | $6.3\sigma$ | $6.4\sigma$ | $2.6\sigma$ |

Table 4.2: Results of the fit of short-baseline data in the 3+1 scheme. The four different possibilities take into account different dataset combinations: all MiniBooNE data (GLO), only the MiniBooNE data above 475 MeV (PrGLO), without MiniBooNE data (noMB) and without LSND data (noLSND). In the first three lines the minimum $\chi^2$ ($\chi^2_{\mathrm{min}}$), the number of degrees of freedom (NDF) and the goodness-of-fit (GoF) are listed. The five lines in the middle give the quantities relevant for the appearance-disappearance (APP-DIS) parameter goodness-of-fit (PG) [253]. In the last three lines we list the difference between the $\chi^2$ without short-baseline oscillations (NO) and $\chi^2_{\mathrm{min}}$ ($\Delta\chi^2_{\mathrm{NO}}$), the corresponding difference of number of degrees of freedom ($\mathrm{NDF}_{\mathrm{NO}}$) and the resulting number of $\sigma$'s ($n\sigma_{\mathrm{NO}}$) for which the absence of oscillations is disfavored. Adapted from [15].

not measure any excess of $\bar{\nu}_e$ events over the background at a distance $L \simeq 18\,\mathrm{m}$. Another experiment, MiniBooNE, was designed to check the LSND signal with about one order of magnitude larger distance and energy, but with the same order of magnitude for the ratio $L/E$. Unfortunately, the results of the MiniBooNE experiment are ambiguous, since the LSND signal was not seen in the neutrino mode ($\nu_\mu \to \nu_e$) [250], while the $\bar{\nu}_\mu \to \bar{\nu}_e$ signal observed in 2010 [251] with the first half of the antineutrino data was not observed in the second half of the antineutrino data [252]. Moreover, in the MiniBooNE data, both for the neutrino and antineutrino modes, an excess in the low-energy bins appears. This is widely considered an anomalous effects, since it cannot be explained with neutrino oscillations [191, 192].

## 4.3 Global Fits of short-baseline Data

Since the discovery of the LSND anomaly, many analyses of short-baseline neutrino oscillation data have been done [177–179, 254–271]. The interest for joint fits of neutrino oscillation data increased after the discoveries of the Gallium neutrino anomaly [194, 231–234, 272–276] and the reactor antineutrino anomaly [187, 189–192, 194, 195, 277–283]. The most recent global fit of SBL neutrino oscillation data was presented in Ref. [15] and it is an update of the analysis of Ref. [199]. These analyses include

- $\overset{(-)}{\nu}_\mu \to \overset{(-)}{\nu}_e$ appearance data from several experiments [247, 249, 252, 284–287];

- $\overset{(-)}{\nu}_e$ disappearance data from several reactor neutrino experiments [217–228] (see Section 4.2.1), from the Gallium radioactive source experiments GALLEX [235–237] and SAGE [229, 238–240] (see Section 4.2.2), from the solar neutrino constraint on $\sin^2 2\vartheta_{ee}$ [194, 288–291] and from the $\nu_e + {}^{12}\mathrm{C} \to {}^{12}\mathrm{N}_{\mathrm{g.s.}} + e^-$ scattering data [278] of KARMEN [292, 293] and LSND [294], with the method discussed in Ref. [192].
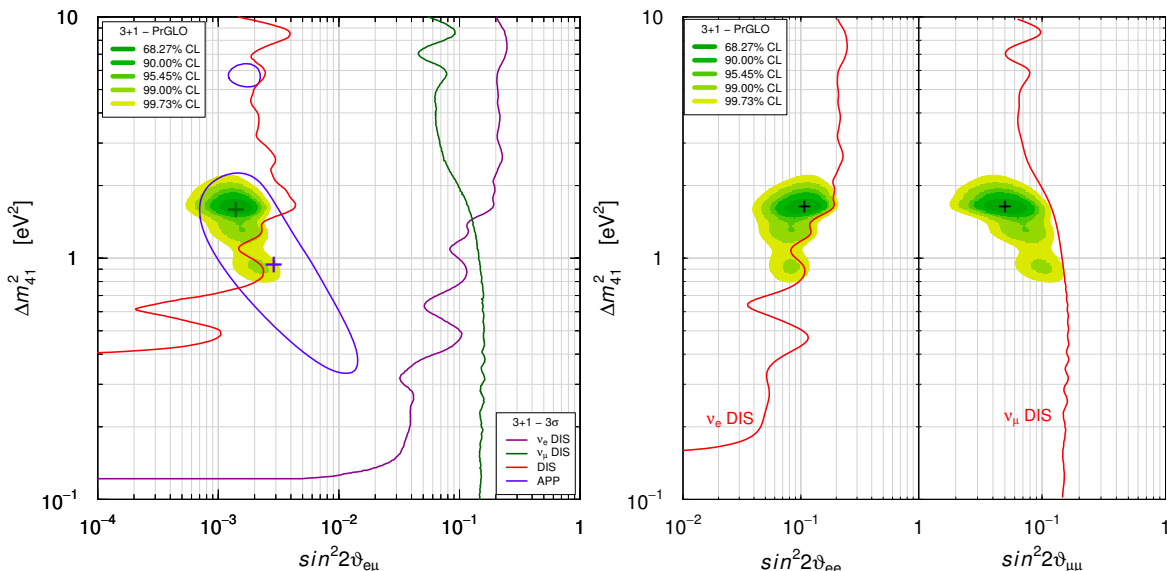
Figure 4.1: Allowed regions in the $\sin^2 2\vartheta_{e\mu}$–$\Delta m_{41}^2$, $\sin^2 2\vartheta_{ee}$–$\Delta m_{41}^2$ and $\sin^2 2\vartheta_{\mu\mu}$–$\Delta m_{41}^2$ planes obtained in the pragmatic 3+1-PrGLO global fit of short-baseline neutrino oscillation data. These are compared with the $3\sigma$ allowed regions obtained from $\overset{(-)}{\nu_\mu} \to \overset{(-)}{\nu_e}$ short-baseline appearance data (APP), the $3\sigma$ constraints obtained from $\overset{(-)}{\nu_e}$ short-baseline disappearance data ($\nu_e$ DIS) and $\overset{(-)}{\nu_\mu}$ short-baseline disappearance data ($\nu_\mu$ DIS), and the combined short-baseline disappearance data (DIS). The best-fit points of the PrGLO and APP fits are indicated by crosses. From Ref. [15].

| CL | $\Delta m_{41}^2[\text{eV}^2]$ | $\sin^2 2\vartheta_{e\mu}$ | $\sin^2 2\vartheta_{ee}$ | $\sin^2 2\vartheta_{\mu\mu}$ |
|---|---|---|---|---|
| 68.27% | $1.57 - 1.72$ | $0.0011 - 0.0018$ | $0.085 - 0.13$ | $0.039 - 0.066$ |
| 90.00% | $1.53 - 1.78$ | $0.00098 - 0.0020$ | $0.071 - 0.15$ | $0.032 - 0.078$ |
| 95.45% | $1.50 - 1.84$ | $0.00089 - 0.0021$ | $0.063 - 0.16$ | $0.030 - 0.085$ |
| 99.00% | $1.24 - 1.95$ | $0.00074 - 0.0023$ | $0.054 - 0.18$ | $0.025 - 0.095$ |
| 99.73% | $0.87 - 2.04$ | $0.00065 - 0.0026$ | $0.046 - 0.19$ | $0.021 - 0.12$ |

Table 4.3: Marginal allowed intervals of the oscillation parameters obtained in the global 3+1-PrGLO fit of short-baseline neutrino oscillation data. From [15].

- $\overset{(-)}{\nu_\mu}$ disappearance obtained from the data of the CDHSW experiment [295], from the analysis [266] of the data of atmospheric neutrino oscillation experiments, from the analysis [191, 296] of the MINOS neutral-current data [297] and from the analysis of the SciBooNE-MiniBooNE neutrino [298] and antineutrino [299] data.

The statistical results obtained from the global fits of the data listed above are summarized in Table 4.2. The global (GLO) fit takes into account all the MiniBooNE data, including the anomalous low-energy bins, which are omitted in the pragmatic global (PrGLO) fit [199]. The last two columns concern the results for a fit without the MiniBooNE data (noMB) and one without the LSND data (noLSND).

From Tab. 4.2, we can see that the absence of short-baseline oscillations is nominally disfavored at about $6\sigma$ in all of the fits which include the LSND data, because the improvement of the $\chi^2$ with short-baseline oscillations is much larger than the number of oscillation parameters. On the other hand, when the LSND data are not considered (noLSND fit), the nominal exclusion of the case of no-oscillations drops dramatically to $2.6\sigma$. Therefore, the LSND experiment is clearly still crucial for the indication in favor of short-baseline $\bar{\nu}_\mu \to \bar{\nu}_e$.

In the GLO analysis, the goodness-of-fit is significantly worse than that in the PrGLO analysis and the same applies for the appearance-disappearance parameter goodness-of-fit. This result confirms the fact that the MiniBooNE low-energy anomaly is not compatible with neutrino oscillations, requiring a small value of $\Delta m_{41}^2$ and a large value of $\sin^2 2\vartheta_{e\mu}$ [191,192], which are excluded by the oscillation data of other experiments (further details are discussed in Ref. [199]). Therefore, it is very likely that the MiniBooNE low-energy anomaly must be explained with some mechanism different from neutrino oscillations. It is interesting to investigate what is the impact of the MiniBooNE experiment on the global analysis of short-baseline neutrino oscillation data. With this aim, we consider also the noMB fit without MiniBooNE data. From Tab. 4.2 we can see that the results of the noMB fit are similar to those of the PrGLO fit and the nominal exclusion of the case of no-oscillations remains at the level of $6\sigma$. Therefore, it is clear that the MiniBooNE experiment has been rather inconclusive. The MicroBooNE experiment at Fermilab [300,301], a large Liquid Argon Time Projection Chamber (LArTPC) in which electrons and photons can be distinguished, is going to investigate the cause of the MiniBooNE low-energy excess of $\nu_e$-like events and to check the LSND signal (see the review in Ref. [302]). Since the low-energy anomaly of MiniBooNE is under discussion, in the following we adopt the "pragmatic approach" advocated in Ref. [199]. The PrGLO fit, that does not take into account the anomalous MiniBooNE low-energy bins, is more reliable than the GLO fit, which includes all the MiniBooNE data.

The allowed regions in the $\sin^2 2\vartheta_{e\mu}$–$\Delta m_{41}^2$, $\sin^2 2\vartheta_{ee}$–$\Delta m_{41}^2$ and $\sin^2 2\vartheta_{\mu\mu}$–$\Delta m_{41}^2$ planes as obtained in the PrGLO fit are shown in Fig. 4.1. These regions are relevant, respectively, for $\overset{(-)}{\nu}_\mu \to \overset{(-)}{\nu}_e$ appearance, $\overset{(-)}{\nu}_e$ disappearance and $\overset{(-)}{\nu}_\mu$ disappearance searches. The corresponding marginal allowed intervals of the oscillation parameters are given in Tab. 4.3. Figure 4.1 shows also the region allowed by $\overset{(-)}{\nu}_\mu \to \overset{(-)}{\nu}_e$ appearance data and the constraints from $\overset{(-)}{\nu}_e$ disappearance and $\overset{(-)}{\nu}_\mu$ disappearance data. We can see that the combined disappearance constraint in the $\sin^2 2\vartheta_{e\mu}$–$\Delta m_{41}^2$ plane excludes a large part of the region allowed by $\overset{(-)}{\nu}_\mu \to \overset{(-)}{\nu}_e$ appearance data, leading to the well-known appearance-disappearance tension [189–192,197,282,283,303], quantified by the parameter goodness-of-fit in Tab. 4.2.

## 4.4 Neutrino and Cosmology

This Section is devoted to extend the treatment presented in the previous Chapters, where we ignored the presence of the neutrino perturbations in the Universe evolution. We will briefly review the impact of the neutrinos on the various cosmological observables we mentioned earlier, with a particular focus on the impact of a light sterile neutrino with a mass at the eV scale. A more detailed discussion is presented, for example, in Ref. [51].

When considering the additional neutrino, which is mostly sterile as explained in Section 4.1, we will denote its mass with the symbol $m_s$. In this section we use this notation, keeping in mind that its real meaning in the 3+1 mixing scheme is $m_s = m_4$. Moreover, in the discussion of the combined analysis of cosmological data and short-baseline oscillation data we consider $m_1, m_2, m_3 \ll m_4$, so that $m_s = m_4 \simeq \sqrt{\Delta m_{41}^2} = \sqrt{\Delta m_{\mathrm{SBL}}^2}$.

This Section is organized as it follows: in Subsection 4.4.1 we introduce the parameterization of the neutrino energy density, in Subsection 4.4.2 we discuss the definitions of the neutrino perturbations, in Subsection 4.4.3 we present the neutrino free-streaming, in Subsection 4.4.4 we briefly review the effects of neutrinos which are relativistic in the early Universe on observables such as the Cosmic Microwave Background (CMB) and the nuclear abundances produced by Big Bang Nucleosynthesis (BBN). In Subsection 4.4.5 we discuss the effects of massive neutrinos, which are important only after the sterile neutrinos became non-relativistic. All these effects can be used to derive constraints on the neutrino properties from the various cosmological data we presented in the previous Chapter. The constraints on the sterile neutrino properties will be discussed in Chapter 5.

### 4.4.1 Neutrino Parameterization

The neutrino contribution to the radiation content in the early Universe can be conveniently parameterized in terms of the effective number of degrees of freedom $N_{\text{eff}}$. This is defined so that the total energy density of relativistic species $\rho_r$ is given by

$$\rho_r = \left[1 + \frac{7}{8}\left(\frac{4}{11}\right)^{4/3} N_{\text{eff}}\right]\rho_\gamma = [1 + 0.2271\, N_{\text{eff}}]\,\rho_\gamma\,, \tag{4.43}$$

where $\rho_\gamma$ is the energy density of photons. $N_{\text{eff}} = 1$ corresponds to the contribution of one single family of active neutrinos which were in equilibrium in the early Universe and passed through an instantaneous decoupling at a temperature of about 1 MeV. The factor $7/8$ is for fermionic degrees of freedom, while the factor $T_\nu^{id}/T_\gamma = (4/11)^{4/3}$ is the consequence of the fact that after neutrino decoupling there is an entropy transfer between electrons and photons, caused by $e^\pm$ annihilations. The superscript "id" indicates that this is the temperature obtained in the instantaneous decoupling limit. This entropy transfer enhances the photon temperature, that becomes higher than the temperature of the decoupled neutrinos. In the real history the neutrinos did not decouple instantaneously and part of them were not completely decoupled from the electron-photon plasma when the $e^\pm$ annihilation occurred. For this reason, the effective number of active neutrinos is slightly larger than three: it is $N_{\text{eff}}^{\text{SM}} = 3.046$ [304, 305]. Assuming that the active neutrino follows the usual thermal history and that the non-standard contribution to the effective number of relativistic species comes only from additional sterile neutrinos, the sterile neutrino contributes to the total radiation energy density with $\Delta N_{\text{eff}} = N_{\text{eff}} - 3.046$. This can be calculated as [306]

$$\Delta N_{\text{eff}} \equiv \frac{\rho_s^{\text{rel}}}{\rho_\nu} = \left[\frac{7}{8}\frac{\pi^2}{15}T_\nu^{id4}\right]^{-1}\frac{1}{\pi^2}\int dp\, p^3 f_s(p)\,, \tag{4.44}$$

where $\rho_\nu$ is the energy density for one active neutrino species, $\rho_s^{\text{rel}}$ is the energy density of the relativistic sterile neutrinos, $p$ is the neutrino momentum and $f_s(p)$ is the momentum distribution. The same formula gives the corresponding contribution of one single active neutrino if the momentum distribution function $f_\nu(p)$ is used instead of $f_s(p)$.

After their non-relativistic transition, neutrinos contribute to the matter energy density of the Universe. The contribution of one single neutrino with mass $m_\nu$ is given by [306]

$$\omega_\nu = \Omega_\nu h^2 = \frac{\rho_\nu}{\rho_c}h^2 = \frac{h^2}{\rho_c}\frac{m_\nu}{\pi^2}\int dp\, p^2 f_\nu(p)\,, \tag{4.45}$$

where $\rho_\nu$ is the energy density of a non-relativistic neutrino, $f_\nu(p)$ is the momentum distribution, $\rho_c$ is the critical density and $h$ is the reduced Hubble parameter. The sterile neutrino contribution can then be parameterized in terms of the dimensionless number [306]

$$\omega_s = \Omega_s h^2 = \frac{\rho_s}{\rho_c}h^2 = \frac{h^2}{\rho_c}\frac{m_s}{\pi^2}\int dp\, p^2 f_s(p)\,, \tag{4.46}$$

where $\rho_s$ is the energy density of a non-relativistic sterile neutrino. Alternatively, $\omega_s$ can be converted in the effective sterile neutrino mass [72]

$$m_s^{\text{eff}} \equiv 94.1\,\omega_s\,\text{eV}\,. \tag{4.47}$$

All the quantities that we introduced depend on the neutrino momentum distribution $f_\nu(p)$ or $f_s(p)$. We focus now on the sterile neutrino with mass of about 1 eV. If the light sterile neutrino decouples from the rest of the plasma when it is still relativistic, $f_s(p)$ does not depend on $m_s$, but it depends only on the production mechanism. The simplest possibility is that one species of light sterile neutrinos is generated by active-sterile oscillations in the early Universe [307–312] and they share the same temperature of the active neutrinos. In this case we have simply $\Delta N_{\text{eff}} = 1$ and $\omega_s \simeq m_s/(94.1\,\text{eV})$.

If for some reasons the light sterile neutrino thermalizes at a temperature $T_s = \alpha T_\nu$, its momentum distribution is given by the standard Fermi-Dirac distribution

$$f_s(p) = \frac{1}{e^{p/T_s} + 1} \,.$$
(4.48)

We name this case the *thermal scenario* (TH), and from Eqs. (4.44) and (4.46) we obtain

$$\Delta N_{\text{eff}} = \alpha^4 \,, \qquad \omega_s = \alpha^3 \frac{m_s}{94.1\,\text{eV}} \,, \qquad m_s^{\text{eff}} = \alpha^3 m_s = \Delta N_{\text{eff}}^{3/4} m_s \,.$$
(4.49)

There are several possible mechanisms that give a non-thermal sterile neutrino production. A popular one is the non-resonant production scenario, also called *Dodelson-Widrow scenario* (DW) [313], which is motivated by early active-sterile neutrino oscillations in the limit of zero lepton asymmetry and small mixing angle. It is possible to calculate the neutrino momentum distribution for the DW scenario:

$$f_s(p) = \frac{\beta}{e^{p/T_\nu} + 1} \,,$$
(4.50)

where $\beta$ is a normalization factor. This momentum distribution leads to

$$\Delta N_{\text{eff}} = \beta \,, \qquad \omega_s = \beta \frac{m_s}{94.1\,\text{eV}} \,, \qquad m_s^{\text{eff}} = \beta m_s = \Delta N_{\text{eff}} m_s \,.$$
(4.51)

We can see from Eqs. (4.49) and (4.51) that the DW and the TH models have an exact degeneracy, since they are related by $\alpha = \beta^{1/4}$ and $m_s^{\text{TH}} = m_s^{\text{DW}} \beta^{1/4}$ [314, 315].

## 4.4.2 Neutrino Perturbations

We want now to extend the treatment of the perturbation theory presented in Chapter 1 with the introduction of the neutrino perturbations. Neutrinos behave differently when relativistic or non-relativistic, and the full treatment must take into account the two possibilities. The treatment of the massless neutrino perturbations can be used to describe any collisionless particle that is still relativistic today, i.e. any particle with mass $m \lesssim 10^{-4}$ eV. Only one out of the three standard neutrinos can be still in this state, given that its mass is sufficiently small. The squared-mass differences obtained from the analyses of the neutrino oscillation data, in fact, tell us that the other two neutrino mass eigenstates are non-relativistic today.

In this Section we will show how it is possible to deal with neutrino perturbations in the evolution equations of the Universe, but we will not show how to find the solutions in the numerical calculation. The interested reader can see Ref. [51] for a detailed treatment.

### Massless Neutrinos

Details of neutrino decoupling would only impact perturbations that were inside the Hubble horizon at the time of neutrino decoupling. These scales are not observable today, since they are suppressed because of diffusion damping, and anyway they are contaminated by foreground emission in real dataset. They are not observable neither in the spectrum of large scale structures, since the non-linear evolution has strong effects that deleted the memory of the previous linear evolution.

Neglecting the non-thermal distortions due to electron-positron annihilation, that are very small, we can consider the neutrino distribution function to be a simple Fermi-Dirac distribution. As a consequence, the neutrino perturbations can be calculated in the same way of the photon perturbations, apart for the sign in the Fermi-Dirac distribution with respect to the Bose-Einstein one. The main difference for the neutrinos, clearly, is the absence of interaction terms with the baryons in all the relevant differential equations.

Using $\mathcal{N}$ to denote the neutrino perturbations, in analogy with $\Theta$ for the photons, we can write the differential equation for the evolution of the neutrino perturbations in the Fourier space:

$$\dot{\mathcal{N}} + ik\mu\mathcal{N} = -\dot{\Phi} - ik\mu\Psi \,.$$
(4.52)

The neutrino perturbation $\mathcal{N}$ can be treated as the photon perturbation $\Theta$, being the only difference in the equations is that for the neutrinos the limit $\sigma_T \to 0$ applies.

This is not the most general treatment that can be developed. To describe the neutrino perturbations when the distribution function is not of the standard Fermi-Dirac type one should generalize the discussion as shown for example in Ref. [51]. The extended treatment can be used if the neutrino has a chemical potential or relevant non-thermal distortions, but also for other decoupled relativistic relics.

**Massive Neutrinos**

To describe massive neutrinos we have to find a set of equations that interpolate from the CDM equations (in the large mass limit) to the massless neutrinos equations (in the small mass limit). The simplest assumption is that neutrinos are decoupled and still relativistic at the time of imposing the initial conditions, so that they have a Fermi-Dirac momentum distribution $f_{\nu,0}$. For the active neutrinos, this would be enough. Since we want to deal with sterile neutrinos, we assume that $f_{\nu,0}$ has a generic form, but we require that it is time-independent after neutrino decoupling.

For massive neutrinos, the mass enters the expression for the energy and some of the simplifications we assumed in Section 1.8 are no more valid. The reason is that the gravitational interactions induce a relative momentum shift that depends on the momentum itself. We can still simplify the Boltzmann equations with the introduction of the relative fluctuations of the phase-space distribution, that we denote with $\Upsilon$:

$$\Upsilon(\eta, \vec{x}, p, \hat{n}) \equiv \frac{f_\nu(\eta, \vec{x}, p, \hat{n})}{f_\nu(\eta, p)} - 1 \,, \tag{4.53}$$

at the first order in perturbations. In the general case, in the relativistic limit we have:

$$\Upsilon(\eta, \vec{x}, p, \hat{n}) = -\frac{1}{4}\mathcal{N}(\eta, \vec{x}, p, \hat{n})\frac{d\ln f_{\nu,0}(y)}{d\ln y} \,, \tag{4.54}$$

where $y = ap$. This expression is valid only when neutrinos are relativistic, since when each neutrino becomes non-relativistic the non-thermal distortions induced by gravity modify the distribution function.

If we write the Boltzmann equation for massive neutrinos and we replicate the calculations developed for photons and massless neutrinos, we obtain the equation of motion for $\Upsilon$ in the real space:

$$\dot{\Upsilon} + \frac{y}{\epsilon}\hat{n} \cdot \vec{\nabla}\Upsilon = \frac{d\ln f_{\nu,0}}{d\ln y}\left(\dot{\Phi} + \frac{\epsilon}{y}\hat{n} \cdot \vec{\nabla}\Psi\right) \,, \tag{4.55}$$

where $\epsilon$ is the neutrino energy. In the relativistic limit, $y/\epsilon \to 1$ and we can use Eq. (4.54) to recover Eq. (4.52).

In analogy with the treatment of the photon perturbations, it is possible to expand $\Upsilon$ in Legendre momenta to obtain an infinite hierarchy of $\Upsilon_l$. From Eq. (4.55), using the axial symmetry around $\hat{n}$ and going to the Fourier space, the equations for the $\Upsilon_l$ are

$$\dot{\Upsilon}_0 = -\frac{yk}{\epsilon}\Upsilon_1 + \dot{\Phi}\frac{d\ln f_{\nu,0}}{d\ln y} \tag{4.56}$$

$$\dot{\Upsilon}_1 = \frac{yk}{3\epsilon}(\Upsilon_0 - 2\Upsilon_2) - \frac{\epsilon k}{3y}\frac{d\ln f_{\nu,0}}{d\ln y}\Psi \tag{4.57}$$

$$\dot{\Upsilon}_l = \frac{yk}{(2l+1)\epsilon}\left[l\,\Upsilon_{l-1} - (l+1)\Upsilon_{l+1}\right], \qquad \forall l \geq 2\,. \tag{4.58}$$

Given that $y/\epsilon \to 0$ in the deeply non-relativistic limit, one could show that the neutrino perturbations evolve exactly as those of CDM after each neutrino becomes non-relativistic. This ca ne seen using the definitions in Eqs. (1.20), (1.89) and (1.90) for massive neutrinos, with the expression of $f_\nu$ at the first order in perturbations.

**Adiabatic initial Conditions in Presence of Neutrinos**

In presence of neutrinos, the relation $\Phi + \Psi = 0$ is no more valid in the early Universe, as a consequence of the neutrino anisotropic stress in Eq. (1.109). The presence of neutrinos induce a constant offset between the metric perturbations $\Phi$ and $\Psi$. The growing adiabatic solution becomes

$$\Phi = -\Psi \left(1 + \frac{2}{5} R_\nu\right), \tag{4.59}$$

where we defined the neutrino ratio $R_\nu$ as

$$R_\nu \equiv \frac{\rho_\nu^{(0)}}{\rho_\gamma^{(0)} + \rho_\nu^{(0)}} = \frac{\frac{7}{8} \left(\frac{4}{11}\right)^{4/3} N_{\rm eff}}{1 + \frac{7}{8} \left(\frac{4}{11}\right)^{4/3} N_{\rm eff}}, \tag{4.60}$$

assuming that all the neutrinos are relativistic at the time of applying the initial conditions. It is possible to show that the updated version of Eqs. (1.117) and (1.118) reads

$$\Theta_0(k, \eta_i) = \mathcal{N}_0(k, \eta_i) = \frac{\delta}{3} = \frac{\delta_b}{3} = -\frac{\Psi}{2}, \tag{4.61}$$

where $\Psi$ can be substituted with $\Phi$ using the relation (4.59).

Equation (4.59) may give the wrong impression that the initial conditions depend on the neutrino anisotropic stress. The shift between $\Phi$ and $\Psi$ is explicit in the conformal Newtonian gauge, but it disappears in other gauges, so that it is clear that $R_\nu$ has no observable consequences. Without changing gauge, this can be seen from the fact that the equations contain the metric perturbations in the $\dot{\Phi}$ and $k\Psi$ terms. The contribution of $R_\nu$ does not affect $\dot{\Phi}$ and the leading term of $k\Psi$ is of order $(k\eta)$. As a consequence, the equations for the evolution are affected by the presence of neutrinos only at the next-to-leading order in a $(k\eta)$ expansion.

### 4.4.3 Neutrino Free-streaming

After decoupling, neutrinos evolve as freely falling particles. Neutrino free-streaming does not affect all the scales, since the Universe expands. The characteristic quantities that describe the distances related to neutrino free-streaming are the *free-streaming scale* $\lambda_{\rm FS}$, indicating the scales at which free-streaming can be ignored, and the *free-streaming horizon* $d_{\rm FS}$, corresponding to the average distance traveled by neutrinos before a given time.

The free-streaming scale $\lambda_{\rm FS}$, or the corresponding wavenumber $k_{\rm FS}$ in comoving Fourier space, can be defined as the product of the neutrino velocity $c_\nu$ by the Hubble time $t_H = 1/H$, normalized in analogy with the Jeans length:

$$\lambda_{\rm FS}(\eta) = a(\eta) \frac{2\pi}{k_{\rm FS}} \equiv 2\pi \sqrt{\frac{2}{3}} \frac{c_\nu(\eta)}{H(\eta)}. \tag{4.62}$$

This is the scale below which the free-streaming particle cannot be confined inside a gravitational potential well.

The free-streaming horizon, instead, is defined as the integral

$$d_{\rm FS}(\eta) = a(\eta) \, r_{\rm FS}(\eta) \equiv a(\eta) \int_{\eta_{\rm in}}^{\eta} c_\nu(\eta) d\eta, \tag{4.63}$$

which is independent of $\eta_{\rm in}$ if $\eta_{\rm in} \ll \eta$ is chosen after the end of inflation.

While a neutrino is relativistic, its speed is $c_\nu = c = 1$ and we have simply

$$\lambda_{\rm FS} = 2\pi \sqrt{\frac{2}{3}} \frac{1}{H}, \qquad d_{\rm FS} = a\eta. \tag{4.64}$$

These quantities are very close to each other, since $a\eta = H^{-1}$ during radiation domination and $a\eta = 2H^{-1}$ during matter domination.

The story is more complicated for neutrinos that become non-relativistic during the Universe evolution. Quantitatively, neutrinos become non-relativistic when their mean momentum $\langle p \rangle$ becomes smaller than their mass $m_\nu$. If neutrinos follow a relativistic Fermi-Dirac distribution with negligible chemical potential, the average momentum can be calculated and it is $\langle p \rangle = 3.15\,T_\nu$. Using the relation between the photon and neutrino temperatures, it is possible to show that a neutrino becomes non-relativistic during matter domination if its mass is

$$5.28 \times 10^{-4}\,\text{eV} \leq m_\nu \lesssim 1.5\,\text{eV}\,. \tag{4.65}$$

Since we are interested in neutrinos below 1.5 eV, we will firstly discuss the free-streaming quantities during matter domination. After the non-relativistic transition, the thermal velocity $c_\nu$ scales with $a^{-1}$ or $\eta^{-2}$, since

$$c_\nu = \frac{\langle p \rangle}{m_\nu} = 158(1+z)\left(\frac{T_\nu}{T_\nu^{id}}\right)\left(\frac{1\,\text{eV}}{m_\nu}\right)\text{Km s}^{-1}\,. \tag{4.66}$$

This means that the free-streaming length increases with $\eta$ and the comoving free-streaming length decreases with $\eta^{-1}$. At the time of the non-relativistic transition, the comoving free-streaming length passes through a maximum that corresponds to the wavenumber $k_{\text{NR}}$. This can be approximated as

$$k_{\text{NR}} \equiv k_{\text{FS}}(\eta_{\text{NR}}) \simeq 0.0178\,\Omega_M^{1/2}\left(\frac{T_\nu^{id}}{T_\nu}\right)^{1/2}\left(\frac{m_\nu}{1\,\text{eV}}\right)^{1/2} h\,\text{Mpc}^{-1}\,, \tag{4.67}$$

valid only if the transition occurs during matter domination. The comoving free-streaming horizon, instead, becomes

$$r_{\text{FS}}(\eta > \eta_{\text{NR}}) \simeq \sqrt{\frac{3}{2}}\frac{4}{k_{\text{NR}}}\left(1 - \frac{1}{2}\left[\frac{1+z}{1+z_{\text{NR}}}\right]^{1/2}\right)\,. \tag{4.68}$$

Also in this case the expression is valid during matter domination only.

For heavier neutrinos that becomes non-relativistic during radiation domination, the things are slightly different. The free-streaming length still increases as $\eta$, but the comoving free-streaming length is constant, since in this case the relation between $a$ and $\eta$ during radiation domination must be considered. Since the comoving free-streaming length starts to decrease after matter-radiation equality, it encounters its maximum between $\eta_{\text{NR}}$ and $\eta_{\text{eq}}$. The minimum value of $k_{\text{FS}}$ is then

$$k_{\text{NR}} \equiv k_{\text{FS}}(\eta_{\text{NR}}) \simeq 0.776\,\Omega_R^{1/2}\left(\frac{T_\nu^{id}}{T_\nu}\right)^{1/2}\left(\frac{m_\nu}{1\,\text{eV}}\right)^{1/2} h\,\text{Mpc}^{-1}\,. \tag{4.69}$$

If we approximate

$$c_\nu = \begin{cases} 1 & \text{for } \eta \leq \eta_{\text{NR}} \\ \eta_{\text{NR}}/\eta & \text{for } \eta_{\text{NR}} < \eta \leq \eta_{\text{eq}} \\ \eta_{\text{NR}}\eta_{\text{eq}}/\eta^2 & \text{for } \eta > \eta_{\text{eq}} \end{cases}\,, \tag{4.70}$$

the comoving free-streaming horizon after matter-radiation equality becomes

$$r_{\text{FS}}(\eta > \eta_{\text{eq}}) \simeq \sqrt{\frac{3}{2}}\frac{2}{\eta_{\text{NR}}}\left[1 + \frac{1}{2}\log\left(\frac{1+z_{\text{NR}}}{1+z_{\text{eq}}}\right) - \frac{1}{2}\left(\frac{1+z}{1+z_{\text{eq}}}\right)^2\right]\,. \tag{4.71}$$

The last term is usually negligible, but the logarithm may be large for heavy particles becoming non-relativistic at high redshift.

In the next Subsections we will use all the defined quantities to describe the neutrino effects on the main cosmological observables. We will try to separate the background from the perturbation effects, both for massless and massive neutrinos.

### 4.4.4 Physical Effects as Radiation in the early Universe

Before discussing the impact of neutrinos on the CMB spectrum, we recall that it is complex to single out the effects of a specific quantity, since it is connected with the other quantities. It is often difficult (or impossible) to separate the contributions of each parameter, but we will do our best to isolate the effects of neutrinos from those of all the others parameters.

The contribution of neutrinos as relativistic particles can be described simply through the parameter $N_{\text{eff}}$ we have already defined. As relativistic components, additional neutrino degrees of freedom change the time of matter-radiation equality (effect **(C3)** in Section 2.5), whose redshift $z_{\text{eq}}$ is given by

$$1 + z_{\text{eq}} = \frac{\rho_m}{\rho_r} = \frac{\omega_m}{\omega_r} = \frac{\omega_m}{\omega_\gamma} \frac{1}{1 + 0.2271\, N_{\text{eff}}}\,, \tag{4.72}$$

where we used Eq. (4.43). To shorten the notation, we define conveniently

$$\alpha \equiv 1 + 0.2271\, N_{\text{eff}}\,. \tag{4.73}$$

A shift in the matter-radiation equality affects the position (effect **(C1)**) and the shape (effect **(C4)**) of the acoustic peaks of the CMB (see Ref. [316]). At recombination, the extra radiation component enhances the expansion rate $H$. This increase of $H$ generates a decrease of the comoving sound horizon $r_{\text{s}} \propto H^{-1}$ [317] and a reduction of the angular scale of the acoustic peaks $\theta_{\text{s}} = r_{\text{s}}/D_A$, leading to a shift of the CMB peaks towards higher multipoles (see Fig. 2(a) of Ref. [316]). In addition, if matter-radiation equality is delayed, the amplitude of the first CMB peak at $\ell \simeq 200$ is increased by the early ISW effect, since decoupling occurs when matter domination is at an earlier stage and the subdominant radiation component causes a slow decrease of the gravitational potential (see Figs. 2(a) and 2(b) of Ref. [316]).

These effects of additional relativistic neutrinos can be partially compensated if other cosmological parameters are simultaneously varied. For example, if the total matter density $\omega_m$ is also increased by a factor $\alpha$ without altering the baryon density $\omega_b$, so that the ratio between odd and even CMB peaks is not altered, according to Eq. (4.72) $z_{\text{eq}}$ can be kept fixed and the two effects discussed above do not appear. After having restored the matter radiation equality, we should consider the coincidence time (effect **(C7)**) that is altered by the increase of $\omega_m$. We can increase also the cosmological constant energy density $\Omega_\Lambda$ and all the important redshifts at which the Universe change its evolution domination are preserved. However, we cannot obtain exactly the same CMB spectrum as in the standard case, because the additional relativistic neutrinos increase the Silk damping effect at high multipoles [317–319]. The damping depends on the ratio $r_{\text{d}}/r_{\text{s}}$, where $r_{\text{d}} \propto H^{-1/2}$ is the photon diffusion length at recombination [317]. Since at fixed $z_{\text{eq}}$ we have $H^2 \propto \rho_r = \alpha\rho_\gamma$, an increase of $N_{\text{eff}}$ corresponds to an increase of $H$ and to an increase of $r_{\text{d}}/r_{\text{s}} \propto \alpha^{1/4}$, which enhances the Silk damping at high-multipoles [317].

The effects of $N_{\text{eff}}$ are summarized in Fig. 4.2 from Ref. [320], where we compare the CMB spectrum predicted by a model with $\Delta N_{\text{eff}} = 0$ (black line) with the spectrum obtained varying $N_{\text{eff}}$ alone (red line with $\Delta N_{\text{eff}} = 2$), the one with changed $N_{\text{eff}}$ and $\omega_m$ (blue line, same $\Delta N_{\text{eff}}$, $\omega_m$ rescaled by $\alpha$) and the last one with rescaled $N_{\text{eff}}$, $\omega_m$ and $\Omega_\Lambda$ (green line, same $\Delta N_{\text{eff}}$ and $\omega_m$, $\Omega_\Lambda$ rescaled by $\alpha$). It is easy to see that the change in the matter-radiation equality has an effect on the amplitude, the position and the envelope of the peaks, that is partially restored changing the total matter density. A residual effect is still present because of the different time of matter-$\Lambda$ equality. Once also the second equality is restored to the initial value, the only remaining background effect is the enhanced diffusion damping at high multipoles, well visible comparing the black and green curves in the lower panel.

The effect of altering $N_{\text{eff}}$ is not limited to the background evolution of the Universe, however. At the level of perturbations, neutrino effects can be important when a mode crosses the sound horizon and acoustic oscillations are driven by metric fluctuations. The presence
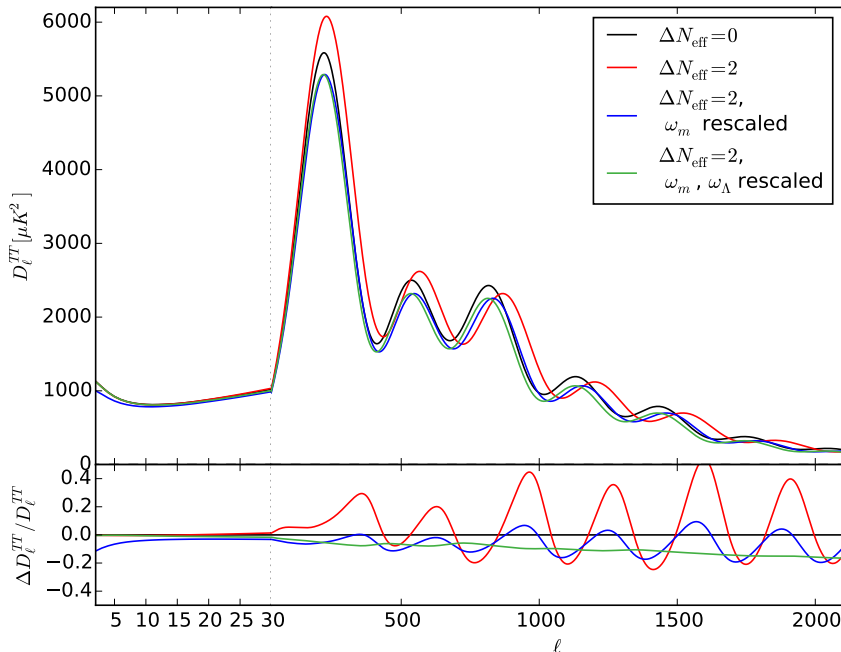
Figure 4.2: Comparison of the CMB spectrum obtained for different values of the effective number of relativistic species $N_{\mathrm{eff}}$ and for different values of $\omega_m$ and $\omega_\Lambda$, rescaled to fix the matter-radiation equality and the coincidence times. The upper panel shows the spectrum $D_l = l(l+1)\,C_l^{TT}/(2\pi)$, while the lower panel shows the relative difference with respect to the model with a standard neutrino content. From Ref. [320].

of neutrinos varies the size of metric fluctuations inside the free-streaming scale, below which neutrino cannot cluster. During radiation domination, neutrinos are a large fraction of the total content of the Universe and they significantly reduce the metric fluctuations at distances smaller than their free-streaming scale. We have seen that temperature fluctuations are boosted by time variations of the metric fluctuations: the presence of neutrinos has hence the result of reducing this boost during the driven oscillation stage. The temperature fluctuations for the modes that enter the sound horizon before decoupling, especially during radiation domination, are then smaller. An analytic approximation of the impact of neutrinos on the driven oscillations has been derived in Ref. [321]. The oscillation amplitude inside the sound horizon is reduced by a factor $(1 + 4/15R_\nu)^{-1}$. With respect to the neutrinoless model the CMB peaks are reduced by the square of:

$$\frac{\Delta C_l}{C_l} = \left(1 + \frac{4}{15}\frac{\alpha - 1}{\alpha}\right)^{-2}. \tag{4.74}$$

For small variations of $N_{\mathrm{eff}}$ around three, the above expression can be approximated with

$$\frac{\Delta C_l}{C_l} = -0.072\,\Delta N_{\mathrm{eff}}, \tag{4.75}$$

valid in the region of acoustic oscillations. A more detailed calculation [319] reported a different formula:

$$\frac{\Delta C_l}{C_l} = \left(1 - 0.2683\,R_\nu + \mathcal{O}(R_\nu^2)\right)^2, \tag{4.76}$$

in good agreement with Eq. (4.74). The authors of Ref. [319] report also that relativistic neutrinos tend to pull temperature perturbations out of gravitational potential wells, since neutrinos moves faster than the temperature perturbations (traveling at a speed $c_s \simeq c/\sqrt{3}$).

This *neutrino drag* effect causes a shift in the phase of the acoustic oscillations, so that the peaks are shifted at smaller $l$. The analytic approximation gives:

$$\Delta l_{\text{peak}} = -\frac{r_s(\eta_{\text{LS}})}{r_A(\eta_{\text{LS}})} \left( 0.1912\, R_\nu + \mathcal{O}(R_\nu^2) \right) . \tag{4.77}$$

Finally, the effective number of relativistic species is connected with BBN: the number of relativistic degrees of freedom fixes the expansion rate during BBN, that in turn fixes the abundances of light elements. BBN can thus give strong constraints on $N_{\text{eff}}$ through the observations of the primordial abundances of light elements [322–325]. According to Ref. [326], BBN limits the effective number of additional relativistic species to $\Delta N_{\text{eff}} < 1$ at 95% C.L., regardless of the inclusion of CMB constraints on the baryon density $\Omega_b h^2$. More recently, the authors of Ref. [327] obtained $\Delta N_{\text{eff}} < 0.2$ at 95% C.L. considering the BBN and CMB data.

### 4.4.5 Physical Effects as massive Component

The parameterization of massive particles as neutrinos is a not trivial step of the description of the cosmological theory. While a single parameter is enough to describe massless particles, the energy density $\omega_\nu$ plays an important role in describing massive neutrinos, but it may not catch all the effects that they induce on cosmology. If one wants to go beyond the minimal picture, for example, the mass of each neutrino mass eigenstate plays a role, as well any modification of the phase-space distribution function due to the presence of chemical potentials or non-thermal distortions. We will assume for simplicity that the three active neutrinos share the same mass, being the effects of the single neutrino masses extremely small to be detected. The effects of different neutrino masses would be easier to detect in the power spectrum of large scale structures, for which the suppression due to neutrino free-streaming is larger. Also the small non-thermal distortions due to electron-positron annihilation after a non-instantaneous neutrino decoupling, that would alter differently the distribution functions of $\nu_e$, $\nu_\mu$ and $\nu_\tau$, have a very small imprint on the observable quantities.

As we are assuming masses below 1.5 eV, neutrinos are still relativistic at matter-radiation equality. The redshift of equality, defined in Eq. (4.72), must be calculated with the neutrinos as relativistic components. The comparison between different masses can be performed at fixed $\omega_m = \omega_b + \omega_c$, or better at fixed ratio $\omega_b / \omega_c$. The matter energy density today, however, is $\omega_m = \omega_b + \omega_c + \omega_\nu$, since neutrinos became non-relativistic. The difference between the model with $\sum m_\nu = 0$ and the one with $\sum m_\nu > 0$ appears only after the neutrino non-relativistic transition, that occurs at $z_{\text{NR}} \propto m_\nu$. The neutrino mass has then an impact only at redshift $z \lesssim z_{\text{NR}}$ on the comoving angular diameter distance to recombination and on the redshift of the dark matter-dark energy equality. For neutrinos that are non-relativistic at photon decoupling ($m_\nu \geq 0.6\,\text{eV}$), there is an additional impact on the comoving sound horizon $r_s(\eta_{\text{LS}})$ and on the damping scale $r_d(\eta_{\text{LS}})$ at recombination.

One between $d_A(\eta_{\text{LS}})$ and $z_\Lambda$ can be fixed changing $h$ or $\Omega_\Lambda$, but not both simultaneously. Since $d_A(\eta_{\text{LS}})$ is related to the scale of the peaks, it is more interesting to fix it and to let $z_\Lambda$ change. Most of the effects **(C1)**–**(C8)** are unchanged for variations of these quantities, with only two exceptions. If $d_A(\eta_{\text{LS}})$ is maintained fixed, the shift in $z_\Lambda$ induces a change in the late ISW effect **(C7)** that alters the spectrum of CMB anisotropies at the largest scales. Moreover, only for neutrinos heavier than 0.6 eV, the additional impact on $r_d(\eta_{\text{LS}})$ causes a variation in the diffusion damping **(C4)**. This concludes what we can say about the modifications of the background evolution, but additional effects appear at the perturbation level.

Neutrino masses can cause perturbation effects through the evolution of the metric perturbations after decoupling (early ISW effect) or through the gravitational driving of photon-baryon oscillations before decoupling, as already discussed for the massless neutrinos. The former effect gives the larger contribution in the multipoles range $20 \lesssim l \lesssim 500$. The depletion

of the spectrum in this range can be roughly approximated with [51, 328]

$$\frac{\Delta C_l}{C_l} \simeq -\left(\frac{m_\nu}{10\,\text{eV}}\right)\%,$$

(4.78)

but the multipoles range that it affects depends on the neutrino free-streaming. Since massive neutrinos can cluster at scales $k < k_{\text{NR}}$, while massless neutrinos free-streams at the same scales, the metric perturbations experience less decay in presence of neutrino masses. For this reason, the early ISW effect is smaller for $k < k_{\text{NR}}$, which is visible above a given angle on the CMB spectra.

# Part II

# Beyond the Standard Model

# Chapter 5

# Light Sterile Neutrino in Cosmology

*This Chapter is based on Refs. [22–24].*

In the previous Chapters we introduced the main ingredients of the analyses we are going to present: the Cosmic Microwave Background (CMB) radiation physics and observations, the other cosmological observations, the physics of neutrino and their effects in cosmology, with a particular attention to the light sterile neutrino (LS$\nu$) with mass of around 1 eV motivated by short-baseline (SBL) neutrino oscillations. In this Chapter we study the constraints on the LS$\nu$ that can be obtained from the analysis of CMB data and we show how other cosmological measurements can influence these constraints.

## 5.1 Light Sterile Neutrino Constraints with Planck 2013 Results

After the Planck collaboration published the 2013 release of data and codes [20, 72], a lively discussions started to grow [140, 324, 329–338] on the value of the effective number of relativistic degrees of freedom $N_{\rm eff}$ before photon decoupling (see [51, 152, 339]), which gives the energy density of radiation $\rho_r$ through the relation presented in Eq. (4.43). Since the value of $N_{\rm eff}$ in the Standard Model (SM) is $N_{\rm eff}^{\rm SM} = 3.046$ [304, 305], a positive measurement of $\Delta N_{\rm eff}$ may be a signal that the radiation content of the Universe was due not only to photons and SM neutrinos, but also to some additional light particle called generically "dark radiation".

In this Chapter we consider the possibility that the dark radiation is made of the light sterile neutrinos (see Chapter 4) whose existence is indicated by the results of SBL neutrino oscillation experiments (see Section 4.2). Here we consider the simplest possibility of the 3+1 scheme presented in Section 4.1, in which the three active flavor neutrinos $\nu_e$, $\nu_\mu$, $\nu_\tau$, are mainly composed of three very light neutrinos $\nu_1$, $\nu_2$, $\nu_3$, with masses much smaller than 1 eV, and there is a sterile neutrino $\nu_s$ which is mainly composed of a new massive neutrino $\nu_4$ with mass $m_4 \sim 1\,{\rm eV}$.

The problem of the determination of $N_{\rm eff}$ from cosmological data is related to that of the Hubble constant $H_0$, because these two quantities are positively correlated in the analysis of the data (see Subsection 4.4.4 and Refs. [15, 22, 23, 316, 317]). Since dedicated local astrophysical experiments obtained values of $H_0$ which are larger than that obtained by the Planck collaboration from the analysis of cosmological data alone [72] (see Section 3.3), there is an indication that $N_{\rm eff}$ may be larger than 3.046, as a consequence of the correlation between $N_{\rm eff}$ and $H_0$. Here, we will consider the local measurement on $H_0$ from HST [121] as a prior in the cosmological analyses.

Since the neutrino oscillation explanation of SBL data requires the existence of a massive neutrino at the eV scale, we discuss also the cosmological bounds on the effective sterile neutrino mass $m_s^{\rm eff}$ defined in Eq. (4.47). For the distribution function of the LS$\nu$, we consider the two cases discussed in the previous Chapter and by the Planck collaboration [72] (see

| | data | $H_0^{\mathrm{gbf}}$ | $H_0^{\mathrm{mbf}} \pm 1\sigma$ | $2\sigma$ |
|---|---|---|---|---|
| no SBL prior | CMB+$H_0$ | 73.6 | $72.7^{+1.9}_{-1.7}$ | $69.0 \div 76.3$ |
| | CMB+$H_0$+BAO | 71.1 | $71.5^{+1.4}_{-1.4}$ | $68.7 \div 74.4$ |
| | CMB+$H_0$+BAO+LGC | 71.1 | $70.4^{+1.5}_{-1.3}$ | $68.1 \div 73.5$ |
| TH SBL prior | CMB | 66.8 | $66.6^{+1.1}_{-1.2}$ | $64.3 \div 68.9$ |
| | CMB+$H_0$ | 68.7 | $68.7^{+1.0}_{-1.1}$ | $66.5 \div 70.7$ |
| | CMB+$H_0$+BAO | 68.7 | $68.8^{+0.8}_{-0.7}$ | $67.3 \div 70.4$ |
| | CMB+$H_0$+BAO+LGC | 69.1 | $69.3^{+0.6}_{-0.6}$ | $68.1 \div 70.6$ |
| DW SBL prior | CMB | 66.5 | $66.9^{+1.2}_{-1.3}$ | $64.6 \div 69.4$ |
| | CMB+$H_0$ | 68.1 | $68.9^{+1.1}_{-1.0}$ | $66.9 \div 71.0$ |
| | CMB+$H_0$+BAO | 69.3 | $69.1^{+0.8}_{-0.8}$ | $67.6 \div 70.6$ |
| | CMB+$H_0$+BAO+LGC | 69.5 | $69.7^{+0.7}_{-0.5}$ | $68.6 \div 71.0$ |

Table 5.1: Global best-fit value $H_0^{\mathrm{gbf}}$, marginal best-fit $H_0^{\mathrm{mbf}} \pm 1\sigma$ (68.27%) and $2\sigma$ (95.45%) limits for $H_0$ obtained from the analysis of the indicated data sets. From Ref. [22].

| | data | $N_{\mathrm{eff}}^{\mathrm{gbf}}$ | $N_{\mathrm{eff}}^{\mathrm{mbf}} \pm 1\sigma$ | $2\sigma$ |
|---|---|---|---|---|
| no SBL prior | CMB+$H_0$ | 3.84 | $3.76^{+0.25}_{-0.23}$ | $3.29 \div 4.26$ |
| | CMB+$H_0$+BAO | 3.59 | $3.71^{+0.23}_{-0.27}$ | $3.17 \div 4.18$ |
| | CMB+$H_0$+BAO+LGC | 3.57 | $3.51^{+0.29}_{-0.29}$ | $3.05 \div 4.01$ |
| TH SBL prior | CMB | 3.29 | $3.26^{+0.21}_{-0.10}$ | $3.05 \div 3.67$ |
| | CMB+$H_0$ | 3.23 | $3.23^{+0.19}_{-0.12}$ | $3.05 \div 3.66$ |
| | CMB+$H_0$+BAO | 3.11 | $3.23^{+0.15}_{-0.11}$ | $3.05 \div 3.55$ |
| | CMB+$H_0$+BAO+LGC | 3.36 | $3.32^{+0.12}_{-0.09}$ | $3.15 \div 3.57$ |
| DW SBL prior | CMB | 3.43 | $3.35^{+0.16}_{-0.15}$ | $3.09 \div 3.73$ |
| | CMB+$H_0$ | 3.19 | $3.31^{+0.18}_{-0.13}$ | $3.08 \div 3.70$ |
| | CMB+$H_0$+BAO | 3.29 | $3.30^{+0.13}_{-0.13}$ | $3.08 \div 3.60$ |
| | CMB+$H_0$+BAO+LGC | 3.30 | $3.42^{+0.11}_{-0.11}$ | $3.22 \div 3.67$ |

Table 5.2: As Tab. 5.1, but for $N_{\mathrm{eff}}$. From Ref. [22].

also [306]): the Thermal (TH) model, for which $m_s^{\mathrm{eff}} = (\Delta N_{\mathrm{eff}})^{3/4} m_s$ (see Eq. (4.49)) and the Dodelson-Widrow (DW) model [313], for which $m_s^{\mathrm{eff}} = \Delta N_{\mathrm{eff}} m_s$ (see Eq. (4.51)). The thermal and the Dodelson-Widrow models are discussed in Subsection 4.4.1.

A further important problem is the compatibility of the cosmological bounds on $N_{\mathrm{eff}}$ and $m_s^{\mathrm{eff}}$ with the active-sterile neutrino mixing required to fit SBL oscillation data. The stringent bounds on $N_{\mathrm{eff}}$ and $m_s^{\mathrm{eff}}$ presented in Ref. [44,72] by the Planck collaboration imply [311] that the production of sterile neutrinos in the early Universe, that should occur given the mixing angles relevant for active-sterile oscillations, is suppressed by some non-standard mechanism. Here we adopt a phenomenological approach similar to the one in Refs. [282, 303, 340]: we use the results of the fit of SBL neutrino oscillation data [199] as a prior for the analysis of cosmological data. In this way, in Subsection 5.1.3 we derive the combined constraints on $N_{\mathrm{eff}}$ and $m_s^{\mathrm{eff}}$ and the related constraints on $H_0$ and $m_s$.

| | data | $m_{s,\mathrm{gbf}}^{\mathrm{eff}}$ | $m_{s,\mathrm{mbf}}^{\mathrm{eff}}$ | $1\sigma$ | $2\sigma$ | $m_s^{\mathrm{gbf}}$ | $m_s^{\mathrm{mbf}}$ | $1\sigma$ | $2\sigma$ | |
|---|---|---|---|---|---|---|---|---|---|---|
| no SBL prior | CMB+$H_0$ | 0 | 0 | $< 0.10$ | $< 0.27$ | 0 | 0 | $< 0.13$ | $< 0.38$ | (TH) |
| | | | | | | | | $< 0.14$ | $< 0.44$ | (DW) |
| | CMB+$H_0$+BAO | 0 | 0 | $< 0.13$ | $< 0.32$ | 0 | 0 | $< 0.18$ | $< 0.51$ | (TH) |
| | | | | | | | | $< 0.21$ | $< 0.65$ | (DW) |
| | CMB+$H_0$+BAO+LGC | 0.41 | 0.42 | $0.28 \div 0.56$ | $0.15 \div 0.70$ | 0.67 | 0.62 | $0.21 \div 1.14$ | $0.00 \div 2.68$ | (TH) |
| | | | | | | 0.79 | 0.92 | $0.00 \div 1.11$ | $0.00 \div 4.81$ | (DW) |
| TH SBL prior | CMB | 0.45 | 0.42 | $0.26 \div 0.67$ | $0.11 \div 0.89$ | 1.30 | 1.28 | $1.09 \div 1.36$ | $0.96 \div 1.42$ | |
| | CMB+$H_0$ | 0.35 | 0.38 | $0.20 \div 0.61$ | $0.05 \div 0.86$ | 1.28 | 1.28 | $1.08 \div 1.35$ | $0.95 \div 1.40$ | |
| | CMB+$H_0$+BAO | 0.17 | 0.37 | $0.20 \div 0.54$ | $0.08 \div 0.75$ | 1.29 | 1.27 | $1.08 \div 1.35$ | $0.95 \div 1.39$ | |
| | CMB+$H_0$+BAO+LGC | 0.47 | 0.48 | $0.35 \div 0.60$ | $0.25 \div 0.74$ | 1.12 | 1.27 | $1.08 \div 1.35$ | $0.95 \div 1.40$ | |
| DW SBL prior | CMB | 0.44 | 0.36 | $0.19 \div 0.57$ | $0.06 \div 0.83$ | 1.13 | 1.28 | $1.08 \div 1.35$ | $0.96 \div 1.42$ | |
| | CMB+$H_0$ | 0.16 | 0.35 | $0.16 \div 0.53$ | $0.04 \div 0.77$ | 1.13 | 1.28 | $1.07 \div 1.35$ | $0.94 \div 1.39$ | |
| | CMB+$H_0$+BAO | 0.32 | 0.28 | $0.16 \div 0.46$ | $0.06 \div 0.64$ | 1.28 | 1.27 | $1.07 \div 1.34$ | $0.95 \div 1.39$ | |
| | CMB+$H_0$+BAO+LGC | 0.32 | 0.45 | $0.33 \div 0.58$ | $0.22 \div 0.72$ | 1.27 | 1.28 | $1.08 \div 1.35$ | $0.95 \div 1.40$ | |
| | SBL [199] | | | | | 1.27 | 1.27 | $1.10 \div 1.36$ | $0.97 \div 1.42$ | |

Table 5.3: As Tab. 5.1, but for $m_s^{\mathrm{eff}}$. We give also the corresponding values for $m_s$, see Eqs. (4.49) and (4.51). From Ref. [22].

### 5.1.1 Cosmological Data and Local $H_0$ Measurements

For our cosmological analysis we used a modified version of the publicly available software CosmoMC[1] [341], a Monte Carlo Markov Chain (MCMC) software which computes the theoretical predictions using CAMB[2] [58]. All the datasets we will use for the analyses have been described extensively in Chapter 3 and we indicate here only the ones we are going to consider, that are:

**Planck** − The full 2013 Planck data [20];

**WP** − The nine-year large-scale $E$-polarization WMAP data [19];

**HighL** − CMB spectra at high multipoles from Atacama Cosmology Telescope (ACT) [65] and South Pole Telescope (SPT) [67, 69]. We will indicate the Planck+WP+highL dataset with **CMB**;

**BAO** − Baryon Acoustic Oscillations (BAO) data from the Sloan Digital Sky Survey (SDSS) Data Release 7 (DR7) [89, 97, 98], the SDSS Baryon Oscillation Spectroscopic Survey (BOSS) Data Release 9 (DR9) [92, 96], and the 6dF Galaxy Survey (6dFGS) [90, 99];

**LGC** − Local Galaxy Cluster data from the Chandra Cluster Cosmology Project [134, 135];

**$H_0$** − the local determination of the Hubble parameter by the Hubble Space Telescope (HST) observations, $H_0 = 73.8 \pm 2.4$ Km s$^{-1}$ Mpc$^{-1}$ [121], used as a prior in the cosmological analyses.

### 5.1.2 Results from Cosmology

Since we are interested in studying the effects on the analyses of cosmological data of a sterile neutrino with a mass motivated by SBL oscillation anomalies, we consider an extension of the standard cosmological model in which both $N_{\mathrm{eff}}$ and $m_s^{\mathrm{eff}}$ are free parameters to be determined by the data. The model we adopt is then an extension of the $\Lambda$CDM model (described in Section 2.5) that includes $N_{\mathrm{eff}}$ and $m_s^{\mathrm{eff}}$, for a total of eight free parameters.

Figure 5.1 and the first parts of Tabs. 5.1, 5.2 and 5.3 shows the results for $H_0$, $N_{\mathrm{eff}}$ and $m_s^{\mathrm{eff}}$ obtained from the fits of CMB, CMB+$H_0$, CMB+$H_0$+BAO and CMB+$H_0$+BAO+LGC data. In Tab. 5.3 we give also the corresponding results for $m_s \simeq m_4$, which depend on
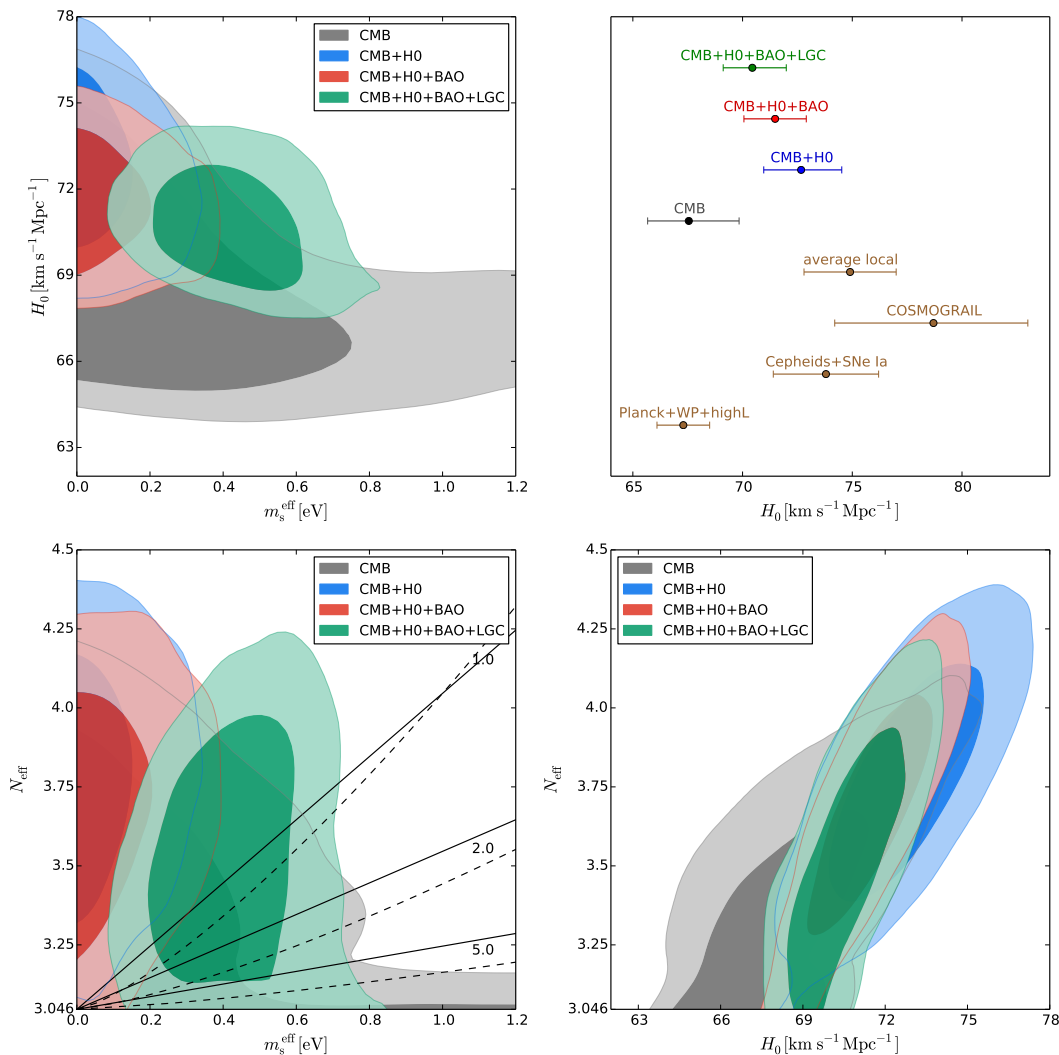
---

[1] http://cosmologist.info/cosmomc/
[2] http://camb.info/

Figure 5.1: Results of the analysis of cosmological data alone. The regions in the 2D plots show, respectively, the $1\sigma$ and $2\sigma$ marginalized posterior probability regions obtained from the analysis of the indicated data sets. The four lower intervals of $H_0$ in the upper-right panel correspond to the measurements from Planck+WP+highL in the $\Lambda$CDM model [72], Cepheids+SNe Ia [121], COSMOGRAIL [125], and a local average obtained combining the two previous measurements (see Ref. [22]). In the bottom-left panel $m_s$ is constant, with the indicated value in eV, along the dashed lines in the thermal model and along the solid lines in the Dodelson-Widrow model. From Ref. [22].

the statistical distribution of sterile neutrinos. Therefore, we distinguish the results for $m_s$ obtained in the thermal (TH) and Dodelson-Widrow (DW) models using, respectively, Eqs. (4.49) and (4.51). In Figs. 5.2, 5.3 and 5.4 we compare graphically the allowed ranges of $N_{\rm eff}$, $m_s^{\rm eff}$ and $m_s$ obtained in the different fits.

From the bottom-left panel in Fig. 5.1, one can see that the fit of CMB data alone restricts $m_s^{\rm eff}$ to small values only for $N_{\rm eff} \gtrsim 3.2$, whereas there is a tail of allowed large values of $m_s^{\rm eff}$ for smaller $N_{\rm eff}$. This is in agreement with Fig. 28-right of Ref. [72], where the tail at small $N_{\rm eff}$ has been explained as corresponding to the case in which the sterile neutrino behaves as warm dark matter, because its mass is large and it becomes non-relativistic well before recombination. This happens in both the thermal and Dodelson-Widrow models, as one can infer from Eqs. (4.49) and (4.51). The presence of this tail of the posterior distribution of $m_s^{\rm eff}$ implies that the posterior distributions of the fitted parameters depend on the arbitrary upper value chosen for $m_s^{\rm eff}$ in the CosmoMC runs (we chose $m_s^{\rm eff} < 5\,{\rm eV}$, whereas the Planck Collaboration chose $m_s^{\rm eff} < 3\,{\rm eV}$). Hence, we do not present in the tables the numerical
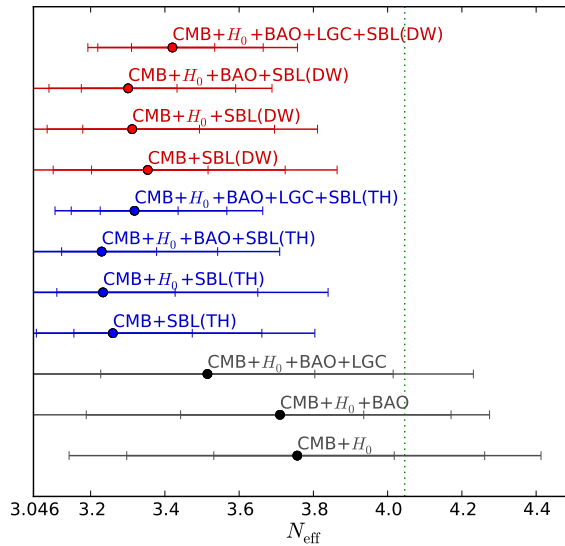
Figure 5.2: Comparison of the allowed intervals of $N_{\rm eff}$ obtained from the fits of CMB, CMB+$H_0$, CMB+$H_0$+BAO and CMB+$H_0$+BAO+LGC data without (black) and with the SBL prior in the thermal (blue) and Dodelson-Widrow (red) models. The segments in each bar correspond to $1\sigma$, $2\sigma$ and $3\sigma$ probability. The dotted vertical line corresponds to $\Delta N_{\rm eff} = 1$. From Ref. [22].
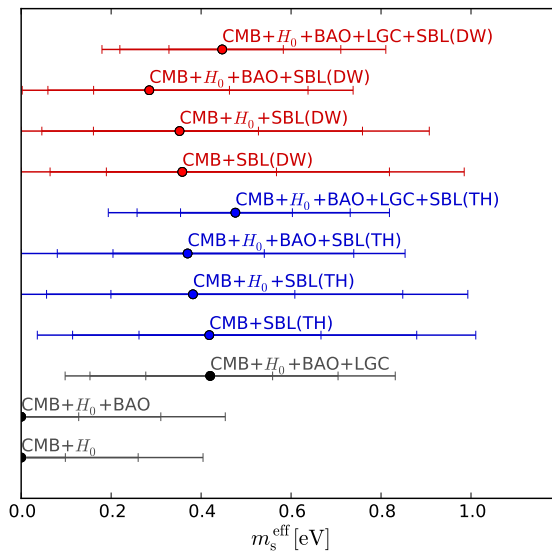


Figure 5.3: As in Fig. 5.2, but for $m_s^{\rm eff}$. From Ref. [22].

results of the fit of CMB data alone, which suffer from this arbitrariness.

The addition of the local $H_0$ prior leads to an increase of $N_{\rm eff}$ which evicts the large-$m_s^{\rm eff}$ and small-$N_{\rm eff}$ region in which the sterile neutrino behaves as warm dark matter. This can be seen from the CMB+$H_0$ allowed regions in Fig. 5.1, the corresponding upper limits for $m_s^{\rm eff}$ ($m_s$) in Figs. 5.3 (5.4) and in Tab. 5.3. The further addition of BAO data slightly lowers the best-fit values and the allowed ranges of $H_0$ and $N_{\rm eff}$ (see Figs. 5.1, 5.2 and Tabs. 5.1, 5.2). Hence, the upper limits for $m_s^{\rm eff}$ and $m_s$ (see Figs. 5.3, 5.4 and Tab. 5.3) are slightly larger, but still rather stringent, of the order of $m_s^{\rm eff} \lesssim 0.3\,{\rm eV}$ and $m_s \lesssim 0.6\,{\rm eV}$ at $2\sigma$.

Comparing the CMB+$H_0$ and CMB+$H_0$+BAO allowed intervals of $m_s$ in Tab. 5.3 and Fig. 5.4 with those obtained from the analysis of SBL data in the framework of 3+1 mixing [199], it is clear that there is a tension[3]: about $5.0\sigma$, $4.6\sigma$, $4.1\sigma$, $3.5\sigma$, respectively, in

---

[3] Possible ways of solving this tension have been discussed before the Planck 2013 data release in Refs. [342–
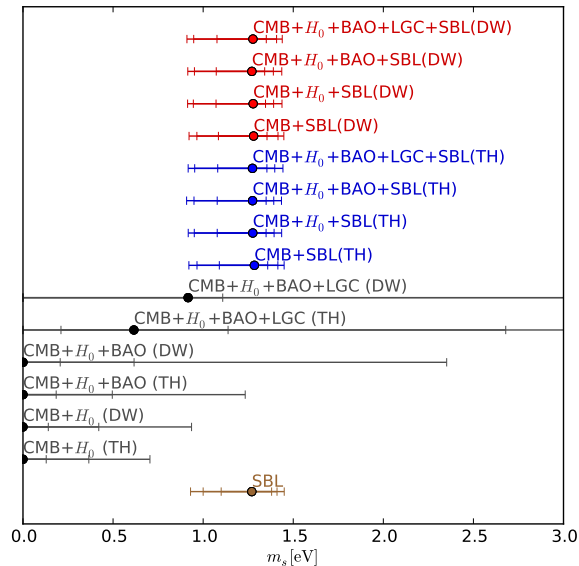
Figure 5.4: As in Fig. 5.2, but for $m_s$. The value indicated with "SBL" is obtained from the 3+1 analysis of SBL data [199]. The out-of-bounds upper limits obtained in the CMB+$H_0$+BAO+LGC analysis are: 7.4 eV ($3\sigma$, TH), 4.8 eV ($2\sigma$, DW), 17.1 eV ($3\sigma$, DW). From Ref. [22].

the CMB+$H_0$(TH), CMB+$H_0$(DW), CMB+$H_0$+BAO(TH) CMB+$H_0$+BAO(DW) fits. The tensions are smaller in the Dodelson-Widrow model and this could be an indication in favor of this case, if SBL oscillations will be confirmed by future experiments (see Refs. [162,345–351]).

Let us now consider the inclusion of the LGC data set in the cosmological fit. As discussed in Section 3.6 and in Ref. [337], the measured amount of clustering of galaxies [134, 135] is smaller than that obtained by evolving the primordial density fluctuations with the relatively large matter density at recombination measured precisely by Planck [72]. The correlation of a relatively large matter density and the clustering of galaxies can be quantified through the approximate relation $\sigma_8 \propto \Omega_m^{0.563}$ [352, 353] which relates the rms amplitude of linear fluctuations today at a scale of $8h^{-1}$ Mpc, $\sigma_8$, with the present matter density $\Omega_m$. The value of $\sigma_8$ and the amount of clustering of galaxies can be lowered by adding hot dark matter in the form of sterile neutrinos with eV-scale masses[4] to the $\Lambda$CDM cosmological model. The free-streaming of these sterile neutrinos suppresses the growth of structures at distances smaller than the free-streaming length, leading to a suppression of $\sigma_8$ with respect to the $\Lambda$CDM approximate relation $\sigma_8 \propto \Omega_m^{0.563}$. In this way, the relatively large Planck value of $\Omega_m$ can be reconciled with the relatively small amount of local galaxy clustering in the LGC data set.

Hence, the inclusion of LGC data in the cosmological fits favors the existence of a sterile neutrino with a mass of the order of that required by SBL data, which is at least partially thermalized in the early Universe [337]. The results of our CMB+$H_0$+BAO+LGC fit given in Figs. 5.1, 5.2, 5.3, 5.4 and Tabs. 5.1, 5.2, 5.3 confirm this expectation. In particular, from the allowed intervals of $m_s$ in Tab. 5.3 and Fig. 5.4 one can see that the tension between cosmological data and SBL 3+1 oscillations disappears with the inclusion of LGC data.

In the following Subsection we analyze the cosmological data using as a prior distribution for $m_s$ the posterior distribution obtained from the analysis of SBL data. This is perfectly consistent in the case of CMB+$H_0$+BAO+LGC cosmological data. However, we present also the results obtained with the CMB, CMB+$H_0$ and CMB+$H_0$+BAO cosmological data, in spite of the tension with SBL data discussed above, because we think that one cannot dismiss

---

344].

[4] Let us note that there was already a tension between LGC data and pre-Planck CMB data and the sterile neutrino solution was proposed in Refs. [135,354]
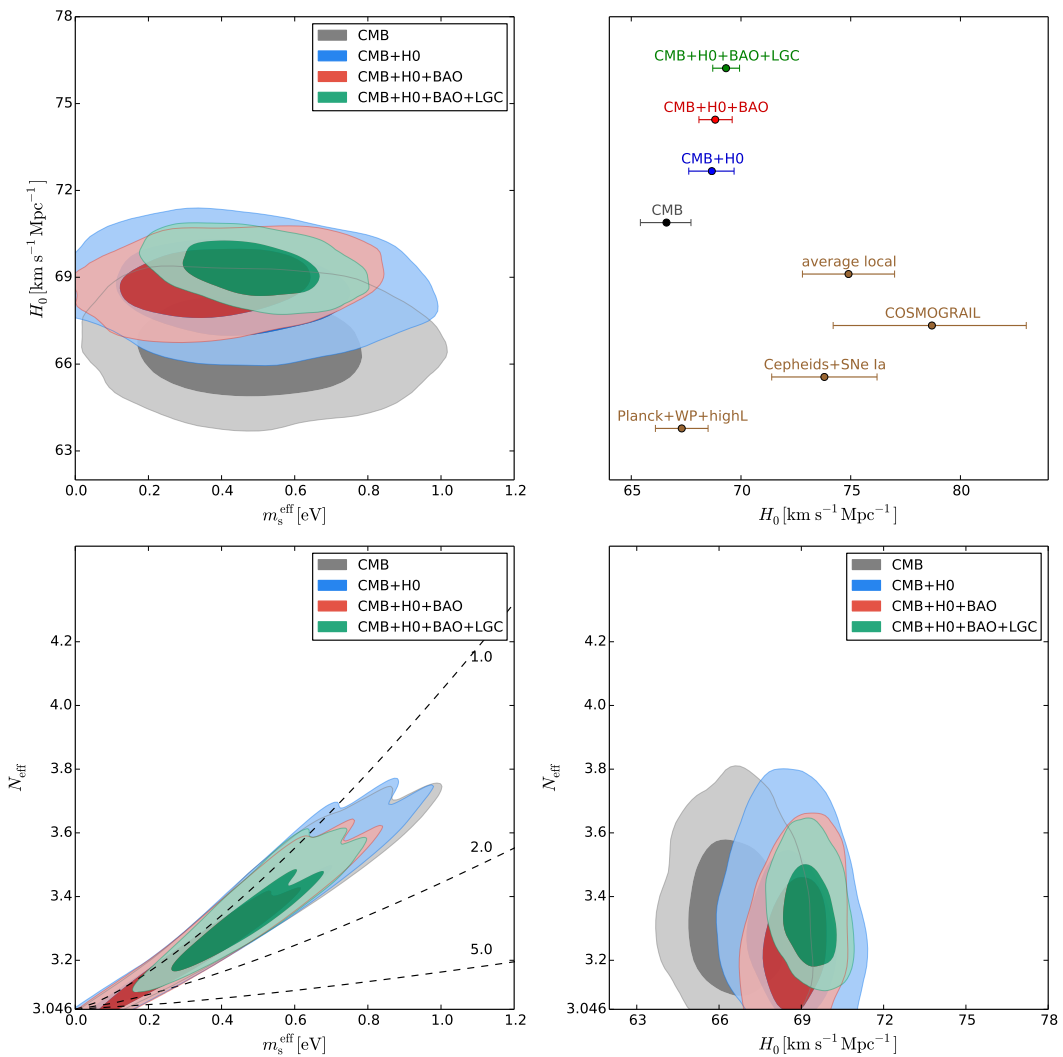
Figure 5.5: As Fig. 5.1, but with the inclusion of the SBL prior for a light sterile neutrino in the thermal model. From Ref. [22].

the results of laboratory experiments on the basis of cosmological observations, which are indirect probes of the neutrino masses and whose interpretation has larger uncertainties.

### 5.1.3 Results with the SBL Prior

The experimental data that motivate the existence of the LS$\nu$ and from which the SBL prior we use here [199] is calculated were presented in the previous Chapter. Following Refs. [282, 303, 340], we use the posterior distribution of $m_s \simeq m_4 \simeq \sqrt{\Delta m_{41}^2}$ obtained from the analysis of SBL data as a prior in the CosmoMC analysis of cosmological data. The range of $m_s$ allowed by the analysis of SBL data [199] is shown in Fig. 5.4 and Tab. 5.3. Note that the SBL prior on $m_s$ has different cosmological implications in the thermal and Dodelson-Widrow models, because the $\Delta N_{\mathrm{eff}}$ dependence of the effective mass $m_s^{\mathrm{eff}}$ is different (see Eqs. (4.49) and (4.51)).

Figure 5.5 shows the results of the analysis of various combinations of datasets (CMB, CMB+$H_0$, CMB+$H_0$+BAO and CMB+$H_0$+BAO+LGC), with the SBL prior in the thermal model. For convenience, the effect of the SBL prior on the allowed regions in the $m_s^{\mathrm{eff}}$–$N_{\mathrm{eff}}$ plane is illustrated clearly in Fig. 5.7, where each panel shows the change of the allowed regions due to the inclusion of the SBL prior in the analysis of the indicated data set. One can see that in all the four analyses the SBL prior forces the allowed region to lie near the dashed line which corresponds to $m_s = 1\,\mathrm{eV}$. In order to keep $m_s$ at the eV scale without
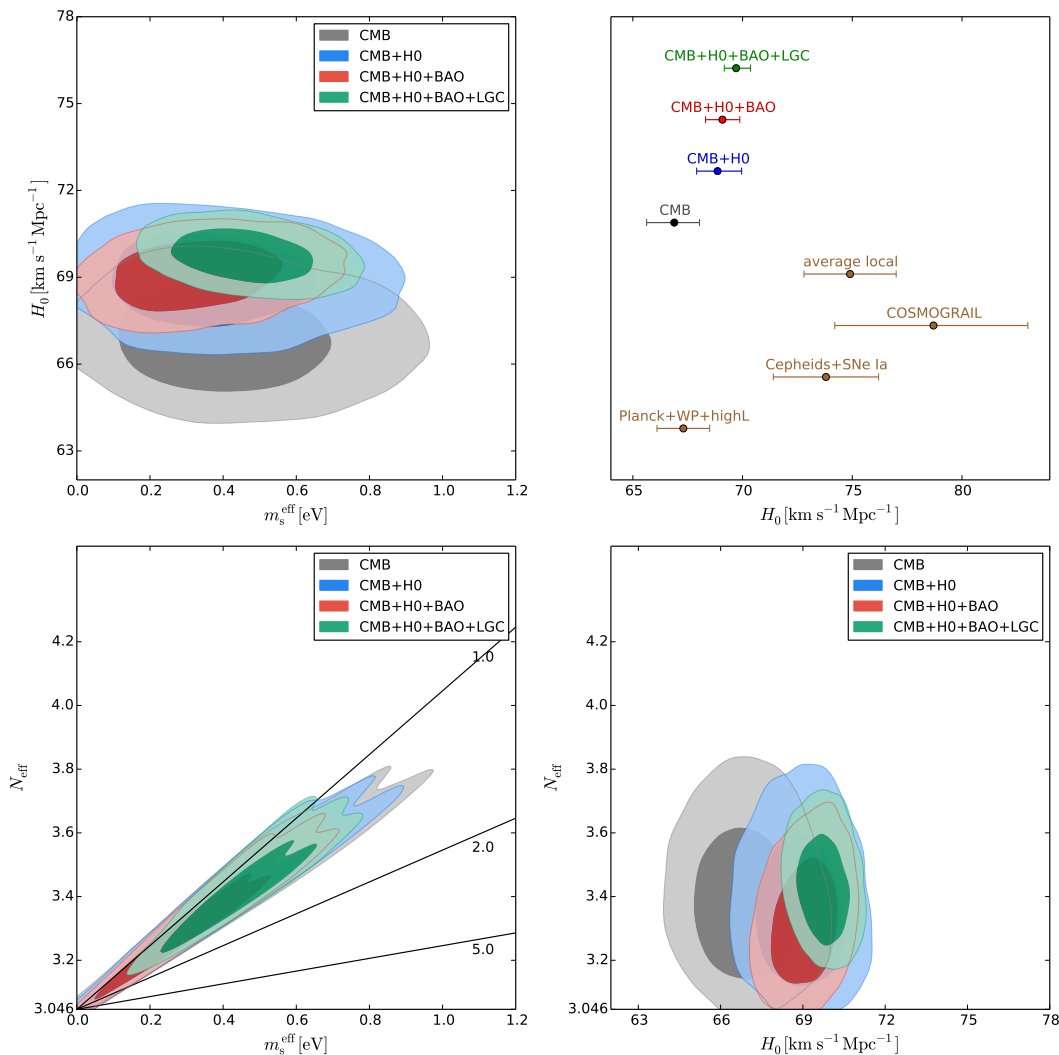
Figure 5.6: As Fig. 5.1, but with the inclusion of the SBL prior for a light sterile neutrino in the Dodelson-Widrow model. From Ref. [22].

increasing too much $m_s^{\mathrm{eff}}$, which is forbidden by the cosmological data, $N_{\mathrm{eff}}$ is forced towards low values.

In the case of the CMB+$H_0$+BAO+LGC cosmological data set, after the addition of the SBL prior the allowed range of $m_s^{\mathrm{eff}}$ (see Fig. 5.3 and Tab. 5.3) is approximately confirmed, but a lower $N_{\mathrm{eff}}$ is required (see Fig. 5.2 and Tab. 5.2), being $N_{\mathrm{eff}} \lesssim 3.7$ with $3\sigma$ probability. As discussed in Ref. [311], in the standard cosmological scenario active-sterile neutrino oscillations generated by values of the mixing parameters allowed by the fit of SBL data imply $\Delta N_{\mathrm{eff}} = 1$. Therefore, it is likely that the compatibility of the neutrino oscillation explanation of the SBL anomalies with cosmological data requires that active-sterile neutrino oscillations in the early Universe are somewhat suppressed by a non-standard mechanism, as, for example, a large lepton asymmetry [310, 355–357].

As one can see from Figs. 5.2, 5.3, 5.6 and 5.7 and from Tabs. 5.2 and 5.3, similar conclusions are reached in the Dodelson-Widrow model. One can note, however, that in this case slightly larger values of $N_{\mathrm{eff}}$ are allowed with respect to the thermal case, and there is a slightly better compatibility of cosmological and SBL data. This happens because for a given value of $m_s$ arising mainly by SBL data and an upper bound on $m_s^{\mathrm{eff}}$ given by cosmological data slightly larger values of $\Delta N_{\mathrm{eff}} \leq 1$ are allowed by Eq. (4.51) in the Dodelson-Widrow model than by Eq. (4.49) in the thermal model.
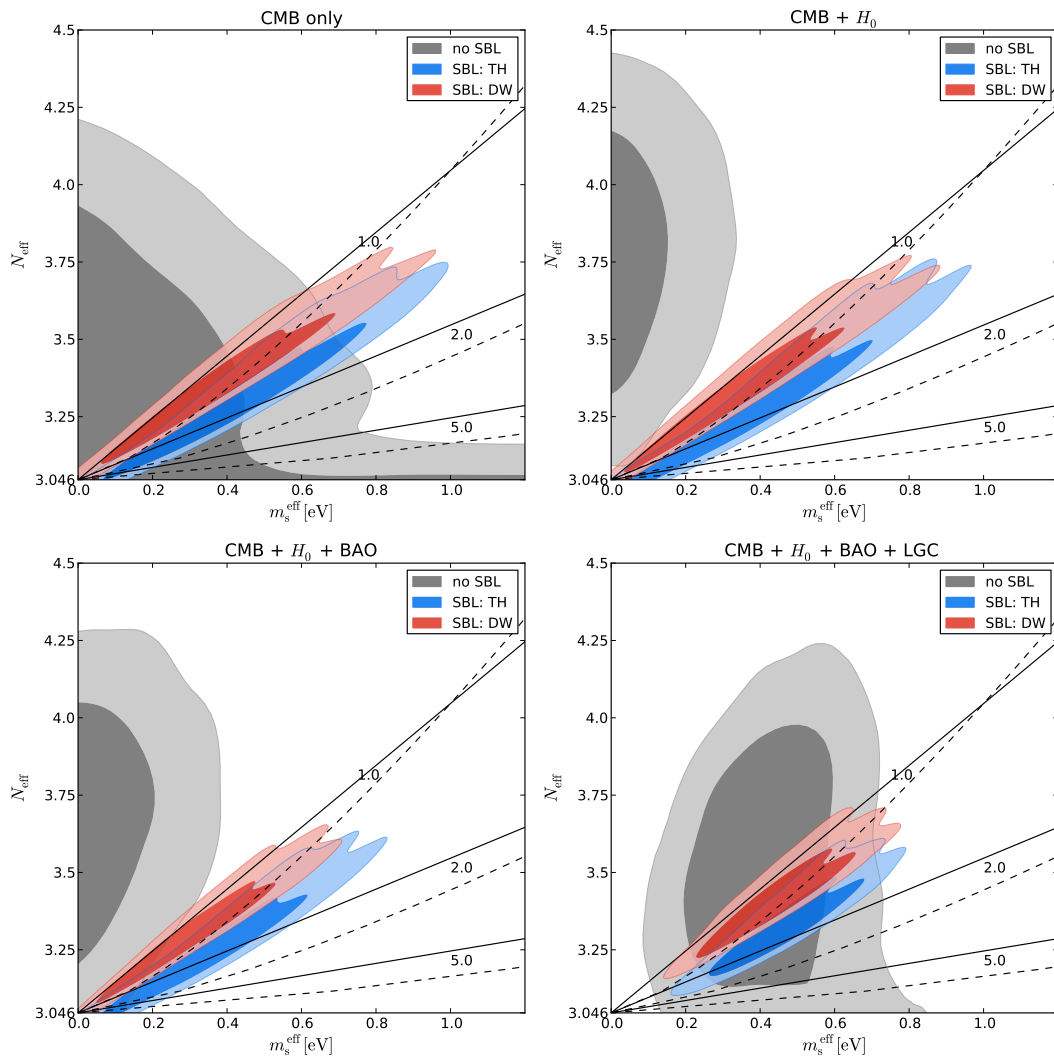
Figure 5.7: Illustrations of the effect of the SBL prior on the results of the fits of CMB, CMB+$H_0$, CMB+$H_0$+BAO and CMB+$H_0$+BAO+LGC data. The value of $m_s$ is constant, equal to the indicated value in eV, along the dashed (solid) lines in the thermal (Dodelson-Widrow) model. From Ref. [22].

### 5.1.4 Discussion

In this section we have analyzed different cosmological data, including those of the Planck experiment [20,72], taking into account the possible existence of a sterile neutrino with a mass $m_s$ at the eV scale, which could have the effect of dark radiation in the early Universe. We investigated three effects: 1) the contribution of local measurements of the Hubble constant $H_0$; 2) the effect of the measurements of the mass distribution of local galaxy clusters [337]; 3) the assumption of a prior distribution for $m_s$ obtained from the analysis of short-baseline oscillation data in the framework of 3+1 mixing, which requires a sterile neutrino mass between about 0.9 and 1.5 eV [199]. For the statistical distribution of the sterile neutrinos we considered the two most studied cases: the thermal model and the Dodelson-Widrow model [313].

We have shown that the local measurements of the Hubble constant $H_0$ induce an increase of the value of the effective number of relativistic degrees of freedom $N_{\text{eff}}$ above the Standard Model value. This is an indication in favor of the existence of sterile neutrinos and their contribution to dark radiation. However, we obtained that the sterile neutrino mass has a $2\sigma$ upper bound of about 0.5 eV in the thermal model and about 0.6 eV in the Dodelson-Widrow model. Hence, there is a tension between cosmological and SBL data. The Dodelson-Widrow

model is slightly more compatible with SBL data and it may turn out that it is favorite if SBL oscillations will be confirmed by future experiments (see Refs. [162, 345–351]).

The tension between cosmological and SBL data disappears if we consider also the measurements of the local galaxy cluster mass distribution, which favor the existence of sterile neutrinos with eV-scale masses which can suppress the small-scale clustering of galaxies through free-streaming [337]. In this case we obtained a cosmologically allowed range for the sterile neutrino mass which at $2\sigma$ can be as large as about 2.7 eV in the thermal model and 4.8 eV in the Dodelson-Widrow model.

In the combined fit of cosmological and SBL data the sterile neutrino mass is restricted around 1 eV by the SBL prior and the cosmological limits on the effective sterile neutrino mass $m_s^{\text{eff}}$ imply that the contribution of the sterile neutrino to the effective number of relativistic degrees of freedom $N_{\text{eff}}$ is likely to be smaller than one. In this case, the production of sterile neutrinos in the early Universe must be somewhat suppressed by a non-standard mechanism, as, for example, a large lepton asymmetry [310, 355–357]. The slightly smaller suppression required by the Dodelson-Widrow model and the slightly better compatibility of cosmological and SBL data in this model may be indications in its favor, with respect to the thermal model.

## 5.2 Degeneracies between Neutrinos and Tensor Modes

Some months after the 2013 release of Planck data, the publication of the new data from the BICEP2 experiment [71] has indicated a high tensor-to-scalar ratio corresponding to the existence of primordial tensor perturbations, that may be significantly correlated with the neutrino-related parameters. We want to investigate how the constraints on eV mass sterile neutrinos are influenced by the BICEP2 claim. We will demonstrate that eV mass sterile neutrinos are not significantly constrained by current cosmological data, given that they contribute with a small amount of relativistic degrees of freedom $\Delta N_{\text{eff}}$. These analyses can be considered a conceptual exercise and not a new set of physical bounds on the LS$\nu$, since we know today that the BICEP2 signal did not concern primordial tensor modes, but it was significantly contaminated by polarized dust emission (see Subsection 3.1.3 and Refs. [73–76]).

This Section is structured in this way: Subsection 5.2.1 contains a discussion of the cosmological parameter estimation, including the cosmological model and the experimental data, in Subsection 5.2.2 (5.2.3) we present the results of the cosmological (joint) analysis and finally Subsection 5.2.4 contains a thorough discussion of these results.

### 5.2.1 The cosmological analysis

As we probed in Section 5.1 that the TH and the DW scenarios give very similar results, we restrict our calculations to the thermal case only. The setup under investigation here is then a model in which the neutrino sector is described by 3 massless or almost massless active species, as well as one additional sterile species characterized by a temperature $T_s$. Since we want to describe only the phenomenology of a TH LS$\nu$, here we decided to use the physical mass $m_s$ as a free parameter, instead of the effective mass $m_s^{\text{eff}}$.

Our cosmological model is a flat $\Lambda$CDM+$r_{0.002}$+$\nu_s$ model with a total of nine parameters

$$\boldsymbol{\theta} = \{\omega_{\text{c}}, \omega_{\text{b}}, \theta_{\text{s}}, \tau, \ln(10^{10}A_s), n_s, r_{0.002}, m_s, \Delta N_{\text{eff}}\}. \tag{5.1}$$

We recall that $\omega_{\text{c}} \equiv \Omega_{\text{c}}h^2$ and $\omega_{\text{b}} \equiv \Omega_{\text{b}}h^2$ are respectively the present-day CDM and baryon energy densities, $\theta_{\text{s}}$ is the angular the sound horizon, $\tau$ is the optical depth to reionization, and $\ln(10^{10}A_s)$ and $n_s$ denote respectively the amplitude and spectral index of the initial scalar fluctuations. The last parameter is $r_{0.002}$ (also indicated with $r$), the tensor-to-scalar ratio at the pivot scale of $0.002\,\text{Mpc}^{-1}$. We assume a flat prior on all of the cosmological parameters, with the exception of $m_s$. For the physical mass of the additional sterile neutrino we shall consider a flat prior only when the SBL data are not included. To perform the joint analysis of SBL and cosmological data, in turn, we shall use the posterior obtained in the analysis of SBL neutrino oscillations (see Sec. 4.2) as a prior on $m_s$.
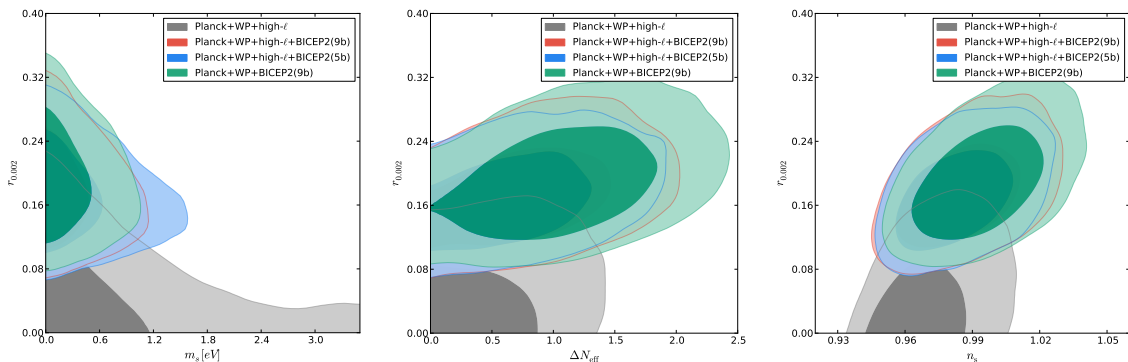
Figure 5.8: $1\sigma$ and $2\sigma$ marginalized contours for different combinations of CMB data sets. From Ref. [23].

In this Section we consider SBL and cosmological data. The latter consist of CMB data, Large Scale Structure (LSS), Hubble constant $H_0$, $\sigma_8$ measurements from the CFHTLenS and the Planck Sunyaev Zel'Dovich (SZ) cluster counts. We briefly resume here the considered datasets, that are extensively described in Chapter 3:

**CMB** – The CMB dataset is based on the one adopted in the previous Section. We additionally include the B-modes autocorrelation power spectrum of the BICEP2 experiment, either using all of the nine channels ($20 < \ell < 340$), or only the first five data points ($\ell < 200$), as in the BICEP2 paper [71].

**LSS** – The information on the matter power spectrum from the WiggleZ Dark Energy Survey [101].

**$H_0$** – the same measurement we used in the previous Section, $H_0 = 73.8 \pm 2.4$ Km s$^{-1}$ Mpc$^{-1}$ [121].

**CFHTLenS** – The weak gravitational lensing signal extracted from the Canada-France Hawaii Telescope Lensing Survey (CFHTLenS) [141, 142], that constrains a combination of the total matter density $\Omega_m$ and the standard deviation of the amplitude of the matter density fluctuations on a sphere of radius $8h^{-1}$Mpc, $\sigma_8$. This result is included in our analysis as a Gaussian prior $\sigma_8(\Omega_m/0.27)^{0.46} = 0.774 \pm 0.040$.

**PSZ** – The number counts of clusters from the Planck Sunyaev Zel'Dovich catalogue [136], incorporated in our analysis as a Gaussian prior $\sigma_8(\Omega_m/0.27)^{0.3} = 0.782 \pm 0.010$.

In addition, we consider the SBL neutrino oscillation data as a prior on the physical mass of the LS$\nu$, as we did in the previous Section. Further details on the parameterization of neutrino oscillations and on the SBL constraints are reported in Chapter 4.

### 5.2.2 Cosmological Results

An interesting question is how the addition of an eventual detection of an high tensor-to-scalar ratio from inflation changes the preferred region in ($m_s$, $\Delta N_{\text{eff}}$) (see Fig. 5.9) space. Therefore, we first look at CMB data only, with and without BICEP2 data included. The result of this analysis can be seen in Fig. 5.8 and in Tab. 5.4. As can be seen in Fig. 5.8, $m_s$ and $r$ are anti-correlated. This happens because $r$ adds power on large scales whereas $m_s$ subtracts power on intermediate and small scales. The inclusion of BICEP2 data therefore tends to strengthen the bound on $m_s$ in order to keep constant the ratio between the small and large scales. Conversely, the addition of the BICEP2 data allows for higher values of $N_{\text{eff}}$, because $N_{\text{eff}}$ is strongly correlated with $n_s$ and the addition of tensors shifts the allowed values for $n_s$ up. For the case of CMB data only, the addition of BICEP2 data therefore strengthens

| Parameters | Planck+WP+high-$\ell$ | Planck+WP+high-$\ell$ +BICEP2(9bins) | Planck+WP+high-$\ell$ +BICEP2(5bins) | Planck+WP +BICEP2(9bins) |
|---|---|---|---|---|
| $\Omega_{\mathrm{b}}h^2$ | $0.02231^{+0.00032\ +0.00078}_{-0.00040\ -0.00072}$ | $0.02251^{+0.00039\ +0.00087}_{-0.00046\ -0.00078}$ | $0.02249^{+0.00035\ +0.00084}_{-0.00045\ -0.00078}$ | $0.02259^{+0.00040\ +0.00094}_{-0.00050\ -0.00082}$ |
| $\Omega_{\mathrm{c}}h^2$ | $0.125^{+0.005\ +0.011}_{-0.007\ -0.010}$ | $0.129^{+0.006\ +0.013}_{-0.007\ -0.012}$ | $0.128^{+0.005\ +0.013}_{-0.008\ -0.012}$ | $0.132^{+0.007\ +0.015}_{-0.008\ -0.014}$ |
| $\theta_{\mathrm{s}}$ | $1.0404^{+0.0009\ +0.0016}_{-0.0008\ -0.0017}$ | $1.0399^{+0.0009\ +0.0017}_{-0.0009\ -0.0017}$ | $1.0401^{+0.0009\ +0.0018}_{-0.0009\ -0.0017}$ | $1.0395^{+0.0009\ +0.0019}_{-0.0009\ -0.0018}$ |
| $\tau$ | $0.094^{+0.013\ +0.031}_{-0.016\ -0.027}$ | $0.097^{+0.013\ +0.031}_{-0.016\ -0.027}$ | $0.096^{+0.013\ +0.030}_{-0.016\ -0.029}$ | $0.098^{+0.014\ +0.031}_{-0.017\ -0.031}$ |
| $n_{\mathrm{s}}$ | $0.970^{+0.011\ +0.033}_{-0.018\ -0.027}$ | $0.986^{+0.016\ +0.035}_{-0.020\ -0.033}$ | $0.983^{+0.014\ +0.034}_{-0.020\ -0.031}$ | $0.995^{+0.017\ +0.038}_{-0.021\ -0.036}$ |
| $\log(10^{10}A_s)$ | $3.106^{+0.029\ +0.068}_{-0.036\ -0.062}$ | $3.120^{+0.030\ +0.071}_{-0.037\ -0.061}$ | $3.167^{+0.047\ +0.080}_{-0.046\ -0.089}$ | $3.145^{+0.052\ +0.090}_{-0.046\ -0.098}$ |
| $r$ | $< 0.145$ | $0.177^{+0.036\ +0.093}_{-0.050\ -0.086}$ | $0.172^{+0.035\ +0.088}_{-0.048\ -0.082}$ | $0.192^{+0.040\ +0.101}_{-0.055\ -0.092}$ |
| $\Delta N_{\mathrm{eff}}$ | $< 1.18$ | $0.82^{+0.40}_{-0.57}; < 1.66$ | $0.73^{+0.31}_{-0.59}; < 1.56$ | $1.08^{+0.49}_{-0.61}; < 2.03$ |
| $m_s[\mathrm{eV}]$ | $< 2.17$ | $< 0.85$ | $< 1.15$ | $< 0.81$ |

Table 5.4: Marginalized $1\sigma$ and $2\sigma$ confidence level limits for the cosmological parameters, given with respect to the mean value. Upper limits are given at $2\sigma$. From Ref. [23].

the bound on $m_s$ slightly while allowing for a much higher $N_{\mathrm{eff}}$. This is consistent with the analysis presented in Ref. [358].

We want now to be more precise. The fact that the BICEP2 data lead to an enhancement of $N_{\mathrm{eff}}$ is due to the correlation between $N_{\mathrm{eff}}$ and the spectral index $n_s$ of the scalar PPS in Eq. (1.144). Keeping fixed the amplitude $A_s$ at $k \sim k_0$, which is constrained by the high-precision Planck data, the scalar contribution to the large-scale temperature fluctuations with $k \ll k_0$ measured by WMAP and Planck can be decreased by an increase[5] of the spectral index $n_s$. In this way, the WMAP and Planck data leave more space for the tensor contribution [361] and the corresponding bounds on $r$ are relaxed. However, the increase of $n_s$ induces an increase of small scale fluctuations with $k \gg k_0$, which would spoil the fit of high-$\ell$ CMB data if the increase is not compensated by an effect beyond the standard cosmological $\Lambda$CDM model. An increase of $N_{\mathrm{eff}}$ above the standard value $N_{\mathrm{eff}}^{\mathrm{SM}} = 3.046$ [305] has just the desired effect of decreasing the small scale fluctuations (see Subsection 4.4.4). In fact, from the fit of CMB data without BICEP2 we obtain $n_s = 0.970^{+0.011}_{-0.018}$ ($1\sigma$) and $\Delta N_{\mathrm{eff}} < 1.18$ ($2\sigma$), and adding BICEP2 data we find $n_s = 0.986^{+0.016}_{-0.020}$ ($1\sigma$) and $\Delta N_{\mathrm{eff}} = 0.82^{+0.40}_{-0.57}$ ($1\sigma$) as reported in Tab. 5.4.

When the inclusion of the BICEP2 data is restricted to the first five bins, the results concerning the basic cosmological parameters remain unchanged within $1\sigma$, whereas the bound on the mass becomes slightly weaker and the constraints on $\Delta N_{\mathrm{eff}}$ are tighter. If we remove the high multipole CMB data the bound on the mass remains almost unchanged, while $\Delta N_{\mathrm{eff}}$ moves towards one additional fully thermalized sterile neutrino.

Having established how the constraints change from CMB data only we now proceed to study the influence of the auxiliary cosmological data. From now on, we will consider only the full CMB dataset that includes the BICEP2 data for all the nine bins.

In Tab. 5.5 we report the mean values and the $1\sigma$ and $2\sigma$ errors on the cosmological parameters and on the neutrino parameters in the different combinations of data sets illustrated above, when the SBL data are not included.

---

[5] One could think to alleviate the tension between BICEP2 and WMAP-Planck by decreasing $n_s$, if the value of $r$ measured by BICEP2 refers to a wavenumber $k_1$ larger than than the wavenumber $k_2 = 0.002\,\mathrm{Mpc}^{-1}$ corresponding to the WMAP and Planck upper bounds [359, 360]. Since $r_{k_2} \simeq r_{k_1}(k_1/k_2)^{n_s-1-n_t}$, where $n_t$ is the tensor spectral index, for $k_2 < k_1$ and $n_s - 1 - n_t < 0$ we have $r_{k_2} < r_{k_1}$ and the ratio $r_{k_2}/r_{k_1}$ decreases by decreasing $n_s$. However, one must take into account that WMAP and Planck did not measure directly the tensor fluctuations as BICEP2, but measured the temperature fluctuations, in which the scalar and tensor contributions are indistinguishable. Hence, decreasing $n_s$ increases the scalar contribution to the temperature fluctuations measured by WMAP and Planck at $k_2 < k_1$ and there is less room for a tensor contribution. Therefore the WMAP and Planck upper bounds on $r_{k_2}$ tighten by about the same amount of the decrease of the BICEP2 value of $r_{k_2}$, maintaining the tension.
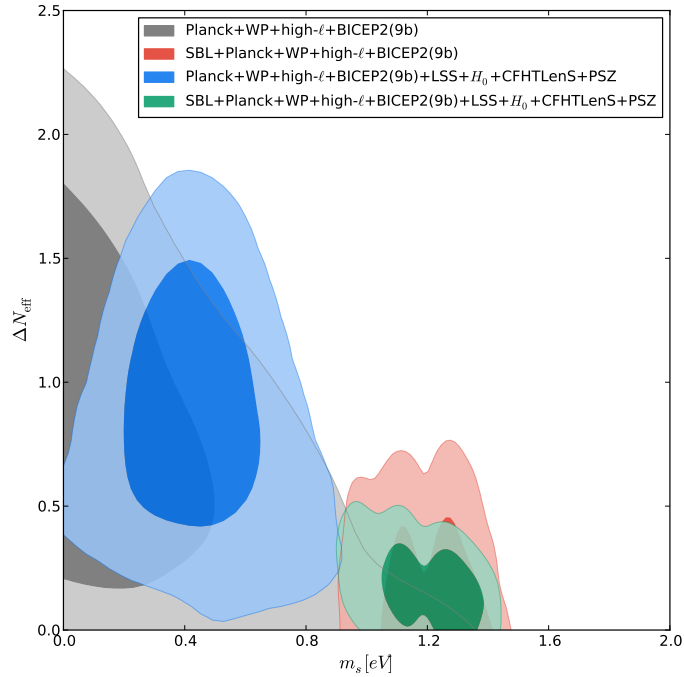
Figure 5.9: $1\sigma$ and $2\sigma$ marginalized contours in the plane $(m_s, \Delta N_{\mathrm{eff}})$. The banana shaped regions allowed by cosmology indicate a sub-eV mass and an excess in $N_{\mathrm{eff}}$, while the inclusion of SBL data forces the mass to be around 1 eV, moving the contours towards the warm dark matter limit, which implies a lower value of $\Delta N_{\mathrm{eff}}$ because of the strong correlation between the two parameters. From Ref. [23].
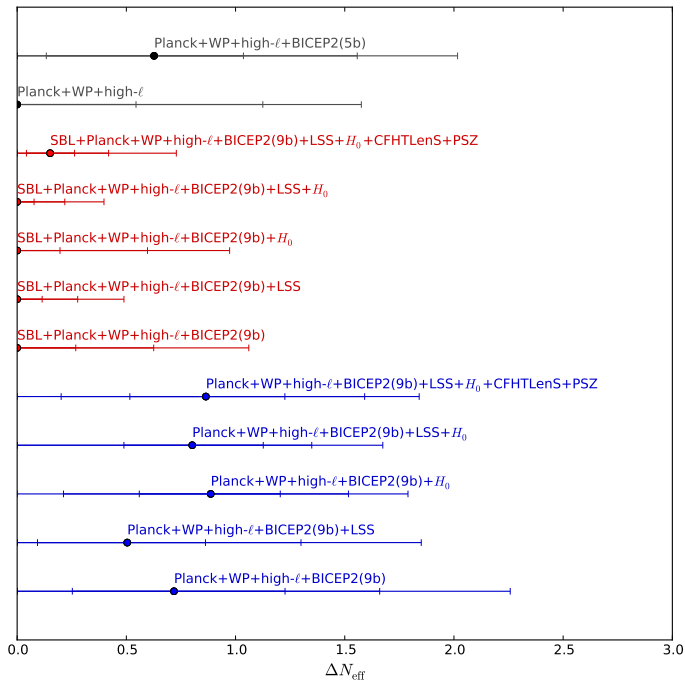


Figure 5.10: $1\sigma$, $2\sigma$ and $3\sigma$ confidence level limits for $\Delta N_{\mathrm{eff}}$, for different dataset combinations. The circles indicate the mean value. From Ref. [23].

95
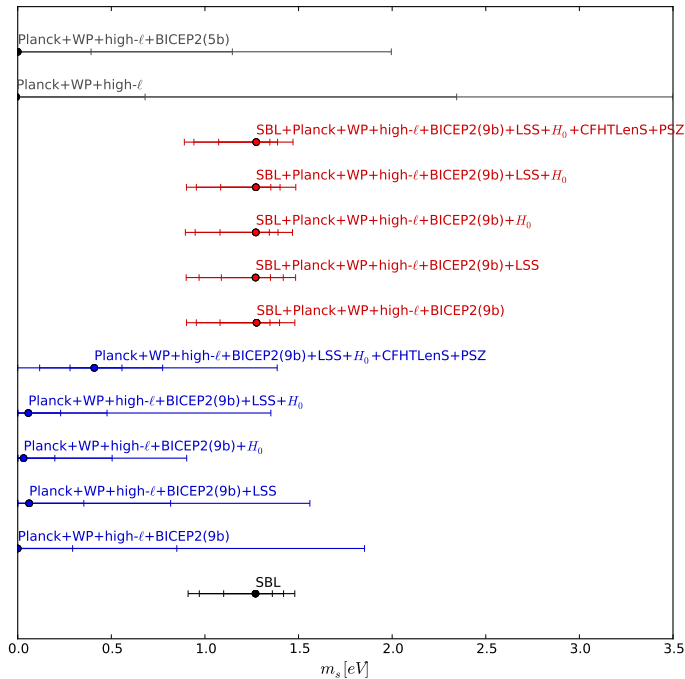
Figure 5.11: As in Fig. 5.10, but for $m_s$. From Ref. [23].

As seen above, the Planck CMB data provide a fairly stringent upper limit on the sterile neutrino mass, except for very low values of $N_{\text{eff}}$, corresponding to the warm dark matter limit. Conversely the preferred value of $N_{\text{eff}}$ is higher than 3, with 4 only being slightly disfavored. The inclusion of BICEP2 data pushes the preferred $N_{\text{eff}}$ up, as it was pointed out by several authors [358, 362, 363]. However, since $m_s$ and $N_{\text{eff}}$ are anti-correlated this actually results in a tighter bound on the sterile neutrino mass from CMB only.

When we include LSS or $H_0$ data the picture remains qualitatively unchanged although, since $m_s$ and $H_0$ are anti-correlated, the addition of the HST $H_0$ data strengthens the upper bound on the sterile neutrino mass. In Fig. 5.11 and Fig. 5.10 we can see how the error bars change for $m_s$ and $\Delta N_{\text{eff}}$ respectively, with various dataset combinations.

The picture changes with the inclusion of weak lensing and cluster data, that leads to an important qualitative change for the preferred range of $m_s$. Both these data sets give a preference for a low value of $\sigma_8$. Given that the amplitude of the fluctuations is fixed on large scales by the CMB measurements, a low value of $\sigma_8$ can be caused by a non-zero neutrino mass which specifically reduces the power on small scales thanks to its free-streaming, while leaving the large scale power unchanged with respect to the standard $\Lambda$CDM prediction. The addition of the CFHTLenS and PSZ data sets yields then a preferred mass for the sterile neutrino of around 0.5 eV, with $\Delta N_{\text{eff}} = 1$ allowed.

### 5.2.3   Results with the SBL prior

At this point we can try to understand if the cosmological and SBL data are really compatible. When we use cosmological data without weak lensing and cluster data we find a relatively stringent upper bound on $m_s$. This is relaxed when $\Delta N_{\text{eff}}$ is low, simply because the suppression of structure formation scales with the total density in neutrinos at late times, i.e. as $\Delta N_{\text{eff}}^{3/4} m_s$. However, since CMB data prefers a high $\Delta N_{\text{eff}}$ this possibility is disfavored, and the conclusion is that CMB and LSS data require the sterile mass to be low. The bound can easily be relaxed in models where additional dark radiation is provided by other particles. When we add weak lensing and cluster data the sterile mass comes out to be around 0.5 eV and fully thermalized sterile neutrinos are allowed.

| Parameters | Planck+WP+high-$\ell$ +BICEP2 | Planck+WP+high-$\ell$ +BICEP2 +LSS | Planck+WP+high-$\ell$ +BICEP2 +$H_0$ | Planck+WP+high-$\ell$ +BICEP2 +LSS+$H_0$ | Planck+WP+high-$\ell$ +BICEP2 +LSS+$H_0$+CFHTLenS+PSZ |
|---|---|---|---|---|---|
| $\Omega_b h^2$ | $0.02251^{+0.00039\ +0.00087}_{-0.00046\ -0.00078}$ | $0.02232^{+0.00033\ +0.00073}_{-0.00039\ -0.00069}$ | $0.02257^{+0.00029\ +0.00059}_{-0.00030\ -0.00057}$ | $0.02248^{+0.00029\ +0.00057}_{-0.00029\ -0.00056}$ | $0.02267^{+0.00027\ +0.00055}_{-0.00028\ -0.00053}$ |
| $\Omega_c h^2$ | $0.129^{+0.006\ +0.013}_{-0.007\ -0.012}$ | $0.128^{+0.005\ +0.011}_{-0.006\ -0.010}$ | $0.130^{+0.006\ +0.011}_{-0.005\ -0.011}$ | $0.129^{+0.005\ +0.011}_{-0.005\ -0.011}$ | $0.127^{+0.006\ +0.011}_{-0.006\ -0.011}$ |
| $\theta_s$ | $1.0399^{+0.0009\ +0.0017}_{-0.0009\ -0.0017}$ | $1.0401^{+0.0009\ +0.0017}_{-0.0008\ -0.0017}$ | $1.0398^{+0.0008\ +0.0018}_{-0.0008\ -0.0016}$ | $1.0399^{+0.0008\ +0.0017}_{-0.0008\ -0.0016}$ | $1.0400^{+0.0009\ +0.0018}_{-0.0009\ -0.0017}$ |
| $\tau$ | $0.097^{+0.013\ +0.031}_{-0.016\ -0.027}$ | $0.093^{+0.013\ +0.027}_{-0.014\ -0.027}$ | $0.099^{+0.013\ +0.029}_{-0.015\ -0.026}$ | $0.095^{+0.013\ +0.028}_{-0.014\ -0.027}$ | $0.091^{+0.013\ +0.028}_{-0.015\ -0.027}$ |
| $n_s$ | $0.986^{+0.016\ +0.035}_{-0.020\ -0.033}$ | $0.977^{+0.012\ +0.028}_{-0.016\ -0.027}$ | $0.989^{+0.011\ +0.021}_{-0.011\ -0.022}$ | $0.985^{+0.011\ +0.020}_{-0.010\ -0.022}$ | $0.993^{+0.010\ +0.021}_{-0.011\ -0.021}$ |
| $\log(10^{10}A_s)$ | $3.120^{+0.030\ +0.071}_{-0.037\ -0.061}$ | $3.182^{+0.042\ +0.073}_{-0.038\ -0.078}$ | $3.124^{+0.030\ +0.060}_{-0.031\ -0.058}$ | $3.116^{+0.029\ +0.060}_{-0.030\ -0.055}$ | $3.124^{+0.031\ +0.063}_{-0.031\ -0.061}$ |
| $r$ | $0.177^{+0.036\ +0.093}_{-0.050\ -0.086}$ | $0.168^{+0.034\ +0.085}_{-0.046\ -0.078}$ | $0.181^{+0.037\ +0.087}_{-0.047\ -0.081}$ | $0.175^{+0.035\ +0.083}_{-0.045\ -0.077}$ | $0.206^{+0.041\ +0.094}_{-0.051\ -0.090}$ |
| $\Delta N_{\rm eff}$ | $0.82^{+0.40}_{-0.57}; < 1.66$ | $0.61^{+0.25}_{-0.52}; < 1.30$ | $0.88^{+0.32\ +0.64}_{-0.32\ -0.67}$ | $0.81^{+0.32}_{-0.32}; < 1.35$ | $0.89^{+0.34\ +0.70}_{-0.37\ -0.69}$ |
| $m_s$[eV] | $< 0.85$ | $< 0.82$ | $< 0.50$ | $< 0.48$ | $0.44^{+0.11\ +0.33}_{-0.16\ -0.32}$ |

Table 5.5: Marginalized $1\sigma$ and $2\sigma$ confidence level limits for the cosmological parameters, given with respect to the mean value, from the analyses of cosmological data only. Upper limits are given at $2\sigma$. From Ref. [23].

In Tab. 5.6 we report the marginalized mean values and the $1\sigma$ and $2\sigma$ errors on the cosmological parameters and on the neutrino parameters in the different combinations of data sets illustrated above, when SBL data are included. As we stated before, it is easy to see that the anti-correlation between $m_s$ and $\Delta N_{\rm eff}$, together with the strong bounds on $m_s$ from the SBL data, leaves a very small space to a fully thermalized sterile neutrino. When adding SBL data, the constraints on $m_s$ come only by the oscillation experiments, with very small dependence on the cosmological data. On the other hand, cosmology provides a strong limit on $\Delta N_{\rm eff}$ that is compatible with 0 within $2\sigma$ in all the cases, as we can see in Fig. 5.10. When LSS data are included, the value of $\Delta N_{\rm eff}$ is even more constrained. Only when CFHTLenS and PSZ are included there is a little evidence that $\Delta N_{\rm eff} > 0$ at more than $1\sigma$: even in this case, however, a fully thermalized sterile neutrino with $\Delta N_{\rm eff} = 1$ is strongly disfavored.

This tension between cosmological and SBL data, has been studied also in past works (see e.g. Ref. [311]): the mass values preferred by SBL data lay above the hot dark matter limit and therefore they are disfavored by cosmology, even if there is only one partially (or fully, $\Delta N_{\rm eff} = 1$) thermalized sterile neutrino. Quantitatively speaking, a model with one fully thermalized sterile neutrino and with a mass fixed at the SBL best-fit has a $\Delta\chi^2 \simeq 18$ compared to the cosmological best-fit model, if Planck+WP+high-$\ell$ data are considered. If also BICEP2 data are considered, the value lowers to $\Delta\chi^2 \simeq 12$: this is possible since the inclusion of the BICEP2 data strengthens the limit on $m_s$, but it weakens the limit on $\Delta N_{\rm eff}$.

If a partial thermalization is taken into account and $\Delta N_{\rm eff}$ is free to vary moving towards lower values, the $\Delta\chi^2$ differences are smaller. For a $m_s = 1.27$ eV neutrino with small $\Delta N_{\rm eff}$ we have $\Delta\chi^2 \simeq 1$ from Planck+WP+high-$\ell$ and $\Delta\chi^2 \simeq 6$ from Planck+WP+high-$\ell$+BICEP2.

We can conclude that a fully thermalized sterile neutrino with a mass fixed at the SBL best-fit is less disfavored by cosmology if the BICEP2 data are included. On the contrary, if the sterile neutrino is not fully thermalized the inclusion of BICEP2 data worsens the consistency of the presence of a 1 eV mass sterile neutrino in cosmology.

### 5.2.4 Discussion

We have performed an analysis of light sterile neutrinos in the context of both cosmology and short baseline neutrino oscillation experiments. Previous analyses have shown that while SBL data points to the existence of a mainly sterile mass state around 1 eV, this is not compatible with cosmological data unless the additional state is somehow prevented from being fully thermalized in the early Universe [282].

If the BICEP2 data were related to primordial tensor modes, they would favor a higher

| Parameters | SBL+Planck+WP +high-$\ell$+BICEP2 | SBL+Planck+WP +high-$\ell$+BICEP2 +LSS | SBL+Planck+WP +high-$\ell$+BICEP2 +$H_0$ | SBL+Planck+WP +high-$\ell$+BICEP2 +LSS+$H_0$ | SBL+Planck+WP +high-$\ell$+BICEP2 +LSS+$H_0$+CFHTLenS+PSZ |
|---|---|---|---|---|---|
| $\Omega_b h^2$ | $0.02214^{+0.00029\ +0.00058}_{-0.00029\ -0.00058}$ | $0.02200^{+0.00026\ +0.00051}_{-0.00025\ -0.00052}$ | $0.02230^{+0.00027\ +0.00060}_{-0.00027\ -0.00054}$ | $0.02214^{+0.00025\ +0.00049}_{-0.00025\ -0.00051}$ | $0.02236^{+0.00023\ +0.00047}_{-0.00023\ -0.00047}$ |
| $\Omega_c h^2$ | $0.121^{+0.003\ +0.008}_{-0.004\ -0.007}$ | $0.121^{+0.002\ +0.006}_{-0.003\ -0.005}$ | $0.118^{+0.003\ +0.007}_{-0.004\ -0.006}$ | $0.118^{+0.002\ +0.005}_{-0.002\ -0.005}$ | $0.117^{+0.002\ +0.006}_{-0.003\ -0.006}$ |
| $\theta_s$ | $1.0408^{+0.0008\ +0.0015}_{-0.0007\ -0.0014}$ | $1.0409^{+0.0006\ +0.0012}_{-0.0006\ -0.0013}$ | $1.0413^{+0.0007\ +0.0013}_{-0.0006\ -0.0015}$ | $1.0413^{+0.0006\ +0.0012}_{-0.0006\ -0.0012}$ | $1.0413^{+0.0006\ +0.0013}_{-0.0006\ -0.0014}$ |
| $\tau$ | $0.092^{+0.012\ +0.026}_{-0.014\ -0.025}$ | $0.088^{+0.012\ +0.027}_{-0.014\ -0.024}$ | $0.094^{+0.012\ +0.028}_{-0.015\ -0.027}$ | $0.091^{+0.012\ +0.026}_{-0.014\ -0.024}$ | $0.086^{+0.012\ +0.026}_{-0.014\ -0.024}$ |
| $n_s$ | $0.962^{+0.008\ +0.016}_{-0.008\ -0.015}$ | $0.958^{+0.006\ +0.013}_{-0.006\ -0.013}$ | $0.967^{+0.007\ +0.015}_{-0.008\ -0.014}$ | $0.962^{+0.006\ +0.012}_{-0.006\ -0.012}$ | $0.970^{+0.005\ +0.011}_{-0.005\ -0.011}$ |
| $\log(10^{10}A_s)$ | $3.213^{+0.031\ +0.063}_{-0.031\ -0.063}$ | $3.220^{+0.030\ +0.059}_{-0.030\ -0.059}$ | $3.091^{+0.026\ +0.057}_{-0.030\ -0.051}$ | $3.085^{+0.025\ +0.052}_{-0.027\ -0.048}$ | $3.169^{+0.027\ +0.053}_{-0.026\ -0.052}$ |
| $r$ | $0.160^{+0.034\ +0.078}_{-0.042\ -0.075}$ | $0.150^{+0.032\ +0.071}_{-0.039\ -0.067}$ | $0.164^{+0.032\ +0.079}_{-0.043\ -0.073}$ | $0.158^{+0.032\ +0.075}_{-0.042\ -0.070}$ | $0.179^{+0.034\ +0.082}_{-0.043\ -0.076}$ |
| $\Delta N_{\text{eff}}$ | $< 0.63$ | $< 0.28$ | $< 0.59$ | $< 0.22$ | $0.19^{+0.07}_{-0.15}$; $< 0.42$ |
| $m_s[\text{eV}]$ | $1.21^{+0.14\ +0.19}_{-0.13\ -0.25}$ | $1.22^{+0.13\ +0.20}_{-0.13\ -0.25}$ | $1.20^{+0.14\ +0.19}_{-0.12\ -0.25}$ | $1.21^{+0.14\ +0.19}_{-0.13\ -0.26}$ | $1.19^{+0.15\ +0.19}_{-0.12\ -0.25}$ |

Table 5.6: As in Tab. 5.5, but from the joint analyses of cosmological and SBL data. From Ref. [23].

dark radiation content, but this actually would tighten the cosmological bounds on the mass of the sterile neutrino, because $m_s$ and $\Delta N_{\text{eff}}$ are strongly anti-correlated. Cosmological data from the CFHTLenS survey and the Planck SZ cluster counts actually favor a non-zero mass of the sterile neutrino, because it alleviates the tension between the value of $\sigma_8$ inferred from the CMB measurements in the context of the minimal $\Lambda$CDM model and the lower values indicated by data CFHTLenS and PSZ data. The inclusion of these two data sets points towards a sterile neutrino mass around 0.5 eV, but with relatively a low $\Delta N_{\text{eff}}$.

The SBL data strongly constrains $m_s$, but not $\Delta N_{\text{eff}}$, and indicates a LS$\nu$ mass not much lower than 1 eV. At the same time the mixing angle is large enough that the additional state should be almost fully thermalized [310, 311, 364]. However, this scenario is highly disfavored by cosmological data (with a $\Delta\chi^2 > 10$), which requires $\Delta N_{\text{eff}}$ to be small if the mass is around 1 eV. Indeed, a model with a mass of 1 eV and a low $\Delta N_{\text{eff}}$ is compatible with cosmology within roughly $2\sigma$ confidence level. The conclusion is that light sterile neutrinos as indicated by SBL data are close to being ruled out by cosmological data, unless they are somehow prevented from thermalizing in the early Universe.

A possible way out of this problem is that sterile neutrinos have new interactions which induce a non-standard matter potential and block thermalization [355, 356, 365–368]. In this case there may be 1 eV sterile neutrinos and an $N_{\text{eff}}$ not much beyond 3, so that the model would be compatible with all existing data. While this scenario certainly works well and can possibly also explain some of the astrophysical anomalies related to cold dark matter, there are without a doubt other possible ways of making eV sterile neutrino compatible with both SBL and cosmological data. For example, some models with low temperature reheating or non-standard expansion rate of the Universe at the MeV scale where the new state is thermalized can also prevent thermalization [369] (see also Section 5.4). In the next Section we will present a model that involves an invisible decay of the sterile neutrino, occurring in cosmological time-scales. This model has the advantage of allowing to reconcile the presence of a massive sterile neutrino with the CMB data, provided that $\Delta N_{\text{eff}} = 1$ is allowed for massless species.

## 5.3 Decaying Sterile Neutrino

### 5.3.1 Motivations and Theoretical Model

In the previous Sections we discussed how a light sterile neutrino could help to reconcile the cosmological and the local determinations of $H_0$ and the observed matter fluctuations at small scale with the value estimated from cosmology. The mass scale of 1 eV that can explain the SBL neutrino oscillations, however, is not the same that emerges from the solution of the $\sigma_8$ problem, that requires masses around 0.5 eV. It turns out that the cosmological and
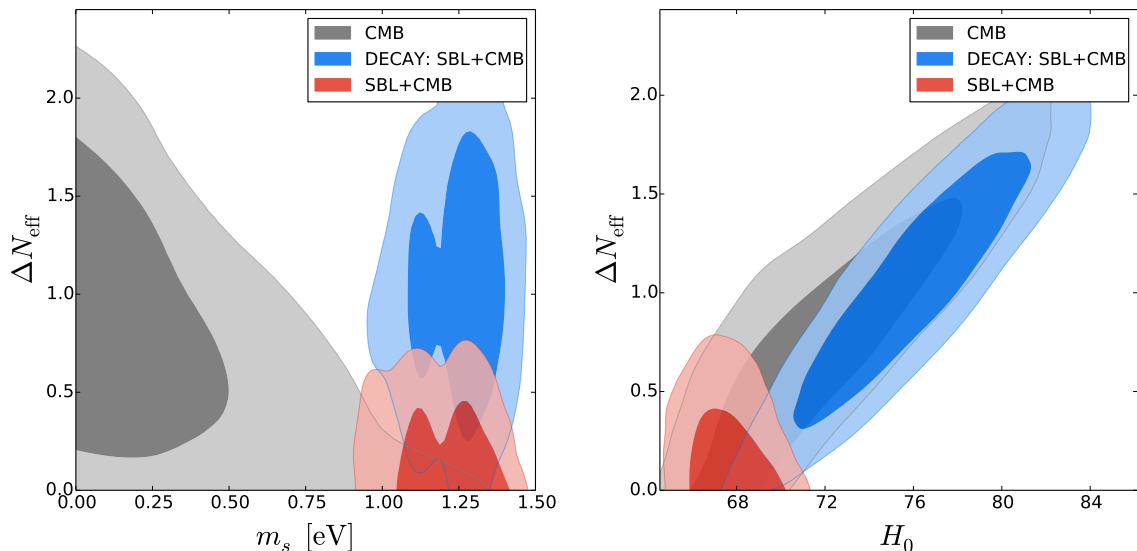
Figure 5.12: $1\sigma$ and $2\sigma$ marginalized allowed regions obtained with CMB data (Planck+WP+high-$\ell$+BICEP2(9bins); see Ref. [23]), without and with the inclusion of SBL data. The gray and red regions are those obtained in Ref. [23] without and with the SBL prior. The blue regions are obtained by adding the possibility of invisible decays for a sterile neutrino that explains the SBL oscillations.

SBL data on the neutrino mass are compatible only if one assumes that the LS$\nu$ with a mass of 1 eV is not fully thermalized in the early Universe ($\Delta N_{\rm eff} = 0.19^{+0.07}_{-0.15}$ at $1\sigma$). The case of a fully thermalized sterile neutrino is disfavored by $\Delta\chi^2 > 10$ [23], even if the (wrong) BICEP2 results would favor an higher $\Delta N_{\rm eff}$. Similar conclusions have been presented also before the BICEP2 results (see e.g. Refs. [22, 303, 311], which take into account the 2013 Planck data [72]) and after the 2015 release of the Planck data [44], that strongly disfavors any departures from $N_{\rm eff} = 3.046$. These results motivated the study of mechanisms which can suppress the thermalization of sterile neutrinos in the early Universe due to active-sterile oscillations before neutrino decoupling [307, 308, 310, 370]. Examples are a large lepton asymmetry [310, 355–357], an enhanced background potential due to new interactions in the sterile sector [365–368, 371–373], a larger cosmic expansion rate at the time of sterile neutrino production [369], and MeV dark matter annihilation [344].

In this Section we propose to solve the problem of the thermalization of the sterile neutrino with an eV-scale mass by introducing an invisible decay of the sterile neutrino. The decay must be invisible in order not to generate unobserved signals. We assume that the decay products are very light (or massless) particles belonging to the sterile sector. For example, the eV-scale sterile neutrino $\nu_s$ could decay into a lighter sterile neutrino $\nu_{s'}$ and a very light invisible (pseudo)scalar boson[6] $\phi$. The lighter sterile neutrino $\nu_{s'}$ must have very small mixing with the active neutrinos, in order to forbid its thermalization in the early Universe and to preserve the effectiveness of the standard three-neutrino mixing paradigm for the explanation of solar and atmospheric neutrino oscillations. Also the very light invisible boson $\phi$ has a negligible thermal distribution before the decay, because it belongs to the sterile sector which may have been in equilibrium at very early times, but has decoupled from the thermal plasma at a very high temperature. In this way the densities of all the particles belonging to the sterile sector have been washed out in the following phase transitions and heavy particle-antiparticle annihilations (see, for example, Ref. [376]). Another possible decay which does not need the presence of a light boson is $\nu_s \to \nu_{s'}\bar{\nu}_{s'}\nu_{s'}$, which needs an effective four-fermion interaction of sterile neutrinos.

---

[6] The new invisible light (pseudo)scalar boson is assumed to interact only with the sterile neutrinos, without the interactions with the active neutrinos studied in Refs. [374, 375] and references therein.

In the invisible decay scenario, the eV-scale sterile neutrino can be fully thermalized in the early Universe through active-sterile oscillations [307, 308, 310, 370] and generates $\Delta N_{\text{eff}} = 1$. In the first radiation-dominated part of the evolution of the Universe the mass of the sterile neutrino is not important, because it is relativistic and it contributes only as radiation. The mass effect is important in the following matter-dominated evolution of the Universe, which leads to the formation of Large Scale Structures (LSS) and the current matter density. The sterile neutrinos which decay into invisible relativistic particles before becoming non-relativistic do not contribute to the matter budget. In this way the eV-scale mass of the sterile neutrino indicated by short-baseline oscillation experiments becomes compatible with a full thermalization of the sterile neutrino in the early Universe.

We analyzed the same cosmological data considered in the previous Section (see Ref. [23]) and we modified the Boltzmann solver `CAMB` [58] in order to take into account the invisible decay of the sterile neutrino. For simplicity[7], we neglected the energy dependence of the sterile neutrino lifetime and we considered a sterile neutrino with a Fermi-Dirac distribution multiplied by

$$N_s(t) = \Delta N_{\text{eff}} \, e^{-t/\tau_s} \, , \tag{5.2}$$

where $t$ is the cosmic time and $\tau_s$ is the effective lifetime of the sterile neutrino. We neglect also the energy distributions of the very light or massless invisible decay products (which depend on the specific decay model) and we parameterize their effect with an effective increase of the amount of radiation by $\Delta N_{\text{eff}} \left(1 - e^{-t/\tau_s}\right)$. Following the analyses of the previous Section, we take into account the SBL constraint on $m_s$ through a prior given by the posterior of the global analysis of SBL oscillation data presented in Ref. [199].

Here we present the same analyses performed in Ref. [24], but with different results for the complete dataset. In fact, we improved the numerical calculations and we fixed an error in the code that affected only the analyses including the CFHTLenS and PSZ datasets. Since the most recent cosmological data disfavor $\Delta N_{\text{eff}} = 1$, however, the final conclusions will be the same.

### 5.3.2 Results

Figure 5.12 shows the $1\sigma$ and $2\sigma$ marginalized allowed regions in the planes ($m_s$–$\Delta N_{\text{eff}}$) and ($H_0$–$\Delta N_{\text{eff}}$) obtained by fitting the CMB data (Planck+WP+high-$\ell$+BICEP2(9bins); see Ref. [23]) with the SBL prior in a model with free $\Delta N_{\text{eff}}$ and a massive sterile neutrino which decays invisibly. The corresponding numerical values of the cosmological parameters are listed in Tab. 5.7.

In Fig. 5.12 we compared the allowed regions obtained with the invisible decay of the sterile neutrino with the corresponding regions shown in Fig. 5.10 for a stable sterile neutrino, without and with the SBL prior. One can see that the invisible decay of the sterile neutrino allows $\Delta N_{\text{eff}} = 1$, which corresponds to the full initial thermalization of the sterile neutrino, even if the SBL prior forces the sterile neutrino mass to assume values around 1.2 eV. In practice, the invisible decay of the sterile neutrino allows us to relax the upper bound of about 0.6 for $\Delta N_{\text{eff}}$ presented in Tab. 5.6 with the SBL prior and bring the allowed range of $\Delta N_{\text{eff}}$ at a level which is similar to that presented in Tab. 5.5 without the SBL prior (see also [358, 362, 363, 377]). This can also be seen in the upper panel of Fig. 5.13, which shows the marginalized allowed interval of $\Delta N_{\text{eff}}$.

Figure 5.12 shows also that by allowing the sterile neutrino to decay one can recover a correlation between $\Delta N_{\text{eff}}$ and $H_0$ which is similar to that obtained in the analysis of CMB data without the SBL prior. Hence, we obtain that large values of $\Delta N_{\text{eff}}$ are correlated to large values of the Hubble constant $H_0$, which are in agreement with the local measurements of $H_0$ (see e.g. Refs. [22, 72]).

---

[7] A precise calculation requires the solution of the coupled Boltzmann equations describing the evolution of the distributions of the sterile neutrino and the decay products. This is beyond the scope of this calculation.

| Parameters | CMB+SBL | CMB+SBL +LSS+$H_0$ +CFHTLenS+PSZ |
|---|---|---|
| $\Omega_{\rm b}h^2$ | $0.02276\,^{+0.00043\,+0.00084}_{-0.00041\,-0.00088}$ | $0.02256\,^{+0.00046\,+0.00070}_{-0.00042\,-0.00088}$ |
| $\Omega_{\rm c}h^2$ | $0.132\,^{+0.007\,+0.014}_{-0.008\,-0.014}$ | $0.116\,^{+0.003\,+0.006}_{-0.003\,-0.005}$ |
| $\theta_{\rm s}$ | $1.0405\,^{+0.0007\,+0.0014}_{-0.0007\,-0.0015}$ | $1.0416\,^{+0.0006\,+0.0013}_{-0.0006\,-0.0012}$ |
| $\tau$ | $0.101\,^{+0.015\,+0.034}_{-0.016\,-0.027}$ | $0.080\,^{+0.012\,+0.024}_{-0.012\,-0.023}$ |
| $n_{\rm s}$ | $1.006\,^{+0.018\,+0.037}_{-0.019\,-0.035}$ | $0.988\,^{+0.011\,+0.021}_{-0.011\,-0.021}$ |
| $\log(10^{10}A_s)$ | $3.123\,^{+0.045\,+0.086}_{-0.045\,-0.094}$ | $3.094\,^{+0.033\,+0.084}_{-0.038\,-0.068}$ |
| $r$ | $0.193\,^{+0.045\,+0.111}_{-0.053\,-0.091}$ | $0.202\,^{+0.043\,+0.099}_{-0.048\,-0.087}$ |
| $\Delta N_{\rm eff}$ | $1.06\,^{+0.46\,+0.88}_{-0.45\,-0.91}$ | $0.30\,^{+0.16}_{-0.23};\ < 0.69$ |
| $m_s[{\rm eV}]$ | $1.27\,^{+0.11\,+0.17}_{-0.15\,-0.23}$ | $1.26\,^{+0.10\,+0.17}_{-0.16\,-0.27}$ |

Table 5.7: Marginalized $1\sigma$ and $2\sigma$ confidence level limits for the cosmological parameters obtained with the invisible sterile neutrino decays. See Fig. 5.15 for the constraints on the decay lifetime $\tau_s$.

Figure 5.14 shows the $1\sigma$ and $2\sigma$ marginalized allowed regions corresponding to those of Fig. 5.12 and obtained by adding the same cosmological data considered in the previous Section: Large Scale Structures (LSS), local $H_0$ measurements, cosmic shear (CFHTLenS) and Sunyaev-Zel'dovich cluster counts from Planck (PSZ). One can see that this wide data set allows more freedom for $\Delta N_{\rm eff}$, but the value $\Delta N_{\rm eff} = 1$ is still excluded by the $3\sigma$ limits (see also Fig. 5.13). This is a consequence of the fact that the CFHTLenS and PSZ datasets require that the massive neutrino free-streams at late times to explain the smaller matter fluctuations that has been observed in the local Universe. Clearly, this restricts the possibilities for the neutrino decay. As we can see in Fig. 5.12, $\Delta N_{\rm eff}$ and $H_0$ are partially correlated, indicating relatively large values of $H_0$ for $\Delta N_{\rm eff} \gtrsim 0.5$, which are in agreement with the local measurements of $H_0$.

The bounds on the decay lifetime $\tau_s$ are not shown in Tab. 5.7. The reason is that the marginalized posterior distribution of $\tau_s$ is rather complicated and it is not simple to define a constraint or an upper limit in this case. The marginalized posterior distributions obtained for $\tau_s$ with the two data combinations are plotted in Fig. 5.15. Let we start discussing the one obtained from the CMB data only. We can see that the curve presents a peak corresponding to $\log_{10}\tau_s \simeq -6$. Since we measure $\tau_s$ in units of the age of the Universe $T_0$, this means that the most likely value for the decay lifetime is $\tau_s \simeq 10^{-6}T_0$, or approximately $10^4$ years: it corresponds to a massive sterile neutrino that decays approximately at the time of its transition to the non-relativistic regime. As a consequence, its mass has an impact on the Universe evolution only for a brief period. All the values $\log_{10}\tau_s \lesssim -7$ are equally feasible, since if the sterile neutrino decays when it is completely relativistic its mass never affects the evolution, and it gives the same contribution of a massless neutrino. For this reason, a marginalized constraint on $\tau_s$ would depend on the lower limit adopted for the prior on $\tau_s$. As a conclusion, the CMB data requires that the sterile neutrino mass affects only a short phase of the Universe evolution, approximately at the time of the sterile neutrino transition to the non-relativistic regime.

As we already mentioned, the situation is different if the complete dataset is considered, because the CFHTLenS and the PSZ data would prefer a massive sterile neutrino at late times, in order to have the suppression in the matter fluctuations that would reconcile the cosmological and the local estimates of $\sigma_8$. If the sterile neutrino decays in the early Universe, it cannot free-stream at late times and the matter fluctuations are not suppressed. This is a reason for which we see a sort of bimodal distribution in the posterior of $\tau_s$ obtained from
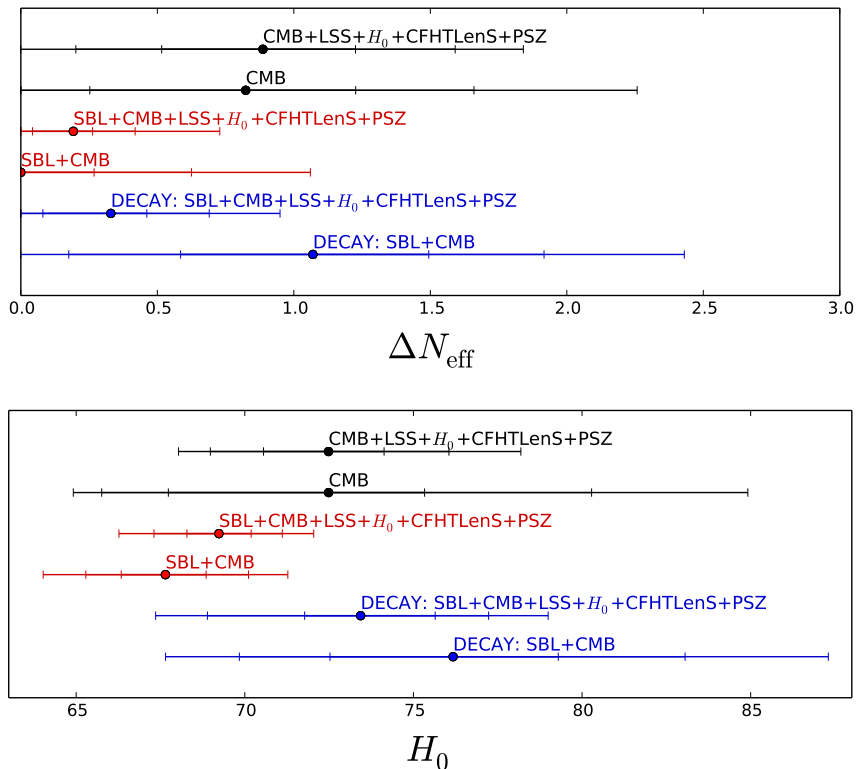
Figure 5.13:    $1\sigma$, $2\sigma$ and $3\sigma$ marginalized error bars for $\Delta N_{\text{eff}}$ and $H_0$ obtained in the different fits of the cosmological data considered in Figs. 5.12 and 5.14. The circles indicate the marginalized best fit values. The black and red intervals are taken from the results in Section 5.2. The blue intervals are obtained by adding the invisible sterile neutrino decay.

the analysis of the complete dataset (red curve in Fig. 5.15): the shape for $\log_{10}\tau_s \lesssim -3$ is similar to the one obtained from the CMB only dataset, with a small shift towards higher values of $\tau_s$, but the posterior is enhanced for $\log_{10}\tau_s \gtrsim -2$ by the phenomenology related to the CFHTLenS and PSZ datasets. We can conclude that the bounds for the decaying sterile neutrino are affected by the tension between the cosmological and local observations, and a clear result cannot be obtained.

## 5.4    Conclusions and Perspectives

In conclusion, we have shown that the cosmological and the SBL data are compatible only if the light sterile neutrino is not fully thermalized. Even if the BICEP2 results about the primordial tensor modes were correct, a fully thermalized sterile neutrino with mass of about 1 eV as indicated by short-baseline neutrino oscillation data would not be compatible with cosmology. Since the mixing parameters obtained from oscillation experiments would allow a full thermalization of the sterile neutrino in the early Universe [307–312], some new mechanism should be found.

The possibility that the sterile neutrino is not stable and decays in cosmological times [24] is not a good solution for two reasons. Firstly, as we pointed out in the previous Section, such a decaying sterile neutrino would not help to solve the tension between CMB data, that would prefer a rapid decay, and the local determinations of the matter fluctuations from CFHTLenS and PSZ, that can be explained only with the free-streaming of relic particle that becomes non-relativistic during the evolution of the structures. Secondly, even if one neglects the local measurements and considers only the CMB data, the decay of the sterile neutrino works well only if $\Delta N_{\text{eff}}$ is allowed to be compatible with 1. The new analyses of
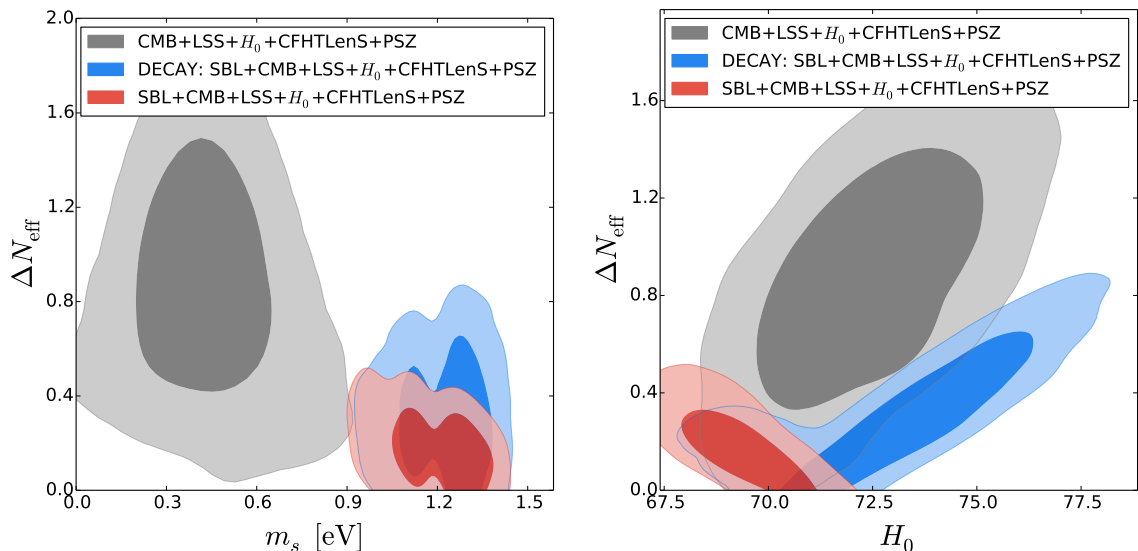
Figure 5.14: As in Fig. 5.12, but for the complete dataset (the same CMB data, plus LSS+$H_0$+CFHTLenS+PSZ).
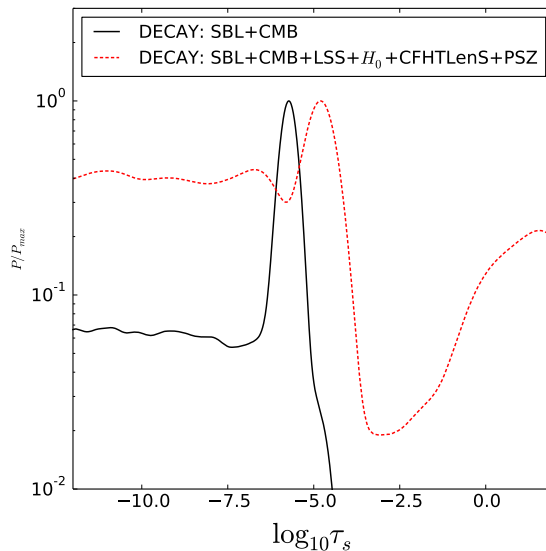


Figure 5.15: Marginalized posterior distributions for $\log_{10} \tau_s$. The decay lifetime $\tau_s$ is given in units of the age of the Universe $T_0$.

the B-mode polarization data showed that the signal measured by BICEP2 does not come from the presence of significant primordial tensor modes [76], but mainly from dust emission. Since the correlation between $r$ and the effective number of relativistic species was responsible of increasing $N_{\text{eff}}$ in the analyses we presented, this is a point against the robustness of the solution we proposed. Moreover, the latest Planck data, in particular about the small scale polarization, strongly disfavor $N_{\text{eff}} > 3.046$ [15, 44]. As a consequence, the decay solution cannot work, since the decay of the sterile neutrino could explain only the full thermalization of a massive neutrino given that $\Delta N_{\text{eff}} = 1$ is allowed for massless species. If $\Delta N_{\text{eff}} = 1$ for massless species is disfavored by cosmology, the decay would not solve the problems and a new solution must be found.

In the past several authors proposed new mechanisms that can relieve the tension: among the others, we list a large lepton asymmetry [310, 355–357, 370, 378–384], new neutrino interactions [365–368, 371, 385–389], entropy production after neutrino decoupling [344], a very

low reheating temperature [390, 391], time varying dark energy components [342], a larger cosmic expansion rate at the time of sterile neutrino production [369].

In the next Chapters we will present two different mechanisms that could alleviate the tensions we discussed. In Chapter 6 we discuss the possibility that the effects on the cosmological observables due to the presence of a sterile neutrino with mass around 1 eV are compensated by an additional freedom in the Primordial Power Spectrum (PPS) of scalar perturbations generated during inflation. If the PPS can have a shape more complicated than a power-law (Eq. (1.144)), a local modification of the initial amplitude of the scalar fluctuations may cancel the Silk damping effect driven by the high $N_{\text{eff}}$ given by the 3+1 neutrino states (see Section 4.4).

A completely different possibility that could give an explanation to the $H_0$ and the $\sigma_8$ tensions is discussed in Chapter 9. We present a model for a phenomenological coupling between Dark Matter (DM) and Dark Energy (DE). If there is an energy transfer from DE to DM, the prediction from the cosmological model gives a smaller $\sigma_8$ and an higher $H_0$, so that local and CMB estimates for these parameters are reconciled. This model, however, does not improve the compatibility between cosmological and SBL data on the presence of a massive sterile neutrino, whose presence is still disfavored.

# Chapter 6

# Inflationary Freedom and Neutrino Properties

*This Chapter is based on Refs. [25, 26].*

In this Chapter we discuss how the constraints on the neutrino properties obtained using the CMB data and several other cosmological data can be biased by the assumption on the Primordial Power Spectrum (PPS) of scalar perturbations. If the PPS presents deviations with respect to the standard power-law (PL), as some inflationary models predict, it is possible to obtain misleading results from the cosmological analyses.

## 6.1   Motivations for Inflationary Freedom

We discussed in Chapter 1 that Inflation is one of the most successful theories that explains the "horizon problem" and the "flatness problem". Moreover, inflation gives origin to the primordial density perturbations that evolved to form the structures we observe today, that we calculated in Subsection 1.9. The standard inflationary paradigm predicts a simple shape for the PPS of scalar perturbations: in this context, the PPS is scale independent and it can be described by the power-law expression in Eq. (1.144). Different models that give an inflationary phase in the early Universe, however, can originate more complicated PPS shapes, with possible features or different behaviors at different scales (see e.g. Refs. [392, 393] or the reviews [394, 395]). It is currently impossible to test directly the physics at the scale of cosmological inflation and consequently it is impossible to check the correctness of the simplest inflationary models. If the theoretical models are wrong or incomplete, any cosmological analysis performed assuming a power-law PPS can lead to biased constraints. The only possibility we have to test the inflationary predictions for the PPS is to reconstruct an unknown PPS starting from the physical observables that we can measure, for example the CMB spectrum.

If one tries to constrain the PPS under the assumption of the $\Lambda$CDM model a non-standard behavior can be found. Firstly, it is necessary to assume a model for the evolution of the Universe and to calculate the transfer function. The physics of the transfer function, introduced in the previous Chapters, is well understood. We mentioned also that the CMB anisotropies can be described very well with a small number of parameters, that are robustly determined from the analyses of the latest experimental data from Planck [21]. Few cosmological parameters that are very well known, indeed, are sufficient to calculate the transfer function. This can be used to calculate the theoretical predictions for the CMB spectra using a completely unknown PPS, and then a comparison with the measured power spectra allows to put constraints on the unknown PPS. This process can be deployed using several methods that were developed in the past: for example we can find regularization methods like Richardson-Lucy iteration [396–399], truncated singular value decomposition [400] and Tikhonov regularization [401, 402], or methods like the maximum entropy deconvolution [403] or the "cosmic inversion" methods [404–408]. In the 2015 release of scientific results, the Planck collaboration presented a wide discussion about inflation and the constraints on the PPS, in Ref. [409].

All these analyses suggest that the PPS may deviate from the expected power-law behavior, especially in the region at small wavemodes: the statistical significances of the deviations are small in some cases, but it is interesting to note that both the CMB power spectra as measured by WMAP [19] and by Planck [20, 21] show similar results. The main source of the difference between the reconstructed PPS and the power-law is in the region at low multipoles, where the cosmic variance is larger. These deviations could be the result of simple statistical fluctuations or be the result of a non-standard inflationary mechanism.

The effects that considering a non-standard PPS has on cosmological parameter estimation have been studied by several authors. for example, the power-law PPS has been simply modified with the introduction of a running in the tilt of the power-law [410–413], a running of the running [414], or a sharp cut-off in the power-law [413]. Our main goal is to study how the freedom of the form of the PPS can affect the existing bounds on different neutrino properties in the early Universe, such as those on the sum of the active neutrino masses $\Sigma m_\nu$, on the effective number of relativistic species $N_{\text{eff}}$ and on the properties of a light sterile neutrino.

Previous analyses of the cosmological data with a standard power-law PPS have found that a fully thermalized sterile neutrino is quite disfavored (see Chapter 5 and Refs. [22, 23, 303, 311, 332]). These results motivated the study of mechanisms which can suppress the thermalization of sterile neutrinos in the early Universe, that would be due to active-sterile oscillations before neutrino decoupling [307, 308]. Examples are a large lepton asymmetry [310, 355–357, 370], an enhanced background potential due to new interactions in the sterile sector [365–368, 371, 386, 387], a larger cosmic expansion rate at the time of sterile neutrino production [369], and MeV dark matter annihilation [344]. We will show in this Chapter that a further possibility consists in the fact that a free PPS can partially compensate the effects of a light sterile neutrino on the cosmological observables.

Besides our main objective, which is to study the robustness of neutrino constraints when the PPS of scalar perturbations is free to vary, we are also interested in obtaining information on the form of the PPS. With these aims, we considered a general form of the PPS that allows the presence of features without forcing a particular shape. In the literature several model-independent parameterizations have been used: for example, a free PPS can be described with wavelets [415–418], principal components [419], top-hat bins without interpolation [420], power-law bins [421, 422], linear interpolation [412, 423–429], broken power-law [422, 430], and interpolating spline functions [413, 431–437]. We decided to follow part of the prescriptions of the interpolating spline form presented in Refs. [434, 436], improving the parametrization by using a "piecewise cubic Hermite interpolating polynomial" (PCHIP), which is described in Section 6.2. This method allows to avoid the spurious oscillating behavior that can appear between the nodes of the interpolating splines.

## 6.2 Primordial Power Spectrum Parameterization

We adopt a non-parametric description for the PPS of scalar perturbations: we describe the function $P_s(k)$ as the interpolation among a series of nodes at fixed wavemodes $k$. We consider twelve nodes $k_j$ ($j \in [1, 12]$) that cover a wide range of values of $k$:

$$k_1 = 5 \times 10^{-6} \, \text{Mpc}^{-1},$$
$$k_2 = 10^{-3} \, \text{Mpc}^{-1},$$
$$k_j = k_2(k_{11}/k_2)^{(j-2)/9} \quad \text{for} \quad j \in [3, 10],$$
$$k_{11} = 0.35 \, \text{Mpc}^{-1},$$
$$k_{12} = 10 \, \text{Mpc}^{-1}. \tag{6.1}$$

The most interesting range is located between $k_2 = 0.001 \, \text{Mpc}^{-1}$ and $k_{11} = 0.35 \, \text{Mpc}^{-1}$, that is approximately the range of wavemodes probed by CMB experiments. In this range we use equally spaced nodes in $\log k$. Additionally, we consider $k_1 = 5 \times 10^{-6} \, \text{Mpc}^{-1}$ and

$k_{12} = 10\,\mathrm{Mpc}^{-1}$ in order to be sure that all the PPS evaluations are inside the covered range: we expect that the nodes at these extreme wavemodes are less constrained by the data.

Having fixed the position of all the nodes, the free parameters that enter our MCMC analyses are the values of the PPS at each node, $P_{s,j} = P_s(k_j)/P_0$, where $P_0$ is the overall normalization. We use $P_0 = 2.36 \times 10^{-9}$ [438] in Section 6.3 and $P_0 = 2.2 \times 10^{-9}$ [44] in the following Sections. Each parameter $P_{s,j}$, whose expected value should be close to 1, is free to vary in the interval $[0.01, 10]$, on which we adopt a flat prior.

The complete $P_s(k)$ at all $k$ is then described as the interpolation among the points $P_{s,j}$:

$$P_s(k) = P_0 \times \texttt{PCHIP}\left(k; P_{s,1}, \ldots, P_{s,12}\right), \tag{6.2}$$

where `PCHIP` stands for "piecewise cubic Hermite interpolating polynomial" [439, 440]. This function is similar to the natural cubic spline, but it has the advantage of avoiding the introduction of spurious oscillations in the interpolation: this is obtained with a condition on the first derivative in the nodes, that is null if there is a change in the monotonicity of the point series. If the monotonicity does not change in the node $P_{s,j}$, the derivative is instead fixed using the secants between $P_{s,j-1}$, $P_{s,j}$ and $P_{s,j+1}$. The price to pay to preserve the original monotonicity of the nodes series is on the second derivative, that becomes discontinue in the nodes, differently from what happens for the natural cubic spline. A more detailed discussion on the `PCHIP` PPS description can be found in Appendix A.

When presenting our results, we will compare the constraints obtained in the context of the standard $\Lambda$CDM model with a standard power-law PPS and those obtained with the free `PCHIP` PPS. In the former case the cosmological model is described by the six parameters described in Section 2.5 ($\Omega_b h^2$, $\Omega_c h^2$, $\theta$, $\tau$, $A_s$, $n_s$), while in the latter case we substitute $A_s$ and $n_s$ with the parameters used to describe the `PCHIP` PPS, $P_{s,j}$ ($j \in [1, 12]$) and we have a model with 16 free parameters ($\Omega_b h^2$, $\Omega_c h^2$, $\theta$, $\tau$, $P_{s,1}, \ldots, P_{s,12}$). These models will be extended to study the properties of neutrinos or other aspects of the cosmological model.

When comparing the PL and the `PCHIP` PPS scenarios, it is convenient to write the values of the `PCHIP` nodes that correspond to the values of the PL PPS at the corresponding wavemodes, given the reference values $n_s^{\mathrm{ref}}$ and $A_s^{\mathrm{ref}}$. These can be converted into reference values to compare the node $P_{s,i}$ with:

$$P_{s,i}^{\mathrm{ref}} \equiv \frac{A_s^{\mathrm{ref}}}{P_0} \left(\frac{k_i}{k_*}\right)^{n_s^{\mathrm{ref}}-1} \qquad \text{with } i \in [1, \ldots, 12]. \tag{6.3}$$

## 6.3 An example: Inflationary Freedom and Light Sterile Neutrinos

### 6.3.1 Parameterization and Data

Before studying separately the degeneracies of the various cosmological parameters with the free PPS, we show that significant variations in the results are allowed if the shape of the PPS is changed. We will follow Ref. [25], where it is shown that the constraints on the properties of a light sterile neutrino change significantly when one analyzes the same set of cosmological data relaxing the hypothesis of a power-law PPS for the scalar perturbations.

To do this, we adopt the same parameterization for the light sterile neutrino and for the cosmological model that we used in Sections 5.2 and 5.3: we use an extended flat $\Lambda$CDM model to accommodate the presence of a sterile neutrino and we consider a scenario involving inflationary freedom in the production of the primordial power spectra. In the analysis with a power-law (PL) PPS we have then a cosmological model with a total of eight parameters:

$$\boldsymbol{\theta} = \{\omega_{\mathrm{c}}, \omega_{\mathrm{b}}, \theta, \tau, \ln(10^{10} A_s), n_s, m_s, \Delta N_{\mathrm{eff}}\}. \tag{6.4}$$

In contrast with previous analyses (see Chapter 5 and Refs. [22–24]), we limit the allowed range of $\Delta N_{\mathrm{eff}}$ in the interval $0 \leq \Delta N_{\mathrm{eff}} \leq 1$, assuming that the additional sterile neutrino

| Parameters | COSMO | COSMO+SBL |
|---|---|---|
| $100\,\omega_{\rm b}$ | $2.263^{+0.026}_{-0.027}{}^{+0.052}_{-0.053}{}^{+0.078}_{-0.080}$ | $2.251^{+0.023}_{-0.025}{}^{+0.049}_{-0.045}{}^{+0.075}_{-0.067}$ |
| $\omega_{\rm c}$ | $0.120^{+0.004}_{-0.005} \pm 0.008\ ^{+0.011}_{-0.009}$ | $0.117^{+0.002}_{-0.003}{}^{+0.006}_{-0.005}{}^{+0.010}_{-0.006}$ |
| $\theta$ | $1.0412 \pm 0.0007 \pm 0.0014\ ^{+0.0020}_{-0.0021}$ | $1.0416 \pm 0.0006 \pm 0.0012\ ^{+0.0018}_{-0.0019}$ |
| $\tau$ | $0.087^{+0.013}_{-0.014}{}^{+0.028}_{-0.026}{}^{+0.045}_{-0.037}$ | $0.087 \pm 0.013\ ^{+0.026}_{-0.025}{}^{+0.040}_{-0.035}$ |
| $\Delta N_{\rm eff}$ | $0.38^{+0.18}_{-0.33}$; No limit; No limit | $0.19^{+0.09}_{-0.12}$; $< 0.41$; $< 0.60$ |
| $m_s$[eV] | $0.61^{+0.31}_{-0.42}$; $< 2.03$; No limit | $1.25^{+0.11}_{-0.16}{}^{+0.17}_{-0.29}{}^{+0.22}_{-0.35}$ |
| $n_{\rm s}$ | $0.979^{+0.011}_{-0.010} \pm 0.020\ ^{+0.030}_{-0.025}$ | $0.969 \pm 0.005 \pm 0.011\ ^{+0.017}_{-0.016}$ |
| $\log(10^{10}A_s)$ | $3.152^{+0.031}_{-0.032}{}^{+0.064}_{-0.058}{}^{+0.094}_{-0.087}$ | $3.178^{+0.024}_{-0.025}{}^{+0.048}_{-0.051}{}^{+0.072}_{-0.075}$ |

Table 6.1:  Marginalized $1\sigma$, $2\sigma$ and $3\sigma$ confidence level limits for the cosmological parameters obtained with the power-law parametrization for the PPS.

cannot contribute to the relativistic energy density more than a standard active neutrino. This is what should happen if sterile neutrinos are produced in the early Universe by neutrino oscillations before neutrino decoupling [307, 308].

We assume a flat prior for all the parameters in Eq. (6.4), except $m_s$, for which we use a flat prior for $0 \leq m_s/\,{\rm eV} \leq 3$ only in the analyses which do not take into account the constraints from short-baseline neutrino oscillation data. In the analyses which take into account these constraints we use as prior for $m_s$ the posterior obtained from the analysis of SBL data presented in Chapter 4. As in the previous Chapter, we neglect the masses of the three light neutrinos $\nu_1$, $\nu_2$, $\nu_3$, which are assumed to be much smaller than 1 eV.

In order to parameterize the free PPS we follow the prescriptions presented in Section 6.2 with $P_0 = 2.36 \times 10^{-9}$ [438]. In the PCHIP PPS analysis we consider a flat $\Lambda$CDM+$\nu_s$ cosmological model with a total of 18 parameters:

$$\boldsymbol{\theta} = \{\omega_{\rm c}, \omega_{\rm b}, \theta, \tau, m_s, \Delta N_{\rm eff}, P_{s,1}, \ldots, P_{s,12}\}, \tag{6.5}$$

where $\omega_{\rm c}$, $\omega_{\rm b}$, $\theta$, $\tau$, $m_s$ and $\Delta N_{\rm eff}$ are the same as in the set (6.4).

In this Section we use the same datasets as in Sections 5.2, 5.3 and Refs. [23, 24], apart from the controversial BICEP2 data on the B-mode polarization of the CMB [71] that we neglect. In the following we will denote the analyses of all the cosmological data alone (Planck 2013 + ACT/SPT + WMAP polarization + LSS + $H_0$ + PSZ + CFHTLenS, see Subsection 5.2.1) as "**COSMO**" and those which include also the prior on the sterile neutrino mass from short-baseline neutrino oscillation as "**COSMO+SBL**".

### 6.3.2   Results

The results of our COSMO and COSMO+SBL analyses are presented in Tab. 6.1 for the standard case of a power-law PPS and in Tab. 6.2 for the free PPS with the PCHIP parameterization. In the upper part of the tables we listed the common parameters of the $\Lambda$CDM model, in the central part we listed the neutrino parameters $\Delta N_{\rm eff}$ and $m_s$, while the lower part concerns the parameters used to parameterize the PPS: $n_{\rm s}$ and $\log(10^{10}A_s)$ for the power-law PPS and the $P_{s,j}$ nodes for the PCHIP PPS. We do not discuss here the constraints on the PPS parameters, that will be presented in the final Section of this Chapter. Here we discuss firstly the results relative to the parameters in the upper part of the Tables 6.1 and 6.2 ($\omega_{\rm b}$, $\omega_{\rm c}$, $\theta$ and $\tau$) and then the results relative to the parameters in the central part of the tables, $\Delta N_{\rm eff}$ and $m_s$.

The bounds on the parameters of the $\Lambda$CDM model change slightly when more freedom is admitted for the PPS. Comparing Tabs. 6.1 and 6.2, one can see that the limits on the parameters of the $\Lambda$CDM model are slightly weakened in the PCHIP PPS case and for some

| Parameters | COSMO | COSMO+SBL |
|---|---|---|
| $100\,\omega_{\mathrm{b}}$ | $2.251^{+0.036\ +0.073\ +0.111}_{-0.036\ -0.072\ -0.106}$ | $2.247^{+0.036\ +0.072\ +0.111}_{-0.038\ -0.078\ -0.117}$ |
| $\omega_{\mathrm{c}}$ | $0.125^{+0.005\ +0.007\ +0.008}_{-0.004\ -0.012\ -0.015}$ | $0.118^{+0.004\ +0.011\ +0.016}_{-0.005\ -0.007\ -0.008}$ |
| $\theta$ | $1.0406^{+0.0007\ +0.0016\ +0.0026}_{-0.0008\ -0.0014\ -0.0019}$ | $1.0413^{+0.0008\ +0.0014\ +0.0020}_{-0.0007\ -0.0016\ -0.0024}$ |
| $\tau$ | $0.086^{+0.014\ +0.031\ +0.052}_{-0.015\ -0.028\ -0.036}$ | $0.090^{+0.014\ +0.033\ +0.051}_{-0.016\ -0.029\ -0.039}$ |
| $\Delta N_{\mathrm{eff}}$ | $> 0.51$; No limit; No limit | $0.25^{+0.13}_{-0.22}$; $< 0.75$; No limit |
| $m_s[\mathrm{eV}]$ | $0.63^{+0.23\ +1.11}_{-0.28\ -0.59}$; No limit | $1.22^{+0.13\ +0.17\ +0.24}_{-0.15\ -0.28\ -0.33}$ |
| $P_{s,1}$ | $< 2.51$; $< 7.97$; No limit | $< 2.75$; $< 8.30$; No limit |
| $P_{s,2}$ | $1.06^{+0.19\ +0.44\ +0.70}_{-0.22\ -0.35\ -0.44}$ | $1.05^{+0.18\ +0.44\ +0.75}_{-0.22\ -0.35\ -0.44}$ |
| $P_{s,3}$ | $0.65^{+0.20\ +0.38\ +0.57}_{-0.19\ -0.37\ -0.54}$ | $0.67^{+0.20\ +0.39\ +0.61}_{-0.19\ -0.36\ -0.52}$ |
| $P_{s,4}$ | $1.14^{+0.12\ +0.23\ +0.36}_{-0.11\ -0.22\ -0.31}$ | $1.13^{+0.11\ +0.23\ +0.34}_{-0.11\ -0.21\ -0.31}$ |
| $P_{s,5}$ | $0.97^{+0.05\ +0.11\ +0.18}_{-0.06\ -0.10\ -0.16}$ | $0.98^{+0.05\ +0.11\ +0.17}_{-0.06\ -0.10\ -0.15}$ |
| $P_{s,6}$ | $0.96 \pm 0.03\ ^{+0.07\ +0.10}_{-0.06\ -0.08}$ | $0.98 \pm 0.03\ ^{+0.07\ +0.11}_{-0.06\ -0.08}$ |
| $P_{s,7}$ | $0.94 \pm 0.03\ ^{+0.06\ +0.10}_{-0.05\ -0.08}$ | $0.94 \pm 0.03 \pm 0.06\ ^{+0.10}_{-0.07}$ |
| $P_{s,8}$ | $0.93 \pm 0.03\ ^{+0.06\ +0.10}_{-0.05\ -0.07}$ | $0.93 \pm 0.03 \pm 0.06\ ^{+0.10}_{-0.07}$ |
| $P_{s,9}$ | $0.93 \pm 0.03\ ^{+0.07\ +0.11}_{-0.06\ -0.08}$ | $0.91 \pm 0.03\ ^{+0.07\ +0.10}_{-0.06\ -0.07}$ |
| $P_{s,10}$ | $0.91 \pm 0.04 \pm 0.08\ ^{+0.12}_{-0.11}$ | $0.88^{+0.03\ +0.08\ +0.14}_{-0.04\ -0.07\ -0.08}$ |
| $P_{s,11}$ | $1.13^{+0.17\ +0.28\ +0.40}_{-0.16\ -0.32\ -0.39}$ | $1.00^{+0.13\ +0.35\ +0.52}_{-0.17\ -0.24\ -0.28}$ |
| $P_{s,12}$ | $< 0.69$; $< 1.18$; $< 1.55$ | $< 0.49$; $< 1.01$; $< 1.33$ |

Table 6.2: Marginalized $1\sigma$, $2\sigma$ and $3\sigma$ confidence level limits for the cosmological parameters obtained with the `PCHIP` parametrization for the PPS. From Ref. [25].

parameters there is also a small shift in the marginalized best-fit value. In all the cases in which this happens, the marginalized best-fit values move inside the $1\sigma$ uncertainties. The freedom of the form of the PPS affects the COSMO results more than the COSMO+SBL results: in the former case the $\omega_{\mathrm{c}}$ and $\theta$ best values change by about $1\sigma$, while a smaller shift is obtained for $100\,\omega_{\mathrm{b}}$. On the other hand, in the COSMO+SBL analysis all the shifts are much smaller than the $1\sigma$ uncertainties, since the degeneracies between $m_s$ and the other parameters are less significant, because the allowed range for $m_s$ is smaller.

The upper points in Figure 6.1 show the marginalized $1\sigma$, $2\sigma$ and $3\sigma$ allowed intervals for $\Delta N_{\mathrm{eff}}$ and $m_s$ that we obtained in the COSMO(PL) and COSMO(PCHIP) analyses, without the SBL prior. Figure 6.2 shows the corresponding marginalized $1\sigma$, $2\sigma$ and $3\sigma$ allowed regions in the $m_s$–$\Delta N_{\mathrm{eff}}$ plane. We can notice some major changes in the allowed values of both $\Delta N_{\mathrm{eff}}$ and $m_s$ in the `PCHIP` PPS case with respect to the power-law PPS case. With a power-law PPS the best-fit value of $\Delta N_{\mathrm{eff}}$ is around 0.4, whereas with the `PCHIP` PPS it is at $\Delta N_{\mathrm{eff}} = 1$, that is the upper limit for $\Delta N_{\mathrm{eff}}$ assumed in the analysis. The reason of this behavior is that the effects of the presence of the additional relativistic energy in the primordial Universe can be compensated by an increase of the `PCHIP` PPS at large $k$ (see Section 6.6). As a result, the marginalized posterior for $\Delta N_{\mathrm{eff}}$ is increased in the region towards $\Delta N_{\mathrm{eff}} = 1$, together with the higher values in the `PCHIP` PPS for $k > 0.35\,\mathrm{Mpc}^{-1}$. In the next Sections we will discuss more in details the reasons that drive to the loosened constraints on the neutrino parameters when a free PPS is assumed.

Without the SBL constraint on $m_s$, the different preferences for the value of $\Delta N_{\mathrm{eff}}$ in the power-law and `PCHIP` PPS analyses correspond to different allowed intervals for $m_s$. As shown in Fig. 6.1, although in both cases the best-fit value of $m_s$ is near 0.6 eV, the intermediate preferred region for $\Delta N_{\mathrm{eff}}$ in the power-law PPS analysis gives for $m_s$ an upper limit of about 2 eV at $2\sigma$, whereas the large preferred values for $\Delta N_{\mathrm{eff}}$ in the `PCHIP` PPS analysis gives a

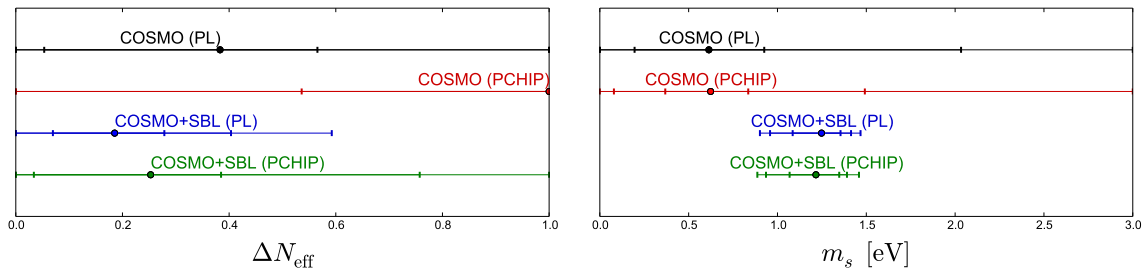Figure 6.1: $1\sigma$, $2\sigma$ and $3\sigma$ marginalized intervals for $\Delta N_{\text{eff}}$ and $m_s$ obtained in the different analyses discussed in the text (considering $0 \leq \Delta N_{\text{eff}} \leq 1$ and $0 \leq m_s/\text{eV} \leq 3$). From Ref. [25].

tighter upper limit of about 1.5 eV at $2\sigma$, since the volume of the posterior distribution is shifted towards lower values of $m_s$.

The SBL prior on the sterile neutrino mass $m_s$ puts a constraint so strong that in practice the value of this parameter does not depend on the inclusion or not of the freedom of the PPS. In fact, the $m_s$ limits in Tabs. 6.1 and 6.2 are similar in the power-law PPS and PCHIP PPS analyses. This can be seen also from the marginalized allowed intervals of $m_s$ in Fig. 6.1, comparing the COSMO+SBL(PL) and COSMO+SBL(PCHIP) allowed intervals.

A major difference appears, instead, in the limits for $\Delta N_{\text{eff}}$, because the effects of the presence of additional relativistic energy in the primordial Universe can be compensated by an increase in the PCHIP PPS at large $k$, as in the case without the SBL constraint on $m_s$. As shown in Fig. 6.1, the best-fit and upper limits on $\Delta N_{\text{eff}}$ in the COSMO+SBL(PL) and COSMO+SBL(PCHIP) are different. In particular, in the COSMO+SBL(PCHIP) the $3\sigma$ upper limit on $\Delta N_{\text{eff}}$ allows the presence of a fully thermalized sterile neutrino compatible with the SBL constraint on $m_s$.

Figure 6.3 shows the contour plots of the marginalized $1\sigma$, $2\sigma$ and $3\sigma$ regions in the $m_s$–$\Delta N_{\text{eff}}$ plane that we obtained in the COSMO+SBL(PL) and COSMO+SBL(PCHIP) analyses. The allowed regions in the left panel are similar[1] to those obtained in Ref. [23] with a standard power-law PPS. One can see that in this case a fully thermalized sterile neutrino is quite disfavored. On the other hand, from the right panel one can see that in the PCHIP PPS analysis a fully thermalized sterile neutrino with a mass just below 1 eV and with $\Delta N_{\text{eff}} = 1$ is even inside the $2\sigma$ region. This means that a fully thermalized sterile neutrino can be accommodated in the cosmological model if the PPS is not forced to be described by a power-law.

At this point we know that the freedom in the inflationary paradigm can have a significant impact on the constraints derived from cosmology. We will study now separately how the PCHIP PPS assumption influences the constraints on the base parameters of the $\Lambda$CDM model (Section 6.5) and on the neutrino properties. We will consider separately the effective number of relativistic degrees of freedom in Section 6.6 and the sum of the neutrino masses in Section 6.7. The following results are based on the Planck 2015 data and they have been presented in Ref. [26].

## 6.4 Base Model and Cosmological Data

The common underlying model that we will extend to study various dark radiation properties is the $\Lambda$CDM model already introduced. From the fundamental cosmological parameters of the $\Lambda$CDM model we will compute other derived quantities, such as the Hubble parameter

---

[1] The only difference is that the analysis in Ref. [23] took into account also the BICEP2 data on the B-mode polarization of the CMB [71].
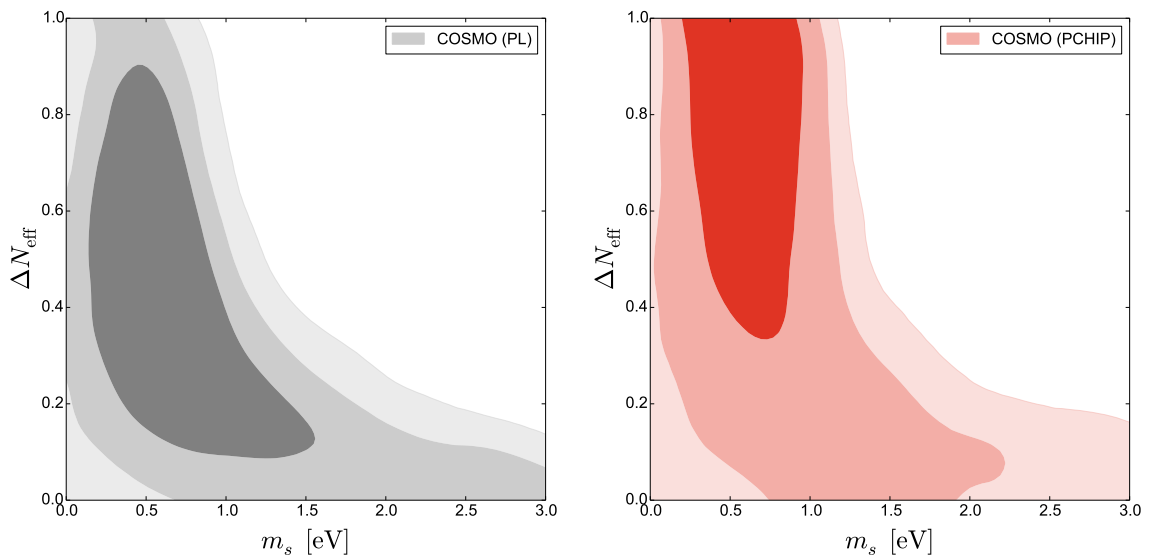
Figure 6.2: $1\sigma$, $2\sigma$ and $3\sigma$ marginalized contours in the $(m_s - \Delta N_{\text{eff}})$ plane in the fits without the SBL prior. The left and right panels correspond, respectively, to the standard power-law PPS and the PCHIP PPS analyses. From Ref. [25].
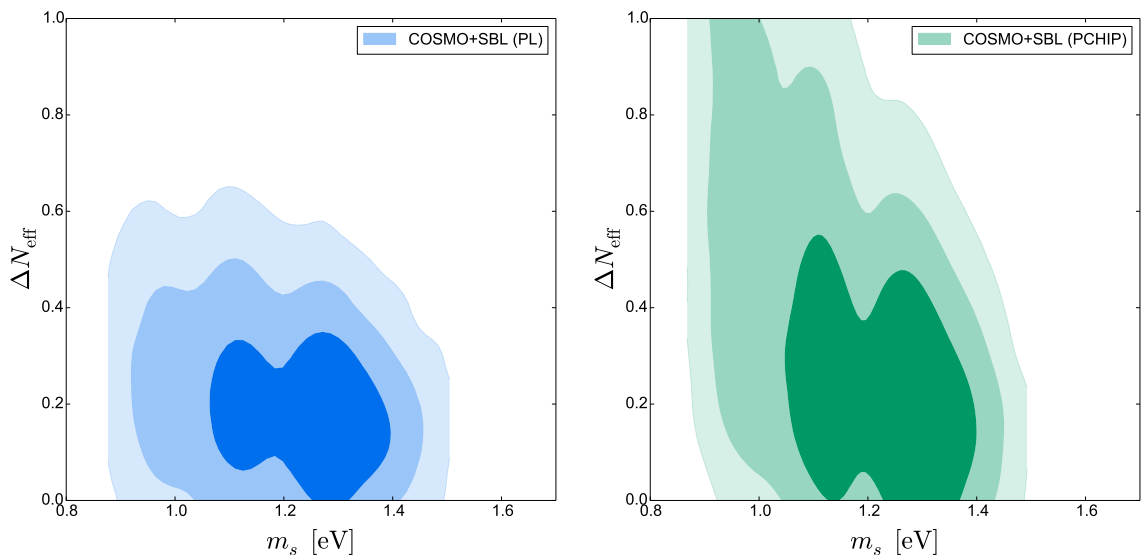


Figure 6.3: As in Fig. 6.2, but with the inclusion of the SBL prior on $m_s$. From Ref. [25].

today $H_0$ and the clustering parameter $\sigma_8$, defined as the mean matter fluctuations inside a sphere of $8h^{-1}$ Mpc radius.

We base our following analyses on the latest data released by the Planck Collaboration [21], of which we consider the full temperature power spectrum at multipoles $2 \leq \ell \leq 2500$ (**Planck TT** hereafter) and the polarization power spectra in the range $2 \leq \ell \leq 29$ (**lowP**). We shall also include the polarization data at $30 \leq \ell \leq 2500$ (**TE, EE**) [62]. Since the polarization spectra at high multipoles are still under discussion and some residual systematics were detected by the Planck Collaboration [44,62], we shall use as baseline dataset the combination **Planck TT+lowP** and the impact of polarization measurements will be separately studied in the dataset **Planck TT,TE,EE+lowP**.

Additionally, we will consider the two CMB datasets above in combination with these additional cosmological measurements (see Chapter 3):

| Parameter | Planck TT+lowP | | Planck TT,TE,EE+lowP | | Planck TT+lowP +MPkW | | Planck TT,TE,EE+lowP +MPkW | |
|---|---|---|---|---|---|---|---|---|
| $100\Omega_b h^2$ | $2.222^{+0.045}_{-0.043}$ | $2.175^{+0.077}_{-0.076}$ | $2.225^{+0.032}_{-0.030}$ | $2.215^{+0.038}_{-0.037}$ | $2.221^{+0.044}_{-0.045}$ | $2.190^{+0.072}_{-0.070}$ | $2.223 \pm 0.031$ | $2.214^{+0.035}_{-0.036}$ |
| $\Omega_c h^2$ | $0.1197^{+0.0043}_{-0.0042}$ | $0.1231^{+0.0061}_{-0.0059}$ | $0.1198 \pm 0.0029$ | $0.1209^{+0.0035}_{-0.0034}$ | $0.1198 \pm 0.0039$ | $0.1223^{+0.0056}_{-0.0053}$ | $0.1200^{+0.0028}_{-0.0027}$ | $0.1210 \pm 0.0033$ |
| $100\theta$ | $1.041 \pm 0.001$ | $1.040 \pm 0.001$ | $1.0408 \pm 0.0006$ | $1.0407 \pm 0.0006$ | $1.041 \pm 0.001$ | $1.041 \pm 0.001$ | $1.0408 \pm 0.0006$ | $1.0407 \pm 0.0006$ |
| $\tau$ | $0.078^{+0.038}_{-0.036}$ | $0.073^{+0.044}_{-0.042}$ | $0.079 \pm 0.034$ | $0.082 \pm 0.040$ | $0.075^{+0.038}_{-0.039}$ | $0.076^{+0.048}_{-0.046}$ | $0.076^{+0.034}_{-0.033}$ | $0.083^{+0.038}_{-0.037}$ |
| $n_S$ | $0.966 \pm 0.012$ | – | $0.964 \pm 0.010$ | – | $0.965 \pm 0.011$ | – | $0.964 \pm 0.009$ | – |
| $\ln[10^{10}A_s]$ | $3.089^{+0.072}_{-0.069}$ | – | $3.094 \pm 0.066$ | – | $3.084^{+0.073}_{-0.074}$ | – | $3.087^{+0.066}_{-0.065}$ | – |
| $H_0\,[\mathrm{km\,s^{-1}\,Mpc^{-1}}]$ | $67.3^{+1.9}_{-1.8}$ | $65.7 \pm 2.7$ | $67.3 \pm 1.3$ | $66.8 \pm 1.5$ | $67.3^{+1.7}_{-1.8}$ | $66.1 \pm 2.5$ | $67.2 \pm 1.2$ | $66.7^{+1.5}_{-1.4}$ |
| $\sigma_8$ | $0.83 \pm 0.03$ | $0.87 \pm 0.06$ | $0.83 \pm 0.03$ | $0.88^{+0.05}_{-0.06}$ | $0.83 \pm 0.03$ | $0.84^{+0.04}_{-0.03}$ | $0.83 \pm 0.03$ | $0.83 \pm 0.03$ |
| $P_{s,1}$ | $\equiv 1.365$ | $< 7.93$ | $\equiv 1.397$ | $< 7.69$ | $\equiv 1.371$ | $< 7.90$ | $\equiv 1.388$ | $< 7.68$ |
| $P_{s,2}$ | $\equiv 1.140$ | $1.15^{+0.38}_{-0.35}$ | $\equiv 1.155$ | $1.14^{+0.39}_{-0.36}$ | $\equiv 1.139$ | $1.14^{+0.39}_{-0.36}$ | $\equiv 1.147$ | $1.14^{+0.38}_{-0.36}$ |
| $P_{s,3}$ | $\equiv 1.115$ | $0.73^{+0.39}_{-0.37}$ | $\equiv 1.128$ | $0.71^{+0.38}_{-0.35}$ | $\equiv 1.113$ | $0.73^{+0.39}_{-0.38}$ | $\equiv 1.120$ | $0.72^{+0.38}_{-0.37}$ |
| $P_{s,4}$ | $\equiv 1.091$ | $1.19^{+0.26}_{-0.25}$ | $\equiv 1.102$ | $1.22^{+0.23}_{-0.22}$ | $\equiv 1.088$ | $1.19 \pm 0.25$ | $\equiv 1.094$ | $1.22 \pm 0.22$ |
| $P_{s,5}$ | $\equiv 1.067$ | $1.07 \pm 0.11$ | $\equiv 1.076$ | $1.08^{+0.11}_{-0.10}$ | $\equiv 1.063$ | $1.07^{+0.12}_{-0.11}$ | $\equiv 1.069$ | $1.08 \pm 0.10$ |
| $P_{s,6}$ | $\equiv 1.043$ | $1.06^{+0.09}_{-0.08}$ | $\equiv 1.051$ | $1.07^{+0.08}_{-0.08}$ | $\equiv 1.040$ | $1.06 \pm 0.09$ | $\equiv 1.044$ | $1.07^{+0.08}_{-0.07}$ |
| $P_{s,7}$ | $\equiv 1.021$ | $1.04^{+0.09}_{-0.08}$ | $\equiv 1.027$ | $1.04 \pm 0.08$ | $\equiv 1.016$ | $1.03 \pm 0.09$ | $\equiv 1.020$ | $1.04^{+0.08}_{-0.07}$ |
| $P_{s,8}$ | $\equiv 0.998$ | $0.99^{+0.09}_{-0.08}$ | $\equiv 1.003$ | $1.01 \pm 0.08$ | $\equiv 0.993$ | $1.00 \pm 0.09$ | $\equiv 0.996$ | $1.01^{+0.08}_{-0.07}$ |
| $P_{s,9}$ | $\equiv 0.976$ | $0.97^{+0.09}_{-0.08}$ | $\equiv 0.980$ | $0.99^{+0.08}_{-0.07}$ | $\equiv 0.971$ | $0.98 \pm 0.09$ | $\equiv 0.973$ | $0.99^{+0.08}_{-0.07}$ |
| $P_{s,10}$ | $\equiv 0.955$ | $0.97^{+0.10}_{-0.09}$ | $\equiv 0.957$ | $0.98 \pm 0.09$ | $\equiv 0.949$ | $0.95 \pm 0.09$ | $\equiv 0.951$ | $0.96 \pm 0.08$ |
| $P_{s,11}$ | $\equiv 0.934$ | $< 4.03$ | $\equiv 0.935$ | $2.44^{+2.00}_{-2.37}$ | $\equiv 0.928$ | $0.82^{+0.45}_{-0.38}$ | $\equiv 0.929$ | $0.81^{+0.45}_{-0.38}$ |
| $P_{s,12}$ | $\equiv 0.833$ | nb | $\equiv 0.829$ | nb | $\equiv 0.825$ | $< 3.93$ | $\equiv 0.823$ | $< 3.44$ |

Table 6.3: Constraints on the cosmological parameters from the Planck TT+lowP and Planck TT,TE,EE+lowP datasets, and also in combination with the matter power spectrum shape measurements from WiggleZ (MPkW), in the $\Lambda$CDM model (*nb* stands for *no bound*). For each combination, we report the limits obtained for the two parameterizations of the primordial power spectrum, namely the power-law model (first column) and the polynomial expansion (second column of each data combination). Limits are at 95% CL around the mean value of the posterior distribution. For each dataset, in the case of the power-law model, the values of $P_{s,i}$ are computed according to Eq. (6.3). From Ref. [26].

**BAO** – Baryon Acoustic Oscillations data as obtained by 6dFGS [90], by the SDSS Main Galaxy Sample (MGS) [91] and by the BOSS experiment in the DR11 release [93];

**MPkW** – the matter power spectrum as measured by the WiggleZ Dark Energy Survey [101];

**lensing** – the reconstruction of the lensing potential obtained by the Planck collaboration with the CMB trispectrum analysis [64].

## 6.5 Constraints in the $\Lambda$CDM Model

In this Section we shall only consider a limited number of data combinations, mostly focusing on the variations driven by the inclusion of the PCHIP PPS in the analyses. We add to the Planck TT+lowP measurements only the datasets that can improve the constraints on the PCHIP PPS at small scales, which are the Planck polarization measurements at high-$\ell$ and the MPkW constraints on the matter power spectrum.

The results we obtain for the $\Lambda$CDM model are reported in Tab. 6.3. For each dataset, we list the constraints on the parameters obtained using both the standard power-law PPS and the model independent approach (PCHIP) for the PPS. In the absence of high multipole polarization or large scale structure data, the errors are generically enlarged for all the parameters: those showing a larger difference between their values in the PCHIP PPS case and in the power-law PPS case are $\Omega_b h^2$, $\Omega_c h^2$, $H_0$ and $\sigma_8$, with deviations of the order of $1\sigma$ in the PCHIP PPS case with respect to the power-law PPS case. This is a consequence of the numerous degeneracies, and we illustrate an example in Fig. 6.4, which depicts the constraints in the ($\Omega_c h^2$, $H_0$) plane for different data combinations, in the $\Lambda$CDM model, assuming the PCHIP PPS description. Simultaneous variations of the parameters can produce effects on the CMB spectrum that can be compensated by the freedom in the PPS.

The differences between the PCHIP and the power-law PPS parameterizations are much smaller for the "Planck TT,TE,EE+lowP+MPkW" dataset, and the two descriptions of the PPS give bounds for the $\Lambda$CDM parameters that are in full agreement.
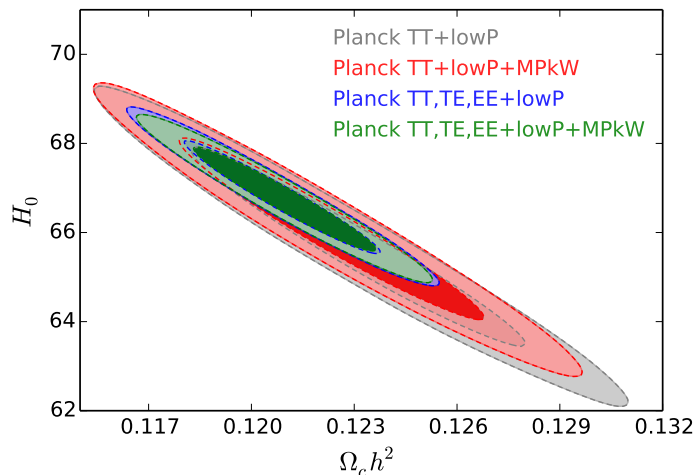
Figure 6.4: 2D constraints at 68% and 95% CL in the $(\Omega_c h^2, H_0)$ plane, obtained in the ΛCDM model considering the `PCHIP` PPS description, for different data combinations. From Ref. [26].

The addition of the high multipole polarization spectra has a profound impact in our analyses. Figure 6.5 depicts the CMB spectra measured by Planck [21], together with the theoretical spectra obtained from the best-fit values arising from our analyses. More concretely, we use the marginalized best-fit values reported in Tab. 6.3 for the ΛCDM model with a power-law PPS obtained from the analyses of the Planck TT+lowP (in black) and Planck TT,TE,EE+lowP (in blue) datasets, plus the best-fit values in the ΛCDM model with a `PCHIP` PPS, from the Planck TT+lowP (red) and Planck TT,TE,EE+lowP (green) datasets. We plot the $D_\ell = \ell(\ell+1)\,C_\ell/(2\pi)$ spectra of the TT and TE anisotropies as well as the relative (absolute for the TE spectra) difference between each spectrum and the one obtained from the Planck TT+lowP data in the ΛCDM model with the power-law PPS. Notice that in the case of TT, the best-fit spectra are in good agreement with the observational data, even if there are variations among the ΛCDM parameters, as they can be compensated by the freedom in the PPS. However, for the TE cross-correlation spectrum, such a compensation is no longer possible and the existing degeneracies are broken. Consequently, the inclusion of the TE spectrum in the analyses has a strong impact on the derived bounds. In particular, in the region between $600 \leq \ell \leq 1200$ in the TE cross-correlation spectra (see the lower panel of Fig. 6.5) it is possible to notice that the line representing the results obtained in the `PCHIP` PPS approach without polarization data deviates significantly from the observational data points. The addition of high multipole polarization data results in a good agreement with the predictions obtained using the power-law PPS.

The bounds on the nodes of the `PCHIP` PPS parameterization are also reported in Tab. 6.3. The most significant deviations from the power-law PPS appear at the extreme wavemodes. At small $k$, the deviations appear because the `PCHIP` PPS can reproduce the fluctuations in the CMB temperature spectrum (see the red and green curves in the upper panel of Fig. 6.5), while at high $k$ the data have smaller precision and therefore the `PCHIP` nodes are less constrained. We will describe the bounds on the `PCHIP` nodes and on the form of the reconstructed PPS in Sec. 6.8, underlying the common aspects and the differences that appear in the various extensions of the ΛCDM model.
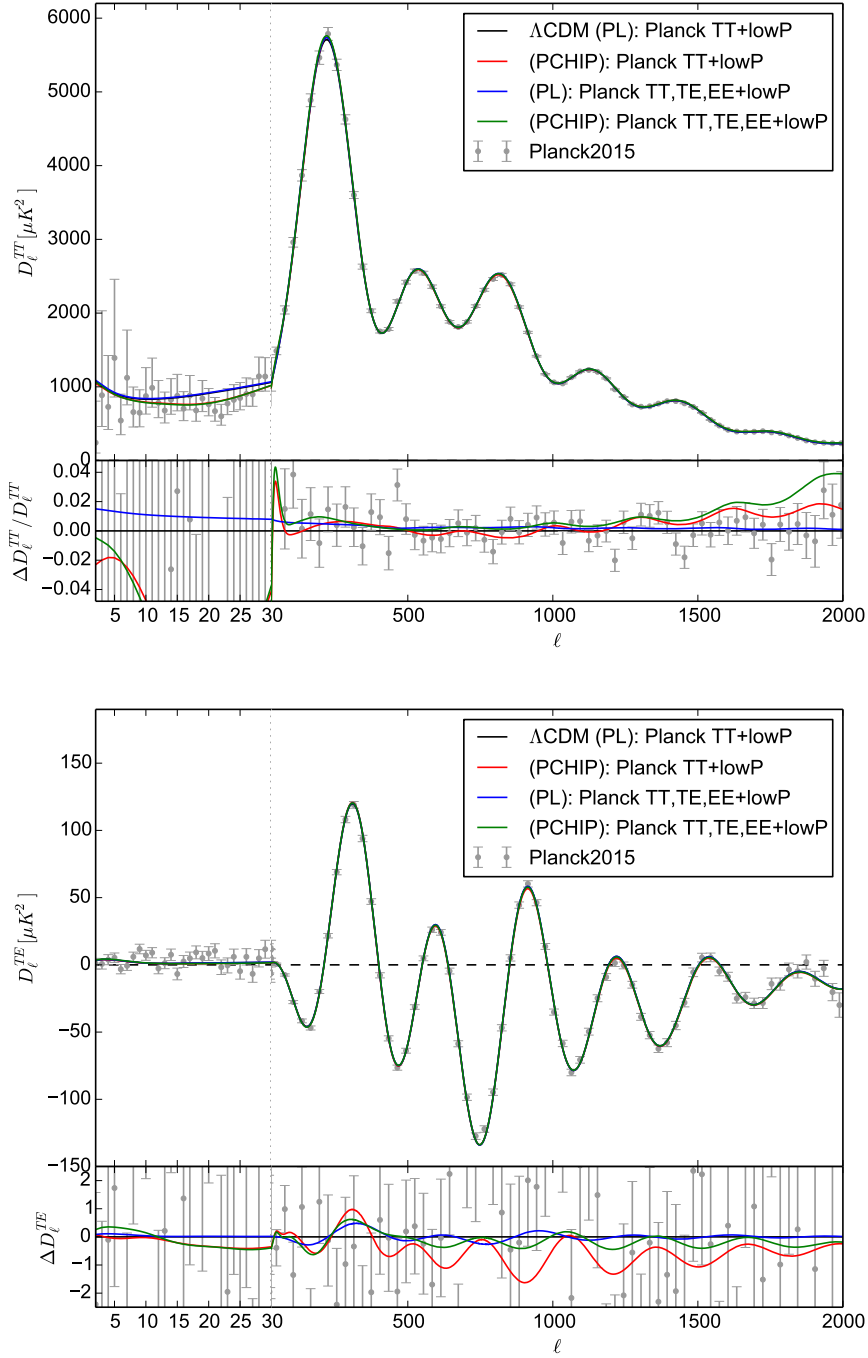
Figure 6.5: Comparison of the Planck 2015 data [21] with the TT and TE spectra obtained using the marginalized best-fit values from the analyses of Planck TT+lowP (black) and Planck TT,TE,EE+lowP (blue) in the ΛCDM model with the power-law (PL) PPS, and from the analyses of Planck TT+lowP (red) and Planck TT,TE,EE+lowP (green) in the ΛCDM model with the PCHIP PPS. The adopted values for each spectrum are reported in Tab. 6.3. We plot the $D_\ell = \ell(\ell+1) C_\ell/(2\pi)$ spectra and the relative (absolute for the TE spectra) difference between each spectrum and the one obtained in the ΛCDM (power-law PPS) model from the Planck TT+lowP data (black line). From Ref. [26].
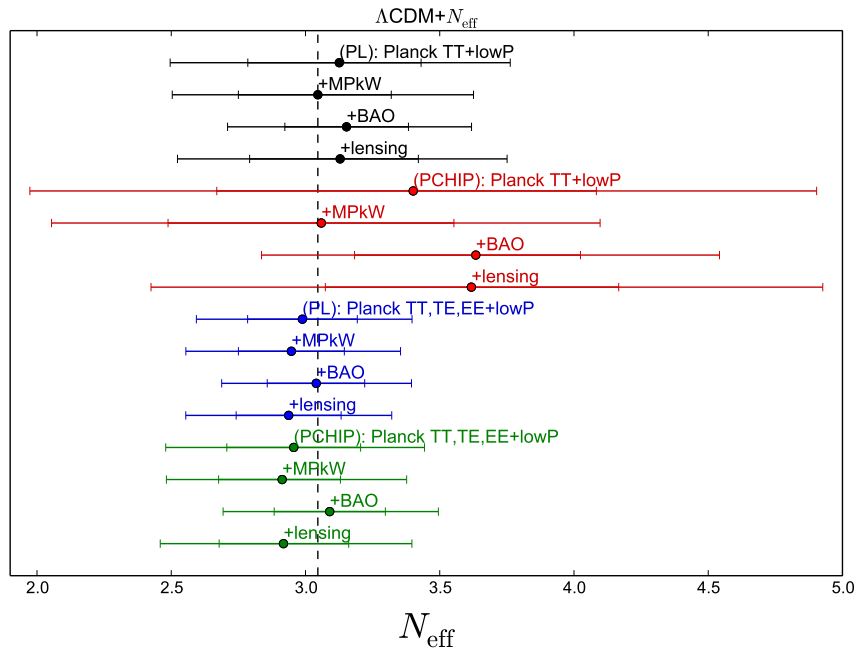
Figure 6.6: 68% and 95% CL constraints on $N_{\rm eff}$, obtained in the $\Lambda$CDM + $N_{\rm eff}$ model. Different colors indicate Planck TT+lowP with PL PPS (black), Planck TT+lowP with PCHIP PPS (red), Planck TT,TE,EE+lowP with PL PPS (blue) and Planck TT,TE,EE+lowP with PCHIP PPS (green). For each color we plot 4 different datasets: from top to bottom, we have CMB only, CMB+MPkW, CMB+BAO and CMB+lensing. From Ref. [26].

## 6.6 Massless Neutrinos

### 6.6.1 Parameterization

We already said that massless species account as radiation during all the evolution of the Universe. The contribution of the relativistic particles to the total energy density can be written using the effective number of degrees of freedom $N_{\rm eff}$, as in Eq. (4.43). The standard value is $N_{\rm eff} = 3.046$ [305] for the three active neutrino standard scenario. Deviations of $N_{\rm eff}$ from its standard value may indicate that the thermal history of the active neutrino is different from what we expect, or that additional relativistic particles are present in the Universe, as additional sterile neutrinos or thermal axions (see Chapter 7 for this last possibility).

We recall that a non-standard value of $N_{\rm eff}$ affects the Big Bang Nucleosynthesis era, and also the matter-radiation equality. A shift in the matter-radiation equality would cause a change in the expansion rate at decoupling, affecting the sound horizon and the angular scale of the peaks of the CMB spectrum, as well as in the contribution of the *early Integrated Sachs Wolfe (ISW) effect* (see Section 4.4.4). To avoid such a shift and its consequences, it is possible to change simultaneously the energy densities of matter and dark energy, in order to keep fixed all the relevant scales in the Universe. In this case, the CMB spectrum is affected only by an increased Silk damping at small scales (see Fig. 4.2).

Considering the $\Lambda$CDM + $N_{\rm eff}$ model, we will now present the constraints on the effective number of relativistic species obtained both in the power-law and the PCHIP PPS scenarios.

### 6.6.2 Results

The constraints on $N_{\rm eff}$ are summarized in Fig. 6.6, where we plot the 68% and 95% CL constraints on $N_{\rm eff}$ obtained with different datasets and PPS combinations for the $\Lambda$CDM + $N_{\rm eff}$ model.
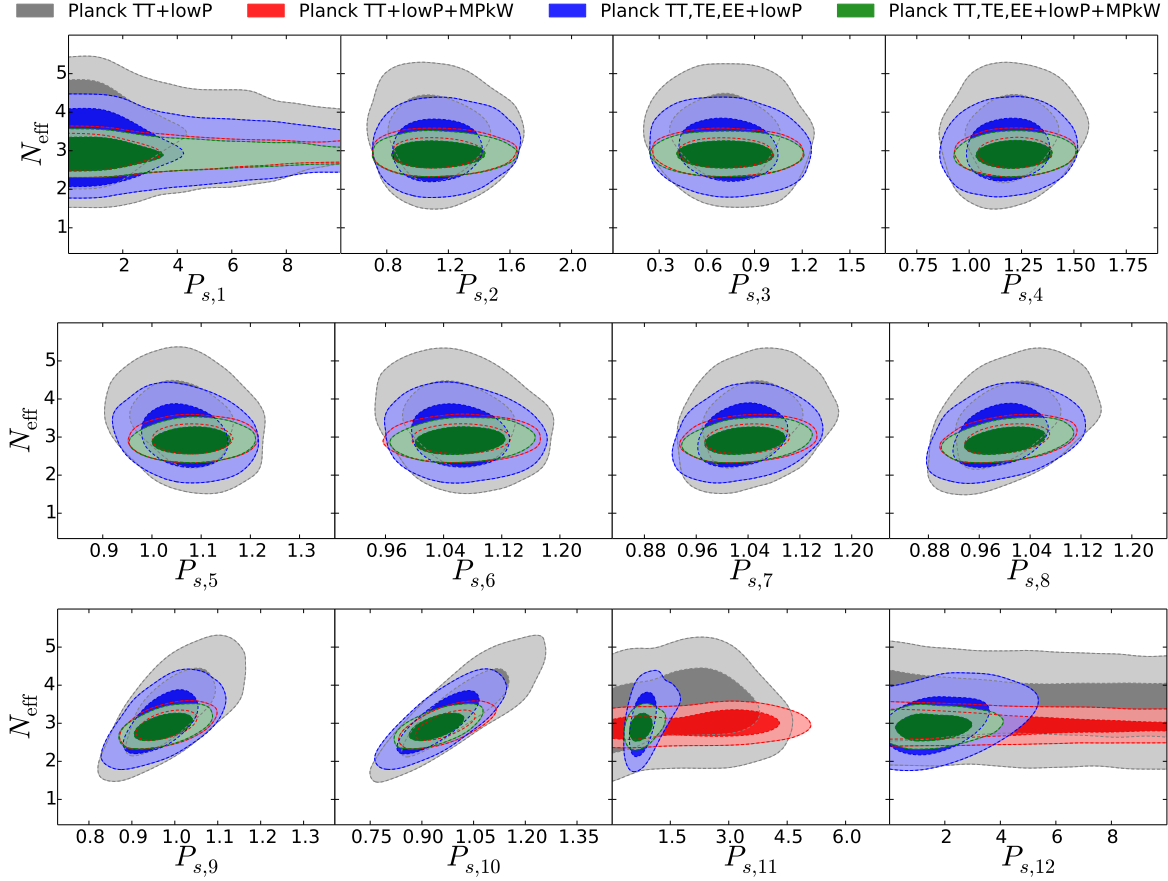
Figure 6.7: 68% and 95% CL constraints in the $(N_{\mathrm{eff}}, P_{s,j})$ planes, obtained in the $\Lambda$CDM + $N_{\mathrm{eff}}$ model. We show the results for Planck TT+lowP (gray), Planck TT+lowP+MPkW (red), Planck TT,TE,EE+lowP (blue) and Planck TT,TE,EE+lowP+MPkW (green). Adapted from Ref. [26].

| Parameter | Planck TT+lowP | | Planck TT+lowP+MPkW | | Planck TT+lowP+BAO | | Planck TT+lowP+lensing | |
|---|---|---|---|---|---|---|---|---|
| $\Omega_b h^2$ | $2.230^{+0.075}_{-0.071}$ | $2.189^{+0.107}_{-0.105}$ | $2.221^{+0.066}_{-0.063}$ | $2.186^{+0.081}_{-0.082}$ | $2.233 \pm 0.047$ | $2.205^{+0.060}_{-0.057}$ | $2.232^{+0.074}_{-0.069}$ | $2.198^{+0.093}_{-0.091}$ |
| $\Omega_c h^2$ | $0.1205^{+0.0081}_{-0.0077}$ | $0.1272^{+0.0189}_{-0.0182}$ | $0.1198^{+0.0077}_{-0.0073}$ | $0.1226^{+0.0148}_{-0.0141}$ | $0.1207^{+0.0077}_{-0.0074}$ | $0.1294^{+0.0153}_{-0.0146}$ | $0.1195^{+0.0079}_{-0.0073}$ | $0.1287^{+0.0169}_{-0.0161}$ |
| $100\theta$ | $1.041 \pm 0.001$ | $1.040 \pm 0.001$ | $1.041 \pm 0.001$ | $1.041 \pm 0.002$ | $1.041 \pm 0.001$ | $1.0400^{+0.0015}_{-0.0014}$ | $1.041 \pm 0.001$ | $1.0401^{+0.0017}_{-0.0015}$ |
| $\tau$ | $0.080^{+0.044}_{-0.042}$ | $0.076^{+0.050}_{-0.047}$ | $0.075^{+0.040}_{-0.039}$ | $0.075^{+0.048}_{-0.043}$ | $0.082^{+0.035}_{-0.036}$ | $0.079^{+0.046}_{-0.041}$ | $0.069^{+0.040}_{-0.038}$ | $0.066^{+0.042}_{-0.038}$ |
| $N_{\mathrm{eff}}$ | $3.13^{+0.64}_{-0.63}$ | $3.40^{+1.50}_{-1.43}$ | $3.05^{+0.58}_{-0.54}$ | $3.06^{+1.04}_{-1.00}$ | $3.15^{+0.47}_{-0.44}$ | $3.63^{+0.91}_{-0.80}$ | $3.13^{+0.62}_{-0.61}$ | $3.62^{+1.31}_{-1.19}$ |
| $n_S$ | $0.969^{+0.032}_{-0.030}$ | – | $0.965^{+0.027}_{-0.026}$ | – | $0.971^{+0.018}_{-0.017}$ | – | $0.971^{+0.030}_{-0.028}$ | – |
| $\ln[10^{10} A_s]$ | $3.096^{+0.095}_{-0.089}$ | – | $3.083^{+0.085}_{-0.084}$ | – | $3.100^{+0.074}_{-0.075}$ | – | $3.070^{+0.085}_{-0.079}$ | – |
| $H_0\,[\mathrm{km\,s^{-1}\,Mpc^{-1}}]$ | $68.0^{+5.7}_{-5.6}$ | $68.2^{+11.4}_{-11.1}$ | $67.3^{+4.8}_{-4.6}$ | $66.0^{+7.4}_{-7.2}$ | $68.3^{+3.0}_{-2.9}$ | $70.2^{+4.6}_{-4.2}$ | $68.5^{+5.6}_{-5.3}$ | $70.2^{+9.4}_{-8.8}$ |
| $\sigma_8$ | $0.83^{+0.05}_{-0.04}$ | $0.88^{+0.10}_{-0.09}$ | $0.83 \pm 0.04$ | $0.84 \pm 0.06$ | $0.84 \pm 0.04$ | $0.90 \pm 0.08$ | $0.82 \pm 0.04$ | $0.88 \pm 0.08$ |
| $P_{s,1}$ | $\equiv 1.337$ | $< 7.96$ | $\equiv 1.369$ | $< 7.97$ | $\equiv 1.318$ | $< 8.06$ | $\equiv 1.279$ | $< 7.87$ |
| $P_{s,2}$ | $\equiv 1.135$ | $1.14^{+0.40}_{-0.37}$ | $\equiv 1.138$ | $1.14^{+0.39}_{-0.36}$ | $\equiv 1.130$ | $1.14^{+0.41}_{-0.38}$ | $\equiv 1.097$ | $1.14^{+0.39}_{-0.37}$ |
| $P_{s,3}$ | $\equiv 1.112$ | $0.73^{+0.41}_{-0.38}$ | $\equiv 1.112$ | $0.73^{+0.40}_{-0.37}$ | $\equiv 1.109$ | $0.72^{+0.41}_{-0.38}$ | $\equiv 1.076$ | $0.70^{+0.39}_{-0.37}$ |
| $P_{s,4}$ | $\equiv 1.090$ | $1.20^{+0.27}_{-0.25}$ | $\equiv 1.087$ | $1.19 \pm 0.25$ | $\equiv 1.088$ | $1.20^{+0.27}_{-0.26}$ | $\equiv 1.056$ | $1.18^{+0.26}_{-0.25}$ |
| $P_{s,5}$ | $\equiv 1.068$ | $1.07^{+0.13}_{-0.12}$ | $\equiv 1.062$ | $1.07 \pm 0.11$ | $\equiv 1.068$ | $1.06 \pm 0.10$ | $\equiv 1.036$ | $1.04 \pm 0.10$ |
| $P_{s,6}$ | $\equiv 1.047$ | $1.06^{+0.10}_{-0.08}$ | $\equiv 1.038$ | $1.06^{+0.09}_{-0.08}$ | $\equiv 1.048$ | $1.06 \pm 0.09$ | $\equiv 1.017$ | $1.03^{+0.07}_{-0.06}$ |
| $P_{s,7}$ | $\equiv 1.026$ | $1.05^{+0.10}_{-0.09}$ | $\equiv 1.015$ | $1.03^{+0.09}_{-0.08}$ | $\equiv 1.028$ | $1.05^{+0.09}_{-0.08}$ | $\equiv 0.998$ | $1.02^{+0.08}_{-0.07}$ |
| $P_{s,8}$ | $\equiv 1.005$ | $1.00^{+0.11}_{-0.10}$ | $\equiv 0.992$ | $1.00^{+0.10}_{-0.09}$ | $\equiv 1.009$ | $1.02 \pm 0.09$ | $\equiv 0.979$ | $0.99 \pm 0.09$ |
| $P_{s,9}$ | $\equiv 0.985$ | $1.00^{+0.14}_{-0.13}$ | $\equiv 0.970$ | $0.97^{+0.11}_{-0.10}$ | $\equiv 0.990$ | $1.02 \pm 0.09$ | $\equiv 0.961$ | $0.99^{+0.12}_{-0.11}$ |
| $P_{s,10}$ | $\equiv 0.965$ | $1.01^{+0.20}_{-0.19}$ | $\equiv 0.948$ | $0.95^{+0.15}_{-0.14}$ | $\equiv 0.972$ | $1.05 \pm 0.12$ | $\equiv 0.943$ | $1.02 \pm 0.17$ |
| $P_{s,11}$ | $\equiv 0.946$ | $< 3.78$ | $\equiv 0.927$ | $0.85^{+0.58}_{-0.45}$ | $\equiv 0.954$ | $< 3.83$ | $\equiv 0.925$ | $< 3.55$ |
| $P_{s,12}$ | $\equiv 0.853$ | nb | $\equiv 0.824$ | $< 4.24$ | $\equiv 0.865$ | nb | $\equiv 0.840$ | nb |

Table 6.4: Constraints on cosmological parameters from the Planck TT+lowP dataset alone and in combination with the matter power spectrum shape measurements from WiggleZ (MPkW), the BAO data and the lensing constraints from Planck, in the $\Lambda$CDM + $N_{\mathrm{eff}}$ model (*nb* stands for *no bound*). For each combination, we report the limits obtained for the two parameterizations of the primordial power spectrum, namely the power-law model (first column) and the polynomial expansion (second column of each pair). Limits are at 95% CL around the mean value of the posterior distribution. For each dataset, in the case of power-law model, the values of $P_{s,i}$ are computed according to Eq. (6.3). From Ref. [26].
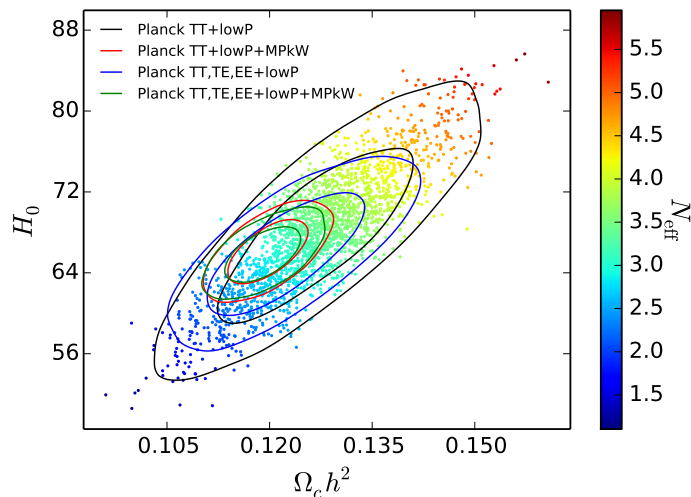
Figure 6.8: 2D constraints at 68% and 95% CL in the $(\Omega_c h^2, H_0)$ plane obtained in the $\Lambda$CDM + $N_{\rm eff}$ model with a PCHIP PPS, for different data combinations. The coloured points are obtained in the same model, from the Planck TT+lowP analysis, and show the correlation with $N_{\rm eff}$. From Ref. [26].

The introduction of $N_{\rm eff}$ as a free parameter does not change significantly the results for the $\Lambda$CDM parameters if a power-law PPS is considered. However, once the freedom in the PPS is introduced, a strong degeneracy between the PCHIP nodes $P_{s,j}$ and $N_{\rm eff}$ appears. Even if the constraints on $N_{\rm eff}$ are loosened for the PCHIP PPS case, all the dataset combinations give constraints on $N_{\rm eff}$ that are compatible with the standard value 3.046 at 95% CL, as we can notice from Fig. 6.6. The mild preference for $N_{\rm eff} > 3.046$ arises mainly as a volume effect in the Bayesian analysis, since the PCHIP PPS parameters can be tuned to reproduce the observed CMB temperature spectrum for a wide range of $N_{\rm eff}$ values. As expected, the degeneracy between the nodes $P_{s,j}$ and $N_{\rm eff}$ shows up at high wavemodes, where the Silk damping effect is dominant, see Fig. 6.7. As a consequence of this correlation, the values preferred for the nodes $P_{s,6}$ to $P_{s,10}$ are slightly larger than the best-fit values of the power-law PPS at the same wavemodes.

The cosmological limits for a number of parameters change as a consequence of the various degeneracies with $N_{\rm eff}$. For example, to compensate the shift of the matter-radiation equality redshift due to the increased radiation energy density, the CDM energy density $\Omega_c h^2$ mean value is slightly shifted and its constraints are weakened. At the same time, the uncertainty on the Hubble parameter $H_0$ is considerably relaxed, because $H_0$ must be also changed accordingly.

It is interesting to note that the introduction of $N_{\rm eff}$ as a free parameter induces a change in the degeneracy between $\Omega_c h^2$ and $H_0$. This effect can be noticed by comparing Fig. 6.4, obtained in the $\Lambda$CDM model, and Fig. 6.8, obtained in the $\Lambda$CDM + $N_{\rm eff}$ model. The reason for which this degeneracy changes is related to the fact that $N_{\rm eff}$ and $\Omega_c h^2$ control the matter-radiation equality redshift. If $N_{\rm eff}$ is freely varying, larger values of this parameter will require a larger matter content $\Omega_c h^2$ to leave unchanged the equality era, and the $H_0$ parameter will move toward larger values. On the other hand, if $N_{\rm eff}$ is fixed to its standard value and $\Omega_c h^2$ is increased, in order to keep unchanged the matter-radiation equality era, a lower value of $H_0$ would be required to compensate the effect.

The results obtained with the inclusion of the full CMB polarization data are shown in Tab. 6.5. The introduction of the polarization data helps in improving the constraints in the models with a PCHIP PPS, since the effects of increasing $N_{\rm eff}$ and changing the PPS are different for the temperature-temperature, the temperature-polarization and the polarization-polarization correlation spectra, as previously discussed in the context of the $\Lambda$CDM model. When the degeneracies are broken, the preferred value of $N_{\rm eff}$ is very close to the standard
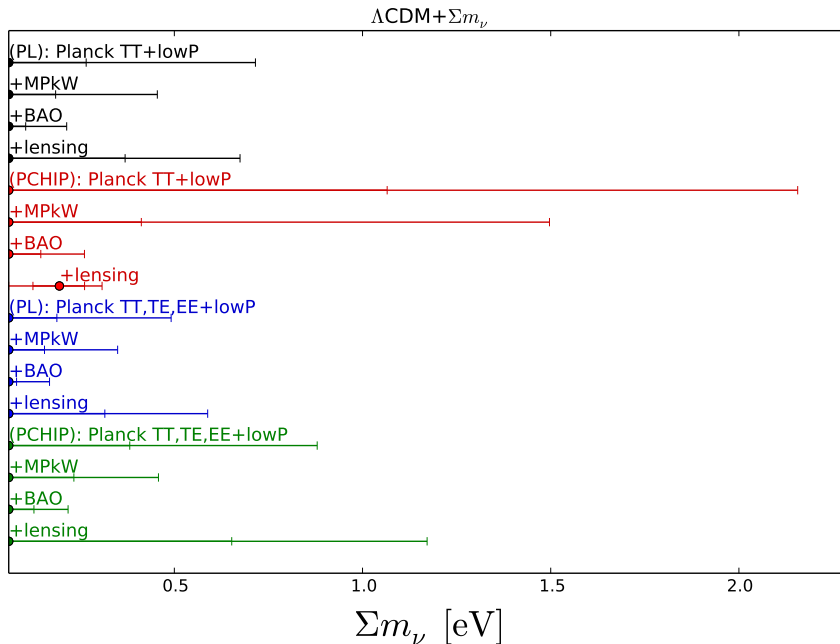
Figure 6.9: As Fig. 6.6 but for the $\Lambda$CDM $+ \Sigma m_\nu$ case. From Ref. [26].

value 3.046. Apparently, the Planck polarization data seem to prefer a value of $N_{\text{eff}}$ slightly smaller than 3.046 for all the datasets except those including the BAO data, but the effect is not statistically significant (see the blue and green points in Fig. 6.6).

As the bounds for $N_{\text{eff}}$ are compatible with 3.046, the $\Lambda$CDM $+ N_{\text{eff}}$ model gives results that are very close to those obtained in the simple $\Lambda$CDM model, but with slightly larger parameter uncertainties, in particular for $H_0$ and $\Omega_c h^2$.

## 6.7 Massive Neutrinos

### 6.7.1 Parameterization

Neutrinos oscillations have robustly established the existence of neutrino masses (see Chapter 4). However, neutrino mixing data only provide information on the squared mass differences and not on the absolute scale of neutrino masses. Cosmology provides an independent tool to test it, as massive neutrinos leave a non negligible imprint in different cosmological observables [362, 411, 441–450]. We recall that the primary effect of varying the neutrino mass scale on the CMB temperature spectrum is related to the early ISW effect (see Subsection 4.4.5). The neutrino transition from the relativistic to the non-relativistic regime affects the decay of the gravitational potentials at the decoupling period, producing an enhancement of the small-scale perturbations, especially near the first acoustic peak.

The baseline scenario we analyze here is an extension of the $\Lambda$CDM model where we assume three active massive neutrino species with degenerate masses. As we did in the previous Section, we will study the $\Lambda$CDM $+ \Sigma m_\nu$ model to test the robustness of the constraints on the neutrino mass scale under the assumption of a free PPS.

### 6.7.2 Results

The 68% and 95% CL bounds on $\Sigma m_\nu$ obtained with different dataset and PPS combinations are summarized in Fig. 6.9. We shall discuss these results in detail below.

Table 6.6 depicts the 95% CL constraints on the sum of the three active neutrino masses arising from Planck TT+lowP CMB data plus other external datasets. Notice that for all the
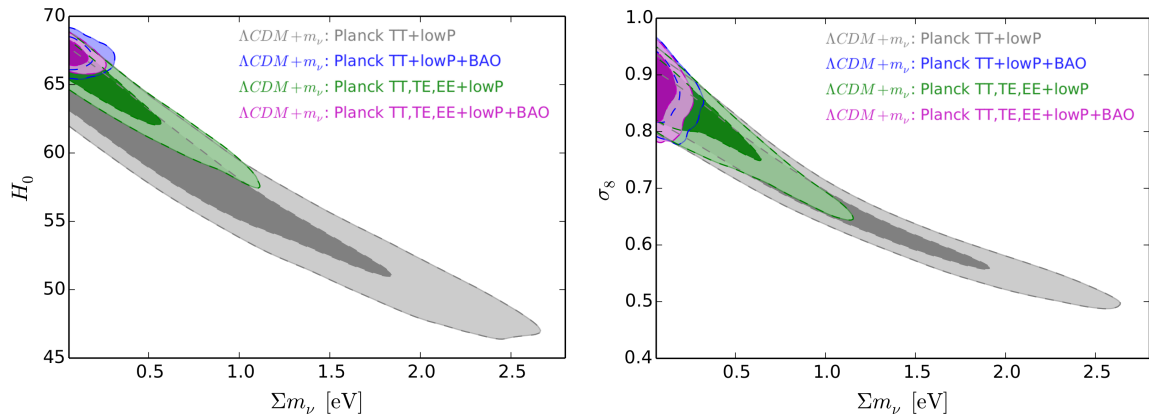
Figure 6.10: 68% and 95% CL allowed regions in the $(\Sigma m_\nu, H_0)$ plane (left panel) and in the $(\Sigma m_\nu, \sigma_8)$ plane (right panel), obtained in the $\Lambda$CDM $+ \Sigma m_\nu$ model within the PCHIP PPS parameterization. From Ref. [26].

data combinations the bounds on neutrino masses are weaker when considering the PCHIP PPS with respect to the power-law PPS case. This loosened bounds are due to the degeneracy between $\Sigma m_\nu$ and the nodes $P_{s,5}$ and $P_{s,6}$, that correspond to the wavenumbers where the contribution of the early ISW effect is located. Therefore, the change induced on these angular scales by a larger neutrino mass could be compensated by increasing $P_{s,5}$ and $P_{s,6}$.

The most stringent constraints on the sum of the three active neutrino masses are obtained when the BAO data are considered. In particular, we have $\Sigma m_\nu < 0.26$ eV ($\Sigma m_\nu < 0.22$ eV) at 95% CL when considering the PCHIP (power-law) PPS parameterization. This is the consequence of the fact that the BAO data strongly constrains the energy densities of the massive species, so that the degeneracy between $\Sigma m_\nu$ and the PPS is broken.

It can be noticed that using the PCHIP PPS parameterization there is a shift not only for the preferred value of $\Sigma m_\nu$, but also for other cosmological parameters, such as the Hubble constant and the clustering parameter $\sigma_8$. This occurs because there exists a strong degeneracy between the neutrino mass and the Hubble constant, as shown in the left panel of Fig. 6.10 and between $\Sigma m_\nu$ and $\sigma_8$, as shown in the right panel of Fig. 6.10. In particular, considering CMB data only, a higher value of $\Sigma m_\nu$ will alter the angular diameter distance to the last scattering surface, change that can be compensated with a smaller value of the Hubble constant $H_0$. The mean values of the clustering parameter $\sigma_8$ are also displaced by $\sim 2\sigma$ (except for the BAO case) toward lower values in the PCHIP PPS approach with respect to those obtained using the power-law PPS, since the free-streaming of a heavier neutrino causes a larger suppression of the perturbations at small scales (see Ref. [51]). The fact that the larger allowed range for $\Sigma m_\nu$ causes a shift in the mean values of $H_0$ and $\sigma_8$ is a simple consequence of volume effects that arise during the Bayesian marginalization.

Table 6.7 presents the constraints on the cosmological parameters from the full CMB data set Planck TT,TE,EE+lowP alone and in combination with the MPkW, BAO and lensing measurements. If one considers the high-$\ell$ polarization measurements, the bounds on the sum of the neutrino masses are larger when using the PCHIP parameterization with respect to the ones obtained with the power-law approach. However, these bounds are more stringent than those obtained using the Planck TT+lowP data only. As we discussed in the previous Sections, the reason for this improvement is due to the fact that the inclusion of the polarization measurements removes many of the degeneracies among the parameters, but in particular between $\Sigma m_\nu$ and the PPS. The constraints on $\Sigma m_\nu$ from all the data combinations and the PPS parameterizations are plotted in Fig. 6.9. Also when the full CMB polarization spectra are included the data combination that gives the most stringent constraints is the one involving BAO datasets, since it provides a 95% CL upper bound $\Sigma m_\nu < 0.22$ eV in the PCHIP PPS case and $\Sigma m_\nu < 0.18$ eV in the power-law PPS case.

## 6.8 Constraints on the Primordial Power Spectrum

From the MCMC analyses presented in the previous sections we obtained constraints on the nodes used to parameterize the `PCHIP` PPS. Using these information, we can obtain a reconstruction of the spectrum shape for the different extensions of the $\Lambda$CDM model. Since the form of the reconstructed PPS is similar for the different models, we discuss now the common features of the `PCHIP` PPS as obtained for the $\Lambda$CDM model.

The results obtained from the dataset combinations that give the most interesting results for the PPS, as for the bounds on the parameters that we reported in Tab. 6.3, are shown: Planck TT+lowP (Fig. 6.11), Planck TT,TE,EE+lowP (Fig. 6.12) and the same plus the MPkW dataset (Fig. 6.13). We also show in Figure 6.14 the results obtained in Ref. [25] from the analyses of the former Planck 2013 spectra, together with the WMAP polarization and the ACT/SPT data at high multipoles. The plotted bands correspond to the constraints reported for the COSMO analysis in Tab. 6.2. In each of these figures we show the marginalized best-fitting reconstruction of the `PCHIP` PPS (solid line), the uncertainty bands at 68%, 95% and 99% CL at different gray-scales and the best-fitting power-law PPS (dotted line) as obtained by the Planck collaboration for the $\Lambda$CDM model [44], as a comparison. The bands are obtained marginalizing over all the values of the PPS separately for each bin in $k$.

Notice that the nodes $P_{s,1}$ and $P_{s,12}$ are badly constrained, due to the fact that these nodes are selected to cover a wide range of wavemodes for computational reasons, but there are no available data to constrain them directly. Also the node $P_{s,11}$ is not very well constrained by the Planck temperature data, as it is possible to see in Fig. 6.11. The bounds on $P_{s,11}$ and $P_{s,12}$ can be improved with the inclusion of the high-multipole polarization data (TE,EE), for which the reconstructed PPS is presented in Fig. 6.12: the improvement is particularly significant for $P_{s,11}$. The inclusion of the MPkW data allows to notably improve the constraints on the last two nodes of the `PCHIP` PPS parameterization, see Fig. 6.13. The impact of the polarization on the nodes at high $k$ is smaller than the one of the matter power spectrum data, since the MPkW dataset provides stronger constraints on the smallest angular scales. The situation is slightly different for the PPS reconstruction presented in Fig. 6.14, for which the tight constraints for $P_{s,11}$ and $P_{s,12}$ arise from the CMB data at high multipoles, provided by the ACT and SPT experiments (see Sec. 3.1).

The bounds on the nodes at small wavemodes ($P_{s,1}$ to $P_{s,4}$) are almost insensitive to the inclusion of additional datasets or to the change in the underlying cosmological model, with only small variations well inside the $1\sigma$ range between the different results. The error bars on the nodes are larger in this part of the spectrum, since it corresponds to low multipoles of the CMB power spectra, where the cosmic variance is larger. In this part of the PPS we have the most evident deviations from the simple power-law PPS. The features are described by the node $P_{s,3}$, for which the value corresponding to the power-law PPS is approximately $2\sigma$ away from the reconstructed result, and by the node $P_{s,4}$, which is mildly discrepant with the power-law value ($1\sigma$ level). These nodes describe the behavior of the CMB temperature spectrum at low-$\ell$, where the observations of the Planck and WMAP experiments show a lack of power at $\ell \simeq 20$ and an excess of power at $\ell \simeq 40$. The detection of these features is in agreement with several previous studies [25, 32, 396–409]. Since this behavior of the CMB spectrum at low multipoles has been reported by analyses of both Planck and WMAP data, it is unlikely that it is the consequence of some instrumental systematics. It is possible that this feature is simply the result of a large statistical fluctuation in a region of the spectrum where cosmic variance is very large. On the other hand, the lack of power at a precise scale can be the signal of some non-standard inflationary mechanism that produced a non standard spectrum for the initial scalar perturbations. Future investigations will possibly clarify these properties of the PPS.

The central part of the reconstructed PPS, from $P_{s,5}$ to $P_{s,10}$, is very well constrained by the data. In this range of wavemodes, no deviations from the power-law PPS are visible, thus confirming the validity of the assumption that the PPS is almost scale-invariant for a wide range of wavemodes. This is also the region where the PPS shape is more sensitive to
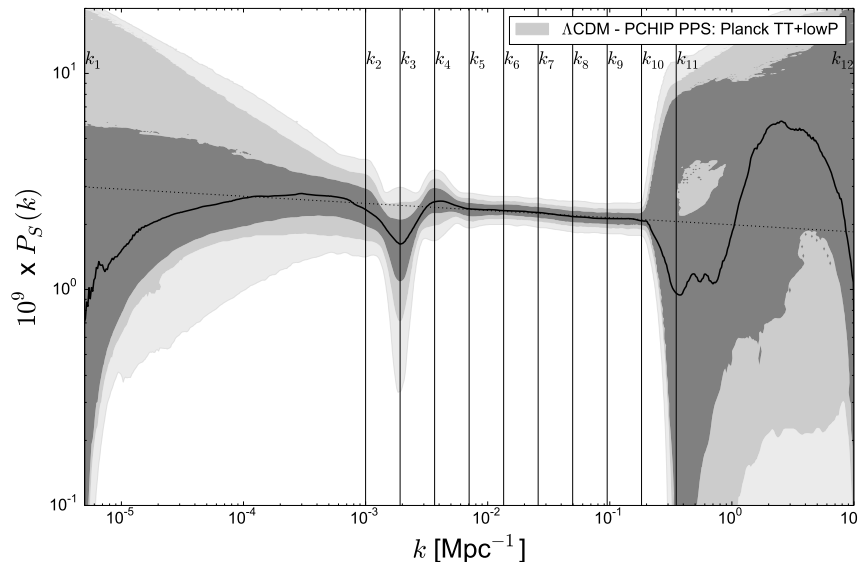
Figure 6.11: Reconstruction of the marginalized best fit `PCHIP` PPS (solid line) with 68%, 95% and 99% confidence bands as obtained in the $\Lambda$CDM model, with the "Planck TT+lowP" dataset. The dotted line represents the power-law PPS corresponding to the Planck best fit [44]. From Ref. [26].

the changes in the $\Lambda$CDM model caused by its extensions. As we can see from the results presented in previous sections, the constraints on the nodes $P_{s,5}$ to $P_{s,10}$ are different for each extension of the $\Lambda$CDM model, in agreement with the results obtained for $\ln[10^{10}A_s]$ and $n_s$ when considering the power-law PPS. In the various tables, when presenting the results on the power-law PPS, we listed the values of the `PCHIP` nodes that would correspond to the best-fitting $A_s$ and $n_s$, to simplify the comparison with the `PCHIP` PPS constraints. These values are calculated using Eq. (6.3). In the range between $k \simeq 0.007$ and $k \simeq 0.2$, the constraints in the `PCHIP` nodes correspond, for most of the cases, to the values expected by the power-law PPS analyses, within their allowed $1\sigma$ range. There are a few exceptions: for example, in the $\Lambda$CDM + $N_{\text{eff}}$ model and with the Planck TT+lowP+BAO dataset, the node $P_{s,10}$ deviates from the expected value corresponding to the power-law PPS by more than $1\sigma$ (see Tab. 6.4). This is a consequence of the large correlation and the large variability range that this dataset allows for $N_{\text{eff}}$. The inclusion of polarization data at high-$\ell$, limiting the range for $N_{\text{eff}}$, does not allow for these deviations from the power-law PPS.

## 6.9 Discussion and Conclusions

The description of the cosmological model may require a non-standard Primordial Power Spectrum (PPS) of scalar perturbations generated during the inflationary phase at the beginning of the Universe. Several analyses have considered the possible deviations from the PPS power-law exploiting both the WMAP and the Planck data measurements of the CMB temperature power spectrum [25, 32, 396–409]. Even if the significance of these deviations is small, it leaves some freedom for the PPS assumed form. Here we test the robustness of the cosmological bounds on several cosmological parameters when the PPS is allowed to have a model-independent shape, that we describe using a `PCHIP` function to interpolate a series of twelve nodes $P_{s,j}$. Our results show that the constraints can significantly change if one considers only the temperature spectrum of the CMB in the data analyses, since the free PPS form can be changed to compensate for the variations in the cosmological parameters. These degeneracies are broken by the inclusion of the polarization spectra measured by Planck. In particular, we show that they are removed due to the inclusion of the temperature-polarization
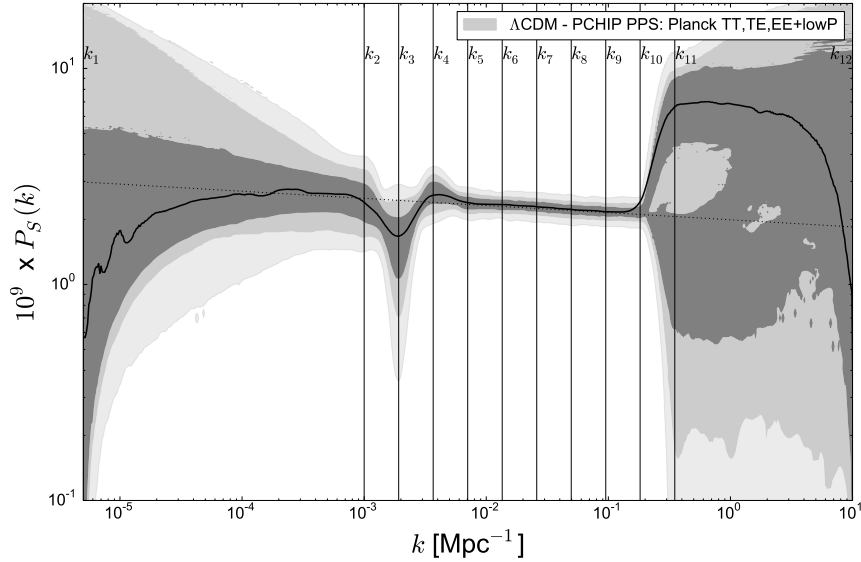
Figure 6.12:    As in Fig. 6.11, but with the "Planck TT,TE,EE+lowP" dataset.    From Ref. [26].
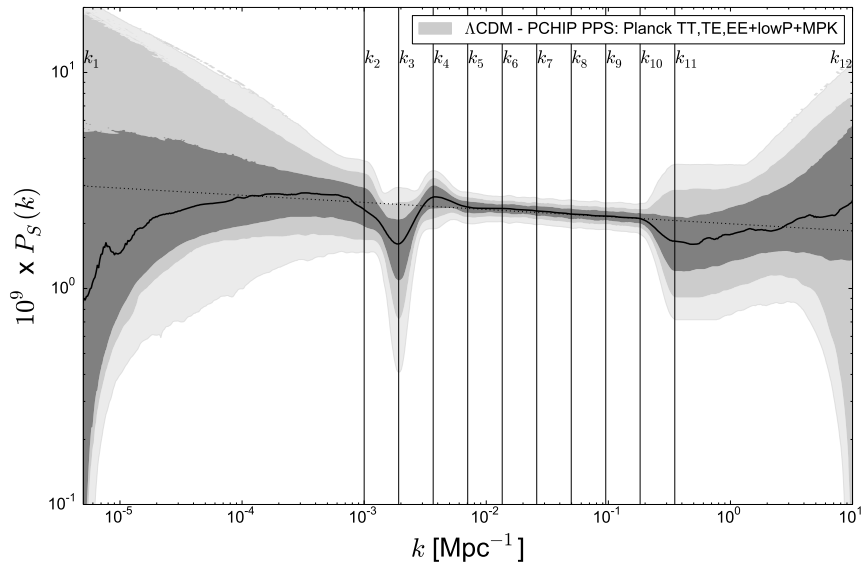


Figure 6.13:    As in Fig. 6.11, but with the "Planck TT,TE,EE+lowP+MPkW" dataset. From Ref. [26].

cross-correlation spectrum. For this reason, we stress here the importance of including several datasets in the analyses, since they are crucial for solving the possible degeneracies between the PPS generated during inflation and the parameters that govern the subsequent evolution, in order to avoid misleading results.

We have explored the impact of a non-canonical PPS in several different extensions of the ΛCDM model, varying the effective number of relativistic species and the masses of the active and the light sterile neutrinos.

Using the 2013 Planck data, we found that the freedom of the form of the PPS does not affect significantly the fitted values of the parameters in the ΛCDM model, while the results concerning the existence of a sterile neutrino in the early Universe can change drastically. If we do not impose any prior on the sterile neutrino mass $m_s$ from the results of short-baseline oscillation experiments (see Chapter 4), a larger value for the sterile neutrino contribution
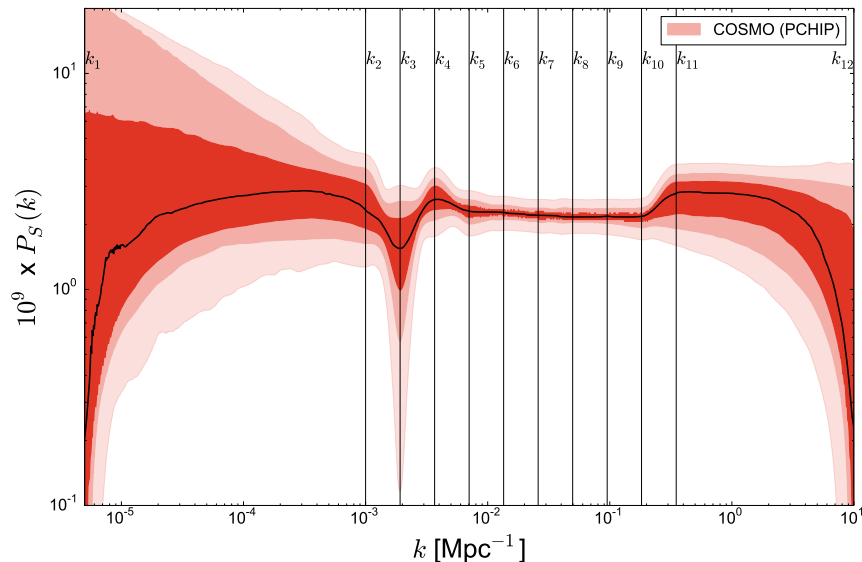
Figure 6.14: Allowed $1\sigma$, $2\sigma$ and $3\sigma$ bands of the `PCHIP` PPS obtained in the analyses without (COSMO) the SBL prior. The bands have been obtained by marginalizing the posterior distribution for each value of the wavenumber $k$ in a fine grid. The black curves correspond to the maximum of the posterior distribution for each value of $k$. From Ref. [25].

$\Delta N_{\rm eff}$ to the effective number of relativistic degrees of freedom before photon decoupling is preferred in the `PCHIP` PPS parameterization with respect to the standard power-law parameterization. The marginalized best fit of $\Delta N_{\rm eff}$ is moved towards one, which corresponds to a fully thermalized sterile neutrino. This shift corresponds to a tightening of the cosmological preferred values for $m_s$.

In the analysis with a prior on $m_s$ obtained from the fit of short-baseline oscillation experiments [199], the freedom of the `PCHIP` PPS affects only the bound on $\Delta N_{\rm eff}$, because the allowed range of $m_s$ is strongly constrained by the SBL prior. We found that a free form of the PPS allows the existence in the early Universe of a fully thermalized sterile neutrino with a mass of about 1 eV [307, 308]. This possibility is quite disfavored by the analysis of cosmological data with a power-law PPS [22, 23, 303, 311, 332]. Hence, the freedom of the PPS may allow us to reconcile the cosmological data with short-baseline neutrino oscillations without the need of an additional mechanism which suppresses the thermalization of the sterile neutrino [310, 344, 355–357, 365–371, 386, 387]. The updated analyses that include the full temperature and polarization data released in 2015 by Planck, however, forbid this reconciliation, since the CMB polarization at high multipoles breaks the degeneracies between $N_{\rm eff}$ and the `PCHIP` nodes.

We studied then the degeneracies between the PPS shape and the different cosmological parameters, separately. We considered the most recent CMB data from the 2015 release of the Planck collaboration.

Concerning the effective number of degrees of freedom $N_{\rm eff}$, we find that the results are in good agreement with the standard value of 3.046, if one assumes the standard power-law PPS. Increasing $N_{\rm eff}$ has the main effect of increasing the Silk damping of the CMB spectrum at small scales and therefore it is easy change the PPS shape at that scales to compensate the increased damping. This results in a strong degeneracy between the relevant `PCHIP` PPS nodes and $N_{\rm eff}$. As a consequence of volume effects in the Bayesian analyses, the constraints on $N_{\rm eff}$ are significantly loosened. For some data combinations we obtain $N_{\rm eff} \simeq 4.8$ allowed at 95% CL. However, the $N_{\rm eff}$ effects can not be compensated by the `PCHIP` nodes in the polarization spectra, in particular in the case of the TE cross-correlation. This is the reason for which the inclusion of CMB polarization measurements in the analyses allows to break the degeneracies and to restore the $N_{\rm eff}$ bounds very close to 3.046 for all the data combinations,

with $N_{\text{eff}} > 3.5$ excluded at more than 95% CL for all the datasets.

In the minimal three active massive neutrinos scenario, the constraints on $\Sigma m_\nu$ from the free PPS scenario are relaxed with respect to the PPS power-law ones. This is due to the degeneracy between $\Sigma m_\nu$ and the nodes $P_{s,5}$ and $P_{s,6}$, that correspond to the scales at which the early Integrated Sachs-Wolfe effect contributes to the CMB spectrum. Also in this case these degeneracies are broken by the inclusion of additional datasets, as the CMB polarization at high multipoles and the BAO measurements. The tightest limits we find is $\Sigma m_\nu < 0.18$ eV (0.22 eV) at 95% CL from the combination of Planck TT,TE,EE+lowP+BAO data, when considering a power-law (`PCHIP`) PPS.

Even if we presented only the results in the $\Lambda$CDM + $N_{\text{eff}}$ and $\Lambda$CDM + $\Sigma m_\nu$ models, similar constraints would be obtained if the neutrino parameters were varied together. The degeneracies with the PPS, in fact, are related to different scales. The results in the $\Lambda$CDM + $N_{\text{eff}}$ + $\Sigma m_\nu$ and $\Lambda$CDM + $N_{\text{eff}}$ + $\Sigma m_\nu$ + $m_s^{\text{eff}}$ models are reported in Ref. [26].

From the MCMC analyses we have also the opportunity to reconstruct and study the shape of the PPS. We find that the reconstructed spectrum is perfectly described by a power-law in the region between $k \simeq 0.007\,\text{Mpc}^{-1}$ and $k \simeq 0.2\,\text{Mpc}^{-1}$, but there are indications that a small dip (at $k \simeq 0.002\,\text{Mpc}^{-1}$) and a statistically less relevant bump (at $k \simeq 0.0035\,\text{Mpc}^{-1}$) appear at large scales. These features are found both considering the WMAP and the Planck CMB spectra. If confirmed by future surveys, they will indicate that the simplest inflationary model is not complete and some new physical mechanism during inflation introduces a scale dependency in the PPS.

In summary, we have shown that dangerous degeneracies among the parameters of the $\Lambda$CDM model (and its possible extensions) and the PPS shape arise when considering CMB temperature power spectrum measurements only. Fortunately, these degeneracies disappear with the inclusion of the CMB polarization data at high multipoles. This is due to the fact that all these cosmological parameters influence the TT, TE and EE spectra in different ways. This confirms the robustness of both the $\Lambda$CDM model and the simplest inflationary models, that predict a power-law PPS that successfully explains the observations at small scales. The large scale fluctuations of the CMB spectrum, however, seem to point towards something new in the scenarios that describe inflation. It must be clarified whether these features are indicating a more complicated inflationary mechanism or they are instead simple statistical fluctuations of the CMB temperature anisotropies.

| Parameter | Planck TT,TE,EE+lowP | | Planck TT,TE,EE+lowP +MPkW | | Planck TT,TE,EE+lowP +BAO | | Planck TT,TE,EE+lowP +lensing | |
|---|---|---|---|---|---|---|---|---|
| $100\Omega_b h^2$ | $2.220 \pm 0.048$ | $2.206^{+0.054}_{-0.055}$ | $2.214^{+0.047}_{-0.046}$ | $2.203 \pm 0.049$ | $2.229 \pm 0.038$ | $2.226^{+0.041}_{-0.040}$ | $2.216^{+0.045}_{-0.046}$ | $2.204^{+0.055}_{-0.053}$ |
| $\Omega_c h^2$ | $0.1191^{+0.0062}_{-0.0061}$ | $0.1197^{+0.0072}_{-0.0071}$ | $0.1186^{+0.0062}_{-0.0061}$ | $0.1191^{+0.0070}_{-0.0067}$ | $0.1192^{+0.0060}_{-0.0059}$ | $0.1203^{+0.0067}_{-0.0068}$ | $0.1178^{+0.0058}_{-0.0057}$ | $0.1184^{+0.0069}_{-0.0067}$ |
| $100\theta$ | $1.0409 \pm 0.0009$ | $1.0408^{+0.0010}_{-0.0009}$ | $1.0409 \pm 0.0009$ | $1.0409 \pm 0.0009$ | $1.0409^{+0.0009}_{-0.0008}$ | $1.0407 \pm 0.0009$ | $1.0410^{+0.0009}_{-0.0008}$ | $1.0410^{+0.0010}_{-0.0009}$ |
| $\tau$ | $0.077 \pm 0.035$ | $0.081^{+0.040}_{-0.039}$ | $0.073^{+0.036}_{-0.035}$ | $0.080^{+0.039}_{-0.037}$ | $0.082 \pm 0.032$ | $0.087 \pm 0.040$ | $0.060 \pm 0.028$ | $0.064^{+0.034}_{-0.032}$ |
| $N_{\rm eff}$ | $2.99^{+0.41}_{-0.39}$ | $2.96^{+0.41}_{-0.48}$ | $2.95^{+0.41}_{-0.39}$ | $2.91^{+0.46}_{-0.43}$ | $3.04 \pm 0.35$ | $3.09 \pm 0.40$ | $2.94 \pm 0.38$ | $2.92^{+0.48}_{-0.46}$ |
| $n_S$ | $0.962 \pm 0.019$ | – | $0.960 \pm 0.019$ | – | $0.966 \pm 0.015$ | – | $0.961^{+0.019}_{-0.018}$ | – |
| $\ln[10^{10}A_s]$ | $3.088 \pm 0.074$ | – | $3.078^{+0.075}_{-0.072}$ | – | $3.098^{+0.067}_{-0.069}$ | – | $3.049^{+0.058}_{-0.056}$ | – |
| $H_0\,[{\rm km\,s^{-1}\,Mpc^{-1}}]$ | $66.8^{+3.2}_{-3.1}$ | $66.1^{+3.9}_{-3.8}$ | $66.5 \pm 3.1$ | $65.8^{+3.6}_{-3.4}$ | $67.5 \pm 2.4$ | $67.6^{+2.6}_{-2.5}$ | $66.7 \pm 3.0$ | $66.2^{+3.9}_{-3.7}$ |
| $\sigma_8$ | $0.83^{+0.04}_{-0.03}$ | $0.87 \pm 0.07$ | $0.82^{+0.04}_{-0.03}$ | $0.83 \pm 0.04$ | $0.83 \pm 0.03$ | $0.88^{+0.06}_{-0.08}$ | $0.81^{+0.03}_{-0.02}$ | $0.86 \pm 0.06$ |
| $P_{s,1}$ | $\equiv 1.415$ | $< 7.62$ | $\equiv 1.427$ | $< 7.79$ | $\equiv 1.377$ | $< 7.27$ | $\equiv 1.373$ | $< 8.15$ |
| $P_{s,2}$ | $\equiv 1.157$ | $1.14^{+0.38}_{-0.35}$ | $\equiv 1.154$ | $1.14^{+0.38}_{-0.35}$ | $\equiv 1.150$ | $1.14^{+0.38}_{-0.36}$ | $\equiv 1.117$ | $1.14^{+0.38}_{-0.35}$ |
| $P_{s,3}$ | $\equiv 1.128$ | $0.72^{+0.37}_{-0.34}$ | $\equiv 1.125$ | $0.72^{+0.37}_{-0.35}$ | $\equiv 1.125$ | $0.73^{+0.38}_{-0.37}$ | $\equiv 1.089$ | $0.68^{+0.36}_{-0.34}$ |
| $P_{s,4}$ | $\equiv 1.101$ | $1.22 \pm 0.22$ | $\equiv 1.096$ | $1.22 \pm 0.22$ | $\equiv 1.100$ | $1.23^{+0.22}_{-0.21}$ | $\equiv 1.062$ | $1.20 \pm 0.21$ |
| $P_{s,5}$ | $\equiv 1.074$ | $1.08 \pm 0.10$ | $\equiv 1.068$ | $1.08^{+0.10}_{-0.09}$ | $\equiv 1.076$ | $1.09^{+0.11}_{-0.10}$ | $\equiv 1.035$ | $1.05^{+0.09}_{-0.08}$ |
| $P_{s,6}$ | $\equiv 1.048$ | $1.06 \pm 0.08$ | $\equiv 1.040$ | $1.06^{+0.08}_{-0.07}$ | $\equiv 1.053$ | $1.07^{+0.09}_{-0.08}$ | $\equiv 1.009$ | $1.03^{+0.07}_{-0.06}$ |
| $P_{s,7}$ | $\equiv 1.022$ | $1.04 \pm 0.08$ | $\equiv 1.013$ | $1.04^{+0.08}_{-0.07}$ | $\equiv 1.030$ | $1.05^{+0.09}_{-0.08}$ | $\equiv 0.984$ | $1.00 \pm 0.06$ |
| $P_{s,8}$ | $\equiv 0.997$ | $1.00^{+0.09}_{-0.08}$ | $\equiv 0.987$ | $1.00^{+0.08}_{-0.08}$ | $\equiv 1.007$ | $1.02^{+0.09}_{-0.08}$ | $\equiv 0.959$ | $0.97 \pm 0.07$ |
| $P_{s,9}$ | $\equiv 0.973$ | $0.98^{+0.09}_{-0.08}$ | $\equiv 0.962$ | $0.98^{+0.09}_{-0.08}$ | $\equiv 0.985$ | $1.00^{+0.09}_{-0.08}$ | $\equiv 0.935$ | $0.95 \pm 0.07$ |
| $P_{s,10}$ | $\equiv 0.949$ | $0.97^{+0.11}_{-0.10}$ | $\equiv 0.937$ | $0.94 \pm 0.10$ | $\equiv 0.964$ | $1.00^{+0.11}_{-0.09}$ | $\equiv 0.912$ | $0.94^{+0.10}_{-0.09}$ |
| $P_{s,11}$ | $\equiv 0.926$ | $< 4.30$ | $\equiv 0.913$ | $0.77^{+0.42}_{-0.37}$ | $\equiv 0.943$ | $2.60^{+2.01}_{-2.52}$ | $\equiv 0.889$ | $2.57^{+1.96}_{-2.17}$ |
| $P_{s,12}$ | $\equiv 0.815$ | nb | $\equiv 0.799$ | $< 3.32$ | $\equiv 0.841$ | nb | $\equiv 0.780$ | nb |

Table 6.5: As Tab. 6.4, but using the Planck TT,TE,EE+lowP dataset. From Ref. [26].

| Parameter | Planck TT+lowP | | Planck TT+lowP+MPkW | | Planck TT+lowP+BAO | | Planck TT+lowP+lensing | |
|---|---|---|---|---|---|---|---|---|
| $\Omega_b h^2$ | $2.214^{+0.054}_{-0.052}$ | $2.127^{+0.097}_{-0.100}$ | $2.217^{+0.054}_{-0.047}$ | $2.161^{+0.089}_{-0.103}$ | $2.228^{+0.041}_{-0.039}$ | $2.219^{+0.063}_{-0.061}$ | $2.210^{+0.048}_{-0.057}$ | $2.136^{+0.081}_{-0.079}$ |
| $\Omega_c h^2$ | $0.1202^{+0.0044}_{-0.0047}$ | $0.1253^{+0.0067}_{-0.0064}$ | $0.1200^{+0.0043}_{-0.0039}$ | $0.1239^{+0.0072}_{-0.0067}$ | $0.1188^{+0.0028}_{-0.0029}$ | $0.1186^{+0.0032}_{-0.0033}$ | $0.1197^{+0.0041}_{-0.0042}$ | $0.1243^{+0.0060}_{-0.0059}$ |
| $100\theta$ | $1.0407^{+0.0010}_{-0.0011}$ | $1.0398 \pm 0.0014$ | $1.041 \pm 0.001$ | $1.0401^{+0.0013}_{-0.0015}$ | $1.0410^{+0.0009}_{-0.0008}$ | $1.0410 \pm 0.0008$ | $1.0408^{+0.0010}_{-0.0009}$ | $1.0399^{+0.0012}_{-0.0011}$ |
| $\tau$ | $0.080 \pm 0.038$ | $0.075^{+0.048}_{-0.044}$ | $0.077^{+0.038}_{-0.037}$ | $0.077^{+0.050}_{-0.043}$ | $0.082^{+0.038}_{-0.037}$ | $0.093^{+0.050}_{-0.047}$ | $0.072^{+0.034}_{-0.032}$ | $0.071^{+0.040}_{-0.037}$ |
| $\Sigma m_\nu[eV]$ | $< 0.75$ | $< 2.16$ | $< 0.46$ | $< 1.15$ | $< 0.22$ | $< 0.26$ | $< 0.63$ | $< 1.64$ |
| $n_S$ | $0.964^{+0.014}_{-0.013}$ | – | $0964 \pm 0.012$ | – | $0.968 \pm 0.009$ | – | $0.963 \pm 0.014$ | – |
| $\ln[10^{10}A_s]$ | $3.095^{+0.074}_{-0.073}$ | – | $3.089^{+0.074}_{-0.070}$ | – | $3.096 \pm 0.073$ | – | $3.077^{+0.061}_{-0.059}$ | – |
| $H_0[\ {\rm Km\ s^{-1}\ Mpc^{-1}}]$ | $65.5^{+5.9}_{-4.4}$ | $58.4^{+8.8}_{-10.4}$ | $66.3^{+3.2}_{-3.8}$ | $62.4^{+6.3}_{-10.9}$ | $67.6 \pm 1.3$ | $67.1^{+1.3}_{-1.4}$ | $65.2^{+3.5}_{-3.8}$ | $58.7^{+7.1}_{-6.8}$ |
| $\sigma_8$ | $0.79^{+0.11}_{-0.08}$ | $0.72^{+0.18}_{-0.20}$ | $0.81^{+0.06}_{-0.07}$ | $0.77^{+0.10}_{-0.19}$ | $0.83 \pm 0.04$ | $0.87^{+0.07}_{-0.07}$ | $0.77^{+0.05}_{-0.06}$ | $0.71^{+0.14}_{-0.14}$ |
| $P_{s,1}$ | $\equiv 1.399$ | $< 8.23$ | $\equiv 1.390$ | $< 7.81$ | $\equiv 1.349$ | $< 8.08$ | $\equiv 1.386$ | $< 7.74$ |
| $P_{s,2}$ | $\equiv 1.156$ | $1.20^{+0.40}_{-0.36}$ | $\equiv 1.149$ | $1.17^{+0.38}_{-0.36}$ | $\equiv 1.139$ | $1.11^{+0.38}_{-0.34}$ | $\equiv 1.140$ | $1.21^{+0.37}_{-0.36}$ |
| $P_{s,3}$ | $\equiv 1.129$ | $0.74^{+0.38}_{-0.37}$ | $\equiv 1.122$ | $0.74^{+0.38}_{-0.37}$ | $\equiv 1.116$ | $0.77^{+0.41}_{-0.40}$ | $\equiv 1.113$ | $0.73 \pm 0.39$ |
| $P_{s,4}$ | $\equiv 1.103$ | $1.22^{+0.28}_{-0.26}$ | $\equiv 1.096$ | $1.20 \pm 0.26$ | $\equiv 1.093$ | $1.21 \pm 0.26$ | $\equiv 1.086$ | $1.23 \pm 0.26$ |
| $P_{s,5}$ | $\equiv 1.077$ | $1.13^{+0.17}_{-0.15}$ | $\equiv 1.071$ | $1.09 \pm 0.13$ | $\equiv 1.070$ | $1.08^{+0.13}_{-0.12}$ | $\equiv 1.060$ | $1.11 \pm 0.12$ |
| $P_{s,6}$ | $\equiv 1.052$ | $1.109^{+0.104}_{-0.097}$ | $\equiv 1.046$ | $1.080^{+0.090}_{-0.087}$ | $\equiv 1.048$ | $1.077^{+0.104}_{-0.100}$ | $\equiv 1.035$ | $1.076^{+0.075}_{-0.073}$ |
| $P_{s,7}$ | $\equiv 1.028$ | $1.049^{+0.093}_{-0.087}$ | $\equiv 1.022$ | $1.044^{+0.091}_{-0.085}$ | $\equiv 1.026$ | $1.054^{+0.100}_{-0.093}$ | $\equiv 1.010$ | $1.034^{+0.069}_{-0.064}$ |
| $P_{s,8}$ | $\equiv 1.004$ | $0.998^{+0.096}_{-0.085}$ | $\equiv 0.998$ | $1.002^{+0.098}_{-0.089}$ | $\equiv 1.005$ | $1.026^{+0.105}_{-0.100}$ | $\equiv 0.986$ | $0.988^{+0.076}_{-0.069}$ |
| $P_{s,9}$ | $\equiv 0.981$ | $0.973^{+0.097}_{-0.084}$ | $\equiv 0.975$ | $0.977^{+0.098}_{-0.089}$ | $\equiv 0.984$ | $1.011^{+0.102}_{-0.097}$ | $\equiv 0.963$ | $0.966^{+0.077}_{-0.069}$ |
| $P_{s,10}$ | $\equiv 0.958$ | $0.966^{+0.098}_{-0.095}$ | $\equiv 0.953$ | $0.956^{+0.097}_{-0.089}$ | $\equiv 0.964$ | $1.005^{+0.106}_{-0.096}$ | $\equiv 0.940$ | $0.968^{+0.085}_{-0.077}$ |
| $P_{s,11}$ | $\equiv 0.936$ | $2.03^{+1.91}_{-2.02}$ | $\equiv 0.930$ | $0.97^{+1.77}_{-0.75}$ | $\equiv 0.944$ | $2.74^{+2.07}_{-2.69}$ | $\equiv 0.918$ | $2.74^{+1.53}_{-2.15}$ |
| $P_{s,12}$ | $\equiv 0.830$ | nb | $\equiv 0.825$ | $< 3.89$ | $\equiv 0.848$ | nb | $\equiv 0.811$ | nb |

Table 6.6: As Tab. 6.4, but for the $\Lambda$CDM $+ \Sigma m_\nu$ model. From Ref. [26].

| Parameter | Planck TT,TE,EE+lowP | | Planck TT,TE,EE+lowP +MPkW | | Planck TT,TE,EE+lowP +BAO | | Planck TT,TE,EE+lowP +lensing | |
|---|---|---|---|---|---|---|---|---|
| $\Omega_b h^2$ | $2.221^{+0.032}_{-0.034}$ | $2.2080^{+0.039}_{-0.040}$ | $2.223^{+0.028}_{-0.027}$ | $2.209^{+0.037}_{-0.038}$ | $2.223 \pm 0.027$ | $2.226 \pm 0.033$ | $2.215 \pm 0.033$ | $2.203 \pm 0.041$ |
| $\Omega_c h^2$ | $0.1200^{+0.0031}_{-0.0030}$ | $0.1212^{+0.0035}_{-0.0034}$ | $0.1199^{+0.0028}_{-0.0027}$ | $0.1212^{+0.0035}_{-0.0033}$ | $0.1192 \pm 0.0023$ | $0.1191^{+0.0024}_{-0.0025}$ | $0.1101 \pm 0.0030$ | $0.1207^{+0.0033}_{-0.0035}$ |
| $100\theta$ | $1.0407 \pm 0.0007$ | $1.0405 \pm -0.0007$ | $1.0407 \pm 0.0007$ | $1.0406 \pm -0.0007$ | $1.0408 \pm 0.0006$ | $1.0408 \pm -0.0007$ | $1.0406 \pm 0.0007$ | $1.0405 \pm -0.0007$ |
| $\tau$ | $0.081^{+0.033}_{-0.034}$ | $0.085^{+0.042}_{-0.040}$ | $0.080 \pm 0.034$ | $0.088 \pm 0.037$ | $0.083^{+0.033}_{-0.032}$ | $0.088^{+0.045}_{-0.040}$ | $0.076^{+0.033}_{-0.032}$ | $0.082 \pm 0.035$ |
| $\Sigma m_\nu[eV]$ | $< 0.50$ | $< 0.88$ | $< 0.35$ | $< 0.46$ | $< 0.18$ | $< 0.22$ | $< 0.63$ | $< 1.17$ |
| $n_S$ | $0.97 \pm 0.01$ | – | $0.964 \pm 0.009$ | – | $0.966 \pm 0.008$ | – | $0.963 \pm 0.009$ | – |
| $\ln[10^{10}A_s]$ | $3.098^{+0.064}_{-0.066}$ | – | $3.095^{+0.065}_{-0.066}$ | – | $3.100^{+0.063}_{-0.064}$ | – | $3.086^{+0.063}_{-0.061}$ | – |
| $H_0[\ {\rm Km\ s^{-1}\ Mpc^{-1}}]$ | $66.3^{+2.9}_{-3.0}$ | $64.3^{+3.9}_{-5.0}$ | $66.7^{+2.3}_{-2.7}$ | $64.4^{+2.1}_{-3.1}$ | $67.5^{+1.1}_{-1.2}$ | $67.1^{+1.3}_{-1.2}$ | $65.0^{+3.3}_{-3.8}$ | $62.8^{+5.1}_{-5.6}$ |
| $\sigma_8$ | $0.81^{+0.06}_{-0.08}$ | $0.82^{+0.11}_{-0.14}$ | $0.82^{+0.05}_{-0.06}$ | $0.81^{+0.05}_{-0.06}$ | $0.83 \pm 0.03$ | $0.87^{+0.07}_{-0.08}$ | $0.78^{+0.05}_{-0.06}$ | $0.71^{+0.12}_{-0.13}$ |
| $P_{s,1}$ | $\equiv 1.405$ | $< 7.52$ | $\equiv 1.399$ | $< 7.43$ | $\equiv 1.380$ | $< 7.59$ | $\equiv 1.399$ | $< 7.91$ |
| $P_{s,2}$ | $\equiv 1.160$ | $1.16^{+0.37}_{-0.35}$ | $\equiv 1.156$ | $1.15^{+0.40}_{-0.36}$ | $\equiv 1.153$ | $1.13^{+0.39}_{-0.36}$ | $\equiv 1.150$ | $1.18^{+0.38}_{-0.36}$ |
| $P_{s,3}$ | $\equiv 1.133$ | $0.73^{+0.39}_{-0.39}$ | $\equiv 1.129$ | $0.73^{+0.39}_{-0.38}$ | $\equiv 1.127$ | $0.73^{+0.39}_{-0.37}$ | $\equiv 1.123$ | $0.73^{+0.37}_{-0.35}$ |
| $P_{s,4}$ | $\equiv 1.107$ | $1.24^{+0.23}_{-0.22}$ | $\equiv 1.103$ | $1.23 \pm 0.23$ | $\equiv 1.103$ | $1.23^{+0.23}_{-0.22}$ | $\equiv 1.096$ | $1.24 \pm 0.23$ |
| $P_{s,5}$ | $\equiv 1.081$ | $1.10 \pm 0.11$ | $\equiv 1.077$ | $1.10 \pm 0.10$ | $\equiv 1.079$ | $1.09^{+0.11}_{-0.10}$ | $\equiv 1.070$ | $1.09 \pm 0.11$ |
| $P_{s,6}$ | $\equiv 1.056$ | $1.073^{+0.091}_{-0.085}$ | $\equiv 1.052$ | $1.079^{+0.078}_{-0.073}$ | $\equiv 1.055$ | $1.069^{+0.093}_{-0.085}$ | $\equiv 1.044$ | $1.065^{+0.076}_{-0.072}$ |
| $P_{s,7}$ | $\equiv 1.031$ | $1.050^{+0.086}_{-0.087}$ | $\equiv 1.028$ | $1.055^{+0.077}_{-0.072}$ | $\equiv 1.032$ | $1.046^{+0.092}_{-0.083}$ | $\equiv 1.019$ | $1.039^{+0.069}_{-0.068}$ |
| $P_{s,8}$ | $\equiv 1.007$ | $1.016 \pm 0.084$ | $\equiv 1.004$ | $1.021^{+0.077}_{-0.073}$ | $\equiv 1.009$ | $1.019^{+0.087}_{-0.088}$ | $\equiv 0.995$ | $1.007^{+0.070}_{-0.072}$ |
| $P_{s,9}$ | $\equiv 0.984$ | $0.996^{+0.082}_{-0.081}$ | $\equiv 0.981$ | $0.998^{+0.075}_{-0.071}$ | $\equiv 0.987$ | $1.003^{+0.083}_{-0.079}$ | $\equiv 0.972$ | $0.988^{+0.068}_{-0.070}$ |
| $P_{s,10}$ | $\equiv 0.961$ | $1.00^{+0.09}_{-0.09}$ | $\equiv 0.958$ | $0.97^{+0.9}_{-0.08}$ | $\equiv 0.966$ | $1.00^{+0.10}_{-0.09}$ | $\equiv 0.948$ | $0.98^{+0.08}_{-0.07}$ |
| $P_{s,11}$ | $\equiv 0.938$ | $2.77^{+1.88}_{-2.63}$ | $\equiv 0.936$ | $0.82^{+0.56}_{-0.45}$ | $\equiv 0.944$ | $2.79^{+2.02}_{-2.72}$ | $\equiv 0.926$ | $3.015^{+1.51}_{-2.14}$ |
| $P_{s,12}$ | $\equiv 0.831$ | nb | $\equiv 0.830$ | $< 3.20$ | $\equiv 0.843$ | nb | $\equiv 0.818$ | nb |

Table 6.7: As Tab. 6.5, but for the $\Lambda$CDM $+ \Sigma m_\nu$ model. From Ref. [26].

# Chapter 7

# Thermal Axion Properties

*This Chapter is based on Refs. [26, 32].*

In the previous Chapters we discussed mainly the properties of active and sterile neutrinos. Among the possible candidates of hot dark matter, however, other particles can be listed. In this Chapter we present the case of the thermal axions, which are introduced in Section 7.1. In the following Section 7.2 we present the cosmological model and the data that we consider in our analyses. The results are presented in Sections 7.3 for the axion mass alone, and in Section 7.4 for the joint constraints on the active neutrino and thermal axion masses.

## 7.1   Introduction

The axion field is the solution proposed by Peccei and Quinn [27, 28, 451, 452] to solve the strong CP problem in Quantum ChromoDynamics, by adding a new global Peccei-Quinn symmetry $U(1)_{PQ}$ that, when spontaneously broken at an energy scale $f_a$, generates a Pseudo-Nambu-Goldstone boson, the axion particle. Non-thermal axions, as those produced by the misalignment mechanism, while being a negligible hot dark matter candidate, may constitute a fraction or the total cold dark matter component of the Universe. We do not explore such a possibility here. Thermal axions [29–31], instead, affect the cosmological observables in a very similar way to that induced by the presence of neutrino masses and/or extra sterile neutrino species. Massive thermal axions as hot relics affect large scale structures, since they only cluster at scales larger than their free-streaming scale when they become non-relativistic, suppressing therefore structure formation at small scales. Concerning the Cosmic Microwave Background (CMB) physics, an axion mass leads to a signature in the CMB photon temperature anisotropies via the early integrated Sachs-Wolfe effect. In addition, extra light species as thermal axions contribute to the dark radiation content of the Universe, or, in other words, lead to an increase of the effective number of relativistic degrees of freedom $N_{\mathrm{eff}}$, defined in Eq. (4.43). The extra contribution to $N_{\mathrm{eff}}$ arising from thermal axions can modify both the CMB anisotropies (via Silk damping) and the primordial abundances of light elements predicted by Big Bang Nucleosynthesis. The former cosmological signatures of thermal axions have been extensively exploited in the literature to derive bounds on the thermal axion mass, see Refs. [362, 453–456].

The most relevant process for the axion thermalization purpose is the interaction with the pion [30]:

$$\pi + \pi \rightarrow \pi + a. \tag{7.1}$$

Assuming this process for the interaction, the axion coupling constant $f_a$ can be related to the axion mass by the following relation [3]:

$$m_a = \frac{f_\pi m_\pi}{f_a} \frac{\sqrt{R}}{1 + R} = 0.6 \text{ eV } \frac{10^7 \text{ GeV}}{f_a} \, , \tag{7.2}$$

where $m_\pi = 135$ MeV is the pion mass, $R = 0.56$ is the up-to-down quark masses ratio, and $f_\pi = 92$ MeV is the pion decay constant. To consider other values of $R$ in the range $0.35 - 0.60$ [3] does not affect in a significant way this relationship [457].

Axions decouple from the primordial plasma at a temperature $T_D$, when the thermally averaged interaction rate $\Gamma(T)$ of the interaction (7.1), falls below the expansion rate of the Universe $H(T)$. This decoupling process is known as the freeze out condition for a thermal relic, and is given by:

$$\Gamma(T_D) = H(T_D) \ , \tag{7.3}$$

where [3]

$$\Gamma = \frac{3}{1024\pi^5} \frac{1}{f_a^2 f_\pi^2} C_{a\pi}^2 I_a \ . \tag{7.4}$$

In this formula the axion-pion coupling constant is $C_{a\pi} = (1-R)/[3(1+R)]$ [30]. The integral $I_a$ can be expressed in the following way [30]:

$$I_a = n_a^{-1} T^8 \int dx_1 dx_2 \frac{x_1^2 x_2^2}{y_1 y_2} f(y_1) f(y_2) \int_{-1}^{1} d\omega \frac{(s - m_\pi^2)^3 (5s - 2m_\pi^2)}{s^2 T^4} \ , \tag{7.5}$$

with $n_a = (\zeta_3/\pi^2) T^3$ the number density for axions in thermal equilibrium and the function $f(y) = 1/(e^y - 1)$ the pion thermal distribution. Moreover, we have three different kinematical variables, $x_i = |\vec{p}_i|/T$, $y_i = E_i/T$ $(i = 1, 2)$ and $s = 2(m_\pi^2 + T^2(y_1 y_2 - x_1 x_2 \omega))$.

The freeze out equation above, Eq. (7.3), can be numerically solved [458], obtaining the axion decoupling temperature $T_D$ as a function of the axion mass $m_a$. The upper left panel of Fig. 7.1 shows the axion decoupling temperature as a function of the axion mass, in eV. Notice that the higher is the axion mass, the lower is the temperature of decoupling. Afterwards it is possible to obtain the present axion number density, that is related to the current photon density $n_\gamma$ by the following equation [458]:

$$n_a = \frac{g_{\star S}(T_0)}{g_{\star S}(T_D)} \times \frac{n_\gamma}{2} \ , \tag{7.6}$$

where $g_{\star S}$ is the number of *entropic* degrees of freedom and $g_{\star S}(T_0) = 3.91$.

The contribution of the relic axion to the total mass-energy density of the Universe is given by the product of the axion mass times the axion number density. The quantity $\Omega_a h^2$ at the present epoch is depicted in the bottom left panel of Fig. 7.1. Notice that a 1 eV axion will give rise to $\Omega_a h^2 \simeq 0.005$ today, while a neutrino of the same mass will contribute to the total mass-energy density of the Universe with $\Omega_\nu h^2 \simeq 0.01$. Notice however that $\Omega_a h^2$ represents the contribution from relic, thermal axion states only. Non-thermal processes, as the misalignment production, could also produce a non-thermal axion population which we do not consider here. See Ref. [459] for the most recent cosmological constraints on such scenario.

The thermal axion can have, as massive neutrinos, the transition between the relativistic to the non relativistic regime. When the thermal axion is still a relativistic particle it increases the effective number of relativistic degrees of freedom $N_{\text{eff}}$, enhancing the amount of radiation in the Universe. The contribution to $N_{\text{eff}}$ from the thermal axion is given by [458]:

$$\Delta N_{\text{eff}} = \frac{4}{7} \left( \frac{3}{2} \frac{n_a}{n_\nu} \right)^{4/3} , \tag{7.7}$$

where $n_a$ is given by Eq. (7.6) and $n_\nu$ refers to the present neutrino plus antineutrino number density per flavor. The upper right panel of Fig. 7.1 shows the axion contribution to the radiation content of the Universe as a function of the axion mass. Notice that the extra dark radiation arising from a 1 eV axion is still compatible (at 95% CL) with the most recent measurements of $N_{\text{eff}}$ from the Planck mission [44].

The last crucial cosmological quantity is the axion free streaming scale, i.e. the wavenumber $k_{\text{FS}}$ below which the axion density perturbations will contribute to clustering once the axion is a non-relativistic particle. This scale is illustrated in Fig. 7.1 (solid line), in the bottom right panel, together with that corresponding to a neutrino of the same mass (dashed
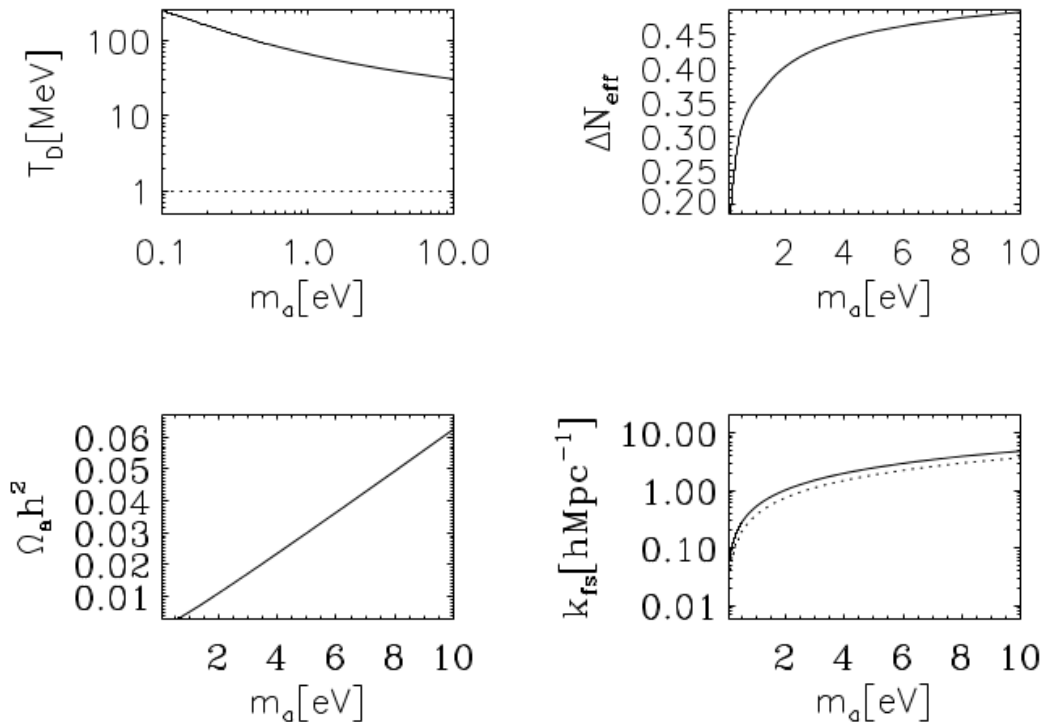
Figure 7.1: The upper left panel shows the temperature of decoupling as a function of the axion mass (solid curve), as well as the Big Bang Nucleosynthesis temperature, $T_{\mathrm{BBN}} \simeq$ 1 MeV (dashed curve). The upper right panel shows the axion contribution to the extra dark radiation content of the Universe, while the bottom right plot depicts the free-streaming scale of an axion (solid curve) or a neutrino (dashed curve) versus the axion/neutrino mass, in eV. The bottom left panel shows the current axion mass-energy density as a function of the axion mass. From Ref. [32].

line). Notice that they cover the same scales for our choice of priors for $m_a$ and $\sum m_\nu$ and therefore one can expect a large correlation between these two quantities in measurements of galaxy clustering.

Several papers in the literature provide bounds on the thermal axion mass, see for example Refs. [362,453–456,459,460]. Here we present the results obtained in Ref. [26,32], studying the constraints on the thermal axion mass, and testing their robustness against the assumption of a free Primordial Power Spectrum (PPS) of scalar perturbations, as we did for the neutrino properties in the previous Chapter. In Section 7.4 we also take into account the fact that thermal axions and massive neutrinos affect the cosmological observables in a very similar way, and we will consider the sum of the neutrino masses and the axion mass free to vary at the same time.

## 7.2 Method

### 7.2.1 Cosmological model

The thermal axion can be parameterized through its coupling constant $f_a$ or through its mass $m_a$. Even if they are equivalent (see Eq. (7.2)), for our purposes it is more convenient to use the axion mass $m_a$. All the other cosmological quantities can be derived as a function of the axion mass $m_a$, as we showed in the previous Section and in Fig. 7.1.

The baseline scenario we consider here is the $\Lambda$CDM model, extended to include the thermal axion. We also adopt the `PCHIP` PPS prescriptions presented in Section 6.2. When

considering the `PCHIP` PPS, for the numerical analyses we use the following set of parameters:

$$\{\omega_b, \omega_c, \theta, \tau, m_a, P_{s,1}, \ldots, P_{s,12}\} \ , \tag{7.8}$$

where the cosmological parameters are the same presented in Section 6.4, with the only exception of $m_a$. The $P_{s,1}, \ldots, P_{s,12}$ nodes describe the `PCHIP` PPS (see Section 6.2). We shall consider a scenario in which massive neutrinos are also present, to explore the expected degeneracy between the sum of the neutrino masses and the thermal axion mass [362], in Section 7.4.

In order to compare the results obtained with the `PCHIP` PPS to the results obtained with the usual power-law PPS model, we describe the latter case with the following set of parameters:

$$\{\omega_b, \omega_c, \theta, \tau, m_a, n_s, \log[10^{10}A_s]\} \ , \tag{7.9}$$

where $n_s$ and $A_s$ are the spectral index and the amplitude of the scalar power-law PPS written in Eq. (1.144) and the other parameters are the same ones described above.

As we discussed extensively the constraints on the reconstructed PPS in Section 6.8, in this Chapter we will not focus on the constraints obtained for the nodes $P_{s,i}$, since they are very similar to those already presented.

## 7.2.2 Cosmological measurements

Our baseline data set consists of CMB measurements. We will adopt the same datasets presented in Section 6.4, and we will use as baseline datasets the CMB data combinations **Planck TT+lowP** and **Planck TT,TE,EE+lowP**. Additionally, we will consider these two CMB datasets in combination with the **BAO**, **MPkW** and **lensing** datasets.

We will also stress the role that the thermal axion can have in solving the tension between local and cosmological determinations of $\sigma_8$. In this case we will indicate with **CMB** the combination of the temperature data from the 2013 release of the Planck satellite [20, 60], the WMAP 9-year polarization measurements [19] and the high multipole data from the South Pole Telescope (SPT) [69] and the Atacama Cosmology Telescope (ACT) [65] experiments. **HST** indicates a gaussian prior on the Hubble constant $H_0 = 70.6 \pm 3.3$ Km s$^{-1}$ Mpc$^{-1}$ [123]. We will present the results obtained studying the weak lensing measurements from CFHTLenS (**CFHT**) [142], described in Section 3.7, and on the cluster normalization condition as measured by the Planck Sunyaev-Zel'dovich (**PSZ**) 2013 catalogue [136], obtained using both the assumption of a fixed mass bias and a free mass bias (see Section 3.6).

Figure 7.2 illustrates the prediction for the cluster normalization condition, $\sigma_8(\Omega_m/0.27)^{0.3}$, as a function of the thermal axion mass. We also show the PSZ measurements [136] with their associated 95% CL uncertainties, including those in which the cluster mass bias parameter is fixed. Notice that the normalization condition decreases as the axion mass increases, as a consequence of the free-streaming nature of the axion: the larger is the axion mass, the larger is the reduction in the matter power spectra, as it happens for massive neutrinos.

Concerning the BAO constraints, we want to point out an interesting effect that affects the results that we will present. Figure 7.3 illustrates the spherically averaged BAO distance, $D_V(z) \propto D_A^2(z)/H(z)$ at a redshift of $z = 0.57$ as a function of the axion mass, as well as the measurement from the BOSS experiment with 95% CL error bars [93]. Notice that, from background measurements only, there exists a strong degeneracy between the CDM and the axion mass-energy densities. The solid black line in Fig. 7.3 shows the spherically averaged BAO distance if all the cosmological parameters are fixed, including $\omega_c$. The spherically averaged BAO distance deviates strongly from the $\Lambda$CDM prediction. However, if $\omega_c$ is varied while $m_a$ is changed, in order to keep the total matter mass-energy density constant the spherically averaged BAO distance approaches its expected value in a $\Lambda$CDM cosmology (see the dotted blue line in Fig. 7.3).
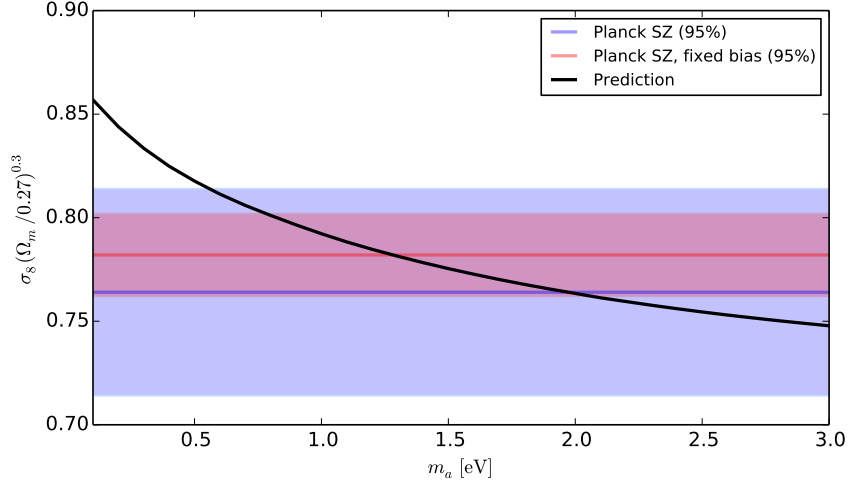
Figure 7.2: Cluster normalization condition, $\sigma_8(\Omega_m/0.27)^{0.3}$, as a function of the thermal axion mass. We also show the current PSZ measurements [136] with their associated 95% CL uncertainties. From Ref. [32].
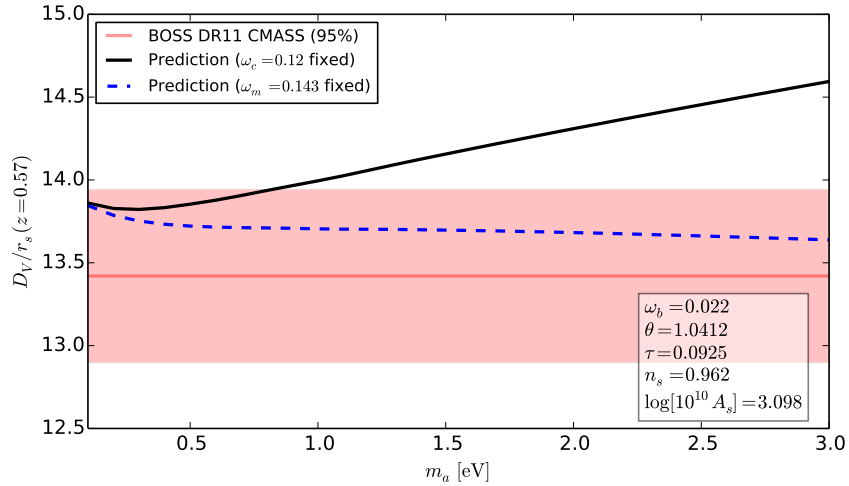


Figure 7.3: The solid black line depicts the spherically averaged BAO distance $D_V(z)$ as a function of the axion mass at a redshift of $z = 0.57$, after keeping fixed all the remaining cosmological parameters, included the cold dark matter energy density. The dashed blue line depicts the equivalent obtained keeping fixed the total matter mass-energy density. The bands show the measurement from the BOSS experiment (DR11) [93] with its associated 95% CL error. From Ref. [32].

## 7.3 Constraints on the Thermal Axion Mass

Tables 7.1 and 7.2 summarize our results for the extended $\Lambda$CDM + $m_a$ scenario, comparing, for each dataset considered here, the constraints arising in the power-law PPS scheme to the bounds obtained in the PCHIP PPS formalism. We can observe that the bounds on the axion mass are relaxed in the PCHIP PPS scenario, as illustrated in Fig. 7.5 and in Tabs. 7.1 and 7.2. This effect is related to the relaxed bound we have on $N_{\rm eff}$ when letting it free to vary in an extended $\Lambda$CDM + $N_{\rm eff}$ scenario that we discussed in Section 6.6. From the results presented in Tab. 6.4, we found $N_{\rm eff} = 3.40^{+1.50}_{-1.43}$ at 95% CL for the PCHIP PPS pa-
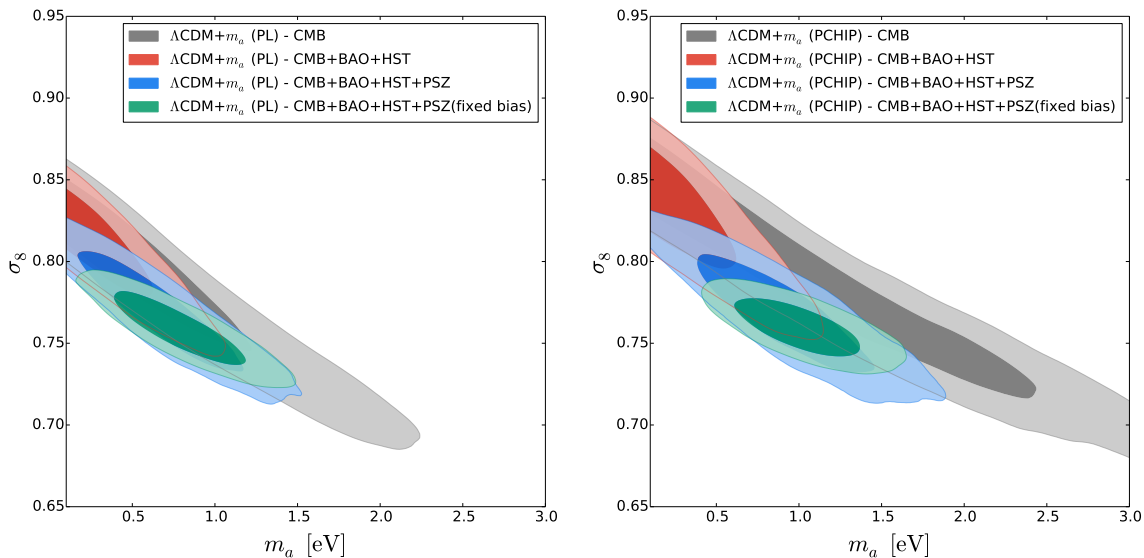
Figure 7.4: 68% and 95% CL allowed regions in the $(m_a, \sigma_8)$ plane for different possible data combinations, when a power-law (left panel) or a `PCHIP` (right panel) PPS is assumed. From Ref. [32].
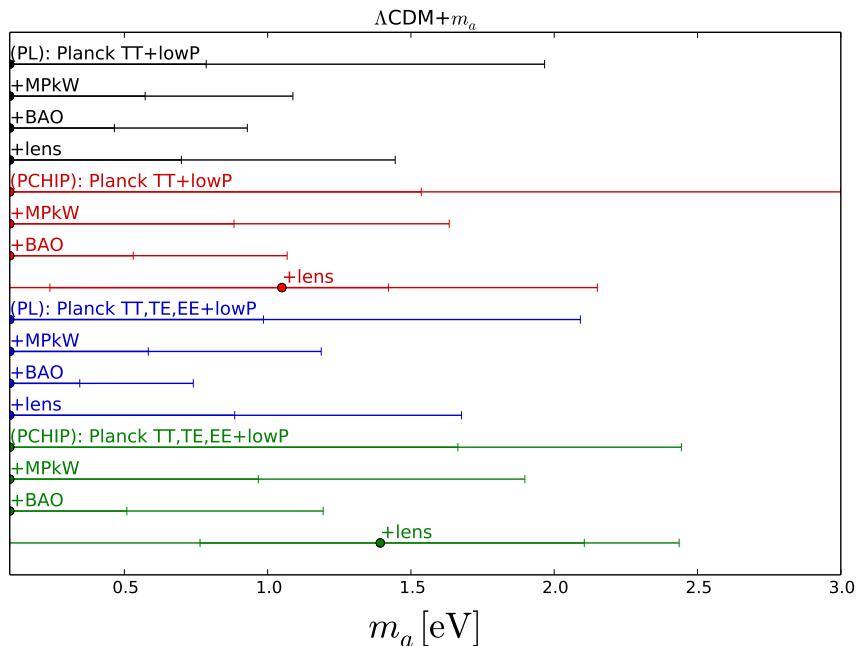


Figure 7.5: As Fig. 6.6 but in the context of the $\Lambda$CDM $+ m_a$ model, focusing on the thermal axion mass $m_a$ parameter. From Ref. [26].

rameterization, implying that the `PCHIP` formalism favors extra dark radiation, and therefore a higher axion mass is allowed. As a consequence, we find that the axion mass is totally unconstrained using the Planck TT+lowP data in the `PCHIP` PPS approach, with respect to the bound $m_a < 1.97$ eV at 95% CL we have for the standard power-law case.

However, when considering the Planck TT,TE,EE+lowP dataset for the $\Lambda$CDM $+ N_{\mathrm{eff}}$ model, we find $N_{\mathrm{eff}} = 2.99^{+0.41}_{-0.39}$ at 95% CL for the power-law PPS, and $N_{\mathrm{eff}} = 2.96^{+0.49}_{-0.48}$ for the `PCHIP` PPS approach (see Tab. 6.5), perfectly in agreement with the standard value $N_{\mathrm{eff}} = 3.046$. First of all, this implies that the axion mass constraints arising from high-$\ell$ polarization data are slightly weaker than those obtained with Planck TT+lowP dataset in

the power-law PPS formalism. In fact, the weakening of these bounds is driven by the fact that $N_{\text{eff}}$ is forced to be greater than standard value, as discussed more in detail in the next Section. Secondly, this means that the `PCHIP` parametrization of the PPS no longer favors an extra dark radiation component, and the effective neutrino number is perfectly in agreement with the bounds obtained by the Planck collaboration. Therefore, these tighter values in the `PCHIP` approach will lead to stronger constraints on the thermal axion mass from CMB data only, finding $m_a < 2.44$ eV with the `PCHIP` PPS, mildly larger than the bound $m_a < 2.09$ eV obtained within the power-law PPS, both at 95% CL.

### 7.3.1 Thermal Axions and Small Scales Perturbations

In parallel to what we did for the massive sterile neutrino in the previous Chapter, we present here some results obtained when the constraints on the small scales matter perturbations are included in the cosmological analyses involving the thermal axions. The data considered here are not the most recent ones. The constraints from CFHTLenS and the Planck SZ cluster counts obtained in the most recent analyses, taking into account a large number of possible astrophysical systematics, tend to show a smaller tension with the CMB data (see Sections 3.6 and 3.7). Therefore, a thermal axion would not be needed to reconcile the two sets of data. It is however possible that future experiments will be able to distinguish the various systematics and to improve the measurements. In the case that the tension will appear again, explanations as the one we provide here will be necessary.

When the CFHT bounds on the $\sigma_8$–$\Omega_m$ relationship are considered in addition to the CMB constraints, the bounds on the thermal axion mass become weaker. The reason is related to the lower $\sigma_8$ values preferred by weak lensing measurements, values that can be achieved by allowing for higher axion masses. The larger is the axion mass, the larger is the reduction of the matter power spectrum at small (i.e. cluster) scales, leading consequently to a smaller value of the clustering parameter $\sigma_8$.

If we instead consider the PSZ data set with fixed cluster mass bias, together with the CMB, BAO and HST measurements, a non-zero value of the thermal axion mass of $\sim 1$ eV ($\sim 0.80$ eV) is favored at $\sim 4\sigma$ ($\sim 3\sigma$) level, when considering the `PCHIP` (standard power-law) PPS approach [32] [1]. However, these results must be regarded as an illustration of what could be achieved with future cluster mass calibrations, as the Planck collaboration has recently shown in their analyses of the 2015 Planck cluster catalogue [137]. When more realistic approaches for the cluster mass bias are used, the errors on the so-called cluster normalization condition are larger, and consequently the preference for a non-zero axion mass of 1 eV is only mild in the `PCHIP` PPS case, while in the case of a standard power-law PPS such an evidence completely disappears.

The left (right) panel of Fig. 7.4 shows the 68% and 95% CL allowed regions in the ($m_a$, $\sigma_8$) plane in the power-law (`PCHIP`) PPS scenario. The lower values of the $\sigma_8$ clustering parameter preferred by PSZ data are translated into a preference for non-zero thermal axion masses. Larger values of $m_a$ will enhance the matter power spectrum suppression at scales below the axion free-streaming scale, leading to smaller values of the $\sigma_8$ clustering parameter, as preferred by PSZ measurements. The evidence for non-zero axion masses is more significant when the cluster mass bias is fixed in the PSZ data analyses. These results are the analogous of what we found for the sterile neutrino in Chapter 5.

### 7.3.2 Planck TT+lowP

The most stringent constraints on the axion properties are obtained with the most recent CMB data, released in 2015 by the Planck collaboration [21], that we are going to consider now.

---

[1] A similar effect when considering PSZ data for constraining either thermal axion or neutrino masses has also been found in Refs. [22, 23, 140, 337, 358, 362].

Table 7.1 shows our results at 95% CL arising from the Planck TT+lowP data alone and in combination with the MPkW, BAO and lensing measurements, for an extended $\Lambda$CDM + $m_a$ scenario, in the context of the two PPS parameterizations explored here.

As we discussed before, the first thing to note is that bounds on the axion mass are largely relaxed when considering the `PCHIP` PPS with respect to the ones obtained in the power-law PPS, in the case of the CMB measurements only. The Planck TT+lowP dataset cannot constrain the axion mass in the `PCHIP` approach. However, when adding the matter power spectrum measurements via the MPkW dataset, the upper limit on the axion mass is reduced by a half in the power-law approach: we have the limit $m_a < 1.09$ eV at 95% CL, that becomes $m_a < 1.63$ eV at 95% CL in the `PCHIP` parametrization.

The most stringent bounds arise when using the BAO data, since they are directly sensitive to the free-streaming nature of the thermal axion. While the MPkW measurements are also sensitive to this small scale structure suppression, BAO measurements are able to constrain better the cold dark matter density $\Omega_c h^2$, strongly correlated with $m_a$. The lower is the thermal axion mass, the lower is the amount of hot dark matter and consequently the lower must be the cold dark matter component, and viceversa. We find $m_a < 0.93$ eV at 95% CL in the standard case, and a slightly weaker constraint in the `PCHIP` case, $m_a < 1.07$ eV at 95% CL, both obtained using the Planck TT+lowP+BAO dataset.

Finally, when considering the lensing dataset, we obtain $m_a < 1.45$ eV at 95% CL in the power-law PPS case, that is slightly relaxed in the `PCHIP` PPS, $m_a < 2.15$ eV at 95% CL. For this combination of datasets, a mild preference appears for an axion mass different from zero: $m_a = 1.05^{+0.37}_{-0.81}$ at 68% CL, only when considering the `PCHIP` approach, as depicted in Fig. 7.5. This is probably due to the existing tension between the Planck data on the lensing reconstruction from the CMB trispectrum and the lensing effect observed in the CMB spectrum, see e.g. Refs. [44, 461].

The weakening of the axion mass constraints in most of the data combinations obtained in the `PCHIP` PPS scheme is responsible for the shift at more than $1\sigma$ of the cold dark matter mass-energy density, due to the existing degeneracy between $m_a$ and $\Omega_c h^2$. Interestingly, this effect has also an impact on the Hubble constant, leading to a shift of about $2\sigma$ towards lower values of the mean value of $H_0$ due to parameter degeneracies, as previously discussed in Chapter 6. Furthermore, a shift in the optical depth towards a lower mean value is also present when analyzing the `PCHIP` PPS scenario. One can explain this shift via the existing degeneracies between $\tau$ and $H_0$ and between $\tau$ and $\Omega_c h^2$. Once BAO measurements are included in the data analyses, the degeneracies are largely removed and there is no significant shift in the values of the $\Omega_c h^2$, $H_0$ and $\tau$ parameters within the `PCHIP` PPS approach, when comparing to their mean values in the power-law PPS.

### 7.3.3   Planck TT,TE,EE+lowP

Table 7.2 shows our results at 95% CL from the Planck TT,TE,EE+lowP data alone and in combination with MPkW, BAO and lensing measurements, for an extended $\Lambda$CDM + $m_a$ scenario, comparing the power-law PPS and the `PCHIP` PPS bounds.

In general, the constraints arising from high-$\ell$ polarization measurements are slightly weaker than those obtained previously. The weakening of the axion mass is driven by the preference of Planck TT,TE,EE+lowP for a lower value of $N_{\rm eff}$, as pointed out before. As shown in Fig. 7.1, the additional contribution to $N_{\rm eff}$ due to thermal axions is a steep function of the axion mass, at least for low thermal axion masses (i.e. below $\sim 1$ eV). The lower value of $N_{\rm eff}$ preferred by small-scale polarization dramatically sharpens the posterior of $m_a$ at low mass (see Fig. 7.6). At higher masses, however, the axion contribution to $N_{\rm eff}$ depends weakly on $m_a$: as a consequence, the posterior distribution flattens at high $m_a$ and overlaps with the one resulting from Planck TT+lowP, since CMB polarization does not help in improving the constraints on $\Omega_m$. We can in fact notice the presence of a bump in the posterior distributions of $\Omega_m$ and $\sigma_8$ for Planck TT,TE,EE+lowP. The mismatch in the values of $\Omega_m$ preferred by low and high thermal axion masses leads to a worsening of the constraints on $m_a$ with respect
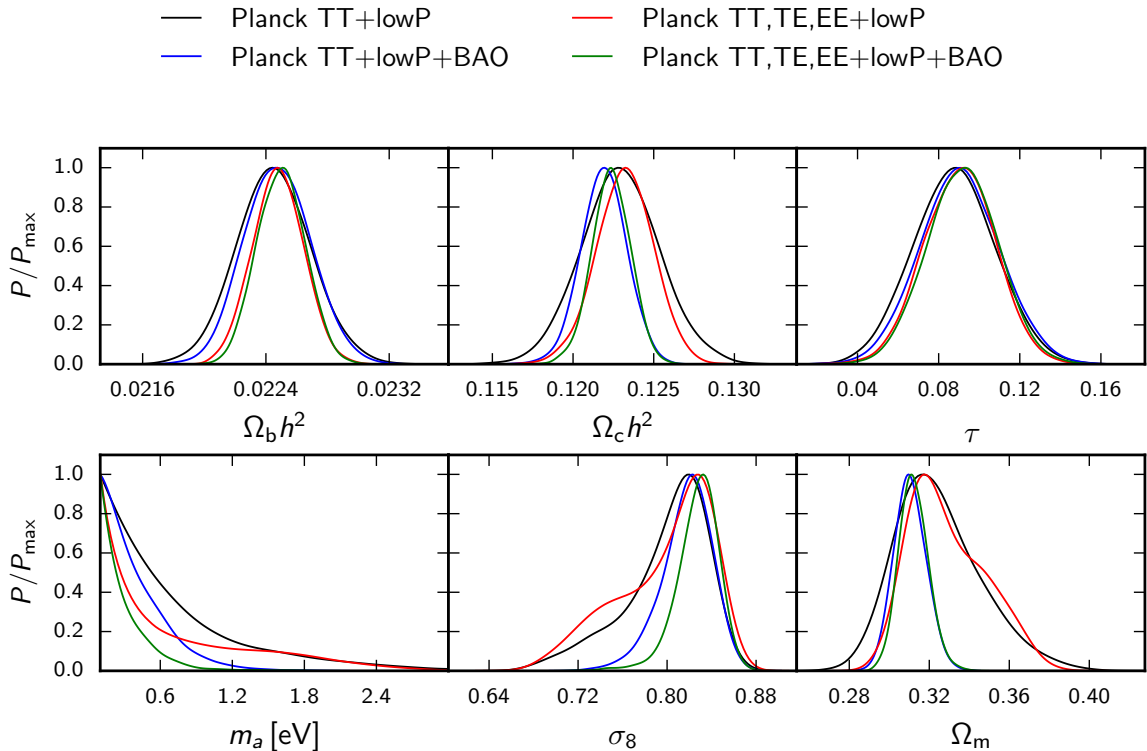
Figure 7.6: One-dimensional posterior probability for the most relevant cosmological parameters for the combination of datasets labeled in the figure, for the power-law approach in the $\Lambda$CDM $+ m_a$ scenario. From Ref. [26].

to the Planck TT+lowP scenario, since the volume of the posterior distribution is now mainly distributed at higher masses. When the BAO data are considered, we get the tightest bounds on $m_a$. In addition, the bump in both the $\Omega_m$ and $\sigma_8$ distributions disappears completely, due to the higher constraining power of the BAO data. As a result, the tail of the $m_a$ distribution is excluded when the BAO measurements are considered, and the constraints do not suffer of the problem related to the volume effects discussed above.

Furthermore, the thermal axion mass bounds are relaxed within the PCHIP PPS formalism. In particular, concerning the CMB measurements only, $m_a < 2.44$ eV at 95% CL in the PCHIP approach, compared to the bound $m_a < 2.09$ eV at 95% CL in the standard power-law PPS description. When adding the matter power spectrum measurements (MPkW), we find upper limits on the axion mass that are $m_a < 1.19$ eV at 95% CL in the power-law PPS and $m_a < 1.90$ eV at 95% CL in the PCHIP parametrization. When considering the lensing dataset, we obtain $m_a < 1.68$ eV at 95% CL in the power-law PPS case, that is relaxed when using the PCHIP PPS, that gives $m_a < 2.44$ eV at 95% CL. A mild preference for an axion mass different from zero appears from this particular data combination ($m_a = 1.39^{+0.71}_{-0.63}$ at 68% CL) only when considering the PCHIP PPS approach, see Fig. 7.5.

It is important to note that, when the CMB polarization at high multipoles is included, the shifts induced in the mean value of the optical depth and in the abundance of the cold dark matter disappear.

## 7.4 Thermal Axions and massive neutrinos

In this Section we show the bounds in a scenario that includes both massive neutrinos and the thermal axion relics. In principle, it should be possible to distinguish between these two relic populations because thermal axions increase the amount of radiation expected in the standard model, where the neutrino contribution is fixed to $N_{\text{eff}} = 3.046$, modifying the $N_{\text{eff}}$
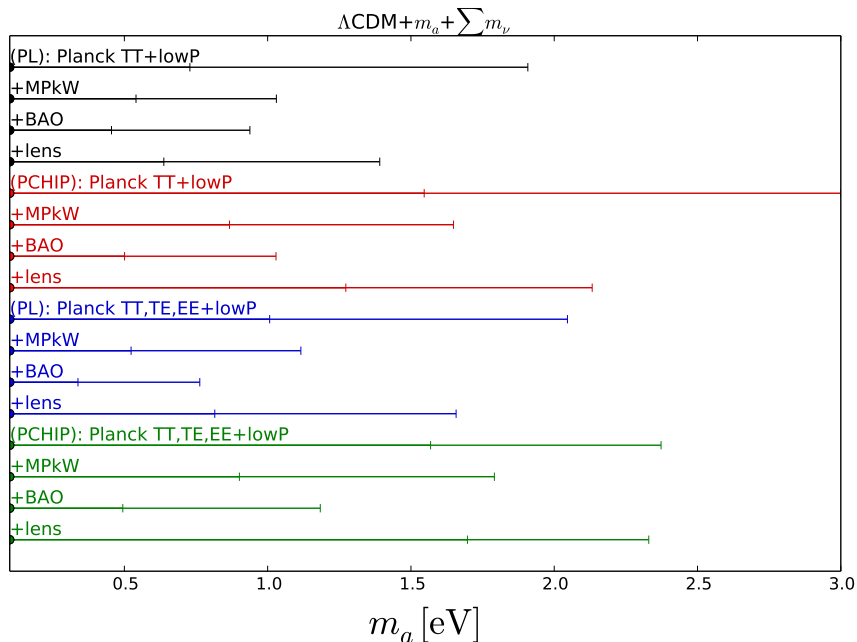
Figure 7.7: As Fig. 6.6 but in the context of a $\Lambda$CDM $+ m_a + \Sigma m_\nu$ model, focusing on the $m_a$ parameter. From Ref. [26].

value through the Eq. (7.7). In addition, axions are expected to be colder and have a larger mass than neutrinos. First of all it is important to note that the thermal axion mass bounds are unchanged in the extended $\Lambda$CDM $+ m_a + \Sigma m_\nu$ model with respect to the $\Lambda$CDM $+ m_a$ scenario. After comparing among the results shown in Tabs. 7.1 (7.2) and 7.3 (7.4) for the Planck TT+lowP (Planck TT,TE,EE+lowP) dataset baseline we can notice that the axion mass constraints are almost identical. In other words, massive neutrinos do not affect the upper limits obtained for the thermal axion mass. On the other hand, the presence of thermal axions tightens the neutrino mass bounds, presented in Sec. 6.7, as both the thermal relics behave as hot dark matter with a free-streaming nature.

### 7.4.1 Results with Planck TT+lowP

Table 7.3 presents our results at 95% CL from the Planck TT+lowP data alone and in combination with the MPkW, BAO and lensing measurements, for an extended $\Lambda$CDM $+ m_a + \Sigma m_\nu$ scenario, in the two PPS parameterizations exploited here. As discussed before for the $\Lambda$CDM $+ m_a$ model, for any combination of datasets the bounds on the axion mass are relaxed when considering the PCHIP PPS with respect to the power-law PPS ones (see Fig. 7.7). In addition, in this case, we can also notice a weakening of the total neutrino mass constraints when using the PCHIP approach (see Fig. 7.8). The only exception appears when considering the BAO measurements, since they are directly sensitive to the free-streaming nature of the two relic particles.

Concerning the CMB measurements only, the Planck TT+lowP data are not able to constrain the axion mass in the PCHIP approach, providing $\Sigma m_\nu < 2.20$ eV at 95% CL versus the $\Sigma m_\nu < 0.62$ eV at 95% CL limit obtained for the power-law approach. When adding the matter power spectrum measurements (MPkW), both the upper limits on the axion mass and on the neutrino masses are reduced by about a half in the canonical power-law PPS scenario, and become $m_a < 1.65$ eV at 95% CL and $\Sigma m_\nu < 1.24$ eV at 95% CL in the PCHIP parameterization. As in the previous sections, the most stringent bounds arise when using the BAO data in both parameterizations: we have $m_a < 1.03$ eV at 95% CL and $\Sigma m_\nu < 0.21$ eV at 95% CL in the PCHIP case. Finally, when considering the lensing dataset with the PCHIP
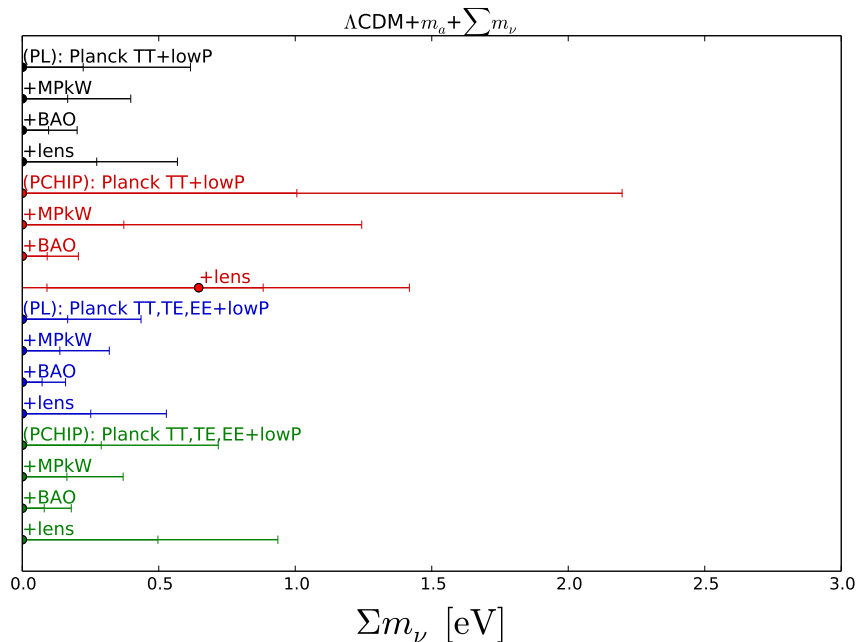
Figure 7.8: As Fig. 7.7, but for the $\Sigma m_\nu$ parameter. From Ref. [26].

PPS, we obtain $m_a < 2.13$ eV at 95% CL and $\Sigma m_\nu < 1.42$ eV at 95% CL.

As in the $\Lambda$CDM $+ m_a$ model, we find a shift of about $2\sigma$ towards lower values of the mean value of the Hubble constant in the PCHIP parameterization, except when BAO data are included in the analyses. However, in this case, the value of $H_0$ is strongly degenerate with the total neutrino mass, as explained in the previous Chapter.

In addition, in this extended scenario with massive neutrinos and within the PCHIP approach, we have a shift of about $2\sigma$ toward higher values in the mean value of the cold dark matter density. These shifts are larger than those reported in the $\Lambda$CDM $+ m_a$ scenario, as now we have one extra degeneracy (between $\Sigma m_\nu$ and $\Omega_c h^2$). A shift in the optical depth $\tau$ is also present in this case, due to the degeneracy between $\Omega_c h^2$ and $\tau$. Once BAO measurements are considered, the shifts in the mean values of the parameters are not significant.

### 7.4.2 Results with Planck TT,TE,EE+lowP

Table 7.4 shows our results at 95% CL from the Planck TT,TE,EE+lowP data alone and in combination with MPkW, BAO and lensing measurements, for an extended $\Lambda$CDM $+ m_a + \Sigma m_\nu$ scenario, comparing the power-law PPS and the PCHIP PPS bounds. As noticed above in the Planck TT+lowP baseline results, the bounds on the axion mass and on the total neutrino mass are relaxed when considering the PCHIP PPS with respect to the power-law PPS ones.

The axion (neutrino) mass constraints are, in general, slightly weaker (stronger) than those obtained using only the temperature power spectrum at small angular scales, for the reasons explained above. In particular, focusing on the CMB measurements alone, the Planck TT,TE,EE+lowP data provides upper limits on the thermal axion mass and on the neutrino masses in the PCHIP approach of $m_a < 2.37$ eV at 95% CL and $\Sigma m_\nu < 0.72$ eV at 95% CL, respectively.

Furthermore, when adding the matter power spectrum measurements (MPkW) we find $m_a < 1.79$ eV at 95% CL and $\Sigma m_\nu < 0.37$ eV at 95% CL in the PCHIP parametrization. This last constraint on the neutrino masses is about half the bound obtained with the Planck TT,TE,EE+lowP dataset. The most stringent bounds on both the axion mass and on the total neutrino mass arise, as usual, from the addition of BAO data. We find $m_a < 1.18$ eV

at 95% CL and $\Sigma m_\nu < 0.18$ eV at 95% CL in the `PCHIP` PPS, respectively. Finally, when considering the lensing dataset within the `PCHIP` PPS we obtain $m_a < 2.33$ eV at 95% CL and $\Sigma m_\nu < 0.94$ eV at 95% CL.

The mean values of the optical depth or of the cold dark matter density do not suffer from the shifts detailed in the absence of high multipole polarization data. There is a (mild) shift, caused by the degeneracy between $\Sigma m_\nu$ and $H_0$, toward lower values in the Hubble constant case within the `PCHIP` approach, which gets accentuated when including the lensing likelihood. As expected, the shift in the mean value of the clustering parameter $\sigma_8$ is larger than in previous cases, due to the presence of two hot dark matter species reducing the small-scale matter fluctuations.

## 7.5 Conclusions

After discussing the cosmological properties of active and sterile neutrinos, that may contribute as hot or warm dark matter components depending on their mass, we studied in this Chapter another possible candidate for hot dark matter: the thermal axion. The contribution of the thermal axion to the cosmological quantities can be described using the scale $f_a$ at which the $U(1)_{PQ}$ symmetry is spontaneously broken, or equivalently its mass $m_a$. Since the thermal axion contributes as a relativitistic particle in the early Universe and as a massive component in the late Universe, its effects are similar to those of the massive neutrinos and a degeneracy exist between the two particles. In particular, the thermal axion free-streaming can explain the discrepancy between local measurements and cosmological estimates of the clustering parameter $\sigma_8$.

The most recent analyses from the Planck collaboration put strong constraints on the additional relativistic particles in the early Universe and no deviations from $N_{\rm eff} = 3.046$ are shown. Our analyses in Chapters 5 and 6 confirmed these results, and the most stringent bound from CMB data only we have found is $N_{\rm eff} = 2.99^{+0.41}_{-0.39}$, obtained from the Planck TT,TE,EE+lowP dataset. The corresponding bound at 68% CL is $N_{\rm eff} = 2.99 \pm 0.20$ with a power-law PPS ($N_{\rm eff} = 2.96 \pm 0.25$ with a `PCHIP` PPS), for which the 68% CL upper constraint is $N_{\rm eff} \simeq 3.2$. The minimum contribution for a thermal axion is $\Delta N_{\rm eff} \simeq 0.2$, corresponding to the minimum value $m_a \simeq 0.1$ eV allowed to perform the calculations for the thermal axion. For smaller axion masses, in fact, the decoupling temperature is above the QCD scale and there are no particles that can efficiently interact with the axion and allow its decoupling [31, 462, 463], that jumps to very high temperatures. In this case, the upper value on $N_{\rm eff}$ allowed by the CMB data at 68% CL is smaller than the minimum value of $N_{\rm eff}$ that is possible when a thermal axion is included, that would be $N_{\rm eff} \simeq 3.25$. As a consequence, the presence of a thermal axion is excluded at 68% CL by CMB data.

Concerning the robustness of the bounds on the axion mass against changes in the assumptions on the power spectrum of initial curvature perturbations, we can notice that the axion mass bounds are largely relaxed when a free PPS is assumed. When including the small scale CMB polarization we find a further weakening of the axion mass constraints. This is due to the fact that polarization constrains significantly the contribution of the axion to $N_{\rm eff}$, but this depends weakly on $m_a$, if it is large. As a consequence, the posterior distribution is smaller at small $m_a$, but is unchanged for large $m_a$. The reduced volume of the posterior distribution for small axion masses is then translated into a broadening of the marginalized constraints towards higher values for $m_a$. The strongest bound we find on the thermal axion mass within the `PCHIP` approach is $m_a < 1.07$ eV at 95% CL when considering the Planck TT+lowP+BAO data combination. In the standard power-law scenario, the most stringent bound is $m_a < 0.74$ eV at 95% CL, obtained with the further inclusion of the polarization at high multipoles (Planck TT,TE,EE+lowP+BAO).

When we vary also the massive neutrino mass to test the degeneracy with the thermal axion mass, we find that the constraints on the total neutrino mass are tighter than those obtained without thermal axions (see Section 6.7), while the bounds on the thermal axion

mass are unchanged. The strongest bounds we find for the thermal axion mass and the total neutrino mass in the `PCHIP` approach are $m_a < 1.03$ eV at 95% CL and $\Sigma m_\nu < 0.18$ eV at 95% CL, when considering the Planck TT+lowP+BAO and Planck TT,TE,EE+lowP+BAO dataset combinations, respectively. In the power-law PPS scenario the strongest bounds are $m_a < 0.76$ eV at 95% CL and $\Sigma m_\nu < 0.16$ eV at 95% CL, obtained both for the Planck TT,TE,EE+lowP+BAO dataset.

Finally, from the analyses we performed in this Chapter it is possible to obtain constraints on the PPS shape. These results are not discussed in this Chapter, however, since they are very similar to those presented in Chapter 6.

| Parameter | Planck TT+lowP | | Planck TT+lowP+MPkW | | Planck TT+lowP+BAO | | Planck TT+lowP+lensing | |
|---|---|---|---|---|---|---|---|---|
| $100\Omega_b h^2$ | $2.245^{+0.048}_{-0.046}$ | $2.178^{+0.080}_{-0.079}$ | $2.240^{+0.045}_{-0.043}$ | $2.191^{+0.074}_{-0.071}$ | $2.248^{+0.043}_{-0.040}$ | $2.224^{+0.065}_{-0.062}$ | $2.245^{+0.046}_{-0.047}$ | $2.182^{+0.082}_{-0.077}$ |
| $\Omega_c h^2$ | $0.1229^{+0.0049}_{-0.0047}$ | $0.1267^{+0.0062}_{-0.0061}$ | $0.1234^{+0.0045}_{-0.0043}$ | $0.1262^{+0.0058}_{-0.0056}$ | $0.1219^{+0.0027}_{-0.0028}$ | $0.1222 \pm 0.0032$ | $0.1222^{+0.0043}_{-0.0044}$ | $0.1253^{+0.0058}_{-0.0059}$ |
| $100\theta$ | $1.041 \pm 0.001$ | $1.0399 \pm 0.0011$ | $1.0405^{+0.0009}_{-0.0010}$ | $1.0401^{+0.0010}_{-0.0011}$ | $1.0407 \pm 0.0008$ | $1.0406^{+0.0008}_{-0.0009}$ | $1.0406 \pm 0.0009$ | $1.0401 \pm 0.0010$ |
| $\tau$ | $0.088^{+0.039}_{-0.038}$ | $0.074^{+0.047}_{-0.043}$ | $0.084^{+0.040}_{-0.039}$ | $0.076^{+0.049}_{-0.043}$ | $0.090 \pm 0.038$ | $0.091^{+0.046}_{-0.043}$ | $0.078 \pm 0.034$ | $0.062^{+0.038}_{-0.037}$ |
| $m_a$ [eV] | $< 1.97$ | nb | $< 1.09$ | $< 1.63$ | $< 0.93$ | $< 1.07$ | $< 1.45$ | $< 2.15$ |
| $n_S$ | $0.974^{+0.014}_{-0.015}$ | – | $0.974 \pm 0.012$ | – | $0.978 \pm 0.010$ | – | $0.977^{+0.012}_{-0.013}$ | – |
| $\ln[10^{10} A_s]$ | $3.119^{+0.075}_{-0.074}$ | – | $3.112 \pm 0.077$ | – | $3.121^{+0.076}_{-0.075}$ | – | $3.096^{+0.062}_{-0.061}$ | – |
| $H_0[\mathrm{Km\,s^{-1}\,Mpc^{-1}}]$ | $67.9^{+2.4}_{-2.8}$ | $65.2 \pm 3.4$ | $68.1^{+2.0}_{-2.3}$ | $66.3^{+2.9}_{-3.1}$ | $68.8 \pm 1.1$ | $68.4 \pm 1.3$ | $68.4^{+2.2}_{-2.5}$ | $66.0 \pm 3.0$ |
| $\sigma_8$ | $0.799^{+0.063}_{-0.086}$ | $0.800^{+0.099}_{-0.097}$ | $0.812^{+0.045}_{-0.050}$ | $0.801^{+0.066}_{-0.070}$ | $0.817^{+0.044}_{-0.049}$ | $0.859^{+0.078}_{-0.081}$ | $0.794^{+0.046}_{-0.059}$ | $0.804^{+0.076}_{-0.085}$ |
| $P_{s,1}$ | $\equiv 1.307$ | $< 7.36$ | $\equiv 1.297$ | $< 8.0$ | $\equiv 1.262$ | $< 7.93$ | $\equiv 1.242$ | $< 7.95$ |
| $P_{s,2}$ | $\equiv 1.138$ | $1.18^{+0.40}_{-0.37}$ | $\equiv 1.131$ | $1.16^{+0.41}_{-0.37}$ | $\equiv 1.123$ | $1.12^{+0.39}_{-0.36}$ | $\equiv 1.100$ | $1.18^{+0.40}_{-0.37}$ |
| $P_{s,3}$ | $\equiv 1.119$ | $0.71^{+0.39}_{-0.37}$ | $\equiv 1.112$ | $0.72^{+0.41}_{-0.40}$ | $\equiv 1.107$ | $0.76^{+0.41}_{-0.39}$ | $\equiv 1.083$ | $0.68 \pm 0.37$ |
| $P_{s,4}$ | $\equiv 1.101$ | $1.20 \pm 0.27$ | $\equiv 1.093$ | $1.20^{+0.27}_{-0.26}$ | $\equiv 1.091$ | $1.22^{+0.27}_{-0.26}$ | $\equiv 1.067$ | $1.19 \pm 0.26$ |
| $P_{s,5}$ | $\equiv 1.082$ | $1.09 \pm 0.12$ | $\equiv 1.075$ | $1.08^{+0.12}_{-0.11}$ | $\equiv 1.076$ | $1.08^{+0.13}_{-0.12}$ | $\equiv 1.051$ | $1.057^{+0.099}_{-0.098}$ |
| $P_{s,6}$ | $\equiv 1.064$ | $1.070^{+0.093}_{-0.089}$ | $\equiv 1.057$ | $1.071^{+0.093}_{-0.083}$ | $\equiv 1.061$ | $1.072^{+0.097}_{-0.093}$ | $\equiv 1.036$ | $1.043^{+0.064}_{-0.066}$ |
| $P_{s,7}$ | $\equiv 1.046$ | $1.047^{+0.090}_{-0.081}$ | $\equiv 1.039$ | $1.042^{+0.091}_{-0.086}$ | $\equiv 1.045$ | $1.056^{+0.095}_{-0.087}$ | $\equiv 1.020$ | $1.011^{+0.064}_{-0.059}$ |
| $P_{s,8}$ | $\equiv 1.029$ | $1.003^{+0.093}_{-0.089}$ | $\equiv 1.021$ | $1.007^{+0.097}_{-0.091}$ | $\equiv 1.031$ | $1.028^{+0.097}_{-0.093}$ | $\equiv 1.005$ | $0.974^{+0.072}_{-0.066}$ |
| $P_{s,9}$ | $\equiv 1.011$ | $0.988^{+0.092}_{-0.087}$ | $\equiv 1.004$ | $0.991^{+0.097}_{-0.090}$ | $\equiv 1.016$ | $1.021^{+0.095}_{-0.091}$ | $\equiv 0.990$ | $0.964^{+0.073}_{-0.072}$ |
| $P_{s,10}$ | $\equiv 0.994$ | $1.00^{+0.10}_{-0.09}$ | $\equiv 0.987$ | $0.987^{+0.099}_{-0.095}$ | $\equiv 1.001$ | $1.03^{+0.11}_{-0.10}$ | $\equiv 0.975$ | $0.986^{+0.084}_{-0.082}$ |
| $P_{s,11}$ | $\equiv 0.978$ | $< 3.69$ | $\equiv 0.971$ | $0.90^{+0.75}_{-0.56}$ | $\equiv 0.987$ | $2.6^{+1.9}_{-2.5}$ | $\equiv 0.961$ | $2.5^{+1.5}_{-1.7}$ |
| $P_{s,12}$ | $\equiv 0.896$ | nb | $\equiv 0.890$ | $< 3.41$ | $\equiv 0.917$ | nb | $\equiv 0.890$ | nb |

Table 7.1: Constraints on cosmological parameters from the Planck TT+lowP dataset alone and in combination with the matter power spectrum shape measurements from WiggleZ (MPkW), the BAO data and the lensing constraints from Planck, in the $\Lambda$CDM $+\ m_a$ model (*nb* stands for *no bound*). For each combination, we report the limits obtained for the two parameterizations of the primordial power spectrum, namely the power-law model (first column) and the polynomial expansion (second column of each pair). Limits are at 95% CL around the mean value of the posterior distribution. For each dataset, in the case of power-law model, the values of $P_{s,i}$ are computed according to Eq. (6.3). From Ref. [26].

| Parameter | Planck TT,TE,EE+lowP | | Planck TT,TE,EE+lowP +MPkW | | Planck TT,TE,EE+lowP +BAO | | Planck TT,TE,EE+lowP +lensing | |
|---|---|---|---|---|---|---|---|---|
| $100\Omega_b h^2$ | $2.248 \pm 0.032$ | $2.241^{+0.039}_{-0.038}$ | $2.245^{+0.030}_{-0.031}$ | $2.236^{+0.037}_{-0.038}$ | $2.250^{+0.030}_{-0.029}$ | $2.248^{+0.038}_{-0.036}$ | $2.248^{+0.033}_{-0.030}$ | $2.242^{+0.039}_{-0.038}$ |
| $\Omega_c h^2$ | $0.1232^{+0.0034}_{-0.0036}$ | $0.1233^{+0.0041}_{-0.0043}$ | $0.1236^{+0.0032}_{-0.0033}$ | $0.1241^{+0.0037}_{-0.0040}$ | $0.1224^{+0.0023}_{-0.0024}$ | $0.1223 \pm 0.0029$ | $0.1231^{+0.0032}_{-0.0033}$ | $0.1224^{+0.0039}_{-0.0043}$ |
| $100\theta$ | $1.0403 \pm 0.0007$ | $1.0402^{+0.0007}_{-0.0006}$ | $1.0403 \pm 0.0007$ | $1.0402 \pm 0.0007$ | $1.0406 \pm 0.0006$ | $1.0405 \pm 0.0006$ | $1.0404 \pm 0.0007$ | $1.0403 \pm 0.0006$ |
| $\tau$ | $0.090^{+0.033}_{-0.034}$ | $0.090^{+0.043}_{-0.042}$ | $0.087 \pm 0.034$ | $0.091 \pm 0.039$ | $0.092 \pm 0.034$ | $0.093^{+0.043}_{-0.042}$ | $0.075 \pm 0.028$ | $0.071^{+0.034}_{-0.032}$ |
| $m_a$ [eV] | $< 2.09$ | $< 2.44$ | $< 1.19$ | $< 1.90$ | $< 0.74$ | $< 1.19$ | $< 1.68$ | $< 2.44$ |
| $n_S$ | $0.972^{+0.011}_{-0.012}$ | – | $0.9734 \pm 0.0098$ | – | $0.9754^{+0.0092}_{-0.0089}$ | – | $0.974^{+0.010}_{-0.011}$ | – |
| $\ln[10^{10} A_s]$ | $3.125^{+0.065}_{-0.067}$ | – | $3.119^{+0.067}_{-0.068}$ | – | $3.125 \pm 0.067$ | – | $3.092 \pm 0.053$ | – |
| $H_0[\mathrm{Km\,s^{-1}\,Mpc^{-1}}]$ | $67.6^{+1.9}_{-2.2}$ | $66.8 \pm 2.2$ | $67.9^{+1.6}_{-1.8}$ | $67.3^{+2.0}_{-2.1}$ | $68.6 \pm 1.0$ | $68.5 \pm 1.1$ | $67.9^{+1.9}_{-2.0}$ | $66.9^{+2.1}_{-1.9}$ |
| $\sigma_8$ | $0.798^{+0.067}_{-0.090}$ | $0.806^{+0.11}_{-0.10}$ | $0.815^{+0.045}_{-0.054}$ | $0.801^{+0.068}_{-0.078}$ | $0.827^{+0.037}_{-0.039}$ | $0.871^{+0.072}_{-0.084}$ | $0.788^{+0.051}_{-0.066}$ | $0.790^{+0.092}_{-0.085}$ |
| $P_{s,1}$ | $\equiv 1.339$ | $< 7.74$ | $\equiv 1.319$ | $< 7.85$ | $\equiv 1.302$ | $< 7.71$ | $\equiv 1.272$ | $< 7.74$ |
| $P_{s,2}$ | $\equiv 1.154$ | $1.15^{+0.39}_{-0.36}$ | $\equiv 1.143$ | $1.14^{+0.40}_{-0.36}$ | $\equiv 1.141$ | $1.12^{+0.39}_{-0.36}$ | $\equiv 1.108$ | $1.18^{+0.40}_{-0.37}$ |
| $P_{s,3}$ | $\equiv 1.133$ | $0.72^{+0.40}_{-0.37}$ | $\equiv 1.123$ | $0.74^{+0.38}_{-0.37}$ | $\equiv 1.122$ | $0.74^{+0.40}_{-0.38}$ | $\equiv 1.090$ | $0.68^{+0.37}_{-0.34}$ |
| $P_{s,4}$ | $\equiv 1.113$ | $1.25 \pm 0.24$ | $\equiv 1.103$ | $1.24 \pm 0.23$ | $\equiv 1.104$ | $1.24 \pm 0.23$ | $\equiv 1.071$ | $1.23^{+0.23}_{-0.22}$ |
| $P_{s,5}$ | $\equiv 1.093$ | $1.11^{+0.12}_{-0.11}$ | $\equiv 1.084$ | $1.11^{+0.11}_{-0.10}$ | $\equiv 1.086$ | $1.10^{+0.12}_{-0.10}$ | $\equiv 1.053$ | $1.071^{+0.092}_{-0.088}$ |
| $P_{s,6}$ | $\equiv 1.073$ | $1.089^{+0.098}_{-0.091}$ | $\equiv 1.065$ | $1.087^{+0.083}_{-0.081}$ | $\equiv 1.069$ | $1.077^{+0.096}_{-0.088}$ | $\equiv 1.036$ | $1.013^{+0.064}_{-0.059}$ |
| $P_{s,7}$ | $\equiv 1.054$ | $1.058^{+0.090}_{-0.087}$ | $\equiv 1.047$ | $1.061^{+0.079}_{-0.077}$ | $\equiv 1.052$ | $1.056^{+0.094}_{-0.087}$ | $\equiv 1.018$ | $1.013^{+0.064}_{-0.059}$ |
| $P_{s,8}$ | $\equiv 1.035$ | $1.035^{+0.091}_{-0.085}$ | $\equiv 1.029$ | $1.037^{+0.080}_{-0.079}$ | $\equiv 1.035$ | $1.036^{+0.093}_{-0.085}$ | $\equiv 1.001$ | $0.995^{+0.066}_{-0.060}$ |
| $P_{s,9}$ | $\equiv 1.016$ | $1.020^{+0.088}_{-0.083}$ | $\equiv 1.011$ | $1.020^{+0.080}_{-0.078}$ | $\equiv 1.018$ | $1.027^{+0.090}_{-0.089}$ | $\equiv 0.984$ | $0.982^{+0.067}_{-0.061}$ |
| $P_{s,10}$ | $\equiv 0.998$ | $1.03^{+0.10}_{-0.09}$ | $\equiv 0.993$ | $1.009^{+0.088}_{-0.085}$ | $\equiv 1.002$ | $1.04 \pm 0.10$ | $\equiv 0.968$ | $0.998^{+0.079}_{-0.071}$ |
| $P_{s,11}$ | $\equiv 0.980$ | $2.8^{+1.6}_{-2.4}$ | $\equiv 0.976$ | $0.94^{+1.0}_{-0.8}$ | $\equiv 0.985$ | $2.9^{+1.8}_{-2.6}$ | $\equiv 0.952$ | $3.1^{+1.4}_{-1.7}$ |
| $P_{s,12}$ | $\equiv 0.892$ | $< 8.89$ | $\equiv 0.891$ | $< 3.06$ | $\equiv 0.906$ | $< 8.66$ | $\equiv 0.872$ | nb |

Table 7.2: As Tab. 7.1, but using the Planck TT,TE,EE+lowP dataset. From Ref. [26].

| Parameter | Planck TT+lowP | | Planck TT+lowP+MPkW | | Planck TT+lowP+BAO | | Planck TT+lowP+lensing | |
|---|---|---|---|---|---|---|---|---|
| $100\Omega_b h^2$ | $2.237^{+0.051}_{-0.055}$ | $2.134^{+0.098}_{-0.093}$ | $2.237 \pm 0.046$ | $2.170^{+0.09}_{-0.10}$ | $2.248^{+0.044}_{-0.042}$ | $2.226^{+0.070}_{-0.065}$ | $2.236 \pm 0.051$ | $2.150^{+0.087}_{-0.082}$ |
| $\Omega_c h^2$ | $0.1234 \pm 0.0048$ | $0.1288^{+0.0068}_{-0.0069}$ | $0.1235^{+0.0045}_{-0.0042}$ | $0.1279^{+0.0075}_{-0.0066}$ | $0.1217^{+0.0030}_{-0.0032}$ | $0.1220^{+0.0033}_{-0.0037}$ | $0.1230^{+0.0049}_{-0.0046}$ | $0.1278 \pm 0.0064$ |
| $100\theta$ | $1.040 \pm 0.001$ | $1.0393^{+0.0013}_{-0.0014}$ | $1.0404^{+0.0009}_{-0.0010}$ | $1.0397^{+0.0013}_{-0.0014}$ | $1.0407 \pm 0.0009$ | $1.0406^{+0.0009}_{-0.0008}$ | $1.040 \pm 0.001$ | $1.0395 \pm 0.0012$ |
| $\tau$ | $0.090^{+0.040}_{-0.039}$ | $0.075^{+0.046}_{-0.042}$ | $0.087^{+0.039}_{-0.037}$ | $0.076^{+0.048}_{-0.046}$ | $0.092 \pm 0.038$ | $0.092^{+0.048}_{-0.047}$ | $0.085^{+0.037}_{-0.035}$ | $0.071^{+0.040}_{-0.037}$ |
| $\Sigma m_\nu$ [eV] | $< 0.62$ | $< 2.20$ | $< 0.40$ | $< 1.24$ | $< 0.20$ | $< 0.21$ | $< 0.57$ | $< 1.42$ |
| $m_a$ [eV] | $< 1.91$ | nb | $< 1.03$ | $< 1.65$ | $< 0.94$ | $< 1.03$ | $< 1.39$ | $< 2.13$ |
| $n_S$ | $0.973^{+0.015}_{-0.016}$ | – | $0.974 \pm 0.012$ | – | $0.978^{+0.010}_{-0.011}$ | – | $0.974^{+0.013}_{-0.014}$ | – |
| $\ln[10^{10} A_s]$ | $3.123^{+0.076}_{-0.075}$ | – | $3.116^{+0.076}_{-0.073}$ | – | $3.123 \pm 0.074$ | – | $3.111^{+0.068}_{-0.064}$ | – |
| $H_0 [\mathrm{Km\,s^{-1}\,Mpc^{-1}}]$ | $66.5^{+4.2}_{-5.1}$ | $59^{+9}_{-10}$ | $67.3^{+3.0}_{-3.4}$ | $63.1^{+6.3}_{-9.4}$ | $68.7 \pm 1.3$ | $68.4 \pm 1.4$ | $66.6^{+4.1}_{-4.7}$ | $60 \pm 7$ |
| $\sigma_8$ | $0.78^{+0.09}_{-0.11}$ | $0.68^{+0.18}_{-0.20}$ | $0.798^{+0.060}_{-0.066}$ | $0.75^{+0.11}_{-0.15}$ | $0.814^{+0.048}_{-0.052}$ | $0.858^{+0.078}_{-0.081}$ | $0.771^{+0.064}_{-0.074}$ | $0.70 \pm 0.13$ |
| $P_{s,1}$ | $\equiv 1.324$ | $< 7.66$ | $\equiv 1.303$ | $< 7.70$ | $\equiv 1.264$ | $< 7.75$ | $\equiv 1.296$ | $< 7.61$ |
| $P_{s,2}$ | $\equiv 1.147$ | $1.23^{+0.40}_{-0.37}$ | $\equiv 1.135$ | $1.20^{+0.40}_{-0.38}$ | $\equiv 1.125$ | $1.12^{+0.40}_{-0.37}$ | $\equiv 1.129$ | $1.23^{+0.39}_{-0.38}$ |
| $P_{s,3}$ | $\equiv 1.128$ | $0.73^{+0.40}_{-0.37}$ | $\equiv 1.116$ | $0.73^{+0.41}_{-0.38}$ | $\equiv 1.109$ | $0.76 \pm 0.43$ | $\equiv 1.110$ | $0.71^{+0.40}_{-0.36}$ |
| $P_{s,4}$ | $\equiv 1.108$ | $1.23^{+0.28}_{-0.27}$ | $\equiv 1.097$ | $1.21^{+0.27}_{-0.26}$ | $\equiv 1.093$ | $1.23^{+0.27}_{-0.26}$ | $\equiv 1.092$ | $1.23^{+0.28}_{-0.27}$ |
| $P_{s,5}$ | $\equiv 1.089$ | $1.15^{+0.18}_{-0.16}$ | $\equiv 1.079$ | $1.10^{+0.14}_{-0.12}$ | $\equiv 1.078$ | $1.08^{+0.13}_{-0.12}$ | $\equiv 1.073$ | $1.11^{+0.13}_{-0.12}$ |
| $P_{s,6}$ | $\equiv 1.070$ | $1.11 \pm 0.11$ | $\equiv 1.061$ | $1.083^{+0.093}_{-0.090}$ | $\equiv 1.063$ | $1.07^{+0.10}_{-0.09}$ | $\equiv 1.055$ | $1.078^{+0.076}_{-0.073}$ |
| $P_{s,7}$ | $\equiv 1.051$ | $1.057^{+0.090}_{-0.082}$ | $\equiv 1.043$ | $1.047^{+0.088}_{-0.086}$ | $\equiv 1.048$ | $1.058^{+0.098}_{-0.095}$ | $\equiv 1.038$ | $1.039^{+0.069}_{-0.065}$ |
| $P_{s,8}$ | $\equiv 1.033$ | $1.007^{+0.091}_{-0.088}$ | $\equiv 1.025$ | $1.007^{+0.095}_{-0.091}$ | $\equiv 1.033$ | $1.03 \pm 0.10$ | $\equiv 1.020$ | $0.995^{+0.078}_{-0.069}$ |
| $P_{s,9}$ | $\equiv 1.015$ | $0.987^{+0.090}_{-0.086}$ | $\equiv 1.008$ | $0.990^{+0.095}_{-0.091}$ | $\equiv 1.018$ | $1.02 \pm 0.10$ | $\equiv 1.003$ | $0.981^{+0.078}_{-0.074}$ |
| $P_{s,10}$ | $\equiv 0.997$ | $1.00 \pm 0.10$ | $\equiv 0.991$ | $0.991^{+0.097}_{-0.096}$ | $\equiv 1.003$ | $1.04^{+0.11}_{-0.10}$ | $\equiv 0.986$ | $1.004^{+0.088}_{-0.081}$ |
| $P_{s,11}$ | $\equiv 0.980$ | $< 3.72$ | $\equiv 0.975$ | $1.1^{+1.3}_{-0.8}$ | $\equiv 0.989$ | $2.6^{+1.9}_{-2.5}$ | $\equiv 0.970$ | $2.8^{+1.5}_{-1.9}$ |
| $P_{s,12}$ | $\equiv 0.895$ | nb | $\equiv 0.893$ | $< 3.14$ | $\equiv 0.919$ | nb | $\equiv 0.889$ | nb |

Table 7.3: As Tab. 7.1, but for the $\Lambda$CDM $+ m_a + \Sigma m_\nu$ model. From Ref. [26].

| Parameter | Planck TT,TE,EE+lowP | | Planck TT,TE,EE+lowP +MPkW | | Planck TT,TE,EE+lowP +BAO | | Planck TT,TE,EE+lowP +lensing | |
|---|---|---|---|---|---|---|---|---|
| $100\Omega_b h^2$ | $2.244^{+0.034}_{-0.035}$ | $2.237 \pm 0.040$ | $2.242^{+0.032}_{-0.031}$ | $2.233^{+0.037}_{-0.036}$ | $2.250^{+0.031}_{-0.030}$ | $2.248^{+0.038}_{-0.036}$ | $2.242^{+0.033}_{-0.037}$ | $2.234^{+0.041}_{-0.040}$ |
| $\Omega_c h^2$ | $0.1235^{+0.0034}_{-0.0036}$ | $0.1235^{+0.0040}_{-0.0043}$ | $0.1236 \pm 0.0033$ | $0.1243^{+0.0037}_{-0.0039}$ | $0.1223 \pm 0.0023$ | $0.1222^{+0.0028}_{-0.0030}$ | $0.1235 \pm 0.0034$ | $0.1230^{+0.0040}_{-0.0042}$ |
| $100\theta$ | $1.0402 \pm 0.0007$ | $1.0401 \pm 0.0007$ | $1.0403 \pm 0.0007$ | $1.0402 \pm 0.0007$ | $1.0405 \pm 0.0007$ | $1.0405 \pm 0.0006$ | $1.0403 \pm 0.0007$ | $1.0401 \pm 0.0007$ |
| $\tau$ | $0.093^{+0.035}_{-0.036}$ | $0.090 \pm 0.043$ | $0.088^{+0.034}_{-0.037}$ | $0.094^{+0.040}_{-0.038}$ | $0.092^{+0.034}_{-0.035}$ | $0.093^{+0.042}_{-0.041}$ | $0.083^{+0.033}_{-0.032}$ | $0.084 \pm 0.037$ |
| $\Sigma m_\nu$ [eV] | $< 0.44$ | $< 0.72$ | $< 0.32$ | $< 0.37$ | $< 0.16$ | $< 0.18$ | $< 0.53$ | $< 0.94$ |
| $m_a$ [eV] | $< 2.05$ | $< 2.37$ | $< 1.12$ | $< 1.79$ | $< 0.76$ | $< 1.18$ | $< 1.66$ | $< 2.33$ |
| $n_S$ | $0.972^{+0.011}_{-0.012}$ | – | $0.973 \pm 0.010$ | – | $0.9754^{+0.0093}_{-0.0089}$ | – | $0.972 \pm 0.011$ | – |
| $\ln[10^{10} A_s]$ | $3.130^{+0.068}_{-0.070}$ | – | $3.120^{+0.067}_{-0.071}$ | – | $3.126^{+0.066}_{-0.068}$ | – | $3.109^{+0.063}_{-0.061}$ | – |
| $H_0 [\mathrm{Km\,s^{-1}\,Mpc^{-1}}]$ | $66.7^{+3.1}_{-3.6}$ | $65.3^{+4.0}_{-4.7}$ | $67.4^{+2.3}_{-2.7}$ | $66.6^{+2.8}_{-3.0}$ | $68.6 \pm 1.1$ | $68.4^{+1.1}_{-1.2}$ | $66.4^{+3.3}_{-3.7}$ | $63.9^{+4.7}_{-5.1}$ |
| $\sigma_8$ | $0.781^{+0.081}_{-0.094}$ | $0.78^{+0.13}_{-0.12}$ | $0.806^{+0.054}_{-0.062}$ | $0.791^{+0.075}_{-0.081}$ | $0.827^{+0.039}_{-0.042}$ | $0.871^{+0.073}_{-0.081}$ | $0.767^{+0.066}_{-0.072}$ | $0.73^{+0.12}_{-0.11}$ |
| $P_{s,1}$ | $\equiv 1.346$ | $< 7.75$ | $\equiv 1.320$ | $< 7.70$ | $\equiv 1.299$ | $< 7.70$ | $\equiv 1.318$ | $< 7.26$ |
| $P_{s,2}$ | $\equiv 1.160$ | $1.17^{+0.39}_{-0.37}$ | $\equiv 1.144$ | $1.15^{+0.39}_{-0.36}$ | $\equiv 1.140$ | $1.13^{+0.38}_{-0.36}$ | $\equiv 1.136$ | $1.19^{+0.39}_{-0.36}$ |
| $P_{s,3}$ | $\equiv 1.139$ | $0.73^{+0.40}_{-0.38}$ | $\equiv 1.124$ | $0.74^{+0.40}_{-0.38}$ | $\equiv 1.122$ | $0.73^{+0.38}_{-0.37}$ | $\equiv 1.115$ | $0.71^{+0.39}_{-0.36}$ |
| $P_{s,4}$ | $\equiv 1.119$ | $1.26^{+0.24}_{-0.23}$ | $\equiv 1.105$ | $1.24^{+0.23}_{-0.23}$ | $\equiv 1.104$ | $1.24^{+0.23}_{-0.22}$ | $\equiv 1.095$ | $1.26 \pm 0.24$ |
| $P_{s,5}$ | $\equiv 1.098$ | $1.11^{+0.12}_{-0.11}$ | $\equiv 1.085$ | $1.11^{+0.11}_{-0.10}$ | $\equiv 1.087$ | $1.10 \pm 0.11$ | $\equiv 1.076$ | $1.11^{+0.11}_{-0.10}$ |
| $P_{s,6}$ | $\equiv 1.079$ | $1.089^{+0.097}_{-0.084}$ | $\equiv 1.066$ | $1.093^{+0.086}_{-0.084}$ | $\equiv 1.069$ | $1.076^{+0.091}_{-0.086}$ | $\equiv 1.056$ | $1.077^{+0.079}_{-0.076}$ |
| $P_{s,7}$ | $\equiv 1.059$ | $1.060^{+0.093}_{-0.087}$ | $\equiv 1.048$ | $1.068^{+0.085}_{-0.076}$ | $\equiv 1.052$ | $1.056^{+0.089}_{-0.083}$ | $\equiv 1.037$ | $1.042^{+0.073}_{-0.071}$ |
| $P_{s,8}$ | $\equiv 1.040$ | $1.036^{+0.092}_{-0.086}$ | $\equiv 1.030$ | $1.042^{+0.084}_{-0.083}$ | $\equiv 1.036$ | $1.036^{+0.090}_{-0.083}$ | $\equiv 1.018$ | $1.021^{+0.074}_{-0.071}$ |
| $P_{s,9}$ | $\equiv 1.021$ | $1.022^{+0.088}_{-0.087}$ | $\equiv 1.012$ | $1.026^{+0.083}_{-0.081}$ | $\equiv 1.019$ | $1.027 \pm 0.087$ | $\equiv 1.000$ | $1.007^{+0.074}_{-0.071}$ |
| $P_{s,10}$ | $\equiv 1.003$ | $1.03^{+0.10}_{-0.09}$ | $\equiv 0.994$ | $1.014^{+0.091}_{-0.085}$ | $\equiv 1.003$ | $1.04 \pm 0.10$ | $\equiv 0.982$ | $1.022^{+0.082}_{-0.080}$ |
| $P_{s,11}$ | $\equiv 0.985$ | $3.0^{+1.5}_{-2.6}$ | $\equiv 0.977$ | $0.94^{+1.1}_{-0.7}$ | $\equiv 0.987$ | $3.0^{+1.8}_{-2.6}$ | $\equiv 0.964$ | $3.3 \pm 1.3$ |
| $P_{s,12}$ | $\equiv 0.896$ | $< 8.61$ | $\equiv 0.892$ | $< 2.99$ | $\equiv 0.909$ | $< 8.53$ | $\equiv 0.878$ | nb |

Table 7.4: As Tab. 7.3, but for the Planck TT, TE, EE+lowP dataset. From Ref. [26].

# Chapter 8

# Inflationary Freedom and Primordial non-Gaussianities

*This Chapter is based on Ref. [33].*

The simplest models of inflation predict small non-Gaussianities and a featureless power spectrum. As we discussed in Chapter 6, however, a large number of well-motivated theoretical scenarios of inflation predict features in the power-spectrum. Hints of these feature have been observed in the CMB temperature spectrum at small multipoles. The scenarios that give origin to the features in the PPS could also generate large non-Gaussianities. We adopt the `PCHIP` parameterization presented in Section 6.2 to study, in a model-independent manner, how the constraints from future large scale structures (LSS) surveys on the local non-Gaussianity parameter $f_{\mathrm{NL}}$ change if the assumption of a power-law (PL) spectrum of initial perturbations is relaxed.

## 8.1  Introduction

We already discussed the fact that inflation has been introduced to explain the flatness problem, the horizon problem and the generation of the primordial perturbations seeding the evolution of our current Universe [36–43, 464–466]. The inflationary theories, however, could be confirmed as responsible for the Universe we observe today only if a signal of primordial gravitational waves would be detected. The different theories, nevertheless, may give different predictions for the power spectrum of the initial curvature perturbations $\mathcal{P}_{\mathcal{R}}(k)$. As we discussed in Subsection 1.9.2, the Primordial Power Spectrum (PPS) is usually assumed to be featureless, described by a simple power-law $\mathcal{P}_{\mathcal{R}}(k) \propto k^{n_s - 1}$ (see Eq. (1.144)), with $n_s$ the scalar spectral index. This might not be the correct case, and a vast number of models proposed in the past predict a non-standard PPS (see e.g. the review [395]). That is the case of slow-roll induced by phase transitions in the early Universe [467–469], by some inflationary potentials [392, 393, 470–491], by resonant particle production [492–496], variation in the sound speed of adiabatic modes [497, 498] or by trans-Planckian physics [499–503]. All the non-standard scenarios, of which this list is just a small fraction, as well as other non-canonical schemes [504–511], could lead to a PPS which may notably differ from the simple power-law parameterization.

Most of the inflationary models we listed above predict also deviations from the pure Gaussian initial conditions. Non-Gaussianities are usually described by a single parameter, $f_{\mathrm{NL}}$. In the matter-dominated Universe, the gauge-invariant Bardeen potential on large scales can be parametrized as [512–515]

$$\Phi_{\mathrm{NG}} = \Phi + f_{\mathrm{NL}} \left( \Phi^2 - \langle \Phi^2 \rangle \right) , \tag{8.1}$$

where $\Phi$ is a Gaussian random field. The non-Gaussianity parameter $f_{\mathrm{NL}}$ is often considered to be a constant, yielding non-Gaussianities of the *local* type.

Traditionally, the standard observable to constrain non-Gaussianities is the Cosmic Microwave Background (CMB), through the three point correlation function, or *bispectrum*. As

the odd power correlation functions vanish for the case of Gaussian random variables, the bispectrum provides the lowest order statistic to test any departure from Gaussianity. The bispectrum is much richer than the power spectrum, as it depends on both the scale and the shape of the power spectra of primordial perturbations. The current bound from the complete Planck mission for the local non-Gaussianity parameter is $f_{\mathrm{NL}} = 0.8 \pm 5.0$ (68% CL) [516].

The large scale structures (LSS) of the Universe provide an independent tool to test primordial non-Gaussianites, as shown in the pioneer works of Refs. [517] and [518]. Dark matter halos will be affected by the presence of non-Gaussianities, and a scale-dependent bias will characterize the non-Gaussian signal at large scales [519–525]. The strongest bounds on primordial non-Gaussianities obtained using exclusively LSS data are those obtained from the DR8 photometric data, see Ref. [526], which exploits 800000 quasars and finds $-49 < f_{\mathrm{NL}} < 31$ (see also Ref. [527]). While current LSS constraints are highly penalized by the systematic uncertainties, it has been shown by a number of authors that upcoming future LSS surveys will reach $\sigma(f_{\mathrm{NL}}) < 1$ [525, 528–538].

Despite the fact that the simplest models of inflation (i.e. single field, slow-rolling with a canonical kinetic term) predict small non-Gaussianities, there are some theoretical scenarios in which large non-Gaussianities could be generated, see e.g. Ref. [539] and references therein. The same deviations from the standard slow-roll inflation that give rise to non-Gaussianities could also be a potential source for other features in the PPS [469], which are absent in the simplest models of inflation. For example, both a non-canonical PPS and large non-Gaussianities can be generated simultaneously in scenarios involving particle production during inflation [496]. These two phenomena could also appear together in single field models with non-standard inflationary potentials [474, 475, 478, 486, 488, 490], as well as in multi-field inflationary models [487] and Brane Inflation [483]. Finally, preheating scenarios [540, 541] are other examples of models that give rise to both a non-standard PPS and non-Gaussianities.

As nature could have chosen other inflationary scenarios rather than the single field slow-roll paradigm, it is interesting to explore how the forecasts for LSS surveys concerning future measurements of $f_{\mathrm{NL}}$ are affected when the assumption of a standard PPS is relaxed, possibly adopting a model-independent description of the PPS. This has never been done before while forecasting errors on the $f_{\mathrm{NL}}$ parameter and it is a mandatory calculation, because models which will produce non-Gaussianities will likely give rise to a non-standard PPS as well. Even if non-Gaussianities and distortions of the PPS are expected to be governed by the same fundamental physics, the underlying inflationary mechanism is unknown a priori. A conservative and general approach is therefore to treat these two physical effects as independent and to be determined simultaneously. In this Chapter we adopt this strategy.

Following Ref. [33] on which this Chapter is based, we structure the discussion in this way: we start describing the parameterization of the PSS used here in Sec. 8.2, we describe the scale-dependent halo bias in the matter power spectrum in Subsection 8.3.1, while Subsection 8.3.2 is about the methodology followed for our calculations as well as the specifications of the future LSS survey illustrated here. We present our results in Subsec. 8.3.3 and we draw our conclusions in Sec. 8.4.

## 8.2   Primordial power spectrum

We discussed in Chapter 6 that, in principle, a non-standard shape for the PPS (see Ref. [395] and references therein), can be generated by many inflationary models (see e.g. Ref. [394] for some compilation) that goes beyond the simplest one. A power-law PPS of scalar and tensor perturbations is the simplest possibility, but it may not be the correct one. In order to explore the robustness of future forecasted errors from LSS surveys on the local non-Gaussianity parameter $f_{\mathrm{NL}}$, we assume a non-parametric form for the PPS, following the prescriptions reported in Section 6.2. This is one of a number of possible methods explored in the literature [396–409, 415, 419, 420, 422, 424, 425, 429, 432, 435–437, 542–550].

In brief, we describe the PPS of the scalar perturbations as a function that interpolates the PPS values in a series of nodes at fixed position. The function we exploit to interpolate is named *piecewise cubic Hermite interpolating polynomial*, the `PCHIP` algorithm [439], described in details in Appendix A. The nodes we use to interpolate the PPS are twelve, located at the values of $k$ listed in Eq. (6.1). The nodes are equally spaced (in logarithmic scale) in the range $(k_2, k_{11})$, that has been shown to be well constrained by current cosmological data [436]. The extreme nodes in $k_1$ and $k_{12}$ are fixed to allow for a non-constant behavior of the PPS outside the well-constrained range. The `PCHIP` PPS is given by Eq. (6.2) and we parameterize the value of the PPS in the nodes with $P_{s,j}$.

## 8.3 Forecasts

### 8.3.1 Non-Gaussian halo bias

Non-Gaussianities as introduced in Eq. (8.1) induce a scale-dependent bias that affects the matter power spectrum at large scales. This scale-dependent bias reads as [517, 519]

$$\delta_g = b\,\delta_{\rm dm} \quad \text{where} \quad b = b_{\rm G} + \Delta b\,, \tag{8.2}$$

where $\delta_g (\delta_{\rm dm})$ are the galaxy (dark matter) overdensities, $b_{\rm G}$ is the Gaussian bias and $\Delta b$ reads as

$$\Delta b = 3 f_{\rm NL} (1 - b_{\rm G}) \delta_{\rm c} \frac{H_0^2 \Omega_{\rm m}}{k^2 T(k) D(a)}\,, \tag{8.3}$$

where $T(k)$ is the linear transfer function. The growth factor $D(a)$ is defined as $\delta_{\rm dm}(a)/\delta_{\rm dm}(a = 1)$ and $\delta_c$ refers to the critical linear overdensity for spherical collapse [551]. The power spectrum with the inclusion of non-Gaussianities is obtained using

$$P_{\rm ng} = P \left( b_G + \Delta b + f\mu_k^2 \right)^2\,, \tag{8.4}$$

where $\mu_k$ is the cosine of the angle between the line of sight and the wave vector $k$ and $f$ is defined as $d\ln\delta_{\rm dm}/d\ln a$. $P$ is the dark matter power spectrum, whose $k$ dependence is driven either by Eq. (6.2) or by the standard power-law PPS in Eq. (1.144) (given the amplitude $A_s$ and the slope $n_s$).

In the top panel of Fig. 8.1 we plot the galaxy power spectrum in absence of non-Gaussianities (i.e. for $f_{\rm NL} = 0$) and for $f_{\rm NL} = 20$. The red dashed line indicates that using a `PCHIP` PPS with $f_{\rm NL} = 0$ it is possible to reproduce the galaxy power spectrum obtained with a standard power-law PPS and $f_{\rm NL} \neq 0$. The $P_{s,j}$ values needed to obtain such an effect were taken within their 95% CL allowed regions [25]. This shows that large degeneracies between the $P_{s,j}$ nodes and the $f_{\rm NL}$ parameter may appear. The large value $f_{\rm NL} = 20$, albeit allowed by the current LSS limits on local non-Gaussianities, is much larger than the expected errors from the upcoming galaxy surveys (see e.g. Refs. [530, 552]). Therefore, we also illustrate in the bottom panel of Fig. 8.1 the equivalent plot for $f_{\rm NL} = 5$. In this case, the values for the PPS nodes $P_{s,j}$ required to match the predictions obtained with the PL PPS lie within their 68% CL allowed regions [25]. We can notice that the degeneracies are still present: we therefore expect that the forecasted errors on $f_{\rm NL}$ are largely affected by the uncertainties on the precise PPS shape.

### 8.3.2 Methodology

We focus here on the future spectroscopic galaxy survey DESI (Dark Energy Spectroscopic Instrument) experiment [553]. Although multi-band, full-sky imaging surveys have been shown to be the optimal setups to constrain non-Gaussianities via LSS measurements [525, 528], the purpose of the current analysis is to explore the degeneracies with the PPS parameterization rather than to optimize the $f_{\rm NL}$ sensitivity. For this reason, we restrict
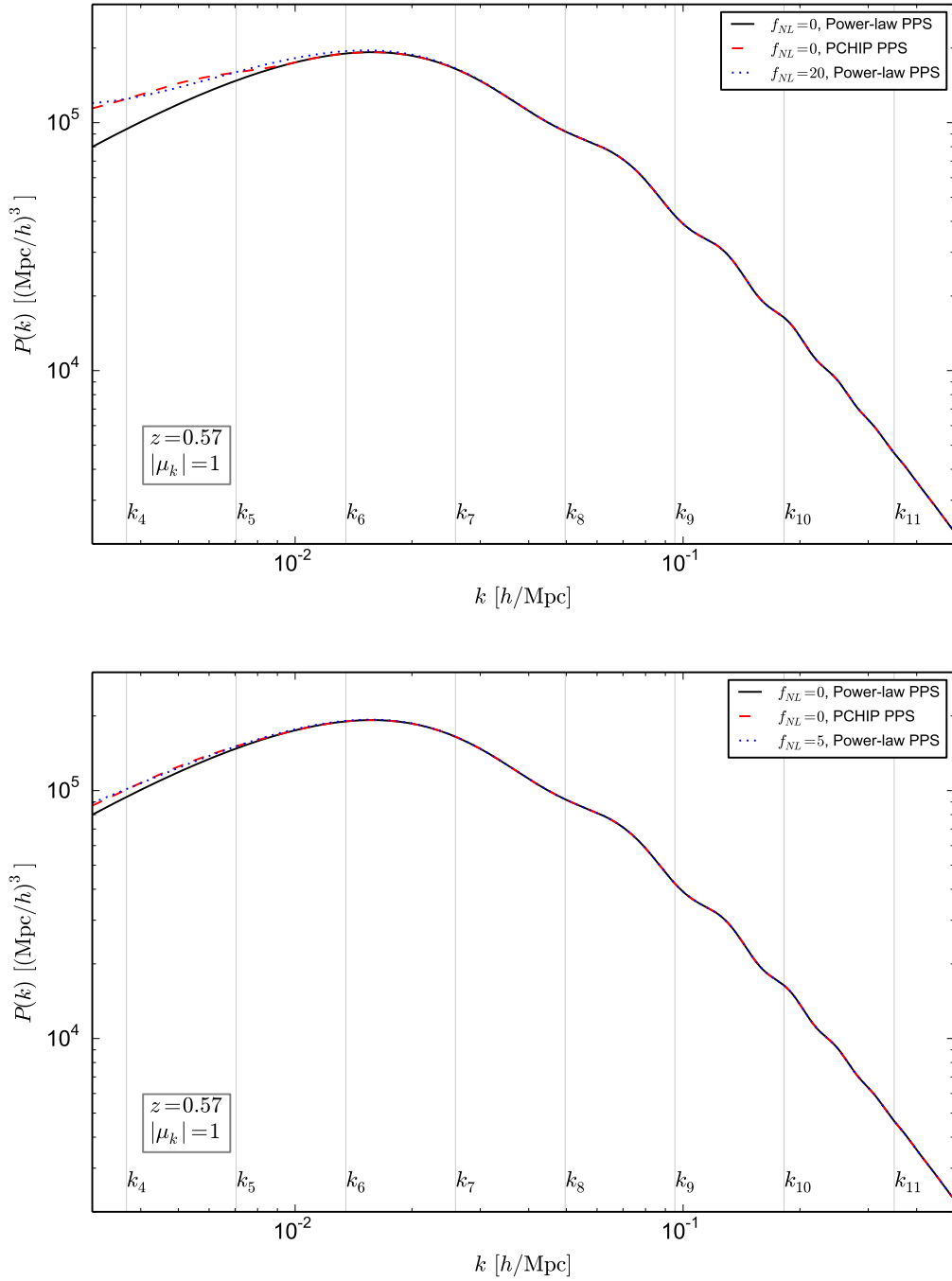
Figure 8.1: The top panel depicts the galaxy power spectrum obtained with the power-law PPS case, for $f_{\mathrm{NL}} = 0$ (black solid curve) and $f_{\mathrm{NL}} = 20$ (blue dotted curve), together with one obtained with a `PCHIP` PPS (red dashed lines) for $f_{\mathrm{NL}} = 0$. The values of the `PCHIP` PPS nodes are chosen accordingly to match the predictions of the $f_{\mathrm{NL}} = 20$ case. The bottom panel shows the same for $f_{\mathrm{NL}} = 5$, with appropriate changes of the values of the `PCHIP` PPS nodes. The labels $k_i$ for $i = 4, \ldots, 11$ indicate the $k$ position of the five nodes considered in our analysis ($i = 5, \ldots, 9$), plus the nodes $k_4$, $k_{10}$, $k_{11}$ that lie outside the $k$ range probed by the DESI experiment. The galaxy power spectra are obtained for $z = 0.57$, $|\mu_k| = 1$ and assuming a constant Gaussian bias $b_G$. From Ref. [33].

ourselves to the DESI galaxy redshift survey, but similar results would be obtained with the results of the ESA Euclid instrument [554].

In order to compute the expected errors on the local non-Gaussianity parameter, we follow here the usual Fisher matrix approach. The elements of the Fisher matrix, as long as the posterior distribution for the parameters can be approximated by a Gaussian function, are [555–557]

$$F_{\alpha\beta} = \frac{1}{2}\mathrm{Tr}\left[C^{-1}C_{,\alpha}C^{-1}C_{,\beta}\right]\;, \tag{8.5}$$

where $C = S + N$ is the total covariance. The covariance matrix contains both the signal $S$ and the noise $N$ terms, and $C_{,\alpha}$ indicates its derivatives with respect to the cosmological parameter $p_\alpha$ in the context of the underlying fiducial model. The 68% CL marginalized errors on a given parameter $p_\alpha$ are $\sigma(p_\alpha) = \sqrt{(F^{-1})_{\alpha\alpha}}$, where $F^{-1}$ is the inverse of the Fisher matrix. In order to highlight the differences in the errors on the $f_{\mathrm{NL}}$ parameter arising from different PPS choices, we only consider information concerning non-Gaussianities from LSS data, and we neglect the information that could be added from the measurements of the CMB bispectrum.

Our LSS Fisher matrix reads as [83]

$$
\begin{aligned}
F^{\mathrm{LSS}}_{\alpha\beta} &= \int_{\vec{k}_{\min}}^{\vec{k}_{\max}} \frac{\partial \ln P_{\mathrm{ng}}(\vec{k})}{\partial p_\alpha} \frac{\partial \ln P_{\mathrm{ng}}(\vec{k})}{\partial p_\beta} V_{\mathrm{eff}}(\vec{k}) \frac{d\vec{k}}{2(2\pi)^3} \\
&= \int_{-1}^{1} \int_{k_{\min}}^{k_{\max}} \frac{\partial \ln P_{\mathrm{ng}}(k,\mu_k)}{\partial p_\alpha} \frac{\partial \ln P_{\mathrm{ng}}(k,\mu_k)}{\partial p_\beta} V_{\mathrm{eff}}(k,\mu_k) \\
&\quad \frac{2\pi k^2 dk d\mu_k}{2(2\pi)^3}\,,
\end{aligned}
\tag{8.6}
$$

where $V_{\mathrm{eff}}$ is the effective volume of the survey. It is calculated as

$$V_{\mathrm{eff}}(k,\mu_k) = \left[\frac{nP_{\mathrm{ng}}(k,\mu_k)}{nP_{\mathrm{ng}}(k,\mu_k)+1}\right]^2 V_{\mathrm{survey}}\,, \tag{8.7}$$

where $P_{\mathrm{ng}}$ is the power spectrum calculated with the inclusion of non-Gaussianities (see Eq. (8.4)) and $n$ refers to the galaxy number density per redshift bin. We assume $k_{\max} = 0.1h/\mathrm{Mpc}$ and we choose $k_{\min} = 2\pi/V^{1/3}$, where $V$ represents the volume of the redshift bin. The DESI survey is expected to cover 14000 deg$^2$ of the sky in the range $0.15 < z < 1.85$, divided in redshift bins of width $\Delta z = 0.1$. We follow Ref. [558] for the number densities $n(z)$ and biases $b_G(z)$ associated to the three types of DESI tracers: Luminous Red Galaxies (LRGs), Emission Line Galaxies (ELGs) and high-redshift quasars (QSOs). We include the redshift dependence of the (fiducial) bias $b_G$ in Eq. (8.4) as follows: $b_G(z)D(z) = 0.84, 1.7, 1.2$ for ELG, LRG and QSO's respectively, where $D(z)$ is the growth factor as a function of the redshift, as in Eq. (8.3). Since we want to combine the three different Fishers matrices from the three DESI tracers (LRGs, ELGs and QSOs), we adopt the multi-tracer formalism developed in Ref. [559]. In the work, the authors present a generic expression for the Fisher information matrix of surveys with any number of tracers. The multi-tracer technique provides constraints that can surpass those set by cosmic variance, since the possible tracers of LSS can present differences in their clustering.

We remind that the observed size of an object or of a feature at a redshift $z$ is obtained in terms of the redshift and the angular quantities $\Delta z$ and $\Delta \theta$. These two quantities are related to the comoving distances $r_\parallel$ and $r_\perp$, along and across the line of sight respectively, through the angular diameter distance $D_A(z)$ and the Hubble rate $H(z)$. The same applies to the Fourier transform associated variables, $k_\parallel$ and $k_\perp$ for the dual coordinates of $r_\parallel$ and $r_\perp$. Therefore, when reconstructing the measurements of galaxy redshifts and positions in some reference cosmological model which differs from a given fiducial cosmology, one has to take into account the geometrical effects [83]:

$$P_{obs}(k_\parallel^{ref}, k_\perp^{ref}) = \frac{D_A(z)|_{ref}^2}{D_A(z)^2} \frac{H(z)}{H(z)|_{ref}} P_{fid}(k_\parallel, k_\perp)\,, \tag{8.8}$$

where the *ref* sub/superscript denote quantities in the reference cosmological model[1]. We properly take into account these effects in our Fisher matrix forecasts when taking numerical derivatives of the galaxy power spectrum with respect to the cosmological parameters at given values of $|\mathbf{k}|$ and $\mu_k$, that are the equivalent of $k_\parallel$ and $k_\perp$.

In addition to the Fisher matrix forecasts, we will also compute the expected shift in the $f_{\rm NL}$ parameter if the $P_{s,j}$ parameters (with $j = 5, \ldots, 9$) describing the PCHIP PPS are incorrectly set to values different from their fiducial ones. For that purpose, we use the method developed by the authors of Ref. [560]. This is the main idea: if the future DESI data are fitted assuming a cosmological model with fixed values of $P_{s,j}$, corresponding to fix both $n_s$ and $A_s$ to their best-fit values, the model is characterized by $n' = 5$ parameters $\mathcal{M}' = \{\Omega_b h^2, \Omega_c h^2, h, f_{\rm NL}, w\}$. If the true underlying cosmology is a model with different values of the $P_{s,j}$ and it is characterized by $n = 10$ parameters $\mathcal{M} = \{\Omega_b h^2, \Omega_c h^2, h, f_{\rm NL}, w, P_{s,j}\}$ (with $j = 5, \ldots, 9$), the values inferred for the $n' = 5$ parameters will be shifted from their true values to compensate for the fact that the model used to fit the data is wrong. Under the assumption of a Gaussian likelihood, the shifts in the $n'$ parameters are [560]

$$\delta\theta'_\alpha = -(F'^{-1})_{\alpha\beta} G_{\beta\zeta} \delta\psi_\zeta \qquad \begin{aligned} &\alpha, \beta = 1 \ldots n', \\ &\zeta = n' + 1 \ldots n, \end{aligned} \tag{8.9}$$

where $F'$ is the Fisher matrix for the model with $n'$ parameters (with fixed $P_{s,j}$) and $G$ denotes the Fisher matrix for the $n$ parameters model (including the previous $n'$ parameters and the PCHIP parameters).

In the following, unless otherwise stated, we adopt the best-fit values from the recent Planck release [44], which corresponds to $A_s = 2.2 \times 10^{-9}$ and $n_s = 0.965$ at the pivot scale $k_{pivot} = 0.05$ for the standard power-law PPS. When we consider the PCHIP parameterization, the best-fit values of the nodes we considered in the numerical analyses are: $P_{s,5} = 1.07099$, $P_{s,6} = 1.04687$, $P_{s,7} = 1.02329$, $P_{s,8} = 1.00024$ and $P_{s,9} = 0.97771$. These values are obtained calculating the value of the best-fit PL PPS at the positions of the nodes $k_5$ to $k_9$ using Eq. (6.3), given the Planck 2015 best-fit values for $A_s$ and $n_s$. The nodes $P_{s,j}$ corresponding to $j < 5$ and $j > 9$ are outside the range of wavemodes that the DESI survey is expected to cover, considering the values of $k_{\rm max}$ and $k_{\rm min}$ that we adopt here.

### 8.3.3 Results

We present now the results obtained from our Fisher matrix calculations, for the two fiducial cosmologies explored here: one in which the PPS is described by the standard power-law form, and a second one where we assume a free PPS, described by the PCHIP parameterization. The parameters describing the model with a PL PPS are the baryon and cold dark matter energy densities $\Omega_b h^2$ and $\Omega_c h^2$, the reduced Hubble parameter $h$, the scalar spectral index $n_s$, the amplitude of the PPS $A_s$ and the equation of state of the dark energy component $w$. The PCHIP PPS case is also described by $\Omega_b h^2$, $\Omega_c h^2$, $h$, $w$, plus five nodes $P_{s,j}$ with $j \in 5, \ldots, 9$. Non-Gaussianities of the local type are included in both the fiducial cosmologies via the $f_{\rm NL}$ parameter. All the results described below, unless otherwise stated, refer to the analysis of the three DESI tracers (ELGs, LRGs and QSOs). This means that they have been obtained exploiting exclusively the scale-dependent biases imprinted in the power spectra of these three types of tracers.

Table 8.1 (8.2) shows the $1\sigma$ marginalized errors for the case of a standard (PCHIP) PPS, for a fiducial value $f_{\rm NL} = 20$ for each of the DESI tracers and from the combination of all of them, obtained using the multi-tracer technique. Even if such a value of the $f_{\rm NL}$ parameter is larger than the expected sensitivity from future probes, it is still allowed by current LSS bounds on primordial non-Gaussianities. Notice that, for the standard PL PPS, the expected error on $f_{\rm NL}$ is 19.9, 10.1 and 8.56 for LRGs, ELGs and QSOs respectively, while in the case of the PCHIP parameterization, we obtain $\sigma(f_{\rm NL}) = 32.2$, 13.3 and 12.6 respectively. Therefore,

---

[1] $k_\parallel = k_\parallel^{ref} D_A(z)|_{ref}/D_A(z)$ and $k_\perp = k_\perp^{ref} H(z)/H(z)|_{ref}$.

| | fiducial | LRG | ELG | QSO | All |
|---|---|---|---|---|---|
| $\Omega_b h^2$ | 0.02267 | $4.78 \times 10^{-3}$ | $4.86 \times 10^{-3}$ | $5.11 \times 10^{-3}$ | $2.38 \times 10^{-3}$ |
| $\Omega_c h^2$ | 0.1131 | $1.75 \times 10^{-2}$ | $1.65 \times 10^{-2}$ | $1.51 \times 10^{-2}$ | $7.70 \times 10^{-3}$ |
| $h$ | 0.705 | $5.02 \times 10^{-2}$ | $5.01 \times 10^{-2}$ | $4.69 \times 10^{-2}$ | $2.42 \times 10^{-2}$ |
| $n_s$ | 0.96 | $5.68 \times 10^{-2}$ | $4.28 \times 10^{-2}$ | $4.12 \times 10^{-2}$ | $1.96 \times 10^{-2}$ |
| $A_s$ | $2.2 \times 10^{-9}$ | 0.341 | 0.331 | 0.302 | 0.156 |
| $f_{\rm NL}$ | 20 | 19.9 | 10.1 | 8.56 | 4.79 |
| $w$ | $-1$ | $5.38 \times 10^{-2}$ | $4.09 \times 10^{-2}$ | $6.18 \times 10^{-2}$ | $2.36 \times 10^{-2}$ |

Table 8.1: Marginalized $1\sigma$ constraints on the parameters associated to the PL PPS assuming a fiducial value $f_{\rm NL} = 20$. The error on the amplitude of the power spectrum is evaluated on $A_s/(2.2 \cdot 10^{-9})$. From Ref. [33].

| | fiducial | LRG | ELG | QSO | All |
|---|---|---|---|---|---|
| $\Omega_b h^2$ | 0.02267 | $7.85 \times 10^{-3}$ | $3.65 \times 10^{-3}$ | $4.70 \times 10^{-3}$ | $2.30 \times 10^{-3}$ |
| $\Omega_c h^2$ | 0.1131 | $2.30 \times 10^{-2}$ | $1.11 \times 10^{-2}$ | $1.41 \times 10^{-2}$ | $6.36 \times 10^{-3}$ |
| $h$ | 0.705 | $7.67 \times 10^{-2}$ | $3.59 \times 10^{-2}$ | $4.62 \times 10^{-2}$ | $2.12 \times 10^{-2}$ |
| $P_{s,5}$ | 1.07099 | 0.340 | 0.169 | 0.212 | 0.111 |
| $P_{s,6}$ | 1.04687 | 0.419 | 0.198 | 0.254 | 0.119 |
| $P_{s,7}$ | 1.02329 | 0.451 | 0.216 | 0.276 | 0.125 |
| $P_{s,8}$ | 1.00024 | 0.479 | 0.229 | 0.293 | 0.132 |
| $P_{s,9}$ | 0.97771 | 0.482 | 0.234 | 0.298 | 0.134 |
| $f_{\rm NL}$ | 20 | 32.2 | 13.3 | 12.6 | 6.43 |
| $w$ | $-1$ | $4.03 \times 10^{-2}$ | $2.80 \times 10^{-2}$ | $4.45 \times 10^{-2}$ | $2.45 \times 10^{-2}$ |

Table 8.2: Marginalized $1\sigma$ constraints on the parameters associated to the non-standard PPS assuming $f_{\rm NL} = 20$. From Ref. [33].

| | fiducial | LRG | ELG | QSO | All |
|---|---|---|---|---|---|
| $\Omega_b h^2$ | 0.02267 | $2.67 \times 10^{-4}$ | $2.63 \times 10^{-4}$ | $2.66 \times 10^{-4}$ | $2.59 \times 10^{-4}$ |
| $\Omega_c h^2$ | 0.1131 | $1.64 \times 10^{-3}$ | $1.44 \times 10^{-3}$ | $1.52 \times 10^{-3}$ | $1.24 \times 10^{-3}$ |
| $h$ | 0.705 | $6.66 \times 10^{-3}$ | $5.24 \times 10^{-3}$ | $5.86 \times 10^{-3}$ | $4.12 \times 10^{-3}$ |
| $n_s$ | 0.96 | $6.72 \times 10^{-2}$ | $6.41 \times 10^{-2}$ | $6.53 \times 10^{-2}$ | $5.84 \times 10^{-3}$ |
| $A_s$ | $2.2 \times 10^{-9}$ | $3.87 \times 10^{-2}$ | $3.28 \times 10^{-2}$ | $3.51 \times 10^{-2}$ | $2.71 \times 10^{-2}$ |
| $f_{\rm NL}$ | 20 | 17.4 | 9.14 | 7.58 | 4.56 |
| $w$ | $-1$ | $4.51 \times 10^{-2}$ | $3.36 \times 10^{-2}$ | $5.44 \times 10^{-2}$ | $2.17 \times 10^{-2}$ |

Table 8.3: As Tab. 8.1 but including CMB priors. From Ref. [33].

the error on $f_{\rm NL}$ is much larger when a `PCHIP` PPS is assumed, up to the 60% level. The constraints on the remaining cosmological parameters are barely affected by the different assumption on the PPS. In some cases, their error is even smaller than in the standard power-law scenario. This is indeed the case of the equation of state parameter $w$, or of $\Omega_b h^2$ and $\Omega_c h^2$. The errors on the latter two parameters are smaller than in the PL PPS approach only when exploiting either ELGs or QSOs tracers. The combination of the data from the three tracers exploiting the multi-tracer technique alleviates the problem with the error on $f_{\rm NL}$. In fact, the value of $\sigma(f_{\rm NL})$ increases only of about 40% when relaxing the assumption of a PL PPS, rather than of 60% as obtained with the separate tracers.

This generic increase in the error on $f_{\rm NL}$ arises from the large degeneracies between the non-Gaussianity parameter and the $P_{s,j}$ nodes, which is reduced when combining the tracers. The top and bottom panels of Fig. 8.2 illustrate the large degeneracies between the $f_{\rm NL}$

|  | fiducial | LRG | ELG | QSO | all |
|---|---|---|---|---|---|
| $\Omega_b h^2$ | 0.02267 | $3.92 \times 10^{-4}$ | $3.79 \times 10^{-4}$ | $3.87 \times 10^{-4}$ | $3.74 \times 10^{-4}$ |
| $\Omega_c h^2$ | 0.1131 | $1.36 \times 10^{-3}$ | $1.10 \times 10^{-3}$ | $1.18 \times 10^{-3}$ | $1.04 \times 10^{-3}$ |
| $h$ | 0.705 | $4.13 \times 10^{-3}$ | $3.14 \times 10^{-3}$ | $3.62 \times 10^{-3}$ | $2.93 \times 10^{-3}$ |
| $P_{s,5}$ | 1.07099 | $2.98 \times 10^{-2}$ | $2.69 \times 10^{-2}$ | $2.77 \times 10^{-2}$ | $2.60 \times 10^{-2}$ |
| $P_{s,6}$ | 1.04687 | $2.89 \times 10^{-2}$ | $2.10 \times 10^{-2}$ | $2.32 \times 10^{-2}$ | $1.99 \times 10^{-2}$ |
| $P_{s,7}$ | 1.02329 | $2.00 \times 10^{-2}$ | $1.73 \times 10^{-2}$ | $1.84 \times 10^{-2}$ | $1.69 \times 10^{-2}$ |
| $P_{s,8}$ | 1.00024 | $1.92 \times 10^{-2}$ | $1.76 \times 10^{-2}$ | $1.86 \times 10^{-2}$ | $1.73 \times 10^{-2}$ |
| $P_{s,9}$ | 0.97771 | $2.59 \times 10^{-2}$ | $2.31 \times 10^{-2}$ | $2.42 \times 10^{-2}$ | $2.22 \times 10^{-2}$ |
| $f_{\rm NL}$ | 20 | 13.0 | 6.85 | 5.64 | 4.75 |
| $w$ | $-1$ | $3.24 \times 10^{-2}$ | $2.46 \times 10^{-2}$ | $4.0 \times 10^{-2}$ | $2.28 \times 10^{-2}$ |

Table 8.4: As Tab. 8.2 but including CMB priors. From Ref. [33].

|  | fiducial | LRG | ELG | QSO | All |
|---|---|---|---|---|---|
| $\Omega_b h^2$ | 0.02267 | $4.78 \times 10^{-3}$ | $5.17 \times 10^{-3}$ | $5.18 \times 10^{-3}$ | $2.45 \times 10^{-3}$ |
| $\Omega_c h^2$ | 0.1131 | $1.73 \times 10^{-2}$ | $1.73 \times 10^{-2}$ | $1.52 \times 10^{-2}$ | $7.88 \times 10^{-3}$ |
| $h$ | 0.705 | $5.0 \times 10^{-2}$ | $5.29 \times 10^{-2}$ | $4.75 \times 10^{-2}$ | $2.48 \times 10^{-2}$ |
| $n_s$ | 0.96 | $5.59 \times 10^{-2}$ | $4.40 \times 10^{-2}$ | $4.11 \times 10^{-2}$ | $2.0 \times 10^{-2}$ |
| $A_s$ | $2.2 \times 10^{-9}$ | 0.339 | 0.347 | 0.305 | 0.160 |
| $f_{\rm NL}$ | 5 | 18.9 | 9.32 | 7.83 | 4.45 |
| $w$ | $-1$ | $5.38 \times 10^{-2}$ | $4.13 \times 10^{-2}$ | $6.19 \times 10^{-2}$ | $2.38 \times 10^{-2}$ |

Table 8.5: Marginalized 1-$\sigma$ constraints on the parameters associated to the PL PPS assuming a fiducial value $f_{\rm NL} = 5$. The error on the amplitude of the power spectrum is evaluated on $A_s/(2.2 \cdot 10^{-9})$. From Ref. [33].

|  | fiducial | LRG | ELG | QSO | All |
|---|---|---|---|---|---|
| $\Omega_b h^2$ | 0.02267 | $7.72 \times 10^{-3}$ | $3.61 \times 10^{-3}$ | $4.61 \times 10^{-3}$ | $2.31 \times 10^{-3}$ |
| $\Omega_c h^2$ | 0.1131 | $2.28 \times 10^{-2}$ | $1.09 \times 10^{-2}$ | $1.38 \times 10^{-2}$ | $6.37 \times 10^{-3}$ |
| $h$ | 0.705 | $7.56 \times 10^{-2}$ | $3.54 \times 10^{-2}$ | $4.52 \times 10^{-2}$ | $2.13 \times 10^{-2}$ |
| $P_{s,5}$ | 1.07099 | 0.342 | 0.169 | 0.215 | 0.113 |
| $P_{s,6}$ | 1.04687 | 0.415 | 0.196 | 0.251 | 0.120 |
| $P_{s,7}$ | 1.02329 | 0.445 | 0.212 | 0.270 | 0.126 |
| $P_{s,8}$ | 1.00024 | 0.472 | 0.225 | 0.287 | 0.133 |
| $P_{s,9}$ | 0.97771 | 0.476 | 0.230 | 0.292 | 0.135 |
| $f_{\rm NL}$ | 5 | 29.3 | 11.9 | 10.7 | 5.97 |
| $w$ | $-1$ | $4.02 \times 10^{-2}$ | $2.79 \times 10^{-2}$ | $4.45 \times 10^{-2}$ | $2.44 \times 10^{-2}$ |

Table 8.6: Marginalized $1\sigma$ constraints on the parameters associated to the non-standard PPS assuming $f_{\rm NL} = 5$. From Ref. [33].

parameter and two of the PCHIP PPS nodes, $P_{s,5}$ and $P_{s,9}$, for the fiducial value $f_{\rm NL} = 20$. We only show the degeneracies with two nodes, but they are similar to the ones with the remaining nodes.

The problem of the degeneracy could be solved in two ways, either exploiting smaller scales in the observed galaxy or quasar power spectra, or using CMB priors. In practice, going to the mildly non-linear regime would require new additional $P_{s,j}$ nodes, with the consequence that new degeneracies between these additional $P_{s,j}$ nodes and the non-Gaussianity parameter $f_{\rm NL}$ would appear. Indeed, we have numerically checked that such a possibility does not solve the problem. Furthermore, a non-linear description of the matter power spectrum would

| | fiducial | LRG | ELG | QSO | All |
|---|---|---|---|---|---|
| $\Omega_b h^2$ | 0.02267 | $2.67 \times 10^{-4}$ | $2.63 \times 10^{-4}$ | $2.67 \times 10^{-4}$ | $2.59 \times 10^{-4}$ |
| $\Omega_c h^2$ | 0.1131 | $1.64 \times 10^{-3}$ | $1.43 \times 10^{-3}$ | $1.52 \times 10^{-3}$ | $1.24 \times 10^{-3}$ |
| $h$ | 0.705 | $6.66 \times 10^{-3}$ | $5.23 \times 10^{-3}$ | $5.85 \times 10^{-3}$ | $4.11 \times 10^{-3}$ |
| $n_s$ | 0.96 | $6.71 \times 10^{-3}$ | $6.40 \times 10^{-3}$ | $6.53 \times 10^{-3}$ | $5.84 \times 10^{-3}$ |
| $A_s$ | $2.2 \times 10^{-9}$ | $3.87 \times 10^{-2}$ | $3.27 \times 10^{-2}$ | $3.51 \times 10^{-2}$ | $2.70 \times 10^{-2}$ |
| $f_{\mathrm{NL}}$ | 5 | 16.8 | 8.56 | 7.12 | 4.27 |
| $w$ | $-1$ | $4.50 \times 10^{-2}$ | $3.36 \times 10^{-2}$ | $5.43 \times 10^{-2}$ | $2.17 \times 10^{-2}$ |

Table 8.7: As Tab. 8.5 but including CMB priors. From Ref. [33].

| | fiducial | LRG | ELG | QSO | all |
|---|---|---|---|---|---|
| $\Omega_b h^2$ | 0.02267 | $3.92 \times 10^{-4}$ | $3.79 \times 10^{-4}$ | $3.86 \times 10^{-4}$ | $3.75 \times 10^{-4}$ |
| $\Omega_c h^2$ | 0.1131 | $1.36 \times 10^{-3}$ | $1.10 \times 10^{-3}$ | $1.18 \times 10^{-3}$ | $1.04 \times 10^{-3}$ |
| $h$ | 0.705 | $4.10 \times 10^{-3}$ | $3.13 \times 10^{-3}$ | $3.59 \times 10^{-3}$ | $2.92 \times 10^{-3}$ |
| $P_{s,5}$ | 1.07099 | $2.98 \times 10^{-2}$ | $2.68 \times 10^{-2}$ | $2.77 \times 10^{-2}$ | $2.60 \times 10^{-2}$ |
| $P_{s,6}$ | 1.04687 | $2.89 \times 10^{-2}$ | $2.11 \times 10^{-2}$ | $2.33 \times 10^{-2}$ | $2.0 \times 10^{-2}$ |
| $P_{s,7}$ | 1.02329 | $2.00 \times 10^{-2}$ | $1.73 \times 10^{-2}$ | $1.84 \times 10^{-2}$ | $1.69 \times 10^{-2}$ |
| $P_{s,8}$ | 1.00024 | $1.92 \times 10^{-2}$ | $1.76 \times 10^{-2}$ | $1.86 \times 10^{-2}$ | $1.73 \times 10^{-2}$ |
| $P_{s,9}$ | 0.97771 | $2.50 \times 10^{-2}$ | $2.31 \times 10^{-2}$ | $2.43 \times 10^{-2}$ | $2.22 \times 10^{-2}$ |
| $f_{\mathrm{NL}}$ | 5 | 12.4 | 6.42 | 5.23 | 4.46 |
| $w$ | $-1$ | $3.23 \times 10^{-2}$ | $2.46 \times 10^{-2}$ | $3.99 \times 10^{-2}$ | $2.27 \times 10^{-2}$ |

Table 8.8: As Tab. 8.6 but including CMB priors. From Ref. [33].

depend on additional parameters, enlarging the number of degeneracies. In contrast, the CMB priors on the PPS parameters, as well as on the dark matter and baryon mass-energy densities, help enormously in solving the problem of the large degeneracies between the PPS parameterization and non-Gaussianities. Tables 8.3 and 8.4 show the equivalent of Tables 8.1 and 8.2 with the inclusion of CMB priors from the Planck mission 2013 data [72]. Notice that the impact of the Planck priors is largely more significant in the PCHIP parameterization case: the $f_{\mathrm{NL}}$ errors arising from the three different dark matter tracers when the CMB information is included are smaller in the PCHIP PSS description than in the PL PSS approach. When the multi-tracer technique is applied, the overall errors after considering Planck 2013 CMB constraints are very similar, regardless on the PPS description and close to $\sigma(f_{\mathrm{NL}}) \simeq 5$.

Table 8.5 (8.6) shows the $1\sigma$ marginalized errors for the case of a PL (PCHIP) PPS, for another possible fiducial value of the non-Gaussianity parameter, $f_{\mathrm{NL}} = 5$. Again, the errors are obtained from each of the DESI tracers, as well as from the multi-tracer technique that combines all of them. As in the case of $f_{\mathrm{NL}} = 20$, the error on the non-Gaussianity parameter increases when the PPS parameterization is changed, reaching in some cases a 60% increment. The results are very similar to those obtained and illustrated before for the larger non-Gaussianities. The errors on the other cosmological parameters remain unaffected by the choice of the PPS parameterization. The dark energy equation of state parameter is extracted with a smaller error in the PCHIP PPS case, and also $\Omega_b h^2$ and $\Omega_c h^2$ are determined with a smaller error in that case from the analyses of the ELGs and QSOs tracers. The multi-tracer technique provides a reduction on the $f_{\mathrm{NL}}$ error that is similar to the one obtained in the previous case with $f_{\mathrm{NL}} = 20$. The top and bottom right panels of Fig. 8.2 illustrate the large degeneracies between the non-Gaussianity parameter $f_{\mathrm{NL}}$ and the nodes $P_{s,5}$ and $P_{s,9}$, for the fiducial value $f_{\mathrm{NL}} = 5$. We can notice that the degeneracy pattern appears to be independent of the value of $f_{\mathrm{NL}}$. The addition of the CMB priors reduces the errors on all the cosmological parameters, including $f_{\mathrm{NL}}$, to the same values in both PPS parameterizations,
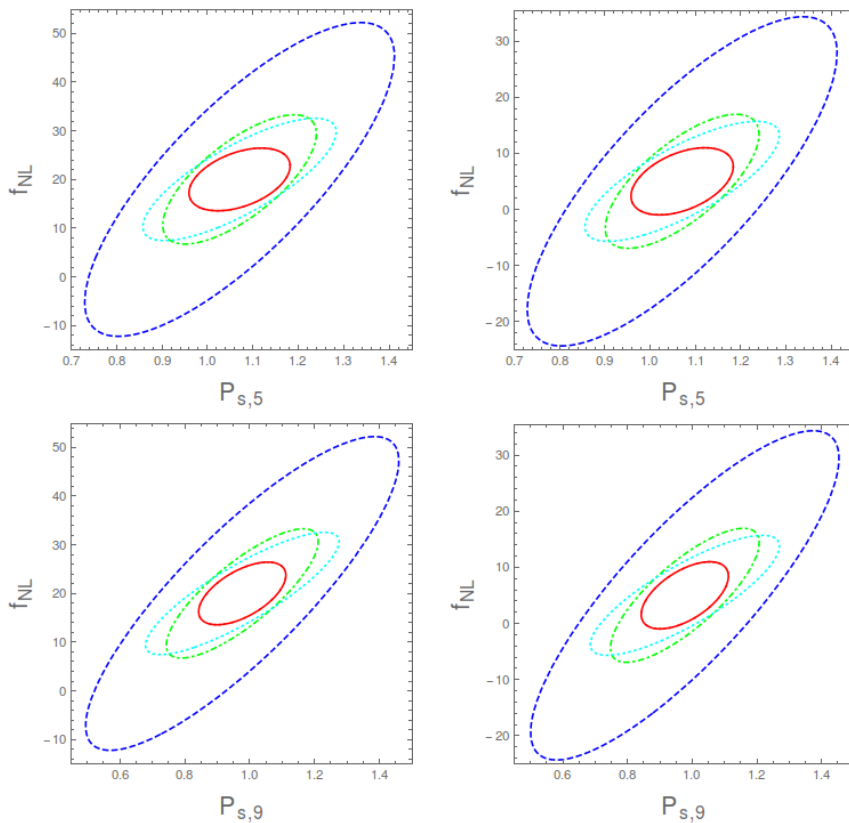
Figure 8.2: The upper left (right) panel shows the degeneracy between $f_{NL}$ and $P_{s,5}$, for a fiducial cosmology with $f_{NL} = 20$ ($f_{NL} = 5$), assuming $k_{max} = 0.1h/\text{Mpc}$. We show the $1\sigma$ marginalized contours associated to the LRGs (in dashed blue lines), ELGs (in dot-dashed green lines), QSOs (in dotted cyan lines) and multi-tracer (in solid red) Fisher matrix analyses. The bottom panels shows the analogous but for the degeneracy between $f_{NL}$ and $P_{s,9}$. From Ref. [33].

as shown in Tabs. 8.7 and 8.8.

We now perform an additional forecast. We focus on the shift induced in the local non-Gaussianity parameter $f_{NL}$, which we set to zero in the two cosmologies $\mathcal{M}$ and $\mathcal{M}'$. For the purpose of this analysis, in the case of the $\mathcal{M}'$ cosmology we fix all the nodes $P_{s,j}$ to their best-fit values according to the Planck 2013 results for the PL PPS (see Eq. (6.3)). A shift in $f_{NL}$ is expected to compensate for the fact that the PCHIP nodes $P_{s,j}$ are additional parameters in $\mathcal{M}$, while they are not considered as free parameters in the $\mathcal{M}'$ analysis. If we displace the $P_{s,j}$ parameters (with $j = 5, \ldots, 9$) from their fixed fiducial values in $\mathcal{M}'$, we are adding them as additional parameters in the cosmological model, so that they must be determined by the data. Referring to the notations of Eq. (8.9) and using a shift $\delta\psi_{P_{s,j}} = 0.1$, which is smaller than the $1\sigma$ expected errors (see Tabs. 8.2 and 8.6), we obtain that the corresponding shift in the $f_{NL}$ parameter is $\delta\theta_{f_{NL}} \simeq 2.5$, regardless of the exploited dark matter tracer. This is a quite large displacement of the local non-Gaussianity parameter which will induce a non-negligible bias in the reconstruction of the inflationary mechanism. While the remaining cosmological parameters are also slightly displaced with respect to their fiducial values, their shifts will not induce a misinterpretation of the underlying true cosmology. The shift of the non-Gaussianity parameter $\delta\theta_{f_{NL}}$ could be a potential problem when extracting the (true) value of the $f_{NL}$ parameter not only from the DESI survey, but also for other future experiments with improved sensitivities to non-Gaussianities, such as SPHEREx [529]. The combination of all the three possible DESI tracers leads to a smaller shift in the $f_{NL}$ parameter ($\delta\theta_{f_{NL}} \simeq 1.6$). If CMB priors are applied the shift is considerably reduced to $\delta\theta_{f_{NL}} \simeq 0.2$,

which is close to the expectations for non-Gaussianities in the most economical inflationary models, i.e. within single field slow-roll inflation [539, 561].

## 8.4 Conclusions

While in the simplest inflationary models the primordial power spectrum (PPS) of the curvature perturbations $\mathcal{P}_{\mathcal{R}}(k)$ can be described by a simple power-law without features, there exists a large number of well-motivated inflationary scenarios that could give rise to a non-standard PPS. The majority of these models will also generate non-Gaussianities. The Large Scale Structures (LSS) of the Universe provide, together with the CMB bispectrum, a tool to test primordial non-Gaussianities.

In the literature, it is possible to find several works devoted to forecast the expectations from upcoming galaxy surveys, such as the Dark Energy Spectroscopic Instrument (DESI) experiment. The forecasted errors and bounds on the non-Gaussianity local parameter $f_{\mathrm{NL}}$ are usually derived under the assumption of a power-law PPS. We relax this assumption and we compute the sensitivity to $f_{\mathrm{NL}}$ expected from the DESI experiment. To do this we assume that the precise shape of the PPS and the non-Gaussianity parameter need to be extracted simultaneously. If the analysis is restricted to LSS data, the standard errors computed assuming a featureless PPS are enlarged by 60% when using the `PCHIP` PPS parameterization and treating each of the possible dark matter tracers individually.

Another potential problem in future galaxy surveys could be induced by the possibly wrong assumption of a featureless PSS, if nature could have chosen a more complicated inflationary mechanism that results in a non-trivial PPS. If future data will be fitted using the wrong PPS cosmology, a shift $|\delta\theta_{f_{\mathrm{NL}}}| \simeq 2.5$ would be inferred (for $k_{\max} = 0.1h/\mathrm{Mpc}$) even if the true cosmology has $f_{\mathrm{NL}} = 0$. The former two problems may be alleviated using the multi-tracer technique. After combining all the DESI possible tracers, when compared to the value obtained with the PL PPS parameterization, the forecasted errors on $f_{\mathrm{NL}}$ will be degraded by 40% and the resulting shift will be reduced to $|\delta\theta_{f_{\mathrm{NL}}}| \simeq 1.6$. The addition of CMB priors from the Planck 2013 data on the PPS parameters and on the energy densities of dark matter and baryons leads to an error on $f_{\mathrm{NL}}$ which is independent of the PPS parameterization used in the analysis. After considering CMB priors, the value of the shift $|\delta\theta_{f_{\mathrm{NL}}}|$ is reduced to 0.2, which is of the order of standard predictions for single-field slow-roll inflation [539, 561].

# Chapter 9

# Coupling between Dark Matter and Dark Energy

*This Chapter is based on Ref. [34].*

In the previous Chapters we presented the constraints coming from cosmology on different dark radiation candidates, as neutrinos and thermal axions. Among the different aims of the analyses, there was the need to find a possible explanation to the small tensions that appear in the context of the $\Lambda$CDM model between local measurements and cosmological estimates of the Hubble parameter $H_0$ and of the small scales matter fluctuations $\sigma_8$.

In this Chapter we show a new possibility that allows to solve these tensions, not involving new particles, but considering a new interaction between the dark components of the present Universe: dark energy and dark matter. A specific theoretical model for the interaction would require a particle physics model that explains the nature of dark matter and dark energy. Several proposed scenarios exist, but we do not have a well established model: therefore we will consider only a phenomenological parameterization for the interaction.

## 9.1 Introduction

The results obtained analyzing the recent data of the Planck collaboration [21] show us that only up to the 5% of the total energy density of the Universe today is provided by baryon matter, while the remaining 95% comes from currently unknown constituents, divided in two different classes, being radiation negligible today. The 26% of the total energy density comes from some matter component that feels gravity, but does not interact with photons and is then named Dark Matter (DM). The remaining 69% comes from a diffuse fluid that is responsible of the accelerated expansion we observe in the recent history of the Universe. The fluid that provides this kind of energy density is named Dark Energy (DE), behaving differently from any other massive component. The leading candidate for DE is the cosmological constant $\Lambda$ that represents the vacuum energy in the equations of General Relativity: it is described by the equation of state (EoS) $p_\Lambda = w_\Lambda \rho_\Lambda$, where $w_\Lambda = -1$ and $p_\Lambda$, $\rho_\Lambda$ are the pressure and the energy density of DE, respectively. Further details on DM and the cosmological constant are discussed in Chapter 1.

It is difficult to understand the value of the cosmological constant in terms of fundamental physics, since it is well below the vacuum energy which can be obtained in the context of quantum field theory, in the Standard Model of Particle Physics. This problem is usually referred to as the "cosmological constant problem". Beside this, there is another problem related to the cosmological constant, that is called "coincidence problem": it appears unnatural that matter and DE, today, contribute to the total energy density with approximately the same amount. Possible solutions to these problems are related to the nature of DE. One possibility is that the DE energy density is not provided by the cosmological constant, but by some dynamical mechanism: for example, it is possible to obtain the same EoS with $w_\Lambda \simeq -1$ by means of a dynamic scalar field, $\phi(t)$, that is rolling down a potential $V(\phi)$. This mechanism is similar to the one we presented in Subsection 1.9.2 for single-field inflation. In fact, a

$\Lambda$-dominated Universe expands exponentially, in analogy with the behavior that appears during an inflationary phase. With such a dynamical mechanism, the "cosmological constant" and "coincidence" problems are partially solved, since the smallness of the vacuum energy and the relative amount of DM and DE energy densities come from a dynamical condition and not from a fine tuning of the parameters.

Cosmology gives us an evidence that DE and DM exist through the determination of their energy densities, but it does not give us the characteristics they have: until particle physics experiments will not give suitable candidates to account for DM and DE, we will not have any information on their characteristics. In particular, any type of non-gravitational interaction involving DE or DM is only constrained by astrophysical observations, with upper bounds on the interaction strength. In this light, it is interesting to extend the $\Lambda$CDM model to study the effects of a new non-gravitational interaction in the dark sector, involving DE and DM (see e.g. Refs. [562–573] and the review [574]). The new interaction can be phenomenologically introduced in cosmology in different ways, see e.g. Refs. [569–572, 575–580] and Ref. [581] for a classification. We will parameterize it through a new term in the stress-energy tensor that enters the Einstein equations. In the coupled scenario, the DE and DM components of the stress-energy tensor $T^{\mu\nu}$ are no longer separately conserved:

$$\nabla_\mu T^{\mu\nu}_{dm} = Q u^\nu_{dm}/a \,, \tag{9.1a}$$
$$\nabla_\mu T^{\mu\nu}_{\rm DE} = -Q u^\nu_{dm}/a \,, \tag{9.1b}$$

where the coefficient $Q$ encodes the interaction rate, $u^\nu_{dm}$ is the dark matter four-velocity and $a$ is the time-dependent scale factor of the Universe [569–572, 575–580]. The introduction of the coupling term in Eqs. (9.1a) and (9.1b) leads to the following conservation equations for the energy densities of DM and DE:

$$\dot\rho_{dm} + 3\mathcal{H}\rho_{dm} = +Q \,, \tag{9.2a}$$
$$\dot\rho_\Lambda + 3\mathcal{H}(1+w_\Lambda)\rho_\Lambda = -Q \,, \tag{9.2b}$$

where $\rho_{\rm DM(\Lambda)}$ is the energy density for DM (DE), $w_\Lambda$ gives the EoS $p_\Lambda = w_\Lambda \rho_\Lambda$ for DE, $\mathcal{H} = \dot a/a$ is the Hubble parameter. With the introduction of the coupling term, the energy densities of the dark components are not individually conserved, because there exists an energy flux between them: if $Q$ is positive the energy flux is from DE to DM and DE decays into DM, while if $Q$ is negative the energy flux has the opposite direction and DM decays into DE.

Several interaction models has been proposed in the literature, for example Refs. [565, 568, 575, 576, 582–584], where the role of Coupled Dark Energy (CDE in the following) is played by a scalar field. In our work, instead of focusing on the theoretical framework that gives origin to a CDE scenario, we use a phenomenological approach and we study a CDE model with [569–572, 575–580]

$$Q = \xi \mathcal{H} \rho_\Lambda \,, \tag{9.3}$$

where $\xi$ is the dimensionless coupling parameter: in this way the coupling is spatially-independent and the time dependency of the interaction rate is governed by the Hubble parameter $\mathcal{H} = \dot a/a$ [577, 578, 585]. Standard cosmology corresponds to $\xi = 0$.

In the following we will test this CDE model against cosmological observables and derive bounds on the relevant model parameters, that in our approach are $w_\Lambda$ and $\xi$. We will also discuss whether the ensuing results help in alleviating the tension on the determination of $H_0$ and $\sigma_8$ which arises from high and low redshift cosmological observables.

The outline of this Chapter is the following: in Section 9.2 we describe our parameterization for the $\Lambda$CDM model, its extension that include a coupling between DE and DM, and the cosmological data we used. In Section 9.3 we present and discuss the results. In Section 9.4 we study the possibility that DM is composed of one interacting fraction and one stable fraction, represented by a sterile neutrino. Finally, we summarize our conclusions in Section 9.5.

## 9.2 Method

### 9.2.1 Parameterization

Our baseline model is the well studied and confirmed $\Lambda$CDM model, already adopted in the previous Chapters and described in Section 2.5. In this Chapter we use the following set of parameters:

$$\boldsymbol{\theta} = \{\Omega_c h^2, \Omega_b h^2, \theta, \tau, \ln(10^{10} A_s), n_s, w_\Lambda, \xi\}, \tag{9.4}$$

where we have the present baryon density $\Omega_b h^2$, the present CDM density $\Omega_c h^2$, the ratio of the sound horizon to the angular diameter distance at decoupling $\theta$, the optical depth at reionization $\tau$, the amplitude $A_s$ and the spectral index $n_s$ of the primordial power spectrum of scalar perturbations. The parameters $w_\Lambda$ and $\xi$ are used for the CDE models, while they are fixed to $\xi = 0$ and $w_\Lambda = -1$ in the $\Lambda$CDM model.

In the first part of our analysis we do not consider the effects of varying the parameters that describe the neutrino sector: the sum of the neutrino masses $\sum m_\nu$, that we fix to the minimal value allowed by the neutrino oscillations, $\sum m_\nu = 0.06$ eV for two almost massless and one massive neutrino, and the effective number of relativistic species $N_{\text{eff}}$, that we fix to the standard value $N_{\text{eff}}^{\text{sm}} = 3.046$ [305] obtained for the three active neutrinos. In Section 9.4, instead, we will study the constraints on an additional light sterile neutrino using the same parameterization adopted in Section 5.1.

We introduce a phenomenological coupling between the dark components in the Universe, parameterized through a coupling term $Q$, written in Eq. (9.3). After introducing the coupling, Eqs. (9.2a) and (9.2b) can be derived from the time component of the stress-energy momentum conservation equation. The decoupled Equations (with $Q = 0$) correspond to $\xi = 0$. Using the coupling term in Eq. (9.3), it is possible to solve Eqs. (9.2a) and (9.2b) and to write explicitly the background equations for the energy densities of DM and DE [570, 578, 586]:

$$\rho_{dm} = \rho_{dm}^0 a^{-3} + \rho_\Lambda^0 a^{-3} \left[ \frac{\xi}{3w_\Lambda + \xi} \left(1 - a^{-3w_\Lambda - \xi}\right) \right], \tag{9.5a}$$

$$\rho_\Lambda = \rho_\Lambda^0 a^{-3(w_\Lambda + 1) - \xi}, \tag{9.5b}$$

where $\rho_i^0$ is the energy density of the species $i$ today. We emphasize that $\xi < 0$ correspond to an energy flux from DM to DE, with DM decaying into DE, whereas $\xi > 0$ correspond to an energy flux from DE to DM, with DE decaying into DM. In the following we will refer to the former case as Model 1 (MOD1) and to the latter case as Model 2 (MOD2) for sake of brevity. From Eq. (9.5b) we can see that DE obeys an effective EoS given by $w_\Lambda^{\text{eff}} = w_\Lambda + \xi/3$: this allows to write Eq. (9.5b) in the usual form $\rho_\Lambda = \rho_\Lambda^0 a^{-3(w_\Lambda^{\text{eff}} + 1)}$.

In the presence of the coupling term in Eq. (9.3), the interaction model does not suffer gravitational instabilities if $w_\Lambda \neq -1$ [568, 575]: for this reason we will consider a constant $w_\Lambda \neq -1$ when $\xi \neq 0$. Early time instabilities can however rise up also when $w_\Lambda \neq -1$ if the coupling is strong [570]: in particular the instability is not present if $\xi$ and $w_\Lambda + 1$ have opposite sign, but they can be present if the two quantities have the same sign. We will consider only constant values $w_\Lambda > -1$ for MOD1, for which $\xi < 0$, and constant values $w_\Lambda < -1$ for MOD2, for which $\xi > 0$, in order to avoid the instabilities. It is worthwhile to note that in the latter case the DM energy density can assume negative values in the past for particular combinations of $w_\Lambda$ and $\xi$ (Eq. (9.5a)), while the DE energy density is always positive (Eq. (9.5b)). To avoid unphysical values of $\rho_{dm}$, we must therefore impose $\xi \lesssim -w_\Lambda$: this is automatic for $\xi < 0$ (MOD1) unless $w_\Lambda$ assumes positive values, but this do not occur since the accelerated expansion of the Universe at late times requires $w_\Lambda < -1/3$. For MOD2, instead, we impose the prior $0 \leq \xi \leq 0.5$, but we will find that the largest values of $\xi$ in this interval are disfavored by our analyses.

From Eq. (9.5b) we note that $\rho_\Lambda$ increases with the scale factor if $w_\Lambda < -1 - \xi/3$: in this region DE has an effective phantom behavior, that is the unbounded increase of $\rho_\Lambda$ in future times. The effective phantom behavior occurs in both the models MOD1 and MOD2.

Even when $w_\Lambda > -1$ and $\xi < 0$ (MOD1) the phantom regime can be present since when $a$ increases $\rho_\Lambda$ can be increased by the energy transfer from DM to DE,, instead of following the decreasing behavior driven by $w_\Lambda > -1$. This effective behavior, however, has the advantage of being free from the instabilities that can occur for a true phantom dark energy [587, 588].

Looking at Eqs. (9.5a) and (9.5b), we notice that it is difficult to disentangle the effects of the DE EoS parameter $w$ and the coupling $\xi$ by only studying the background evolution. We must include the perturbation evolution equations, which are also affected by the additional coupling. To obtain the new equations for the linear perturbation in DM and DE one has to perform the calculations in the perturbed space time, following the method we presented in Section 1.8. As a result, the coupled perturbation equations in the synchronous gauge can be obtained [578]:

$$\dot{\delta}_{dm} = -\left(kv_{dm} + \frac{\dot{h}}{2}\right) + \xi\mathcal{H}\frac{\rho_\Lambda}{\rho_{dm}}(\delta_\Lambda - \delta_{dm}) ; \tag{9.6a}$$

$$\dot{v}_{dm} = -\mathcal{H}v_{dm}\left(1 + \xi\frac{\rho_\Lambda}{\rho_{dm}}\right) ; \tag{9.6b}$$

$$\dot{\delta}_\Lambda = -(1 + w_\Lambda)\left(kv_\Lambda + \frac{\dot{h}}{2}\right) - 3\mathcal{H}(1 - w_\Lambda) \cdot \left(\delta_\Lambda\mathcal{H}(3(1 + w_\Lambda) + \xi)\frac{v_\Lambda}{k}\right) ; \tag{9.6c}$$

$$\dot{v}_\Lambda = -2\mathcal{H}\left(1 + \frac{\xi}{1 + w_\Lambda}\right)v_\Lambda + k\frac{\delta_\Lambda}{1 + w_\Lambda} ; \tag{9.6d}$$

where $h = 6\phi$ is the synchronous gauge metric perturbation and the DM peculiar velocity $v_{dm}$ is fixed to zero using the gauge freedom. Moreover, the DE sound speed is fixed: $c_{s,\Lambda} = 1$. The uncoupled equations for $\delta_{dm}$ and $v_{dm}$ have been presented in Eqs. (1.92) and (1.93) in the conformal Newtonian gauge. They can be recovered using $\xi = 0$ and changing appropriately the gauge. We adopt the adiabatic initial conditions (see Section 1.9) for the CDE component [568, 575, 579] as for all the other cosmological constituents [54].

The effects of the additional coupling are visible in different ways on the cosmological observables. Since we expect a strong degeneracy between the coupling parameter $\xi$ and the DM density today $\Omega_c h^2$, due to the conversion of DM into DE (or vice versa) that reduce (increase) the DM abundance at different times, we briefly list the effects that the dark coupling has on cosmology when we consider $\Omega_c h^2$ fixed. The DM density today will be degenerate with the variations in the coupling strength $\xi$, since $\xi$ impacts the CMB spectra through the corresponding DM energy density at the matter-radiation equality epoch or at the CMB decoupling, that is higher (smaller) if the coupling parameter is negative (positive). When $\Omega_c h^2$ is fixed, the presence of the coupling provides a shift in the position and a change in the envelope of the CMB peaks, due mainly to the different background evolution and to the different DM density in the early Universe, and a change in the low-$\ell$ spectrum, due to a different contribution to the integrated Sachs-Wolfe (ISW) effect [577, 580]. The upper panel of Fig. 9.1 shows the dependence of the CMB spectrum on $\xi$. The DE EoS parameter $w_\Lambda$, in turn, has an impact mainly on the low-$\ell$ part of the spectrum and on the position of the acoustic peaks, leaving their envelope almost unchanged: this gives the opportunity of breaking the degeneracy arising from the background evolution Equations (9.5a) and (9.5b) when studying the CMB spectrum in a wide range of multipoles.

The DM abundance, instead, is relevant for the matter-radiation equality and for the expansion rate at the time of CMB decoupling, that influences the comoving sound horizon and consequently the angular scale of the peaks: it is difficult to distinguish the impact of the DM energy density and the coupling strength from CMB data alone, as it is possible to see comparing the panels of Fig. 9.1. The degeneracy with the DM density can be studied with additional data on the gravitational lensing and on the clustering, since the coupling introduces a non-standard time-dependency of the DM density. The fact of having different amounts of DM at different epochs leads to different evolution histories of the small scale fluctuations under the effect of gravity. If DM decays into DE, for example, there is much more
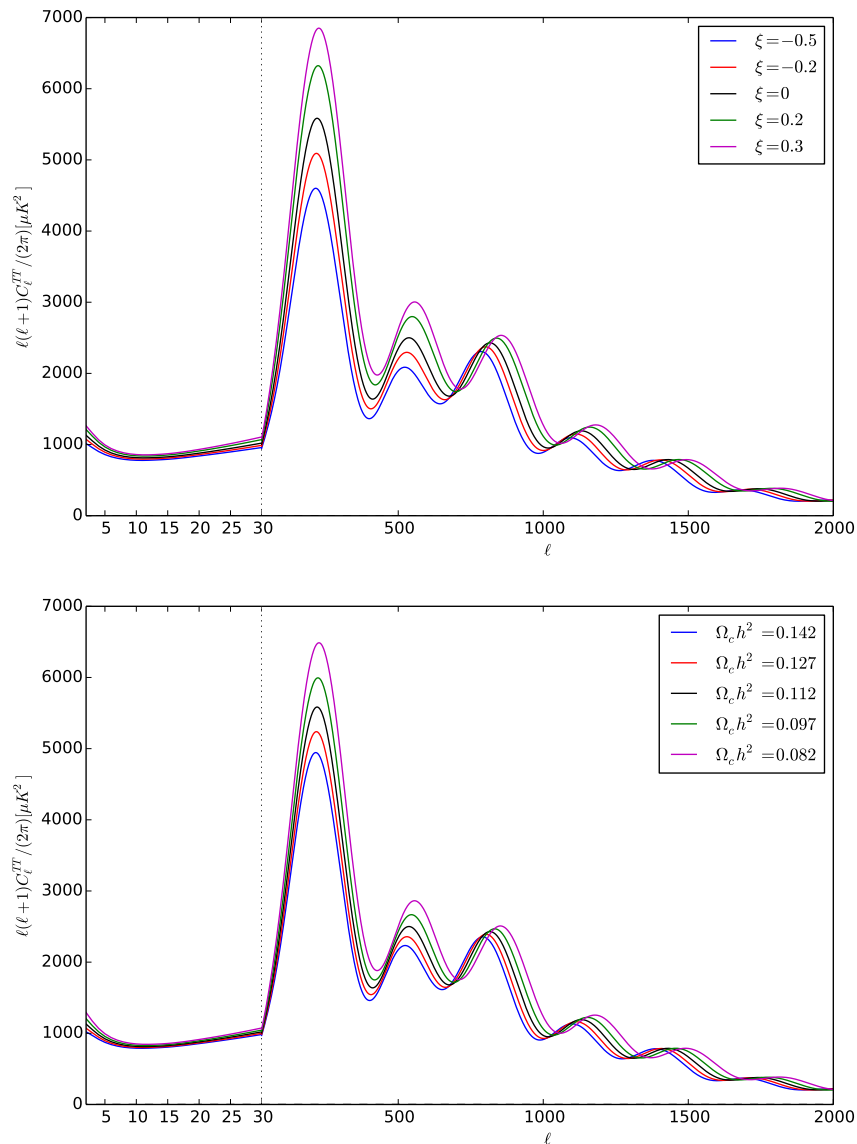
Figure 9.1: Dependence of the CMB spectrum on two cosmological parameters: the coupling strength $\xi$ (upper panel) and the DM energy density today $\Omega_c h^2$ (lower panel). All the other parameters are kept fixed. The black curve is the same in the different panels. From Ref. [34].

DM in the early Universe, leading to a stronger clustering and to an anticipated nonlinear regime for the evolution of the perturbations.

For our cosmological analyses we implemented all the relevant equations into the numerical Boltzmann solver `CAMB` [58] and we modified the Markov Chain Monte Carlo (MCMC) code `CosmoMC` [341] in order to include $\xi$ as an additional parameter. We then use `CosmoMC` to obtain the cosmological constraints and we compare the results obtained in the standard $\Lambda$CDM model with those obtained considering the CDE scenarios, MOD1 and MOD2. We restrict $\xi$ and $w_\Lambda$ to the intervals in Tab. 9.1 for the reasons explained above and we consider flat priors in these ranges for our MCMC analyses.

Finally, we want to underline the connections of the parameters used in the Equations presented above with the parameters that appear in the $\Lambda$CDM model and in the `CAMB` / `CosmoMC` software that we use for the analyses. The DM energy density $\rho_{dm}$ is proportional to the parameter $\Omega_c h^2$, since $\Omega_c = \rho_{dm}/\rho_c \propto \rho_{dm}/h^2$ (see Section 1.5): the physical energy density of DM today is then proportional to $\Omega_c h^2$. On the contrary, $\Omega_c$ depends on Hubble parameter today. This observation will be useful when we will discuss the results for the CDE

| Parameter | Prior | | |
|---|---|---|---|
| | ΛCDM | MOD1 | MOD2 |
| $w_\Lambda$ | -1 | [-0.999, -0.1] | [-2.5, -1.001] |
| $\xi$ | 0 | [-1, 0] | [0, 0.5] |
| | no interaction | DM decays into DE | DE decays into DM |

Table 9.1: The priors on parameters for the coupling scenario, the coupling parameter $\xi$ and the DE EoS parameter $w_\Lambda$, that we use for the analyses of the different models. All the priors are flat in the listed intervals. From Ref. [34].

models. On the contrary, we will present the results for $\Omega_\Lambda = 1 - \Omega_k - (\Omega_\gamma + \Omega_b + \Omega_c + \Omega_\nu)$, where we always consider $\Omega_k = 0$ (flat Universe). $\Omega_\Lambda$ is a derived parameter in our analyses, and it is not proportional to the physical energy density $\rho_\Lambda$, but it depends on the Hubble parameter today ($\Omega_\Lambda \propto \rho_\Lambda/h^2$).

### 9.2.2 Cosmological Data

We base our analyses on the Cosmic Microwave Background (CMB) data (see Section 3.1) from the 2015 Planck release [21], in particular we consider as our minimal data combination the full temperature autocorrelation spectrum in the range $2 \leq \ell \leq 2500$ (denoted as **PlanckTT**) plus the low-$\ell$ Planck polarization spectra in the range $2 \leq \ell \leq 29$ (denoted as **lowP**) [62]. Additionally, we consider and add separately the high-$\ell$ Planck polarization spectra in the range $30 \leq \ell < 2500$ (hereafter **highP**) [62].

Since the coupling between DE and DM introduces a time-dependency in the background evolution of DE and DM (see Eqs. (9.5a) and (9.5b)), it is important to test our theoretical models using data at many different redshift with respect to the CMB measurements. In particular, in MOD1 we expect a higher amount of DM in the early Universe than in the ΛCDM model, with stronger gravitational effects in the initial phases of the evolution. On the opposite side, in the MOD2 the amount of DM is smaller in the early Universe and the gravitational clustering is reduced until enough DE is decayed into DM. For these reasons, it is important to consider observations at various redshift to constrain the CDE models, as they can distinguish the different evolution histories.

One of the most important probes of the expansion and of the existence of DE are the Supernovae (SNe) of type Ia. We consider the luminosity distances of SN Ia from the SNLS and SDSS catalogs as re-analyzed in the joint analysis [126] (**JLA** hereafter), introduced in Section 3.4.

Another interesting probe of the Universe evolution comes from the Redshift Space Distortions (RSD, see Subsection 3.2.4), namely distortions of the shape of galaxy clusters in the redshift space due to peculiar motions of the single objects along the line of sight. We include also the Baryon Acoustic Oscillations (BAO) data as determined by 6dFGS [90], SDSS-MGS [91] and BOSS DR11 [93], together with the RSD determinations from BOSS DR11 [115]. We will refer to the combination of these measurements as to the **BAO/RSD** dataset.

The amount of DM affects also the strength of the gravitational lensing. We include information on the power spectrum of the lensing potential reconstructed by Planck from the trispectrum detection [64] (hereafter **lens**). We do not consider weak lensing determinations obtained from the cosmic shear measurements of the CFHTLenS survey [589] for the reasons explained in Section 3.7. We also do not consider the other local determinations of $\sigma_8$ from local measurements (see Section 3.6) for the same reasons, nor any constraints on the Hubble parameter $H_0$, the expansion rate of the Universe today, due to the tensions that exist between local determinations and CMB estimates also for this observable (see Section 3.3).

| Parameter | $\Lambda$CDM | MOD1 | MOD2 |
|---|---|---|---|
| $100\Omega_b h^2$ | $2.222\,^{+0.047}_{-0.043}$ | $2.216\,^{+0.046}_{-0.045}$ | $2.226\,^{+0.047}_{-0.046}$ |
| $\Omega_c h^2$ | $0.120\,^{+0.004}_{-0.004}$ | $0.069\,^{+0.053}_{-0.065}$ | $0.133\,^{+0.019}_{-0.016}$ |
| $100\theta$ | $1.0409\,^{+0.0009}_{-0.0009}$ | $1.0441\,^{+0.0052}_{-0.0040}$ | $1.0402\,^{+0.0013}_{-0.0013}$ |
| $\tau$ | $0.078\,^{+0.039}_{-0.037}$ | $0.077\,^{+0.039}_{-0.038}$ | $0.077\,^{+0.039}_{-0.038}$ |
| $n_s$ | $0.965\,^{+0.012}_{-0.012}$ | $0.964\,^{+0.013}_{-0.012}$ | $0.966\,^{+0.013}_{-0.012}$ |
| $\log(10^{10}A_s)$ | $3.089\,^{+0.074}_{-0.072}$ | $3.088\,^{+0.073}_{-0.073}$ | $3.087\,^{+0.073}_{-0.074}$ |
| $\xi$ | $0$ | $(-0.789, 0]$ | $[0, 0.269)$ |
| $w_\Lambda$ | $-1$ | $[-1, -0.703)$ | $-1.543\,^{+0.524}_{-0.447}$ |
| $H_0$ [ Km s$^{-1}$ Mpc$^{-1}$ ] | $67.28\,^{+1.92}_{-1.89}$ | $67.91\,^{+7.44}_{-7.87}$ | $> 68.32$ |
| $\sigma_8$ | $0.830\,^{+0.029}_{-0.028}$ | $1.464\,^{+1.948}_{-1.037}$ | $0.898\,^{+0.163}_{-0.160}$ |

Table 9.2: Marginalized limits at $2\sigma$ for various parameters considered in our analyses, obtained with the "PlanckTT+lowP" dataset for the three different models ($\Lambda$CDM, MOD1 and MOD2). When an interval denoted with parenthesis is given, it refers to the $2\sigma$ C.L. range starting from the prior extreme, listed in Tab. 9.1. $H_0$ is limited to the range $[20, 100]$. From Ref. [34].

| Parameter | $\Lambda$CDM | MOD1 | MOD2 |
|---|---|---|---|
| $100\Omega_b h^2$ | $2.229\,^{+0.028}_{-0.028}$ | $2.228\,^{+0.030}_{-0.030}$ | $2.227\,^{+0.031}_{-0.030}$ |
| $\Omega_c h^2$ | $0.119\,^{+0.002}_{-0.002}$ | $0.091\,^{+0.029}_{-0.033}$ | $0.135\,^{+0.014}_{-0.014}$ |
| $100\theta$ | $1.0409\,^{+0.0006}_{-0.0006}$ | $1.0426\,^{+0.0022}_{-0.0019}$ | $1.0400\,^{+0.0010}_{-0.0010}$ |
| $\tau$ | $0.062\,^{+0.025}_{-0.025}$ | $0.063\,^{+0.027}_{-0.026}$ | $0.059\,^{+0.028}_{-0.027}$ |
| $n_s$ | $0.966\,^{+0.008}_{-0.008}$ | $0.966\,^{+0.009}_{-0.009}$ | $0.966\,^{+0.009}_{-0.009}$ |
| $\log(10^{10}A_s)$ | $3.055\,^{+0.045}_{-0.046}$ | $3.058\,^{+0.049}_{-0.049}$ | $3.050\,^{+0.050}_{-0.051}$ |
| $\xi$ | $0$ | $(-0.463, 0]$ | $[0, 0.300)$ |
| $w_\Lambda$ | $-1$ | $[-1, -0.829)$ | $(-1.129, -1]$ |
| $H_0$ [ Km s$^{-1}$ Mpc$^{-1}$ ] | $67.72\,^{+1.01}_{-0.97}$ | $67.57\,^{+1.81}_{-1.79}$ | $67.83\,^{+1.90}_{-1.75}$ |
| $\sigma_8$ | $0.812\,^{+0.017}_{-0.017}$ | $0.994\,^{+0.294}_{-0.219}$ | $0.749\,^{+0.069}_{-0.063}$ |

Table 9.3: The same as in Tab. 9.2, for the results obtained with the "ALL" dataset. From Ref. [34].

It is important, however, to discuss and possibly solve the small tensions that currently are present between the CMB observations and the local measurements, and new physics beyond the standard cosmological model can help in this direction. As we will show in the next Section, the CDE model can reconcile local and cosmological measurements for both $H_0$ and $\sigma_8$.

In our analyses we will explore different combinations of the listed dataset: our starting point will be the CMB-only dataset **PlanckTT+lowP**, then we will add one of the other datasets at a time (highP, lens, JLA, BAO/RSD) and finally we will consider a combination involving all the dataset, "PlanckTT+lowP + highP + lens + JLA + BAO/RSD", that we will indicate with **ALL** for sake of brevity. For each of these data combinations we will test the three cosmological models ($\Lambda$CDM, MOD1, MOD2) to study how the constraints change.
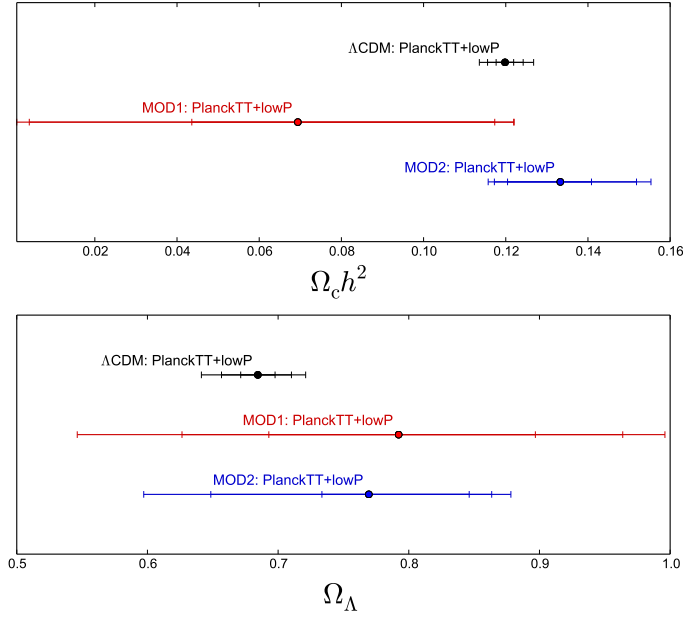
Figure 9.2: Marginalized 1, 2 and $3\sigma$ limits from the "PlanckTT+lowP" dataset for $\Omega_c h^2$ and $\Omega_\Lambda$, for the three different cosmological models: $\Lambda$CDM, MOD1 and MOD2. MOD1 predicts a smaller amount of DM today with respect to $\Lambda$CDM, as one would expect in a model in which the energy flux is from DM to DE; on the other hand, MOD2 predicts more DM today compared to $\Lambda$CDM, since in that model the energy flux is opposite, i.e. DE decays into DM. From Ref. [34].

## 9.3 Results

In this section we present the result obtained in the cosmological analyses. We compare the three different models ($\Lambda$CDM, MOD1, MOD2) and the constraints provided by the different datasets. We list in Tables 9.2 ("CMB only") and 9.3 ("ALL" dataset) the $2\sigma$ constraints for the parameters we considered. Most of the standard $\Lambda$CDM parameters are not sensitive to the coupling in the dark sector and the ensuing results are unchanged when moving from the $\Lambda$CDM model to the MOD1 and MOD2 scenarios: the baryon density today $\Omega_b h^2$, the optical depth at reionization $\tau$, the tilt $n_s$ and the amplitude $\log(10^{10}A_s)$ of the power spectrum of scalar perturbations. Their determination is therefore robust against modified expansion histories induced by the new DM/DE coupling.

Slightly larger variations occur for the ratio of the sound horizon to the angular diameter distance at decoupling, $\theta$, but even in this case the differences between the various models are well inside the mutual $2\sigma$ limits. Interestingly, the addition of the external data in the "ALL" dataset reduces the uncertainties on various parameters, but requires a shift towards lower values for the optical depth at reionization $\tau$ and for the amplitude of the scalar perturbations power spectrum $\log(10^{10}A_s)$. These parameters suffer of a mild tension in the recent Planck results, as discussed in [44], since the analyses that consider the low-$\ell$ temperature spectrum point towards higher values of $\tau$ with respect to the results obtained from the polarization spectra only. If one considers the lensing information and the BAO measurements together with the temperature spectrum, the results are in good agreement with the indications in favor of a small $\tau$ coming from the Planck polarization spectra. As the CMB observations constrain the combination $A_s e^{-2\tau}$, a smaller $\tau$ reflects in a smaller $A_s$.

As we would expect, there is a strong correlation between the coupling parameter $\xi$ and the current DM energy density $\Omega_c h^2$. For $\xi < 0$ (MOD1), the bigger is the interaction, the smaller is the DM abundance today, i.e. more DM decayed into DE during the evolution. Conversely, in $\xi > 0$ (MOD2) a larger current DM abundance is predicted. Since CMB data
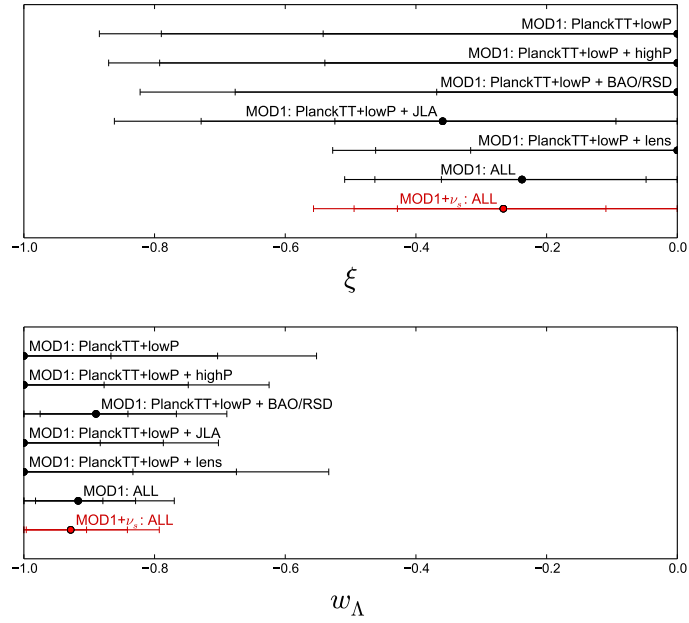
Figure 9.3:  Marginalized 1, 2 and 3σ limits on ξ and $w_\Lambda$ in the MOD1, for different datasets. When the error bars are not visible, they coincide with the limit in the prior, as listed in Tab. 9.1. The red point is for the MOD1+$\nu_s$ model, discussed in Section 9.4. From Ref. [34].
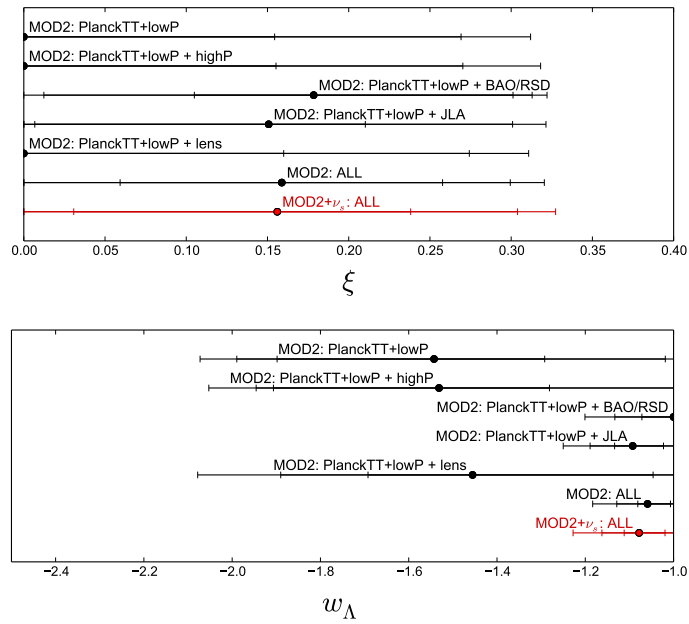


Figure 9.4:   Marginalized 1, 2 and 3σ limits from ξ and $w_\Lambda$ in the MOD2, for different datasets. When the error bars are not visible, they coincide with the limit in the prior, as listed in Tab. 9.1. The red point is for the MOD2+$\nu_s$ model, discussed in Section 9.4. From Ref. [34].

mainly constrain the DM abundance in the early Universe, the best fit values for $\Omega_c h^2$ can be very different in the ΛCDM, MOD1 or MOD2 cases, as it is possible to see from Tabs. 9.2 and 9.3 and the upper panel in Fig. 9.2, where the 1, 2 and 3σ limits for $\Omega_c h^2$ in the different models are shown. Given a flat Universe, this reflects also in different values for the DE energy density today in the different models (see the 1, 2 and 3σ limits for $\Omega_\Lambda$ in the lower panel in Fig. 9.2).
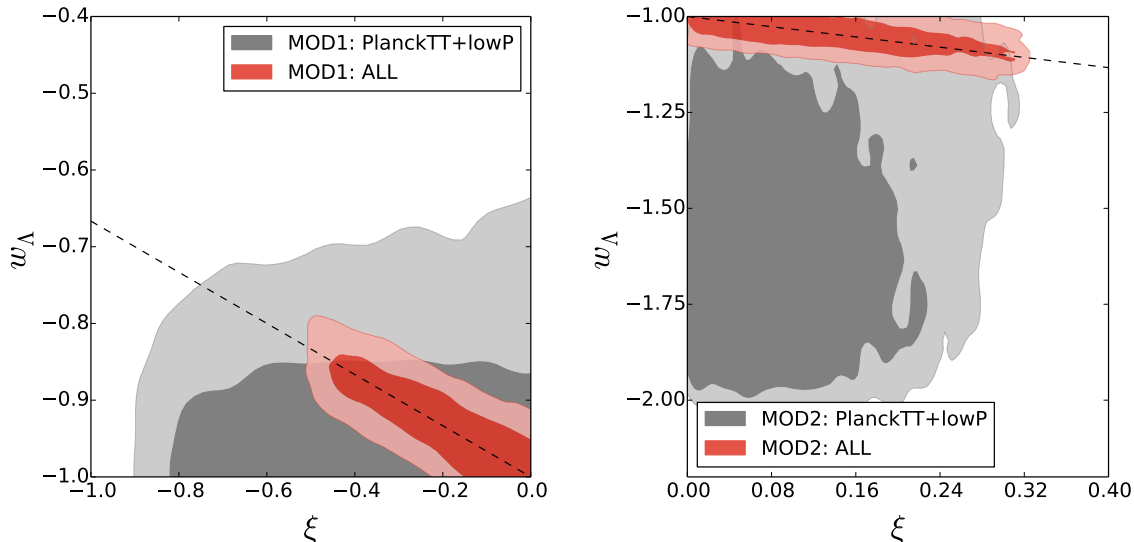
Figure 9.5: Marginalized 1 and $2\sigma$ allowed regions in the $(\xi, w_\Lambda)$ plane in the MOD1 (left) and MOD2 (right) scenarios, for different datasets. Points in the regions below the dashed lines (representing $w_\Lambda^{\mathrm{eff}} = w_\Lambda + \xi/3 = -1$) correspond to an increasing energy density for DE in the future. From Ref. [34].

Figs. 9.3 and 9.4 show the 1, 2 and $3\sigma$ limits on $\xi$ (upper panels) and $w_\Lambda$ (lower panels) obtained with different datasets, for both the CDE models MOD1 (Fig. 9.3) and MOD2 (Fig. 9.4). The constraints are almost insensitive to the addition of the CMB polarization at high multipoles ("highP"). The lensing information, instead, leads to stronger constraints for $\xi$ in MOD1: as expected, this comes from the bounds on the DM abundance during the expansion history that are provided by the lensing detection. Both in MOD1 and MOD2, the addition of the JLA and BAO/RSD dataset leads to stronger bounds on the DE EoS $w_\Lambda$, that is constrained towards -1. Actually the cosmological data constrains the effective DE EoS parameter $w_\Lambda^{\mathrm{eff}} = w_\Lambda + \xi/3$ that drives the background evolution in Eq. (9.5b). As we can see in Fig. 9.5, for both MOD1 (left panel) and MOD2 (right panel) the marginalized regions in the $(\xi, w_\Lambda)$ plane are well constrained around the $w_\Lambda^{\mathrm{eff}} = -1$ (dashed) line, thus indicating a preference for a DE energy density that is effectively constant over time.

From Tab. 9.2 we can also see how the CMB data only gives poor constraints on both the derived quantities $H_0$ and $\sigma_8$. For the Hubble parameter, this is due to the strong correlation between $H_0$ and the DE EoS parameter: as we can see in Eq. (9.5b), when $w_\Lambda < -1$ the DE density today is larger for larger values of $|w_\Lambda|$. Since the Universe is DE-dominated at late times, the total energy density $\rho_{\mathrm{tot}}$ increases with $\rho_\Lambda$ and consequently the Hubble rate today $H \propto \sqrt{\rho_{\mathrm{tot}}}$ is larger. When $w_\Lambda > -1$, instead, the situation is opposite and values for $H_0$ lower than the CMB predictions can be found. The CMB alone, however, is not a good way to constrain the DE EoS: with the introduction of additional data, in particular the BAO/RSD and JLA datasets, the constraints on $w_\Lambda$ are much stronger, especially in MOD2, and consequently the allowed regions for $H_0$ are better identified.

It is interesting to note that MOD1 predicts a value for $\sigma_8$ significantly larger than the $\Lambda$CDM prediction (see both Tab. 9.2 and Tab. 9.3): since MOD1 predicts a larger amount of DM in the early Universe, there is more clustering in the primordial Universe, that results in an earlier transition to the nonlinear evolution and hence to unavoidably larger values for $\sigma_8$ with respect to the $\Lambda$CDM predictions. Even if the $\sigma_8$ values as determined by local measurements are underestimates of the true value, as the CMB determinations within the $\Lambda$CDM model seems to suggest, this can be a strong argument against a CDE parameterization through MOD1. On the contrary, in MOD2 the DM abundance is bigger in the late Universe with respect to the earlier epochs: the nonlinear evolution is entered later during
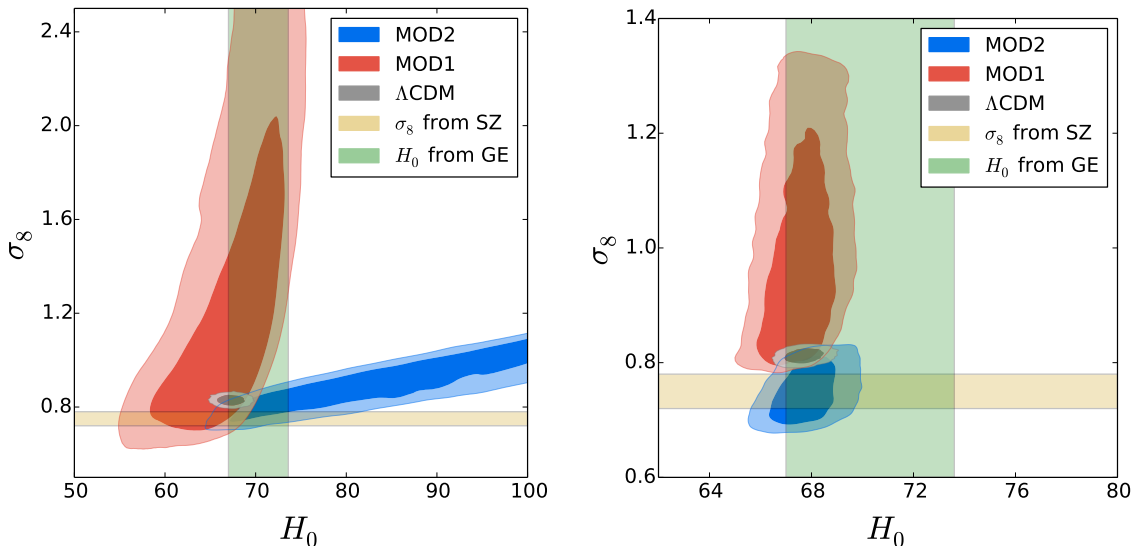
Figure 9.6: Marginalized 1 and $2\sigma$ allowed regions in the $(\sigma_8, H_0)$ plane for different models: $\Lambda$CDM (gray), MOD1 (red) and MOD2 (blue). The left panel correspond to the CMB only dataset "PlanckTT+lowP", while the panel on the right correspond to the full combination considered here ("ALL"). The green band is $H_0 = 70.6 \pm 3.3$ Km s$^{-1}$ Mpc$^{-1}$ [123] (GE), while the dark yellow band is $\sigma_8 = 0.75 \pm 0.03$ [136] (SZ). From Ref. [34].

the Universe evolution and $\sigma_8$ does not increase significantly, because at late times the DE is dominant and prevents clustering. A hint for late-time appearance of DM was found also in the recent study [590], thus giving another point in favor of MOD2.

In Fig. 9.6 we summarize the results on $H_0$ and $\sigma_8$ in the three models ($\Lambda$CDM, MOD1, MOD2) for both the CMB only (left panel) and the "ALL" (right panel) datasets. As reference, we plot two bands representing the local determinations of $\sigma_8 = 0.75 \pm 0.03$ from Planck [136], obtained leaving the mass bias free to vary, and $H_0 = 70.6 \pm 3.3$ [123] as a comparison. Both the plots display that in MOD1 it is impossible to obtain high $H_0$ values with low $\sigma_8$ values and the uncertainty on $\sigma_8$ reflects also in an uncertainty on $H_0$ [591]. On the contrary, in MOD2 $H_0$ can assume larger values without implying very large values for $\sigma_8$. This is due to the opposite correlation of $\sigma_8$ with the coupling parameter $\xi$: whereas in MOD1 a larger $\sigma_8$ arises from a larger interaction rate, MOD2 shows an opposite behavior, namely lower values of $\sigma_8$ correspond to a stronger coupling in the dark sector and possibly to high values of $H_0$. In this sense, MOD2 should be preferred over MOD1, since in this context the cited tensions regarding $\sigma_8$ and $H_0$ can be solved.

## 9.4 Sterile neutrinos as stable DM component

Up to now we did not consider the possibility that the total amount of DM energy density is provided by two or more different species, with only one of them coupled to DE. In this situation, the DM is composed by a stable and an interacting fraction, with the consequence that only part of the DM can feed (or be fed by) DE during the Universe evolution. A model with an interacting DM component combined with a stable one was studied for example in Ref. [592], where the authors report a preference for the existence of two separate components.

Among the most investigated DM candidates, sterile neutrinos have been widely studied in the past (see e.g. Chapters 4, 5 and 6). We present here a comparison of the bounds obtained for the sterile neutrino properties when the underlying cosmological model is changed from the $\Lambda$CDM model to the CDE scenarios MOD1 and MOD2, to test the possibility that the additional neutrino represents the stable DM fraction.

| | Prior | |
|---|---|---|
| Parameter | $\Lambda$CDM | $\nu_s$ |
| $m_s^{\text{eff}}$ | 0 | [0,15] |
| $N_{\text{eff}}$ | 3.046 | [3.046, 6] |

Table 9.4: The priors on the neutrino parameters $N_{\text{eff}}$ and $m_s^{\text{eff}}$, flat in the listed intervals. From Ref. [34].

To include the additional neutrino in the cosmological analysis we use the parameterization presented in Ref. [72] and adopted in Section 5.1. The additional neutrino acts as a relativistic component in the early Universe and gives a contribution to the effective number of relativistic species $N_{\text{eff}}$ that is $\Delta N_{\text{eff}} = N_{\text{eff}} - N_{\text{eff}}^{\text{sm}}$ and it can be obtained from Eq. (4.44). In the late Universe, when the sterile neutrino becomes non-relativistic, its mass becomes important and it behaves as a massive component. Since we will not study the compatibility of the cosmological constraints with SBL neutrino oscillations, in this case it is more convenient to use the effective mass $m_s^{\text{eff}}$ (see Eq. (4.47)) instead of the physical mass $m_s$. The effective mass is more convenient than $m_s$ also because we are particularly interested in the degeneracy between $\Omega_s h^2 \propto m_s^{\text{eff}}$ and the DM energy density $\Omega_c h^2$. For both $N_{\text{eff}}$ and $m_s^{\text{eff}}$ we adopt flat priors in the intervals listed in Tab. 9.4.

We study the constraints on the sterile neutrino properties using only the full data combination "ALL", that gives the strongest constraints on the CDE models. We compare the results obtained in the $\Lambda$CDM+$\nu_s$, MOD1+$\nu_s$ and MOD2+$\nu_s$ models in Tab. 9.5 for all the relevant parameters. The inclusion of an additional neutrino do not change significantly the constraints on the $\Lambda$CDM parameters, with the only exception of $\Omega_c h^2$. For the baryon energy density there is a small shift of less than $1\sigma$, while the errors on $\tau$, $n_s$ and $\log(10^{10} A_s)$ are slightly increased, but these changes are independent on the CDE model.

As expected, the quantity that varies most is the CDM energy density $\Omega_c h^2$, that is lower and more uncertain in all the models. This is due to the fact that the sterile neutrino acts as a massive component in the late Universe and it contributes to the total amount of matter with $\Omega_s h^2 \propto m_s^{\text{eff}}$: a degeneracy with DM exists. The degeneracy is shown in Fig. 9.7, where it is clear that a higher DM energy density corresponds to a lower $m_s^{\text{eff}}$, for all the models. The differences in $\Omega_c h^2$ between the CDE+$\nu_s$, MOD1+$\nu_s$ and MOD2+$\nu_s$ models, however, are the same we discussed without the sterile neutrino.

Constraints on the parameters $N_{\text{eff}}$ and $m_s^{\text{eff}}$ are almost the same in the different models, with only very small differences: this means that the properties of the sterile neutrino as DM are robust against the introduction of the new interaction. In parallel, also the constraints on the coupling parameter $\xi$ and on the DE EoS parameter $w_\Lambda$ are almost insensitive to the presence of the additional neutrino. The 1, 2 and $3\sigma$ limits on $\xi$ and $w_\Lambda$ are plotted in red in Figures 9.3 and 9.4 for MOD1 and MOD2 respectively: the "ALL" dataset, independently of the $\nu_s$ presence, gives a $1\sigma$ preference for a non-zero interaction in the dark sector.

The presence of an additional component that acts as a relativistic particle in the early Universe and a non-relativistic one in the late Universe gives a suppression in the clustering, due to the free-streaming effect, and an increase of the Hubble parameter, due to the necessity of increasing both the DM and DE energy densities in the Universe to avoid a shift of the matter-radiation equality and of the coincidence time. As a consequence, the inclusion of the sterile neutrino shifts the predictions for $H_0$ towards slightly higher values and lowers those for $\sigma_8$. In Fig. 9.8 we show the equivalent of Fig. 9.6 for the models with the additional neutrino. Apart for the fact that the regions are slightly wider, there are no significant variations with respect to the right panel of Fig. 9.6. As a consequence of the lowering of $\sigma_8$, however, models with the sterile neutrino show a higher compatibility with the low-$\sigma_8$ measurements as, for example, the Planck cluster counts (SZ, yellow band in the plots).

| Parameter | $\Lambda$CDM | MOD1 | MOD2 |
|---|---|---|---|
| $100\Omega_b h^2$ | $2.237\,^{+0.034}_{-0.031}$ | $2.237\,^{+0.036}_{-0.032}$ | $2.236\,^{+0.035}_{-0.032}$ |
| $\Omega_c h^2$ | $0.113\,^{+0.014}_{-0.019}$ | $0.083\,^{+0.034}_{-0.033}$ | $0.129\,^{+0.024}_{-0.025}$ |
| $100\theta$ | $1.0408\,^{+0.0006}_{-0.0007}$ | $1.0426\,^{+0.0022}_{-0.0020}$ | $1.0400\,^{+0.0010}_{-0.0011}$ |
| $\tau$ | $0.063\,^{+0.032}_{-0.033}$ | $0.064\,^{+0.034}_{-0.035}$ | $0.060\,^{+0.034}_{-0.035}$ |
| $n_s$ | $0.969\,^{+0.012}_{-0.011}$ | $0.968\,^{+0.013}_{-0.012}$ | $0.968\,^{+0.012}_{-0.012}$ |
| $\log(10^{10}A_s)$ | $3.059\,^{+0.066}_{-0.067}$ | $3.061\,^{+0.068}_{-0.070}$ | $3.054\,^{+0.070}_{-0.069}$ |
| $\xi$ | $0$ | $(-0.494, 0]$ | $[0, 0.304)$ |
| $w_\Lambda$ | $-1$ | $[-1, -0.841)$ | $(-1.162, -1]$ |
| $m_s^{\rm eff}$ [eV] | $< 2.1$ | $< 1.9$ | $< 2.2$ |
| $N_{\rm eff}$ | $< 3.34$ | $< 3.38$ | $< 3.35$ |
| $H_0$ [ Km s$^{-1}$ Mpc$^{-1}$] | $67.91\,^{+1.33}_{-1.26}$ | $68.23\,^{+2.21}_{-2.00}$ | $68.43\,^{+2.16}_{-2.07}$ |
| $\sigma_8$ | $0.789\,^{+0.039}_{-0.045}$ | $0.988\,^{+0.300}_{-0.229}$ | $0.727\,^{+0.073}_{-0.072}$ |

Table 9.5: Marginalized limits at $2\sigma$ for various parameters considered in our analyses, obtained with the "ALL" dataset for the three different models ($\Lambda$CDM+$\nu_s$, MOD1+$\nu_s$ and MOD2+$\nu_s$). When an interval denoted with parenthesis is given, it refers to the $2\sigma$ C.L. range starting from the prior extreme. These are listed in Tabs. 9.1 and 9.4. From Ref. [34].
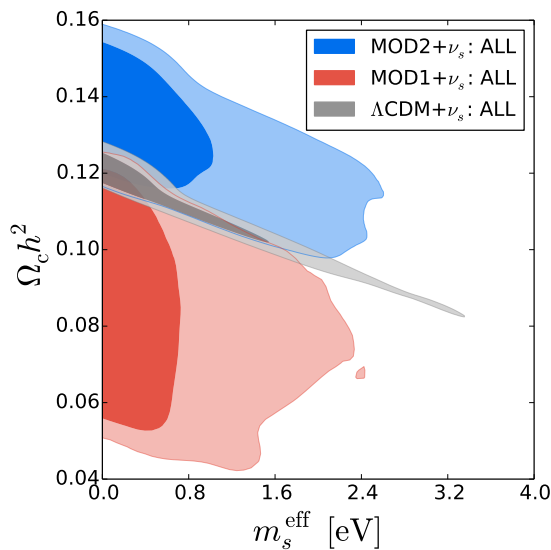


Figure 9.7: Marginalized 1 and $2\sigma$ allowed regions in the ($\Omega_c h^2$, $m_s^{\rm eff}$) plane for different models: $\Lambda$CDM+$\nu_s$ (gray), MOD1+$\nu_s$ (red) and MOD2+$\nu_s$ (blue), obtained with the full data combination considered here ("ALL"). From Ref. [34].

## 9.5 Conclusions

The largest part of the energy density of our Universe is represented by a dark sector, formed by dark matter and dark energy. Both these components are known only for they gravitational effects, but we still ignore if they can be explained in the context of fundamental physics: while many candidates of DM have been proposed, the true nature of DE is completely unknown from this point of view. Apart for gravity, we ignore how DM and DE interact with the other particles. The existence of a non-gravitational coupling involving DE or DM cannot be excluded: this additional interaction would have an impact on cosmology and it can be tested, in principle, studying the various cosmological observables. A coupling with
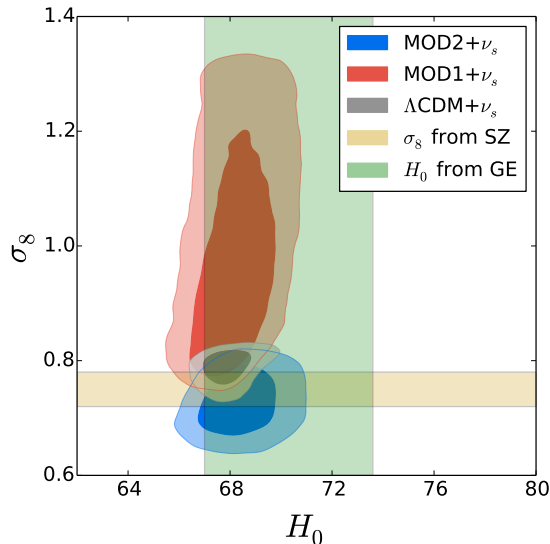
Figure 9.8: Marginalized 1 and $2\sigma$ allowed regions in the $(\sigma_8,\ H_0)$ plane for different models: $\Lambda$CDM$+\nu_s$ (gray), MOD1$+\nu_s$ (red) and MOD2$+\nu_s$ (blue), obtained with the full data combination considered here ("ALL"). The green band is $H_0 = 70.6 \pm 3.3$ Km s$^{-1}$ Mpc$^{-1}$ [123] (GE), while the dark yellow band is $\sigma_8 = 0.75 \pm 0.03$ [136] (SZ). From Ref. [34].

standard matter is disfavored by observations both for DE and DM, but it is possible that the interaction does not involve baryons nor photons or other particles in the standard model. We studied the possibility that DM and DE are coupled to each other in a non-gravitational way. We introduced a phenomenological interaction rate $Q = \xi H \rho_\Lambda$ [577,578,585], where the dimensionless parameter $\xi$ encodes the coupling strength: for our choice, positive $\xi$ values correspond to DM decaying in DE, while a negative $\xi$ gives a scenario with DE decaying in DM.

We test the coupled model using several cosmological data: CMB data and gravitational lensing reconstructions from the 2015 Planck release, SuperNovae distance calibrations, BAO and RSD measured by several experiments. All these measurements have the aim to constrain the evolution of the Universe at different redshifts and to test the gravitational interaction at different epochs. The time-dependency of DE and DM energy densities is indeed modified by the introduction of the coupling that influences both the background and the perturbations evolution.

In the context of an extended $\Lambda$CDM model, we obtained constraints on the coupling parameter $\xi$ and on the DE Equation of State (EoS) $w_\Lambda$. We base our analysis on the Planck observations for CMB temperature and polarization [21, 62], but we obtain the strongest constraints from the inclusion of additional information at several different redshifts. The introduction of Supernovae data from the joint analysis of Ref. [126] strongly constrains the effective DE EoS $w_\Lambda^{\text{eff}} = w_\Lambda + \xi/3$ to be -1, while the BAO/RSD [90,91,93,115] data gives a mild preference for a non-zero coupling, both for MOD1 and MOD2.

If we consider the predicted values of the Hubble parameter $H_0$ and of $\sigma_8$, however, we note that the phenomenology of MOD1, that was more studied in the past (see e.g. Refs. [577, 578]), increases the tension with the low-redshift measurements of $H_0$ [121,123] and the local determinations of $\sigma_8$ [134,136,137,589,593,594]. The reason is that in MOD1 a higher amount of DM in the early Universe is required to have some residual DM today. This higher DM amount increases the clustering effect and drives the evolution to nonlinear scales earlier. In MOD2, on the contrary, $\sigma_8$ is smaller than in the $\Lambda$CDM model and CMB estimates can be reconciled with low-redshift probes.

We studied also the possible presence of a sterile neutrino [15, 22–25, 595–597] as an additional and stable dark matter component. In this case we find that the sterile neutrino

parameters are completely insensitive to the parameters of the CDE model and the constraints are practically the same for the $\Lambda$CDM+$\nu_s$, the MOD1+$\nu_s$ and the MOD2+$\nu_s$ models.

In conclusion, a coupled DM/DE cosmology is a viable option, compatible with a large host of cosmological data. Moreover, a model where DE decays into DM during the evolutionary history of the Universe can help solving the small tensions that currently exist between different high- and low-redshift observations in the context of the $\Lambda$CDM model, therefore providing an interesting new opportunity of investigation for models of the dark sectors of the Universe.

# Chapter 10

# Summary and Conclusions

Our knowledge of the Universe is rather robust. Most of the predictions of the theoretical model based on the theory of General Relativity proposed by A. Einstein have been experimentally confirmed. The last, exciting probe of General Relativity is the recent first detection of the gravitational waves by the LIGO/VIRGO collaboration [598]. Modern cosmology is based on the models derived from the Einstein's theory, that are tested using the numerous experimental data collected in several different observations. The strongest tools to study the models of the Universe evolution are the observations of the Cosmic Microwave Background (CMB), that is the relic photon radiation emitted in the early Universe. This Thesis is devoted to study several aspects of the cosmological evolution using mainly the CMB results obtained by the Planck experiment. We considered different extensions of the standard $\Lambda$CDM model: we included additional particles (neutrinos, axions), we assumed non-standard inflationary scenarios and we introduced an additional coupling between dark matter and dark energy.

The first results that we reported concern the cosmological constraints on the light sterile neutrino. We found that the CMB data disfavor the presence of an additional massive neutrino, if it is thermalized with the active neutrinos. A light neutrino relic is favored, instead, by the local measurements of $\sigma_8$ and $H_0$ (see Chapter 5), because the free-streaming nature of the neutrino allows to reduce the amount of matter fluctuations at small scales even if $H_0$ is simultaneously increased, as a consequence of the correlation with the presence of additional relativistic particles. The mass required to reconcile the $H_0$ and $\sigma_8$ tensions, however, is smaller than the one required by SBL neutrino oscillations.

As a consequence of the anticorrelation between the sterile neutrino mass $m_s$ and its contribution $\Delta N_{\mathrm{eff}}$ to the effective number of relativistic species $N_{\mathrm{eff}}$ (see Chapter 5), the presence of a neutrino with 1 eV mass is allowed only if its contribution to $N_{\mathrm{eff}}$ is much smaller than the one from each active neutrino. The strongest constraints on $\Delta N_{\mathrm{eff}}$ can be obtained considering the 2015 data on the CMB anisotropies by the Planck collaboration, from which it is possible to obtain $\Delta N_{\mathrm{eff}} \lesssim 0.4$ at 95% C.L., with small variations due to the inclusion of different datasets (see Section 6.6). This confirms the problem of the missing thermalization of the sterile neutrino. Previous studies [310,356,364] have shown that the mixing parameters derived from the SBL analyses are large enough to allow the sterile neutrino to be in equilibrium with the active neutrinos. Since this does not happen, some new physical mechanism should operate. Some of the possibilities include: a large lepton asymmetry [310, 355–357, 370, 378–384], new neutrino interactions [365–368, 371, 385–389], entropy production after neutrino decoupling [344], very low reheating temperatures [390, 391], time varying dark energy components [342], a larger cosmic expansion rate at the time of sterile neutrino production [369].

The mechanism of the sterile neutrino decay proposed originally in Ref. [24] has been studied in Section 5.3. We showed that the decay of the light sterile neutrino may help in solving the incomplete thermalization problem only if the CMB data would allow $\Delta N_{\mathrm{eff}} = 1$ for massless species. In this case, indeed, if the fully thermalized sterile neutrino decays into

massless species when it is still relativistic, its mass is not relevant for the evolution, but the amount of radiation is given by $N_{\text{eff}} \simeq 4$. In the decay scenario we found a tension between the measurements at low-redshift and the CMB: if the local determinations of $\sigma_8$ would favor the presence of a massive neutrino in the late-times evolution, in order to suppress the matter fluctuations through the free-streaming effect, the CMB data strongly prefer a rapid decay of the sterile neutrino. These requirements are clearly incompatible. For this reason and since $N_{\text{eff}} \simeq 4$ is strongly disfavored by the current data, the sterile neutrino decay scenario is not a viable solution to reconcile the presence of the light sterile neutrino in cosmology.

Another possibility that we proposed is to assume a scenario that we denoted as "Inflationary Freedom". With this name we indicated the possibility that the Primordial Power Spectrum (PPS) of scalar perturbations generated during inflation can be more complicated than a simple power-law, as the simplest inflationary models predict. Since the final CMB spectrum is the convolution of the scalar PPS and of the transfer function, robustly calculated from the theory discussed in Chapter 2, changes in the transfer function can be compensated by variations in the PPS. Previous analyses of the WMAP and Planck (2013, 2015) CMB spectra showed that there are indications for deviations from the power-law shape of the PPS, especially at large scales [25, 26, 32, 396–409].

We used a model independent parameterization for the free PPS and we showed that strong degeneracies between the PPS parameters and the neutrino parameters exist, in particular at small scales. The effective number of relativistic species is degenerate with the PPS because the presence of additional radiation leads to an enhanced Silk damping effect (see Section 4.4), that can be compensated with an enhancement of the PPS at the relevant scales. One of the main effects of the neutrino mass in cosmology is to alter the contribution of the early ISW effect (see Section 4.4). Also in this case a variation of the PPS at the scales corresponding to the early ISW contribution can partially compensate the effects of increasing the neutrino masses. The result is that the bounds on $N_{\text{eff}}$ and on the neutrino mass scale are significantly relaxed, if only the temperature spectrum of CMB anisotropies is considered. Since the impact of the cosmological parameters and of the PPS are different in the temperature and polarization spectra, however, the degeneracy between the PPS and the neutrino parameters can be broken with the inclusion of the TE and EE spectra at high multipoles measured by the Planck collaboration. If the results obtained without the CMB polarization data in the context of "Inflationary Freedom" would allow the presence of a fully thermalized sterile neutrino (see Section 6.3), this is no more true when the polarization data are included (see Sections 6.6 and 6.7).

In Chapter 7 we studied a different candidate for hot dark matter: the thermal axion. Axions are pseudo-Nambu-Goldstone bosons generated by the spontaneous breaking of the global Peccei-Quinn symmetry $U(1)_{PQ}$, introduced to solve the strong CP problem in Quantum ChromoDynamics. The new symmetry is spontaneously broken at the scale $f_a$, to which the thermal axion mass is connected by Eq. (7.2). Since it is relativistic in the early Universe, contributing to $N_{\text{eff}}$, and non-relativistic at late times, the thermal axion contribution to the cosmological evolution is similar to that of a massive neutrino. Thanks to its free-streaming properties, a thermal axion can reduce the matter fluctuations at small scales and help to reconcile the $\sigma_8$ tension. Also in this case, however, we found that the full CMB data from the 2015 release of Planck disfavor the presence of the additional thermal axion in cosmology. The constraint comes in particular from the fact that a thermal axion gives a minimum contribution $\Delta N_{\text{eff}} \simeq 0.2$ to the amount of radiation in the early Universe, but this is outside the limits at 68% C.L. obtained from the full Planck dataset.

Despite the fact that the presence of the axion is disfavored by the CMB data at 68% C.L., the significance of this result is not high and the presence of a thermal axion is still allowed by the at 95% C.L. constraints. For this reason, we studied the bounds on the axion mass in the context of a power-law and of a free PPS. When we varied also the neutrino masses to test the degeneracy with the thermal axion mass, we found that the constraints on the total neutrino mass are tighter than those obtained without thermal axions, while the

bounds on the thermal axion mass are unchanged. In both cases we find only upper limits on the axion and neutrino masses, unless the Planck SZ cluster counts data are included in the analyses. In the latter case we found the only evidence for a non-null axion mass (see Subsection 7.3.1). As we discussed in Chapter 3, however, the local determinations of $\sigma_8$ may suffer the presence of unaccounted systematics. If these present results will be confirmed in future experiments, the evidence of a non-zero axion mass will be strengthened. As of today, anyhow, the evidence for $m_a > 0$ must be treated with caution, because the CMB results that disfavor the presence of massive thermal axions are more robust than the local determinations of $\sigma_8$.

The majority of the models that generate a non-standard PPS also generate primordial non-Gaussianities, that can be studied using the Large Scale Structures (LSS) of the Universe and the CMB bispectrum. In Chapter 8 we studied how the expectations for the Dark Energy Spectroscopic Instrument (DESI) experiment, an upcoming galaxy survey, change when the hypothesis of a power-law PPS is relaxed. To do this, we assumed that the precise shape of the PPS and the non-Gaussianity parameter $f_{NL}$ need to be extracted simultaneously from the data. We considered three different DESI tracers of the matter distribution at various redshifts: luminous red galaxies, emission line galaxies and high-redshift quasars. If the analysis is restricted to LSS data, the standard errors computed assuming a power-law PPS are enlarged by 60% when using the free PPS parameterization and treating each of the possible dark matter tracers individually. The problem is then that determining the PPS and $f_{NL}$ simultaneously may cause a degrading of the obtained constraints. Another problem could be induced in this way: if nature have chosen a more complicated inflationary mechanism that results in a non-trivial PPS, all the analyses performed under the possibly wrong assumption of a power-law PPS may give biased results, as a consequence of the degeneracy between the PPS and the non-Gaussianities. This degeneracy may be reduced using the multi-tracer technique, or combining the DESI tracers with the CMB priors on the PPS parameters. The addition of CMB priors on the PPS parameters and on the energy densities of dark matter and baryons leads to an error on $f_{NL}$ which is independent of the PPS parameterization used in the analysis.

In the context of the $\Lambda$CDM model, it is possible to obtain predictions on values of the Hubble parameter $H_0$ and of the clustering parameter $\sigma_8$ today from the analyses of CMB data. These predictions are in tension with the low-redshift measurements of $H_0$ [121,123] and the local determinations of $\sigma_8$ [134, 136, 137, 589, 593, 594]. These tensions may be alleviated by the presence of a massive neutrino, that can reduce the perturbations at small scales thanks to its free-streaming properties that influence the Universe evolution, but this is not the only possibility. In Chapter 9 we proposed a solution that involves the introduction of a phenomenological non-gravitational coupling between dark matter and dark energy. Dark matter and dark energy are known only for their gravitational effects, but we still ignore if they can be explained in the context of fundamental physics. The existence of a non-gravitational coupling involving DE or DM cannot be excluded: this additional interaction would have an impact on cosmology and it can be tested studying the various cosmological observables. We introduced a phenomenological interaction rate that describes the energy transfer from dark matter to dark energy. For our choice, a positive coupling (MOD1 for sake of brevity) corresponds to DM decaying in DE, while a negative coupling (MOD2) gives a scenario with DE decaying in DM. We tested the coupled model using several cosmological data at different redshifts, since the time-dependency of the DE and DM energy densities is modified by the introduction of the coupling, that influences both the background and the perturbations evolution. In the context of an extended $\Lambda$CDM model, we obtained constraints on the coupling parameter $\xi$ and on the dark energy equation of state parameter $w_\Lambda$. The introduction of Supernovae data from the joint analysis of Ref. [126] strongly constrains the effective DE EoS parameter $w_\Lambda^{\text{eff}} = w_\Lambda + \xi/3$ (see Subsection 9.2.1) to be $-1$, while the BAO/RSD [90, 91, 93, 115] data gives a preference for a non-zero coupling, both for MOD1 and MOD2. We noticed that the phenomenology of MOD1, that was more studied in the

past (see e.g. Refs. [577, 578]), increases the tension with the low-redshift measurements of $H_0$ [121, 123] and of $\sigma_8$ [134, 136, 137, 589, 593, 594]. The reason is that in MOD1 a higher amount of DM in the early Universe is required to have some residual DM today, and this higher DM amount increases the clustering effect and accelerates the nonlinear evolution. In MOD2, on the contrary, $\sigma_8$ is smaller than in the $\Lambda$CDM model and CMB estimates can be reconciled with low-redshift probes.

In conclusion, the $\Lambda$CDM model is extremely robust and most of the currently available cosmological data disfavor (or strongly constrain) any deviation from the simplest description of the Universe. Despite this, some small tensions are present. It is still not clear if they are the consequence of unaccounted systematics, incomplete or approximated calculations, or unaccounted astrophysical effects in the analyses of low-redshift observations. Maybe they are just hints that some new physics exists. Some new mechanism during inflation may be responsible of the features at large scales observed in the power spectrum of initial scalar fluctuations. A coupled DM/DE cosmology is a viable option to solve the tensions that exists between different high- and low-redshift observations of $H_0$ and $\sigma_8$, if DE decays into DM during the evolution of the Universe. This is also an interesting new opportunity of investigation for models of the dark sector of the Universe. This solution, however, does not help to solve the problem of the thermalization of the sterile neutrino. Future neutrino oscillation experiments will confirm if the sterile neutrino with mass around 1 eV exists. If its existence will be proved, we will have to understand the reasons for which neutrino oscillations, that would allow its thermalization, are suppressed in the hot and dense primordial plasma.

# Part III

# Appendix

# Appendix A

# `PCHIP` Parametrization of the Primordial Power Spectrum

*This Chapter appears as Appendix A in Ref. [25].*

In this work we parameterized the PPS with a "piecewise cubic Hermite interpolating polynomial" (`PCHIP`) [439, 440]. We decided to adopt this interpolating function in order to avoid spurious oscillations of the interpolating function between the nodes which is often obtained in spline interpolations. This problem occurs because a natural cubic spline requires the values of the function, the first and the second derivatives to be continuous in the nodes [599].

The `PCHIP` function, instead, is constructed in order to preserve the shape of the set of points to be interpolated. This is achieved with a modification of the "monotone piecewise cubic interpolation" [439] which can accommodate non-monotone functions and preserves the local monotonicity.

Let us consider a function with known values $y_j$ in N nodes $x_j$, with $j = 1, \ldots, N$. A piecewise cubic interpolation is performed with $N-1$ cubic functions between the nodes. The determination of these $N-1$ cubic functions requires the determination of $4(N-1)$ coefficients. Besides the $2(N-1)$ constraints obtained by requiring that the initial and final point of each cubic function match the known values of the original function in the corresponding nodes, one needs a prescription for the other $2(N-1)$ necessary constraints. In the case of a natural cubic spline interpolation one gets $2(N-2)$ constraints by requiring the continuity of the first and second derivatives in the nodes and the remaining two constraints are obtained by requiring that the second derivatives in the first and last nodes vanish. The drawback of this method is that the interpolating curve is determined by a set of linear equations without any local control. In fact, all the interpolating curve is affected by the change of a single point.

Local control of the interpolating curve can be achieved by relaxing the requirement of continuity of the second derivatives in the nodes and using the resulting freedom to adjust the first derivatives with a local prescription. In order to see how it can be done, it is convenient to write the cubic interpolating polynomial between the nodes $x_j$ and $x_{j+1}$ in the Hermite form

$$f(x; y_1, \ldots, y_N) = \frac{(h_j + 2t)\,(h_j - t)^2}{h_j^3} y_j + \frac{(3h_j - 2t)\,t^2}{h_j^3} y_{j+1} + \frac{(h_j - t)^2\,t}{h_j^2} d_j + \frac{t^2\,(h_j - t)}{h_j^2} d_{j+1},$$

$$(A.1)$$

where $t = x - x_j$ and $h_j = x_{j+1} - x_j$. Here $d_j$ and $d_{j+1}$ are the values of the derivatives in the two nodes. In the `PCHIP` method the derivatives are chosen in order to preserve the local monotonicity of the interpolated points. This is done by considering the relative differences

$$\delta_j = \frac{y_{j+1} - y_j}{x_{j+1} - x_j}.$$

$$(A.2)$$

The `PCHIP` prescription is:

- If $\delta_{j-1}$ and $\delta_j$ have opposite signs, then $x_j$ is a discrete local minimum or maximum and $d_j = 0$.
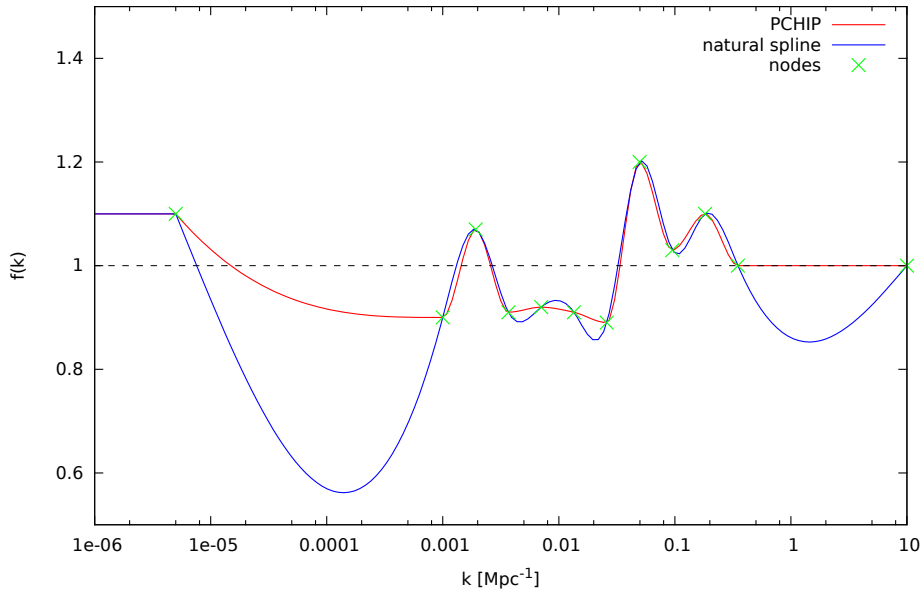
Figure A.1: Illustration of the difference between the `PCHIP` (red line) and the natural spline (blue line) interpolations $f(\log k; y_1, \ldots, y_{12})$ of a function with known values $y_1, \ldots, y_{12}$ in 12 nodes (green crosses) at the values of $k$ in Eq. (6.1). The values $y_1, \ldots, y_{12}$ in the nodes are 1.1, 0.9, 1.07, 0.91, 0.92, 0.91, 0.89, 1.2, 1.03, 1.1, 1.0, 1.0.

- If $\delta_{j-1}$ and $\delta_j$ have the same sign, then $d_j$ is determined by the weighted harmonic mean

$$\frac{w_1 + w_2}{d_j} = \frac{w_1}{\delta_{j-1}} + \frac{w_2}{\delta_j}, \tag{A.3}$$

  with $w_1 = 2h_j + h_{j-1}$ and $w_2 = h_j + 2h_{j-1}$.

- The derivatives in the first and last nodes are determined by a shape-preserving prescription based on a quadratic fit of three points. For $d_1$ we consider the three points $(x_1, y_1)$, $(x_2, y_2)$, $(x_3, y_3)$. The derivative in $x_1$ of the parabola which passes through these three points is given by

$$d(h_1, h_2, \delta_1, \delta_2) = \frac{(2h_1 + h_2)\,\delta_1 - h_1\delta_2}{h_1 + h_2}. \tag{A.4}$$

  The shape-preserving prescription for $d_1$ is:

  - If the signs of $d(h_1, h_2, \delta_1, \delta_2)$ and $\delta_1$ are different, then $d_1 = 0$.
  - If the signs of $\delta_1$ and $\delta_2$ are different and $|d(h_1, h_2, \delta_1, \delta_2)| > 3|\delta_1|$, then $d_1 = 3\delta_1$.
  - Else $d_1 = d(h_1, h_2, \delta_1, \delta_2)$.

  For $d_N$ one must replace $1 \to N-1$ and $2 \to N-2$.

We fit the power spectrum $P_s(k)$ with Eq. (6.2), in which the function $\texttt{PCHIP}(k; P_{s,1}, \ldots, P_{s,12})$ is calculated with the `PCHIP` prescription in the logarithmic scale of $k$:

$$\texttt{PCHIP}(k; P_{s,1}, \ldots, P_{s,12}) = f(\log k; P_{s,1}, \ldots, P_{s,12}). \tag{A.5}$$

A comparison between the natural cubic spline and the `PCHIP` interpolations of the PPS is presented in Fig. A.1. We choose the same nodes positions that we used for the PPS parametrization in our cosmological analysis and we choose the values of the function in the nodes in order to show the difference between the natural cubic spline and the `PCHIP` interpolations. One can see that the `PCHIP` interpolation can reproduce the shape of the points without adding the spurious features between the points that are clearly visible in the natural cubic spline interpolation.

# Bibliography

[1] B. Pontecorvo, "Mesonium and antimesonium," *Sov. Phys. JETP* **6** (1957) 429. [Zh. Eksp. Teor. Fiz. 33, 549 (1957)].

[2] Z. Maki, M. Nakagawa, and S. Sakata, "Remarks on the unified model of elementary particles," *Prog. Theor. Phys.* **28** (1962) 870–880.

[3] **Particle Data Group** Collaboration, K. A. Olive *et al.*, "Review of Particle Physics," *Chin. Phys.* **C38** (2014) 090001.

[4] K. Abe *et al.*, "Measurements of neutrino oscillation in appearance and disappearance channels by the T2K experiment with $6.6 \times 10^{20}$ protons on target," *Phys. Rev.* **D91** (Feb., 2015) 072010, `1502.01550`.

[5] S. M. Bilenky and C. Giunti, "Neutrinoless Double-Beta Decay: a Probe of Physics Beyond the Standard Model," *Int. J. Mod. Phys.* **A30** (Nov., 2015) 1530001, `1411.4791`.

[6] O. Dragoun and D. Vénos, "Searches for Active and Sterile Neutrinos in Beta-Ray Spectra," `arXiv:1504.07496 [hep-ex]`.

[7] C. Weinheimer, "Direct neutrino mass search," in *Proceedings, International School of Physics "Enrico Fermi", 152$^{nd}$ Course, "Neutrino Physics"*. 2002. `arXiv:hep-ex/0210050 [hep-ex]`. `http://alice.cern.ch/format/showfull?sysnb=2346428`.

[8] **KATRIN** Collaboration, S. Mertens, "Status of the KATRIN Experiment and Prospects to Search for keV-mass Sterile Neutrinos in Tritium $\beta$-decay," *Phys. Procedia* **61** (2015) 267–273.

[9] L. Wolfenstein, "Neutrino Oscillations in Matter," *Phys. Rev.* **D17** (1978) 2369–2374.

[10] S. P. Mikheev and A. Yu. Smirnov, "Resonance Amplification of Oscillations in Matter and Spectroscopy of Solar Neutrinos," *Sov. J. Nucl. Phys.* **42** (1985) 913–917. [Yad. Fiz.42,1441(1985)].

[11] S. P. Mikheev and A. Yu. Smirnov, "Resonant amplification of neutrino oscillations in matter and solar neutrino spectroscopy," *Nuovo Cim.* **C9** (1986) 17–26.

[12] **IceCube PINGU** Collaboration, M. G. Aartsen *et al.*, "Letter of Intent: The Precision IceCube Next Generation Upgrade (PINGU)," `arXiv:1401.2046 [physics.ins-det]`.

[13] S. Adrian-Martinez *et al.*, "Letter of Intent for KM3NeT2.0," `arXiv:1601.07459 [astro-ph.IM]`.

[14] F. An *et al.*, "Neutrino Physics with JUNO," *J. Phys.* **G43** (July, 2016) 030401, `1507.05613`.

[15] S. Gariazzo, C. Giunti, M. Laveder, Y. F. Li, and E. M. Zavanin, "Light sterile neutrinos," *J. Phys.* **G43** (2016) 033001, arXiv:1507.08204 [hep-ph].

[16] A. Einstein, "Die Grundlage der allgemeinen Relativitätstheorie," *Annalen der Physik* **354** no. 7, (1916) 769–822.

[17] A. A. Penzias and R. W. Wilson, "A Measurement of excess antenna temperature at 4080-Mc/s," *Astrophys. J.* **142** (1965) 419–421.

[18] G. F. Smoot *et al.*, "Structure in the COBE differential microwave radiometer first year maps," *Astrophys. J.* **396** (1992) L1–L5.

[19] **WMAP** Collaboration, C. L. Bennett *et al.*, "Nine-Year Wilkinson Microwave Anisotropy Probe (WMAP) Observations: Final Maps and Results," *Astrophys. J. Suppl.* **208** (2013) 20, arXiv:1212.5225 [astro-ph.CO].

[20] P. A. R. Ade *et al.*, "Planck 2013 results. I. Overview of products and scientific results," *Astron. Astrophys.* **571** (Nov., 2014) A1, arXiv:1303.5062.

[21] R. Adam *et al.*, "Planck 2015 results. I. Overview of products and scientific results," 1502.01582.

[22] S. Gariazzo, C. Giunti, and M. Laveder, "Light Sterile Neutrinos in Cosmology and Short-Baseline Oscillation Experiments," *JHEP* **11** (2013) 211, arXiv:1309.3192 [hep-ph].

[23] M. Archidiacono, N. Fornengo, S. Gariazzo, C. Giunti, S. Hannestad, and M. Laveder, "Light sterile neutrinos after BICEP-2," *JCAP* **1406** (2014) 031, arXiv:1404.1794 [astro-ph.CO].

[24] S. Gariazzo, C. Giunti, and M. Laveder, "Cosmological Invisible Decay of Light Sterile Neutrinos," arXiv:1404.6160 [astro-ph.CO].

[25] S. Gariazzo, C. Giunti, and M. Laveder, "Light Sterile Neutrinos and Inflationary Freedom," *JCAP* **1504** (2015) 023, arXiv:1412.7405 [astro-ph.CO].

[26] E. Di Valentino, S. Gariazzo, M. Gerbino, E. Giusarma, and O. Mena, "Dark Radiation and Inflationary Freedom after Planck 2015," arXiv:1601.07557 [astro-ph.CO].

[27] R. D. Peccei and H. R. Quinn, "CP Conservation in the Presence of Instantons," *Phys. Rev. Lett.* **38** (1977) 1440–1443.

[28] R. D. Peccei and H. R. Quinn, "Constraints Imposed by CP Conservation in the Presence of Instantons," *Phys. Rev.* **D16** (1977) 1791–1797.

[29] M. S. Turner, "Thermal Production of Not SO Invisible Axions in the Early Universe," *Phys. Rev. Lett.* **59** (1987) 2489. [Erratum: Phys. Rev. Lett.60,1101(1988)].

[30] S. Chang and K. Choi, "Hadronic axion window and the big bang nucleosynthesis," *Phys. Lett.* **B316** (1993) 51–56, arXiv:hep-ph/9306216 [hep-ph].

[31] E. Masso, F. Rota, and G. Zsembinszki, "On axion thermalization in the early universe," *Phys. Rev.* **D66** (2002) 023004, arXiv:hep-ph/0203221 [hep-ph].

[32] E. Di Valentino, S. Gariazzo, E. Giusarma, and O. Mena, "Robustness of cosmological axion mass limits," *Phys. Rev.* **D91** (2015) 123505, arXiv:1503.00911 [astro-ph.CO].

[33] S. Gariazzo, L. Lopez-Honorez, and O. Mena, "Primordial Power Spectrum features and $f_{NL}$ constraints," *Phys. Rev.* **D92** (2015) 063510, `arXiv:1506.05251` `[astro-ph.CO]`.

[34] R. Murgia, S. Gariazzo, and N. Fornengo, "Constraints on the Coupling between Dark Energy and Dark Matter from CMB data," `arXiv:1602.01765 [astro-ph.CO]`.

[35] S. Dodelson, *Modern Cosmology*. Academic Press. Academic Press, 2003. ISBN: 9780122191411.

[36] A. H. Guth, "The Inflationary Universe: A Possible Solution to the Horizon and Flatness Problems," *Phys. Rev.* **D23** (Jan., 1981) 347–356.

[37] A. D. Linde, "A New Inflationary Universe Scenario: A Possible Solution of the Horizon, Flatness, Homogeneity, Isotropy and Primordial Monopole Problems," *Phys. Lett.* **B108** no. 6, (Feb., 1982) 389–393.

[38] V. F. Mukhanov and G. V. Chibisov, "Quantum Fluctuation and Nonsingular Universe. (In Russian)," *JETP Lett.* **33** (1981) 532–535. [Pisma Zh. Eksp. Teor. Fiz.33,549(1981)].

[39] A. A. Starobinsky, "Dynamics of Phase Transition in the New Inflationary Universe Scenario and Generation of Perturbations," *Phys. Lett.* **B117** no. 3-4, (Nov., 1982) 175–178.

[40] S. W. Hawking, "The Development of Irregularities in a Single Bubble Inflationary Universe," *Phys. Lett.* **B115** no. 4, (Sept., 1982) 295.

[41] A. Albrecht and P. J. Steinhardt, "Cosmology for Grand Unified Theories with Radiatively Induced Symmetry Breaking," *Phys. Rev. Lett.* **48** (Apr., 1982) 1220–1223.

[42] F. Lucchin and S. Matarrese, "Power Law Inflation," *Phys. Rev.* **D32** (Sept., 1985) 1316.

[43] V. F. Mukhanov, H. A. Feldman, and R. H. Brandenberger, "Theory of cosmological perturbations. Part 1. Classical perturbations. Part 2. Quantum theory of perturbations. Part 3. Extensions," *Phys. Rept.* **215** no. 5-6, (June, 1992) 203–333.

[44] P. A. R. Ade *et al.*, "Planck 2015 results. XIII. Cosmological parameters," `1502.01589`.

[45] E. W. Kolb and M. S. Turner, *The Early Universe*. Addison-Wesley, 1990. Frontiers in Physics, 69.

[46] A. H. Guth and E. J. Weinberg, "Could the Universe Have Recovered from a Slow First Order Phase Transition?," *Nucl. Phys.* **B212** (1983) 321.

[47] S. W. Hawking, I. G. Moss, and J. M. Stewart, "Bubble Collisions in the Very Early Universe," *Phys. Rev.* **D26** (1982) 2681.

[48] E. R. Harrison, "Fluctuations at the threshold of classical cosmology," *Phys. Rev.* **D1** (1970) 2726–2730.

[49] R. A. Sunyaev and Y. B. Zeldovich, "Small-Scale Fluctuations of Relic Radiation," *Astrophysics and Space Science* **7** (Apr., 1970) 3–19.

[50] P. J. E. Peebles and J. T. Yu, "Primeval adiabatic perturbation in an expanding universe," *Astrophys. J.* **162** (1970) 815–836.

[51]  J. Lesgourgues, G. Mangano, G. Miele, and S. Pastor, *Neutrino Cosmology*. Cambridge University Press, 2013. ISBN: 9781139012874.

[52]  W. T. Hu, *Wandering in the Background: A CMB Explorer*. PhD thesis, UC Berkeley, 1995. `astro-ph/9508126`. `http://alice.cern.ch/format/showfull?sysnb=0207836`.

[53]  M. Zaldarriaga and D. D. Harari, "Analytic approach to the polarization of the cosmic microwave background in flat and open universes," *Phys. Rev.* **D52** (1995) 3276–3287, `arXiv:astro-ph/9504085 [astro-ph]`.

[54]  C.-P. Ma and E. Bertschinger, "Cosmological perturbation theory in the synchronous and conformal Newtonian gauges," *Astrophys. J.* **455** (1995) 7–25, `arXiv:astro-ph/9506072 [astro-ph]`.

[55]  U. Seljak and M. Zaldarriaga, "A Line of sight integration approach to cosmic microwave background anisotropies," *Astrophys. J.* **469** (1996) 437–444, `astro-ph/9603033`.

[56]  R. K. Sachs and A. M. Wolfe, "Perturbations of a cosmological model and angular variations of the microwave background," *Astrophys. J.* **147** (1967) 73–90. [Gen. Rel. Grav.39,1929(2007)].

[57]  J. Silk, "Cosmic black body radiation and galaxy formation," *Astrophys. J.* **151** (1968) 459–471.

[58]  A. Lewis, A. Challinor, and A. Lasenby, "Efficient computation of CMB anisotropies in closed FRW models," *Astrophys. J.* **538** (2000) 473–476, `astro-ph/9911177`.

[59]  S. Weinberg, "Damping of tensor modes in cosmology," *Phys. Rev.* **D69** (2004) 023503, `arXiv:astro-ph/0306304 [astro-ph]`.

[60]  P. A. R. Ade *et al.*, "Planck 2013 results. XV. CMB power spectra and likelihood," *Astron. Astrophys.* **571** (Nov., 2014) A15, `arXiv:1303.5075`.

[61]  **WMAP** Collaboration, G. Hinshaw *et al.*, "Nine-Year Wilkinson Microwave Anisotropy Probe (WMAP) Observations: Cosmological Parameter Results," *Astrophys. J. Suppl.* **208** (2013) 19, `arXiv:1212.5226 [astro-ph.CO]`.

[62]  N. Aghanim *et al.*, "Planck 2015 results. XI. CMB power spectra, likelihoods, and robustness of parameters," *Submitted to: Astron. Astrophys.* (July, 2015) , `1507.02704`.

[63]  P. A. R. Ade *et al.*, "Planck 2013 results. XVII. Gravitational lensing by large-scale structure," *Astron. Astrophys.* **571** (Nov., 2014) A17, `arXiv:1303.5077`.

[64]  P. A. R. Ade *et al.*, "Planck 2015 results. XV. Gravitational lensing," `1502.01591`.

[65]  S. Das *et al.*, "The Atacama Cosmology Telescope: temperature and gravitational lensing power spectrum measurements from three seasons of data," *JCAP* **1404** (2014) 014, `arXiv:1301.1037 [astro-ph.CO]`.

[66]  E. M. George *et al.*, "A measurement of secondary cosmic microwave background anisotropies from the 2500-square-degree SPT-SZ survey," *Astrophys. J.* **799** no. 2, (2015) 177, `arXiv:1408.3161 [astro-ph.CO]`.

[67]  R. Keisler *et al.*, "A Measurement of the Damping Tail of the Cosmic Microwave Background Power Spectrum with the South Pole Telescope," *Astrophys. J.* **743** (2011) 28, `arXiv:1105.3182 [astro-ph.CO]`.

[68] K. T. Story *et al.*, "A Measurement of the Cosmic Microwave Background Damping Tail from the 2500-square-degree SPT-SZ survey," *Astrophys. J.* **779** (2013) 86, `arXiv:1210.7231 [astro-ph.CO]`.

[69] C. L. Reichardt *et al.*, "A measurement of secondary cosmic microwave background anisotropies with two years of South Pole Telescope observations," *Astrophys. J.* **755** (2012) 70, `arXiv:1111.0932 [astro-ph.CO]`.

[70] J. Dunkley *et al.*, "The Atacama Cosmology Telescope: likelihood for small-scale CMB data," *JCAP* **1307** (2013) 025, `arXiv:1301.0776 [astro-ph.CO]`.

[71] **BICEP2** Collaboration, P. A. R. Ade *et al.*, "Detection of *B*-Mode Polarization at Degree Angular Scales by BICEP2," *Phys. Rev. Lett.* **112** (2014) 241101, `arXiv:1403.3985 [astro-ph.CO]`.

[72] P. A. R. Ade *et al.*, "Planck 2013 results. XVI. Cosmological parameters," *Astron. Astrophys.* **571** (Nov., 2014) A16, `arXiv:1303.5076 [astro-ph.CO]`.

[73] R. Adam *et al.*, "Planck intermediate results. XXX. The angular power spectrum of polarized dust emission at intermediate and high Galactic latitudes," *Astron. Astrophys.* **586** (Sept., 2016) A133, `arXiv:1409.5738`.

[74] P. A. R. Ade *et al.*, "BICEP2 / Keck Array V: Measurements of B-mode Polarization at Degree Angular Scales and 150 GHz by the Keck Array," *Astrophys. J.* **811** (2015) 126, `arXiv:1502.00643 [astro-ph.CO]`.

[75] P. A. R. Ade *et al.*, "BICEP2 / Keck Array VI: Improved Constraints On Cosmology and Foregrounds When Adding 95 GHz Data From Keck Array," *Phys. Rev. Lett.* **116** (Oct., 2016) 031302, `1510.09217`.

[76] **Planck Collaborations** Collaboration, P. Ade *et al.*, "Joint Analysis of BICEP2/*Keck Array* and *Planck* Data," *Phys. Rev. Lett.* **114** (2015) 101301, `arXiv:1502.00612 [astro-ph.CO]`.

[77] K. T. Story *et al.*, "A Measurement of the Cosmic Microwave Background Gravitational Lensing Potential from 100 Square Degrees of SPTpol Data," *Astrophys. J.* **810** (2015) 50, `arXiv:1412.4760 [astro-ph.CO]`.

[78] R. Keisler *et al.*, "Measurements of Sub-degree B-mode Polarization in the Cosmic Microwave Background from 100 Square Degrees of SPTpol Data," *Astrophys. J.* **807** (2015) 151, `arXiv:1503.02315 [astro-ph.CO]`.

[79] B. A. Bassett and R. Hlozek, "Baryon Acoustic Oscillations," `arXiv:0910.5224 [astro-ph.CO]`.

[80] É. Aubourg *et al.*, "Cosmological implications of baryon acoustic oscillation measurements," *Phys. Rev.* **D92** (Nov., 2015) 123516, `1411.1074`.

[81] A. D. Sakharov, "Nachal'naia stadija rasshirenija Vselennoj i vozniknovenije neodnorodnosti raspredelenija veshchestva," *Zh. Eksp. Teor. Fiz.* **49** no. 1, (1966) 345–358. [Sov. Phys. JETP22,241(1966)].

[82] C. Blake and K. Glazebrook, "Probing dark energy using baryonic oscillations in the galaxy power spectrum as a cosmological ruler," *Astrophys. J.* **594** (2003) 665–673, `arXiv:astro-ph/0301632 [astro-ph]`.

[83] H.-J. Seo and D. J. Eisenstein, "Probing dark energy with baryonic acoustic oscillations from future large galaxy redshift surveys," *Astrophys. J.* **598** (2003) 720–740, `arXiv:astro-ph/0307460 [astro-ph]`.

[84] M. Hamuy, M. M. Phillips, N. B. Suntzeff, R. A. Schommer, and J. Maza, "BVRI Light Curves for 29 Type Ia Supernovae," *Astron. J.* **112** (1996) 2408–2437, `arXiv:astro-ph/9609064 [astro-ph]`.

[85] **Supernova Search Team** Collaboration, A. G. Riess *et al.*, "Observational evidence from supernovae for an accelerating universe and a cosmological constant," *Astron. J.* **116** (1998) 1009–1038, `arXiv:astro-ph/9805201 [astro-ph]`.

[86] **Supernova Cosmology Project** Collaboration, S. Perlmutter *et al.*, "Measurements of Omega and Lambda from 42 high redshift supernovae," *Astrophys. J.* **517** (1999) 565–586, `astro-ph/9812133`.

[87] D. J. Eisenstein, H.-j. Seo, and M. J. White, "On the Robustness of the Acoustic Scale in the Low-Redshift Clustering of Matter," *Astrophys. J.* **664** (2007) 660–674, `arXiv:astro-ph/0604361 [astro-ph]`.

[88] D. J. Eisenstein, W. Hu, and M. Tegmark, "Cosmic complementarity: H(0) and Omega(m) from combining CMB experiments and redshift surveys," *Astrophys. J.* **504** (1998) L57–L61, `arXiv:astro-ph/9805239 [astro-ph]`.

[89] N. Padmanabhan, X. Xu, D. J. Eisenstein, R. Scalzo, A. J. Cuesta, K. T. Mehta, and E. Kazin, "A 2 per cent distance to $z=0.35$ by reconstructing baryon acoustic oscillations - I. Methods and application to the Sloan Digital Sky Survey," *Mon. Not. Roy. Astron. Soc.* **427** no. 3, (2012) 2132–2145, `arXiv:1202.0090 [astro-ph.CO]`.

[90] F. Beutler, C. Blake, M. Colless, D. H. Jones, L. Staveley-Smith, L. Campbell, Q. Parker, W. Saunders, and F. Watson, "The 6dF Galaxy Survey: Baryon Acoustic Oscillations and the Local Hubble Constant," *Mon. Not. Roy. Astron. Soc.* **416** (2011) 3017–3032, `arXiv:1106.3366 [astro-ph.CO]`.

[91] A. J. Ross, L. Samushia, C. Howlett, W. J. Percival, A. Burden, and M. Manera, "The clustering of the SDSS DR7 main Galaxy sample – I. A 4 per cent distance measure at $z = 0.15$," *Mon. Not. Roy. Astron. Soc.* **449** no. 1, (2015) 835–847, `arXiv:1409.3242 [astro-ph.CO]`.

[92] L. Anderson *et al.*, "The clustering of galaxies in the SDSS-III Baryon Oscillation Spectroscopic Survey: Baryon Acoustic Oscillations in the Data Release 9 Spectroscopic Galaxy Sample," *Mon. Not. Roy. Astron. Soc.* **427** no. 4, (2013) 3435–3467, `arXiv:1203.6594 [astro-ph.CO]`.

[93] **BOSS** Collaboration, L. Anderson *et al.*, "The clustering of galaxies in the SDSS-III Baryon Oscillation Spectroscopic Survey: baryon acoustic oscillations in the Data Releases 10 and 11 Galaxy samples," *Mon. Not. Roy. Astron. Soc.* **441** no. 1, (2014) 24–62, `arXiv:1312.4877 [astro-ph.CO]`.

[94] A. J. Cuesta *et al.*, "The clustering of galaxies in the SDSS-III Baryon Oscillation Spectroscopic Survey: Baryon Acoustic Oscillations in the correlation function of LOWZ and CMASS galaxies in Data Release 12," *Mon. Not. Roy. Astron. Soc.* **457** (2016) 1770, `arXiv:1509.06371 [astro-ph.CO]`.

[95] H. Gil-Marín *et al.*, "The clustering of galaxies in the SDSS-III Baryon Oscillation Spectroscopic Survey: BAO measurement from the LOS-dependent power spectrum of DR12 BOSS galaxies," `arXiv:1509.06373 [astro-ph.CO]`.

[96] **SDSS Collaboration** Collaboration, C. P. Ahn *et al.*, "The Ninth Data Release of the Sloan Digital Sky Survey: First Spectroscopic Data from the SDSS-III Baryon Oscillation Spectroscopic Survey," *Astrophys. J. Suppl.* **203** (2012) 21, `arXiv:1207.7137 [astro-ph.IM]`.

[97] **SDSS** Collaboration, K. N. Abazajian *et al.*, "The Seventh Data Release of the Sloan Digital Sky Survey," *Astrophys. J. Suppl.* **182** (2009) 543–558, `arXiv:0812.0649 [astro-ph]`.

[98] **SDSS** Collaboration, W. J. Percival *et al.*, "Baryon Acoustic Oscillations in the Sloan Digital Sky Survey Data Release 7 Galaxy Sample," *Mon. Not. Roy. Astron. Soc.* **401** (2010) 2148–2168, `arXiv:0907.1660 [astro-ph.CO]`.

[99] D. H. Jones *et al.*, "The 6dF Galaxy Survey: Final Redshift Release (DR3) and Southern Large-Scale Structures," *Mon. Not. Roy. Astron. Soc.* **399** (2009) 683, `arXiv:0903.5451 [astro-ph.CO]`.

[100] C. Blake *et al.*, "The WiggleZ Dark Energy Survey: mapping the distance-redshift relation with baryon acoustic oscillations," *Mon. Not. Roy. Astron. Soc.* **418** (2011) 1707–1724, `arXiv:1108.2635 [astro-ph.CO]`.

[101] D. Parkinson *et al.*, "The WiggleZ Dark Energy Survey: Final data release and cosmological results," *Phys. Rev.* **D86** (2012) 103518, `arXiv:1210.2130 [astro-ph.CO]`.

[102] N. G. Busca *et al.*, "Baryon Acoustic Oscillations in the Ly-$\alpha$ forest of BOSS quasars," *Astron. Astrophys.* **552** (2013) A96, `arXiv:1211.2616 [astro-ph.CO]`.

[103] A. Slosar *et al.*, "Measurement of Baryon Acoustic Oscillations in the Lyman-alpha Forest Fluctuations in BOSS Data Release 9," *JCAP* **1304** (2013) 026, `arXiv:1301.3459 [astro-ph.CO]`.

[104] D. Kirkby *et al.*, "Fitting Methods for Baryon Acoustic Oscillations in the Lyman-$\alpha$ Forest Fluctuations in BOSS Data Release 9," *JCAP* **1303** (2013) 024, `arXiv:1301.3456 [astro-ph.CO]`.

[105] A. Slosar *et al.*, "The Lyman-alpha forest in three dimensions: measurements of large scale flux correlations from BOSS 1st-year data," *JCAP* **1109** (2011) 001, `arXiv:1104.5244 [astro-ph.CO]`.

[106] W. J. Percival, L. Samushia, A. J. Ross, C. Shapiro, and A. Raccanelli, "Redshift-space distortions," *Philosophical Transactions of the Royal Society A: Mathematical, Physical and Engineering Sciences* **369** no. 1957, (Nov., 2011) 5058– Since 5067.

[107] N. Kaiser, "Clustering in real space and in redshift space," *Monthly Notices of the Royal Astronomical Society* **227** no. 1, (July, 1987) 1–21.

[108] A. J. S. Hamilton, "Linear redshift distortions: A Review," in *Ringberg Workshop on Large Scale Structure Ringberg, Germany, September 23-28, 1996*. 1997. `arXiv:astro-ph/9708102 [astro-ph]`. `http://alice.cern.ch/format/showfull?sysnb=0255366`.

[109] M. C. Chu, "Precise measurement of $\theta_{13}$ at Daya Bay," *JCAP* **0910** (2008) 004, `arXiv:0810.0807 [astro-ph]`. `http://inspirehep.net/record/798511/files/arXiv:0810.0807.pdf`.

[110] J. A. Peacock and S. J. Dodds, "Nonlinear evolution of cosmological power spectra," *Mon. Not. Roy. Astron. Soc.* **280** (1996) L19, `arXiv:astro-ph/9603031 [astro-ph]`.

[111] R. Scoccimarro, "Redshift-space distortions, pairwise velocities and nonlinearities," *Phys. Rev.* **D70** (2004) 083007, `arXiv:astro-ph/0407214 [astro-ph]`.

[112] E. Jennings, C. M. Baugh, and S. Pascoli, "Modelling redshift space distortions in hierarchical cosmologies," *Mon. Not. Roy. Astron. Soc.* **410** (2011) 2081, `arXiv:1003.4282 [astro-ph.CO]`.

[113] A. Taruya, T. Nishimichi, and S. Saito, "Baryon Acoustic Oscillations in 2D: Modeling Redshift-space Power Spectrum from Perturbation Theory," *Phys. Rev.* **D82** (2010) 063522, `arXiv:1006.0699 [astro-ph.CO]`.

[114] H. Gil-Marín *et al.*, "The clustering of galaxies in the SDSS-III Baryon Oscillation Spectroscopic Survey: RSD measurement from the LOS-dependent power spectrum of DR12 BOSS galaxies," `arXiv:1509.06386 [astro-ph.CO]`.

[115] L. Samushia *et al.*, "The clustering of galaxies in the SDSS-III Baryon Oscillation Spectroscopic Survey: measuring growth rate and geometry with anisotropic clustering," *Mon. Not. Roy. Astron. Soc.* **439** no. 4, (2014) 3504–3519, `arXiv:1312.4899 [astro-ph.CO]`.

[116] F. Beutler, C. Blake, M. Colless, D. H. Jones, L. Staveley-Smith, G. B. Poole, L. Campbell, Q. Parker, W. Saunders, and F. Watson, "The 6dF Galaxy Survey: z ≈ 0 measurement of the growth rate and $sigma_8$," *Mon. Not. Roy. Astron. Soc.* **423** (2012) 3430–3444, `arXiv:1204.4725 [astro-ph.CO]`.

[117] C. Blake *et al.*, "The WiggleZ Dark Energy Survey: the growth rate of cosmic structure since redshift z=0.9," *Mon. Not. Roy. Astron. Soc.* **415** (2011) 2876, `arXiv:1104.2948 [astro-ph.CO]`.

[118] **BOSS** Collaboration, F. Beutler *et al.*, "The clustering of galaxies in the SDSS-III Baryon Oscillation Spectroscopic Survey: Testing gravity with redshift-space distortions using the power spectrum multipoles," *Mon. Not. Roy. Astron. Soc.* **443** no. 2, (2014) 1065–1089, `arXiv:1312.4611 [astro-ph.CO]`.

[119] B. A. Reid, H.-J. Seo, A. Leauthaud, J. L. Tinker, and M. White, "A 2.5 per cent measurement of the growth rate from small-scale redshift space clustering of SDSS-III CMASS galaxies," *Mon. Not. Roy. Astron. Soc.* **444** no. 1, (2014) 476–502, `arXiv:1404.3742 [astro-ph.CO]`.

[120] S. de la Torre *et al.*, "The VIMOS Public Extragalactic Redshift Survey (VIPERS). Galaxy clustering and redshift-space distortions at z=0.8 in the first data release," *Astron. Astrophys.* **557** (2013) A54, `arXiv:1303.2622 [astro-ph.CO]`.

[121] A. G. Riess, L. Macri, S. Casertano, H. Lampeitl, H. C. Ferguson, A. V. Filippenko, S. W. Jha, W. Li, and R. Chornock, "A 3% Solution: Determination of the Hubble Constant with the Hubble Space Telescope and Wide Field Camera 3," *Astrophys. J.* **730** (2011) 119, `arXiv:1103.2976 [astro-ph.CO]`.

[122] E. M. L. Humphreys, M. J. Reid, J. M. Moran, L. J. Greenhill, and A. L. Argon, "Toward a New Geometric Distance to the Active Galaxy NGC 4258. III. Final Results and the Hubble Constant," *Astrophys. J.* **775** (2013) 13, `arXiv:1307.6031 [astro-ph.CO]`.

[123] G. Efstathiou, "H0 Revisited," *Mon. Not. Roy. Astron. Soc.* **440** (2014) 1138–1152, `arXiv:1311.3461 [astro-ph.CO]`.

[124] W. L. Freedman, B. F. Madore, V. Scowcroft, C. Burns, A. Monson, S. E. Persson, M. Seibert, and J. Rigby, "Carnegie Hubble Program: A Mid-Infrared Calibration of the Hubble Constant," *Astrophys. J.* **758** (2012) 24, `arXiv:1208.3281 [astro-ph.CO]`.

[125] S. H. Suyu *et al.*, "Two accurate time-delay distances from strong lensing: Implications for cosmology," *Astrophys. J.* **766** (2013) 70, `arXiv:1208.6010 [astro-ph.CO]`.

[126] **SDSS** Collaboration, M. Betoule *et al.*, "Improved cosmological constraints from a joint analysis of the SDSS-II and SNLS supernova samples," *Astron. Astrophys.* **568** (2014) A22, `arXiv:1401.4064 [astro-ph.CO]`.

[127] S. Bird, M. Viel, and M. G. Haehnelt, "Massive Neutrinos and the Non-linear Matter Power Spectrum," *Mon. Not. Roy. Astron. Soc.* **420** (2012) 2551–2561, `arXiv:1109.4416 [astro-ph.CO]`.

[128] F. Marulli, C. Carbone, M. Viel, L. Moscardini, and A. Cimatti, "Effects of Massive Neutrinos on the Large-Scale Structure of the Universe," *Mon. Not. Roy. Astron. Soc.* **418** (2011) 346, `arXiv:1103.0278 [astro-ph.CO]`.

[129] **VIRGO Consortium** Collaboration, R. E. Smith, J. A. Peacock, A. Jenkins, S. D. M. White, C. S. Frenk, F. R. Pearce, P. A. Thomas, G. Efstathiou, and H. M. P. Couchmann, "Stable clustering, the halo model and nonlinear cosmological power spectra," *Mon. Not. Roy. Astron. Soc.* **341** (2003) 1311, `arXiv:astro-ph/0207664 [astro-ph]`.

[130] N. Kaiser, "On the Spatial correlations of Abell clusters," *Astrophys. J.* **284** (1984) L9–L12.

[131] S. W. Allen, A. E. Evrard, and A. B. Mantz, "Cosmological Parameters from Observations of Galaxy Clusters," *Ann. Rev. Astron. Astrophys.* **49** (2011) 409–470, `arXiv:1103.4829 [astro-ph.CO]`.

[132] D. H. Weinberg, M. J. Mortonson, D. J. Eisenstein, C. Hirata, A. G. Riess, and E. Rozo, "Observational Probes of Cosmic Acceleration," *Phys. Rept.* **530** (2013) 87–255, `arXiv:1201.2434 [astro-ph.CO]`.

[133] E. Rozo, E. S. Rykoff, J. G. Bartlett, and A. E. Evrard, "Cluster Cosmology at a Crossroads: Neutrino Masses," `arXiv:1302.5086 [astro-ph.CO]`.

[134] A. Vikhlinin *et al.*, "Chandra Cluster Cosmology Project III: Cosmological Parameter Constraints," *Astrophys. J.* **692** (2009) 1060–1074, `arXiv:0812.2720 [astro-ph]`.

[135] R. A. Burenin and A. A. Vikhlinin, "Cosmological parameters constraints from galaxy cluster mass function measurements in combination with other cosmological data," *Astron. Lett.* **38** (2012) 347, `arXiv:1202.2889 [astro-ph.CO]`.

[136] **Planck** Collaboration, P. A. R. Ade *et al.*, "Planck 2013 results. XX. Cosmology from Sunyaev–Zeldovich cluster counts," *Astron. Astrophys.* **571** (2014) A20, `arXiv:1303.5080 [astro-ph.CO]`.

[137] P. A. R. Ade *et al.*, "Planck 2015 results. XXIV. Cosmology from Sunyaev-Zeldovich cluster counts," `1502.01597`.

[138] R. A. Sunyaev and Ya. B. Zeldovich, "Microwave background radiation as a probe of the contemporary structure and history of the universe," *Ann. Rev. Astron. Astrophys.* **18** (1980) 537–560.

[139] A. B. Mantz *et al.*, "Weighing the giants – IV. Cosmology and neutrino mass," *Mon. Not. Roy. Astron. Soc.* **446** (2015) 2205–2225, `arXiv:1407.4516 [astro-ph.CO]`.

[140] J. Hamann and J. Hasenkamp, "A new life for sterile neutrinos: resolving inconsistencies using hot dark matter," *JCAP* **1310** (2013) 044, `arXiv:1308.3255 [astro-ph.CO]`.

[141] M. Kilbinger *et al.*, "CFHTLenS: Combined probe cosmological model comparison using 2D weak gravitational lensing," *Mon. Not. Roy. Astron. Soc.* **430** no. 3, (2013) 2200–2220, `arXiv:1212.3338 [astro-ph.CO]`.

[142] C. Heymans *et al.*, "CFHTLenS tomographic weak lensing cosmological parameter constraints: Mitigating the impact of intrinsic galaxy alignments," *Mon. Not. Roy. Astron. Soc.* **432** (2013) 2433, `arXiv:1303.1808 [astro-ph.CO]`.

[143] P. A. R. Ade *et al.*, "Planck 2015 results. XIV. Dark energy and modified gravity," `1502.01590`.

[144] M. Raveri, "Are cosmological data sets consistent with each other within the Λ cold dark matter model?," *Phys. Rev.* **D93** (2016) 043522, `arXiv:1510.00688 [astro-ph.CO]`.

[145] L. Verde, R. Jimenez, and S. Feeney, "The importance of local measurements for cosmology," *Phys. Dark Univ.* **2** (2013) 65–71, `arXiv:1303.5341 [astro-ph.CO]`.

[146] S. Joudaki *et al.*, "CFHTLenS revisited: assessing concordance with Planck including astrophysical systematics," `arXiv:1601.05786 [astro-ph.CO]`.

[147] T. D. Kitching, L. Verde, A. F. Heavens, and R. Jimenez, "Discrepancies between CFHTLenS cosmic shear & Planck: new physics or systematic effects?," `arXiv:1602.02960 [astro-ph.CO]`.

[148] C. L. Cowan, F. Reines, F. B. Harrison, H. W. Kruse, and A. D. McGuire, "Detection of the free neutrino: A Confirmation," *Science* **124** (1956) 103–104.

[149] S. L. Glashow, "Partial symmetries of weak interactions," *Nucl. Phys.* **22** (1961) 579–588.

[150] S. Weinberg, "A model of leptons," *Phys. Rev. Lett.* **19** (1967) 1264–1266.

[151] A. Salam, "Weak and electromagnetic interactions,".

[152] C. Giunti and C. W. Kim, "Fundamentals of Neutrino Physics and Astrophysics,".

[153] S. Bilenky, *Introduction to the physics of massive and mixed neutrinos*, vol. 817. Springer, 2010.

[154] Z.-z. Xing and S. Zhou, *Neutrinos in particle physics, astronomy and cosmology*. Zhejiang University Press, 2011.

[155] M. C. Gonzalez-Garcia, M. Maltoni, J. Salvado, and T. Schwetz, "Global fit to three neutrino mixing: critical look at present precision," *JHEP* **12** (2012) 123, `1209.3023 [hep-ph]`.

[156] G. Bellini, L. Ludhova, G. Ranucci, and F. L. Villante, "Neutrino oscillations," *Adv. High Energy Phys.* **2014** (2014) 191960, `1310.7858 [hep-ph]`.

[157] **Particle Data Group** Collaboration, J. Beringer *et al.*, "The Review of Particle Physics," *Phys. Rev.* **D86** (2012) 010001. `http://pdg.lbl.gov`.

[158] R. R. Volkas, "Introduction to sterile neutrinos," *Prog. Part. Nucl. Phys.* **48** (2002) 161–174, `hep-ph/0111326`.

[159] R. N. Mohapatra and P. B. Pal, *Massive neutrinos in physics and astrophysics*. World Scientific, 2004.

[160] R. N. Mohapatra and A. Y. Smirnov, "Neutrino Mass and New Physics," *Ann. Rev. Nucl. Part. Sci.* **56** (2006) 569–628, `hep-ph/0603118`.

[161] A. Boyarsky, O. Ruchayskiy, and M. Shaposhnikov, "The Role of sterile neutrinos in cosmology and astrophysics," *Ann. Rev. Nucl. Part. Sci.* **59** (2009) 191–214, `0901.0011 [hep-ph]`.

[162] K. N. Abazajian *et al.*, "Light Sterile Neutrinos: A White Paper," `1204.5379 [hep-ph]`.

[163] M. Drewes, "The Phenomenology of Right Handed Neutrinos," *Int. J. Mod. Phys.* **E22** (2013) 1330019, `1303.6912 [hep-ph]`.

[164] S. M. Bilenky and S. T. Petcov, "Massive neutrinos and neutrino oscillations," *Rev. Mod. Phys.* **59** (1987) 671.

[165] S. L. Glashow, J. Iliopoulos, and L. Maiani, "Weak interactions with lepton – hadron symmetry," *Phys. Rev.* **D2** (1970) 1285–1292.

[166] J. Schechter and J. W. F. Valle, "Neutrino masses in SU(2) x U(1) theories," *Phys. Rev.* **D22** (1980) 2227.

[167] **ALEPH, DELPHI, L3, OPAL, SLD, LEP Electroweak Working Group, SLD Electroweak Group, SLD Heavy Flavour Group** Collaboration, S. Schael *et al.*, "Precision electroweak measurements on the $Z$ resonance," *Phys. Rept.* **427** (2006) 257–454, `hep-ex/0509008`.

[168] C. Jarlskog, "Neutrino Counting at the $Z$ Peak and Right-handed Neutrinos," *Phys. Lett.* **B241** (1990) 579.

[169] S. M. Bilenky, W. Grimus, and H. Neufeld, "A Lower bound on the number of neutrino species measured at Z0 peak," *Phys. Lett.* **B252** (1990) 119–122.

[170] S. M. Bilenky, "On the phenomenology of neutrino oscillations in vacuum," `1208.2497 [hep-ph]`.

[171] S. M. Bilenky, "Some comments on high precision study of neutrino oscillations," *Phys. Part. Nucl. Lett.* **12** (2015) 453–461, `arXiv:1502.06158 [hep-ph]`.

[172] S. Bilenky, "On atmospheric neutrino mass-squared difference in the precision era," `arXiv:1512.04172 [hep-ph]`.

[173] H. A. Bethe, "A Possible Explanation of the Solar Neutrino Puzzle," *Phys. Rev. Lett.* **56** (1986) 1305.

[174] F. Capozzi, G. L. Fogli, E. Lisi, A. Marrone, D. Montanino, and A. Palazzo, "Status of three-neutrino oscillation parameters, circa 2013," *Phys. Rev.* **D89** (2014) 093018, `1312.2878 [hep-ph]`.

[175] D. V. Forero, M. Tortola, and J. W. F. Valle, "Neutrino oscillations refitted," *Phys. Rev.* **D90** no. 9, (2014) 093006, `arXiv:1405.7540 [hep-ph]`.

[176] M. C. Gonzalez-Garcia, M. Maltoni, and T. Schwetz, "Updated fit to three neutrino mixing: status of leptonic CP violation," *JHEP* **11** (Sept., 2014) 052, `1409.5439`.

[177] N. Okada and O. Yasuda, "A Sterile neutrino scenario constrained by experiments and cosmology," *Int. J. Mod. Phys.* **A12** (1997) 3669–3694, `arXiv:hep-ph/9606411 [hep-ph]`.

[178] S. M. Bilenky, C. Giunti, and W. Grimus, "Neutrino mass spectrum from the results of neutrino oscillation experiments," *Eur. Phys. J.* **C1** (1998) 247–253, `arXiv:hep-ph/9607372 [hep-ph]`.

[179] S. M. Bilenky, C. Giunti, W. Grimus, and T. Schwetz, "Four neutrino mass spectra and the Super-Kamiokande atmospheric up - down asymmetry," *Phys. Rev.* **D60** (1999) 073007, `arXiv:hep-ph/9903454 [hep-ph]`.

[180] M. Maltoni, T. Schwetz, M. A. Tortola, and J. W. F. Valle, "Status of global fits to neutrino oscillations," *New J. Phys.* **6** (2004) 122, `hep-ph/0405172`.

[181] A. de Gouvêa, K. J. Kelly, and A. Kobach, "$CP$-invariance violation at short-baseline experiments in $3+1$ neutrino scenarios," *Phys. Rev.* **D91** no. 5, (2015) 053005, `arXiv:1412.1479 [hep-ph]`.

[182] N. Klop and A. Palazzo, "Imprints of CP violation induced by sterile neutrinos in T2K data," *Phys. Rev.* **D91** (2015) 073017, `arXiv:1412.7524 [hep-ph]`.

[183] J. M. Berryman, A. de Gouvêa, K. J. Kelly, and A. Kobach, "Sterile neutrino at the Deep Underground Neutrino Experiment," *Phys. Rev.* **D92** (July, 2015) 073012, `1507.03986`.

[184] H. W. Long, Y. F. Li, and C. Giunti, "CP-violating Phases in Active-Sterile Solar Neutrino Oscillations," *Phys. Rev.* **D87** no. 11, (2013) 113004, `arXiv:1304.2207 [hep-ph]`.

[185] T. A. Mueller *et al.*, "Improved Predictions of Reactor Antineutrino Spectra," *Phys. Rev.* **C83** (2011) 054615, `1101.2663 [hep-ex]`.

[186] P. Huber, "On the determination of anti-neutrino spectra from nuclear reactors," *Phys. Rev.* **C84** (2011) 024617, `1106.0687 [hep-ph]`.

[187] G. Mention, M. Fechner, T. Lasserre, T. A. Mueller, D. Lhuillier, M. Cribier, and A. Letourneau, "The Reactor Antineutrino Anomaly," *Phys. Rev.* **D83** (2011) 073006, `1101.2755 [hep-ex]`.

[188] V. V. Sinev, "Joint analysis of spectral reactor neutrino experiments," `arXiv:1103.2452 [hep-ex]`.

[189] J. Kopp, M. Maltoni, and T. Schwetz, "Are there sterile neutrinos at the eV scale?," *Phys. Rev. Lett.* **107** (2011) 091801, `1103.4570 [hep-ph]`.

[190] C. Giunti and M. Laveder, "3+1 and 3+2 Sterile Neutrino Fits," *Phys. Rev.* **D84** (2011) 073008, `1107.1452 [hep-ph]`.

[191] C. Giunti and M. Laveder, "Status of 3+1 Neutrino Mixing," *Phys. Rev.* **D84** (2011) 093006, `1109.4033 [hep-ph]`.

[192] C. Giunti and M. Laveder, "Implications of 3+1 Short-Baseline Neutrino Oscillations," *Phys. Lett.* **B706** (2011) 200–207, `1111.1069 [hep-ph]`.

[193] E. Ciuffoli, J. Evslin, and H. Li, "The Reactor Anomaly after Daya Bay and RENO," *JHEP* **12** (2012) 110, `arXiv:1205.5499 [hep-ph]`.

[194] C. Giunti, M. Laveder, Y. F. Li, Q. Y. Liu, and H. W. Long, "Update of Short-Baseline Electron Neutrino and Antineutrino Disappearance," *Phys. Rev.* **D86** (2012) 113014, `arXiv:1210.5715 [hep-ph]`.

[195] C. Giunti, M. Laveder, Y. F. Li, and H. W. Long, "Short-baseline electron neutrino oscillation length after troitsk," *Phys. Rev.* **D87** no. 1, (2013) 013004, `arXiv:1212.3805 [hep-ph]`.

[196] C. Zhang, X. Qian, and P. Vogel, "Reactor Antineutrino Anomaly with known $\theta_{13}$," *Phys. Rev.* **D87** no. 7, (2013) 073018, `arXiv:1303.0900 [nucl-ex]`.

[197] J. Kopp, P. A. N. Machado, M. Maltoni, and T. Schwetz, "Sterile Neutrino Oscillations: The Global Picture," *JHEP* **05** (2013) 050, 1303.3011 [hep-ph].

[198] A. N. Ivanov, R. Höllwieser, N. I. Troitskaya, M. Wellenzohn, O. M. Zherebtsov, and A. P. Serebrov, "Deficit of reactor antineutrinos at distances smaller than 100 m and inverse $\beta$ decay," *Phys. Rev.* **C88** no. 5, (2013) 055501, arXiv:1306.1995 [hep-ph].

[199] C. Giunti, M. Laveder, Y. F. Li, and H. W. Long, "Pragmatic View of Short-Baseline Neutrino Oscillations," *Phys. Rev.* **D88** (2013) 073008, arXiv:1308.5288 [hep-ph].

[200] F. Von Feilitzsch, A. A. Hahn, and K. Schreckenbach, "EXPERIMENTAL BETA SPECTRA FROM PU-239 AND U-235 THERMAL NEUTRON FISSION PRODUCTS AND THEIR CORRELATED ANTI-NEUTRINOS SPECTRA," *Phys. Lett.* **B118** (1982) 162–166.

[201] K. Schreckenbach, G. Colvin, W. Gelletly, and F. Von Feilitzsch, "DETERMINATION OF THE ANTI-NEUTRINO SPECTRUM FROM U-235 THERMAL NEUTRON FISSION PRODUCTS UP TO 9.5-MEV," *Phys. Lett.* **B160** (1985) 325–330.

[202] A. A. Hahn, K. Schreckenbach, G. Colvin, B. Krusche, W. Gelletly, and F. Von Feilitzsch, "Anti-neutrino Spectra From $^{241}$Pu and $^{239}$Pu Thermal Neutron Fission Products," *Phys. Lett.* **B218** (1989) 365–368.

[203] N. Haag, F. von Feilitzsch, L. Oberauer, W. Potzel, K. Schreckenbach, and A. A. Sonzogni, "Re-publication of the data from the BILL magnetic spectrometer: The cumulative $\beta$ spectra of the fission products of $^{235}$U, $^{239}$Pu, and $^{241}$Pu," arXiv:1405.3501 [nucl-ex].

[204] M. Fallot *et al.*, "New antineutrino energy spectra predictions from the summation of beta decay branches of the fission products," *Phys. Rev. Lett.* **109** (2012) 202504, arXiv:1208.3877 [nucl-ex].

[205] A. C. Hayes, J. L. Friar, G. T. Garvey, G. Jungman, and G. Jonkmans, "Systematic Uncertainties in the Analysis of the Reactor Neutrino Anomaly," *Phys. Rev. Lett.* **112** (2014) 202501, arXiv:1309.4146 [nucl-th].

[206] D. A. Dwyer and T. J. Langford, "Spectral Structure of Electron Antineutrinos from Nuclear Reactors," *Phys. Rev. Lett.* **114** no. 1, (2015) 012502, arXiv:1407.1281 [nucl-ex].

[207] X. B. Ma, L. Z. Wang, Y. X. Chen, W. L. Zhong, and F. P. An, "Uncertainties analysis of fission fraction for reactor antineutrino experiments," arXiv:1405.6807 [nucl-ex].

[208] A. A. Sonzogni, T. D. Johnson, and E. A. McCutchan, "Nuclear structure insights into reactor antineutrino spectra," *Phys. Rev.* **C91** no. 1, (2015) 011301.

[209] D.-L. Fang and B. A. Brown, "Effect of first forbidden decays on the shape of neutrino spectra," *Phys. Rev.* **C91** no. 2, (2015) 025503, arXiv:1502.02246 [nucl-th].

[210] **IGISOL** Collaboration, A. A. Zakari-Issoufou *et al.*, "Total Absorption Spectroscopy Study of $^{92}$Rb Decay: A Major Contributor to Reactor Antineutrino Spectrum Shape," *Phys. Rev. Lett.* **115** no. 10, (2015) 102503, arXiv:1504.05812 [nucl-ex].

[211] A. C. Hayes, J. L. Friar, G. T. Garvey, D. Ibeling, G. Jungman, T. Kawano, and R. W. Mills, "Possible origins and implications of the shoulder in reactor neutrino spectra," *Phys. Rev.* **D92** no. 3, (2015) 033015, arXiv:1506.00583 [nucl-th].

[212] **RENO** Collaboration, S.-H. Seo, "New Results from RENO and The 5 MeV Excess,"
*AIP Conf. Proc.* **1666** (2015) 080002, `arXiv:1410.7987 [hep-ex]`.

[213] **Double Chooz** Collaboration, J. I. Crespo-Anadón, "Double Chooz: Latest results,"
*Nucl. Part. Phys. Proc.* **265-266** (2015) 99–104, `arXiv:1412.3698 [hep-ex]`.

[214] **Daya Bay** Collaboration, L. Zhan, "Recent Results from Daya Bay," *PoS*
**NEUTEL2015** (2015) 017, `arXiv:1506.01149 [hep-ex]`.

[215] C. Bemporad, G. Gratta, and P. Vogel, "Reactor based neutrino oscillation
experiments," *Rev. Mod. Phys.* **74** (2002) 297, `arXiv:hep-ph/0107277 [hep-ph]`.

[216] M. Fukugita and T. Yanagida, *Physics of neutrinos and applications to astrophysics*.
2003.

[217] Y. Declais *et al.*, "Study of reactor anti-neutrino interaction with proton at Bugey
nuclear power plant," *Phys. Lett.* **B338** (1994) 383–389.

[218] A. A. Kuvshinnikov, L. A. Mikaelyan, S. V. Nikolaev, M. D. Skorokhvatov, and A. V.
Etenko, "Measuring the anti-electron-neutrino + p —> n + e+ cross-section and beta
decay axial constant in a new experiment at Rovno NPP reactor. (In Russian),"
*JETP Lett.* **54** (1991) 253–257. [Sov. J. Nucl. Phys.52,300(1990)].

[219] **Bugey** Collaboration, B. Achkar *et al.*, "Search for neutrino oscillations at 15-meters,
40-meters, and 95-meters from a nuclear power reactor at Bugey," *Nucl. Phys.* **B434**
(1995) 503–534.

[220] **CALTECH-SIN-TUM** Collaboration, G. Zacek *et al.*, "Neutrino Oscillation
Experiments at the Gosgen Nuclear Power Reactor," *Phys. Rev.* **D34** (1986)
2621–2636.

[221] A. Hoummada, S. L. Mikou, G. Bagieu, J. Cavaignac, and D. H. Koang, "Neutrino
oscillations I.L.L. experiment reanalysis," *Applied Radiation and Isotopes* **46** (1995)
449–450.

[222] G. S. Vidyakin, V. N. Vyrodov, I. I. Gurevich, Yu. V. Kozlov, V. P. Martemyanov,
S. V. Sukhotin, V. G. Tarasenkov, and S. K. Khakimov, "Bounds on the neutrino
oscillation parameters for reactor anti-neutrinos," *Sov. Phys. JETP* **71** (1990)
424–426. [Zh. Eksp. Teor. Fiz.98,764(1990)].

[223] A. I. Afonin, S. N. Ketov, V. I. Kopeikin, L. A. Mikaelyan, M. D. Skorokhvatov, and
S. V. Tolokonnikov, "A Study of the Reaction $\bar{\nu}_e + P \to e^+ + N$ on a Nuclear
Reactor," *Sov. Phys. JETP* **67** (1988) 213–221. [Zh. Eksp. Teor. Fiz.94N2,1(1988)].

[224] Z. D. Greenwood *et al.*, "Results of a two position reactor neutrino oscillation
experiment," *Phys. Rev.* **D53** (1996) 6054–6064.

[225] **CHOOZ** Collaboration, M. Apollonio *et al.*, "Search for neutrino oscillations on a
long baseline at the CHOOZ nuclear power station," *Eur. Phys. J.* **C27** (2003)
331–374, `arXiv:hep-ex/0301017 [hep-ex]`.

[226] F. Boehm *et al.*, "Final results from the Palo Verde neutrino oscillation experiment,"
*Phys. Rev.* **D64** (2001) 112001, `arXiv:hep-ex/0107009 [hep-ex]`.

[227] **Double Chooz** Collaboration, Y. Abe *et al.*, "Improved measurements of the
neutrino mixing angle $\theta_{13}$ with the Double Chooz detector," *JHEP* **10** (2014) 086,
`arXiv:1406.7763 [hep-ex]`. [Erratum: JHEP02,074(2015)].

[228] **Daya Bay** Collaboration, C. Zhang, "Recent Results from the Daya Bay
Experiment," *AIP Conf. Proc.* **1666** (2015) 080003, `arXiv:1501.04991 [hep-ex]`.

[229] **SAGE** Collaboration, J. N. Abdurashitov *et al.*, "Measurement of the response of a Ga solar neutrino experiment to neutrinos from an Ar-37 source," *Phys. Rev.* **C73** (2006) 045805, `nucl-ex/0512041`.

[230] M. Laveder, "Unbound neutrino roadmaps," *Nucl. Phys. Proc. Suppl.* **168** (2007) 344–346.

[231] C. Giunti and M. Laveder, "Short-Baseline Active-Sterile Neutrino Oscillations?," *Mod. Phys. Lett.* **A22** (2007) 2499–2509, `hep-ph/0610352`.

[232] M. A. Acero, C. Giunti, and M. Laveder, "Limits on nu(e) and anti-nu(e) disappearance from Gallium and reactor experiments," *Phys. Rev.* **D78** (2008) 073009, `0711.4222 [hep-ph]`.

[233] C. Giunti and M. Laveder, "VSBL Electron Neutrino Disappearance," *Phys. Rev.* **D80** (2009) 013005, `arXiv:0902.1992 [hep-ph]`.

[234] C. Giunti and M. Laveder, "Statistical Significance of the Gallium Anomaly," *Phys. Rev.* **C83** (2011) 065504, `1006.3244 [hep-ph]`.

[235] **GALLEX** Collaboration, P. Anselmann *et al.*, "First results from the Cr-51 neutrino source experiment with the GALLEX detector," *Phys. Lett.* **B342** (1995) 440–450.

[236] **GALLEX** Collaboration, W. Hampel *et al.*, "Final results of the Cr-51 neutrino source experiments in GALLEX," *Phys. Lett.* **B420** (1998) 114–126.

[237] F. Kaether, W. Hampel, G. Heusser, J. Kiko, and T. Kirsten, "Reanalysis of the GALLEX solar neutrino flux and source experiments," *Phys. Lett.* **B685** (2010) 47–54, `arXiv:1001.2731 [hep-ex]`.

[238] D. Abdurashitov *et al.*, "The Russian-American gallium experiment (SAGE) Cr neutrino source measurement," *Phys. Rev. Lett.* **77** (1996) 4708–4711.

[239] **SAGE** Collaboration, J. N. Abdurashitov *et al.*, "Measurement of the response of the Russian-American gallium experiment to neutrinos from a Cr-51 source," *Phys. Rev.* **C59** (1999) 2246–2263, `arXiv:hep-ph/9803418 [hep-ph]`.

[240] **SAGE** Collaboration, J. N. Abdurashitov *et al.*, "Measurement of the solar neutrino capture rate with gallium metal. III: Results for the 2002–2007 data-taking period," *Phys. Rev.* **C80** (2009) 015807, `arXiv:0901.2200 [nucl-ex]`.

[241] J. N. Bahcall, "Gallium solar neutrino experiments: Absorption cross-sections, neutrino spectra, and predicted event rates," *Phys. Rev.* **C56** (1997) 3391–3409, `arXiv:hep-ph/9710491 [hep-ph]`.

[242] W. C. Haxton, "Cross-section uncertainties in the gallium neutrino source experiments," *Phys. Lett.* **B431** (1998) 110–118, `arXiv:nucl-th/9804011 [nucl-th]`.

[243] D. Krofcheck *et al.*, "GAMOW-TELLER STRENGTH FUNCTION IN GE-71 VIA THE (P, N) REACTION AT MEDIUM-ENERGIES," *Phys. Rev. Lett.* **55** (1985) 1051–1054.

[244] D. Krofcheck, "Gamow-Teller strength distributions for solar neutrino detectors via the (p,n) reaction,". PhD Thesis, Ohio State University.

[245] D. Frekers *et al.*, "The Ga-71(He-3, t) reaction and the low-energy neutrino response," *Phys. Lett.* **B706** (2011) 134–138.

[246] **LSND** Collaboration, C. Athanassopoulos *et al.*, "Candidate events in a search for anti-muon-neutrino —> anti-electron-neutrino oscillations," *Phys. Rev. Lett.* **75** (1995) 2650–2653, `arXiv:nucl-ex/9504002 [nucl-ex]`.

[247] **LSND** Collaboration, A. Aguilar-Arevalo *et al.*, "Evidence for neutrino oscillations from the observation of anti-neutrino(electron) appearance in a anti-neutrino(muon) beam," *Phys. Rev.* **D64** (2001) 112007, `hep-ex/0104049`.

[248] B. Armbruster *et al.*, "Search for anti-nu/mu –> anti-nu/e oscillations with KARMEN2," *Nucl. Phys.* **A663** (2000) 803–806.

[249] **KARMEN** Collaboration, B. Armbruster *et al.*, "Upper limits for neutrino oscillations muon-anti-neutrino —> electron-anti-neutrino from muon decay at rest," *Phys. Rev.* **D65** (2002) 112001, `arXiv:hep-ex/0203021 [hep-ex]`.

[250] **MiniBooNE** Collaboration, A. A. Aguilar-Arevalo *et al.*, "Unexplained Excess of Electron-Like Events From a 1-GeV Neutrino Beam," *Phys. Rev. Lett.* **102** (2009) 101802, `arXiv:0812.2243 [hep-ex]`.

[251] **MiniBooNE** Collaboration, A. A. Aguilar-Arevalo *et al.*, "Event Excess in the MiniBooNE Search for $\bar{\nu}_\mu \to \bar{\nu}_e$ Oscillations," *Phys. Rev. Lett.* **105** (2010) 181801, `arXiv:1007.1150 [hep-ex]`.

[252] **MiniBooNE** Collaboration, A. A. Aguilar-Arevalo *et al.*, "Improved Search for $\bar{\nu}_\mu \to \bar{\nu}_e$ Oscillations in the MiniBooNE Experiment," *Phys. Rev. Lett.* **110** (2013) 161801, `arXiv:1207.4809 [hep-ex]`.

[253] M. Maltoni and T. Schwetz, "Testing the statistical compatibility of independent data sets," *Phys. Rev.* **D68** (2003) 033020, `arXiv:hep-ph/0304176 [hep-ph]`.

[254] J. J. Gomez-Cadenas and M. C. Gonzalez-Garcia, "Future tau-neutrino oscillation experiments and present data," *Z. Phys.* **C71** (1996) 443–454, `arXiv:hep-ph/9504246 [hep-ph]`.

[255] S. Goswami, "Accelerator, reactor, solar and atmospheric neutrino oscillation: Beyond three generations," *Phys. Rev.* **D55** (1997) 2931–2949, `arXiv:hep-ph/9507212 [hep-ph]`.

[256] C. Giunti, M. C. Gonzalez-Garcia, and C. Pena-Garay, "Four-neutrino oscillation solutions of the solar neutrino problem," *Phys. Rev.* **D62** (2000) 013005, `arXiv:hep-ph/0001101 [hep-ph]`.

[257] V. D. Barger, B. Kayser, J. Learned, T. J. Weiler, and K. Whisnant, "Fate of the sterile neutrino," *Phys. Lett.* **B489** (2000) 345–352, `arXiv:hep-ph/0008019 [hep-ph]`.

[258] O. L. G. Peres and A. Yu. Smirnov, "(3+1) spectrum of neutrino masses: A Chance for LSND?," *Nucl. Phys.* **B599** (2001) 3, `arXiv:hep-ph/0011054 [hep-ph]`.

[259] W. Grimus and T. Schwetz, "Four neutrino mass schemes and the likelihood of (3+1) mass spectra," *Eur. Phys. J.* **C20** (2001) 1–11, `arXiv:hep-ph/0102252 [hep-ph]`.

[260] A. Strumia, "Interpreting the LSND anomaly: Sterile neutrinos or CPT violation or...?," *Phys. Lett.* **B539** (2002) 91–101, `arXiv:hep-ph/0201134 [hep-ph]`.

[261] M. Maltoni, T. Schwetz, M. A. Tortola, and J. W. F. Valle, "Ruling out four neutrino oscillation interpretations of the LSND anomaly?," *Nucl. Phys.* **B643** (2002) 321–338, `arXiv:hep-ph/0207157 [hep-ph]`.

[262] R. Foot, "Are four neutrino models ruled out?," *Mod. Phys. Lett.* **A18** (2003) 2079–2082, `arXiv:hep-ph/0210393 [hep-ph]`.

[263] C. Giunti, "Last CPT invariant hope for LSND neutrino oscillations," *Mod. Phys. Lett.* **A18** (2003) 1179–1186, `arXiv:hep-ph/0302173 [hep-ph]`.

[264] M. Sorel, J. M. Conrad, and M. Shaevitz, "A Combined analysis of short baseline neutrino experiments in the (3+1) and (3+2) sterile neutrino oscillation hypotheses," *Phys. Rev.* **D70** (2004) 073004, `arXiv:hep-ph/0305255 [hep-ph]`.

[265] V. Barger, D. Marfatia, and K. Whisnant, "LSND anomaly from CPT violation in four neutrino models," *Phys. Lett.* **B576** (2003) 303–308, `arXiv:hep-ph/0308299 [hep-ph]`.

[266] M. Maltoni and T. Schwetz, "Sterile neutrino oscillations after first MiniBooNE results," *Phys. Rev.* **D76** (2007) 093005, `arXiv:0705.0107 [hep-ph]`.

[267] S. Goswami and W. Rodejohann, "MiniBooNE results and neutrino schemes with 2 sterile neutrinos: Possible mass orderings and observables related to neutrino masses," *JHEP* **10** (2007) 073, `arXiv:0706.1462 [hep-ph]`.

[268] T. Schwetz, "LSND versus MiniBooNE: Sterile neutrinos with energy dependent masses and mixing?," *JHEP* **02** (2008) 011, `arXiv:0710.2985 [hep-ph]`.

[269] G. Karagiorgi, Z. Djurcic, J. M. Conrad, M. H. Shaevitz, and M. Sorel, "Viability of Delta m**2 1- eV**2 sterile neutrino mixing models in light of MiniBooNE electron neutrino and antineutrino data from the Booster and NuMI beamlines," *Phys. Rev.* **D80** (2009) 073001, `arXiv:0906.1997 [hep-ph]`. [Erratum: Phys. Rev.D81,039902(2010)].

[270] E. Akhmedov and T. Schwetz, "MiniBooNE and LSND data: Non-standard neutrino interactions in a (3+1) scheme versus (3+2) oscillations," *JHEP* **10** (2010) 115, `arXiv:1007.4171 [hep-ph]`.

[271] A. E. Nelson, "Effects of CP Violation from Neutral Heavy Fermions on Neutrino Oscillations, and the LSND/MiniBooNE Anomalies," *Phys. Rev.* **D84** (2011) 053001, `arXiv:1010.3970 [hep-ph]`.

[272] C. Giunti and M. Laveder, "electron-neutrino Disappearance in MiniBooNE," *Phys. Rev.* **D77** (2008) 093002, `arXiv:0707.4593 [hep-ph]`.

[273] C. Giunti and M. Laveder, "Short-Baseline Electron Neutrino Disappearance, Tritium Beta Decay and Neutrinoless Double-Beta Decay," *Phys. Rev.* **D82** (2010) 053005, `arXiv:1005.4599 [hep-ph]`.

[274] C. Giunti and M. Laveder, "Hint of CPT Violation in Short-Baseline Electron Neutrino Disappearance," *Phys. Rev.* **D82** (2010) 113009, `arXiv:1008.4750 [hep-ph]`.

[275] C. Giunti and M. Laveder, "Short-Baseline $\bar{\nu}_m u \rightarrow \bar{\nu}_e$ Oscillations," *Phys. Rev.* **D82** (2010) 093016, `arXiv:1010.1395 [hep-ph]`.

[276] C. Giunti and M. Laveder, "Large Short-Baseline antinu_mu Disappearance," *Phys. Rev.* **D83** (2011) 053006, `arXiv:1012.0267 [hep-ph]`.

[277] A. Donini, P. Hernandez, J. Lopez-Pavon, and M. Maltoni, "Minimal models with light sterile neutrinos," *JHEP* **07** (2011) 105, `arXiv:1106.0064 [hep-ph]`.

[278] J. M. Conrad and M. H. Shaevitz, "Limits on Electron Neutrino Disappearance from the KARMEN and LSND $\nu_e$ - Carbon Cross Section Data," *Phys. Rev.* **D85** (2012) 013017, `arXiv:1106.5552 [hep-ex]`.

[279] G. Karagiorgi, M. H. Shaevitz, and J. M. Conrad, "Confronting the Short-Baseline Oscillation Anomalies with a Single Sterile Neutrino and Non-Standard Matter Effects," `arXiv:1202.1024 [hep-ph]`.

[280] E. Kuflik, S. D. McDermott, and K. M. Zurek, "Neutrino Phenomenology in a 3+1+1 Framework," *Phys. Rev.* **D86** (2012) 033015, `arXiv:1205.1791 [hep-ph]`.

[281] A. Donini, P. Hernandez, J. Lopez-Pavon, M. Maltoni, and T. Schwetz, "The minimal 3+2 neutrino model versus oscillation anomalies," *JHEP* **07** (2012) 161, `arXiv:1205.5230 [hep-ph]`.

[282] M. Archidiacono, N. Fornengo, C. Giunti, and A. Melchiorri, "Testing 3+1 and 3+2 neutrino mass models with cosmology and short baseline experiments," *Phys. Rev.* **D86** (2012) 065028, `arXiv:1207.6515 [astro-ph.CO]`.

[283] J. M. Conrad, C. M. Ignarra, G. Karagiorgi, M. H. Shaevitz, and J. Spitz, "Sterile Neutrino Fits to Short Baseline Neutrino Oscillation Measurements," *Adv. High Energy Phys.* **2013** (2013) 163897, `1207.4765 [hep-ex]`.

[284] L. Borodovsky *et al.*, "Search for muon-neutrino oscillations muon-neutrino —> electron-neutrino (anti-muon-neutrino —> anti-electron-neutrino in a wide band neutrino beam," *Phys. Rev. Lett.* **68** (1992) 274–277.

[285] **NOMAD** Collaboration, P. Astier *et al.*, "Search for nu(mu) —> nu(e) oscillations in the NOMAD experiment," *Phys. Lett.* **B570** (2003) 19–31, `arXiv:hep-ex/0306037 [hep-ex]`.

[286] **ICARUS** Collaboration, M. Antonello *et al.*, "Search for anomalies in the $\nu_e$ appearance from a $\nu_\mu$ beam," *Eur. Phys. J.* **C73** (2013) 2599, `arXiv:1307.4699 [hep-ex]`.

[287] **OPERA** Collaboration, N. Agafonova *et al.*, "Search for $\nu_\mu \to \nu_e$ oscillations with the OPERA experiment in the CNGS beam," *JHEP* **07** (2013) 004, `arXiv:1303.3953 [hep-ex]`. [Addendum: JHEP07,085(2013)].

[288] C. Giunti and Y. F. Li, "Matter Effects in Active-Sterile Solar Neutrino Oscillations," *Phys. Rev.* **D80** (2009) 113007, `arXiv:0910.5856 [hep-ph]`.

[289] A. Palazzo, "Testing the very-short-baseline neutrino anomalies at the solar sector," *Phys. Rev.* **D83** (2011) 113013, `arXiv:1105.1705 [hep-ph]`.

[290] A. Palazzo, "An estimate of $\theta_{14}$ independent of the reactor antineutrino flux determinations," *Phys. Rev.* **D85** (2012) 077301, `arXiv:1201.4280 [hep-ph]`.

[291] A. Palazzo, "Phenomenology of light sterile neutrinos: a brief review," *Mod. Phys. Lett.* **A28** (2013) 1330004, `1302.1102 [hep-ph]`.

[292] **KARMEN** Collaboration, B. E. Bodmann *et al.*, "Neutrino interactions with carbon: Recent measurements and a new test of electron-neutrino, anti-muon-neutrino universality," *Phys. Lett.* **B332** (1994) 251–257.

[293] B. Armbruster *et al.*, "KARMEN limits on electron-neutrino —> tau-neutrino oscillations in two neutrino and three neutrino mixing schemes," *Phys. Rev.* **C57** (1998) 3414–3424, `arXiv:hep-ex/9801007 [hep-ex]`.

[294] **LSND** Collaboration, L. B. Auerbach *et al.*, "Measurements of charged current reactions of nu(e) on 12-C," *Phys. Rev.* **C64** (2001) 065501, `arXiv:hep-ex/0105068 [hep-ex]`.

[295] F. Dydak *et al.*, "A Search for Muon-neutrino Oscillations in the Delta m**2 Range 0.3-eV**2 to 90-eV**2," *Phys. Lett.* **B134** (1984) 281.

[296] D. Hernandez and A. Yu. Smirnov, "Active to sterile neutrino oscillations: Coherence and MINOS results," *Phys. Lett.* **B706** (2012) 360–366, `arXiv:1105.5946 [hep-ph]`.

[297] **MINOS** Collaboration, P. Adamson *et al.*, "Active to sterile neutrino mixing limits from neutral-current interactions in MINOS," *Phys. Rev. Lett.* **107** (2011) 011802, `arXiv:1104.3922 [hep-ex]`.

[298] **SciBooNE, MiniBooNE** Collaboration, K. B. M. Mahn *et al.*, "Dual baseline search for muon neutrino disappearance at $0.5eV^2 \Delta m^2 40eV^2$," *Phys. Rev.* **D85** (2012) 032007, `arXiv:1106.5685 [hep-ex]`.

[299] **SciBooNE, MiniBooNE** Collaboration, G. Cheng *et al.*, "Dual baseline search for muon antineutrino disappearance at $0.1eV^2 \Delta m^2 100eV^2$," *Phys. Rev.* **D86** (2012) 052009, `arXiv:1208.0322`.

[300] **MicroBooNE** Collaboration, H. Chen *et al.*, "A Proposal for a New Experiment Using the Booster and NuMI Neutrino Beamlines: MicroBooNE,". FERMILAB-PROPOSAL-0974.

[301] **ArgoNeuT, MicroBooNE** Collaboration, A. M. Szelc, "Recent results from ArgoNeuT and status of MicroBooNE," *AIP Conf. Proc.* **1666** (2015) 180001.

[302] T. Katori and J. Conrad, "Beyond Standard Model Searches in the MiniBooNE Experiment," *Adv. High Energy Phys.* **2015** (2015) 362971, `arXiv:1404.7759 [hep-ex]`.

[303] M. Archidiacono, N. Fornengo, C. Giunti, S. Hannestad, and A. Melchiorri, "Sterile neutrinos: Cosmology versus short-baseline experiments," *Phys. Rev.* **D87** no. 12, (2013) 125034, `arXiv:1302.6720 [astro-ph.CO]`.

[304] G. Mangano, G. Miele, S. Pastor, and M. Peloso, "A Precision calculation of the effective number of cosmological neutrinos," *Phys. Lett.* **B534** (2002) 8–16, `arXiv:astro-ph/0111408 [astro-ph]`.

[305] G. Mangano, G. Miele, S. Pastor, T. Pinto, O. Pisanti, and P. D. Serpico, "Relic neutrino decoupling including flavor oscillations," *Nucl. Phys.* **B729** (2005) 221–234, `hep-ph/0506164`.

[306] M. A. Acero and J. Lesgourgues, "Cosmological constraints on a light non-thermal sterile neutrino," *Phys. Rev.* **D79** (2009) 045026, `arXiv:0812.2249 [astro-ph]`.

[307] A. D. Dolgov and F. L. Villante, "BBN bounds on active sterile neutrino mixing," *Nucl. Phys.* **B679** (2004) 261–298, `hep-ph/0308083`.

[308] M. Cirelli, G. Marandella, A. Strumia, and F. Vissani, "Probing oscillations into sterile neutrinos with cosmology, astrophysics and experiments," *Nucl. Phys.* **B708** (2005) 215–267, `hep-ph/0403158`.

[309] A. Melchiorri, O. Mena, S. Palomares-Ruiz, S. Pascoli, A. Slosar, and M. Sorel, "Sterile Neutrinos in Light of Recent Cosmological and Oscillation Data: A Multi-Flavor Scheme Approach," *JCAP* **0901** (2009) 036, `arXiv:0810.5133 [hep-ph]`.

[310] S. Hannestad, I. Tamborra, and T. Tram, "Thermalisation of light sterile neutrinos in the early universe," *JCAP* **1207** (2012) 025, 1204.5861 [astro-ph].

[311] A. Mirizzi, G. Mangano, N. Saviano, E. Borriello, C. Giunti, G. Miele, and O. Pisanti, "The strongest bounds on active-sterile neutrino mixing after Planck data," *Phys. Lett.* **B726** (2013) 8–14, arXiv:1303.5368 [astro-ph.CO].

[312] S. Hannestad, R. S. Hansen, T. Tram, and Y. Y. Y. Wong, "Active-sterile neutrino oscillations in the early Universe with full collision terms," *JCAP* **1508** (2015) 019, arXiv:1506.05266 [hep-ph].

[313] S. Dodelson and L. M. Widrow, "Sterile-neutrinos as dark matter," *Phys. Rev. Lett.* **72** (1994) 17–20, arXiv:hep-ph/9303287 [hep-ph].

[314] S. Colombi, S. Dodelson, and L. M. Widrow, "Large scale structure tests of warm dark matter," *Astrophys. J.* **458** (1996) 1, arXiv:astro-ph/9505029 [astro-ph].

[315] A. Cuoco, J. Lesgourgues, G. Mangano, and S. Pastor, "Do observations prove that cosmological neutrinos are thermally distributed?," *Phys. Rev.* **D71** (2005) 123501, arXiv:astro-ph/0502465 [astro-ph].

[316] M. Archidiacono, E. Giusarma, S. Hannestad, and O. Mena, "Cosmic dark radiation and neutrinos," *Adv. High Energy Phys.* **2013** (2013) 191047, 1307.0637 [astro-ph].

[317] Z. Hou, R. Keisler, L. Knox, M. Millea, and C. Reichardt, "How Massless Neutrinos Affect the Cosmic Microwave Background Damping Tail," *Phys. Rev.* **D87** (2013) 083008, arXiv:1104.2333 [astro-ph.CO].

[318] R. Bowen, S. H. Hansen, A. Melchiorri, J. Silk, and R. Trotta, "The Impact of an extra background of relativistic particles on the cosmological parameters derived from microwave background anisotropies," *Mon. Not. Roy. Astron. Soc.* **334** (2002) 760, arXiv:astro-ph/0110636 [astro-ph].

[319] S. Bashinsky and U. Seljak, "Neutrino perturbations in CMB anisotropy and matter clustering," *Phys. Rev.* **D69** (2004) 083002, arXiv:astro-ph/0310198 [astro-ph].

[320] S. Gariazzo, "Light Sterile Neutrinos In Cosmology," in *17th Lomonosov Conference on Elementary Particle Physics. Moscow, Russia, August 20–26, 2015*, A. Studenikin, ed. World Scientific Publ. Co., 2016. arXiv:1601.01475 [astro-ph.CO]. http://inspirehep.net/record/1414175/files/arXiv:1601.01475.pdf.

[321] W. Hu and N. Sugiyama, "Small scale cosmological perturbations: An Analytic approach," *Astrophys. J.* **471** (1996) 542–570, arXiv:astro-ph/9510117 [astro-ph].

[322] G. Steigman, "Neutrinos And Big Bang Nucleosynthesis," *Adv. High Energy Phys.* **2012** (2012) 268321, arXiv:1208.0032 [hep-ph].

[323] F. Iocco, G. Mangano, G. Miele, O. Pisanti, and P. D. Serpico, "Primordial Nucleosynthesis: from precision cosmology to fundamental physics," *Phys. Rept.* **472** (2009) 1–76, arXiv:0809.0631 [astro-ph].

[324] T. D. Jacques, L. M. Krauss, and C. Lunardini, "Additional Light Sterile Neutrinos and Cosmology," *Phys. Rev.* **D87** no. 8, (2013) 083515, arXiv:1301.3119 [astro-ph.CO]. [Erratum: Phys. Rev.D88,no.10,109901(2013)].

[325] B. D. Fields, P. Molaro, and S. Sarkar, "Big-Bang Nucleosynthesis," *Chin. Phys.* **C38** (Dec., 2014) 090001, 1412.1408.

[326] G. Mangano and P. D. Serpico, "A robust upper limit on $N_{eff}$ from BBN, circa 2011," *Phys. Lett.* **B701** (2011) 296–299, arXiv:1103.1261 [astro-ph.CO].

[327] R. H. Cyburt, B. D. Fields, K. A. Olive, and T.-H. Yeh, "Big Bang Nucleosynthesis: 2015," arXiv:1505.01076 [astro-ph.CO].

[328] J. Lesgourgues and S. Pastor, "Neutrino cosmology and Planck," *New J. Phys.* **16** (2014) 065002, 1404.1740 [hep-ph].

[329] P. Di Bari, S. F. King, and A. Merle, "Dark Radiation or Warm Dark Matter from long lived particle decays in the light of Planck," *Phys. Lett.* **B724** (2013) 77–83, arXiv:1303.6267 [hep-ph].

[330] C. Boehm, M. J. Dolan, and C. McCabe, "A Lower Bound on the Mass of Cold Thermal Dark Matter from Planck," *JCAP* **1308** (2013) 041, arXiv:1303.6270 [hep-ph].

[331] C. Kelso, S. Profumo, and F. S. Queiroz, "Non-thermal WIMPs as "Dark Radiation" in Light of ATACAMA, SPT, WMAP9 and Planck," *Phys. Rev.* **D88** no. 2, (2013) 023511, arXiv:1304.5243 [hep-ph].

[332] E. Di Valentino, A. Melchiorri, and O. Mena, "Dark radiation sterile neutrino candidates after Planck data," *JCAP* **1311** (2013) 018, arXiv:1304.5981.

[333] N. Said, E. Di Valentino, and M. Gerbino, "Planck constraints on the effective neutrino number and the CMB power spectrum lensing amplitude," *Phys. Rev.* **D88** no. 2, (2013) 023513, arXiv:1304.6217 [astro-ph.CO].

[334] S. Weinberg, "Goldstone Bosons as Fractional Cosmic Neutrinos," *Phys. Rev. Lett.* **110** no. 24, (2013) 241301, arXiv:1305.1971 [astro-ph.CO].

[335] L. Verde, P. Protopapas, and R. Jimenez, "Planck and the local Universe: Quantifying the tension," *Phys. Dark Univ.* **2** (2013) 166–175, arXiv:1306.6766 [astro-ph.CO].

[336] L. Verde, S. M. Feeney, D. J. Mortlock, and H. V. Peiris, "(Lack of) Cosmological evidence for dark radiation after Planck," *JCAP* **1309** (2013) 013, arXiv:1307.2904 [astro-ph.CO].

[337] M. Wyman, D. H. Rudd, R. A. Vanderveld, and W. Hu, "Neutrinos Help Reconcile Planck Measurements with the Local Universe," *Phys. Rev. Lett.* **112** no. 5, (Feb., 2014) 051302, 1307.7715.

[338] R. A. Battye and A. Moss, "Evidence for Massive Neutrinos from Cosmic Microwave Background and Lensing Observations," *Phys. Rev. Lett.* **112** no. 5, (Feb., 2014) 051303, 1308.5870.

[339] J. Lesgourgues and S. Pastor, "Neutrino mass from Cosmology," *Adv. High Energy Phys.* **2012** (2012) 608515, arXiv:1212.6154 [hep-ph].

[340] J. R. Kristiansen, Ø. Elgarøy, C. Giunti, and M. Laveder, "Cosmology with sterile neutrino masses from oscillation experiments," arXiv:1303.4654 [astro-ph.CO].

[341] A. Lewis and S. Bridle, "Cosmological parameters from CMB and other data: A Monte Carlo approach," *Phys. Rev.* **D66** (2002) 103511, astro-ph/0205436.

[342] E. Giusarma, M. Archidiacono, R. de Putter, A. Melchiorri, and O. Mena, "Sterile neutrino models and nonminimal cosmologies," *Phys. Rev.* **D85** (2012) 083522, arXiv:1112.4661 [astro-ph.CO].

[343] H. Motohashi, A. A. Starobinsky, and J. Yokoyama, "Cosmology Based on f(R) Gravity Admits 1 eV Sterile Neutrinos," *Phys. Rev. Lett.* **110** no. 12, (2013) 121302, `arXiv:1203.6828 [astro-ph.CO]`.

[344] C. M. Ho and R. J. Scherrer, "Sterile Neutrinos and Light Dark Matter Save Each Other," *Phys. Rev.* **D87** (2013) 065016, `1212.1689 [hep-ph]`.

[345] M. Cribier, M. Fechner, T. Lasserre, A. Letourneau, D. Lhuillier, G. Mention, D. Franco, V. Kornoukhov, and S. Schonert, "A proposed search for a fourth neutrino with a PBq antineutrino source," *Phys. Rev. Lett.* **107** (2011) 201801, `arXiv:1107.2335 [hep-ex]`.

[346] A. Bungau *et al.*, "Proposal for an Electron Antineutrino Disappearance Search Using High-Rate $^8$Li Production and Decay," *Phys. Rev. Lett.* **109** (2012) 141802, `arXiv:1205.4419 [hep-ex]`.

[347] C. Rubbia, A. Guglielmi, F. Pietropaolo, and P. Sala, "Sterile neutrinos: the necessity for a 5 sigma definitive clarification," `arXiv:1304.2047 [hep-ph]`.

[348] **Borexino** Collaboration, G. Bellini *et al.*, "SOX: Short distance neutrino Oscillations with BoreXino," *JHEP* **08** (2013) 038, `arXiv:1304.7721 [physics.ins-det]`.

[349] **OscSNS** Collaboration, M. Elnimr *et al.*, "The OscSNS White Paper," in *Community Summer Study 2013: Snowmass on the Mississippi (CSS2013) Minneapolis, MN, USA, July 29-August 6, 2013.* 2013. `arXiv:1307.7097`. `http://inspirehep.net/record/1244668/files/arXiv:1307.7097.pdf`.

[350] X. Qian, C. Zhang, M. Diwan, and P. Vogel, "Unitarity Tests of the Neutrino Mixing Matrix," `arXiv:1308.5700 [hep-ex]`.

[351] **nuSTORM** Collaboration, D. Adey *et al.*, "nuSTORM - Neutrinos from STORed Muons: Proposal to the Fermilab PAC," `arXiv:1308.6822 [physics.acc-ph]`.

[352] W. Hu and B. Jain, "Joint galaxy - lensing observables and the dark energy," *Phys. Rev.* **D70** (2004) 043009, `arXiv:astro-ph/0312395 [astro-ph]`.

[353] W. Hu, "Dark energy probes in light of the CMB," *ASP Conf. Ser.* **339** (2005) 215, `arXiv:astro-ph/0407158 [astro-ph]`.

[354] R. A. Burenin, "Possible indication for non-zero neutrino mass and additional neutrino species from cosmological observations," *Astron. Lett.* **39** (2013) 357–366, `arXiv:1301.4791 [astro-ph.CO]`.

[355] A. Mirizzi, N. Saviano, G. Miele, and P. D. Serpico, "Light sterile neutrino production in the early universe with dynamical neutrino asymmetries," *Phys. Rev.* **D86** (2012) 053009, `1206.1046 [hep-ph]`.

[356] N. Saviano, A. Mirizzi, O. Pisanti, P. D. Serpico, G. Mangano, and G. Miele, "Multi-momentum and multi-flavour active-sterile neutrino oscillations in the early universe: role of neutrino asymmetries and effects on nucleosynthesis," *Phys. Rev.* **D87** (2013) 073006, `1302.1200 [astro-ph]`.

[357] S. Hannestad, R. S. Hansen, and T. Tram, "Can active-sterile neutrino oscillations lead to chaotic behavior of the cosmological lepton asymmetry?," *JCAP* **1304** (2013) 032, `1302.7279 [astro-ph]`.

[358] C. Dvorkin, M. Wyman, D. H. Rudd, and W. Hu, "Neutrinos help reconcile Planck measurements with both the early and local Universe," *Phys. Rev.* **D90** no. 8, (2014) 083503, `arXiv:1403.8049 [astro-ph.CO]`.

[359] A. Ashoorioon, K. Dimopoulos, M. M. Sheikh-Jabbari, and G. Shiu, "Non-Bunch–Davis initial state reconciles chaotic models with BICEP and Planck," *Phys. Lett.* **B737** (2014) 98–102, `arXiv:1403.6099 [hep-th]`.

[360] B. Audren, D. G. Figueroa, and T. Tram, "A note of clarification: BICEP2 and Planck are not in tension," `arXiv:1405.1390 [astro-ph.CO]`.

[361] L. Knox and M. S. Turner, "Detectability of tensor perturbations through CBR anisotropy," *Phys. Rev. Lett.* **73** (1994) 3347–3350, `arXiv:astro-ph/9407037 [astro-ph]`.

[362] E. Giusarma, E. Di Valentino, M. Lattanzi, A. Melchiorri, and O. Mena, "Relic Neutrinos, thermal axions and cosmology in early 2014," *Phys. Rev.* **D90** (2014) 043507, `arXiv:1403.4852 [astro-ph.CO]`.

[363] J.-F. Zhang, Y.-H. Li, and X. Zhang, "Sterile neutrinos help reconcile the observational results of primordial gravitational waves from Planck and BICEP2," *Phys. Lett.* **B740** (2015) 359–363, `arXiv:1403.7028 [astro-ph.CO]`.

[364] A. C. Vincent, E. F. Martinez, P. Hernández, M. Lattanzi, and O. Mena, "Revisiting cosmological bounds on sterile neutrinos," *JCAP* **1504** (2015) 006, `arXiv:1408.1956 [astro-ph.CO]`.

[365] S. Hannestad, R. S. Hansen, and T. Tram, "How Self-Interactions can Reconcile Sterile Neutrinos with Cosmology," *Phys. Rev. Lett.* **112** (2014) 031802, `1310.5926 [astro-ph]`.

[366] B. Dasgupta and J. Kopp, "Cosmologically Safe eV-Scale Sterile Neutrinos and Improved Dark Matter Structure," *Phys. Rev. Lett.* **112** (2014) 031803, `1310.6337 [hep-ph]`.

[367] T. Bringmann, J. Hasenkamp, and J. Kersten, "Tight bonds between sterile neutrinos and dark matter," *JCAP* **1407** (2014) 042, `1312.4947 [hep-ph]`.

[368] P. Ko and Y. Tang, "$\nu\Lambda$MDM: A model for sterile neutrino and dark matter reconciles cosmological and neutrino oscillation data after BICEP2," *Phys. Lett.* **B739** (2014) 62–67, `1404.0236 [hep-ph]`.

[369] T. Rehagen and G. B. Gelmini, "Effects of kination and scalar-tensor cosmologies on sterile neutrinos," *JCAP* **1406** (2014) 044, `1402.0607 [hep-ph]`.

[370] Y.-Z. Chu and M. Cirelli, "Sterile neutrinos, lepton asymmetries, primordial elements: How much of each?," *Phys. Rev.* **D74** (2006) 085015, `astro-ph/0608206`.

[371] M. Archidiacono, S. Hannestad, R. S. Hansen, and T. Tram, "Cosmology with self-interacting sterile neutrinos and dark matter - A pseudoscalar model," *Phys. Rev.* **D91** (2015) 065021, `1404.5915 [astro-ph.CO]`.

[372] M. Archidiacono and S. Hannestad, "Efficient calculation of cosmological neutrino clustering with both linear and non-linear gravity," `arXiv:1510.02907 [astro-ph.CO]`.

[373] M. Archidiacono, S. Hannestad, R. S. Hansen, and T. Tram, "Sterile neutrinos with pseudoscalar self-interactions and cosmology," *Phys. Rev.* **D93** (2016) 045004, `arXiv:1508.02504 [astro-ph.CO]`.

[374] J. F. Beacom, N. F. Bell, and S. Dodelson, "Neutrinoless universe," *Phys. Rev. Lett.* **93** (2004) 121302, `arXiv:astro-ph/0404585 [astro-ph]`.

[375] S. Hannestad and G. Raffelt, "Constraining invisible neutrino decays with the cosmic microwave background," *Phys. Rev.* **D72** (2005) 103514, `arXiv:hep-ph/0509278 [hep-ph]`.

[376] A. D. Dolgov, "Neutrinos in cosmology," *Phys. Rept.* **370** (2002) 333–535, `arXiv:hep-ph/0202122 [hep-ph]`.

[377] J.-F. Zhang, Y.-H. Li, and X. Zhang, "Cosmological constraints on neutrinos after BICEP2," *Eur. Phys. J.* **C74** (2014) 2954, `arXiv:1404.3598 [astro-ph.CO]`.

[378] R. Foot and R. R. Volkas, "Reconciling sterile neutrinos with big bang nucleosynthesis," *Phys. Rev. Lett.* **75** (1995) 4350, `arXiv:hep-ph/9508275 [hep-ph]`.

[379] R. Foot and R. R. Volkas, "Studies of neutrino asymmetries generated by ordinary sterile neutrino oscillations in the early universe and implications for big bang nucleosynthesis bounds," *Phys. Rev.* **D55** (1997) 5147–5176, `arXiv:hep-ph/9610229 [hep-ph]`.

[380] N. F. Bell, R. Foot, and R. R. Volkas, "Relic neutrino asymmetries and big bang nucleosynthesis in a four neutrino model," *Phys. Rev.* **D58** (1998) 105010, `arXiv:hep-ph/9805259 [hep-ph]`.

[381] N. F. Bell, R. R. Volkas, and Y. Y. Y. Wong, "Relic neutrino asymmetry evolution from first principles," *Phys. Rev.* **D59** (1999) 113001, `arXiv:hep-ph/9809363 [hep-ph]`.

[382] X.-D. Shi, G. M. Fuller, and K. Abazajian, "Neutrino mixing generated lepton asymmetry and the primordial He-4 abundance," *Phys. Rev.* **D60** (1999) 063002, `arXiv:astro-ph/9905259 [astro-ph]`.

[383] P. Di Bari and R. Foot, "On the sign of the neutrino asymmetry induced by active sterile neutrino oscillations in the early universe," *Phys. Rev.* **D61** (2000) 105012, `arXiv:hep-ph/9912215 [hep-ph]`.

[384] P. Di Bari and R. Foot, "Active sterile neutrino oscillations in the early universe: Asymmetry generation at low —delta m**2— and the Landau-Zener approximation," *Phys. Rev.* **D65** (2002) 045003, `arXiv:hep-ph/0103192 [hep-ph]`.

[385] L. Bento and Z. Berezhiani, "Blocking active sterile neutrino oscillations in the early universe with a Majoron field," *Phys. Rev.* **D64** (2001) 115015, `arXiv:hep-ph/0108064 [hep-ph]`.

[386] N. Saviano, O. Pisanti, G. Mangano, and A. Mirizzi, "Unveiling secret interactions among sterile neutrinos with big-bang nucleosynthesis," *Phys. Rev.* **D90** no. 11, (2014) 113009, `arXiv:1409.1680 [astro-ph.CO]`.

[387] A. Mirizzi, G. Mangano, O. Pisanti, and N. Saviano, "Collisional production of sterile neutrinos via secret interactions and cosmological implications," *Phys. Rev.* **D91** (Oct., 2015) 025019, `1410.1385`.

[388] Y. Tang, "More Is Different: Reconciling eV Sterile Neutrinos with Cosmological Mass Bounds," *Phys. Lett.* **B750** (2015) 201–208, `arXiv:1501.00059 [hep-ph]`.

[389] X. Chu, B. Dasgupta, and J. Kopp, "Sterile neutrinos with secret interactions—lasting friendship with cosmology," *JCAP* **1510** no. 10, (2015) 011, `arXiv:1505.02795 [hep-ph]`.

[390] G. Gelmini, S. Palomares-Ruiz, and S. Pascoli, "Low reheating temperature and the visible sterile neutrino," *Phys. Rev. Lett.* **93** (2004) 081302, `arXiv:astro-ph/0403323 [astro-ph]`.

[391] A. Yu. Smirnov and R. Zukanovich Funchal, "Sterile neutrinos: Direct mixing effects versus induced mass matrix of active neutrinos," *Phys. Rev.* **D74** (2006) 013001, `arXiv:hep-ph/0603009 [hep-ph]`.

[392] A. G. Cadavid and A. E. Romano, "Effects of discontinuities of the derivatives of the inflaton potential," *Eur. Phys. J.* **C75** (2015) 589, `arXiv:1404.2985 [astro-ph.CO]`.

[393] N. Kitazawa and A. Sagnotti, "Pre-inflationary clues from String Theory?," *JCAP* **1404** (2014) 017, `arXiv:1402.1418 [hep-th]`.

[394] J. Martin, C. Ringeval, and V. Vennin, "Encyclopædia Inflationaris," *Phys. Dark Univ.* **5-6** (2014) 75–235, `arXiv:1303.3787 [astro-ph.CO]`.

[395] J. Chluba, J. Hamann, and S. P. Patil, "Features and New Physical Scales in Primordial Observables: Theory and Observation," *Int. J. Mod. Phys.* **D24** no. 10, (2015) 1530023, `arXiv:1505.01834 [astro-ph.CO]`.

[396] A. Shafieloo and T. Souradeep, "Primordial power spectrum from WMAP," *Phys. Rev.* **D70** (2004) 043523, `arXiv:astro-ph/0312174 [astro-ph]`.

[397] G. Nicholson and C. R. Contaldi, "Reconstruction of the Primordial Power Spectrum using Temperature and Polarisation Data from Multiple Experiments," *JCAP* **0907** (2009) 011, `arXiv:0903.1106 [astro-ph.CO]`.

[398] D. K. Hazra, A. Shafieloo, and T. Souradeep, "Cosmological parameter estimation with free-form primordial power spectrum," *Phys. Rev.* **D87** no. 12, (2013) 123528, `arXiv:1303.5336 [astro-ph.CO]`.

[399] D. K. Hazra, A. Shafieloo, and T. Souradeep, "Primordial power spectrum from Planck," *JCAP* **1411** (2014) 011, `arXiv:1406.4827 [astro-ph.CO]`.

[400] G. Nicholson, C. R. Contaldi, and P. Paykari, "Reconstruction of the Primordial Power Spectrum by Direct Inversion," *JCAP* **1001** (2010) 016, `arXiv:0909.5092 [astro-ph.CO]`.

[401] P. Hunt and S. Sarkar, "Reconstruction of the primordial power spectrum of curvature perturbations using multiple data sets," *JCAP* **1401** (2014) 025, `arXiv:1308.2317 [astro-ph.CO]`.

[402] P. Hunt and S. Sarkar, "Search for features in the spectrum of primordial perturbations using Planck and other datasets," *JCAP* **1512** (2015) 052, `arXiv:1510.03338 [astro-ph.CO]`.

[403] G. Goswami and J. Prasad, "Maximum Entropy deconvolution of Primordial Power Spectrum," *Phys. Rev.* **D88** no. 2, (2013) 023522, `arXiv:1303.4747 [astro-ph.CO]`.

[404] M. Matsumiya, M. Sasaki, and J. Yokoyama, "Cosmic inversion: Reconstructing primordial spectrum from CMB anisotropy," *Phys. Rev.* **D65** (2002) 083007, `arXiv:astro-ph/0111549 [astro-ph]`.

[405] M. Matsumiya, M. Sasaki, and J. Yokoyama, "Cosmic inversion. 2. An iterative method for reproducing the primordial spectrum from the CMB data," *JCAP* **0302** (2003) 003, `arXiv:astro-ph/0210365 [astro-ph]`.

[406] N. Kogo, M. Matsumiya, M. Sasaki, and J. Yokoyama, "Reconstructing the primordial spectrum from WMAP data by the cosmic inversion method," *Astrophys. J.* **607** (2004) 32–39, `arXiv:astro-ph/0309662 [astro-ph]`.

[407] N. Kogo, M. Sasaki, and J. Yokoyama, "Constraining cosmological parameters by the cosmic inversion method," *Prog. Theor. Phys.* **114** (2005) 555–572, `arXiv:astro-ph/0504471 [astro-ph]`.

[408] R. Nagata and J. Yokoyama, "Reconstruction of the primordial fluctuation spectrum from the five-year WMAP data by the cosmic inversion method with band-power decorrelation analysis," *Phys. Rev.* **D78** (2008) 123002, `arXiv:0809.4537 [astro-ph]`.

[409] **Planck Collaboration** Collaboration, P. A. R. Ade *et al.*, "Planck 2015 results. XX. Constraints on inflation," `arXiv:1502.02114 [astro-ph.CO]`.

[410] M. Archidiacono, E. Giusarma, A. Melchiorri, and O. Mena, "Dark Radiation in extended cosmological scenarios," *Phys. Rev.* **D86** (2012) 043509, `arXiv:1206.0109 [astro-ph.CO]`.

[411] G.-B. Zhao *et al.*, "The clustering of galaxies in the SDSS-III Baryon Oscillation Spectroscopic Survey: weighing the neutrino mass using the galaxy power spectrum of the CMASS sample," *Mon. Not. Roy. Astron. Soc.* **436** (2013) 2038–2053, `arXiv:1211.3741 [astro-ph.CO]`.

[412] J. A. Vazquez, M. Bridges, Y.-Z. Ma, and M. P. Hobson, "Constraints on the tensor-to-scalar ratio for non-power-law models," *JCAP* **1308** (2013) 001, `arXiv:1303.4014 [astro-ph.CO]`.

[413] K. N. Abazajian, G. Aslanyan, R. Easther, and L. C. Price, "The Knotted Sky II: Does BICEP2 require a nontrivial primordial power spectrum?," *JCAP* **1408** (2014) 053, `arXiv:1403.5922 [astro-ph.CO]`.

[414] C. Cheng, Q.-G. Huang, and W. Zhao, "Constraints on the extensions to the base ΛCDM model from BICEP2, Planck and WMAP," *Sci. China Phys. Mech. Astron.* **57** (2014) 1460–1465, `arXiv:1404.3467 [astro-ph.CO]`.

[415] P. Mukherjee and Y. Wang, "Wavelet band powers of the primordial power spectrum from CMB data," *Astrophys. J.* **593** (2003) 38, `arXiv:astro-ph/0301058 [astro-ph]`.

[416] P. Mukherjee and Y. Wang, "Direct wavelet expansion of the primordial power spectrum: Results from pre-MAP CMB data," *Astrophys. J.* **598** (2003) 779–784, `arXiv:astro-ph/0301562 [astro-ph]`.

[417] P. Mukherjee and Y. Wang, "Model-independent reconstruction of the primordial power spectrum from WMAP data," *Astrophys. J.* **599** (2003) 1–6, `arXiv:astro-ph/0303211 [astro-ph]`.

[418] P. Mukherjee and Y. Wang, "Primordial power spectrum reconstruction," *JCAP* **0512** (2005) 007, `arXiv:astro-ph/0502136 [astro-ph]`.

[419] S. M. Leach, "Measuring the primordial power spectrum: Principal component analysis of the cosmic microwave background," *Mon. Not. Roy. Astron. Soc.* **372** (2006) 646–654, `arXiv:astro-ph/0506390 [astro-ph]`.

[420] Y. Wang, D. N. Spergel, and M. A. Strauss, "Cosmology in the next millennium: Combining MAP and SDSS data to constrain inflationary models," *Astrophys. J.* **510** (1999) 20, `arXiv:astro-ph/9802231 [astro-ph]`.

[421] S. Hannestad, "Reconstructing the inflationary power spectrum from CMBR data," *Phys. Rev.* **D63** (2001) 043009, `arXiv:astro-ph/0009296 [astro-ph]`.

[422] D. K. Hazra, A. Shafieloo, and G. F. Smoot, "Reconstruction of broad features in the primordial spectrum and inflaton potential from Planck," *JCAP* **1312** (2013) 035, `arXiv:1310.3038 [astro-ph.CO]`.

[423] Y. Wang and G. Mathews, "A Measurement of the primordial power spectrum from Maxima and Boomerang data," *Astrophys. J.* **573** (2002) 1, `arXiv:astro-ph/0011351 [astro-ph]`.

[424] S. L. Bridle, A. M. Lewis, J. Weller, and G. Efstathiou, "Reconstructing the primordial power spectrum," *Mon. Not. Roy. Astron. Soc.* **342** (2003) L72, `arXiv:astro-ph/0302306 [astro-ph]`.

[425] S. Hannestad, "Reconstructing the primordial power spectrum - A New algorithm," *JCAP* **0404** (2004) 002, `arXiv:astro-ph/0311491 [astro-ph]`.

[426] M. Bridges, A. N. Lasenby, and M. P. Hobson, "A bayesian analysis of the primordial power spectrum," *Mon. Not. Roy. Astron. Soc.* **369** (2006) 1123–1130, `arXiv:astro-ph/0511573 [astro-ph]`.

[427] **WMAP Collaboration** Collaboration, D. N. Spergel *et al.*, "Wilkinson Microwave Anisotropy Probe (WMAP) three year results: implications for cosmology," *Astrophys. J. Suppl.* **170** (2007) 377, `arXiv:astro-ph/0603449 [astro-ph]`.

[428] M. Bridges, A. N. Lasenby, and M. P. Hobson, "WMAP 3-year primordial power spectrum," *Mon. Not. Roy. Astron. Soc.* **381** (2007) 68–74, `arXiv:astro-ph/0607404 [astro-ph]`.

[429] M. Bridges, F. Feroz, M. P. Hobson, and A. N. Lasenby, "Bayesian optimal reconstruction of the primordial power spectrum," *Mon. Not. Roy. Astron. Soc.* **400** (2009) 1075–1084, `arXiv:0812.3541 [astro-ph]`.

[430] D. K. Hazra, A. Shafieloo, G. F. Smoot, and A. A. Starobinsky, "Ruling out the power-law form of the scalar primordial spectrum," *JCAP* **1406** (2014) 061, `arXiv:1403.7786 [astro-ph.CO]`.

[431] C. Sealfon, L. Verde, and R. Jimenez, "Smoothing spline primordial power spectrum reconstruction," *Phys. Rev.* **D72** (2005) 103520, `arXiv:astro-ph/0506707 [astro-ph]`.

[432] L. Verde and H. V. Peiris, "On Minimally-Parametric Primordial Power Spectrum Reconstruction and the Evidence for a Red Tilt," *JCAP* **0807** (2008) 009, `arXiv:0802.1219 [astro-ph]`.

[433] H. V. Peiris and L. Verde, "The Shape of the Primordial Power Spectrum: A Last Stand Before Planck," *Phys. Rev.* **D81** (2010) 021302, `arXiv:0912.0268 [astro-ph.CO]`.

[434] R. Hlozek *et al.*, "The Atacama Cosmology Telescope: a measurement of the primordial power spectrum," *Astrophys. J.* **749** (2012) 90, `arXiv:1105.4887 [astro-ph.CO]`.

[435] C. Gauthier and M. Bucher, "Reconstructing the primordial power spectrum from the CMB," *JCAP* **1210** (2012) 050, `arXiv:1209.2147 [astro-ph.CO]`.

[436] R. de Putter, E. V. Linder, and A. Mishra, "Inflationary Freedom and Cosmological Neutrino Constraints," *Phys. Rev.* **D89** (2014) 103502, `arXiv:1401.7022 [astro-ph.CO]`.

[437] B. Hu, J.-W. Hu, Z.-K. Guo, and R.-G. Cai, "Reconstruction of the primordial power spectra with Planck and BICEP2 data," *Phys. Rev.* **D90** (2014) 023544, `arXiv:1404.3690 [astro-ph.CO]`.

[438] D. Larson *et al.*, "Seven-Year Wilkinson Microwave Anisotropy Probe (WMAP) Observations: Power Spectra and WMAP-Derived Parameters," *Astrophys. J. Suppl.* **192** (2011) 16, `arXiv:1001.4635 [astro-ph.CO]`.

[439] F. Fritsch and R. Carlson, "Monotone Piecewise Cubic Interpolation," *SIAM Journal on Numerical Analysis* **17** no. 2, (1980) 238.

[440] F. Fritsch and J. Butland, "A Method for Constructing Local Monotone Piecewise Cubic Interpolants," *SIAM Journal on Scientific and Statistical Computing* **5** no. 2, (1984) 300.

[441] B. A. Reid, L. Verde, R. Jimenez, and O. Mena, "Robust Neutrino Constraints by Combining Low Redshift Observations with the CMB," *JCAP* **1001** (2010) 003, `arXiv:0910.0008`.

[442] J. Hamann, S. Hannestad, J. Lesgourgues, C. Rampf, and Y. Y. Y. Wong, "Cosmological parameters from large scale structure - geometric versus shape information," *JCAP* **1007** (2010) 022, `arXiv:1003.3999 [astro-ph.CO]`.

[443] R. de Putter *et al.*, "New Neutrino Mass Bounds from Sloan Digital Sky Survey III Data Release 8 Photometric Luminous Galaxies," *Astrophys. J.* **761** (2012) 12, `arXiv:1201.1909 [astro-ph.CO]`.

[444] E. Giusarma, R. De Putter, and O. Mena, "Testing standard and nonstandard neutrino physics with cosmological data," *Phys. Rev.* **D87** no. 4, (2013) 043515, `arXiv:1211.2154 [astro-ph.CO]`.

[445] Z. Hou *et al.*, "Constraints on Cosmology from the Cosmic Microwave Background Power Spectrum of the 2500 deg$^2$ SPT-SZ Survey," *Astrophys. J.* **782** (2014) 74, `arXiv:1212.6267 [astro-ph.CO]`.

[446] M. Archidiacono, E. Giusarma, A. Melchiorri, and O. Mena, "Neutrino and dark radiation properties in light of recent CMB observations," *Phys. Rev.* **D87** no. 10, (2013) 103519, `arXiv:1303.0143 [astro-ph.CO]`.

[447] E. Giusarma, R. de Putter, S. Ho, and O. Mena, "Constraints on neutrino masses from Planck and Galaxy Clustering data," *Phys. Rev.* **D88** no. 6, (2013) 063515, `arXiv:1306.5544 [astro-ph.CO]`.

[448] S. Riemer-Sørensen, D. Parkinson, and T. M. Davis, "Combining Planck data with large scale structure information gives a strong neutrino mass constraint," *Phys. Rev.* **D89** (2014) 103505, `arXiv:1306.4153 [astro-ph.CO]`.

[449] J.-W. Hu, R.-G. Cai, Z.-K. Guo, and B. Hu, "Cosmological parameter estimation from CMB and X-ray cluster after Planck," *JCAP* **1405** (2014) 020, `arXiv:1401.0717 [astro-ph.CO]`.

[450] E. Di Valentino, E. Giusarma, O. Mena, A. Melchiorri, and J. Silk, "Cosmological limits on neutrino unknowns versus low redshift priors," `arXiv:1511.00975 [astro-ph.CO]`.

[451] S. Weinberg, "A New Light Boson?," *Phys. Rev. Lett.* **40** (1978) 223–226.

[452] F. Wilczek, "Problem of Strong p and t Invariance in the Presence of Instantons," *Phys. Rev. Lett.* **40** (1978) 279–282.

[453] A. Melchiorri, O. Mena, and A. Slosar, "An improved cosmological bound on the thermal axion mass," *Phys. Rev.* **D76** (2007) 041303, `arXiv:0705.2695 [astro-ph]`.

[454] S. Hannestad, A. Mirizzi, G. G. Raffelt, and Y. Y. Y. Wong, "Cosmological constraints on neutrino plus axion hot dark matter," *JCAP* **0708** (2007) 015, `arXiv:0706.4198 [astro-ph]`.

[455] S. Hannestad, A. Mirizzi, G. G. Raffelt, and Y. Y. Y. Wong, "Neutrino and axion hot dark matter bounds after WMAP-7," *JCAP* **1008** (2010) 001, `arXiv:1004.0695 [astro-ph.CO]`.

[456] M. Archidiacono, S. Hannestad, A. Mirizzi, G. Raffelt, and Y. Y. Y. Wong, "Axion hot dark matter bounds after Planck," *JCAP* **1310** (2013) 020, `arXiv:1307.0615 [astro-ph.CO]`.

[457] M. Archidiacono, T. Basse, J. Hamann, S. Hannestad, G. Raffelt, and Y. Y. Y. Wong, "Future cosmological sensitivity for hot dark matter axions," *JCAP* **1505** (2015) 050, `arXiv:1502.03325 [astro-ph.CO]`.

[458] S. Hannestad, A. Mirizzi, and G. Raffelt, "New cosmological mass limit on thermal relic axions," *JCAP* **0507** (2005) 002, `arXiv:hep-ph/0504059 [hep-ph]`.

[459] E. Di Valentino, E. Giusarma, M. Lattanzi, O. Mena, A. Melchiorri, and J. Silk, "Cosmological Axion and neutrino mass constraints from Planck 2015 temperature and polarization data," *Phys. Lett.* **B752** (2016) 182–185, `arXiv:1507.08665 [astro-ph.CO]`.

[460] E. Di Valentino, E. Giusarma, M. Lattanzi, A. Melchiorri, and O. Mena, "Axion cold dark matter: status after Planck and BICEP2," *Phys. Rev.* **D90** (2014) 043534, `arXiv:1405.1860 [astro-ph.CO]`.

[461] E. Di Valentino, A. Melchiorri, and J. Silk, "Beyond six parameters: extending ΛCDM," *Phys. Rev.* **D92** no. 12, (2015) 121302, `arXiv:1507.06646 [astro-ph.CO]`.

[462] P. Graf and F. D. Steffen, "Thermal axion production in the primordial quark-gluon plasma," *Phys. Rev.* **D83** (2011) 075011, `arXiv:1008.4528 [hep-ph]`.

[463] A. Salvio, A. Strumia, and W. Xue, "Thermal axion production," *JCAP* **1401** (2014) 011, `arXiv:1310.6982 [hep-ph]`.

[464] D. H. Lyth and A. Riotto, "Particle physics models of inflation and the cosmological density perturbation," *Phys. Rept.* **314** (1999) 1–146, `hep-ph/9807278`.

[465] B. A. Bassett, S. Tsujikawa, and D. Wands, "Inflation dynamics and reheating," *Rev. Mod. Phys.* **78** (2006) 537–589, `astro-ph/0507632`.

[466] D. Baumann and H. V. Peiris, "Cosmological Inflation: Theory and Observations," *Adv. Sci. Lett.* **2** (2009) 105–120, `arXiv:0810.3022 [astro-ph]`.

[467] J. A. Adams, G. G. Ross, and S. Sarkar, "Multiple inflation," *Nucl. Phys.* **B503** (1997) 405–425, `arXiv:hep-ph/9704286 [hep-ph]`.

[468] P. Hunt and S. Sarkar, "Multiple inflation and the WMAP 'glitches'," *Phys. Rev.* **D70** (2004) 103518, `arXiv:astro-ph/0408138 [astro-ph]`.

[469] S. Hotchkiss and S. Sarkar, "Non-Gaussianity from violation of slow-roll in multiple inflation," *JCAP* **1005** (2010) 024, `arXiv:0910.3373 [astro-ph.CO]`.

[470] A. A. Starobinsky, "Spectrum of adiabatic perturbations in the universe when there are singularities in the inflation potential," *JETP Lett.* **55** (1992) 489–494. [Pisma Zh. Eksp. Teor. Fiz.55,477(1992)].

[471] S. M. Leach, M. Sasaki, D. Wands, and A. R. Liddle, "Enhancement of superhorizon scale inflationary curvature perturbations," *Phys. Rev.* **D64** (2001) 023512, `arXiv:astro-ph/0101406 [astro-ph]`.

[472] J.-O. Gong, "Breaking scale invariance from a singular inflaton potential," *JCAP* **0507** (2005) 015, `arXiv:astro-ph/0504383 [astro-ph]`.

[473] J. A. Adams, B. Cresswell, and R. Easther, "Inflationary perturbations from a potential with a step," *Phys. Rev.* **D64** (2001) 123514, `arXiv:astro-ph/0102236 [astro-ph]`.

[474] X. Chen, R. Easther, and E. A. Lim, "Large Non-Gaussianities in Single Field Inflation," *JCAP* **0706** (2007) 023, `arXiv:astro-ph/0611645 [astro-ph]`.

[475] X. Chen, R. Easther, and E. A. Lim, "Generation and Characterization of Large Non-Gaussianities in Single Field Inflation," *JCAP* **0804** (2008) 010, `arXiv:0801.3295 [astro-ph]`.

[476] R. N. Lerner and J. McDonald, "Space-Dependent Step Features: Transient Breakdown of Slow-roll, Homogeneity and Isotropy During Inflation," *Phys. Rev.* **D79** (2009) 023511, `arXiv:0811.1933 [astro-ph]`.

[477] C. Dvorkin and W. Hu, "Generalized Slow Roll for Large Power Spectrum Features," *Phys. Rev.* **D81** (2010) 023518, `arXiv:0910.2237 [astro-ph.CO]`.

[478] P. Adshead, C. Dvorkin, W. Hu, and E. A. Lim, "Non-Gaussianity from Step Features in the Inflationary Potential," *Phys. Rev.* **D85** (2012) 023531, `arXiv:1110.3050 [astro-ph.CO]`.

[479] H. M. Hodges, G. R. Blumenthal, L. A. Kofman, and J. R. Primack, "Nonstandard Primordial Fluctuations From a Polynomial Inflaton Potential," *Nucl. Phys.* **B335** (1990) 197.

[480] S. M. Leach and A. R. Liddle, "Inflationary perturbations near horizon crossing," *Phys. Rev.* **D63** (2001) 043508, `arXiv:astro-ph/0010082 [astro-ph]`.

[481] M. Joy, V. Sahni, and A. A. Starobinsky, "A New Universal Local Feature in the Inflationary Perturbation Spectrum," *Phys. Rev.* **D77** (2008) 023514, `arXiv:0711.1585 [astro-ph]`.

[482] R. K. Jain, P. Chingangbam, and L. Sriramkumar, "On the evolution of tachyonic perturbations at super-Hubble scales," *JCAP* **0710** (2007) 003, `arXiv:astro-ph/0703762 [astro-ph]`.

[483] R. Bean, X. Chen, G. Hailu, S. H. H. Tye, and J. Xu, "Duality Cascade in Brane Inflation," *JCAP* **0803** (2008) 026, `arXiv:0802.0491 [hep-th]`.

[484] A. Ashoorioon and A. Krause, "Power Spectrum and Signatures for Cascade Inflation," `arXiv:hep-th/0607001 [hep-th]`.

[485] A. Ashoorioon, A. Krause, and K. Turzynski, "Energy Transfer in Multi Field Inflation and Cosmological Perturbations," *JCAP* **0902** (2009) 014, `arXiv:0810.4660 [hep-th]`.

[486] R. Saito, J. Yokoyama, and R. Nagata, "Single-field inflation, anomalous enhancement of superhorizon fluctuations, and non-Gaussianity in primordial black hole formation," *JCAP* **0806** (2008) 024, `arXiv:0804.3470 [astro-ph]`.

[487] A. Achucarro, J.-O. Gong, S. Hardeman, G. A. Palma, and S. P. Patil, "Features of heavy physics in the CMB power spectrum," *JCAP* **1101** (2011) 030, `arXiv:1010.3693 [hep-ph]`.

[488] G. Goswami and T. Souradeep, "Power spectrum nulls due to non-standard inflationary evolution," *Phys. Rev.* **D83** (2011) 023526, `arXiv:1011.4914 [astro-ph.CO]`.

[489] P. Brax and E. Cluzel, "Perturbation Theory in k-Inflation Coupled to Matter," *JCAP* **1104** (2011) 014, `arXiv:1102.1917 [hep-th]`.

[490] F. Arroja, A. E. Romano, and M. Sasaki, "Large and strong scale dependent bispectrum in single field inflation from a sharp feature in the mass," *Phys. Rev.* **D84** (2011) 123503, `arXiv:1106.5384 [astro-ph.CO]`.

[491] J. Liu and Y.-S. Piao, "A Multiple Step-like Spectrum of Primordial Perturbation," *Phys. Lett.* **B705** (2011) 1–4, `arXiv:1106.5608 [hep-th]`.

[492] D. J. H. Chung, E. W. Kolb, A. Riotto, and I. I. Tkachev, "Probing Planckian physics: Resonant production of particles during inflation and features in the primordial power spectrum," *Phys. Rev.* **D62** (2000) 043508, `arXiv:hep-ph/9910437 [hep-ph]`.

[493] G. J. Mathews, D. J. H. Chung, K. Ichiki, T. Kajino, and M. Orito, "Constraints on resonant particle production during inflation from the matter and CMB power spectra," *Phys. Rev.* **D70** (2004) 083505, `arXiv:astro-ph/0406046 [astro-ph]`.

[494] A. E. Romano and M. Sasaki, "Effects of particle production during inflation," *Phys. Rev.* **D78** (2008) 103522, `arXiv:0809.5142 [gr-qc]`.

[495] N. Barnaby, Z. Huang, L. Kofman, and D. Pogosyan, "Cosmological Fluctuations from Infra-Red Cascading During Inflation," *Phys. Rev.* **D80** (2009) 043501, `arXiv:0902.0615 [hep-th]`.

[496] N. Barnaby, "Nongaussianity from Particle Production During Inflation," *Adv. Astron.* **2010** (2010) 156180, `arXiv:1010.5507 [astro-ph.CO]`.

[497] A. Achúcarro, J.-O. Gong, G. A. Palma, and S. P. Patil, "Correlating features in the primordial spectra," *Phys. Rev.* **D87** no. 12, (2013) 121301, `arXiv:1211.5619 [astro-ph.CO]`.

[498] G. A. Palma, "Untangling features in the primordial spectra," *JCAP* **1504** no. 04, (2015) 035, `arXiv:1412.5615 [hep-th]`.

[499] R. H. Brandenberger and J. Martin, "The Robustness of inflation to changes in superPlanck scale physics," *Mod. Phys. Lett.* **A16** (2001) 999–1006, `arXiv:astro-ph/0005432 [astro-ph]`.

[500] U. H. Danielsson, "A Note on inflation and transPlanckian physics," *Phys. Rev.* **D66** (2002) 023511, `arXiv:hep-th/0203198 [hep-th]`.

[501] K. Schalm, G. Shiu, and J. P. van der Schaar, "The Cosmological vacuum ambiguity, effective actions, and transplanckian effects in inflation," *AIP Conf. Proc.* **743** (2005) 362–392, `arXiv:hep-th/0412288 [hep-th]`. [,362(2004)].

[502] B. Greene, K. Schalm, J. P. van der Schaar, and G. Shiu, "Extracting new physics from the CMB," *eConf* **C041213** (2004) 0001, `arXiv:astro-ph/0503458` `[astro-ph]`.

[503] R. Easther, W. H. Kinney, and H. Peiris, "Boundary effective field theory and trans-Planckian perturbations: Astrophysical implications," *JCAP* **0508** (2005) 001, `arXiv:astro-ph/0505426 [astro-ph]`.

[504] C. P. Burgess, J. M. Cline, F. Lemieux, and R. Holman, "Are inflationary predictions sensitive to very high-energy physics?," *JHEP* **02** (2003) 048, `arXiv:hep-th/0210233` `[hep-th]`.

[505] Y.-S. Piao, B. Feng, and X.-m. Zhang, "Suppressing CMB quadrupole with a bounce from contracting phase to inflation," *Phys. Rev.* **D69** (2004) 103520, `arXiv:hep-th/0310206 [hep-th]`.

[506] B. A. Powell and W. H. Kinney, "The pre-inflationary vacuum in the cosmic microwave background," *Phys. Rev.* **D76** (2007) 063512, `arXiv:astro-ph/0612006` `[astro-ph]`.

[507] G. Nicholson and C. R. Contaldi, "The large scale CMB cut-off and the tensor-to-scalar ratio," *JCAP* **0801** (2008) 002, `arXiv:astro-ph/0701783` `[astro-ph]`.

[508] A. Lasenby and C. Doran, "Closed universes, de Sitter space and inflation," *Phys. Rev.* **D71** (2005) 063502, `arXiv:astro-ph/0307311 [astro-ph]`.

[509] R. H. Ribeiro, "Inflationary signatures of single-field models beyond slow-roll," *JCAP* **1205** (2012) 037, `arXiv:1202.4453 [astro-ph.CO]`.

[510] G. Dvali and S. Kachru, "Large scale power and running spectral index in new old inflation," `arXiv:hep-ph/0310244 [hep-ph]`.

[511] D. Langlois and F. Vernizzi, "From heaviness to lightness during inflation," *JCAP* **0501** (2005) 002, `arXiv:astro-ph/0409684 [astro-ph]`.

[512] D. S. Salopek and J. R. Bond, "Nonlinear evolution of long wavelength metric fluctuations in inflationary models," *Phys. Rev.* **D42** (1990) 3936–3962.

[513] A. Gangui, F. Lucchin, S. Matarrese, and S. Mollerach, "The Three point correlation function of the cosmic microwave background in inflationary models," *Astrophys. J.* **430** (1994) 447–457, `arXiv:astro-ph/9312033 [astro-ph]`.

[514] L. Verde, L.-M. Wang, A. Heavens, and M. Kamionkowski, "Large scale structure, the cosmic microwave background, and primordial non-gaussianity," *Mon. Not. Roy. Astron. Soc.* **313** (2000) L141–L147, `arXiv:astro-ph/9906301 [astro-ph]`.

[515] E. Komatsu and D. N. Spergel, "Acoustic signatures in the primary microwave background bispectrum," *Phys. Rev.* **D63** (2001) 063002, `arXiv:astro-ph/0005036` `[astro-ph]`.

[516] P. A. R. Ade *et al.*, "Planck 2015 results. XVII. Constraints on primordial non-Gaussianity," `1502.01592`.

[517] N. Dalal, O. Dore, D. Huterer, and A. Shirokov, "The imprints of primordial non-gaussianities on large-scale structure: scale dependent bias and abundance of virialized objects," *Phys. Rev.* **D77** (2008) 123514, `arXiv:0710.4560 [astro-ph]`.

[518] S. Matarrese and L. Verde, "The effect of primordial non-Gaussianity on halo bias," *Astrophys. J.* **677** (2008) L77–L80, `arXiv:0801.4826 [astro-ph]`.

[519] A. Slosar, C. Hirata, U. Seljak, S. Ho, and N. Padmanabhan, "Constraints on local primordial non-Gaussianity from large scale structure," *JCAP* **0808** (2008) 031, `arXiv:0805.3580 [astro-ph]`.

[520] N. Afshordi and A. J. Tolley, "Primordial non-gaussianity, statistics of collapsed objects, and the Integrated Sachs-Wolfe effect," *Phys. Rev.* **D78** (2008) 123507, `arXiv:0806.1046 [astro-ph]`.

[521] C. Carbone, L. Verde, and S. Matarrese, "Non-Gaussian halo bias and future galaxy surveys," *Astrophys. J.* **684** (2008) L1–L4, `arXiv:0806.1950 [astro-ph]`.

[522] M. Grossi, L. Verde, C. Carbone, K. Dolag, E. Branchini, F. Iannuzzi, S. Matarrese, and L. Moscardini, "Large-scale non-Gaussian mass function and halo bias: tests on N-body simulations," *Mon. Not. Roy. Astron. Soc.* **398** (2009) 321–332, `arXiv:0902.2013 [astro-ph.CO]`.

[523] V. Desjacques, U. Seljak, and I. Iliev, "Scale-dependent bias induced by local non-Gaussianity: A comparison to N-body simulations," *Mon. Not. Roy. Astron. Soc.* **396** (2009) 85–96, `arXiv:0811.2748 [astro-ph]`.

[524] A. Pillepich, C. Porciani, and O. Hahn, "Universal halo mass function and scale-dependent bias from N-body simulations with non-Gaussian initial conditions," *Mon. Not. Roy. Astron. Soc.* **402** (2010) 191–206, `arXiv:0811.4176 [astro-ph]`.

[525] M. Alvarez *et al.*, "Testing Inflation with Large Scale Structure: Connecting Hopes with Reality," `arXiv:1412.4671 [astro-ph.CO]`.

[526] B. Leistedt, H. V. Peiris, and N. Roth, "Constraints on Primordial Non-Gaussianity from 800 000 Photometric Quasars," *Phys. Rev. Lett.* **113** no. 22, (2014) 221301, `arXiv:1405.4315 [astro-ph.CO]`.

[527] N. Agarwal, S. Ho, and S. Shandera, "Constraining the initial conditions of the Universe using large scale structure," *JCAP* **1402** (2014) 038, `arXiv:1311.2606 [astro-ph.CO]`.

[528] R. de Putter and O. Doré, "Designing an Inflation Galaxy Survey: how to measure $\sigma(f_{\mathrm{NL}}) \sim 1$ using scale-dependent galaxy bias," `arXiv:1412.3854 [astro-ph.CO]`.

[529] O. Doré *et al.*, "Cosmology with the SPHEREX All-Sky Spectral Survey," `arXiv:1412.4872 [astro-ph.CO]`.

[530] J. Byun and R. Bean, "Non-Gaussian Shape Discrimination with Spectroscopic Galaxy Surveys," *JCAP* **1503** no. 03, (2015) 019, `arXiv:1409.5440 [astro-ph.CO]`.

[531] A. Raccanelli, O. Dore, and N. Dalal, "Optimization of spectroscopic surveys for testing non-Gaussianity," `arXiv:1409.1927 [astro-ph.CO]`.

[532] D. Yamauchi, K. Takahashi, and M. Oguri, "Constraining primordial non-Gaussianity via a multitracer technique with surveys by Euclid and the Square Kilometre Array," *Phys. Rev.* **D90** no. 8, (2014) 083520, `arXiv:1407.5453 [astro-ph.CO]`.

[533] S. Camera, M. G. Santos, and R. Maartens, "Probing primordial non-Gaussianity with SKA galaxy redshift surveys: a fully relativistic analysis," *Mon. Not. Roy. Astron. Soc.* **448** no. 2, (2015) 1035–1043, `arXiv:1409.8286 [astro-ph.CO]`.

[534] L. D. Ferramacho, M. G. Santos, M. J. Jarvis, and S. Camera, "Radio galaxy populations and the multitracer technique: pushing the limits on primordial non-Gaussianity," *Mon. Not. Roy. Astron. Soc.* **442** no. 3, (2014) 2511–2518, `arXiv:1402.2290 [astro-ph.CO]`.

[535] S. Ferraro and K. M. Smith, "Using large scale structure to measure $f_{NL}, g_{NL}$ and $\tau_{NL}$," *Phys. Rev.* **D91** no. 4, (2015) 043506, arXiv:1408.3126 [astro-ph.CO].

[536] C. Fedeli, C. Carbone, L. Moscardini, and A. Cimatti, "The clustering of galaxies and galaxy clusters: constraints on primordial non-Gaussianity from future wide-field surveys," *Mon. Not. Roy. Astron. Soc.* **414** (2011) 1545–1559, arXiv:1012.2305 [astro-ph.CO].

[537] C. Carbone, O. Mena, and L. Verde, "Cosmological Parameters Degeneracies and Non-Gaussian Halo Bias," *JCAP* **1007** (2010) 020, arXiv:1003.0456 [astro-ph.CO].

[538] T. Giannantonio, C. Porciani, J. Carron, A. Amara, and A. Pillepich, "Constraining primordial non-Gaussianity with future galaxy surveys," *Mon. Not. Roy. Astron. Soc.* **422** (2012) 2854–2877, arXiv:1109.0958 [astro-ph.CO].

[539] N. Bartolo, E. Komatsu, S. Matarrese, and A. Riotto, "Non-Gaussianity from inflation: Theory and observations," *Phys. Rept.* **402** (2004) 103–266, arXiv:astro-ph/0406398 [astro-ph].

[540] A. Chambers and A. Rajantie, "Lattice calculation of non-Gaussianity from preheating," *Phys. Rev. Lett.* **100** (2008) 041302, arXiv:0710.4133 [astro-ph]. [Erratum: Phys. Rev. Lett.101,149903(2008)].

[541] J. R. Bond, A. V. Frolov, Z. Huang, and L. Kofman, "Non-Gaussian Spikes from Chaotic Billiards in Inflation Preheating," *Phys. Rev. Lett.* **103** (2009) 071301, arXiv:0903.3407 [astro-ph.CO].

[542] A. Shafieloo, T. Souradeep, P. Manimaran, P. K. Panigrahi, and R. Rangarajan, "Features in the Primordial Spectrum from WMAP: A Wavelet Analysis," *Phys. Rev.* **D75** (2007) 123502, arXiv:astro-ph/0611352 [astro-ph].

[543] K. Ichiki and R. Nagata, "Brute force reconstruction of the primordial fluctuation spectrum from five-year Wilkinson Microwave Anisotropy Probe observations," *Phys. Rev.* **D80** (2009) 083002.

[544] J. A. Vazquez, M. Bridges, M. P. Hobson, and A. N. Lasenby, "Model selection applied to reconstruction of the Primordial Power Spectrum," *JCAP* **1206** (2012) 006, arXiv:1203.1252 [astro-ph.CO].

[545] G. Aslanyan, L. C. Price, K. N. Abazajian, and R. Easther, "The Knotted Sky I: Planck constraints on the primordial power spectrum," *JCAP* **1408** (2014) 052, arXiv:1403.5849 [astro-ph.CO].

[546] D. Tocchini-Valentini, M. Douspis, and J. Silk, "Are there features in the primordial power spectrum?," *Mon. Not. Roy. Astron. Soc.* **359** (2005) 31–35, arXiv:astro-ph/0402583 [astro-ph].

[547] P. Paykari, F. Lanusse, J. L. Starck, F. Sureau, and J. Bobin, "PRISM: Sparse Recovery of the Primordial Power Spectrum," *Astron. Astrophys.* **566** (2014) A77, arXiv:1402.1983 [astro-ph.CO].

[548] N. Kogo, M. Sasaki, and J. Yokoyama, "Reconstructing the primordial spectrum with CMB temperature and polarization," *Phys. Rev.* **D70** (2004) 103001, arXiv:astro-ph/0409052 [astro-ph].

[549] J. Hamann, A. Shafieloo, and T. Souradeep, "Features in the primordial power spectrum? A frequentist analysis," *JCAP* **1004** (2010) 010, arXiv:0912.2728 [astro-ph.CO].

[550] A. Iqbal, J. Prasad, T. Souradeep, and M. A. Malik, "Joint Planck and WMAP Assessment of Low CMB Multipoles," *JCAP* **1506** (2015) 014, `arXiv:1501.02647 [astro-ph.CO]`.

[551] T. Kitayama and Y. Suto, "Formation rate of gravitational structures and the cosmic x-ray background radiation," *Mon. Not. Roy. Astron. Soc.* **280** (1996) 638, `arXiv:astro-ph/9602076 [astro-ph]`.

[552] B. Sartoris *et al.*, "Next Generation Cosmology: Constraints from the Euclid Galaxy Cluster Survey," `arXiv:1505.02165 [astro-ph.CO]`.

[553] **DESI** Collaboration, M. Levi *et al.*, "The DESI Experiment, a whitepaper for Snowmass 2013," `arXiv:1308.0847 [astro-ph.CO]`.

[554] **the Euclid Collaboration** Collaboration, R. Scaramella *et al.*, "Euclid space mission: a cosmological challenge for the next 15 years," *IAU Symp.* **306** (2015) 375–378, `arXiv:1501.04908 [astro-ph.CO]`. `http://inspirehep.net/record/1340291/files/arXiv:1501.04908.pdf`.

[555] M. Tegmark, A. Taylor, and A. Heavens, "Karhunen-Loeve eigenvalue problems in cosmology: How should we tackle large data sets?," *Astrophys. J.* **480** (1997) 22, `arXiv:astro-ph/9603021 [astro-ph]`.

[556] G. Jungman, M. Kamionkowski, A. Kosowsky, and D. N. Spergel, "Cosmological parameter determination with microwave background maps," *Phys. Rev.* **D54** (1996) 1332–1344, `astro-ph/9512139`.

[557] R. A. Fisher, "The Fiducial Argument in Statistical Inference," *Annals Eugen.* **6** (1935) 391–398.

[558] A. Font-Ribera, P. McDonald, N. Mostek, B. A. Reid, H.-J. Seo, and A. Slosar, "DESI and other dark energy experiments in the era of neutrino mass measurements," *JCAP* **1405** (2014) 023, `arXiv:1308.4164 [astro-ph.CO]`.

[559] L. R. Abramo and K. E. Leonard, "Why multi-tracer surveys beat cosmic variance," *Mon. Not. Roy. Astron. Soc.* **432** (2013) 318, `arXiv:1302.5444 [astro-ph.CO]`.

[560] A. F. Heavens, T. D. Kitching, and L. Verde, "On model selection forecasting, Dark Energy and modified gravity," *Mon. Not. Roy. Astron. Soc.* **380** (2007) 1029–1035, `arXiv:astro-ph/0703191 [astro-ph]`.

[561] J. M. Maldacena, "Non-Gaussian features of primordial fluctuations in single field inflationary models," *JHEP* **05** (2003) 013, `arXiv:astro-ph/0210603 [astro-ph]`.

[562] J. A. Frieman and B.-A. Gradwohl, "Dark matter and the equivalence principle," *Phys. Rev. Lett.* **67** (1991) 2926–2929.

[563] B.-A. Gradwohl and J. A. Frieman, "Dark matter, long range forces, and large scale structure," *Astrophys. J.* **398** (1992) 407–424.

[564] C. Wetterich, "The Cosmon model for an asymptotically vanishing time dependent cosmological 'constant'," *Astron. Astrophys.* **301** (1995) 321–328, `arXiv:hep-th/9408025 [hep-th]`.

[565] L. Amendola, "Coupled quintessence," *Phys. Rev.* **D62** (2000) 043511, `astro-ph/9908023`.

[566] L. Amendola, "Linear and non-linear perturbations in dark energy models," *Phys. Rev.* **D69** (2004) 103524, `arXiv:astro-ph/0311175 [astro-ph]`.

[567] V. Pettorino and C. Baccigalupi, "Coupled and Extended Quintessence: theoretical differences and structure formation," *Phys. Rev.* **D77** (2008) 103003, arXiv:0802.1086 [astro-ph].

[568] J. Valiviita, E. Majerotto, and R. Maartens, "Instability in interacting dark energy and dark matter fluids," *JCAP* **0807** no. 07, (July, 2008) 020, 0804.0232.

[569] J.-H. He and B. Wang, "Effects of the interaction between dark energy and dark matter on cosmological parameters," *JCAP* **0806** (2008) 010, arXiv:0801.4233 [astro-ph].

[570] M. B. Gavela, D. Hernandez, L. Lopez Honorez, O. Mena, and S. Rigolin, "Dark coupling," *JCAP* **0907** (2009) 034, arXiv:0901.1611 [astro-ph.CO].

[571] J.-H. He, B. Wang, and Y. P. Jing, "Effects of dark sectors' mutual interaction on the growth of structures," *JCAP* **0907** (2009) 030, arXiv:0902.0660 [gr-qc].

[572] E. Abdalla, E. G. M. Ferreira, J. Quintin, and B. Wang, "New evidence for interacting dark energy from BOSS," arXiv:1412.2777 [astro-ph.CO].

[573] V. Salvatelli, N. Said, M. Bruni, A. Melchiorri, and D. Wands, "Indications of a late-time interaction in the dark sector," *Phys. Rev. Lett.* **113** no. 18, (2014) 181301, arXiv:1406.7297 [astro-ph.CO].

[574] Yu. L. Bolotin, A. Kostenko, O. A. Lemets, and D. A. Yerokhin, "Cosmological Evolution With Interaction Between Dark Energy And Dark Matter," *Int. J. Mod. Phys.* **D24** no. 03, (2014) 1530007, arXiv:1310.0085 [astro-ph.CO].

[575] J.-H. He, B. Wang, and E. Abdalla, "Stability of the curvature perturbation in dark sectors' mutual interacting models," *Phys. Lett.* **B671** (2009) 139–145, arXiv:0807.3471 [gr-qc].

[576] B. M. Jackson, A. Taylor, and A. Berera, "On the large-scale instability in interacting dark energy and dark matter fluids," *Phys. Rev.* **D79** no. 4, (Feb., 2009) 043526, 0901.3272.

[577] V. Salvatelli, A. Marchini, L. Lopez-Honorez, and O. Mena, "New constraints on Coupled Dark Energy from the Planck satellite experiment," *Phys. Rev.* **D88** no. 2, (July, 2013) 023531, 1304.7119.

[578] A. A. Costa, X.-D. Xu, B. Wang, E. G. M. Ferreira, and E. Abdalla, "Testing the Interaction between Dark Energy and Dark Matter with Planck Data," *Phys. Rev.* **D89** no. 10, (2014) 103531, arXiv:1311.7380 [astro-ph.CO].

[579] M. B. Gavela, L. Lopez Honorez, O. Mena, and S. Rigolin, "Dark Coupling and Gauge Invariance," *JCAP* **1011** (2010) 044, 1005.0295.

[580] J.-H. He, B. Wang, and E. Abdalla, "Testing the interaction between dark energy and dark matter via latest observations," *Phys. Rev.* **D83** (2011) 063515, arXiv:1012.3904 [astro-ph.CO].

[581] K. Koyama, R. Maartens, and Y.-S. Song, "Velocities as a probe of dark sector interactions," *JCAP* **0910** (2009) 017, arXiv:0907.2126 [astro-ph.CO].

[582] L. Amendola, G. Camargo Campos, and R. Rosenfeld, "Consequences of dark matter-dark energy interaction on cosmological parameters derived from SNIa data," *Phys. Rev.* **D75** no. 8, (Apr., 2007) 083506, astro-ph/0610806.

[583] G. Caldera-Cabral, R. Maartens, and B. M. Schaefer, "The Growth of Structure in Interacting Dark Energy Models," *JCAP* **0907** no. 07, (July, 2009) 027, 0905.0492.

[584] A. B. Pavan, E. G. M. Ferreira, S. Micheletti, J. C. C. de Souza, and E. Abdalla, "Exact cosmological solutions of models with an interacting dark sector," *Phys. Rev.* **D86** (2012) 103521, `1111.6526`.

[585] W. Zimdahl and D. Pavon, "Interacting quintessence," *Phys. Lett.* **B521** (2001) 133–138, `arXiv:astro-ph/0105479 [astro-ph]`.

[586] G. Izquierdo and D. Pavon, "Limits on the parameters of the equation of state for interacting dark energy," *Phys. Lett.* **B688** (2010) 115–124, `arXiv:1004.2360 [astro-ph.CO]`.

[587] G. Huey and B. D. Wandelt, "Interacting quintessence. The Coincidence problem and cosmic acceleration," *Phys. Rev.* **D74** (2006) 023519, `arXiv:astro-ph/0407196 [astro-ph]`.

[588] S. Das, P. S. Corasaniti, and J. Khoury, "Super-acceleration as signature of dark sector interaction," *Phys. Rev.* **D73** (2006) 083509, `arXiv:astro-ph/0510628 [astro-ph]`.

[589] C. Heymans *et al.*, "CFHTLenS: The Canada-France-Hawaii Telescope Lensing Survey," *Mon. Not. Roy. Astron. Soc.* **427** (2012) 146, `arXiv:1210.0032 [astro-ph.CO]`.

[590] C. Pigozzo, S. Carneiro, J. S. Alcaniz, H. A. Borges, and J. C. Fabris, "Evidence for cosmological particle creation?," `arXiv:1510.01794 [astro-ph.CO]`.

[591] I. Odderskov, M. Baldi, and L. Amendola, "The effect of interacting dark energy on local measurements of the Hubble constant," `arXiv:1510.04314 [astro-ph.CO]`.

[592] Z. Berezhiani, A. D. Dolgov, and I. I. Tkachev, "Reconciling Planck results with low redshift astronomical measurements," *Phys. Rev.* **D92** (2015) 061303, `arXiv:1505.03644 [astro-ph.CO]`.

[593] C. L. Reichardt *et al.*, "Galaxy clusters discovered via the Sunyaev-Zel'dovich effect in the first 720 square degrees of the South Pole Telescope survey," *Astrophys. J.* **763** (2013) 127, `arXiv:1203.5775 [astro-ph.CO]`.

[594] H. Böhringer, G. Chon, and C. A. Collins, "The extended ROSAT-ESO Flux Limited X-ray Galaxy Cluster Survey (REFLEX II) IV. X-ray Luminosity Function and First Constraints on Cosmological Parameters," *Astron. Astrophys.* **570** (2014) A31, `arXiv:1403.2927 [astro-ph.CO]`.

[595] A. Merle, "keV Neutrino Model Building," *Int. J. Mod. Phys.* **D22** (2013) 1330020, `arXiv:1302.2625 [hep-ph]`.

[596] J. Bergström, M. C. Gonzalez-Garcia, V. Niro, and J. Salvado, "Statistical tests of sterile neutrinos using cosmology and short-baseline data," *JHEP* **10** (2014) 104, `arXiv:1407.3806 [hep-ph]`.

[597] A. Merle, V. Niro, and D. Schmidt, "New Production Mechanism for keV Sterile Neutrino Dark Matter by Decays of Frozen-In Scalars," *JCAP* **1403** (2014) 028, `arXiv:1306.3996 [hep-ph]`.

[598] **Virgo, LIGO Scientific** Collaboration, B. h. Abbott *et al.*, "Observation of Gravitational Waves from a Binary Black Hole Merger," *Phys. Rev. Lett.* **116** no. 6, (2016) 061102, `arXiv:1602.03837 [gr-qc]`.

[599] W. H. Press, S. A. Teukolsky, W. T. Vetterling, and B. P. Flannery, *Numerical Recipes 3rd Edition: The Art of Scientific Computing.* Cambridge University Press, New York, NY, USA, 3 ed., 2007.

# List of Figures

# List of Tables